High-Pressure Crystallography

NATO Science for Peace and Security Series

This Series presents the results of scientific meetings supported under the NATO Programme: Science for Peace and Security (SPS).

The NATO SPS Programme supports meetings in the following Key Priority areas: (1) Defence Against Terrorism; (2) Countering other Threats to Security and (3) NATO, Partner and Mediterranean Dialogue Country Priorities. The types of meeting supported are generally "Advanced Study Institutes" and "Advanced Research Workshops". The NATO SPS Series collects together the results of these meetings. The meetings are co-organized by scientists from NATO countries and scientists from NATO's "Partner" or "Mediterranean Dialogue" countries. The observations and recommendations made at the meetings, as well as the contents of the volumes in the Series, reflect those of participants and contributors only; they should not necessarily be regarded as reflecting NATO views or policy.

Advanced Study Institutes (ASI) are high-level tutorial courses intended to convey the latest developments in a subject to an advanced-level audience

Advanced Research Workshops (ARW) are expert meetings where an intense but informal exchange of views at the frontiers of a subject aims at identifying directions for future action

Following a transformation of the programme in 2006 the Series has been re-named and re-organised. Recent volumes on topics not related to security, which result from meetings supported under the programme earlier, may be found in the NATO Science Series.

The Series is published by IOS Press, Amsterdam, and Springer, Dordrecht, in conjunction with the NATO Public Diplomacy Division.

Sub-Series

A.	Chemistry and Biology	Springer
B.	Physics and Biophysics	Springer
C.	Environmental Security	Springer
D.	Information and Communication Security	IOS Press
E.	Human and Societal Dynamics	IOS Press

http://www.nato.int/science
http://www.springer.com
http://www.iospress.nl

Series B: Physics and Biophysics

High-Pressure Crystallography

From Fundamental Phenomena to Technological Applications

edited by

Elena Boldyreva
Novosibirsk State University
Institute of Solid State Chemistry and Mechanochemistry
Novosibirsk, Russia

and

Przemyslaw Dera
University of Chicago
Center for Advanced Radiation Sources
Chicago, U.S.A.

Published in cooperation with NATO Public Diplomacy Division

Proceedings of the NATO Advanced Study Institute on
High-Pressure Crystallography: Advanced Armor Materials
and Protection from Explosives
Erice, Italy
4–14 June 2009

Library of Congress Control Number: 2010930225

ISBN 978-90-481-9260-1 (PB)
ISBN 978-90-481-9257-1 (HB)
ISBN 978-90-481-9258-8 (e-book)

Published by Springer,
P.O. Box 17, 3300 AA Dordrecht, The Netherlands.

www.springer.com

Printed on acid-free paper

Dedication

This book is dedicated to the memory of Prof. Lodovico Riva di san Severino. Lodovico has dedicated a big part of his life to support, organization and leadership of the Erice crystallographic schools. He was a phenomenal organizer, a charming and very hospitable host and a great evening singer. Lodovico passed away shortly after the conclusion of the 2010 Erice school. He will be greatly missed.

PREFACE

Figure 1. Audience, including local organizers (orange scarfs) and student participants during one of the lectures.

This volume is a collection of lectures presented during the 2009 International School on High-pressure Crystallography, which took place at the Ettore Majorana Center for Scientific Culture, between June 4 and 14, 2009, in the very picturesque Sicilian town of Erice. The 2009 school was the 41st course of the "International School of Crystallography" organized at the Majorana Center and was directed by Elena Boldyreva (Novosibirsk University) and Przemyslaw Dera (University of Chicago). Unmatched support and excellent on-site organization was provided by the expert team consisting of Prof. Paola Spadon (Uniersity of Padova), Prof. Lodovico Riva di San Severino (University of Bologna), Elena Papinutto and Prof. John Irvin (University of California, San Franciso), aided by great team of young local organizers ("orange scarfs").

Major part of funding for the school was provided by a grant from the NATO Science for Peace and Security program, through which the 2009 Erice school was recognized as a NATO Advanced Study Institute (ASI). The theme of the Erice ASI was "High-pressure Crystallography: Advanced Armor Materials and Protection from Explosives." Additional financial support for the event was provided by the United States National Science Foundation EAR Geophysics Program, Consortium for Materials Properties Research in Earth Sciences, International Union of Crystallography, European Crystallographic Association, International Center for Diffraction Data, Psi-kappa, and several industrial sponsors, including (in alphabetic order) Almax Industries, Bruker AXS, Crystal Impact, D'Anvils, Oxford Diffraction and Stoe.

Figure 2. Marsala social evening.

The 2009 Erice school was very well attended, with 122 participants including 46 lecturers and 76

student participants (undergraduate, graduate and post-graduate), and included 10 days of intensive study, hands-on instruction and panel discussions.

The meeting agenda included a unique blend of topics and disciplines that are never found covered at a single event. The format of school with emphasis on education, rather, than review of recent accomplishments allowed all attendees, both students, as well as lectures, to significantly broaden their perception of the synergy of the multidisciplinary facets of high-pressure science and its applications in everyday life, technology and security. In addition to 45-minute lecture presentations, the school offered several excellent and widely attended hands-on and follow-me workshops, which allowed the student participants to learn many advanced tricks of the trade from the top experts in the field.

The topics covered by the lectures focused on several important aspects of high-pressure science: physics (properties and structure), chemistry (chemical reactions, transport), materials science (new materials) and engineering (mechanical properties); implications for geology, geophysics and planetary science (minerals in their natural, deep earth environments), biology and medicine. In addition, direct or indirect (e.g. economic) applications of the high-pressure science in several fields of modern technology have been considered. Such a variety of topics, explains a very "densely packed" program, which "kept the participants under pressure" during the 10 days.

The contents of this book are organized in six rough thematic blocks: (A) Experimental techniques and introduction to fundamental phenomena and their description, (B) Superhard materials and materials science (C) Computational approaches in high-pressure science (D) Geophysics and high-pressure transformations of minerals and rocks, (E) Molecular materials and explosives under high stress, (F) High-pressure effects on biomimetics and biological matter.

The first theme introduces the most modern experimental techniques used to generate high-pressure and temperature conditions, as well as study the behavior of samples at these conditions. Special emphasis is placed on experimental methods used in mineral physics research.

Several excellent chapters review the field of hard and superhard materials with potential technological applications. Synthetic routes in terms of chemistry, technical approaches to the synthesis at extreme conditions (e.g., using diamond anvil cell, large volume press, or novel detonation techniques), both ex-situ and in-situ methods of characterization of the structure and properties of the novel materials are presented.

Figure 3. Panel discussion of software for high-pressure crystallography.

Several expert lecturers reviewed computational approaches to predicting structures and properties of materials at high pressure as well as designing new materials with specific properties.

Another large block of presentations deals with the issues of geophysical applications of high-pressure experiments and starts with a general introduction to the issue of phase transitions in the deep earth and their relation to seismic phenomena and seismic observations. Other general topics discussed include possibilities and mechanisms of incorporation of water into rock-forming minerals (e.g. during the process of subduction) and its consequences for seismically active areas, the phenomenon and consequences of spin transitions that occur in iron-containing minerals present in the Earth's lower mantle, as well as general trends in the structural transformations in upper mantle minerals. The geophysics session concludes with the discussion of the important issue of plastic deformation, defect formation and texture development in rocks and minerals.

Also, a large and very exciting segment of presentations is focused on the behavior of molecular materials at extreme conditions, many with significant relevance for planetary science. Problems such as in-situ crystallization at high-pressure, solvothermal crystallization, polymorphism control, hydrogen bond transformations, and conformational transformations were introduced.

Figure 4. Hands-on workshop on in-situ crystallization.

The final theme of the book is biological matter and biomimetics at extreme conditions, including environmental and geobiological aspects, deep-sea environments, habitability limits, as well as deactivation of viruses and bacteria.

Majority of the multimedia presentations shown at the Erice ASI are available online at:

http://cars9.uchicago.edu/surfacewiki/HPCrystallography/Erice2009/LecturePresentations

An important outcome of the "round table" discussion on data processing software was the birth of a set of three new online resources for the high-pressure crystallography community: Digital Resources for High Pressure Crystallography (DigResHPX). The DigResHPX package includes:

1. High Pressure Crystallography blog:
   http://hpdac.net/
2. High Pressure Crystallography mailing list:
   hpdac@hpc.amu.edu.pl
3. High Pressure Crystallography wiki:
   http://cars9.uchicago.edu/surfacewiki/HPCrystallography

These online tools and services are meant to provide a communication platform for exchange of technical information, advice, references, discussions etc. relevant for high-pressure crystallography.

This book is the final fruit of the Erice ASI, and with it we are hoping to provide current and future students and researchers in high-pressure field with a valuable and unique reference that offers both background information, as well as an overview of the numerous facets of the modern high-pressure science and technology.

Finally, we would like to express our sincere thanks to all that helped make the 2009 Erice ASI happen: the sponsors, local organizers, lecturers and student participants – you all contributed to the success of the school and to this book! We also gratefully acknowledge the most valuable technical assistance in preparing the manuscript for the publication by our colleagues at home institutions: Nancy Lazarz in Chicago, Elena Achkasova, Antonina Polyakova and Vasily Minkov in Novosibirsk.

School directors,

Elena Boldyreva and Przemyslaw Dera

TABLE OF CONTENTS

Preface vii
E. Boldyreva and P. Dera

1. Introduction to High Pressure Science 1
   P. Dera

2. All Different Flavors of Synchrotron Single Crystal X-Ray Diffraction Experiments 11
   P. Dera

3. Synchrotron High-Pressure High-Temperature Techniques 23
   M. Mezouar

4. Mineral Physics of Earth Core: Iron Alloys at Extreme Condition 35
   L. Dubrovinsky, J.-F. Lin and N. Dubrovinskaia

5. Synchrotron-Based Spectroscopic Techniques: Mössbauer and High-Resolution Inelastic Scattering 43
   J.M. Jackson

6. High-Pressure X-Ray Absorption Spectroscopy: Application to the Local Aspects of Phase Transitions in Ferroelectric Perovskites 51
   J.-P. Itié, A.-M. Flank, P. Lagarde, S. Ravy and A. Polian

7. Present-Day High-Intensity and High-Resolution Neutron Diffraction and Neutron Scattering Under High Pressure 69
   A.M. Balagurov

8. Large Volume Presses for High-Pressure Studies Using Synchrotron Radiat 81
   Y. Wang

9. Rheology at High Pressures and High Temperatures 97
   Y. Wang and N. Hilairet

10. Radial Diffraction in the Diamond Anvil Cell: Methods and Applications 111
    S. Merkel

11. Reduction and Analysis of Two-Dimensional Diffraction Data Including Texture Analysis 123
S.C. Vogel

12. Equations of State and Their Applications in Geosciences 135
T. Boffa Ballaran

13. Anisotropic Compression. What can it Teach us About Intermolecular Interactions? 147
E. Boldyreva

14. High-Pressure Structural Evolution of Molecular Crystals 161
N. Casati

15. Introduction into the Theory of Phase Transitions 171
V. Dmitriev

16. Phase Transitions in AB Systems. Symmetry Aspects 183
H. Sowa

17. The Charm of Subtle H-Bonds Transformations 193
A. Katrusiak

18. Carrier Bandwidth Physical Phenomena in Strongly Correlated Magnetic Oxides: Lessons from Neutron Diffraction at High Pressures 203
D.P. Kozlenko

19. Jahn-Teller Systems at High Pressure 215
F. Rodriguez

20. Effect of Spin Transitions in Iron on Structure and Properties of Mantle Minerals 231
L. Dubrovinsky, O. Narygina and I. Kantor

21. Boron and Boron-Rich Solids at High Pressures 241
A. Polian, S.V. Ovsyannikov, M. Gauthier, P. Munsch, J.-C. Chervin and G. Lemarchand

22. Non-Molecular Carbon Dioxide at High Pressure 251
M. Santoro

23. Simple Metals at High Pressures 261
O. Degtyareva

24. Light Metal Hydrides Under Non-Ambient Conditions: Probing Chemistry by Diffraction? 281
Y. Filinchuk

25. Evolutionary Crystal Structure Prediction and Novel High-Pressure Phases 293
A.R. Oganov, Y. Ma, A.O. Lyakhov, M. Valle and C. Gatti

26. Ab Initio Quantum Chemistry and Semi-Empirical Description of Solid State Phases Under High Pressure: Chemical Applications 325
P. Macchi

27. First-Principles Simulations of Alloy Thermodynamics in Megabar Pressure Range 341
I.A. Abrikosov

28. First-Principles Molecular Dynamics and Applications in Planetary Science 353
S. Scandolo

29. Molecular Orbital Approach to Interpret High Pressure Phenomena – Case of Elusive Gold Monofluoride 357
W. Grochala and D. Kurzydłowski

30. High-Pressure Synthesis of Materials 373
P.F. McMillan

31. High-Pressure Synthesis of Novel Superhard Phases in the B–C–N–O System 385
V.L. Solozhenko

32. Synthesis and Structure-Property Relations of Binary Transition Metal Carbides at Extreme Conditions 397
B. Winkler, A. Friedrich, L. Bayarjargal and E.A. Juarez-Arellano

33. High Pressure and Superconductivity: Intercalated Graphite CaC_6 as a Model System 407
A. Gauzzi, N. Bendiab, M. D'Astuto, B. Canny, M. Calandra, F. Mauri, G. Loupias, S. Takashima, H. Takagi, N. Takeshita, C. Terakura, N. Emery, C. Herold, P. Lagrange, M. Hanfland and M. Mezouar

34. Structure-Property Relationships in Novel High-Pressure Superhard Materials 419
N. Dubrovinskaya and L. Dubrovinsky

35. Carbon Nanotubes Under High Pressure Probed by Resonance Raman Scattering 435
A. San-miguel, C. Cailler, D. Machon, E.B. Barros, A.L. Aguiar and A.G.S. Filho

36. High-Pressure Studies of Energetic Materials 447
C.R. Pulham, D.I.A. Millar, I.D.H. Oswald and W.G. Marshall

37. Amorphous Materials at High Pressure 459
C. Sanloup

38. Amorphous X-Ray Diffraction at High Pressure: Polyamorphic Silicon and Amyloid Fibrils 469
P.F. McMillan, D. Daisenberger, R.Q. Cabrera and F. Meersman

39. Microporous Materials at High-Pressure: Are they Really Soft? 481
G.D. Gatta

40. Hydrogen Bonding in Minerals at High Pressures 493
B. Winkler

41. Nanomaterials at High Pressure: Spectroscopy and Diffraction Techniques 503
G.R. Hearne

42. Analysis of the Total Scattering Using the Quantitative High Pressure Pair Distribution Function: Practical Considerations 513
J.B. Parise, L. Ehm and F.M. Michel

43. Analysis of the Total Scattering Using the Quantitative High Pressure Pair Distribution Function: Case Studies 523
L. Ehm, F.M. Michel and J.B. Parise

44. High-Pressure Studies of Pharmaceuticals and Biomimetics. Fundamentals and Applications. A General Introduction 533
E. Boldyreva

45. New Frontiers in Physical form Discovery: High-Pressure Recrystallization of Pharmaceuticals and Other Molecular Compounds 545
F.P.A. Fabbiani

46. Pressure-Induced Phase Transitions in Crystalline Amino Acids. Raman Spectroscopy and X-Ray Diffraction 559
P.T.C. Freire

47. Exploring the Energy and Conformational Landscape of Biomolecules Under Extreme Conditions 573
R. Winter

48. High-Pressure Crystallography of Biomolecules: Recent Achievements. I. Introduction, Materials and Methods 591
R. Fourme, I. Ascone, M. Mezouar, A.-C. Dhaussy, R. Kahn and E. Girard

49. High-Pressure Crystallography of Biomolecules: Recent Achievements. II. Applications 603
R. Fourme, I. Ascone, R. Kahn and E. Girard

INTRODUCTION TO HIGH-PRESSURE SCIENCE

PRZEMYSLAW DERA*
Center for Advanced Radiation Sources, *The University of Chicago, Argonne National Laboratory Bldg. 434A, 9700 S Cass Ave., Argonne, IL 60439, USA*

Abstract To a common person pressure is just one of the parameters that describe a thermodynamic state. We all hear about it in everyday weather forecasts, and most of us do not associate it with anything particularly unique. Probably the most intuitive idea of the effect of high-pressure comes from movies, where submarine sinking to the bottom of the ocean is gradually crushed by the surrounding water, until its hull implodes. Why, then hundreds of scientists throughout the world spent their lifelong careers studying high-pressure phenomena? Despite all the developments in experimental technologies and instrumentation, modern scientist has very few tools that allow him or her to "grab" two atoms and bring them, in a very controllable way, closer together. Being able to achieve this task means the ability to directly probe interatomic interaction potentials and can cause transformations as dramatic as turning of a common gas into solid metal. Before the reader delves into more advanced topics described later in this book, this introductory chapter aims to explain several elementary, but extremely important concepts in high-pressure science. We will start with a brief discussion of laboratory devices used to produce pressure, address the issue of hydrostaticity, elastic and plastic compression, and will conclude with a short discussion of unique effects of anisotropic stress.

Keywords: High pressure, pressure-induced phenomena, diamond anvil cell, elastic deformation, plastic deformation, yield stress

* E-mail: dera@cars.uchicago.edu

E. Boldyreva and P. Dera (eds.), *High-Pressure Crystallography: From Fundamental Phenomena to Technological Applications*, DOI 10.1007/978-90-481-9258-8_1,

1. Introduction

1.1. IN SITU VERSUS EX SITU

Experiments that explore the effects of pressure on matter can be classified into two general categories: ***in situ*** experiments, which probe the properties of the sample *while* it is subject to compression, and ***ex situ*** experiments, which examine changes in the sample *after* it has been compressed to the pressure of interest, and then decompressed. *Ex situ* experimental studies of decompressed samples do not differ from ambient experiments, as the sample is retrieved from the pressure generating apparatus, prior to the measurements, but relay on irreversibility of pressure-induced changes. Probably the most popular laboratory high-pressure device for *ex situ* high-pressure studies is a large volume press (see chapter 8 by *Wang*). *Ex situ* experiments work quite well for studies of transformations such as chemical reactions or reconstructive structural phase transitions that occur during heating at high pressure, but do not revert when decompression is performed at ambient temperature. *Ex situ* approach has been successfully used to study pressure-temperature-composition phase diagrams of simple systems (*e.g. Stewart and Schmidt*, 2007), as well as melting curves, in which case the *ex situ* examination of the samples (usually done with electron microprobe) involves search for melt-specific morphologies in the sample. One of the great advantages of the *ex situ* approach is that it allows for a detailed chemical analysis of the quench sample, which is never possible *in situ*. This advantage has been used, e.g. for study of the pressure-dependence of partitioning of elements.

Unfortunately, many of the most interesting pressure-induced phenomena are reversible, and cannot be studied *ex situ. In situ* studies bring the advantage of allowing to watch the high-pressure phenomena as they happen, however, it is usually necessary to modify the experimental technique used, to accommodate the pressure generating device in which the sample is enclosed.

Before we start the short introduction to the pressure generating devices, it is worthwhile to think for a moment about the definition of the term “high” pressure. High-pressure scientists study effects of pressure on a whole variety of objects, from superhard materials like diamond and boron nitride, through metals, molecular solids, to living organisms. The adjective “high” implies conditions that produce some extraordinary (not found at “normal”, ambient conditions) effects or behavior for the given object of study.

Of course, the definition of "high" is very different in biophysics, where most objects of interest (macromolecules, microorganisms) are destroyed below pressure of 1 GPa (10,000 atm) than in geophysics, where conditions of interest (deep earth) are measured in hundreds of gigapascal. Despite these differences, however, there are many parallels between these so different systems in the underlying physics of interatomic interactions, thermodynamics governing transformations, and chemistry.

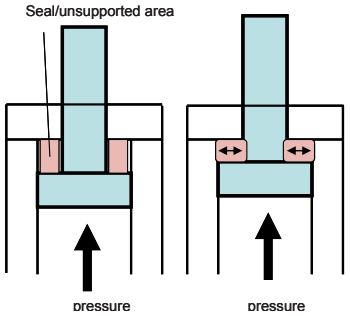

Figure 1. Bridgman's concept of unsupported area seal, which revolutionized high-pressure research at the beginning of twentieth century (After *Spain and Paauwe* (1977)).

1.2. SOME NOTES ON THE HISTORY OF PRESSURE GENERATING DEVICE

The main factors that control the progress of the high-pressure science are the availability of high-pressure devices with required capabilities (pressure range, sample size, optical access, *etc.*), and (for *in situ* experiments) availability of experimental probes/techniques with sufficient sensitivity that allow working with samples inside the high pressure devices. It is worth noting that majority of the most influential high-pressure researchers throughout the last century have significantly contributed to the development of pressure generating devices.

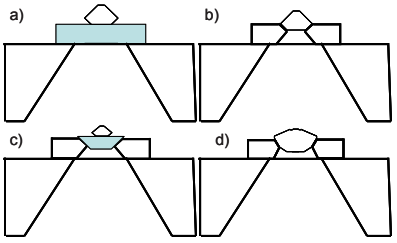

Figure 2. Modern modifications of the diamond anvil cell geometry maximizing angular access to the sample: (**a**) *Yamanaka et al.* (2001) flat-disk single-crystal diamond backing plate (**b**) *Boehler and de Hantsetters* (2004) conically shaped anvil with matching WC backing plate (**c**) *Krauss and Steurer* (2005) design utilizing compression-fitting-shaped single-crystal diamond backing plate (**d**) *Sowa and Ahsbahs* (2006) design with obtuse-angle conical anvil.

Unquestionably, the first to significantly revolutionize high-pressure science (which before him was basically nonexistent) by introducing new ideas into generation of high pressure in laboratory was Percy W. Bridgman, who received the 1946 Nobel prize in physics. Bridgman introduced the then-revolutionary idea of unsupported area seal (see Figure 1), which allowed him to extend pressure range in his high-pressure apparatus from 0.3 GPa to as much as 10 GPa (for more information on Bridgman's scientific legacy see *W.L. Maila*, 1991 and *McMillan*, 2005).

The device which dominates the current high-pressure research, diamond anvil cell (DAC), was invented in 1950s, almost simultaneously at two different research laboratories: the National Bureau of Standards (now NIST) and the University of Chicago (for detailed historical account see *Hazen*, 1993; *Piermarini*, 1993, 2001; *Bassett*, 2009). The ingenuity of the basic concept is well demonstrated by the fact that the design of the device has not changed almost at all over the last half a century. The recent decade witnessed very dramatic and dynamic developments in synchrotron-based *in situ* experiments at ultrahigh pressure (above 100 GPa, for an overview see chapter 3 by *Mezouar*). Motivated by the fact that majority of the synchrotron high-pressure experiments involve x-ray diffraction and require large angular access to the sample, in recent years several interesting modifications have been proposed (see Figure 2), which implement either backing plates made of single crystal diamond (*Yamanaka et al.*, 2001; *Krauss and Steurer*, 2005) or conically shaped anvils (*Boehler and de Hantsetters*, 2004; *Sowa and Ahsbahs*, 2006) that can be mounted in wide angular access non-transparent backing plates with matching conical surfaces.

For an extensive treatment on pressure-generating devices and techniques see books by *Eremets* (1996), *Holtzapfel and Isaacs* (1997), *Hazen and Downs* (2000), and *Chen et al.* (2005).

2. Hydrostaticity, Nonhydrostaticity and Compressive Deformation Regimes

2.1. PRESSURE AND STRESS

Pressure is usually referred to as a scalar parameter. According to the definition, pressure is the force acting on a unit area. Obviously, in three dimensions, forces acting on an object from different directions can have different values, therefore, in most real high-pressure experiments scalar description of pressure is insufficient. In 1827 *Cauchy* (1827) introduced the concept of stress tensor, which provides a generalized description of the forces acting along different directions at a point in a body. The Cauchy stress is a second order Cartesian tensor of the form:

$$\boldsymbol{\sigma} = \sigma_{ij} = \begin{bmatrix} \sigma_{11} & \sigma_{12} & \sigma_{13} \\ \sigma_{21} & \sigma_{22} & \sigma_{23} \\ \sigma_{31} & \sigma_{32} & \sigma_{33} \end{bmatrix}.$$

The diagonal elements of the stress tensor are called *normal stresses*, whereas the off-diagonal elements are *shear stresses*. Because of the

symmetry of the stress tensor (for a body in equilibrium $\sigma_{ij} = \sigma_{ji}$), stress can also be expressed in the *Voigt* form, as a six-dimensional vector:

$$\boldsymbol{\sigma} = \begin{bmatrix} \sigma_{11} & \sigma_{22} & \sigma_{33} & \sigma_{23} & \sigma_{13} & \sigma_{12} \end{bmatrix}^T = \begin{bmatrix} \sigma_1 & \sigma_2 & \sigma_3 & \sigma_4 & \sigma_5 & \sigma_6 \end{bmatrix}^T$$

Hydrostatic conditions can be defined in terms of the components of the stress tensor. Ideal hydrostaticity requires all the *normal stresses* to be equal, and all the *shear stresses* to be zero. In real experiments ideal hydrostaticity can be achieved only with the use of fluid pressure media. Once pressure medium solidifies (either in crystalline or amorphous state) the stress tensor can be at best described as quasi-hydrostatic. In high-pressure experiments carried in solid pressure media the components of the stress tensor are not only non-hydrostatic, but usually differ from one point in space, to another. *E.g.*, in diamond anvil cell, assuming radial symmetry, stress usually varies laterally, as a function of distance from the center of the diamond anvil (in such case stress is in fact a tensor field). Two good recent references regarding effective hydrostatic limits of various pressure-transmitting media are *Angel et al.* (2007) and *Klotz et al.* (2009).

2.2. ELASTIC DEFORMATION AND ITS LIMITS

A macroscopic response of an object to applied compressive stress is a deformation (change in the shape and/or size), which can be quantitatively described by means of a second order Cartesian strain tensor ε_{ij}. Similar to σ_{ij}, ε_{ij} can also be expressed in the vector *Voigt* notation. *Macroscopic strain* is usually measured during *in situ* experiments by means of x-ray radiography or computed tomography (see chapter 9 in this book by *Wang and Hilairet*).

Most phenomena studied in high-pressure research occur during compression in *elastic regime*. Elastic deformation is reversible by definition (once the compressive forces are no longer applied, the object returns to its original shape and size). Elastic deformation is governed by Hooke's law, which in the tensor form can be written as:

$$\begin{bmatrix} \sigma_1 \\ \sigma_2 \\ \sigma_3 \\ \sigma_4 \\ \sigma_5 \\ \sigma_6 \end{bmatrix} = \begin{bmatrix} C_{11} & C_{12} & C_{13} & C_{14} & C_{15} & C_{16} \\ C_{12} & C_{22} & C_{23} & C_{24} & C_{25} & C_{26} \\ C_{13} & C_{23} & C_{33} & C_{34} & C_{35} & C_{36} \\ C_{14} & C_{24} & C_{34} & C_{44} & C_{45} & C_{46} \\ C_{15} & C_{25} & C_{35} & C_{45} & C_{55} & C_{56} \\ C_{16} & C_{26} & C_{36} & C_{46} & C_{56} & C_{66} \end{bmatrix} \begin{bmatrix} \varepsilon_1 \\ \varepsilon_2 \\ \varepsilon_3 \\ \varepsilon_4 \\ \varepsilon_5 \\ \varepsilon_6 \end{bmatrix}$$

where C_{ij} is the stiffness tensor. Inverse of the stiffness tensor, $S_{ij} = (C_{ij})^{-1}$, is referred to as elastic compliance tensor. The number of independent stiffness coefficients depends on the symmetry of the object, *e.g.* for a cubic crystal there are only three independent coefficients (*Nye*, 1985). Elastic compliances are related with adiabatic bulk modulus as follows:

$$K = \frac{1}{S_{11} + S_{22} + S_{33} + 2\left(S_{12} + S_{23} + S_{31}\right)}.$$

Extensive treatment of the topic of bulk moduli can be found in chapter 12 by *Boffa Balaran*.

In the elastic regime, *macroscopic stain* of a single crystal sample is proportional to the *lattice strain* ε_L (deformation of the unit cell of the crystal). The lattice strain tensor can be calculated from the unit cell parameters (a, b, c, α, β, γ) using the direct-to-Cartesian transformation matrix A (*Hazen et al.*, 2000)*:*

$$A = \begin{bmatrix} a\sin\beta & -b\sin\alpha\cos\gamma^* & 0 \\ 0 & b\sin\alpha\sin\gamma^* & 0 \\ a\cos\beta & b\cos\alpha & c \end{bmatrix},$$

where asterisk denotes reciprocal cell parameters. *Lattice strain* between two states denoted by subscripts 0 and 1 can be calculated from the equation:

$$\varepsilon'_L A_0 = A_1 - A_0,$$

by following the symmetrization routine (*Nye*, 1985):

$$\varepsilon_L = 1/2\left(\varepsilon'^T_L + \varepsilon'_L\right).$$

More detailed information about strain and its anisotropy can be found in chapter 13 by *Boldyreva*. With the knowledge of stiffness coefficient estimates at a given pressure it is possible to calculate the full stress tensor from the lattice strain, using the Hooke's law (*Downs and Singh*, 2006).

2.3. LIMITS OF ELASTIC COMPRESSION

The elastic range ends when the material reaches its *yield strength*, at which point plastic deformation begins. The *yield strength* or *yield point* of a material is defined in engineering and materials science as the stress at which a material begins to deform plastically (the stress–strain relation is no longer linear and deformation is no longer reversible). In the three-dimensional space of the *normal stresses*, an infinite number of *yield points*

form together a *yield surface*. Knowledge of the *yield point* is vital when designing a mechanical component, since it generally represents an upper limit to the load that can be applied.

There are different models describing the conditions of stress that define the yield surface. Among the most popular ones is the *Tresca–Guest yield surface* (TGYS), also known as maximum shear stress yield criterion. In terms of the principal stresses the Tresca criterion is expressed as

$$\max(|\sigma_1 - \sigma_2|, |\sigma_2 - \sigma_3|, |\sigma_3 - \sigma_1|) = \sigma_Y$$

where σ_Y is *yield stress*. TGYS defines the limits when the material remains elastic in terms of equality of the three principal stresses (a nearly hydrostatic case). If the maximum difference between the normal stresses is lower than the yield stress, no matter how much the material is compressed or stretched, it remains elastic. This assumption is the basis for studying the elastic behavior of materials subject to ultrahigh pressure utilizing quasi-hydrostatic pressure transmitting media. According to TGYS, when one of principal stresses becomes smaller (or larger) than the others the material is subject to shearing. In such situations, if the shear stress reaches the yield limit, the material enters the plastic domain.

Another model describing the shape of the yield surface is Huber–von Mises–Hencky (HMHYS) criterion, which relates the elastic limit to the sum of squares of principal stress differences:

$$(\sigma_1 - \sigma_2)^2 + (\sigma_1 - \sigma_2)^2 + (\sigma_1 - \sigma_2)^2 = 2\sigma_Y^2 .$$

It should be noted that that both the TGYS and HMHYS criteria are isotropic and do not relate to the possible anisotropy of the material.

Beyond the yield surface, the deformation is not reversible. However, an object in the plastic deformation range must have first undergone elastic deformation, which was reversible, so upon release of the stress it will return part way to its original shape. The plastic character of the deformation past the yield limit results from formation of defects and dislocations within the sample. For a detailed introduction to plastic deformation see chapter 10 by *Merkel.*

2.4. UNIQUE EFFECTS OF ANISOTROPIC STRESS

While in most high-pressure experiments anisotropy of the stress is an unwanted factor, there are some unique effects that stress anisotropy may have, which are not achievable under hydrostatic conditions. Perhaps best known examples here are shear-induced chemical reactions and structural phase transitions specific to nonhydrostatic conditions.

It has been known since the early work of *Bridgman* (1935) that shear stress can cause athermal chemical reactions, such as substitution of aluminum into Fe_2O_3 hematite structure. Reaction mechanisms usually utilize energy stored in strained bonds, resulting from defects and dislocations formed during plastic deformation (*Gilman*, 1996; *Levitas*, 2004).

Among the nonhydrostatic phase transition probably the best known is the compression behavior of inorganic spin-Peierls compound, $CuGeO_3$. $CuGeO_3$ undergoes two different sequences of phase transitions in a hydrostatic and quasi-hydrostatic pressure media (*Jayaraman et al.*, 1995; *Dera et al.*, 2002). The high-pressure phases differ in color, depending on the stress anisotropy, and some of the nonhydrostatic phases can be quenched to ambient conditions. Another example of structural phase transition that requires anitropic stress is the formation of penta-coordinated silica phase in SiO_2 (*Badro et al.*, 1997).

References

Angel R.J., Bujak M., Zhao J., Gatta G.D., and Jacobsen S.D. (2007) "Effective hydrostatic limits of pressuremedia for high-pressure crystallographic studies." J. Appl. Cryst. 40, 26–32.

Badro J., Teter D.M., Downs R.T., Gillet P., Hemley R.J., and Barrat J-L. (1997) "Theoretical study of a five-coordinated silica polymorph." Phys. Rev. B 56, 5797–5806.

Bassett W.A. (2009) "Diamond anvil cell, 50th birthday." High Press. Res. 29, 163–186.

Boehler R., and de Hantsetters K. (2004) "New anvil designs in diamond-cells." High Press. Res. 24, 391–396.

Bridgman P.W. (1935) "Effects of high shearing stress combined with high hydrostatic pressure." Phys. Rev. 48, 825.

Cauchy A.L. (1827) "On the pressure or tension in a solid body." Exercices de Mathématiques 2, 42.

Chen J., Wang Y., Duffy T.S., Shen G., and Dobrzhinetskaya L.P. (2005) "Advances in High-Pressure Techniques for Geophysical Applications." Elsevier, Amsterdam.

Dera P., Jayaraman A., Prewitt C.T., and Gramsch S.A. (2002) "Structural basis for high-pressure polymorphism in $CuGeO_3$." Phys. Rev. B 65, 134105.

Downs R.T., and Singh A.K. (2006) "Analysis of deviatoric stress from nonhydrostatic pressure on a single crystal in a diamond anvil cell: the case of monoclinic aegirine, $NaFeSi_2O_6$." J. Phys. Chem. Solids 67, 1995–2000.

Eremets M.I. (1996) "High Pressure Experimental Methods." Oxford Science Publication, Oxford.

Gilman J.J. (1996) "Mechanochemistry." Science 274, 65.

Hazen R.M. (1993) "The New Alchemists. Breaking Through the Barriers of High Pressure." Random House, New York.

Hazen R.M., and Downs R.T. (Eds.) (2000) "Reviews in Mineralogy and Geochemistry, vol. 41, High-Temperature and High-Pressure Crystal Chemistry." Mineralogical Society of America, Washington DC.

Hazen R.M., Downs R.T., and Prewitt C.T. (2000) "Principles of comparative crystal chemistry" in: Hazen R.M., and Downs R.T. (Eds.), Reviews in Mineralogy and Geochemistry, vol. 41, High-Temperature and High-Pressure Crystal Chemistry, Mineralogical Society of America, Washington DC.

Holtzapfel W.B., and Isaacs N.S. (Eds.) (1997) "High Pressure Techniques in Chemistry and Physics: A Practical Approach." Oxford University Press, Oxford.

Jayaraman A., Wang S.Y., Ming L.C., and Cheong S-W. (1995) "Pressure-induced intercalation and amorphization in the spin-Peierls compound $CuGeO_3$." Phys. Rev. Lett. 75, 2356–2359.

Klotz S., Chervin J.-C., Munsch P., and Le Marchand G. (2009) "Hydrostatic limits of 11 pressure transmitting media." J. Phys. D: Appl. Phys. 42, 075413.

Krauss H.R., and Steurer W. (2005) "Conically shaped single-crystalline diamond backing plates for a diamond anvil cell." Rev. Sci. Instrum. 76, 105104.

Levitas V.I. (2004) "High pressure mechanochemistry: conceptual multiscale theory and interpretation of experiments." Phys. Rev. B 70, 1–24.

McMillan P.F. (2005) "Pressing on: the legacy of Percy W. Bridgman," Nat. Mater. 4, 715–718.

Nye J.F. (1985) "Physical Properties of Crystals – Their Representation by Tensors and Matrices." Clarendon Press, Oxford, England.

Piermarini G.J. (1993) "Alvin Van Valkenburg and the diamond anvil cell." High Press. Res. 11, 279–284.

Piermarini G.J. (2001) "High-pressure X-ray crystallography with the diamond anvil cell." J. Res. Natl. Inst. Stand. Technol. 106, 889–920.

Sowa H. and Ahsbahs H. (2006) "High-pressure X-ray investigation of zincite ZnO single crystals using diamond anvils with an improved shape." J. Appl. Cryst. 39, 169–175.

Spain I.L., and Paauwe J. (Eds.) (1977) "High pressure technology. Vol. I Equipment designs, materials and properties." Marcel Dekker, New York.

Stewart A.J., and Schmidt M.W. (2007) "Sulfur and phosphorus in the Earth's core: the Fe-P-S system at 23 GPa." Geophys. Res. Lett. 34, L13201.

Walter M.L. (1991) "Science and Cultural Crisis: An Intellectual Biography of Percy Williams Bridgman (1882–1961)." Stanford University Press, Palo Alto, CA.

Yamanaka T., Fukuda T., Hattori T., and Sumiya H. (2001) "New diamond anvil cell for single-crystal analysis." Rev. Sci. Instrum. 72, 1458.

ALL DIFFERENT FLAVORS OF SYNCHROTRON SINGLE CRYSTAL X-RAY DIFFRACTION EXPERIMENTS

PRZEMYSLAW DERA*
Center for Advanced Radiation Sources, The University of Chicago, Argonne National Laboratory Bldg. 434A, 9700 S Cass Ave., Argonne, IL 60439, USA

Abstract This lecture reviews the main concepts, applications and capabilities of different non-conventional approaches to single-crystal x-ray diffraction (SXD) experiment utilizing synchrotron radiation for applications in high-pressure research. You will learn how such experiment can be designed and performed to best answer the scientific goals of your study and, at the same time overcome the main technical limitations imposed by the high-pressure device and type of measurement. The emphasis will be placed on experiments that cannot be performed using laboratory instruments, *e.g.* involving ultrahigh (>50 GPa) pressures, poor quality samples, laser heating in diamond anvil cell (DAC), *etc.* The main goal of the presentation is to convince you that even if you are not an expert crystallographer, with good understanding of the general basic principles of synchrotron SXD experiments in a DAC you can successfully use these techniques as valuable and easy tools in your own high-pressure research.

Keywords: Synchrotron experiments, structure determination, single-crystal diffraction, phase transitions

1. Introduction

Conventional methodology (utilizing monochromatic beam and four circle diffractometer with point detector) for single-crystal XRD experiments has been developed and optimized shortly after the first automated diffractometers became available in late 1960s and has served the crystallographic

* E-mail: dera@cars.uchicago.edu

E. Boldyreva and P. Dera (eds.), *High-Pressure Crystallography: From Fundamental Phenomena to Technological Applications*, DOI 10.1007/978-90-481-9258-8_2,

community very well since then (see *e.g. Arndt and Willis*, 1966; *Busing and Levy*, 1967). The introduction of area detectors in the 1990s has brought some revolutionary improvements into the data collection time, ease of diffractometer operation and sensitivity (*e.g. Burns*, 1998), but at the same time turned the diffractometer more into a black box that operates in a push-button mode. This mode usually works very well in application to crystals in air, but often is not quite adequate for experiments involving samples enclosed in diamond anvil cells (DACs). DAC introduces several important obstacles into the experiment, which significantly affect the quality of the intensity data and the coverage of reciprocal space (amount of independent observations that can be acquired). Since the very beginning of the automated diffractometry high-pressure crystallographers have strived to define optimal data collection and data reduction strategies geared towards retrieving highest-possible quality data from the SXD experiment in a DAC and developed such custom solutions as the $\phi = 0°$ positioning mode (*Finger and King*, 1978), 8-position peak centering (*Hamilton*, 1974; *King and Finger*, 1979; *Dera and Katrusiak*, 1999), multiple-ψ intensity measurement (*Loveday et al.*, 1990). *Miletich et al.* (2001) presented a thorough review of the high-pressure crystallographic solutions and techniques for SXD experiments with lab diffractometer.

The availability of synchrotron x-ray sources, and development of beam-lines specializing in high-pressure diffraction experiments has brought yet another significant revolution into high-pressure crystallography, enabling researchers to work with much smaller samples, reach much higher pressure and study more complex solids (*e.g.* proteins). However, despite all the great advantages of SXD techniques, synchrotron single crystal experiments remain much less frequently utilized than synchrotron powder diffraction experiments. The main reasons for this situation are lack of understanding of basic principles and (mostly unjustified) fear of sophistication. I will try to convince you that a well designed and executed synchrotron SXD experiment can, in fact, be much easier than a powder experiment, and will, in most cases, provide you with data characterized by a far superior information content and quality.

While the conventional experimental strategy for SXD experiments is ideal for crystals of reasonable (above 0.020 mm) size in air, and large incident beams (above 0.100 mm), characteristic of laboratory diffractometers, it is often suboptimal or even inadequate for experiments in diamond anvil cell involving synchrotron radiation. The main reasons for that are:

- Access limitations introduced by the design of the DAC
- Presence of additional diffraction signal (backing plates, diamonds, pressure medium)

- Time constraints (*e.g.* necessity to collect data containing maximum information at multiple pressure steps within the constraint of synchrotron beamtime)
- Instrument imprecision (for beam sizes below 0.005 mm and very small crystals (0.001–0.005 mm) keeping the illuminated volume of the crystal constant during rotation is almost impossible)
- DAC rotation limitations (*e.g.* for experiments at high pressure during laser heating)

Because of these reasons, a lot of developmental efforts have recently been devoted to designing and testing alternative ways of performing SXD experiments at synchrotron high-pressure beamlines. These new experimental approaches, which retrieve the same information content and provide the same (or superior) data quality as the conventional methods, allow to circumvent most of the problems intrinsic to DAC.

The main objective of this lecture is to provide a comprehensive introduction to SXD crystallography at high pressure as well as critical review of the most promising experimental approaches alternative to conventional monochromatic SXD experiment.

2. Why SXD Experiment is Usually Better than a Powder Experiment

A typical single crystal XRD experiment provides three classes of direct observations: (i) crystal orientations and diffracted beam orientations at which diffraction peaks occur (ii) intensities of the diffracted beams (iii) energies/wavelengths of the diffracted beams. From these measurements, the following secondary and directly interpretable information can be derived:

- Lengths of reciprocal vectors corresponding to each diffraction peak
- Orientation of reciprocal vectors corresponding to each diffraction peak
- Orientation matrix
- Miller indices
- Structure factor amplitudes
- Systematic absences/space group
- Structure factor phases
- Structure model (atomic positions, occupancies, thermal displacement parameters)
- Electron density distribution

The main difference between single crystal and powder experiment is that in the latter it is not possible to measure/determine orientations of reciprocal vectors, but only their lengths. While this may seem like a small loss, it has very significant consequences for data analysis/information retrieval:

- In powder diffraction determination of the unit cell, space group and assignment of Miller indices are usually ambiguous.
- Because of one dimensional character of the powder XRD data peak profiles often overlap and peak intensities cannot be measured independently.
- Peaks at high resolution (small d-spacings, below ~1.5 Å) contribute very little to indexing and unit cell refinement as their Miller index assignment is very ambiguous).

In addition to the above general shortcomings of powder diffraction, there are also important high-pressure specific limitations such as insufficient particle statistics, especially after laser heating treatment (due to recrystallization), uniaxial strain induced peak broadening and coexistence of multiple phases within one sample. It cannot be denied that powder XRD at high pressure is a well established and very successful technique, but it has to be realized that majority of its successes apply to very simple systems (elements, oxides, binary compounds).

3. Basic Principles of SXD

Diffraction (scattering of intense and directional diffracted beam(s) originating from the crystal) occurs when the Bragg condition for the given reciprocal vector is satisfied at a given *crystal orientation* and for the *available incident wavelength*. At a given crystal orientation each reciprocal vector requires a different specific wavelength for the diffraction to occur. At a given fixed wavelength there is a set of crystal positions (defined by rotation of the reciprocal vector on a surface of cone with axis along the incident beam) at which diffraction for a given reciprocal vector occurs. In order to observe sufficient number of peaks one of the variables has to be varied. Diffraction occurs regardless of the detector used, and the detector position, but the detector is needed to provide the observation.

Capturing the diffraction event on a detector constrains the intensity, direction and energy (only if the incident beam is monochromatic, or with a polychromatic incident beam, if the detector has energy resolution) of the diffracted beam. The angle between the diffracted and transmitted beams (Bragg angle), together with diffracted beam energy define the length of the corresponding reciprocal vector.

In a polychromatic experiment with stationary sample the crystal orientation is constant, therefore measuring the directions, intensities and energies of the diffracted beams provides complete SXD information. In a monochromatic experiment with area detector, on the other hand, diffraction images are collected while the sample is rotated, and the complete

measurement involves determination of the directions and intensities of diffracted beams as well as crystal orientations at which these intensities reach maximum.

4. Differences and Similarities Between Monochromatic SXD Experiments with Point Detector and with Area Detector

The conventional monochromatic SXD technique using 4-circle diffractometer and point detector, and utilizing the high-pressure specific data collection strategy can be successfully applied at synchrotrons to pressures as high as 50 GPa (*Friedrich et al.*, 2007) however, the long data collection time, and user-attention-intense data collection process are often prohibitive for synchrotron environments.

One of the major advantages of using point detector is the ability to collimate the diffracted beam and discriminate the signal originating from the sample crystal from other signals (powder diffraction from the backing plates, diamond reflections, parasitic scattering, *etc.*). Additionally, point detector experiments provide a much more detailed information about the evolution of crystal mosaicity (related to *e.g.* to uniaxial strain) by allowing to measure high resolution rocking curves (*e.g. Angel et al.*, 2007). High quality of the intensity data that can be achieved through diffracted beam collimation often allows more advanced data analysis such as retrieval of deformation electron density using maximum entropy method (*e.g. Yamanaka*, 2005).

SXD experiments require as large as possible angular access to the sample and are usually performed with DACs equipped in x-ray semi-transparent backing plates. The plates most commonly used in lab experiments are made of Be metal. With the use of point detector the powder diffraction signal which originates from the transmitted beam passing through the downstream Be backing plate can be rejected by collimation of the diffracted beam. Use of Be backing plates in synchrotron SXD experiments with area detectors is not very convenient, as the very textured Be powder pattern significantly contaminates the signal originating from the studied sample.

One of the most important differences between monochromatic SXD (mSXD) experiment with point and area detector is peak positioning. In point detector experiment the sample is positioned individually for measurement of every peak. As a result, the data collection time depends significantly on the number of reflections measured (and as a consequence on the size of the unit cell and crystal symmetry). This strategy requires that the orientation matrix of the crystal is determined very precisely prior to the actual data collection.

In area detector experiments peak intensities are captured in the diffraction image "on the fly", while the sample rotates. Since the surface area has a large angular coverage, multiple diffraction events are recorded in the same image without the necessity to "aim" for each peak specifically. In principle, it is possible to record a good quality dataset without any prior knowledge of the crystal orientation. This significantly speeds up the experiment, and makes it lees attention-demanding. Availability of diffraction images with multiple diffraction peaks is also very convenient in experiments involving phase transitions, as it provides an immediate qualitative evidence that a discontinuous change has happened.

There is a general belief that SXD experiments with area detectors produce unit cell information with quality inferior to that coming out from point detector instruments, however this is mostly due to hardware configurations (mostly very short sample-to-detector distance) used in CCD lab diffractometers which do not emphasize high quality unit cell parameter measurements and result in relatively large uncertainties of peak d-spacing determination. In fact, in a properly designed synchrotron SXD experiment the unit cell parameter determination can be more precise than in a powder experiment, because peaks at very large Bragg angle can be unambiguously indexed (using their three-dimensional coordinates, instead of just the lengths) and used in the unit cell refinement.

Monochromatic SXD experiments utilizing area detectors (CCD and image plate) have been successfully carried out at GSECARS, Sector 13 APS and several other high pressure beamlines throughout the world to pressures as high as 200 GPa.

5. Monochromatic Experiments with Area Detectors

5.1. STANDARD STEP-SCAN APPROACH

Standard monochromatic SXD experiments are performed using small angular step technique, in which the step size is adjusted to capture every diffraction peak in several consecutive images and allow determination of the angle at which the maximum peak intensity occurs by peak fitting (of peak intensity integrated within one image as a function of the rotation angle). Unfortunately, step scan mSXD experiments performed at synchrotrons bring several inconveniences:

1. They produce very large volumes of data. With a standard 0.3 degree step scan a single dataset at one pressure point usually consists of more than 1,000 images. Processing of such large numbers of images is quite time consuming and their storage is expensive.

2. Data collected only is step-scan mode does not provide an easy way of looking at "global picture". If data processing is not performed in real time an interesting phenomenon can be overlooked at the time of performing the data collection.
3. Collecting every image involves time spent for a detector readout, which for certain types of detectors can be very significant (for MAR345 image plate detector readout of one image in full resolution mode takes over 2 min). With large number of images collected the total time lost for readout quickly becomes prohibitive.
4. With high quality and very small crystals and with tightly focused beam peak profiles are often much narrower than the typical 0.3 degree angular step.
5. With very short exposure times (often in the sub-second range) the synchronization of the rotation motor speed with the shutter becomes challenging.

The simplest solution to most of the above problems, which is applicable to crystals of small to medium unit cell is to follow up the step scan with a data collection involving accumulation of the whole (or large part) of the accessible angular range or simply algebraically merging the step images. Such wide-rotation image provides the "global" picture of the diffraction, assures constant rotation speed and significantly shortens the data processing time. There are, however, also few disadvantages of the wide-rotation approach, such as:

- It is not possible to avoid strong diamond peaks which are captured in the same single image as all of the sample peaks.
- With large unit cell crystals the spacial overlap of the peaks might become a problem.

5.2. DUAL-SLEW APPROACH

From the point of view of best possible utilization of the valuable synchrotron beam time it would be optimal if a complete SXD information could be retrieved from a single wide rotation (WR) image. This would mean that a full data collation at a single pressure could be accomplished in a matter of seconds. Such data would most likely be of mediocre coverage and redundancy, but could provide possible insight into slower dynamical processes. Unfortunately, single wide-rotation image does not carry the information about the rotation angle at which each peak maximum occurred. This information is not needed, as long as a sufficiently accurate orientation matrix is available (*e.g.* determined at lower pressure), but in case of a displacive phase transitions peak indexing for the new phase without step scan data becomes very challenging.

In order to solve this problem a new data collection approach, referred to as Dual Slew Approach (DSA) inspired by a method recently patented by Bruker AXS (*Hooft*, 2008, private communication) has been introduced and tested at high pressure beamlines of GSECARS and HPCAT, Advanced Photon Source, ANL.

In a DSA data collection no step scan images are needed. The experiment consists of collecting only two WR images. During the first image accumulation the sample is rotated (usually about the vertical, omega/phi axis) and the detector remains still. When the second image is recorded, the sample rotation is the same as in the first image, but it is accompanied by a second continuous motion, which changes the position of the diffraction peaks on the detector e.g. (detector rotation or translation along, or across the incident beam, chi-rotation, etc.). The magnitude of shift of the detector position for each peak depends on when, during the accumulation the peak passed through its diffraction maximum. Therefore, the maximum intensity rotation angle for each peak can be retrieved by measuring the shifts of the detector pixel coordinates. The DSA method brings several important advantages:

- Complete SXD information can be obtained in a much shorter time just (two accumulations). The gain is especially significant for image plate detectors that have readout times as long as 2–3 min per image.
- The second DSA image records information about peak rocking curves and thus provides some more insight into the strain/mosaicity conditions.
- The precision of the peak rotation angle determination can be controlled by adjusting the magnitude of the second motion, and precision much higher than usually achievable in step scans can easily be accomplished.

6. Beyond Monochromatic Experiments – Polychromatic and Variable Energy SXD Techniques

In addition to monochromatic experiments, single crystal diffraction at high pressure can also be successfully performed with polychromatic incident beam. The two varieties of this method utilize solid-state energy-dispersive point detector (the EDX approach) and non-energy dispersive area detector (Laue method). The EDX method was very popular and quite successfully used in the 1980, but currently fell out of fashion mostly because of the relatively long data collection time (comparable to point detector mSXD experiments) and much more complicated than in mSXD peak intensity corrections. The classical Laue approach has never been widely utilized at high pressure because it does not provide direct information about reciprocal vector lengths and therefore does not allow determination of equation of state.

6.1. VARIABLE MONOCHROMATIC EXPERIMENT (VMSXD)

Ice et al. (2005) described the concept and first experimental tests of high-pressure variable monochromatic (energy scan) experiments with area detector. In vmSXD experiment the sample remains still and incident energy is varied to bring multiple diffraction peaks to a diffracting condition. The diffraction images are collected in a step scan mode, with each image collected at a different energy. Peak energies are determined by fitting of the energy-rocking curves in a manner analogous to angular rocking curve fitting in the mSXD experiment. The vmSXD can be conveniently combined with a wide energy range (WER) image accumulation (analogous to RW images in mSXD), which then provides a global picture of diffraction in one image and can be used conveniently for structure amplitude retrieval. The WER image, is essentially a limited-range (pink beam) Laue image, and alone does not contain the information about the reciprocal vector lengths. The vmSXD approach can also utilize the concept of DSA. If two WER images are recorded, and during the second image acquisition, the continuous energy change is accompanied by a continuous sample rotation (or detector motion), the peak energies can be retrieved my measuring the magnitudes of the peak shifts.

7. Structure Solution and Refinement at Ultrahigh Pressures

In general the information retrieved from an SXD experiment can be used for the purpose of determining the crystal structure if the following conditions are satisfied:

- The unit cell and space group are determined correctly, or at least a proper but unconventional unit cell/space group is assigned.
- The peak intensities are measured with sufficient precision and accuracy. The measure of precision is internal consistency factor of measured intensities R_{int}, which reflects agreement between the measured values of peak intensity for symmetry dependent peaks.
- Sufficient signal to noise level for the peak intensities is obtained.
- Necessary corrections (Lorenz, polarization, absorption, extinction) are applied.
- Sufficient number of peaks intensities are measured and sufficient coverage of the asymmetric part of the reciprocal space is available. From the experimental point of view the above requirements should be satisfied if:
- The sample crystal is of sufficient quality.

- The stress field is sufficiently isotropic.
- The illuminated sample volume remains sufficiently constant.

8. Between Single Crystal and Powder

While the information content of a single-crystal experiment is usually far better than that that of a powder experiment, it is not always possible to preserve the integrity of a single crystal throughout the whole pressure range of interest. Reconstructive phase transitions, anisotropic stresses, as well as high temperature gradients can irreversibly turn the single crystal sample to a powder (*e.g. Sowa and Ahsbahs*, 2006). There are multiple examples that even in such cases pursuing single-crystal style analysis of the coarse powder/bad single crystal samples can lead to retrieval of important and not obtainable by other means information (*e.g. McMahon*, 2005).

It is possible today to deal relatively routinely with crystal twinning and occurrence of multiple grains of one or several different phases present in the incident beam at the same time. In fact, recent reports demonstrate feasibility of single crystal analysis with samples composed of hundreds of such grains (see *e.g. Vaughan et al.*, 2004). The ease of peak indexing and ability to determine structures of unknown phases are not the only benefits of SXD approach. With application of methods known as 3D x-ray microscopy (see *Poulsen*, 2004 for a recent review) details of texture, strain and stress state, and epitaxial relations can be deduced from multigranular samples. Even in case if the sample is composed of small grains and of relatively poor diffraction quality, but exhibits high preferred orientation, collection of three-dimensional data in an SXD manner (pole figure measurement) may yield very valuable information (e.g. decomposition of overlapping peaks) that can be critical in deciphering the nature of the crystal structure (*Wessels et al.*, 1999; *Baerlocher*, 2004).

9. Conclusions

Synchrotron single crystal x-ray diffraction experiments can undoubtedly serve as a very valuable tool in studying structure and behavior of solids under high pressure. The unequivocal determination of the unit cell and space group, the structure factor amplitude information free from ambiguities caused by peak overlap and broadening characteristic of powder diffraction, and the ability to efficiently work with crystals in 1–10 μm size range, as well as reach pressures in excess of 200 GPa make it a truly unique experimental method.

With the recent significant efforts located at the synchrotron beamlines specializing in high-pressure research and focused on creating custom setups, optimized new methodology and specialized data acquisition and analysis software for SXD experiments at ultrahigh pressures the technique becomes not only more and more easily available to the broad community of high-pressure scientists, but also significantly less sophisticated and more user friendly.

ACKNOWLEDGEMENTS

Development of novel high-pressure synchrotron SXD methodology and instrumentation at GSECARS, Sector 13, APS was supported by a grant from the MRI Program, Division of Materials Research, National Science Foundation (NSF-DMR-0521179). X-ray data were collected at GSECARS and HPCAT sectors, APS, Argonne National Laboratory. GSECARS is supported by the National Science Foundation, the U.S. Department of Energy, the W.M Keck Foundation, the U.S. Department of Agriculture and the State of Illinois. Use of the APS was supported by DOE-BES, under Contract No. DE-AC02-06CH11357. Help from and collaboration with Robert T. Downs, Charles T. Prewitt, Barbara Lavina, Lauren A. Borkowski, Oliver Tschauner, Hans-Peter Liermann, Wenge Yang, Vitali B. Prakapenka, Mark Rivers and Steven Sutton is gratefully acknowledged.

References

Angel, R.J., Bujak, M., Zhao, J., Gatta, G.D., & Jacobsen, S.D. (2007) "Effective hydrostatic limits of pressure media for high-pressure crystallographic studies" *J. Appl. Cryst*., **40**, 26–32.

Arndt, U.W. & Willis, B.T.M. (1966) Single Crystal Diffractometry. Cambridge: Cambridge University Press.

Baerlocher, C., McClusker L.B., et al. (2004). "Exploiting texture to estimate the relative intensities of overlapping reflections" *Z. Kristallogr.*, **219**, 803–812.

Burns, P.C. (1998) "CCD X-ray area detectors applied to the analysis of mineral structures" *Canad. Mineral.*, **36**, 847–853.

Busing, W.R. & Levy, H.A. (1967) "Angle calculations for 3- and 4-circle X-ray and neutron diffractometers" *Acta Cryst.*, **22**, 457–464.

Dera, P. & Katrusiak, A. (1999) "Diffractometric crystal centering" *J. Appl. Cryst.*, **32**, 510–515.

Finger, L.W. & King, H. (1978) "A revised method of operation of the single-crystal diamond cell and refinement of the structure of NaCl at 32 kbar" *Am. Mineral.*, **63**, 337–342.

Friedrich, A., Haussühl, E., Boehler, R., Morgenroth, W., Juarez-Arellano, E.A., & Winkler, B. (2007) "Single-crystal structure refinement of diaspore at 50 GPa" *Amer. Mineral*., **97**, 1640–1644.

Hamilton, W.C. (1974) International Tables for X-ray Crystallography, Vol. IV, pp. 273–284. Birmingham: Kynoch Press. (Present distributor Kluwer, Dordrecht.)

Ice, G.E., Dera P., Liu, W., & Mao, H.K. (2005) "Adapting polychromatic X-ray micro-diffraction techniques to high-pressure research: energy scan approach" *J. Synchrotr. Rad*., **12**, 608–617.

King, H.E. Jr & Finger, L.W. (1979). "Diffracted beam crystal centering and its application to high-pressure crystallography" *J. Appl. Cryst.*, **12**, 374–378.

Loveday, J.S., McMahon, M.I., & Nelmes R.J. (1990) "The effect of diffraction by the diamonds of a diamond-anvil cell on single-crystal sample intensities" *J. Appl. Cryst.*, **23**, 392–396.

McMahon, M.I. (2005) "Structures from powders and poor-quality single crystals at high pressure" *J. Synchrotron Rad.*, **12**, 549–553.

Miletich, R., Allan, D.R., & Kuhs, W.F. (2001) "High-pressure single-crystal techniques" chapter 14 in Hazen, R.M., Downs, R.T. (eds.), Comparative Crystal Chemistry, Reviews in Mineralogy Vol. XLI, pp. 445–519. Washington, DC: Mineralogical Society of America and Geochemical Society.

Poulsen, H.F. (2004) "Three dimensional X-ray diffraction microscopy" Springer Tracts in Modern Physics. Springer, Berlin.

Sowa, H. & Ahsbahs, H. (2006) "High-pressure X-ray investigation of zincite ZnO single crystals using diamond anvils with an improved shape." *J. Appl. Cryst.*, **39**, 169–175.

Vaughan, G.B.M., Schmidt, S., et al. (2004) "Multicrystal approach to crystal structure solution and refinement" *Z. Kristallogr.*, **219**, 813–825.

Wessels, T., Baerlocher, C., et al. (1999) "Single-crystal-like diffraction from polycrystalline materials" *Science*, **284**: 477–479.

Yamanaka, T. (2005) "Structural changes induced by lattice-electron interactions: SiO_2 stishovite and $FeTiO_3$ ilmenite" *J. Synchrotron Rad.*, **12**, 566–576.

SYNCHROTRON HIGH-PRESSURE HIGH-TEMPERATURE TECHNIQUES

MOHAMED MEZOUAR*
ESRF, BP220, 38000 Grenoble, France

Abstract This chapter is devoted to the description of a state-of-the-art synchrotron beamline fully optimised for monochromatic x-ray diffraction at high pressure and high (or low) temperature. This beamline exhibits outstanding performance in terms of photon flux and focusing capabilities at high x-ray energies. The main components of this instrument are described in some details. In particular, the choices in terms of x-ray source, x-ray optics, detectors and sample environment are discussed.

Keywords: Synchrotron beamline, x-ray diffraction, high pressure, high temperature, diamond anvil cell, Paris-Edinburgh cell

1. Introduction

The investigation of matter under extreme conditions is one of the natural issues addressed at a synchrotron radiation source (*Shimomura et al*., 1992; *Nelmes and Mc Mahon*, 1994). Indeed, the highly collimated and intense x-ray beam available at third generation high energy machines such as the ESRF, APS and SPRING8 is the ideal tool for probing microscopic samples at maximum pressures and temperatures and for reducing the effects of gradients in these variables. Several state-of the-art x-ray diffraction (XRD) high pressure (HP) beamlines operate at these large facilities. Here, I will focus on beamline ID27 at the ESRF, a recently constructed instrument, and I will describe its main components. This instrument is fully optimised for monochromatic high resolution XRD under extreme P and T. It has two dedicated experimental hutches respectively optimised for the Paris-Edinburgh cell and diamond anvil cell experimentation. The large volume

* E-mail: mezouar@esrf.fr

E. Boldyreva and P. Dera (eds.), *High-Pressure Crystallography: From Fundamental Phenomena to Technological Applications*, DOI 10.1007/978-90-481-9258-8_3,

programme at ID27 is focused on measurements of phase equilibrium (*Crichton et al*., 2001), thermo-elastic properties of solids (*Stolen et al*., 2000), the structures of melts and glasses (*Crichton et al*., 2001) and *in situ* chemistry at high pressures and temperatures (*Solozhenko et al*., 2002). The diamond-cell facility is optimised for accurate structure determinations at ultrahigh pressures (*Akahama et al*., 2002) and allowed simultaneous laser or resistive heating at P–T conditions reproducing those of planetary interiors (*Schultz et al.*, 2005; *Andrault et al.*, 1997). The main components of beamline ID27 are presented in the following.

2. General Beamline Description

A general view of the beamline ID27 is presented in Figure 1 and is composed of an optical hutch (OH), two specialised experimental hutches (EH), two control cabins and two high-pressure laboratories. The first experimental hutch, EH1, is 6 m long and 2.5 m wide (on average) and is fully dedicated to large volume cell experiments using the Paris–Edinburgh (P–E) press. The second hutch, EH2, is 8 m long and 3 m wide and is fully optimised for diamond anvil cell (DAC) experiments at high temperature

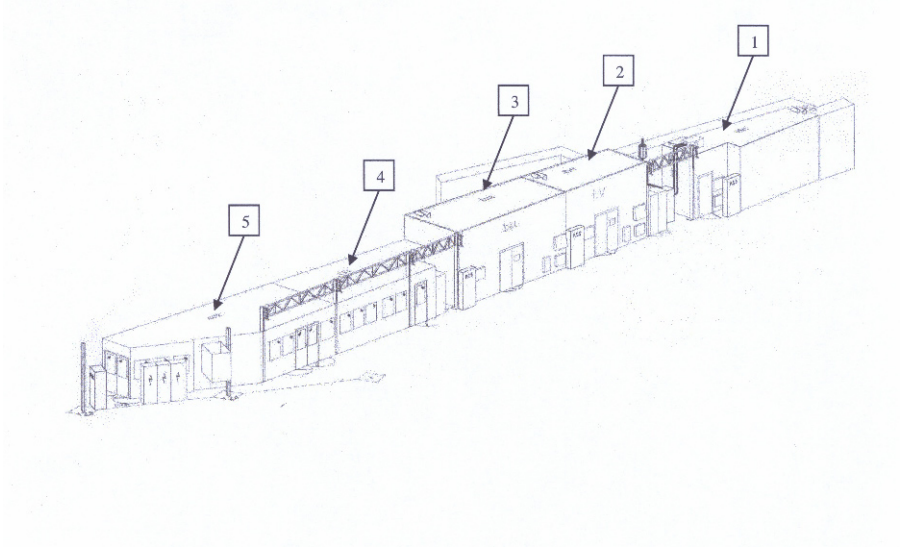

Figure 1. General beamline overview. (1) Optics hutch, (2) Experimental hutch 1, (3) Experimental hutch 2, (4) Diamond anvil cell laboratory, (5) Paris–Edinburgh press laboratory.

using laser or resistive heating and low temperature using helium flow cryostats. Two sample preparation laboratories adapted to diamond cell and large volume cell loading are located at the beamline for convenience. The centre of the experimental hutches EH1 and EH2 are respectively located at 41 and 48 m from the x-ray source. This x-ray source is composed of two small-gap in-vacuum undulators of 23 mm period that can be used simultaneously at a minimum magnetic gap of 6 mm. The monochromatic beam is selected using a nitrogen cooled silicon (111) monochromator and focused on the sample using multilayer mirrors in the Kirkpatrick–Baez geometry. EH1 and EH2 are respectively equipped with an XYZ translation to accommodate the P–E press and a versatile high-precision two-circle diffractometer suitable for powder and single crystal diffraction in DACs. The diffraction signal is collected on a MAR165 CCD or a MAR345 detectors that are easily interchanged using high precision motorized translations.

3. The X-ray Source, Optics and Detectors for High-Pressure Diffraction

3.1. THE X-RAY SOURCE

A very intense and highly focused x-ray beam is crucial for *in situ* diffraction experiments at high pressure because of the very small sample dimensions. For pressures above 100 GPa, the typical sample dimensions are of the order of 20 μm or smaller. Moreover, high-pressure diffraction experiments require high photon flux at high x-ray energies because of the limited x-ray aperture of high pressure cells and the highly absorbing pressure windows. Therefore, the choice of an optimized x-ray source is of primary importance (*Chavanne et al.*, 1998). Beamline ID27 is equipped with 2 in-vacuum small-gap undulators on a low-ß section (small source but higher divergence in the horizontal direction). The energy dependence of the photon intensity of the U23 in vacuum undulators installed at beamline ID27, a wide gap U40 undulator and a wiggler W70 are compared in Figure 2. The calculation was conducted for an incident beam size of 1 mm in the horizontal direction and 0.5 mm in the vertical direction at 30 m from the source. The two U23 available at ID27 can reach minimum magnetic gaps of 6 mm and generate extremely bright beams in the x-ray energy region of interest. The gain in intensity, compared to the U40 and W70 varies between 3 and 4 in the x-ray energy domain between 30 and 50 keV, which is the optimum energy region for high pressure diffraction experiments.

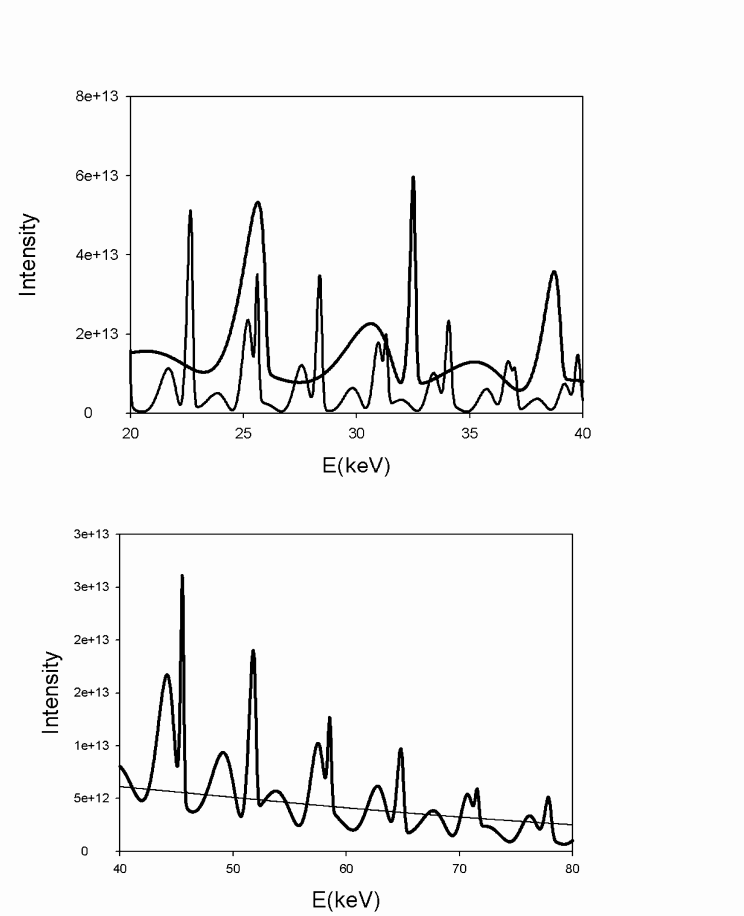

Figure 2. Comparison of different insertion devices in 20–40 keV (U23 vs U40) and 40–80 keV (U23 and W70) x-ray energy domains.

3.2. THE X-RAY OPTICS

The x-ray optics installed at beamline ID27 have been selected for their simplicity and flexibility. The optical elements are composed of a nitrogen cooled channel-cut silicon (111) monochromator located in the optics hutch at 30 m from the source and a pair of multilayer mirrors in the Kirkpatrick–Baez (KB) geometry installed in each experimental hutch to focus the monochromatic beam on the pressurized sample. The dimensions of this monochromator are optimised to select a broad energy domain from 6 keV (λ = 2 Å) to 90 keV (λ = 0.14 Å) which largely covers the energy band needed for high-pressure diffraction experiments.

As already mentioned, the quality of focussing optics at high x-ray energies is of primary importance in high-pressure experiments because of the very small sample volume. ID27 is equipped with two 300 mm long multilayer mirrors developed by the ESRF optics group (*Hignette et al.*, 2003). These multilayer mirrors are made of iridium-alumina multilayer deposited on silicon wafers. They possess a very broad energy band pass from 6 to 80 keV with a maximum of 80% reflectivity at 30 keV. A photograph of these new mirrors is shown in Figure 3. Large focal distances of 800 and 1,200 mm are respectively used for the horizontal and the vertical mirrors in order to avoid serious loss of spatial resolution. The focal spot measured by translating a 1 mm tungsten wire across the x-ray beam is shown in Figure 4, a 6 μm beam spot diameter at full width half maximum (FWHM) is routinely obtained.

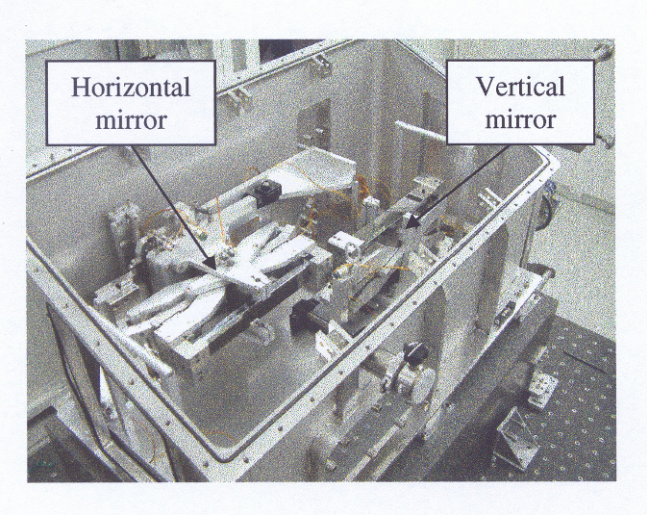

Figure 3. Photograph of a pair of 300 mm long Kirkpatrick–Baez mirrors.

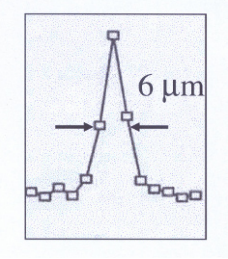

Figure 4. Beam spot size along the horizontal direction measured by translating a tungsten wire at the focal point.

3.3. DETECTORS

The criteria for a detector suitable for high pressure experiments are mostly dictated by the cell geometry (limited 2θ angle), composition (diamonds for the DACs, boron gaskets for the P–E press) and by working x-ray energies. These criteria impose a large input surface of more than 150 mm diameter, a high spatial resolution (point spread function of 150 μm FWHM or less), low noise and high dynamic range (14 bits or more), a good sensitivity at high x-ray energies above 30 keV, stable and easily tractable spatial distortions with fast reading (a few seconds or less) and erasing times. The MAR345 image plate detector fulfils most of the above criteria but has long readout time of 1 min or more depending on the choice of the pixel size. This becomes problematic when compared to exposure times of the order of 1 s or less because of the high photon flux available at beamline ID27. This situation is improved with a large area MAR165 CCD detector because the readout time is reduced to 4 s in full binning but the detection area is much smaller.

4. Beamline Performance

The beamline performance have been tested on a lanthanum hexaboride powder LaB_6 sample (SRM 660a) from the National Institute of Standards and Technology (NIST, USA). The sample was loaded in a hole of 150 μm diameter and 40 μm thickness of an indented stainless steel gasket in order to reproduce the typical sample geometry in a DAC. The wavelength of the incident x-ray beam was $\lambda = 0.3738$ Å which corresponds to the iodine K-edge, the standard wavelength used at beamline ID27 for DAC experiments. The exposure time is set using an electro-mechanical fast-shutter with a minimum opening-closing time of 10 ms. The diffraction patterns were collected on a MAR345 image plate scanner and circularly integrated using the software Fit2D (*Hammersley et al.*, 1996). A typical diffraction pattern of LaB_6 and the corresponding one-dimensional spectrum is presented in Figure 5, the sample to detector distance was approximately 360 mm. In this case, the focusing mirrors were not used, the x-ray beam was simply collimated down to 50×50 μm^2 using a pair of tungsten carbide slits in order to prevent any contamination from the gasket material. The detector saturation was reached after only 5 s of exposure confirming the important gain in intensity. The relative d-spacing variation $\Delta d/d$ obtained from the pseudo-Voight fitting of the diffraction lines of the LaB_6 pattern is $\Delta d/d = 1.5.10^{-4}$. Another set of diffraction patterns were collected with the focusing mirrors in place in order to estimate the loss of spatial resolution they induce. The focal spot diameter obtained with the KB mirrors was 5 μm

(FWHM) with an incident x-ray beamsize of 0.5×0.8 mm^2. In this case, the exposure time was reduced to less than a second because of the large angular acceptance of the mirrors. The $\Delta d/d$ value increases to $3.1.10^{-4}$ when the mirrors were employed. This degradation of the spatial resolution is an acceptable compromise for high-pressure diffraction experiments where focusing optics are mandatory.

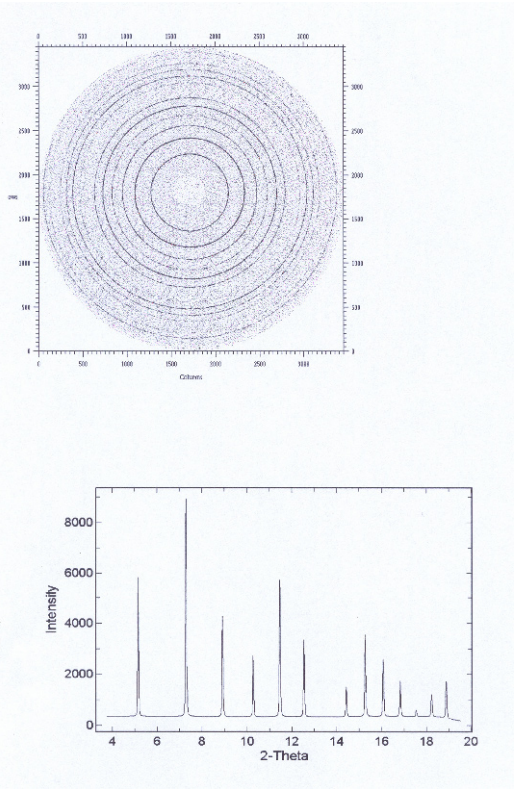

Figure 5. Two-dimensional x-ray diffraction pattern of LaB_6 and the corresponding one dimensional spectrum collected at ID27.

5. Diffractometer and Sample Environment

High-pressure cells of two types are available at beamline ID27, the diamond and Paris–Edinburgh cell. Static ultrahigh (megabar) pressures are achieved in diamond anvil cells (*LeToullec et al.*, 1988; *Chervin et al.*, 1995) that can concentrate high stresses at a very small area. These cells generally have 0.1–0.4 mm culet tips and are therefore suitable for generating pressures above 100 GPa. These cells can be used with simultaneous resistive heating to temperatures up to 1,000 K, laser heating to temperatures above 5,000 K or

helium cryocooling to temperatures lower than 10 K. The Paris–Edinburgh press can simultaneously generate stable pressures up to 8 GPa and temperatures up to 2,200 K on several cubic millimetre sample volumes using tungsten carbide anvils (*Mezouar et al.*, 1999) and pressures up to 17 GPa and temperatures up to 1,500 K using sintered diamond anvils. The P–E press is complementary to the diamond anvil cell because of its much larger sample volume which for instance, allows *in situ* chemistry at high pressure and high temperature with control of the stoichiometry (*Nieto Sanz et al.*, 2004).

5.1. THE PARIS-EDINBURGH SETUP

The large volume cell diffractometer is installed in a fully dedicated experimental hutch (EH1) and is composed of an XYZ cell stage that allows micro positioning of the press, a Soller slits system (*Mezouar et al.*, 2002) to eliminate most of the background signal coming from the sample environment, a large area detector (MAR345) and a fast imaging system to *in situ* visualize the sample. A photograph of the large volume cell setup is shown in Figure 6.

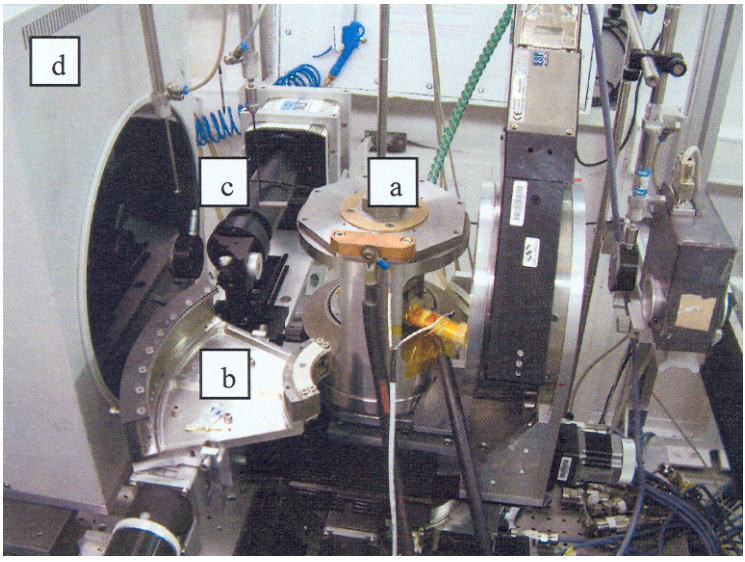

Figure 6. Paris–Edinburgh XRD setup at ID27- **a**: VX5 Paris-Edinburgh press, **b**: Soller slits system, **c**: Fast imaging camera, **d**: MAR Image Plate.

5.2. THE DOUBLE-SIDED LASER HEATING SYSTEM

The second experimental hutch is dedicated to experiments at very high P and T in the double-sided laser heating DACs. The laser-heated diamond anvil cell (DAC) is the only technique that can create extreme temperatures at extreme pressures (P > 100 GPa). Temperatures in excess of 5,000 K can be achieved for samples under pressure in diamond cells by heating with high-power infrared lasers. This dedicated hutch is equipped with a high-precision two-circle goniometer (rotations are about a vertical ω-axis and a χ-axis in the horizontal plane) installed on a stacking of three orthogonal translation tables XYZ. This goniometer can accommodate different types of diamond-anvil cells. Positioning (including that of independent-jaws micron-size slits) and centering the sample to accuracy better than 1 μm is standard. A photograph of the laser heating setup and the corresponding schematic are presented in Figure 7. The laser heating system is composed of a high-power diode pump Nd–YAG infrared laser, several guiding optics, optimized focusing and collecting optics and a visible spectrometer. The laser beam penetrates on both sides of the DAC at an incidence angle of 20 degrees and creates a homogenous temperature area probed by the focused x-ray beam. Temperature is measured by multi-wavelength spectral radiometry on both sides of the sample. The thermal signal emitted by the sample is collected by optimized collecting optics that also serves as imaging optics. The thermal radiation is focused via these optics to the entrance slit of a visible spectrometer where the thermal light is wavelength dispersed. The system is equipped with two collecting optics (CO). A hole is drilled on the upstream CO along the x-ray beam path in order to perform *in situ* temperature measurements. The downstream CO largely intercepts the x-ray diffraction cone and is removed during the x-ray exposure. However, it allows the control of the temperature stability and temperature gradients via measurements done shortly before and after x-ray data collection. In addition, the COs also serves as imaging optics. In this case, the light coming from the sample is directly focused on a infra-red sensitive CCD camera. This system enables the *in situ* visualization of the sample in the DAC during heating and x-ray exposure and allows the accurate alignment of the x-ray beam with the hot spot induced by the laser beam.

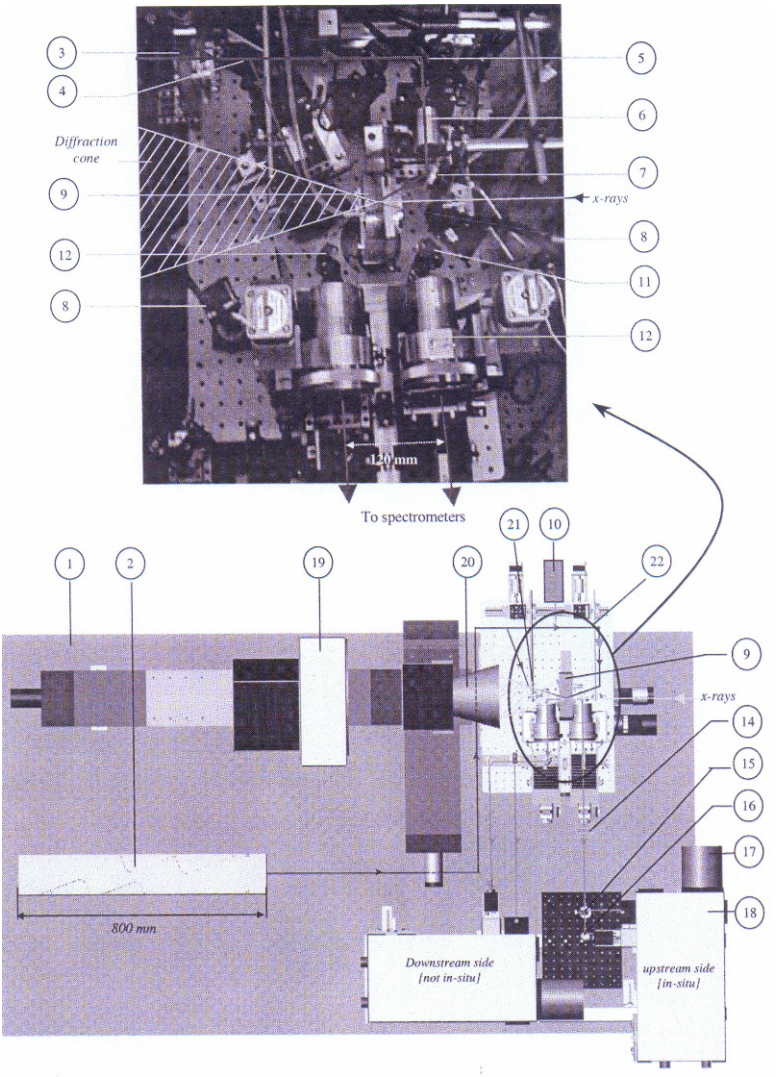

Figure 7. Set-up for the double-sided laser-heated DAC at the high-pressure beamline ID27; (1) Optical table, (2) CW diode-pumped TEM_{00} Nd:YAG laser; (3) waveplate; (4) Beam-splitter cube; (5) laser mirror oriented at 45°; (6) laser focusing objective; (7) laser mirror oriented at 35°; (8) laser beamstop; (9) Diamond anvil cell placed in a cooling unit; (10) Argon laser emitting at a wavelength of 488 nm for pressure measurements using the ruby fluorescence technique; (11) Upstream mirror oriented at 45° with a hole drilled in its centre enabling the x-rays to get through; (12) Downstream mirror oriented at 45°; (13) collecting and imaging optics: Schwarzfield-type telescopes; (14) filters (KG, NG and/or RG) and Nd:YAG laser mirrors with 0° incidence; (15) Beamsplitter cube (50/50); (16) mirror oriented at 45°; (17) Thermoelectrically cooled CCD; (18) Imaging spectrometer; (19) large-area CCD; (20) Image Plate detector; (21): x-ray beamstop; (22) pinhole.

References

Akahama, Y., Kawamura, H. & Le Bihan, T. (2002). J. Phys.: Cond. Matt. 14, 10583–10588.
Andrault, D., Fiquet, G., Kunz, M., Visocekas, F. & Haeusermann, D. (1997). Science 278, 831–834.
Besson, J.M., Nelmes, R.J., Hamel, G., Loveday, J.S., Weill, G. & Hull, S. (1992). Physica B 180/181, 907–910.
Chavanne, J., Elleaume, P. & Van Vaerenbergh, P. (1998). J. Synch. Rad. 5, 196–201.
Chervin, J.C., Canny, B., Besson, J.M. & Pruzan, P. (1995). Rev. Sci. Instrum. 66, 2595–2598.
Crichton, W.A., Vaughan, G.B.M. & Mezouar, M. (2001). Z. Krystallogr. 216, 417–419.
Crichton, W.A., Mezouar, M., Grande, T., Stolen, S. & Grzechnik, A. (2001). Nature 414, 622–625.
Hammersley, A.P., Svensson, S.O., Hanfland, M., Fitch, A.N. & Hausermann, D. (1996). High Press. Res. 14, 235–248.
Hignette, O., Cloetens, P., Lee, W.K., Ludwig, W. & Rostaing, G. (2003). J. Phys. IV 104, 231–234.
Le Toullec, R., Pinceaux, J.P. & Loubeyre, P. (1988). High Press. Res. 1, 77–81.
Mezouar, M., Le Bihan, T., Libotte, H., Le Godec, Y. & Haeusermann, D. (1999). J. Synch. Rad. 6, 1115–1119.
Mezouar, M., Faure, P., Crichton, W., Rambert, N., Bauchau, S. & Blattmann, G. (2002). Rev. Sci. Instr. 73, 3770–3774.
Nelmes, R.J. & Mc Mahon, M.I. (1994). J. Synch. Rad. 1, 69–73.
Nieto Sanz, D., Loubeyre, P., Crichton, W.A. & Mezouar M. (2004). Phys. Rev. B 70, 214108–214114.
Schultz, E., Mezouar, M., Crichton, W.A., Bauchau, S., Blattmann, G., Andrault, D., Fiquet, G., Boehler, R., Rambert, N., Sitaud, B. & Loubeyre, P. (2005). High Press. Res. 25, 71–83.
Shimomura, O., Takemura, K., Fujihisa, H., Fujii, Y., Ohishi, Y., Kikegawa, T., Amemiya, Y. & Matsushita, T. (1992). Rev. Sci. Instrum. 63, 967–973.
Solozhenko, V.L., Turkevich, V.Z., Kurakevych, O.O., Crichton, W.A. & Mezouar, M. (2002). J. Phys. Chem. B 106, 6634–6637.
Stolen, S., Grzechnik, A., Grande, T. & Mezouar, M. (2000). Sol. State Com. 115, 249–252.

MINERAL PHYSICS OF EARTH CORE: IRON ALLOYS AT EXTREME CONDITION

LEONID DUBROVINSKY[*1], JUNG-FU LIN[2], NATALIA DUBROVINSKAIA[3]
[1]*Bayerisches Geoinstitut, Universität Bayreuth, D-95440 Bayreuth, Germany,* [2]*Department of Geological Sciences, Jackson School of Geosciences, the University of Texas at Austin, USA,* [3]*Mineralphysik, Institut für Geowissenschaftent, Universität Heidelberg, D-69120 Heidelberg, Germany and Lehrstuhl für Kristallographie, Physikalisches Institut, Universität Bayreuth, D-95440 Bayreuth, Germany*

Abstract Mineral physics and high-pressure crystallography research provide crucial information on the enigmatic properties of the Earth's interior and is motivating multidisciplinary efforts to re-evaluate our understanding of the past and current states of the planet. We discuss the structures, melting temperatures, sound velocities of the dominant core-forming iron–nickel-light element alloys, as well as seismic anisotropy, thermal and chemical states of the Earth core in view of structural studies of iron-based alloys at multimegabar pressure range.

Keywords: Earth core, iron alloys, high pressure

1. Introduction

The Earth's core is the most remote region on our planet (Figure 1). The boundary of the core is at about 2,900 km in depth. Not only do we not have samples from the core, we do not even expect to get any. To date, the most direct observations of the core have come from seismological studies using remote-sensing techniques. Due to the complex internal structure of the Earth, seismic investigations require extensive data coverage and appropriate

[*] E-mail: Leonid.Dubrovinsky@uni-bayreuth.de

E. Boldyreva and P. Dera (eds.), *High-Pressure Crystallography: From Fundamental Phenomena to Technological Applications*, DOI 10.1007/978-90-481-9258-8_4,

models. Decoding geochemical signature of the core carried by mantle plumes faces similar challenges. Experimental and computational simulations have been hindered by the necessity to approach pressures over 140 GPa and temperatures above 3,000 K, prevalent in the core. For these reasons, many fundamental issues concerning the Earth's core remain controversial and poorly understood.

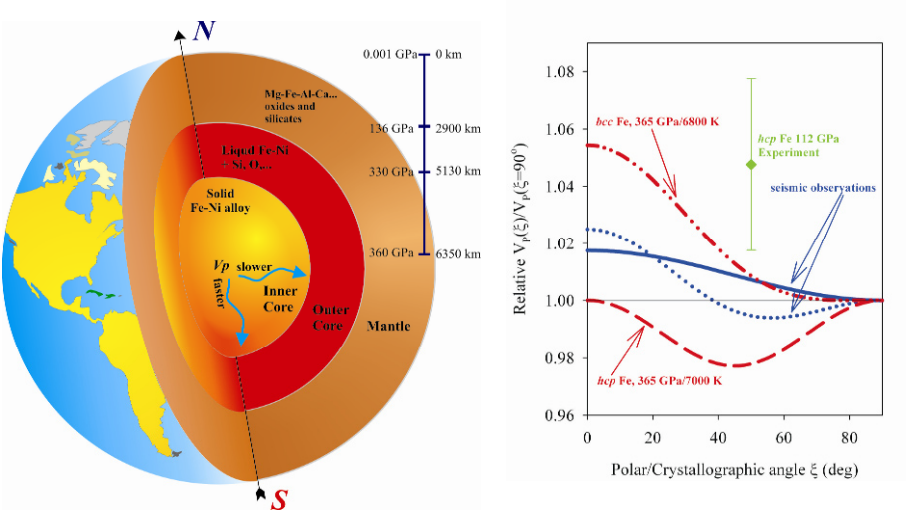

Figure 1. A cutaway of the Earth's interior (left) reveals seismic anisotropy of the inner core (right). Representative elastic anisotropies of single-crystal hcp dashed line) and bcc (solid line) iron from theory (*Belonoshko et al.*, 2008), prefer-oriented hcp iron from static experiments at 112 GPa (diamond) (*Antonangeli et al.*, 2004), and seismic observations in the inner core are shown for comparison.

Despite all these difficulties, the Earth's core is in focus of the highest research interest due to development of experimental and computational methods, as well as steady improvement in observational techniques. Recent studies reveal a number of unusual and enigmatic phenomena related to the core properties and dynamics. Among them is the discovery of the inner core anisotropy, *i.e.*, seismic waves travel faster along the Earth's polar axis than in the equatorial direction. There is also evidence for differential rotation between the inner core and the rest of the Earth and fine–scale heterogeneity. Earth's magnetic field strongly links to the core dynamics. Acceleration of the movement of magnetic poles over the last 150 years is a clear manifestation of the importance of understanding of the Earth core properties for human society.

2. Composition of the Earth's Core

Composition of the Earth's core is a geochemical parameter crucial for understanding the evolution and current dynamics of our planet. Since the discovery of the Earth's core about a century ago, the idea of iron being the dominant component of the core gained firm support from cosmochemical and geochemical observations, seismic data, theory of geomagnetism, and high-pressure studies. Cosmochemical data and studies of iron meteorites give evidence that the Earth's core contains significant (5–15%) amounts of nickel. Already in the early 1950s it was recognized that the outer core is less dense than iron or an iron–nickel alloy at corresponding conditions. Current estimates for the density deficit relative to solid iron vary between 6% and 10% for the outer core and 2–5% for inner core (*Dubrovinsky et al.*, 2000, 2007; *Dewale et al.*, 2006). Uncertainties are in part related to the experimental difficulties in measurements of the properties of iron (or iron–nickel alloys) at multimegabar pressure range and high temperatures, but the fundamental problem is the absence of a universal pressure scale that has led to significant discrepancies in the inter-laboratory studies (see, for example, *Dubrovinsky et al.*, 2007). Nevertheless, the core is expected to contain other element(s) apart from iron and nickel. In order to be considered as an important component of Earth's outer core, an element lighter than iron must be geochemically abundant, alloying readily with iron, and partitioning preferably to liquid rather than to a solid iron phase. These constraints have resulted in S, O, Si, C, and H being the preferred candidates, but practically all geochemically abundant elements which are lighter than iron were suggested and have their proponents. Additional constrains come up from the analysis of elements depletion in the mantle (*e.g.* how much of a certain element was available to be incorporated into the bulk core in the past (on stage of the Earth differentiation) and at present), the comparison of physical properties (density, compressibility, sound velocities, *etc.*) of Fe–(Ni)-light element compounds with corresponding properties of the core, the observation of the partitioning of elements at the core–mantle and inner-outer core boundaries. Available information suggests that none of elements alone could satisfy all constrains simultaneously. Studies of elements solubility in molten iron in laser-heated diamond anvil cells at megabar pressure range and temperatures in excess of 3,000 K by means of analytical transmission electron microscopy (*Takafuji et al.*, 2005) and measurements of compressional sound velocities in light element alloys of iron at high-pressure by inelastic X-ray scattering (*Badro et al.*, 2007) gave consistent results. The preferred model derived form these experimental works is the outer core containing about 5.3 wt.% oxygen and 2.8 wt.% silicon, and the inner core with about 2.3 wt.% silicon. Note that these

conclusions depend on the structure of the iron–nickel-light element(s) alloys at core conditions and on the assumed temperature of the Earth's core.

3. Melting of Iron and Temperature of the Earth' Core

One of the major uncertainties in the modern geophysics is temperature of the Earth's core. This is a basic parameter, essential for modeling thermal budget and dynamics of the planet, including such surface processes as volcanism and tectonics. There is no way to obtain temperature distribution in the Earth core from direct observations. However, temperature of solidification of the core material at inner-outer core boundary (ICB, ~330 GPa) could provide a good estimate of temperature at the depth of ~5,100 km, and melting temperature of core-forming material would give low bound of the temperature at core–mantle boundary (CMB, depth ~2,900 km and pressure ~136 GPa). Assuming that iron is the main component of the Earth's core, necessary information could be extracted from an experimentally measured melting curve of iron at multimegabar pressures (Figure 2). At ICB conditions the only experiments possible at the moment are those based on shock waves (see, for example, *Nguyen and Holmes*, 2004). In these experiments temperature estimations are difficult and require significant assumptions. Studies in laser-heated diamond anvil cells (DACs) could be

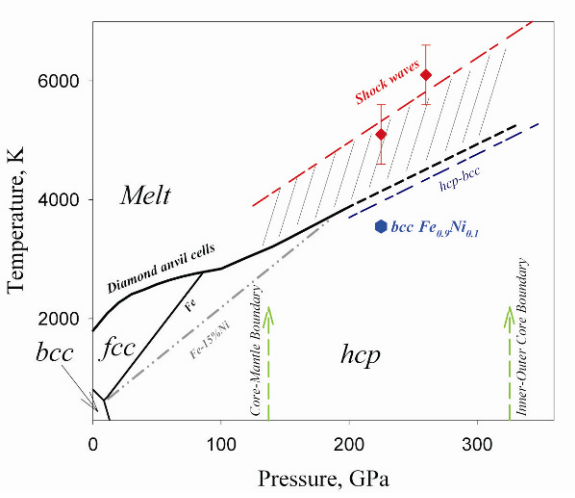

Figure 2. Representative phase diagram of iron and iron–nickel alloys at high pressures and temperatures. hcp iron is stable over a wide range of pressures and temperatures, while bcc iron is predicted to exist in the inner core (dashed line) and a bcc $Fe_{0.9}Ni_{0.1}$ alloy is experimentally observed at 225 GPa and 3,400 K (hexagon). Melting curves of iron from shockwave measured (diamonds) are much higher than static diamond cell results (dashed line). Shaded area: current survey of the melting temperatures of iron at core pressures.

extended to over 200 GPa, but a detection of the melting event in DACs is not easy and even at a moderate pressure below 100 GPa there is no unambiguous consensus. Currently the difference between the shock wave and DAC results on iron melting at ICB is more than 1,000 K (Figure 2) with different theoretical calculations supporting either of the estimates (*e.g. Alfè et al.*, 2003; *Belonoshko et al.*, 2003). The effect of light elements on melting temperature and sub-solidus relations in iron-based alloys at Earth's core conditions adds further uncertainties in guessing temperature of the Earth's core.

4. Structure of Iron and Iron-Based Alloys in the Earth's Inner Core

Iron has been reported to have several phases based on x-ray diffraction at high pressure and temperature, *i.e.*, α and δ, body-centered-cubic (*bcc*); γ, face-centered-cubic (*fcc*); ε, hexagonal closed-packed (*hcp*); β, double-hcp phase (*dhcp*) or orthorhombic phase. The α-, δ-, and γ-phases at lower pressures are well established and broadly accepted. The ε-phase has been proved to be a dominant phase in a wide pressure–temperature range approaching the Earth's core conditions. The β-phase, observed at pressures above 30 GPa and high temperature, is probably metastable, or stabilizes due to contaminations.

While studying of pure iron at multimegabar pressures draw considerable attention and have provided rich experimental data, the knowledge of the behavior and properties of Fe–Ni alloys at conditions of the Earth's core is still limited. At ambient pressure iron–nickel alloys with up to 25 at% of Ni have the *bcc* structure, while higher nickel contents promote crystallization of the *fcc*-structured phase (Figure 2). Compression of *bcc*-structured alloys at ambient temperature results in their transformation to the *hcp*-phase at pressures between 7 and 14 GPa (depending on composition and conditions of experiments). Like in case of pure iron, no further transformations were observed up to a pressure of ~300 GPa on compression of the Fe–Ni alloys with up to 20 at% Ni. However, the presence of nickel significantly affects phase relations in the Fe–Ni system at high temperatures and pressures. While the slope of the *hcp–fcc* phase boundary for pure iron is 35–40 K/GPa, there are indications that the phase boundaries of Fe-Ni alloys with 10 to 30% Ni might have much lower slopes (15–25 K/GPa). Simple extrapolation of experimental results (Figure 2) for Fe with 10–20 wt.% Ni suggests that the stable phase at the inner core conditions is either hexagonal close packed, or a mixture of *hcp* and *fcc* phases (*Lin et al.*, 2002; *Mao et al.*, 2006; *Dubrovinsky et al.*, 2007).

Unlike experiments, theoretical calculations do not require extrapolation in modeling the state and properties of iron and iron-based alloys at conditions of the Earth's core and suggest that at sufficiently high pressures (above 100 GPa) and temperatures close to the melting point iron transforms into *bcc* structured phase (*Belonoshko et al.*, 2003). Although for pure iron this prediction has not been confirmed yet, the *hcp–bcc* transformation of the $Fe_{0.9}Ni_{0.1}$ alloy was observed at pressures above 225 GPa and temperatures over 3,400 K (*Dubrovinsky et al.*, 2007). Moreover, both experimental (*Lin et al.*, 2003) and theoretical (*Vocadlo et al.*, 2003) works point out towards stabilization of the *bcc*-structured phase due to the elements (particularly, silicon) important for the Earth's inner core chemistry.

If *bcc*-structured phase is indeed dominant in the Earth's inner core, it could help to clarify at least one of its enigmatic properties – elastic anisotropy (Figure 1b). Preferred orientation of crystals of the *hcp*-structured iron-based alloy could, in principle, explain why sound waves propagate faster along Earth's spin axis than in the equatorial plane. However, elastic anisotropy of *hcp* iron rapidly decreases with increasing temperature. In contrast, according to molecular dynamic simulations (*Belonoshko et al.*, 2008) cubic *bcc* iron is extremely anisotropic and can account for 12% of the seismic wave anisotropy sufficient for explanation of anisotropy of the inner core. Simulations reveal also that abundant grain boundaries and defects formed in *bcc* iron at high temperatures could lead to drastic decrease of the shear modulus and shear wave velocity, as compared to those estimates obtained from the averaged single-crystal values, thus providing possible explanation of low rigidity of the Earth's inner core.

5. Conclusions

The emerging picture of the Earth's core shows that it as a very dynamic region. Functioning of the geodynamo requires the outer core liquid with small enough viscosity to permit fluid motion with typical velocities of 20 km/year. Intensive convection in the outer core is powered by secular cooling which results in solidification at the inner core boundary and growth of the inner core. Preferential fractionation of elements during crystallization of the inner core changes composition, density, and chemical activity of outer core. Continuous changes of the outer core provoke its continuous reactions with the mantle and induce small-scale dynamic processes at the core–mantle boundary. Mineral physics plays a key role in providing data about the state and properties of the materials at conditions of the Earth's core. The main challenge of the studies of mineralogy of the Earth's core is to find a common ground for explanation of different,

sometimes seemingly unconnected or controversial, properties – the chemical and phase composition, temperature and the heat flow, nature of the dynamics and geomagnetism, convection and elasticity.

References

Alfè, D., M. J. Gillan, G. D. Price (2003) Thermodynamics from first principles: temperature and composition of the Earth's core. *Mineral. Mag.*, *67*, 113–123.

Antonangeli, D., Occelli, F., Requardt, H., Badro, J., Fiquet, F., Krisch, M., et al. (2004) Elastic anisotropy in textured hcp-iron to 112 GPa from sound wave propagation measurements. *Earth Planet. Sci. Lett.*, *225*, 243–251.

Badro, J., et al. (2007) Effect of light elements on the sound velocities in solid iron: Implications for the composition of Earth's core. *Earth Planet. Sci. Lett.*, *254*, 233–238.

Belonoshko, A. B., R. Ahuja, B. Johansson, (2003) Stability of the body-centred-cubic phase of iron in the Earth's inner core. *Nature*, *424*, 1032–1034.

Belonoshko, A. B., et al. (2008), Elastic anisotropy of Earth's inner core. *Science*, *319*, 797–800.

Dubrovinsky, L., et al. (2000) X-ray study of thermal expansion and phase transition of iron at multimegabar pressure. *Phys. Rev. Lett.*, *84*, 1720–1723.

Dubrovinsky, L., et al. (2007) Body-centered cubic iron-nickel alloy in Earth's core. *Science*, *316*, 1880–1883.

Dewaele, A., et al., (2006) Quasihydrostatic equation of state of iron above 2 Mbar. *Phys. Rev. Lett.*, *97*, 215504.

Lin, J.-F. et al. (2002) Iron-nickel alloy in the Earth's core. *Geophys. Res. Lett.*, *29*, 1471, doi:10.1029/2002GL015089.

Lin, J.-F., et al. (2003) Iron-silicon alloy in Earth's core? *Science*, *295*, 313–315.

Mao, W. L., et al. (2006) Phase relations of Fe-Ni alloys at high pressure and temperature. *Phys. Earth Planet. Interiors*, *155*, 146–150.

Nguyen, J. H., N. C. Homes (2004) Melting of iron at the physical conditions of the Earth's core. *Nature*, *427*, 339–341.

Takafuji, N., et al. (2005) Solubilities of O and Si in liquid iron in equilibrium with $(Mg,Fe)SiO_3$ perovskite and the light elements in the core. *Geophys. Res. Lett.*, *32*, L06313, doi:10.1029/2005GL022773.

Vocadlo, L., et al. (2003) Possible thermal and chemical stabilization of body-centred-cubic iron in the Earth's core. *Nature*, *424*, 536–539.

SYNCHROTRON-BASED SPECTROSCOPIC TECHNIQUES: MÖSSBAUER AND HIGH-RESOLUTION INELASTIC SCATTERING

JENNIFER M. JACKSON*
Seismological Laboratory, Division of Geological and Planetary Sciences, California Institute of Technology, Pasadena, CA (USA)

Abstract We summarize recent developments in selected synchrotron-based spectroscopy methods like nuclear resonant forward scattering ("synchrotron Mössbauer spectroscopy"), nuclear resonant inelastic x-ray scattering ("NRIXS"), and momentum-resolved inelastic x-ray scattering ("IXS"). The inelastic methods provide specific vibrational information, e.g., the phonon density of states, and in combination with diffraction data permits the determination of sound velocities under high pressure and high temperature. The Mössbauer method gives hyperfine interactions between the resonant nucleus and electronic environment like isomer shifts, quadrupole splittings, and magnetic fields, which provide important information on valence, spin state, and magnetic ordering. Both nuclear resonant methods use a nuclear resonant isotope as a probe and can be applied under high pressure and high temperature. The physical mechanism of the scattering processes will be discussed and several high-pressure high-temperature examples will be given.

Keywords: Synchrotron Mössbauer spectroscopy, valence states, inelastic x-ray scattering, phonon density of states, sound velocities

1. Synchrotron Mössbauer Spectroscopy (SMS)

Conventional Mössbauer spectroscopy as well as SMS are based on the often appreciable probability that the resonant nuclei absorb x-rays without participation of lattice vibrations, i.e., recoilless. Similar to conventional

* E-mail: jackson@gps.caltech.edu

E. Boldyreva and P. Dera (eds.), *High-Pressure Crystallography: From Fundamental Phenomena to Technological Applications*, DOI 10.1007/978-90-481-9258-8_5,

Mössbauer spectroscopy (MBS), the SMS method permits us to determine distortions of electronic charges at the position of the ^{57}Fe nuclei. The configuration of the electron shell and the deviation of the local environment from cubic symmetry expresses itself in two parameters that are accessible to SMS measurements, the splitting of the excited nuclear state caused by an electric-field-gradient tensor (quadrupole splitting) and a shift of the nuclear states caused by the s-electron density in the nuclear volume (isomer shift).

The comparison of the different experimental approaches of more traditional methods of MBS and SMS reduces to an evaluation of the properties of the used radiation source. Synchrotron radiation and γ-rays emitted by a radioactive source have very different properties. However, both types of sources permit Mössbauer experiments aiming at the extraction of hyperfine parameters, e.g., quadrupole splittings and isomer shifts. Synchrotron radiation is emitted in short (<100 ps) intense pulses that repeat periodically. On the other hand, the emission of photons from radioactive sources is random in time. The situation is inverted if we analyze the energy bandwidths, which are on the order of millielectronvolt for monochromatized synchrotron radiation but only about the natural line width (Γ = 4.66 neV for the 14.4125 keV resonance of the ^{57}Fe isotope) for a suitable radioactive source. This reciprocal behavior strongly suggests that the experimental techniques should be similarly reciprocal, i.e., energy-resolved spectroscopy with radioactive sources (MBS) and time-resolved spectroscopy with synchrotron radiation (SMS). Figure 1 illustrates the spectra of a material for which the iron nuclei experience a quadrupole splitting, Δ. In conventional MBS, we observe two dips separated by Δ in the energy-dependent transmission through the material. The time-dependent transmission that is observed in SMS shows oscillations with a period of $2h/\Delta$, where h is Planck's constant. In both cases, we directly obtain the quadrupole splitting from the data. Isomer shifts are only observable in a relative sense; in the case of MBS, with respect to the source emission line, and in the case of SMS, with respect to a reference absorber that must be inserted into the beam path. In comparison to the traditional Mössbauer spectroscopy, the high brilliance of the synchrotron radiation reduces the synchrotron Mössbauer data collection times tremendously, allows easier access for high-pressure studies, and reduces pressure gradients in the observed data.

For SMS measurements, the energy bandwidth of the excitation source should be as small as practicably achievable with reasonable efficiency. The high-resolution monochromator is tuned to the nuclear transition energy and kept as stable as possible. X-rays that are transmitted through the sample

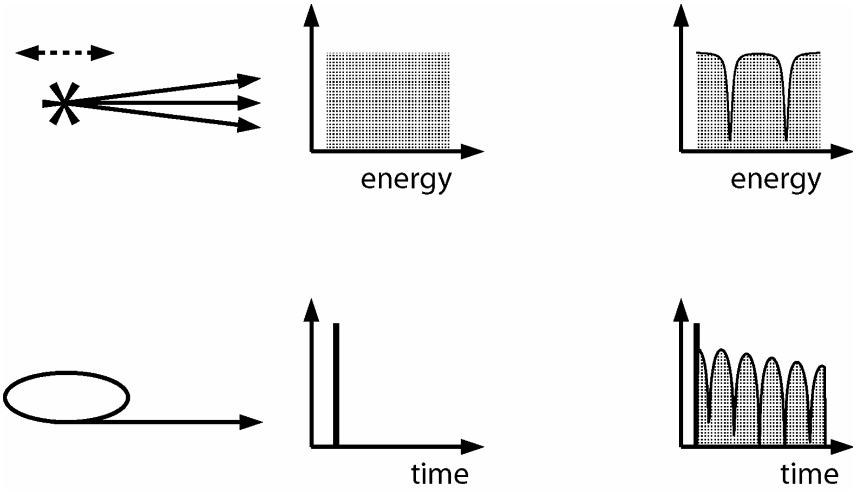

Figure 1. Reciprocal properties of radioactive sources (*top*) and synchrotron radiation (*bottom*) lead to reciprocal experimental techniques (From *Jackson et al.* (2005)).

excite the resonant nuclei coherently and are observed with an avalanche photo diode detector that is placed far enough away from the sample to avoid contamination from incoherent scattering. The delayed events are mapped as a function of elapsed time between arrival of a synchrotron radiation pulse and detection of transmitted x-ray photon – this constitutes the time spectrum of the nuclei in the sample. The delayed transmitted intensity can be expressed in terms of the nuclear contribution to the index of refraction of the sample. The reader is referred to *Sturhahn* (2000, 2004) for more details on SMS and details of data evaluation. At present, there are three facilities capable of such measurements: the European Synchrotron Radiation Facility in Grenoble (France), the Advanced Photon Source in the Chicago, IL area (USA), and the Super Photon Ring in Kansai (Japan).

1.1. VALENCE AND SPIN STATE

Most of the minerals and polymorphs expected in Earth's interior are believed to incorporate low concentrations of Fe^{2+} and/or Fe^{3+} of about 10 at% or less. They are not expected to be magnetically ordered in Earth's lower mantle because of the low Fe content and the elevated temperatures. However, valence and spin state of the Fe in minerals may still be relevant with respect to density, iron partitioning, partial melting, radiative thermal conductivity, and compositional layering. The SMS method provides quadrupole splittings and isomer shifts similarly to traditional Mössbauer spectroscopy but the high brilliance of the synchrotron radiation reduces the data

collection times tremendously, allows easier access for high-pressure studies, and reduces pressure gradients in the observed data. The assignment of a set of parameter values to valence and spin state is usually based on a fingerprinting scheme.

Recently the SMS method has been applied to silicates, oxides, and metals to pressures above 1 Mbar. For a recent review of these studies, the reader is referred to Sturhahn and Jackson (2007).

1.2. MAGNETISM

Magnetic ordering in a material causes a characteristic Zeeman splitting of the nuclear levels of the resonant isotope. The SMS time spectrum carries the signature of such a magnetic splitting. The SMS method has been used to investigate magnetism under high pressure using the ^{57}Fe isotope, the ^{151}Eu isotope, the ^{119}Sn isotope, and the ^{149}Sm isotope.

2. Nuclear Resonant Inelastic X-ray Scattering (NRIXS)

For NRIXS measurements, the energy bandwidth of the incident x-rays determines the resolution of the phonon spectra of the samples. The high-resolution monochromator is tuned around the nuclear transition energy, and the x-rays excite the resonant nuclei in the sample. The incoherently re-emitted radiation is observed with an avalanche photo diode detector that is placed as close as possible to the sample but away from any strong coherent scattering directions. The integrated delayed counting rate is recorded. The NRIXS method directly provides the Fourier-transformed self-intermediate scattering function, $S(\mathrm{k},E)$. The quasi-harmonic model of lattice vibrations is then used to extract the partial (due to information about motions of the resonant nuclei only) and projected (due to a potential angular dependence on the wave-vector, k) phonon DOS from $S(\mathrm{k},E)$. Typical acquisition times for a NRIXS spectrum range between 1 h for iron-rich samples under ambient conditions and days for dilute samples under very high pressures. The evaluation of the measured NRIXS spectra can be performed using the PHOENIX software. The reader is referred to *Sturhahn* (2000, 2004) for a theoretical and technical review on nuclear resonant inelastic scattering of synchrotron radiation. At present, there are three facilities capable of NRIXS measurements: the European Synchrotron Radiation Facility in Grenoble (France), the Advanced Photon Source in the Chicago, IL area (USA), and the Super Photon Ring in Kansai (Japan).

2.1. SOUND VELOCITIES

The starting point for sound velocity measurements is the phonon DOS that is extracted from the NRIXS data. The connection between the phonon DOS and sound velocities may not be immediately obvious. In solids, sound waves and acoustic phonons of wavelengths much larger than inter-atomic distances describe the same physical phenomenon. The "phonon-picture" emphasizes microscopic properties, like inter-atomic force constants, whereas the macroscopic descriptors like elastic moduli and density dominate the understanding of the "sound-wave picture." A quantitative description of the low-energy region of the phonon DOS provides the Debye sound velocity, V_D. For a recent review of such investigations under high-pressure, the reader is referred to Sturhahn and Jackson (2007). For an isotropic solid, the Debye sound velocity is related to the compressional, V_P, and shear, V_S, velocities, using (*Sturhahn* and *Jackson* 2007; *Jackson et al*., 2009) (Figure 2):

$$(3/V_D^3) = (1/V_P^3) + (2/V_S^3).$$

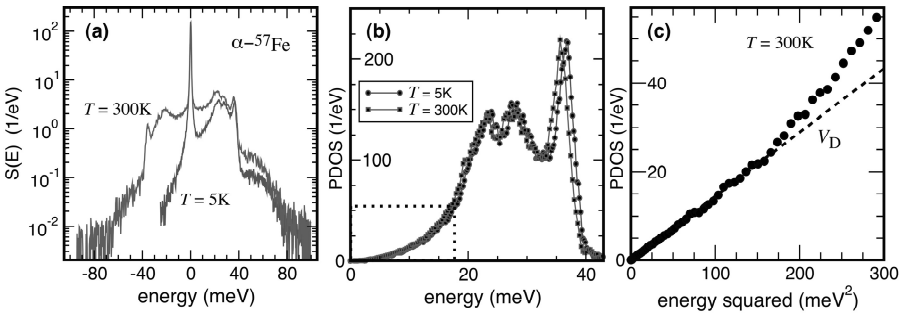

Figure 2. Typical procedure for NRIXS data collection and sound velocity analysis: (**a**) raw NRIXS spectra of polycrystalline α-iron at 300 K and at 5 K, (**b**) extraction of the phonon density of states, and (**c**) the determination of the Debye sound velocity (V_D). The decrease in intensity of the anti-Stokes scattering portion of the spectrum (left side, a) at low temperatures is due to the lower thermal vibrations in the crystal. The data points in (**c**) are taken from the PDOS within the dashed rectangle in (**b**) and are used to determine V_D (dashed straight line, c). Spectra are from *Sturhahn* (2004) and *Angel et al.* (2009).

2.2. TEMPERATURE

The NRIXS raw data has a very fundamental property which is independent of the material under investigation: the spectra follow a detailed balance principle. If the NRIXS data are given by *I(E)* with $E = 0$ as the exact nuclear transition energy, we can write

$$I(-E) = e^{-\beta E} I(E),$$

where $\beta = 1/(k_B T)$ is the inverse temperature, and k_B is Boltzmann's constant. The above relation permits us to determine the temperature of the sample from the spectral intensity ratios of phonon creation ($E > 0$) and annihilation ($E < 0$) parts (Figure 2a).

3. Momentum Resolved Inelastic X-ray Scattering (IXS)

Notes in this section are taken from portions of Jackson's contribution to *Angel et al.* (2009). The physical processes that underlie momentum resolved inelastic scattering of x-rays (IXS) are similar to those described for inelastic scattering of light (e.g., Brillouin Spectroscopy). The difference between IXS and Brillouin scattering lies in the particle probe. X-rays have shorter wavelengths ($\lambda \sim 0.1$ nm) and therefore provides access to large sections of the dispersion scheme. This is in contrast to inelastic light scattering methods such as Brillouin or Raman scattering that can only determine the acoustic and optic modes, respectively, at very long wavelengths (or small momentum transfers) close to the Brillouin zone center. IXS investigations carried out on polycrystalline samples routinely provide orientationally averaged longitudinal acoustic velocities, whereas measurements on single-crystals provide single-crystal elastic moduli.

Synchrotron x-rays with a given energy and bandwidth interact with quantized lattice vibrations (phonons) in the sample and are inelastically scattered at a known angle. Focus spot sizes are as low as 30 μm (horizontal) by 10 μm (vertical). The scattered photons are analyzed by several analyzers, which are mounted on a Rowland circle at a distance of several meters. The monochromator design, focus spot sizes, number of analyzers, and sample-to-analyzer distance varies depending on the instrument. At present, there are five instruments dedicated to IXS for the study of phonons: ID16 and ID28 at the European Synchrotron Radiation Facility in Gernoble (France), 3ID and 30ID at the Advanced Photon Source in the Chicago, IL area (USA), and BL35XU at the Super Photon Ring in Kansai (Japan). The reader is referred to *Burkel* (2001) and *Krisch et al.* (2007) for details on the theoretical background and recent status of IXS.

3.1. SOUND VELOCITIES AND ELASTIC ANISOTROPY

If the sample is a single crystal, directional dependence of the acoustic modes are obtained and with known density, the C_{ij}'s can be determined. In the cases where the sample is crystalline, the sample must be oriented on a Bragg reflection and selection rules apply. Probing phonon excitations using IXS requires a relative high energy resolution of at least $\Delta E/E = 10^{-7}$.

The acoustic modes are determined by probing their respective phonon dispersion curves close to the Brillouin zone center. In order to obtain accurate sound velocities from the slopes of these phonon dispersion curves, the energy resolution must be high ($\sim 10^{-9}$ eV) at low-energy transfer (near the Brillouin zone center). Therefore, practical use of IXS to determine the sound velocities of materials has only been made possible in the last decade due to advances in x-ray optics and the advent of third generation synchrotron sources.

Together with the extraction of the sound velocities and known density, the single-crystal elastic moduli may be determined with a high degree of accuracy and therefore provide direct information on elastic anisotropy. Aggregate elastic properties can also be obtained from polycrystalline samples, but is generally restricted to the longitudinal acoustic mode due to lower signal to noise ratios (see *Bosak et al.*, 2007). A lower resolution ($>10^{-9}$ eV) could be employed if the studies are not aimed at obtaining sound velocities, but rather the general shape of the dispersion curve.

In general, the higher the resolution is, the longer the collection times are. IXS measurements can be performed on very small sample volumes ($\sim 10^{-4}$ mm^3) that can be optically transparent or opaque. The scattering cross-section is a function of absorption coefficient (μ), physical density, and probing energy. The optimal signal for DAC experiments is generally obtained if the absorption length ($t = 1/\mu$) is of the order of 10–40 μm, which span elements with Z between 30 and 50. IXS has proven to be successful for samples in DACs with lower and higher Z (see *Antonangelli et al.*, 2004 for recent reviews).

References

Angel R., Jackson, J.M., Speziale, S., and Reichmann, H-J., (2009), Elasticity measurements of minerals: A review. *European Journal of Mineralogy*: *HP-HT Mineral Physics: Implications for Geosciences*, doi:10.1127/0935-1221/2009/0021-1925.

Antonangeli, D., Occelli, F., Requardt, H., Badro, J., Fiquet, G., and Krisch, M., (2004), Elastic anisotropy in textured hcp-iron to 112 GPa from sound wave propagation measurements. *Earth and Planetary Science Letters*, 225(1–2):243–251.

Bosak, A., Krisch, M., Fischer, I., Huotari, S., and Monaco, G., (2007), Inelastic x-ray scattering from polycrystalline materials at low momentum transfer. *Physical Review B*, 75(064106).

Burkel, E., (2001), Determination of phonon dispersion curves by means of inelastic x-ray scattering. *Journal of Physics: Condensed Matter*, 13:7627–7644.

Jackson, J.M., Hamecher, E.A., and Sturhahn, W., (2009): Nuclear resonant X-ray spectroscopic study on (Mg,Fe)SiO_3 orthoenstatites, *European Journal of Mineralogy*; *HP-HT Mineral Physics: Implications for Geosciences*, doi:10.1127/0935-1221/2009/0021-1932.

Jackson, J.M., Sturhahn, W., Shen, G., Zhao, J., Hu, M., Errondonea, D., Bass, J.D., and Fei, Y., (2005), A synchrotron Mössbauer spectroscopy study of (Mg,Fe)SiO_3 perovskite up to 120 GPa. *American Mineralogist*, 90:199–205.

Krisch, M., and Sette, F., (2007), *Inelastic x-ray scattering from phonons.* In M. Cardona, and R. Merlin, Eds. Light Scattering in Solid IX, 108, pp. 317–370. Springer-Verlag Berlin, Heidelberg.

Sturhahn, W., (2000), CONUSS and PHOENIX: Evaluation of nuclear resonant scattering data. *Hyperfine Interactions*, 125:149–172.

Sturhahn, W., (2004), Nuclear resonant spectroscopy. *Journal of Physics: Condensed Matter*, 16:5497–5530.

Sturhahn, W., and Jackson, J.M., (2007), *Geophysical applications of nuclear resonant spectroscopy.* In E. Ohtani, Ed. Advances in High-Pressure Mineralogy, 421, pp. 157–174. The Geological Society of America, Washington DC.

HIGH-PRESSURE X-RAY ABSORPTION SPECTROSCOPY: APPLICATION TO THE LOCAL ASPECTS OF PHASE TRANSITIONS IN FERROELECTRIC PEROVSKITES

JEAN-PAUL ITIE[1,*], ANNE-MARIE FLANK[1], PIERRE LAGARDE[1], SYLVAIN RAVY[1], ALAIN POLIAN[2]
[1]*Synchrotron SOLEIL, L'Orme des Merisiers, St Aubin, BP48, 91192 Gif-sur-Yvette Cedex, France,* [2]*PMD, IMPMC, CNRS UMR 7590, Université P. et M. Curie-Paris 6, 140 rue de Lourmel 75015 Paris France*

Abstract X-ray absorption spectroscopy (XAS) provides information on the local order around a given atom. Under high pressure, this technique has been shown to be very sensitive to phase transitions. The evolution of the local structure of ferroelectric titanates under high pressure is obtained using XAS showing that the Ti atom remains out of the center of the surrounding oxygen octahedron just above the transition to the cubic structure and goes to the center at higher pressure. For $BaTiO_3$ this effect is directly related to the lost of diffuse lines observed in the x-ray diffraction pattern.

Keywords: High pressure, ferroelectrics, x-ray absorption spectroscopy, titanate

1. Introduction

The phase diagram of titanate perovskites in the PT plane is extremely rich and is dominated by the competition between the ferroelectric and the antiferrodistorsive instabilities. The first one corresponds to the displacement of the Ti atom from the centre of the oxygen octahedron while the second one is related to the rotation and/or the tilt of the oxygen octahedra.

From the "long-range point of view", these instabilities induce phase transitions to lower symmetry structures as observed by x-ray or neutron

*E-mail: jean-paul.itie@synchrotron-soleil.fr

E. Boldyreva and P. Dera (eds.), *High-Pressure Crystallography: From Fundamental Phenomena to Technological Applications*, DOI 10.1007/978-90-481-9258-8_6,

diffraction. Therefore these techniques are very sensitive to the antiferrodistorsive instability. But diffraction provides information averaged over a large number of unit cells and does not reflect always what the local situation is. On the contrary, x-ray Absorption Spectroscopy (XAS) is a local probe (*Lytle et al.*, 1975; *Sayers et al.*, 1971; *Stern et al.*, 1975) and is able to provide valuable information around a given atom (Ti in our case), which can be directly related to the ferroelectric instability and its evolution with pressure (*Itie et al.*, 2006; *Jaouen et al.*, 2007). Therefore the two techniques are complementary for the study of perovskites under pressure.

In Section 2 we will give an introduction to XAS. Section 3 will be devoted to the analysis of the pre-edge part of the absorption spectrum of titanate perovskites at the Ti K edge in relation to the off-centre position of Ti with respect to the oxygen octahedron. In Section 4 we will discuss the effect of pressure on the XAS spectra of titanate perovskites. Section 5 will show the relation between the diffuse scattering lines observed for some perovskites and the local ferroelectricity. Conclusion and perspectives will be presented in Section 6.

2. X-ray Absorption Spectroscopy

2.1. ATOMIC ABSORPTION

X-ray absorption spectroscopy, as any absorption measurement, is in fact a measure of the transmission of a given sample, i.e. the ratio between the number of photons before and after the sample. If we call I_0 the current before the sample and I_1 the current after the sample, the transmission T is written as

$$T = I_1 / I_0 \tag{1}$$

The transmission is related to the absorption coefficient α (or absorption cross section) by

$$T = e^{-\alpha d} \tag{2}$$

d being the thickness of the sample.

Combining Eqs (1)–(2) we obtain:

$$\alpha = \ln(I_0 / I_1) \tag{3}$$

For a given element, we observe as a function of the incident photons some discontinuities in the absorption cross-section. These discontinuities are related to the extraction of an electron from a deep atomic shell. This is possible if the energy of the incident photons is superior or equal to the

binding energy of the electron. The interaction between the photon and the electron is larger when the energy of the photon is close to the binding energy (resonance phenomena). Then the absorption decreases slightly with increasing photon energy. For the different atomic shells that constitute the atom (1s, 2s, $2p_{1/2}$, $2p3_{/2}$, 3s, $3p_{1/2}$, $3p_{1/2}$, $3d_{1/2}$ $3d_{3/2}$, $3d_{5/2}$, …) we observe a succession of discontinuity defined as absorption edges (respectively K, L_1, L_2, L_3, M_1, M_2, M_3, M_4, M_5, …).

The absorption of silver is shown in Figure 1.

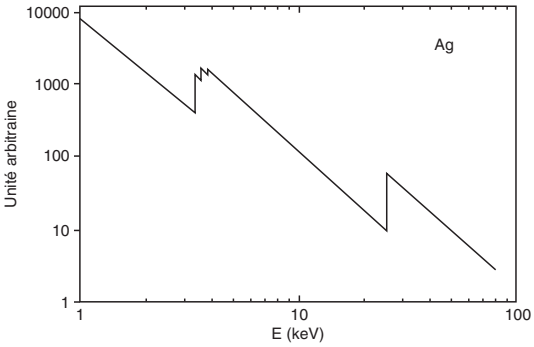

Figure 1. X-ray absorption of Ag function of the photon energy.

The binding energy of an electron of a given atomic shell depends on the interaction between this electron and the core and the other electrons. Therefore this energy is a fingerprint of the considered atom.

2.2. FINAL STATE EFFECTS

We have seen that the absorption of x-ray photons in a material presents some discontinuities called absorption edge related to the extraction of an electron from a deep atomic shell of a given atom. The absorption edge depends on the initial state of the extracted electron (through the nature of the shell from where the electron is extracted). We can also ask what happens to the electron after the extraction and if it has the possibility to go anywhere. The initial state of the electron has a given energy and a given symmetry. In order to be extracted it must interact with the photon. Moreover, there are some constrains limiting its ability to go into another state defined by a given energy and a given symmetry:

- The final state must be empty.
- The final state must be compatible in terms of symmetry and energy with the interaction between the photon and the electron. This interaction can be treated in the dipolar approximation. Within this approximation, some selection rules can be applied. Going from an *s* level, the final

state must have p symmetry for example. These rules are called the dipolar selection rules.

If we apply these rules for the K edge of germanium (Figure 2), we see that the *4p* levels are not filled and in this case we expect a large absorption of the x-rays corresponding to the transition of an electron from an *1s* state to a *4p* state (this absorption is called the white line).

At higher energy, the empty states of the atoms are mixed and form what is called the continuum. The transition of an electron toward the continuum is always allowed because the states are empty and include all the symmetries (*s,p,d,…*). Therefore we see that the discontinuities are slightly more complicated and can differ depending on the nature of the edge, the existence or not of binding states with the good symmetry (compatible with the selection rules) that do not belong to the continuum.

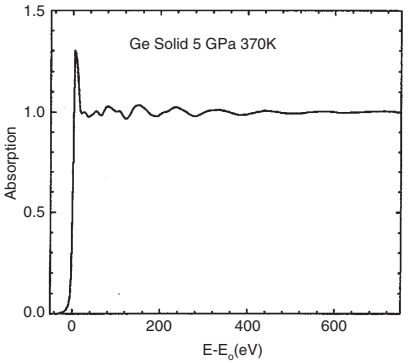

Figure 2. X-ray absorption spectrum of germanium.

In the case of rare gas (Kr) and for the K edge, the first free states do not have the good symmetry (the *4p* states are full for Kr) and the absorption does not show a strong absorption (white line) in the gas phase (see Figure 3).

The x-ray absorption depends on the initial and on the final state and on the interaction process between the incident photon and the electron. The existence of localised states in energy (binding states) with symmetry compatible with the selection rules will modify the intensity of the absorption at this energy. The binding states are strongly influenced by the existence of an atomic bonding between two (or more) atoms. From the same edge, we will have different forms of absorption spectrum for an isolated atom (gas form) or for an atom, which is bound with other atoms. Here we begin to see the sensitivity of the x-ray absorption to the neighbours (nature of the neighbouring atoms and type of bonding). A good example is given in Figure 3 where the x-ray absorption spectrum of krypton at the K edge of Kr is shown at different pressures and therefore for different forms of

krypton: gas, liquid, solid. One can notice some modulation of the absorption edge in the liquid and in the solid phase with a larger intensity. An onset of a white line is already seen in the liquid phase and becomes more important in the solid phase.

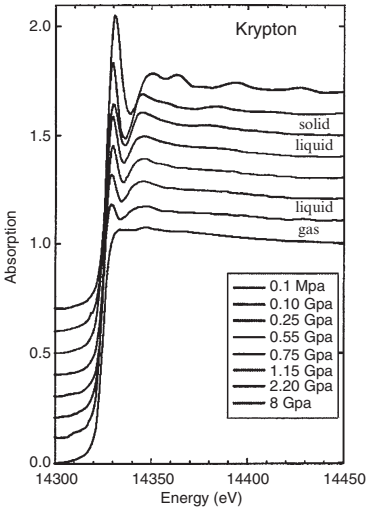

Figure 3. Evolution of the x-ray absorption spectrum of krypton in the gas, liquid and solid phases.

2.3. FROM THE FERMI GOLDEN RULE TO THE EXAFS FORMULA

In a quantum mechanical formalism the absorption phenomena can be described by the Fermi golden rule

$$\alpha = 4\pi^2 n\left(e^2/\hbar c\right)\sum\left|\left\langle i\left|\vec{E}.\vec{r}\right|f\right\rangle\right|^2 \delta\left(E_i+\hbar\omega-E_f\right) \tag{4}$$

- n is the atom density.
- $|i\rangle$ is the wave function of the electron in the initial state.
- $|f\rangle$ is the wave function describing the final state of the electron ejected from the atom.
- $\vec{E}.\vec{r}$ is the interaction Hamiltonian in the dipolar approximation.
- δ (x) is the Dirac function.

The oscillating part χ(E) of the absorption coefficient is defined by

$$\chi(E)=\frac{\alpha(E)-\alpha_0(E)}{\alpha_O(E)} \tag{5}$$

Using Eq (4) it can be shown, in the plane wave approximation, that

$$\chi(k)=-\frac{1}{k}\sum_j N_j \frac{F_j(\pi,k)}{R_j^2}\sin(2kR_j+\theta_j)\exp(-2\sigma_j^2k^2)\exp(-\frac{2R_j}{\lambda(k)}) \qquad (6)$$

where k is defined by $\frac{\hbar k^2}{2m}=E-E_0$, E_0 being the threshold energy, F_j (π, k) is the backscattering amplitude, θ_j is the phase function, λ the mean free path of the photoelectron, N_j the number of neighbours at the distance R_j, σ_j the pseudo Debye–Waller factor which measures both static and dynamic disorder.

3. The Pre-edge Part of the Absorption Spectrum of Titanate at the Ti K edge

3.1. QUALITATIVE INTERPRETATION OF THE PRE-EDGE FOR TITANATE PEROVSKITES

Figure 4 shows the pre-edge of $SrTiO_3$ at room pressure in the cubic phase. The spectrum has been recorded on the LUCIA beamline (*Flank et al.*, 2006) at SLS, PSI. Three pre-edge features labelled A, B, C (C_1 and C_2) are clearly observable.

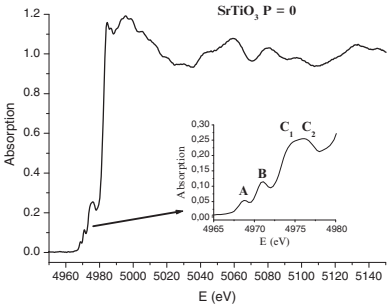

Figure 4. XAS spectrum of $SrTiO_3$ at the Ti K edge at room pressure. The insert shows the pre-edge part.

Depending on the material, the intensities of these features vary strongly (*Vedrinskii et al.*, 1998) (Figure 5). For $PbTiO_3$ and $BaTiO_3$, which are ferroelectric materials with a tetragonal distortion of the cubic structure, the B feature is intense while for $SrTiO_3$, $CaTiO_3$ and $EuTiO_3$, which are not ferroelectrics with a cubic or an orthorhombic structure, the same feature is weak. Therefore, it appears that the intensity of the B feature in titanate perovskite can be used as a measure of the ferroelectric distortion around the Ti atom, at the atomic scale since XAS is a local probe.

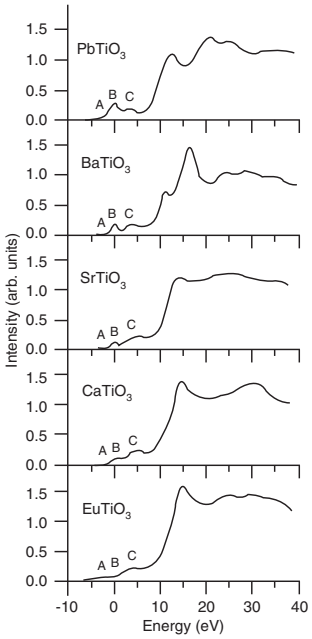

Figure 5. Pre-edge part of the XAS Ti K edge for various titanate perovskite (*Vedrinskii et al.*, 1998).

3.2. ORIGIN OF THE PRE-EDGE FEATURES IN TITANATE PEROVSKITES

The origin of the pre-edge features has been recently discussed in many papers (*Fujita et al.*, 2004; *Nozawa et al.*, 2005; *Tanaka et al.*, 2005; *Yamamoto et al.*, 2004). As we will see, using recent codes (*Cabaret et al.*, 2007; *Joly*, 2001) it becomes possible to reproduce these features. However, while in the Section 1 we have been able to reproduce the EXAFS oscillations in the dipole approximation, here we need to include also the quadrupole contributions to the absorption spectrum. This will modify slightly the selection rules, allowing transition from *1s* to *3d* for the transition metals K edge. In order to attribute the origin of the pre-edge features we will follow the calculations performed by *Cabaret et al*. (2007), using a plane wave electronic structure code based on density functional theory in the local density approximation, in which the calculation of x-ray absorption spectra in electric dipole (E_1) and quadrupole (E_2) approximations has been implemented (*Cabaret et al.*, 2005; *Taillefumier et al.*, 2002). The results of the calculation for $SrTiO_3$ in a non-distorted cubic structure are shown in Figure 6.

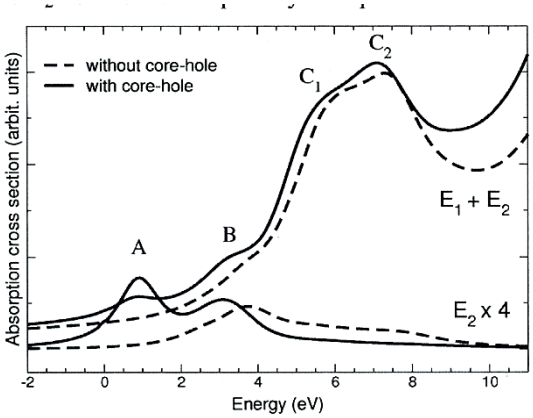

Figure 6. Calculated Ti K-pre-edge (*Cabaret et al.*, 2007) with and without core-hole for the cubic ambient phase of $SrTiO_3$. The total cross section is labeled E_1+ E_2 and the isotropic E_2 quadrupole contribution is multiplied by a factor 4.

From the comparison with the experimental curve (insert of Figure 4), it appears that the core-hole interaction has to be taken into account to reproduce the features A and B. These features come from the quadrupole contribution (*1s-3d*). The C features are also well reproduced and come from E_1 contribution due to the empty *p* states of Ti absorbing atom hybridized with the $3d$-e_g states of neighbouring Ti via O-*p* states. The feature B has also a very weak E_1 contribution resulting from the hybridization of *p* states of absorbing Ti and $3d$-t_{2g} states of neighbouring Ti. Still, the intensity of the feature B remains too small as compared to the experimental one. When Ti is not in a centrosymmetric site, the mixing between *p* and $3d$-e_g states of absorbing Ti becomes allowed and the intensity of the feature B increases. This is illustrated in Figure 7, which shows the calculated spectra obtained

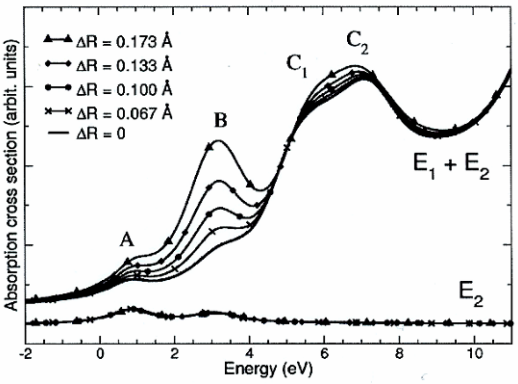

Figure 7. Theoretical spectra (*Cabaret et al.*, 2007) of Ti K-pre-edge for $SrTiO_3$ with various off-site Ti positions. ΔR is the shift of Ti along the [111] direction.

when Ti is displaced along the [111] direction. An assumption of a displacement of 0.1 Å is sufficient to reproduce the experimental spectrum, in agreement with recent EXAFS analysis (*Kodre et al.*, 2007) where a value of 0.08 Å has been found.

4. High Pressure Effect on the Ti K-pre-edge of Titanate Perovskites

4.1. EXPERIMENTAL

All the experiments at the Ti K edge have been performed at the LUCIA beamline of SLS (PSI, Switzerland) or on the ID12 beamline of ESRF (Grenoble, France). The main advantages of this beamline were a very small spot size (<5*10 μm^2 FWHM), a high flux (2 10^{11} ph/s/0.1%bw) in the x-ray spot and a high stability of the beam (<1 μm) during the energy scan. Absorption measurements have been done in transmission under vacuum in order to avoid the air absorption. Due to the strong absorption of the x-rays by the diamond at the energy of the Ti K edge (4.966 keV), a specific diamond anvil cell with mini diamonds (0.5 mm thick each with a total transmission at 5 keV equal to 2 10^{-3}) mounted on perforated diamonds (*Dadashev et al.*, 2001; *Itie et al.*, 2005, 2007) has been used. Pressure has been measured using the ruby scale.

4.2. RESULTS

4.2.1. *$CaTiO_3$*

Figure 8 shows the results obtained for $CaTiO_3$ at the Ti K edge up to 8.4 GPa. A small shift of the XANES peaks due to the pressure induced shortening of the interatomic distance is observed. But in the pre-edge part of the absorption spectrum there is no pressure effect, both in the intensities and in the position of the features. In this compound the Ti atom is at the centre of the oxygen octahedron at ambient pressure and remains in its position whatever the pressure is.

4.2.2. *$SrTiO_3$*

$SrTiO_3$ has been studied both on single crystals and on powder samples. Two phase transformation have been observed, the first one above 5 GPa and the second one close to 14 GPa. Strong modifications of the absorption spectrum are observed as shown in Figures 9 and 10. The first transition corresponds to the onset of the antiferrodistorsive instability, which leads to a small rotation of the oxygen octahedra. At the transition a decrease of the B feature intensity occurs (Figure 9), which indicates, that in the new phase

the Ti atom shifts to the center of the oxygen octahedron. The increase in the C feature intensity is correlated to the modification of the Ti-O-Ti path due to the rotation of the octahedra (the C features correspond to the dipole transition 1s-p, the p states of the absorbing Ti being hybridized with the 3d e_g states of the neighboring Ti).

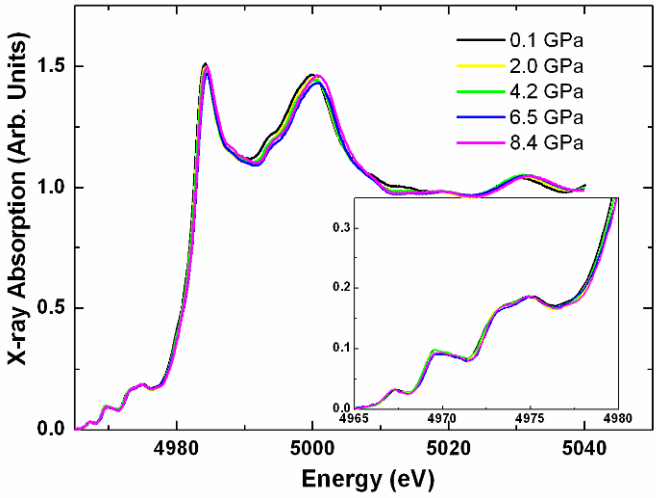

Figure 8. Experimental Ti K-XANES for $CaTiO_3$ at various pressures. Insert shows pre-edge features.

At higher pressure a second transition is observed. At Figure 10, we can see that the XANES part of the spectrum has changed and that there are some modifications in the pre-edge (see insert of Figure 10). The EXAFS part is quite similar with a large shift to higher energy of the oscillations, which indicates, that there is a shortening of the interatomic distances, and that the local environment of the Ti atom does not change drastically. The pre-edge modifications affect the feature A which has been described (see Section 3.2) as a transition from *1s* to *3d*-t_{2g}. It seems that the energy splitting between t_{2g} and e_g *d* levels has increased in the new phase. The C features are also different which indicate that there are some modifications in the Ti–Ti interaction.

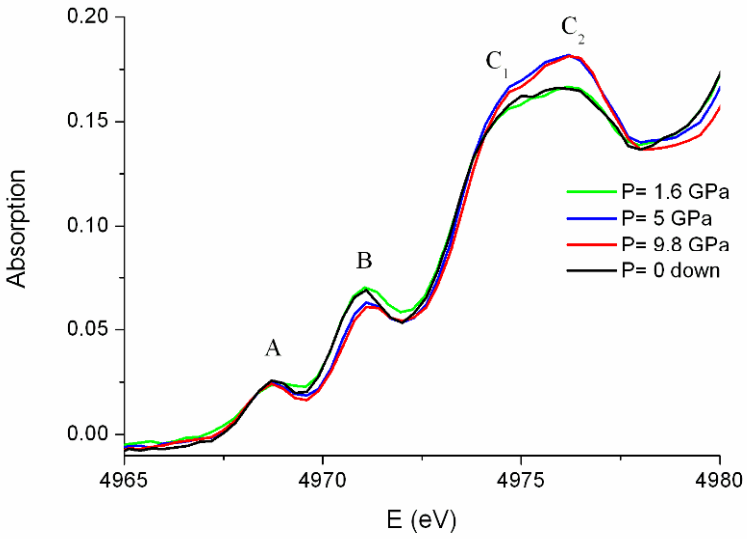

Figure 9. Evolution of the pre-edge part of the absorption spectrum for $SrTiO_3$ with pressure.

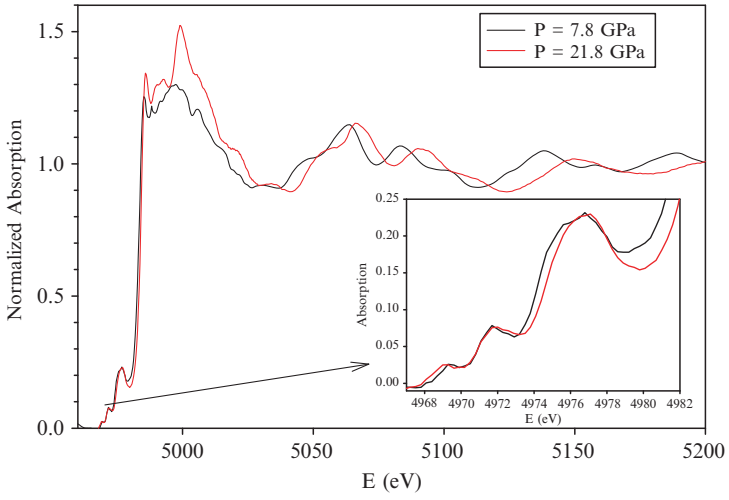

Figure 10. Comparison of the XAFS spectrum at the Ti K edge for $SrTiO_3$ at 7.8 GPa (black line) and 21.8 GPa (red line). The insert shows the pre-edge part of the spectrum.

4.2.3. *$BaTiO_3$*

At room pressure, $BaTiO_3$ is ferroelectric and crystallizes in a tetragonal structure. At 2 GPa a transition to a cubic structure occurs (*Ishidate et al.*, 1997; *Pruzan et al.*, 2002; *Venkateswaran et al.*, 1998) with a lost of the

ferroelectricity. Figure 11 shows the evolution with pressure of the Ti K pre-edge for $BaTiO_3$. A strong decrease in the intensity of the feature B is observed up to 10 GPa. Then the intensity remains constant up to the highest pressure. Following the interpretation of the pre-edge features, this result indicates, that at the transition to the cubic non-ferroelectric phase, the Ti atom remains off- centre with respect to the oxygen octahedron. With increasing pressure the Ti atom shifts to the centre of the oxygen octahedron, i.e. to the position, which is reached at 10 GPa. Above this pressure the Ti atom remains at the centre.

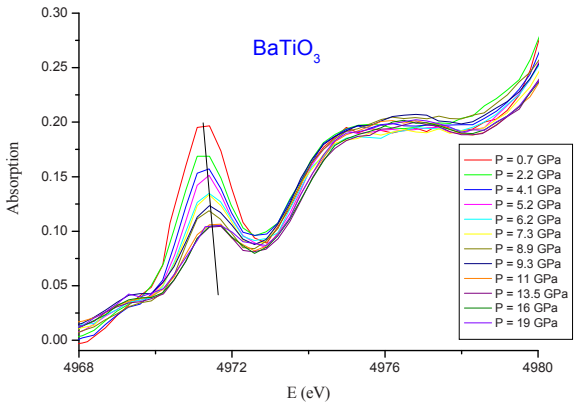

Figure 11. Evolution of the pre-edge part of the absorption spectrum for $BaTiO_3$ with pressure.

Because the structure above 2 GPa is cubic, the off-centre position of the Ti atom must be disordered (if it were ordered, we should have at least a tetragonal distortion). In fact the cubic structure can be seen as an average of a local tetragonal distortion. This can explain, why the thermal parameter for the Ti atom in the high pressure cubic structure is larger than the same one in the tetragonal structure (*Hayward et al.*, 2005). It is also noticeable, that under pressure the Ti atom shifts to the center of the oxygen octahedron. At high temperature, where a similar cubic structure is observed, this is not the case: the Ti remains off-centre, whatever the temperature is.

4.2.4. *$PbTiO_3$*

Similarly to $BaTiO_3$, $PbTiO_3$ is ferroelectric at room pressure, but in this compound both Pb and Ti contribute to the polarization. Under pressure, close to 11 GPa, a phase transformation to a cubic structure occurs (*Sani et al.*, 2002). This can be observed also by the modification of the Ti K-pre-edge features (*Jaouen et al.*, 2007). These features have been simulated using the FDMNES code (*Joly*, 2001) (Figure 12), showing that on the transition

to the cubic phase the Pb atoms shift in the oxygen plane and the Ti atom remains slightly out of the centre of the oxygen octahedron (Figure 13). The increase of the δ' feature is due to the shift of the Pb atom, while the decrease of the β (B) feature is due to the centering of the Ti atom. As for $BaTiO_3$, the Ti atom goes to the centre of the oxygen octahedron at higher pressure (>15 GPa) and remains in this position between 20 and 30 GPa, what excludes the reappearance of the ferroelectricity in this pressure range.

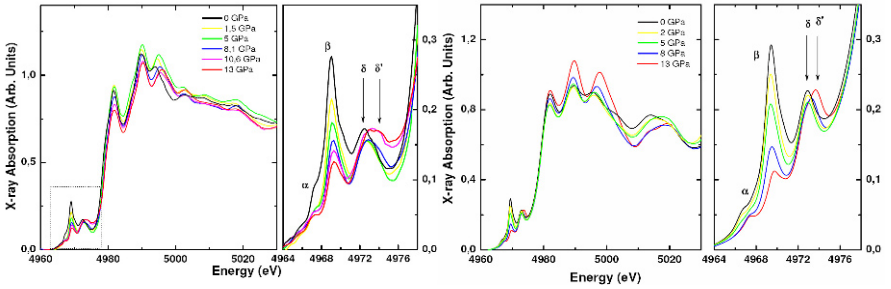

Figure 12. Evolution with pressure of the experimental (*left*) and calculated (*right*) Ti K-pre-edge for $PbTiO_3$.

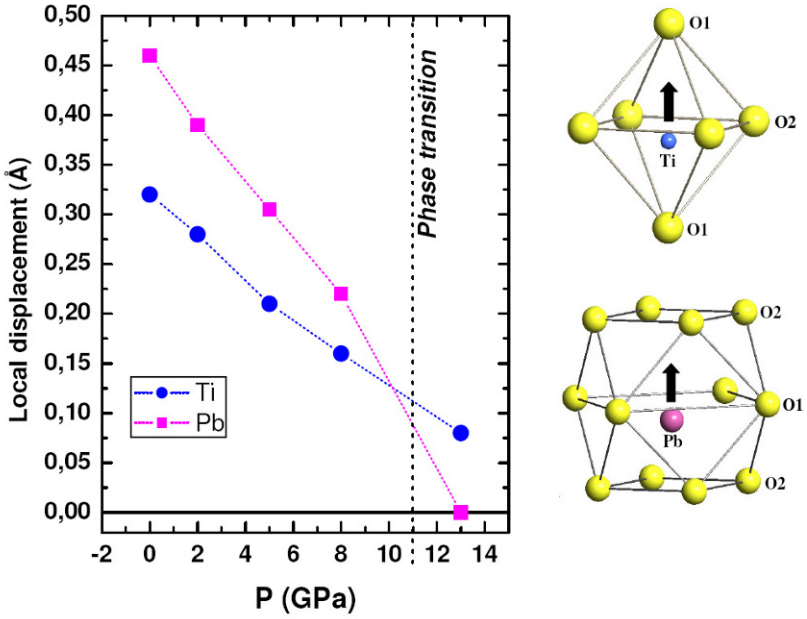

Figure 13. Variation with pressure of the local displacement of Pb and Ti in $PbTiO_3$ (*Jaouen et al.,* 2007).

5. Diffuse Lines of $BaTiO_3$ Under High Pressure

The diffraction pattern of $BaTiO_3$ exhibits diffuse lines both in the tetragonal phase at room temperature and in the cubic phase at high temperature (*Comes et al.*, 1970). These diffuse lines are related to the displacement of the Ti atoms with respect to the centre of the pseudo cubic unit cell, but it is not clear, if this displacement is static or dynamic. Recently (*Ravy et al.*, 2007), the diffuse scattering lines have been recorded as a function of pressure and it has been shown, that their intensity decreases with increasing pressure and that they vanish close to 11 GPa (Figures 14 and 15). These results are in perfect agreement with Ti K-the pre-edge measurements.

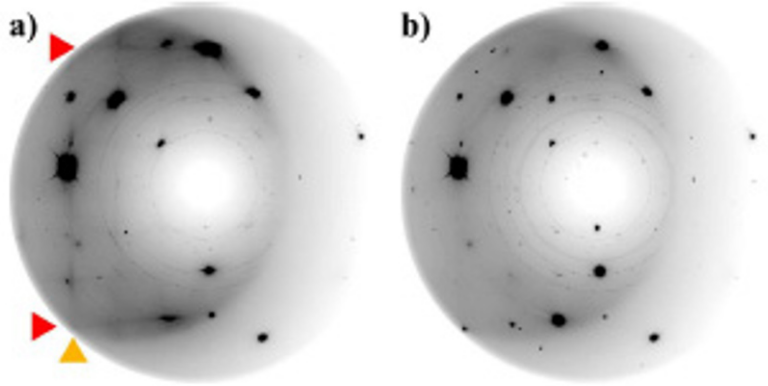

Figure 14. Diffraction pattern of $BaTiO_3$ at (**a**) 2.6 GPa and (**b**) 11.3 GPa. The arrows point to (010) and (100) diffuse lines.

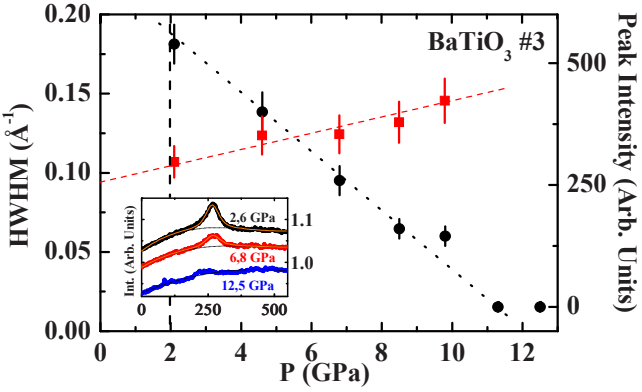

Figure 15. Pressure dependence of the peak intensity (*right scale*) and the HWHM (*left scale*) of the diffuse lines of $BaTiO_3$. Lines are guide for the eyes. The vertical line indicates the tetragonal cubic transition pressure. The insert shows the profiles of the diffuse lines at 2.6, 6.8 and 12.5 GPa.

The decrease in the intensity of the diffuse lines corresponds also to the decrease of the feature B in the pre-edge part of the absorption spectrum (Figure 16). Therefore, the diffuse lines exist, when the Ti is off-centre and vanish, when the Ti shifts to the center of the oxygen octahedron. From the absorption measurement we can say, that the Ti displacement is essentially static.

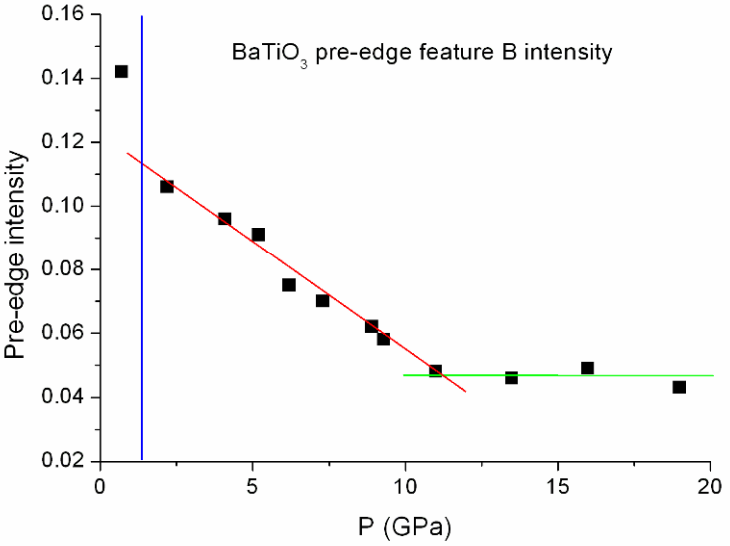

Figure 16. Evolution with pressure of the intensity of Ti K-pre-edge feature B.

6. Conclusion and Perspectives

We have shown, that ferroelectricity in titanate perovskite can be suppressed by the application of pressure. The pre-edge part of the absorption spectrum has been used to follow the pressure-induced transformation. XAS is not limited to this part of the spectrum. In many other cases, XANES or EXAFS are very useful to follow pressure-induced modifications (*Itie*, 1992; *Itie et al.*, 1993, 1997).

In this paper we have also demonstrated one of the most interesting features of the high-pressure experiments: a phenomenon observed at ambient pressure (in our case – the existence of diffuse lines in the diffraction pattern) can be "killed" by the application of high pressure (disappearance of these diffuse lines). Under the same conditions another observation (the intensity of the pre-edge feature B decreases with pressure) is made and is correlated to the first one. Therefore, the explanation of the second observation gives

the explanation of the first one as well. Application of high pressure allows one to interpret a phenomenon, which exists under ambient conditions, but which cannot be explained if we have the data at these ambient conditions only. Pressure is more efficient than temperature, because pressure acts on the volume (which can be determined quite easily) while temperature acts on the entropy (which is more difficult to measure).

References

Cabaret, D., Gaudry, E., Taillefumier, M., Sainctavit, P., and Mauri, F., 2005, Calculation with an efficient "non muffin-tin" method: application to the angular dependence of the Al K-edge in corundum, *Physica Scripta, Proc. XAFS-12 conference* **T115**: 131–135.

Cabaret, D., Couzinet, B., Flank, A.M., Itié, J.P., Lagarde, P., and Polian, A., 2007, Ti K pre-edge in $SrTiO_3$ under pressure: experiments and full-potential first-principles calculations. 13th International conference on X-ray absorption fine structure - XAFS13 - Stanford (US), 9–14 July 2006, AIP Conference Proceedings, **882**: 120–122.

Comes, R., Lambert, M., and Guinier, A., 1968, The chain structure of $BaTiO_3$ and $KNbO_3$. *Solid State Com*. **6**: 715–719.

Comes, R., Lambert, M., and Guinier, A., 1970, Désordre linéaire dans les cristaux (cas du silicium, du quartz, et des pérovskites ferroélectriques). *Acta Cryst. A* **26**: 244–254.

Dadashev, A., Pasternak, M. P., Rozenberg G. Kh., and Taylor, R.D., 2001, Applications of perforated diamond anvils for very high-pressure research. *Rev. Sci. Instr*. **72**: 2633–2637.

Flank, A.-M., Cauchon, G., Lagarde, P., Bac, S., Janousch, M., Wetter, R., Dubuisson, J.-M., Idir, M., Langlois, F., Moreno, T., and Vantelon, D., 2006, LUCIA, A Microfocus soft XAS beamline. *NIM Phys. Res. B* **246**: 269–274.

Fujita, M., Nakamatsu, H., Sugihara, S., Aihara, J., and Sekine, R., 2004, Origin of Low-Energy peaks in the Ti-K XANES spectra of $SrTiO_3$ and $CaTiO_3$. *J. Comput. Chem. Jpn.* **3**(1): 21–26.

Hayward, S.A., Redfern, S.T., Stone, H.J., Tucker, M.G., Whittle, K.R., and Marshall, W.G., 2005, Phase transitions in $BaTiO_3$: a high-pressure neutron diffraction study. *Z. Kristallogr.* **220**: 735–739.

Ishidate, T., Abe, S., Takahashi, H., and Mori, N., 1997, Phase Diagram of $BaTiO_3$. *Phys. Rev. Lett*. **78**(12): 2397–2400.

Itié, J.P., 1992, X-ray absorption spectroscopy under high pressure. *Phase Trans*. 39 (1–4): 81–98.

Itié, J.P., San-Miguel, A., and Polian, A., 1993, Contribution of XAFS to the understanding of material behavior under high pressure. *Jpn J. Appl. Phys*. **32**(Suppl.2): 711–715.

Itié, J.P., Polian, A., Martinez, D., Briois, V., DiCicco, A., Filipponi, A., and San-Miguel, A., 1997, X-ray absorption spectroscopy under extreme conditions. *Journal de Physique IV France* **7**: C2-31–C2-38.

Itié, J.P., Baudelet, F., Congeduti, A., Couzinet, B., Farges F., and Polian, A., 2005, High pressure x-ray absorption spectroscopy at lower energy in the dispersive mode: application to Ce and $FePO_4$. *J. Phys.: Condens. Matter*. **17**(11): S883–S888.

Itié, J.P., Couzinet, B., Polian, A., Flank, A.M., and Lagarde, P., 2006, Pressure-induced disappearance of the local rhombohedral distortion in BaTiO3. *Europhys. Lett*. **74**: 706–711.

Itié, J.P., Flank, A.M., Lagarde, P., Polian, A., Couzinet, B., & Idir, M. Extension to low energies (<7keV) of high-pressure X-ray absorption spectroscopy. Ninth international conference on synchrotron radiation instrumentation Daegu (KO) 28 May–2 June 2006, AIP Conference Proceedings 2007, **879**: 1329–1332.

Jaouen, N., Dhaussy, A.C., Itié, J.P., Rogalev, A., Marinel, S., and Joly, Y., 2007, High-pressure dependent ferroelectric phase transition in lead titanate. *Phys. Rev. B.* **75**: 224115.

Joly, Y., 2001, X-ray absorption near-edge structure calculations beyond the muffin-tin approximation. *Phys. Rev. B*. **63**: 125120.

Kodre, A., Arcon, I., Gomilsek, J.P., and Zalar, B., 2007, EXAFS study of disorder in $SrTiO_3$ perovskite, AIP Conference Proceedings, X-ray absorption fine structure – XAFS13, edited by B. Hedman and P. Pianetta, American Institute of Physics 978-0-7354-0384-0/07, Melvile, New York, **882**: 481–483.

Kornev, I.A., Bellaiche, L., Bouvier, P., Janolin, P.E., Dkhil, B., and Kreisel, J., 2006, Ferroelectricity of perovskites under pressure. *Phys. Rev. Lett*. **95**: 196804.

Lytle, F.W., Sayers, D.E., and Stern, E.A., 1975, Extended X-ray-absorption fine-structure technique. II. Experimental practice and selected results. *Phys. Rev. B* **11**: 4825–4835.

Nozawa, S., Iwazumi, T., and Osawa, H., 2005, Direct observation of the quantum fluctuation controlled by ultraviolet irradiation in $SrTiO_3$. *Phys. Rev. B.* **72**: 121101.

Pruzan, Ph., Gourdain, D., Chervin, J.C., Canny, B., Couzine, B., and Hanfland, M., 2002, Equation of state of $BaTiO_3$ and $KNbO_3$ at room temperature up to 30 GPa. *Sol. Stat. Com.* **123**(1–2): 21–26.

Ravy, S., Itié, J.P., Polian, A., and Hanfland, M., 2007, High-pressure study of X-ray diffuse scattering in ferroelectric perovskites. *Phys. Rev. Lett.* **99**: 117601.

Sani, A., Hanfland, M., and Levy, D., 2002, The equation of state of $PbTiO_3$ up to 37 GPa: a synchrotron X-ray powder diffraction study. *J. Phys. Condens. Matter.* **14**: 10601–10604.

Sayers, D.E., Stern, E.A., and Lytle, F.W., 1971, New technique for investigating non-crystalline structures: Fourier analysis of the extended X-ray-absorption fine structure. *Phys. Rev. Lett.* **27**: 1204–1207.

Stern, E., Sayers, D., and Lytle, F., 1975, Extended X-ray-absorption fine-structure technique. III. Determination of physical parameters. *Phys. Rev. B.* **11**: 4836–4846.

Taillefumier, M., Cabaret, D., Flank, A.-M., and Mauri, F., 2002, X-ray absorption near-edge structure calculations with the pseudopotentials: application to the *K* edge in diamond and α-quartz. *Phys. Rev. B* **66**: 195107.

Tanaka, I., Mezoguchi, T., and Yamamoto, T., 2005, XANES and ELNES in ceramic science. *J. Am. Ceram. Soc.* **88**(8): 2013–2029.

Vedrinskii, R.V., Kraizman, V.L., Novakovich, A.A., Demekhin, Ph. V., and Urazdhin, S.V., 1998, Pre-edge fine structure of the 3d atom K X-ray absorption spectra and quantitative atomic structure determinations for ferroelectric perovskite structure crystals. *J. Phys.: Condens. Matter.* **10**(42): 9561–9580.

Venkateswaran, U.D., Naik, V.M., and Naik, R., 1998, High-pressure Raman studies of polycrystalline $BaTiO_3$. *Phys. Rev. B* **58**: 14256–14260.

Yamamoto, T., Mizoguchi, T., and Tanaka, I., 2004, Core-hole effect on dipolar and quadrupolar transitions of $SrTiO_3$ and $BaTiO_3$ at Ti *K* edge. *Phys. Rev. B* **71**: 245113.

PRESENT-DAY HIGH-INTENSITY AND HIGH-RESOLUTION NEUTRON DIFFRACTION AND NEUTRON SCATTERING UNDER HIGH PRESSURE

ANATOLY M. BALAGUROV*
Joint Institute for Nuclear Research, Frank Laboratory of Neutron Physics Dubna, Moscow reg

Abstract The use of neutron scattering continues to evolve quickly both in traditional and in new fields. Basically, it is connected with general technical progress and realization of new ideas in the spectrometer performance. The principal event of the last years is the appearance of third-generation pulsed neutron sources. It is only at these sources that the construction of new spectrometers can be realized, which would offer new possibilities in high-pressure experiments: widening of pressure range and improvement of experimental data quality. In the lecture, general problems of elastic neutron scattering and new opportunities for experiments under high pressure are discussed, and examples of studies are given.

Keywords: Neutron scattering, crystal, atomic and magnetic structure, high pressure

1. Introduction

Fundamental properties of low energy neutrons make them a powerful experimental tool for investigation of structure and dynamics of condensed matter at atomic or molecular level. Another important factor is the potentiality to optimize a neutron experiment over intensity, resolution, background level, energy and momentum range, etc. The well-known major drawback of neutron scattering is comparatively **low intensity** of neutron beams produced at steady state or pulsed sources. At present, there are several dozens of neutron scattering centers in the world, but only in several, the most advanced of them, high-pressure experiments can be realized.

* E-mail: bala@nf.jinr.ru

E. Boldyreva and P. Dera (eds.), *High-Pressure Crystallography: From Fundamental Phenomena to Technological Applications*, DOI 10.1007/978-90-481-9258-8_7,

Moreover, even at high flux neutron sources the **elastic mode** is used as a rule for high-pressure studies, as the most intensive part of neutron scattering cross-section. This is why only elastic scattering, which is used for obtaining data about atomic, molecular or magnetic structures, is considered in this lecture.

Elementary introduction to the basic principles of low energy neutron scattering can be found, for instance at the sites (http://library.lanl.gov/cgi-bin/getfile?00326651.pdf). Useful information is placed also at the European Neutron Portal web site (http://neutron.neutron-eu.net/).

2. General Questions of Neutron Scattering

According to a general quantum-mechanical consideration of the interaction between a neutron and the ensemble of scattering centers (atomic nuclei) (van Hove, 1954), the scattering intensity and sample properties can be connected by the relation:

$$S(\boldsymbol{q}, \omega) \sim \iint e^{i(\boldsymbol{q}\boldsymbol{r} - \omega t)} G(\boldsymbol{r}, t) d\boldsymbol{r} dt. \quad (1)$$

Here $S(\boldsymbol{q},\omega)$, to which the intensity is proportional, is the so-called **scattering law**, $\boldsymbol{q}$ and ω are proportional to the momentum and energy transferred in the scattering process, $G(\boldsymbol{r},t)$ is the time and space **correlation function**. In the classical limit $G(\boldsymbol{r},t)$ is connected with the probability to find two different particles at given locations and times.

Formula (1) is the **Fourier transformation** of $G(\boldsymbol{r},t)$ into $S(\boldsymbol{q},\omega)$ and in accordance with its properties any features of $S(\boldsymbol{q},\omega)$ at q_c and ω_c can be linked with typical dimensions, l_c, and times, t_c, by simple relations: $l_c \approx 2\pi/q_c$ and $t_c \approx 2\pi/\omega_c$. The advanced neutron spectrometers offer the possibility of measuring scattering patterns in extremely wide range over q and ω. For instance, for elastic scattering the range from $q_{min} \approx 1 \cdot 10^{-3}$ Å^{-1} to $q_{max} \approx 60$ Å^{-1} is absorbed perfectly. This means that we can observe some structural peculiarities of an object in the range of dimensions $(0.1–6 \cdot 10^3)$ Å. This is a huge interval, and to overlap it, we need several **different types** of spectrometers.

2.1. HOW DIFFRACTION LIMIT CAN BE OVERCOME

The most general task of neutron diffraction structural experiments is the reconstruction of scattering density (nuclear or magnetic), $b(\boldsymbol{r})$, using the measured intensity distribution as a function of momentum transfer. This task can be successfully solved if $b(\boldsymbol{r})$ exhibits a long-range order; for good crystals precise positions of all atoms can be determined. On the contrary,

for large molecules in a solvent only a limited amount of data about their geometrical shape can be obtained.

The relation $l_c \approx 2\pi/q_c$, which can be sometimes rewritten as $l_{min} \approx \lambda_{min}/2$, is known as **diffraction limit** for observation of structural details of an object if wavelength λ_{min} is used. In a conventional neutron diffraction experiment $\lambda_{min} \approx 1$ Å, which means that l_{min} is around 0.5 Å. At the same time, it is well-known, that the precision in the determination of the interatomic distances in crystal is about 0.002 Å, and the uncertainties in lattice parameters are often ~0.0001 Å, i.e. much smaller than the diffraction limit. So, high precision in structural information is obtained owing to the description of diffraction data by **parametric models** in the course of special refinement procedure. In this case, the precision in structural parameters is limited by experimental data statistics and **correspondence** of the model to the real structure. For the analysis of data obtained in experiments under high pressure, just parametric models are used, as a rule.

2.2. NEUTRON INTERACTIONS AND MODES OF EXPERIMENTS

If a slow neutron with energy $E \approx 0.02$ eV is scattered in a crystal or by a large molecule, the energy exchange could be very small: $\Delta E/E \sim$ m/M, where m is the neutron mass, M is the crystal mass, i.e. $\sim 10^{-24}$. We can put $\Delta E = 0$ and it is just this process which is known as **elastic** scattering. On the contrary, if $\Delta E \sim E$, the process is said to be **inelastic**.

According to quantum mechanics, both elastic and inelastic neutron scattering can be **coherent** or **incoherent**. Here, the regularity in phase relations of scattered waves is meant by coherence. Failures in regularity are connected with randomness in isotope distribution and mutual nucleus and neutron spin orientation.

Finally, depending on the interaction mode, neutron scattering can be classified as **nuclear** or **magnetic** scattering. The first one takes place, if the neutron interacts with the atomic nucleus; the second one is realized after the interaction between neutron and magnetic moment of an atom. Nuclear scattering always occurs, while magnetic scattering is added to nuclear scattering if the atom has unpaired electrons or orbital magnetic moment.

In principle, each mode of scattering (there are **eight altogether**, Figure 1) could be utilized for realization of some particular experiment. For high-pressure studies the **elastic coherent nuclear** or **elastic coherent magnetic** scattering are used as a rule.

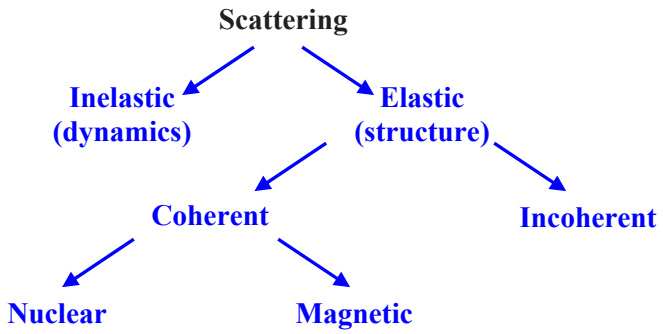

Figure 1. Modes of slow neutron scattering by matter. If one wants to obtain data about nuclear (magnetic) structure, the elastic coherent nuclear (magnetic) scattering must be used.

3. Neutron Spectrometers: New Capabilities

Neutron spectrometers for elastic scattering can be roughly divided into **three groups**: diffractometers, small angle scattering (SANS) spectrometers and reflectometers. **Diffractometers** are used for experiments with single- or polycrystals for measuring Bragg scattering (diffraction peaks). With **SANS spectrometer** the intensity in the range of small (<10°) angles is measured for analysis of large ($R >> \lambda$) inhomogeneities: molecules in a solvent, pores in a matrix. With **reflectometers** the reflection or scattering from external or internal interfaces can be measured, which is important for studies of thin films or multilayers.

For each spectrometer data acquisition can be organized either with monochromatic incident neutron beam (**λ = const technique**), or with polychromatic ("white") beam (**time-of-flight technique**). The first one is used at steady-state reactors; the second one is natural for pulsed neutron sources. These two types of data acquisition methods are considered now as complementary ones, i.e. depending on a problem, the first or the second one is preferable. Sometimes, for solution of a complex problem, or if there exist any doubts in the reliability of experimental data, it is recommended to use both techniques for data acquisition. For high-pressure experiments TOF-spectrometers have been traditionally considered as more appropriate, because with them spectra are collected in a fixed-angle scattering geometry in the energy-dispersive mode. Now high-pressure cells are successfully adapted for the λ = const technique as well, with the data collection in the angle-dispersive mode.

Comparing topics of neutron scattering experiments, which are carried out nowadays and which were performed 15–20 years ago, it should be admitted that the range of topics has broadened significantly. First of all it is connected with the appearance of necessary conditions for performing new experiments, which seemed unfeasible before. As to diffraction, two crucial parameters – intensity and resolution of neutron diffractometers – have been radically improved. With the new generation of neutron guides, monochromators and detectors, the data acquisition rate has increased in hundreds of times. Neutron detectors have undergone extremely noticeable changes in recent years. Two-dimensional position-sensitive detectors of large size and with good positional resolution are now widely used. Large-area multipixel detectors with solid angle up to 4 sr are constructed for new diffractometers at pulsed neutron sources (see, for instance, *Day et al*., 2004).

The D20 (λ = const) instrument at ILL (*Hansen*, 2002) is a prominent example of an advanced powder diffractometer, which combines both high intensity and good resolution. As to pulsed sources (with TOF instruments), more or less similar capabilities exist at the IBR-2 pulsed reactor in Dubna (*Balagurov and Mironova*, 1993) and at ISIS (RAL) (http://www.isis.rl.ac.uk/instruments/index.htm).

4. Neutron Scattering Under High Pressure

The main problem of neutron scattering under high pressure is a comparatively low neutron flux, which is ~10^{14} lower than the flux of synchrotron radiation even at advanced sources. Consequently, sample volume should be rather large, and maximum achievable pressure is now around some **dozens of GPa** (~30 GPa). Nevertheless, even within this range, a great number of tasks exist, whose solution can be hardly provided with X-ray or synchrotron radiation scattering. A traditional list includes the refinement of structures, which are a mixture of light and heavy atoms, or, on the contrary, consist of chemical elements with close atomic numbers; the analysis of magnetic structures, i.e. the determination of magnitude and direction of atomic magnetic moments; the investigation of thermal motion of atoms and molecules. Often the success of a structural experiment crucially depends on the unique sensitivity of neutrons for the isotopes of elements and light atoms, first of all for hydrogen and deuterium.

Until 1980s high-pressure neutron studies were carried out in the range of up to ~2 GPa. This pressure can be obtained in the piston-cylinder cells with sample volume of around 500 mm^3. In the beginning of the 1980s the specialized low-background multidetector diffractometer has been designed in Russia (*Glazkov et al.*, 1988), and single-crystal anvil cells for the first

time started to be used in neutron scattering experiments. This arrangement provides a possibility to study samples of 0.1–10 mm^3 volume up to ~10 GPa (with sapphire anvils), and to ~30 GPa (with diamond anvils). In the 1990s a cell based on WC anvils with toroidal geometry was developed by physicists from Paris and Edinburgh (*Besson et al.*, 1992) for TOF diffractometers. In this device pressures up to ~15 GPa were obtained, if sample volume was around 100 mm^3.

High-pressure technique based on diamond or sapphire anvils has been developed mostly in the joint work performed by the scientists from the "Kurchatov Institute" (Moscow) and LLB (Saclay). A new cell design (**"Kurchatov–LLB" cell**) and incident neutron beam focusing helped to increase the pressure limit up to ~50 GPa. These very compact cells (Figure 2) make it possible to measure diffraction patterns at temperatures as low as 0.1 K and at magnetic fields up to 7.5 T (*Goncharenko*, 2004).

The "**Paris–Edinburgh (PE) press**" have been recently adopted for the λ = const diffraction (*Klotz et al.*, 2005). Unlike a standard setup, the scattering plane is in the equatorial plane of the anvils (Figure 3), for which cubic boron nitride (BN) is used. Since as a sample holder (gasket) TiZr alloy (zero-matrix material) is used, there are no additional peaks in diffraction patterns. With this device several successful experiments have been performed. For instance, magnetism and Verwey transition in Fe_3O_4 were studied under pressure in the range of 0–10 GPa and at temperatures of 130–300 K at the D20 (ILL) diffractometer (*Klotz et al.*, 2008).

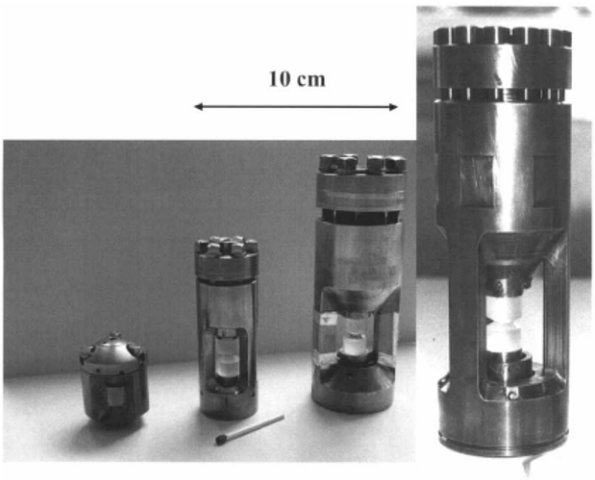

Figure 2. Kurchatov-LLB high-pressure cells for low-temperature neutron diffraction (From *Goncharenko*, 2004).

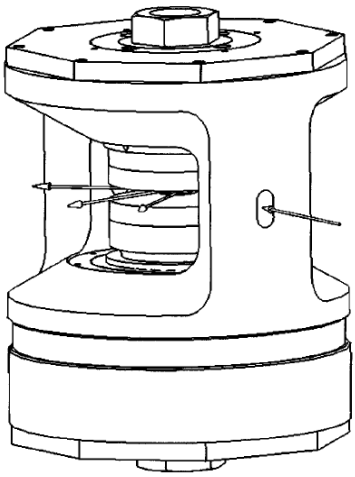

Figure 3. VX Paris–Edinburgh press indicating the scattering geometry with the incident and diffracted neutron beams. The diameter of the press is 250 mm, its mass is 60 kg (From *Klotz et al.*, 2005).

At present, it is these two types of cells that are used in neutron diffraction experiments if pressure around 10 GPa and higher is needed. In studies of molecular compounds or biological objects ("soft matter") pressure not higher than 1 GPa is conventionally used, and consequently there are no any impediments for applying neutron scattering technique.

5. Examples of Studies

A typical example of neutron structural experiment under high pressure is the analysis of compressibilities of lattice and interatomic distances. In (*Balagurov et al.*, 1999) for HTSC compound $HgBa_2CuO_{4+\delta}$ (Hg-1201) with three doping levels (δ = 0.06, 0.13, and 0.19) structural data were obtained at the D2B (ILL) diffractometer up to ~1 GPa with a high-pressure cell of the "cylinder-piston" type. The compressibilities of the unit-cell parameters and the main interatomic distances in Hg-1201 are presented in Figure 4 as a function of δ. One can see that the oxygen content does not strongly affect the lattice compressibility. On the contrary, the compressibility of the apical bond distances, Cu–O_2 and Hg–O_2, is significantly dependent on the doping level.

The analysis of variations of interatomic distances allows one to suggest that in the under and optimally doped states (δ = 0.06 and 0.13) the charge transfer under pressure from the reservoir to the (CuO_2) layers plays a minor role. It is important that the precision in the determination of interatomic

distances Hg–O and Cu–O in this experiment was better than 0.005 Å, which makes it possible to analyze the dependence of the compressibilities on oxygen content with confidence.

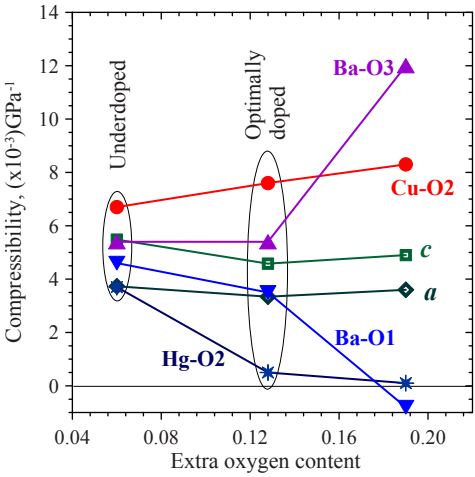

Figure 4. Compressibilities of the main Hg-1201 structural parameters for underdoped (δ = 0.06), optimally doped (δ = 0.13), and overdoped (δ = 0.19) states; *a* and *c* are the lattice constants, Cu–O_2 and Hg–O_2 are the apical bonds (from *Balagurov et al.*, 1999).

Many interesting investigations were performed with high-pressure anvil cells. At present, they are successfully used at both types (λ = const and TOF) of neutron spectrometers. As an example, low-temperature diffraction patterns measured at the TOF diffractometer with a sapphire anvil cell are shown in Figure 5. The quality of patterns is quite good even at large d_{hkl}.

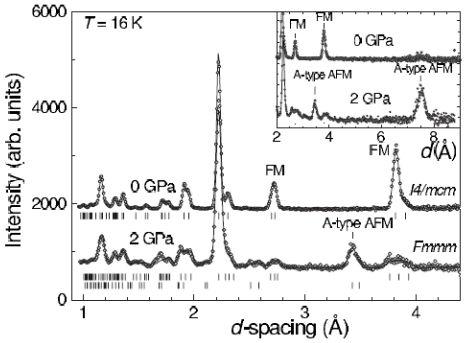

Figure 5. Neutron diffraction patterns of $Pr_{0.52}Sr_{0.48}MnO_3$ measured at P = 0 and 2 GPa, T = 16 K at fixed scattering angles 2θ = 90° and 45.5° (inset) with the DN-12 diffractometer at the pulsed IBR-2 reactor (From *Kozlenko et al.*, 2007).

An example of high-quality diffraction patterns obtained with the modified PE press (Figure 3) at the λ = const HRPT (PSI) diffractometer is shown in Figure 6. In this study of the $(Nd,Tb)_{0.55}Sr_{0.45}MnO_3$ compound a possible influence of the oxygen isotope substitution on the lattice compressibility was sought, but up to ~8 GPa no influence has been found (Figure 7).

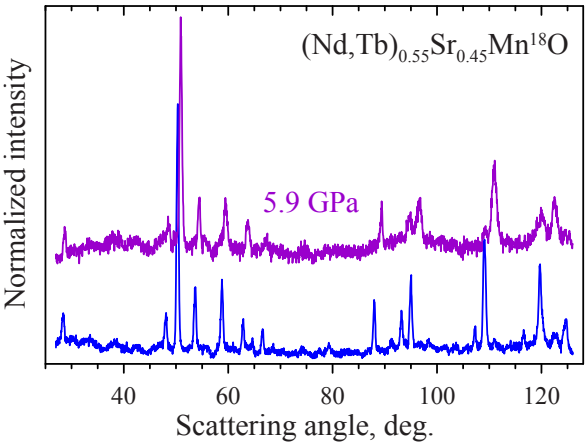

Figure 6. Neutron diffraction patterns of $(Nd,Tb)_{0.55}Sr_{0.45}MnO_3$, measured at P = 0 and 5.9 GPa (room temperature) with VX Paris–Edinburgh press at the HRPT diffractometer (SINQ, PSI) with λ = 1.886 Å.

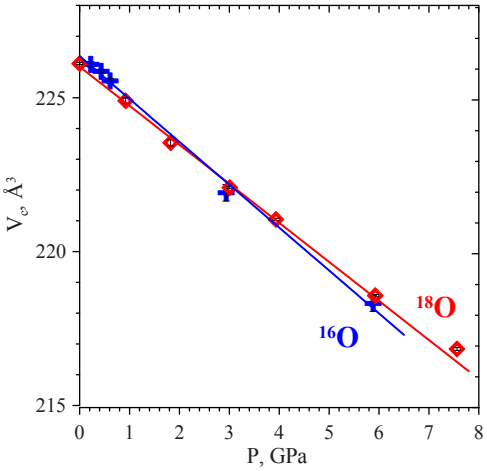

Figure 7. The cell volume of $(Nd,Tb)_{0.55}Sr_{0.45}MnO_3$ with ^{16}O and ^{18}O isotopes as a function of external pressure, as measured with VX Paris–Edinburgh press at the HRPT diffractometer (SINQ, PSI) (*I.A. Bobrikov, A.M. Balagurov, D.V. Sheptyakov*, 2008, unpublished results).

6. Prospects of Neutron Scattering Under High Pressure

Investigations of condensed matter by means of neutron scattering continue to be of great current importance in all traditional fields of application of this experimental tool. Analysis of a crystal structure of hydrides, oxides, fluorides, etc., determination of magnetic structure, utilization of various isotope-contrasting (labeling) techniques in the studies of organic and biological materials, investigation of atomic and molecular dynamics – in all these topics high-pressure experiments are carried out and undoubtedly will be continued.

At present, there are around 15 neutron scattering centers, where experiments under high pressure up to (2–3) GPa can be realized. In a few centers well-adopted range is 10 GPa, and in a couple of them even higher pressure (up to 50 GPa) can be used.

The appearance of **third-generation pulsed neutron sources** (http://neutron.neutron-eu.net/) with an average power of about 1 MW (SNS in USA and J-SNS in Japan), together with the modernized IBR-2 reactor (W = 2 MW) will open up totally new possibilities. The range of high pressures will be widened and the quality of experimental data will be improved considerably. This scenario was in a sense predicted by R.M. Brugger in the late 1960s (*Brugger*, 1968): "High-flux pulsed sources would replace the generation of steady-state research reactors".

References

Balagurov, A.M., Sheptyakov, D.V., Aksenov, V.L., Antipov, E.V., Putilin, S.N., Radaelli, P.G., Marezio, M., 1999, Structure of $HgBa_2CuO_{4+\delta}$ ($0.06 \leq \delta \leq 0.19$) at ambient and high pressure, Phys. Rev. B. 59: 7209.

Balagurov, A.M., Mironova, G.M., 1993, Phase transformations in materials studied by TOF neutron thermo-diffractometry, Mater. Sci. Forum. 133–136: 397.

Besson, J.M., Nelmes, R.J., Hamel, G., Loveday, J.S., Wilson, R.M., Hull, S., 1992, Neutron powder diffraction above 10 GPa, Physica B. 180, 181: 907.

Brugger, R.M., 1968, We need more intense thermal-neutron beams, Phys. Today. 21: 23.

Day, P., Enderby, J.E., Williams, W.G., Chapon, L.C., Hannon, A.C., Radaelli, P.G., Soper, A.K., 2004, GEM: the general materials diffractometer at ISIS – multibank capabilities for studying crystalline and disordered materials, Neutron News. 15: 19.

Glazkov, V.P., Naumov, I.V., Somenkov, V.A., Shil'shtein, S.Sh., 1988, Superpositional many-detector systems and neutron diffraction of microsamples, Nucl. Instr. Meth. A. 264: 367.

Goncharenko, I.N., 2004, Neutron diffraction experiments in diamond and sapphire anvil cells, High Press. Res. 24: 193.

Hansen T., 2002, Future trends in high intensity neutron diffraction on D20 at ILL, EPDIC-8, Uppsala, 23 to 26 May.

van Hove, L., 1954, Correlations in space and time and Born approximation scattering in systems of interacting particles, Phys. Rev. 95: 249.

Klotz, S., Strässle, Th., Rousse, G., Hamel, G., Pomjakushin, V., 2005, Angle-dispersive neutron diffraction under high pressure to 10 GPa, Appl. Phys. Lett. 86: 031917.

Klotz, S., Steinle-Neumann, G., Strässle, Th., Philippe, J., Hansen, Th., Wenzel, M.J., 2008, Magnetism and the Verwey transition in Fe_3O_4 under pressure, Phys. Rev. B. 77: 012411.

Kozlenko, D.P., Dubrovinsky, L.S., Jirák, Z., Savenko, B.N., Martin, C., Vratislav, S., 2007, Pressure-induced antiferromagnetism and compression anisotropy in $Pr_{0.52}Sr_{0.48}MnO_3$, Phys. Rev. B, 76: 09440859.

LARGE VOLUME PRESSES FOR HIGH-PRESSURE STUDIES USING SYNCHROTRON RADIATION

YANBIN WANG*
Center for Advanced Radiation Sources, *The University of Chicago*, *Chicago*, *IL*

Abstract The large-volume press (LVP) is an indispensable technique in high-pressure research that complements capabilities of the diamond anvil cell (DAC). While maximum attainable temperature (T) and pressure (P) are limited, compared to the DAC, LVP offers more uniform P-T conditions, with sample volumes about 10^3–10^6 times those of the DAC. These features make LVP an ideal tool for accurate measurements of bulk physical properties and systematic studies on complex systems. Advents in high-pressure technology and synchrotron radiation have revolutionized LVP research in the past 2 decades. The employment of sintered diamond anvils has dramatically expanded the LVP pressure range (currently about 90 GPa) at high temperatures. New diffraction techniques have made it possible to determine atomic structures of both crystalline and non-crystalline materials under extreme P and T conditions. Efforts in incorporating other in-situ techniques at synchrotron sources have made it possible to measure many physical properties simultaneously with x-ray diffraction. This lecture provides a brief description of the various types of LVPs in use at synchrotron sources and scientific applications.

Keywords: High pressure, large-volume press, synchrotron, diffraction, imaging

1. Introduction

The large-volume press is one of the primary tools for studying matters under high pressure and temperature. The interface with synchrotron and neutron radiation has made it possible to investigate various physical–chemical

* E-mail: wang@cars.uchicago.edu

E. Boldyreva and P. Dera (eds.), *High-Pressure Crystallography: From Fundamental Phenomena to Technological Applications*, DOI 10.1007/978-90-481-9258-8_8,

phenomena and measure properties of materials at simultaneous high P (currently ~ 90 GPa) and T (~3,000 K), on millimeter-sized samples. With resistive heating, stable temperatures can be maintained for extended period of time (hours to days), and temperature gradients are on the order of 10–100 K/mm. The large sample volume allows robust characterization of bulk properties of materials (especially multi-phased materials) with a combination of various characterization techniques applied to the sample simultaneously.

2. Types of LVPs Used at Synchrotron Sources

LVPs came into use in the 1950s, through efforts in generating high pressures on bulk specimens for synthesis reactions, especially for making diamond (e.g., see *Bundy*, 1989). Significant developments were initiated in earth science communities in the late 1960s, to simulate P–T conditions corresponding to earth and planetary interiors (e.g., *Kawai*, 1970; *Kumazawa*, 1973; *Onodera*, 1987). The earliest efforts known to the author in studying materials using laboratory x-ray sources were in the 1970s (*Inoue and Asada*, 1973), leading to the first synchrotron-based LVP facility at the Photon Factory (Japan) in the 1980s (*Shimomura et al*., 1985). Since then, LVPs have become a major player in high-P–T research using synchrotron and neutron sources.

LVP systems for synchrotron use generally consist of the following key components: (1) a hydraulic press with a load control system, (2) a pressure module or tooling (a set of "guide blocks") within which a sample assembly is compressed to generate quasi-hydrostatic pressure, (3) an electrical heating system for temperature control, (4) x-ray optical components for diffraction and imaging, (5) x-ray and image detectors, and (6) a "goniometer" capable of carrying the press and locating the sample in the diffraction volume defined by the x-ray optics. Details of the system design vary and operation procedures can be found in a number of publications (*Utsumi et al*., 1998; *Katsura et al*., 2004; *Wang et al*., 2009, etc.). In this chapter, a brief description is given of various pressure modules, which have evolved rather rapidly in recent years.

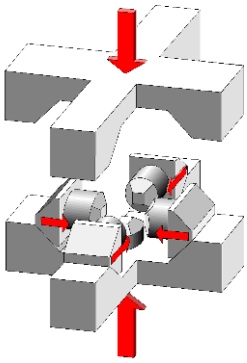

Figure 1. Conceptual diagram illustrating the principles of the DIA cubic anvil apparatus.

The first tooling is the cubic-anvil apparatus, known as the DIA (*Osugi et al.*, 1964), which consists of six anvils (Figure 1). Two anvils are along the center line of the loading axis

(large opposed arrows) and are fixed opposite to each other on each guide block. The other four anvils are horizontally placed, forming a cubic nest bounded by the flat faces of the six anvils. A ram force applied along the vertical axis is decomposed, by the 45° sliding surfaces, into three pairs acting along three orthogonal directions, forcing the six anvils to advance (retract) synchronously towards (away from) the center of the cube. X-ray access is through vertical gaps between the side anvils. The diffraction vector is vertical, with possible 2θ angles up to ~25°.

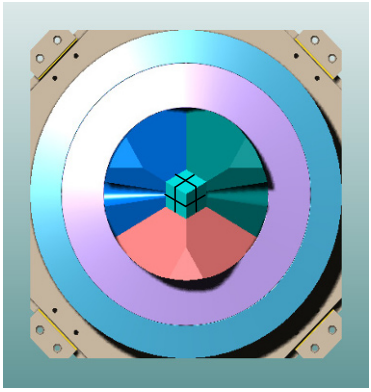

Figure 2. Top view of the T-25 module. The geometry is identical to Kawai-type systems used in most high-pressure laboratories in the US and in Japan, with the [111] axis of the eight-cube assembly along the loading axis. X-ray diffraction is through the gaps between WC anvils, inclined from the loading axis at 35.26°.

The second is the so-called Kawai-type apparatus, consisting of a first-stage hardened steel cylinder cut into six parts, each having the inner tip truncated into a square surface, enclosing a cubic cavity, with the [111] axis of the cube along the ram load direction. Inside the cubic cavity is a second-stage assembly (known as the Kawai assembly), consisting of eight WC cubes, separated by spacers. Each cube has one corner truncated into a triangular face; the eight truncations form an octahedral cavity in which the pressure medium is compressed.

Several variations of such apparatus exist. At beamline 13-ID-D of the APS (GSECARS), a Kawai-type module is used to compress 25 mm edge-length WC cubic anvils (named T-25) (Figure 2). A miniaturized version of this apparatus (*Vaughan et al.*, 1998) is used both at the APS and the NSLS. These pressure modules, called T-10 or T-cup, have an overall module diameter of ~200 mm and compress 10 mm WC second-stage cubes. Diffracted x-rays pass through the

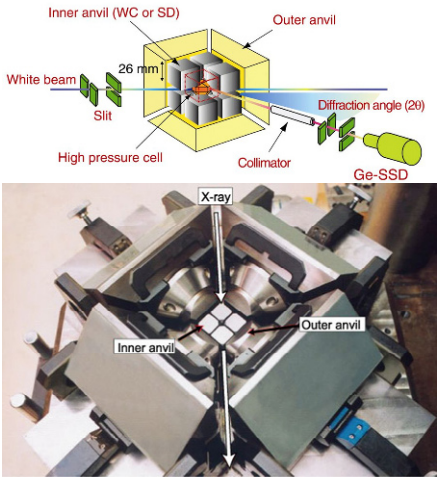

Figure 3. SPEED-1500, a 6/8 system at SPring-8. Mk.II is an improved version of this apparatus and MAX-90 is a smaller version of the same concept. (SPring-8 website)

gaps between the second-stage cubic anvils in a plane inclined at an angle of 35.26° from the loading direction. Conical access notches are made in the first-stage wedges, to allow a range of 2θ angles up to 10–12°.

The third configuration is a hybrid system using a set of large DIA anvils to compress the Kawai-assembly (*Shimomura et al.*, 1992). Figure 3 shows such a configuration used at Beamline BL04B1 at SPring-8 (*Utsumi et al.*, 1998). Hydraulic load is parallel to the [100] direction of the eight-cube Kawai cell, and x-ray access is through horizontal anvil gaps if WC cubes are used. Notches are made in the first-stage DIA anvils to allow x-ray access. With sintered diamond cubes, vertical diffraction is also possible. This apparatus is the most successful in generating "ultrahigh" pressures towards megabar (100 GPa) using sintered diamond anvils. Current records are 90 GPa at room temperature, about 60 GPa at temperatures over 1,500 K (e.g., *Tange et al*., 2008). In this chapter, I will use the term "Kawai-cell" for the T-25 systems and "Kawai in DIA" for the hybrid systems described in Figure 3.

Several new devices have been developed in recent years, with specific features addressing certain particular needs in high-pressure science. *Wang et al.* (2003) developed the deformation-DIA (D-DIA) for studying deformation under high P and T. The D-DIA is a modification of the DIA apparatus, with additional independent control of one pair of anvils provided by two additional hydraulic actuators (differential rams). These differential rams are located within the guide blocks (Figure 4) and react against the platens driven by the main hydraulic ram, which provides quasi-hydrostatic pressurization. Each differential ram is driven by a precision positive-displacement pump, so its speed is controllable. Strain rates of ~10^{-3}–10^{-7} s^{-1} can be imposed on a 1-mm-long sample. The D-DIA is capable of shortening and lengthening the sample, thereby deforming the sample in stress-strain loops; a typical method in conventional deformation studies. It also has advantages in quasi-hydrostatic pressure generation. The differential rams can be used to compensate elastic deformation in the apparatus at various loads. By adjusting differential rams, one can generate conditions closer to hydrostatic than a regular DIA. These advantages have inspired a new generation of multi-anvil systems for applications in the Kawai-in-DIA configuration.

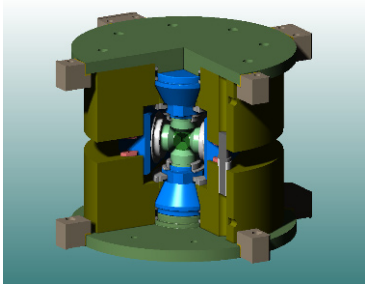

Figure 4. Cutaway view of the D-DIA with differential rams in the upper and lower guide block, showing locations of the differential rams (*Wang et al.*, 2003).

Another new type of multi-anvil device has been installed at the Institute for Study of Earth's Interior, Okayama University, Japan. This apparatus has a DIA-like geometry, but with each of the six anvils independently controlled by a hydraulic system (*Ito et al*., 2009). It is argued that alignment of the six outer–stage anvils will improve significantly, making it possible to compress the Kawai-cell with greater degree of accuracy, thereby generating higher pressures with sintered diamond anvils.

Not all LVPs are multi-anvil apparatus. The toroid anvil cell, first developed in the former Soviet Union (*Khvostantsev et al*., 1977), operates on the principle of opposed anvils. Instead of flat anvil tips as in the DAC, both toroid anvils have a half spherical depression (Figure 5). *Besson et al.* (1992) integrated this device with a compact hydraulic system, allowing greater flexibility. Paris–Edinburgh (P/E) cells, as they are known now, are currently in use at many synchrotron and neutron sources. Sample size is typically in the millimeter range. X-ray access is through the gaps between the two anvils for synchrotron diffraction. In neutron scattering studies, it is common to drill a hole through the loading axis so that incident beam enters the sample through the upper anvil (Figure 5). Many high pressure studies have been conducted using this device, primarily in physics communities at ambient and low temperatures (e.g., *Nelmes and McMahon*, 1998). The compact hydraulic press has the advantage of flexibility, and has been used to accommodate smaller multianvil devices such as T-10 (*Le Godec et al*., 2009).

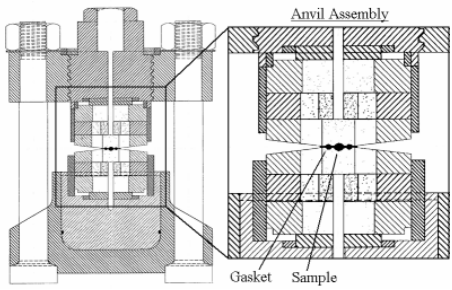

Figure 5. The Paris-Edinburgh cell. This is an opposed anvil device, with depressions machined in the anvil tops, compressing a semi-spherical sample assembly. Press frame and hydraulic ram are designed as an integrated entityresulting in a compact system.

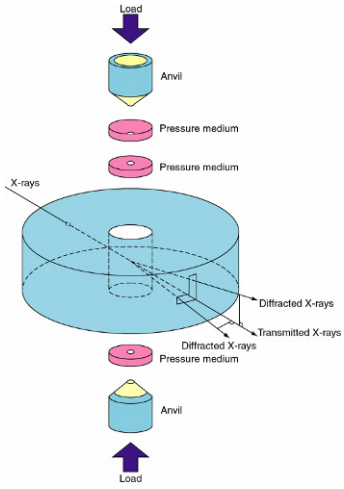

Figure 6. The Drickamer cell. With sintered diamond as anvil material, it can generate over 30 GPa pressure, with a sample about 0.2–0.3 mm in linear dimensions.

The Drickamer cell (*Balchan & Drickamer*, 1961) has two large anvils (diameters 10 mm or above) with an

optimal tapered angle. The anvils are compressed inside a containment ring, made of WC or hardened steel, with x-ray access holes for diffraction (Figure 6). Such devices have been used at Photon Factory (*Funamori et al.*, 1993; *Gotou et al*., 2006) for some time. Devices for monochromatic diffraction and sample imaging have been developed (*Nishiyama et al.*, 2009). Several variations of the Drickamer apparatus have been developed for special applications, such as the rotational (shear) deformation apparatus (RDA) developed by *Yamazaki and Karato* (2001) and the high-P tomography apparatus by *Wang et al*. (2005). Due to space limitations, we will not discuss these special apparatus further.

3. Interfacing LVPs with Synchrotron Radiation

3.1. MAJOR COMPONENTS

Each LVP system has unique features in its operation, depending on the beamline characteristics, diffraction techniques used, and scientific objectives, but they all share certain common components. In what follows, I will describe one configuration as an example to illustrate the principles in synchrotron related operations. More detailed discussions on choice of diffraction techniques will be given in the following chapter.

Figure 7 illustrates major components of the LVP operation at GSECARS. For energy-dispersive operations, white x-rays enter the station with a predefined beam size (1–2 mm), which is then collimated by a set of slits made of heavy metal to the desired dimensions (typically 0.05–0.1 mm) for diffraction. The collimated beam then enters the high-pressure device, through gaps between the anvils, to illuminate the sample. Diffracted x-rays are collected on the down-stream side, again through anvil gaps, by a solid-state detector (SSD). The incident beam position is fixed, and the SSD detector is aligned using a set of translation and rotation stages at a fixed 2θ angle. An additional set of collimators and slits is inserted between the sample and the SSD, to tightly define a diffracting volume (the intersecting volume defined by the incident beam size and the diffracted

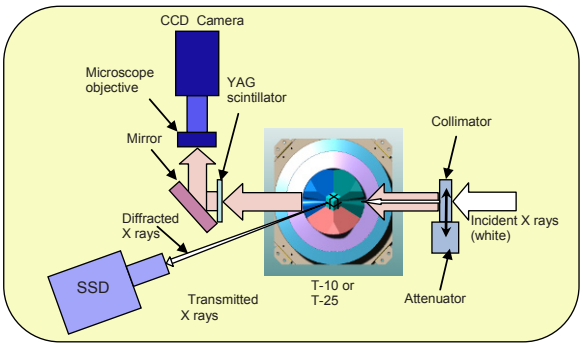

Figure 7. A typical beamline setup for energy-dispersive x-ray diffraction and imaging in the LVP.

beam size), so that scattering of the pressure media surrounding the sample does not contaminate sample diffraction signal.

3.2. MANEUVERING THE LVP

The LVP needs to be carried by a positioning table, so that the sample can be located in the diffracting volume defined by the diffraction optics at any hydraulic load. Press rotation is sometimes necessary to maximize anvil gaps along the beam path. Figure 8 shows the positioning and control systems at beamline 13-ID-D of GSECARS. The 10 MN press (A), weighing ~7 t, is held by a positioning table (B). Linear actuators drive the press in three orthogonal directions, with position repeatabilities of 2–3 μm. A roller table top (C) is used to slide pressure modules in and out of the press. A positive displacement pump is used to apply hydraulic load and is remotely controlled with programmable feedback. An independent stand (E) on the upstream side of the LVP carries the entrance slit system for controlling incident beam size. A detector support frame (F), located at the down-stream side of the LVP, is independently operated. This support frame is capable of positioning single and multi-element SSDs, as well as monochromatic detectors for diffraction work, with linear positioning accuracies of 1–2 μm and angular repeatability of 0.001°. All motors are computer-controlled so the detector can mimic a mechanical 2θ arm, scanning though a segment of a circle centered at the sample, at virtually any prescribed inclination angle.

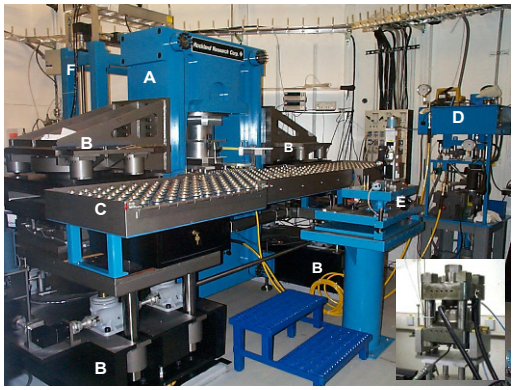

Figure 8. The 1,000 ton (10 MN) LVP system at GSECARS, beamline 13-ID-D. The inset shows a P/E cell at ID27 of the ESRF (with built-in hydraulic ram and frame) the sizes of the two systems are shown approximately to scale.

3.3. HIGH-PRESSURE CELL ASSEMBLY

Given the nature of the LVP devices, solid materials are used as pressure medium in most cases. The choice of pressure media, heater material, thermocouples, etc., is often dictated by the device, the sample and the P–T conditions desired. Every experiment is unique in its own way, and there is no single cell assembly that can satisfy all the needs. The only one

requirement in common is that the cells must be transparent to the x-rays. Each cell requires careful design effort and many tests. It is impossible to give a comprehensive review of all the successful cell assemblies.

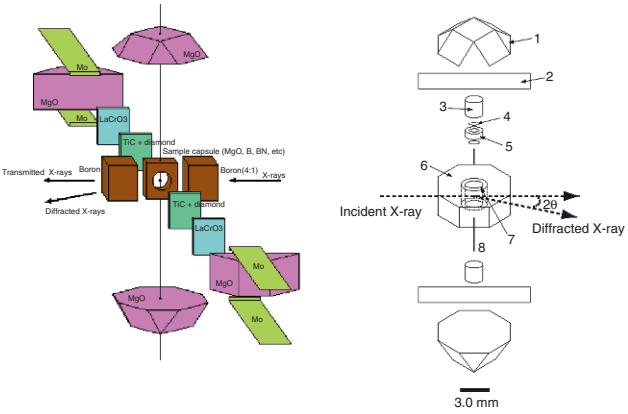

Figure 9. A: A cell designed for T-10 at GSECARS (*Uchida et al.*, 2001). Sample stacking is along a direction that is inclined at 35.26° from vertical, coinciding with the diffraction vector. B: Cell design by *Nishiyama et al.* (2004) at SPring-8. In SPEED-1500, the diffraction vector is horizontal. Labeled parts are: 1, MgO; 2, Mo; 3, ZrO_2; 4, rhenium; 5, sample container (graphite); 6, pressure medium (ZrO_2), 7, heater ($LaCrO_3$); 8, thermocouple.

Figure 9 shows two examples, both taking into account the diffraction geometry of the device used. In both cases the pressure medium is no longer a single piece of pre-fabricated octahedron; this allows double sample chambers to be oriented relative to the diffraction vector, so that sample and diffraction pressure standard are separated. Because of the complex shapes of certain parts, it is necessary to use a CNC machine for part preparation.

3.4. VIEWING THE SAMPLE WITH X RAYS

Radiographic imaging became a powerful tool to locate the sample (*Wang et al.*, 2000). By driving out the incident collimating slits, an attenuator is positioned in the beam, to damp unwanted low-energy photons, allowing optimized absorption contrast through the cell assembly. *Uchida et al.* (2001 described the typical setup. Figure 10 is an example of the radiographic image taken from a T-10 cell. Here, two samples are loaded in the cell, with a thermocouple

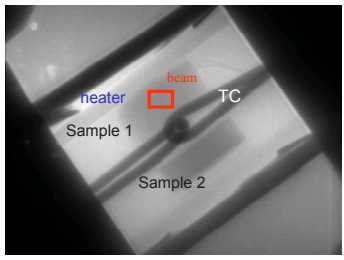

Figure 10. An example of cell image recorded by the radiography setup (*Uchida et al.*, 2001).

(TC) in between. Disc heater plates (TiC and diamond powder – light gray) and $LaCrO_3$ thermal insulator plates (dark) can be seen. Once the sample is centered relative to the large incident beam, collimators are driven in the beam path to cut the beam size to that shown by the red box in Figure 10. The location of the beam relative to the entire cell image is immediately known.

4. Diffraction Techniques

4.1. ENERGY-DISPERSIVE DIFFRACTION (EDD)

The energy-dispersive diffraction (EDD) technique, carried out on polycrystalline samples at a fixed 2θ angle (Figure 11A), is still a commonly used approach. Data collection is fast (from seconds to minutes) and the incident and diffracted beams well collimated, so that clean diffraction data can be obtained, despite pressure media surrounding the sample. Metal capsules are often used to control sample environment oxygen fugacity, water content, etc.). EDD is an ideal for phase boundary determination and equation of state studies. However, EDD provides limited sampling of the crystallites in the sample because of the fixed 2θ angle, and is not suitable for experiments near melting or with rapid crystal growth. This limitation may be circumvented somewhat by using ADD with an area detector. In studies of liquids and amorphous materials, EDD data are collected at multiple 2θ angles, to increase coverage in the reciprocal space for accurate determination of the radial distribution function (e.g., *Tsuji et al*., 1989). The synchrotron incident beam is simulated using the Monte Carlo approach and Compton scattering effects are typically dealt with based on theoretical predictions (*Funakoshi*, 1997).

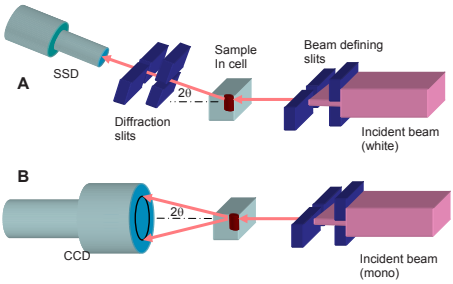

Figure 11. Two diffraction techniques used. A: EDD. The incident white beam is collimated by the beam defining slits. Another set of collimators on the diffraction side ensures only diffraction signals from the sample enter the SSD. B: An area detector is used for ADD. Diffraction signals in a finite solid angle cone are collected. Sometimes Soller slits can be used in between the sample and the detector for beam collimation.

However, EDD does not provide reliable crystal structure information such as bonding characteristics and atomic positions. Various efforts have been made to extract quantitative crystallographic information from EDD data, with limited success (e.g., *Yamanaka et al*., 1992; *Ballirano and Caminiti*, 2001).

4.2. ANGLE-DISPERSIVE DIFFRACTION (ADD)

ADD has become more widely used technique in LVP systems, especially with area detectors (Figure 11B). However, diffraction of the pressure media, gaskets, pressure marker, etc., as well as Compton scattering of the materials involved, all contribute to the background, reducing signal-to-noise ratio, sometimes severely overlapping with sample diffraction signal (e.g., see *Angel et al*., 2000, for a review). To overcome the background problem, a Soller slit system is used, which consists of multiple collimators that are in a radial alignment, centered at the sample (e.g., *Yaoita et al*., 1997; *Mezouar et al*., 2002). By oscillating the Soller slits in between the sample and the 2-D detector, background scattering can be significantly reduced.

5. Other In-situ Probes

Many in-situ characterization techniques have been used in the LVP, some simultaneously with x-ray diffraction and imaging. Ultrasonic interferometry is now commonly used (e.g., *Li et al*., 2005). This technique has yielded elasticity data with specific density from diffraction, and has the promising prospect to refine diffraction-based pressure scales for self-consistency. Acoustic emission (*Dobson et al*., 2004; *Jung et al.*, 2006), electrical conductivity (*Kusaba et al*., 1993; *Yoshino et al*., 2008), thermal conductivity and diffusivity (*Osako et al*., 2004), differential thermal analysis (*Maeda et al*., 1981), etc. have all been applied to the LVP.

6. Applications and Future Prospects

LVP techniques have been used in wide range of high pressure studies. Here, we give a few examples of results from the LVP in conjunction with synchrotron radiation that have unique advantages and have made important contributions to certain scientific problems. It is impossible to give a comprehensive review, given the limited space here; only selected results are given here as examples.

The homogeneous and stable temperature generation makes LVP an ideal tool for studies of phase relations. Phase boundaries can be determined in-situ along multiple P–T paths in a single experiment. Phase diagrams for essentially all the major constituents of the Earth's rocky interior have been studied, including, e.g., SiO_2 (*Zhang et al.*, 1996), $(Mg,Fe)_2SiO_4$ (*Fei et al*., 2004), $MgSiO_3$ (*Ono et al*., 2001), $Mg_3Al_2Si_3O_{12}$ (*Hirose et al*., 2001), etc.

Kinetics of phase transformations plays an important role in understanding the dynamics of the Earth. Pyroxene – garnet transformation in the $CaO–MgO–Al_2O_3–SiO_2$ system (*Nishi et al*., 2008), olivine to wadsleyite in

Mg_2SiO_4 (*Kubo et al*., 2004), and to $MgSiO_3$ perovskite+MgO (*Kubo et al*., 2002), garnet to perosvkite (*Kubo et al*., 2008). Effects of water on the kinetics have been studied on the following boundaries: olivine – wadsleyite (*Hosoya et al*., 2005), and garnet – perovskite in MORB composition (*Sano et al*., 2008). Atomic evolution during the olivine – spinel transition in Fe_2SiO_4 has been investigated (*Chen et al*., 2001).

Elasticity of minerals and materials at high P and T has been studied using x-ray diffraction, imaging, and ultrasonic interferometry (e.g., *Li et al*., 2005). These measurements combine several pieces of information simultaneously: specific density (from unit cell), macroscopic sample length (from imaging), and travel time of sound waves through the sample (ultrasonic interferometry). From these measurements, information on longitudinal and shear wave velocities of mantle minerals were obtained, and compared with earth models basic on seismic observations: single-crystal and polycrystalline olivine (*Darling et al*., 2004); pyroxenes (*Kung et al*., 2005); wadsleyite (*Li et al*., 2001); ringwoodite (*Higo et al*., 2008); garnets (*Gwanmesia et al*., 2006, 2009) etc. Using the redundant P-V-Vp-Vs-T data, self-consistent equations of state can be constructed. *Kono et al*. (2007) recently investigated equation of state for MgO using this technique.

Viscosities of melts are studied using falling sphere techniques with radiographic imaging. Measurements have been conducted on various materials from simple elements such as S (*Terasaki et al*., 2004), Fe (*Rutter et al*., 2002; *Terasaki et al*., 2002), etc., to alloys such as Fe-S (*Terasaki et al*., 2006), Fe–C (*Terasaki et al*., 2006), to silicate minerals such as diopside (*Reid et al*., 2003), albite (*Poe et al*., 2006), to complex systems such as dacite (*Tinker et al*., 2004) and peridotite (*Liebske et al*., 2005). Interfacial tension between Fe–S–P and silicate melts at high pressure (*Terasaki et al*., 2008).

Structures of many melts and liquids have been investigated (see *Katayama and Tsuji*, 2003 for a review). Equations of state of melts are currently being approached by two techniques: x-ray absorption measurement (*Katayama et al*., 1998) and x-ray microtomography (*Lesher et al*., 2009).

High pressure, high temperature deformation is another area where LVP has unique advantages. Because of the large sample dimensions, strain and strain rates can be controlled or monitored during deformation, so that stress-strain curves can be established at various strain rates. This capability allows quantitative investigation into flow laws of materials at various conditions. Another chapter is devoted to this subject, please see *Wang and Hilairet* (this volume).

Still another new area is high-pressure microtomography. A number of studies have emerged using this technique: measuring interfacial tension of

liquids under pressure (*Terasaki et al*., 2008), glass and liquid volume and density (*Lesher et al*., 2009), and segregation of Fe–S melts in silicates (*Wang et al*., 2008). This is a new direction and its potential has not been fully explored.

With the development of the double-stage system (Kawai-cell in DIA), simultaneous P–T conditions of 50 GPa and 2,000 K can be reached using sintered diamond anvils, making it possible to study petrology under lower mantle conditions (*Tange et al*., 2008). P–V–T equations of state data to such P–T range are now available (*Tange et al*., 2008); simultaneous acoustic velocity measurements coupled with P–V–T determination are emerging (*Kono et al.*, 2007). Crystal structures of materials that cannot be quenched and recovered to ambient condition are being refined under transition zone and lower mantle conditions (e.g., *Wang et al.*, 2004; *Uchida et al*., 2009).

ACKNOWLEDGMENTS

Several LVP technical developments at GSECARS were supported by NFS grants EAR-0001088, 0652574, and 0711057. GSECARS is supported by the National Science Foundation – Earth Sciences (EAR-0622171) and Department of Energy – Geosciences (DE-FG02-94ER14466). Use of the Advanced Photon Source was supported by the U.S. Department of Energy, Office of Science, Office of Basic Energy Sciences, under Contract No. DE-AC02-06CH11357.

References

Angel RJ, RT Downs, LW Finger (2000) *High-Temperature and High-Pressure Crystal Chemistry* (Eds. R.M. Hazen and R.T. Downs), MSA, Washington, D.C., pp. 559–596.

Balchan AS, HG Drickamer (1961) High pressure electrical resistance cell, and calibration points above 100 kilobars. *Rev. Sci. Instrum*., **32**, 308–313.

Ballirano P, R Caminti (2001) Rietveld refinements on laboratory energy dispersive X-ray diffraction (EDXD) data. *J. Appl. Cryst*., **34**, 757–762.

Besson JM, RJ Nelmes, G Hamel, JS Loveday, G Weill, S Hull (1992) Neutron powder diffraction above 10 GPa. *Physica B*, **180**, 907–910.

Bundy FP (1989) Pressure-temperature phase diagram of elemental carbon. *Physica A*, 156, 169–178.

Chen JH, DJ Weidner, JB Parise, MT Vaughan, P Raterron (2001) Observation of cation reordering during the olivine-spinel transition in fayalite by in situ synchrotron x-ray diffraction at high pressure and temperature. *Phys. Rev. Lett.*, **86**(18), 4072–4075.

Darling K, GD Gwanmesia, J Kung, B Li, RC Liebermann (2004) Ultrasonic measurements of the sound velocities in polycrystalline San Carlos olivine in multi-anvil, high-pressure apparatus. *Phys. Earth Plant. Int*., **143**–**144**, 19–31.

Dobson DP, PG Meredith, SA Boon (2004) Detection and analysis of microseismicity in multi anvil experiments. *Phys. Earth Planet. Int*., **143**–**144**, 337–346.

Fei Y, J Van Orman, J Li, W van Westrenen, C Sanloup, W Minarik, K Hirose, T Komabayashi, M Walter, K Funakoshi (2004) Experimentally determined postspinel transformation boundary in Mg_2SiO_4 using MgO as an internal pressure standard and its geophysical implications. *J. Geophys. Res.*, **109**, B02305, doi:10.1029/2003JB002562.

Funakoshi K (1997) Energy-dispersive x ray diffraction study for alkali silicate melts using synchrotron radiation under high pressure and temperature. *PhD Thesis*, Tokyo Institute of Technology, pp. 117.

Funamori N, T Yagi (1993) High pressure and high temperature in situ x-ray observation of $MgSiO_3$ perovskite under lower mantle conditions. *Geophys. Res. Lett*., **25**, 387–390.

Gotou H, T Yagi, DJ Frost, DC Rubie (2006) Opposed-anvil-type high-pressure and high-temperature apparatus using sintered diamond. *Rev. Sci. Instrum*., **77**, 035113, doi:10.1063/1.2182855.

Gwanmesia GD, J Zhang, K Darling, J Kung, B Li, L Wang, D Neuville, RC Liebermann (2006) Elasticity of polycrystalline pyrope ($Mg_3Al_2Si_3O_{12}$) to 9 Gpa and 1000 C. *Phys. Earth Planet. Int*., **155**, 179–190.

Gwanmesia GD, L Wang, R Triplett, RC Liebermann (2009) Pressure and temperature dependence of the elasticity of pyrope-majorite [Py60Mj40 and Py50Mj50] garnets solid solution measured by ultrasonic interferometry technique, *Phys. Earth Plant. Int*., **174**, 105–112.

Higo Y, T Inoue, T Irifune, K Funakoshi, B Li (2008) Elastic wave velocities of $(Mg_{0.91}Fe_{0.09})SiO_4$ ringwoodite under P-T conditions of the mantle transition zone region, *Phys. Earth Planet. Int*., **166**, 167–174.

Hirose K, YW Fei, S Ono, T Yagi, K Funakoshi (2001) *In situ* measurements of the phase transition boundary in $Mg_3Al_2Si_3O_{12}$: implications for the nature of the seismic discontinuities in the Earth's mantle. *Earth Planet. Sci. Lett.*, **184** (3–4), 567–573.

Hosoya T, T Kubo, E Ohtani, A Sano, K-I Funakoshi (2005), Water controls the fields of metastable olivine in cold subducting slabs. *Geophys. Res. Lett*., **32**, L17305, doi:10.1029/2005GL023398.

Inoue K, T Asada (1973) Cubic anvil X-ray diffraction press up to 100 kbar and 1000C. *Jpn. J. Appl. Phys*., **12**, 1786–1793.

Ito E, T Katsura, D Yamazaki, A Yoneda, M Tado, T Ochi, E Nishibara, A Nakamura (2009) A new 6-axis apparatus to squeeze the Kawai-cell of sintered diamond cubes. *Phys. Earth Planet. Int.*, **174**, 264–269.

Jung H, Y Fei, PG Silver, HW Green Ii (2009) Frictional sliding in serpentine at very high pressure. *Earth Planet. Sci. Lett.*, **277**, 273–279.

Katayama Y, K Tsuji, O Shimomura, T Kikegawa, M Mezouar, D Martinez-Garcia, JM Besson, D Hausermann, M Hanfland (1998) Density measurements of liquid under high pressure and high temperature. *J. Synchrotron Rad.*, **5**, 1023–1025.

Katayama Y, K Tsuji (2003) X-ray structural studies on elemental liquids under high pressures. *J. Phys.: Condens. Matter*, **15**, 6085–6103.

Katsura T, K Funakoshi, A Kubo, N Nishiyama, Y Tange, Y Sueda, T Kubo, W Utsumi (2004) A large-volume high-pressure and high-temperature apparatus for *in situ* X-ray observation, 'SPEED-Mk.II', *Phys. Earth Planet. Int.*, **143**–**144**, 497–506.

Kawai N, Endo S (1970) The generation of ultrahigh hydrostatic pressure by a split sphere apparatus. *Rev. Sci. Instrum.* **41**, 1178–1181.

Khvostantsev LG, LF Vereshchagin, AP Novikov (1977) Device of toroid type for high pressure generation, *High Temp.- High Press.*, **9**, 637–639.

Kono Y, Y Higo, T Inoue, T Irifune (2007) Ultrasonic elastic wave velocity measurements of MgO at high pressures and high temperatures with standard free pressure calibration, Eos Trans. Am. Goephys Union, Fall Meeting, MR53A 06.

Kubo T, E Ohtani, T Kato, S Urakawa, A Suzuki, Y Kanbe, K-I Funakoshi, W Utsumi, T Kikegawa, K Fujino (2002) Mechanisms and kinetics of the post-spinel transformation in Mg_2SiO_4. *Phys. Earth Planet. Int.*, **129**, 153–171.

Kubo T, E Ohtani, K Funakoshi (2004) Nucleation and growth kinetics of the α–β transformation in Mg_2SiO_4 determined by in situ synchrotron powder x-ray diffraction. *Am. Miner*., **89**, 285–293.

Kubo T, E Ohtani, T Kato, T Kondo, T Hosoya, A Sano, T Kikegawa (2008) Kinetics of the post-garnet transformation: implications for density and rheology of subducting slabs. *Phys. Earth Planet. Int*., **170**, 181–192.

Kumazawa M (1973) Theory of generation of very high static pressures by an external force. *High Temp.-High Press*., **5**, 599–619.

Kung J, B Li, T Uchida, Y Wang (2005) In-situ elasticity measurement for the unquenchable high-pressure clinopyroxene phase: implication for the upper mantle, *Geophys. Res. Lett.*, **32**, doi:10.1029/2004GL021661.

Kusaba K, L Galoisy, Y Wang, MT Vaughan, DJ Weidner (1993) Determination of phase transition pressures of ZnTe under quasihydrostatic conditions. *PAGEOPH*, **141**, 643–652.

Le Godec Y, G Hamel, VL Solozhenko, D Martinez-Garcia, J Philippe, T Hammouda, M Mezouar, WA Crichton, G Morard, S Klotz (2009) Portable multi-anvil device for in situ angle-dispersive synchrotron diffraction measurements at high pressure and high temperature. *J. Synchr. Radiat*., **16**, 513–523.

Lesher CE, Y Wang, S Gaudio, A Clark, N Nishiyama, M Rivers (2009) Densities of magnesium silicate glasses and melts at high pressure by X-ray microtomography. *Phys. Earth Planet. Int*., **174**, 292–301.

Li B, RC Liebermann, DJ Weidner (2001) P-V-V_P-V_S-T measurements on wadsleyite to 7 GPa and 873K: Implications for the 410-km seismic discontinuity. *J. Geophys. Res*., **106**: 30575–30591.

Li B, J Kung, T Uchida, Y Wang (2005) Pressure calibration to 20 GPa by simultaneous use of ultrasonic and x-ray techniques, *J. Appl. Phys*., **98**, 013521, doi:10.1063/1.1946905.

Liebske C, B Schmickler, H Terasaki, BT Poe, A Suzuki, K Funakoshi, R Ando, DC Rubie, (2005) Viscosity of peridotite liquid up to 13 GPa: Implications for magma ocean viscosities. *Earth Planet. Sci. Lett*., **240**, 589–604.

Maeda Y, H Kanetsuna, K Tagashira, T Takemura (1981) DTA and x-ray studies on extended-chain crystals of polyethylene under high pressure. *J. Polym. Sci*.: Polymer Physics Edition, 19, 1325–1331.

Mezouar M, P Faure, W Crichton, N Rambert, B Sitaud, S Bauchau, G Blattmann (2002) Multichannel collimator for structural investigations of liquids and amorphous materials at high pressures and temperatures. *Rev. Sci. Instrum.*, **73**, 3570–3574.

Nelmes RJ, MI McMahon (1998) in: Semiconductors and Seimimetals (Eds. R.K. Willardson and E.R. Weber), Academic, New York, 1998, vol. 54, p. 145.

Nishi M, T Kato, T Kubo, T Kikegawa (2008) Survival of pyropic garnet in subducting plates, *Phys. Earth Planet. Int.*, **170**, 274–280.

Nishiyama N, T Irifune, T Inoue, J Ando, K Funakoshi (2004) Precise determination of phase relations in pyrolite across the 660 km seismic discontinuity by in situ X-ray diffraction and quench experiments. *Phys. Earth Planet. Int*., **143**–**144**, 185–199.

Nishiyama N, Y Wang, T Irifune, T Sanehira, ML Rivers, SR Sutton, D Cookson (2009) Development of a combination of a Drickamer apparatus and monochromatic X-rays for stress and strain measurements under high pressure. *J. Synchtr. Rad*., **16**(6), doi:10.1107/S0909049509033342.

Ono S, T Katsura, E Ito, M Kanzaki, A Yoneda, MJ Walter, S Urakawa, W Utsumi, K Funakoshi (2001) *In situ* observation of ilmenite-perovskite phase transition in $MgSiO_3$ using synchrotron radiation. *Geophys. Res. Lett.*, **28** (5), 835–838.

Onodera A (1987) Octahedral-anvil high-pressure devices. *High Temp.-High Press.*, **19**, 579–609.

Osako M, E Ito, A Yoneda (2004) Simultaneous measurements of thermal conductivity and thermal diffusivity for garnet and olivine under high pressure. *Phys. Earth Planet. Inter.*, **143**–**144**, 311–320.

Osugi J, K Shimizu, K Inoue, K Yasunami (1964) A compact cubic anvil high pressure apparatus. *Rev. Phys. Chem. Jpn.*, **34**, 1–6.

Poe BT, C Romano, C Liebske, DC Rubie, Terasaki, H, A Suzuki, K Funakoshi (2006) High-temperature viscosity measurements of hydrous albite liquid using in-situ falling-sphere viscometry at 2.5 GPa. *Chem. Geol.*, **229**, 2–9.

Reid JE, A Suzuki, K Funakoshi, H Terasaki, BT Poe, DC Rubie (2003) The viscosity of diopside ($CaMgSi_2O_6$) liquid at pressures up to 13 GPa. *Phys. Earth Planet. Int*., **139**, 45–54.

Rutter MD, RA Secco, H Liu, T Uchida, ML Rivers, SR Sutton, Y Wang (2002a) Viscosity of liquid Fe at high pressure, *Phys. Rev. B*, **66**, 060102-1:4.

Sano A, E Ohtani, K Litasov, T Kubo, T Hosoya, K Funakoshi, T Kikegawa (2006) In situ X-ray diffraction study of the effect of water on the garnet–perovskite transformation in MORB and implications for the penetration of oceanic crust into the lower mantle. *Phys. Earth Planet. Int.*, **159**, 118–126.

Shimomura O, S Yamaoka, T Yagi, M Wakatsuki, K Tsuji, H Kawamura, N Hamaya, O Fukuoga, K Aoki, S Akimoto (1985) Multi-anvil type X-ray system for synchrotron radiation, in Solid State Physics Under Pressure (Ed. S Minomura), Terra Scientific Publishing Co., Tokyo, pp. 351–356.

Shimomura O, W Utsumi, T Taniguchi, T Kikegawa, T Nagashima (1992) A new high pressure and high temperature apparatus with sintered diamond anvils for synchrotron radiation use, in High-Pressure Research: Application to Earth and Planetary Sciences (Eds. Y. Syono and M.H. Manghnani), TERRAPUB, Tokyo, pp. 3–11.

Tange Y, T Irifune, K Funakoshi (2008) Pressure generation to 80 GPa using multiamvil apparatus with sintered diamond anvils. *High Pres. Res*., **28**, 245–254.

Terasaki H, T Kato, S Urakawa, K Funakoshi, K Sato, A Suzuki, T Okada (2002) Viscosity change and structural transition of Molten Fe at 5 GPa. *Geophys. Res. Lett*., **29**(8), (2002), doi:10.1029/2001GL014321.

Terasaki H, T Kato, K Funakoshi, A Suzuki, S Urakawa (2004) Viscosity of liquid sulfur under high pressure. *J. Phys.: Condens Matter*., **16**, 1707–1714.

Terasaki H, A Suzuki, E Ohtani, K Nishida, T Sakamaki, K Funakoshi (2006) Effect of pressure on the viscosity of Fe-S and Fe-C liquids up to 16 GPa. *Geophys. Res. Lett*., **33**, doi:10.1029/2006GL027147.

Terasaki H, S Urakawa, K Funakoshi, Y Wang, Y Shibazaki, T Sanehira, Y Ueda, E Ohtani (2008) Interfacial tension measurement of Ni-S liquid using high pressure X-ray micro-tomography. *High Press. Res*., **28**, 327–334, doi:10.1080/08957950802208902.

Tinker D, CE Lesher, GB Baxter, T Uchida, Y Wang (2004) High-pressure viscometry of polymerized silicate melts and limitations of the Eyring equation. *Am. Min*., **89**, 1701–1708.

Tsuji K, K Yaoita, M Imai, O Shimomura, T Kikegawa (1989) Measurements of x-ray diffraction for liquid metals under high pressure. *Rev. Sci. Instrum*., **60**, 2425–2428.

Uchida T, Y Wang, ML Rivers, SR Sutton (2001) Stability field and thermal equation of state of epsilon-iron determined by synchrotron X-ray diffraction in a multianvil apparatus. *J. Geophys. Res*., **106**, 21,799–21,810.

Uchida T, Y Wang, N Nishiyama, R Von Dreele, A Nozawa, K Funakoshi, H Kaneko, T Irifune, Y Yamada (2009) Structure of $CaSiO_3$ perovskite to 1300 K and 25 GPa. *Earth Plant. Sci. Lett.* (in press).

Utsumi W, K Funakoshi, S Urakawa, M Yamakata, K Tsuji, H Konishi, O Shimomura, (1998) SPring-8 beamlines for high pressure science with multi-anvil apparatus. *Rev. High Press. Sci. Technol.* **7**, 1484–1486.

Vaughan MT, DJ Weidner, YB Wang, JH Chen, CC Koleda, IC Getting (1998) T-CUP: A new high-pressure apparatus for X-ray studies. *Rev. High Press. Sci. Technol.* **7**, 1520–1522.

Wang Y, M Rivers, T Uchida, P Murray, G Shen, S Sutton, J Chen, Y Xu, D Weidner (2000), High pressure research using large-volume presses at GeoSoilEnviroCARS, Advanced Photon Source, in: *Proceedings of the International Conference on High Pressure Science and Technology (AIRAPT-17)*, Science and Technology of High Pressure, vol. 2, pp. 1047–1052.

Wang Y, WB Durham, IC Getting, DJ Weidner (2003) The deformation DIA: a new apparatus for high temperature triaxial deformation to pressures up to 15 GPa, *Rev. Sci. Instrum*., **74**, 3002–3011.

Wang Y, T Uchida, RB Von Dreele, ML Rivers, N Nishiyama, K Funakoshi, A Nozawa, H Kaneko (2004) A new technique for angle-dispersive powder diffraction using an energy-dispersive setup and synchrotron radiation. *J. Appl. Cryst.*, **37**, 947–956.

Wang Y, T Uchida, F Westferro, ML Rivers, N Nishiyama, J Gebhardt, CE Lesher, SR Sutton (2005) High-pressure x-ray tomography microscope: synchrotron computed microtomography at high pressure and temperature. *Rev. Sci. Instrum*., **76**, 073709, doi:10.1063/1.1979477.

Wang Y, CE Lesher, S Gaudio, A Clark, J Roberts, T Sanehira, H Watson (2008) High pressure tomography in studies of core formation mechanisms, Eos Trans., AGU 89(53) Fall Meet. Suppl., Abstract MR43A-1800.

Wang Y, ML Rivers, SR Sutton, N Nishiyama, T Uchida, T Sanehira (2009) Large-volume high pressure facility at GSECARS: a "Swiss-Army-Knife" approach to synchrotron-based experimental studies. *Phys. Earth Planet. Int.*, **174**, 270–281.

Yamanaka T, K Sugiyama, K Ogata (1992) Kinetic study of the GeO2 transition under high pressures using synchrotron X-radiation. *J. Appl. Cryst*., **25**, 11–15.

Yamazaki D, S Karato (2001) High pressure rotational deformation apparatus to 15 GPa. *Rev. Sci. Instrum.*, **72**, 4207–4211.

Yaoita K, Y Katayama, K Tsuiji, T Kikegawa, O Shimomura (1997) Angle-dispersive diffraction measurement system for high-pressure experiments using a multichannel collimator. *Rev. Sci. Instrum*., **68**, 2106–2110.

Yoshino T, G Manthilake, T Matsuzaki, T Katsura (2008) Dry mantle transition zone inferred from the conductivity of wadsleyite and ringwoodite. *Nature*, **451**, 326–329.

Zhang J, B Li, W Utsumi, RC Liebermann (1996) *In situ* X-ray observations of the coesite – stishovite transition: reversed phase boundary and kinetics. *Phys. Chem. Mineral.*, **23**, 1–10.

RHEOLOGY AT HIGH PRESSURES AND HIGH TEMPERATURES

YANBIN WANG*, NADEGE HILAIRET
Center for Advanced Radiation Sources,
The University of Chicago

Abstract We review recent progress in studying deformation at simultaneous high pressure and high temperature using in-situ diffraction and imaging in the large volume press (LVP). Current state-of-the-art deformation devices and diffraction and imaging techniques are introduced, along with theoretical background for stress measurements based on diffraction. Examples are given to illustrate the kind of information that can be extracted using these techniques. Future prospects are discussed.

Keywords: Rheology, deformation, diffraction, high pressure and high temperature

1. Introduction

The physics of deformation of solids plays a vital role in earth science, materials science, and engineering. While materials scientists try to understand the mechanical behavior of ceramics and metals in discovering new materials capable of withstanding severe pressure (P) and temperature (T) conditions or to save cost of matter and energy, earth scientists aim at extrapolating laboratory deformation data on earth materials to large strains and low strain rates, to understand geodynamic processes over time scales of millions of years, under extreme P–T conditions.

Deformation is a kinetic process involving transport of matter. A successful technique for studying this process requires measurements on stress (the driving force for mass transport), strain (the amount of transport), and strain rate (the speed of transport). Many experimental techniques are available to study plastic deformation. Here we are primarily interested in those that can be applied to high P–T, especially those involved with x-ray (and neutron) diffraction. We will restrict our scope to the large-volume press (LVP),

* E-mail: wang@cars.uchicago.edu

E. Boldyreva and P. Dera (eds.), *High-Pressure Crystallography: From Fundamental Phenomena to Technological Applications*, DOI 10.1007/978-90-481-9258-8_9,

which has many advantages in studying plastic deformation: it offers relatively homogeneous and sustained P–T conditions for controlled deformation over a long period of time; it offers sufficient sample size so that strain and strain rates can be measured, with large number of crystallites providing robust diffraction statistics and allowing examination of grain size dependence in rheological properties; it allows texture to be determined during the cause of deformation.

Unlike the elastic Hookean behavior, where stress and strain responses are instantaneous, linear, and path independent, plastic behavior is non-linear and time dependent (Figure 1). Strain and strain rate are vital parameters in describing this behavior. Here we do not consider the brittle behavior, where the sample may fail catastrophically above a certain stress or strain level.

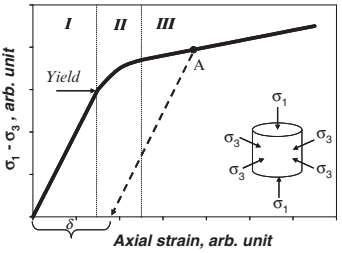

Figure 1. A schematic illustration of a typical stress–strain curve during triaxial deformation. Stage I: elastic; stage II: primary creep; stage III: steady-state creep. Note yield point where non-linearity begins.

The macroscopic variables describing plastic deformation are stress (σ), strain (ε), strain rate ($\dot{\varepsilon}$), T, and P. Which variables are chosen as independent depends on the applications one is interested in.

For geodynamics, it is usually more convenient to treat $\dot{\varepsilon}$, T, and P as independent variables. Since temperatures in the Earth are high and stress levels are low, mineral deformation often follow the power-law:

$$\dot{\varepsilon} = Af_1(fO_2)f_2(H_2O)f_3(d)\sigma^n \exp\left(\frac{E_a + PV_a}{RT}\right), \quad (1)$$

where A is a material constant, f_1, f_2, and f_3 describe the dependence of the deformation process on oxygen fugacity (fO_2), volatile content (exemplified here as H_2O), and grain size (d); n is the stress exponent, E_a the activation energy, V_a activation volume, and R the gas constant.

2. Experimental Devices for Diffraction Based Deformation Studies at High P and T

It this section we describe devices used for large-volume high P–T deformation studies. Techniques with the diamond anvil cell are covered in a separate chapter (*Merkel*, this volume). We further restrict discussions to the devices that can provide both stress and plastic strain information.

2.1. DEFORMATION DIA (D-DIA)

Operation principles are given in *Wang et al.* (2003). Here we focus on the diffraction specifics and designs of cell assemblies. Figure 2 illustrates the anvil configuration for x-ray diffraction. At least two x-ray transparent anvils must be used, on the diffraction side, to ensure that diffraction patterns at various azimuth angles to be recorded. This is the key in stress measurement. Both sintered diamond (SD) and cubic boron nitride (cBN) anvils have been used. For SD, lighter binding materials (such as Si) are preferred. On the other hand, Co-based SD anvils tend to have higher strength, allowing attainment of higher pressures.

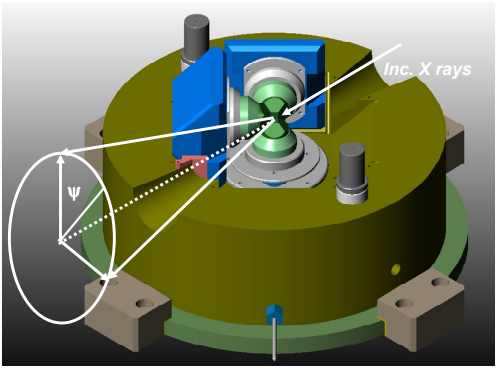

Figure 2. Diffraction configuration in the D-DIA. The circle on the left represents a Debye ring, with the azimuth angle Ψ indicated. The maximum 2θ angle is determined by the conical angle in the cut out in the guide block.

A representative cell assembly is shown in Figure 3. Thermocouple is protected by the ceramic tubing, which is also used as a deformation piston. The thermocouple junction tends to cause uneven deformation at the sample-thermocouple interface, making total strain measurement uncertain and difficult. Often the power-temperature relation is calibrated before hand, and deformation experiments are conducted based on the calibration only. This results in large uncertainties in temperature estimate and is an area for further technical developments.

Many materials have been studied using the D-DIA. The highest pressure achieved so far is about 19 GPa (*Nishiyama et al*., 2007), and maximum temperature to date is about 1,600 K (*Durham et al*., 2009).

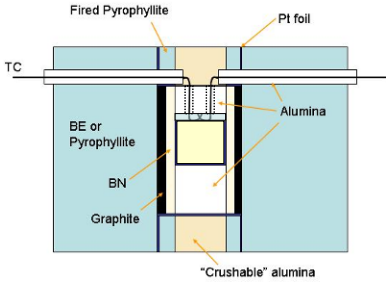

Figure 3. A typical cell assembly used in D-DIA experiments.

2.2. DRICKAMER APPARATUS

The Drickamer anvil apparatus has been used in a way similar to side diffraction in the DAC for measuring lattice strain (e.g., *Funamori et al*., 1994). This apparatus offers larger samples and more stable T (to ~2,000 K)

than the DAC. Although stress and pressure are coupled, like in the case of the DAC, this apparatus can generate pressures in excess of 40 GPa using sintered diamond anvils, making it possible to study plastic deformation under lower mantle conditions. *Nishiyama et al*. (2009) modified the Drickamer apparatus for both stress and strain measurement using monochromatic radiation. X-ray windows are machined into the steel containment ring (Figure 4a) to allow beam passage. Conical path on the diffraction side makes it possible to record complete Debye rings up to ±10° in 2θ. With specially designed cell assemblies, *Nishiyama et al*. (2009) studied bulk samples about 0.3–0.5 mm in diameter and 0.3–0.4 mm in thickness to pressures above 30 GPa.

New high T cells have recently been developed (e.g., *Gotou et al.,* 2006), using a mixture of TiC + diamond powder as heating material, making it possible to investigate deformation at simultaneous high pressure and temperature conditions corresponding to the lower mantle.

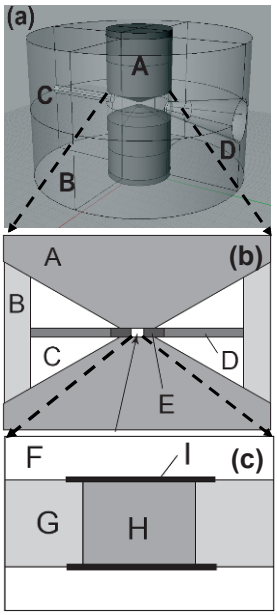

Figure 4. (a) A 3D view. A: anvil; B: containment ring; C: path for incident x rays; D: path for diffracted x rays. (b) Cell assembly. A: anvil, B: outer gasket (PEEK); C: pyrophyllite; D: inner gasket (PBI); E: pressure medium (boron epoxy). (c) An expanded view from (b) showing the sample environment. F: pyrophyllite; G: graphite; H: sample; I: gold foil.

2.3. ROTATIONAL DRICKAMER APPARATUS (RDA)

The RDA is a modification of the Drickamer apparatus, with details described by *Yamazaki and Karato* (2001). A small (~70 T) hydraulic press is used to compress the Drickamer cell. Torque is applied by connecting the top anvil to a rotational actuator, so that the top anvil rotates relative to the bottom anvil, which is fixed to the hydraulic press frame. Large shear strains can be generated. Figure 5 shows schematics of a sample assembly. Magnitude of the shear strain increases with distance from the center, strain determination is not accurate, but this is compensated by the very large strains generated. Temperatures are estimated based on power-temperature calibrations or geothermobarometry. Due to the large amounts of pressure media surrounding the sample, EDD with a multi-element detector is the diffraction technique of choice, which can significantly reduce background scattering.

A non-negligible axis stress component is present throughout the experiment in the Drickamer apparatus. Hence, the stress boundary condition acting

on the sample may be considered a combination of simple shear and a uniaxial compression. The treatment of lattice strain must take into account this complexity (*Xu et al*., 2005; *Nishihara et al*., 2008a).

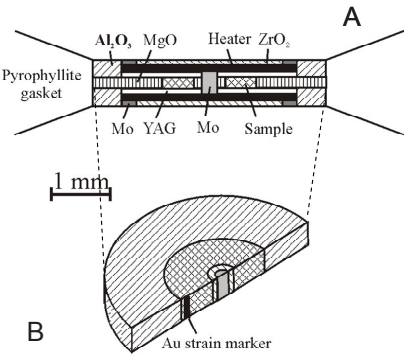

Figure 5. A typical cell assembly in the RDA. A: cross section view of the entire cell assembly sandwiched in between two anvils. B: one half of the sample, which is in a shape of a doughnut, with the center hole filled by a Mo rod. A strain marker (Au) is located near the outer diameter of the sample, inside an MgO "doughnut". No thermocouple is used to avoid x-ray damping by the wires. Modified after *Xu et al.* (2005)

2.4. DEFORMATION T-CUP AND KATD

Two new developments may be noteworthy for future applications. The deformation T-cup is under development at the National Synchrotron Light Source (NSLS) and Stony Brook. This is a modified T-cup apparatus (See chapter on large-volume techniques), compressing the Kawai-type eight-cube assembly along the [111] direction, with the top-most and lower-most anvils driven independently by build-in differential rams in the guide-blocks.

A Kawai-type apparatus for triaxial deformation (KATD) was being tested at the Magma Factory, Tokyo Institute of Technology (*Nishihara*, 2008b). This apparatus uses a large D-DIA to compress a Kawai-type assembly, along the [100] direction (Figure 6). The cell assembly has an octahedral shape, nesting in the center of the eight-cube assembly. When the differential rams are advanced, the top four cubic anvils will be pressed against the bottom four anvils, causing the octahedral pressure medium to deform, resulting in deformation in the sample inside

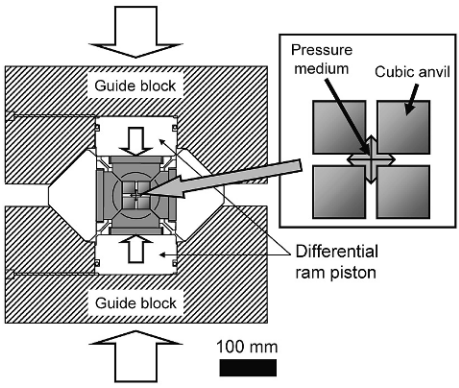

Figure 6. Cross section of the KATD. The six DIA anvils (four are shown) compress a Kawai-type eight cubic anvils in a large D-DIA. Inset shows the configuration of the second-stage cubic anvils with the octahedral pressure medium.

the octahedron. Deformation generally can only be conducted in one direction, as gasket flow between the cubic anvils cannot be reversed.

2.5. EXPERIMENTAL SETUP AT SYNCHROTRON SOURCES

Experimental setup varies depending on the apparatus and the nature of the x-ray source. Here we describe the setup at GSECARS to illustrate typical components and functions in a deformation experiment (Figure 7). For diffraction, the incident beam (monochromatic) is collimated by two pairs of WC slits, to dimensions on the order of 0.1×0.1 mm^2. Diffracted x-rays are detected by an area detector over the solid angle defined by the conical cut in the D-DIA module (±12°). No beam collimation is attempted on the diffraction side. The wavelength of the incident beam is tunable, and is optimized by considering the d-spacing range of interest, absorption of the sample and pressure media, and exposure time. Available photon energies are up to 65 keV.

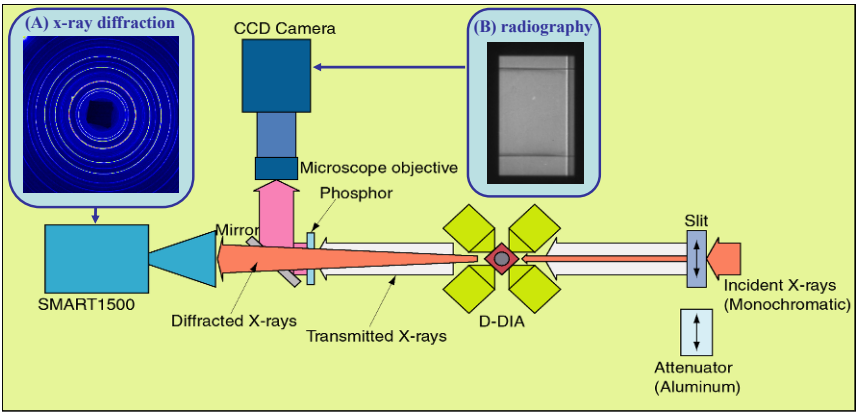

Figure 7. Experimental setup at GSECARS, APS, top view. Narrower, darker arrows passing though the cell assembly represent the diffraction beam path, whereas white arrows represent imaging beam path. An area detector (SMART1500 as an example) is used to collect diffraction signal. The phosphor/mirror assembly and the CCD camera are driven out when diffraction pattern is being recorded. (A): an example of diffraction pattern showing completely Debye rings. (B): an example of image showing markers for length determination.

The angle-dispersive diffraction (ADD) technique is exclusively used at GSECARS, where an area detector (MAR 165) is mounted perpendicular to the incident x-ray beam. Major advantages of this approach are: (1) complete Debye rings can be recorded, allowing accurate determination of lattice strains, which are the basis for stress determination (e.g., *Uchida et al*., 2004; *Nishiyama et al*., 2005, 2007; *Hilairet et al*., 2007), and (2) real-time

monitoring of texture development, which, when analyzed later, provides information on preferred orientation and slip systems (e.g., *Wenk et al.,* 2005; *Miyagi et al*., 2007). The lack of diffraction beam collimation requires that no strong scattering materials are used in the beam path. Special "windows" are inserted in the cell assembly along the beam path to eliminate scattering from the pressure media.

Another approach employs energy-dispersive diffraction (EDD) with a multi-element detector (see *Karato and Weidner*, 2008), by positioning the detector elements strategically at several points on a circle, with conical slits to collimate the diffracted signal. This significantly reduces scattering from surrounding materials in the cell assembly, but also discards vast majority of the diffraction information. As a result, no textural information can be obtained.

The incident slits can be translated or opened up to allow a large beam (on the order of 2–3 mm in linear dimensions) to illuminate the sample. This is used for imaging total sample length. Strain markers are placed on both ends of the sample, and the absorption contrast is converted into visible light by a scintillator (Ce-doped YAG single crystal). A CCD camera is used to record the image. During deformation, switching between the imaging and diffraction modes is automatic: driving the incident slits in, scintillator and CCD camera out for diffraction and driving incident slits out, scintillator and camera in for imaging.

3. Measuring Stress and Strain

Diffraction based on the Braggs relation detects changes in lattice spacings at various azimuth angles relative to the given stress field. This distortion in the lattice spacing is referred to as lattice strains, which are elastic response of the lattice to the imposed stress field and are fully recoverable when the stress is removed. This not to be confused with the total sample strain, which is the macroscopic shape change of the sample. Sample strains in our case are primarily plastic. Lattice strains do not contribute to plastic strain, which is due to the creation and motion of various defects. Both lattice strain and sample strain can be determined from x-rays, the former by diffraction and latter by imaging.

3.1. MEASURING STRESS USING DIFFRACTION

X-ray diffraction is governed by the relation between wavelength (λ), scattering angle (2θ) and the spacing between lattice planes (d) by the Bragg's law:

$$\lambda = 2d \sin\theta. \tag{2}$$

Measuring d requires that either λ or θ is held constant as the other is scanned, corresponding to angle-dispersive (ADD) or energy-dispersive diffraction (EDD), respectively. The simultaneous identification of λ and θ for a given diffraction peak defines the value of d for that lattice spacing.

Theory describing diffraction-based lattice strain under non-hydrostatic constraint has been developed for all crystallographic systems (*Singh,* 1993; *Singh and Balasingh*, 1994; *Uchida et al*., 1996). Here we concentrate on some details of the data analysis techniques using the ADD technique (*Uchida et al.*, 2004) and consider the stress geometry shown in the inset of Figure 1. Each 2-D diffraction pattern (Figure 8a) is converted into Cartesian coordinates (Figure 8b) using the software package FIT2D (*Hammersley*, 1998). In our case, $\chi = 0$ is arbitrarily defined to lie in the vertical direction, parallel to the maximum principal stress axis. Data in Cartesian coordinates are then converted into a series of 1-D (intensity vs 2θ) diffraction patterns, by binning the data in 1–5° intervals of the detector χ angle (Figure 8c). The d-spacings for (hkl) reflections are determined as a function of true azimuth angle φ (Figure 8d), which is modified based on the dependence of the detector azimuth χ on the 2θ angle: $\cos\varphi = \cos\theta\cos\chi$.

As in conventional deformation experiments, we denote the "triaxial" stress field at the center of the sample as (*Singh* [1993]),

$$\sigma_{ij} = \begin{pmatrix} \sigma_1 & 0 & 0 \\ 0 & \sigma_3 & 0 \\ 0 & 0 & \sigma_3 \end{pmatrix} = \begin{pmatrix} \sigma_p & 0 & 0 \\ 0 & \sigma_p & 0 \\ 0 & 0 & \sigma_p \end{pmatrix} + \begin{pmatrix} 2t/3 & 0 & 0 \\ 0 & -t/3 & 0 \\ 0 & 0 & -t/3 \end{pmatrix}, \tag{3}$$

where σ_1 and σ_3 are the maximum and minimum principal stresses, respectively, with compression being positive. Hydrostatic and differential stresses are defined as $\sigma_p (= (\sigma_1 + 2\sigma_3)/3)$ and $t (= \sigma_1 - \sigma_3)$, respectively. The lattice strain $\varepsilon(\varphi, hkl)$ of any d-spacing with Miller index (hkl) in a polycrystalline sample with random grain orientation is expressed as

$$\varepsilon(\varphi, hkl) = \varepsilon_p - \varepsilon_t(hkl)\left(1 - 3\cos^2\varphi\right) \tag{4}$$

where ε_p is hydrostatic lattice strain and $\varepsilon_t(hkl)$ the "differential lattice strain" due to the differential stress. The magnitude of $\varepsilon_t(hkl)$ is obtained by fitting each reflection distortion as a function of azimuth angle (Figure 8d).

The value of t is related to the differential stress by multiplying an appropriate elastic constant. It is computed from the lattice strain $\varepsilon_t(hkl)$ assuming Reuss bound (where stress is assumed continuous through all the grains) by

$$t = 6G(hkl)\varepsilon_t(hkl), \tag{5}$$

where the modulus $G(hkl)$ can be obtained from elastic compliances S_{ij} for the Voigt model (*Uchida et al.*, 1996). Note that throughout this treatment (and all that derived by Singh, 1993), crystallites are assumed randomly oriented. For samples with severe lattice preferred orientation, the azimuth dependence described in Eq (4) may breakdown (e.g., *Merkel et al.*, 2009a). It is a good practice to plot $\varepsilon(hkl)$ against $(1-3\cos^2\varphi)$ and examine the linearity of the measurement.

Once yielding occurs, even in a small population of the crystallites, grains stressed along the "softer" directions will yield and transfer loads to those along "stronger" directions (*Uchida et al.*, 2004; *Weidner et al.*, 2004). Currently the most common approach is to obtain stress level for each available Miller index individually, based on the iso-stress (Reuss) model, and then assume that the average of all the individual stresses reasonably represents macroscopic stress in the sample (*Uchida et al.*, 2004, 2005; *Li et al.*, 2006; *Durham et al.*, 2009). Elasto-plastic self-consistent modeling (e.g., *Clausen and Lorentzen*, 1997) may provide an improved technique in defining a unique macroscopic stress from lattice strain measurement. The technique is discussed by *Merkel* (2009b, this volume) and *Burnley and Zhang* (2008).

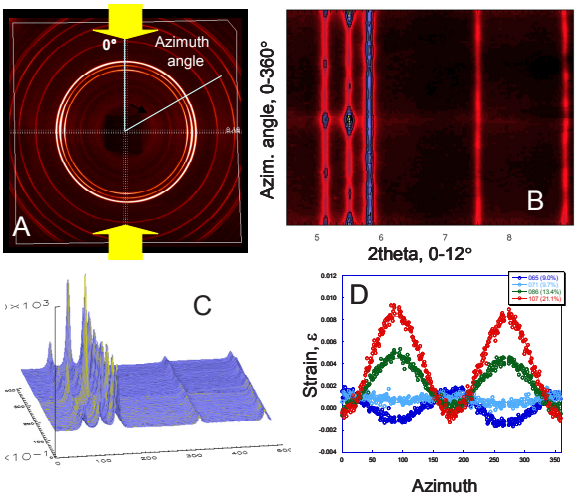

Figure 8. Data processing for lattice strain analysis using monochromatic diffraction. (a): area detector data, polar coordinates of reciprocal *d*-spacing versus detector azimuth χ. Unique principal stress direction σ_1 is indicated by the large arrows. (b): after conversion to Cartesian coordinates. (c): Intensity versus 2θ plots for various azimuthal bins. (d): Dependence of d-spacing on azimuth angle determined from the 1D plots in (c).

3.2. MEASURING STRAIN USING RADIOGRAPHY

Markers of contrasting materials at strategic locations allow tracking of deformation on radiographs of the sample. For the D-DIA, the cylindrical ends of the sample are the best locations; for RDA, a small marker foil loaded parallel to compression axis is more convenient to detect shear strain. Accuracy of measured strains depends critically on how precisely the positions of the strain markers are defined. Image quality can be enhanced by processing images with a median filter to remove zingers and salt-and-pepper noise. One can simply define marker positions by the minima in intensity values on columns of the image, but this has limited precision. The best resolution to date is obtained using the approach described by *Li et al.* (2003), inspired by classical image analysis methods. 2D cross-correlation of a region containing the marker is applied to a pair of consecutive images, to find an area on the second image with the 2D distribution of intensities closest to the first one. A spline of the sum of squared differences (SSD) in the direction of deformation is then sampled at sub-pixel intervals to refine the shift to a sub-pixel resolution. The area shift from one image to the next is assumed to represent the marker position shift. Irregular shapes or shadows then become an advantage, provided that only small (a few pixels) shifts are occurring between two images.

The strain rate is defined as the variation of strain over time. The precision of the strain rate depends on the precision on the time measure, the absolute sample length, and the strain measurement. The response of the sample and its surrounding medium to the applied strain depends on the rigidity of the cell assembly and of the apparatus itself. Therefore even though the apparatus is controlled at constant displacement, sample deformation may not flow at a constant strain rate. Strain rate usually becomes almost constant when the sample flows at a pseudo-steady state; this strain rate is obtained by linear regression of strain over time and over several percent of strain.

4. What Information can be Obtained and How?

Here we briefly review the wide range of information on plastic flow that can be obtained using the current high P–T deformation methods, illustrating with recent works. Readers are encouraged to consult publications cited.

4.1. STRESS–STRAIN CURVES AND DETERMINATION OF FLOW LAWS

Flow stresses obtained for different P–T-ε conditions are fitted to flow laws. By carefully controlling the confining pressure during deformation, isobaric and isothermal stress–strain curves can be obtained in the D-DIA

(e.g., *Nishiyama et al*., 2005, 2007; *Hilairet et al*., 2007 using ADD; *Ratterron et al*., 2007, *Li et al*., 2006 and *Durham et al*., 2009 using EDD). For the RDA, an approximately constant pressure can also be maintained during shear deformation (e.g., *Kawazoe et al*., 2007). Less straightforward is the use of the modified Drickamer cell, where pressure and stresses are generally coupled, much as in the DAC. One would expect that in D-T-cup and KATD, pressure and stress are also coupled.

High pressure with control on differential stress has been the key to obtaining rheological properties of complex materials such as phyllosilicates, which exhibit a semi-brittle behavior at lower confining pressures and may amorphize under too high a non-hydrostatic stress. Quantifying antigorite rheology, for instance, showed it plays an important role in controlling stress build-up and deformation in the subduction zones (*Hilairet et al*., 2007).

4.2. TEXTURE ANALYSIS AND LATTICE PREFERRED ORIENTATION

Lattice preferred orientation (LPO) can be measured using ADD technique. Defining and quantifying these LPO at relevant P and T conditions allow an understanding of slip systems and elastic anisotropy due to deformation (e.g. *Wenk et al.* (2005) on Mg_2SiO_4 ringwoodite, and *Miyagi et al.*, 2007 on post-perovskite $CaIrO_3$).

4.3. ELASTO-PLASTIC SELF-CONSISTENT MODELING

Diffraction data on deformed polycrystalline samples reveal a great deal of information of deformation physics but are complex to extract. One of the challenges is how to correlate differential stresses calculated from different reflections to the macroscopic stress. A widely adopted approach is to use the averaged value of all stresses measured for available reflections in the experiment. *Burnley and Zhang* (2008) employed elastic-plastic self-consistent (EPSC) modeling to address this problem in quartz (also see *Merkel*, 2009b, this volume). It is worth pointing out that EPSC models work best for low temperature creep, where dislocation glide is the dominant deformation mechanism. With increasing temperature, diffusion related process become more important. Dislocation climb, recrystallization etc. may not be modeled by the EPSC technique at present.

5. Future Prospects and Conclusion

Using x-ray diffraction to conduct quantitative studies on high pressure and high temperature deformation is relatively new. Although significant advances have been made in the past few years, many more are needed to improve our understanding of the deformation process, especially at grain-to-grain level. Efforts are currently being devoted to the following directions:

Improve resolution in stress and strain measurement. Current stress resolution is at about 50 MPa level. In order to measure creep strength at high temperatures accurately, a stress resolution to 10 MPa is needed. Multi-element detectors are being considered for EDD techniques, whereas larger area detectors with smaller pixel size will help experiments with ADD technique. For the latter, focused beam will help reduce data collection time, to improve time resolution. For strain measurement, absolute length resolution of 0.1 μm or better will be essential. For a 1 mm long sample, this corresponds to a strain of 10^{-5}.

Larger cell and sample volume. In order to examine effects of grain size and oxygen fugacity on deformation, larger cell and sample volume is the key. Larger devices are therefore needed. Larger DDIA's represent development in this direction.

Higher P-T capabilities. Single-stage DDIA is potentially limited to pressure. Double-stage systems such as KATD and modified Drickamer apparatus may allow deformation of large sample to higher pressure and temperature conditions.

Understanding micro-mechanisms of deformation. Theoretical investigations are needed to understand polycrystal behavior at grain-to-grain level.

Eventually, an integrated approach using all above mentioned techniques will help us in gaining insight of the rheological processes under high pressure and temperature.

ACKNOWLEDGMENTS

GSECARS is supported by the National Science Foundation – Earth Sciences (EAR-0622171) and Department of Energy – Geosciences (DE-FG02-94ER14466). M. Rivers, S. Sutton, T. Uchida, N. Nishiyama have contributed greatly to the GSECARS deformation facility. Many past users also have contributed to the development; special thanks go to S. Merkel, H. Wenk, L. Miyagi, B. Reynard, and I. Daniel. We thank S. Merkel for stress analysis software and L. Li for code for strain analysis, on which our present code is based. Use of the APS was supported by the U.S. Department of Energy, Office of Science, Office of Basic Energy Sciences, under Contract No. DE-AC02-06CH11357. We acknowledge the generous support from NSF (EAR0652574 and 0711057) for portions of the work reported here.

References

Burnley, P.C., Zhang, D., (2008), Interpreting in situ x-ray diffraction data from high pressure deformation experiments using elastic-plasticc self-consistent models: an example using quartz. *J. Phys.: Condens. Matter*, **20**, 285201 (10 pp), doi:10.1088/0953-8984/20/28/28501.

Clausen, B., Lorentzen, T., (1997), A self-consistent model for polycrystal deformation, description and implementation, Riso National Laboratory *Risø-R-970 (EN)* Roskilde, Denmark, pp 42.

Durham, W.B., Mei, S., Kohlstedt, D.L., Wang, L., Dixon, N.A., (2009), New measurements of activation volume in olivine under anhydrous conditions. *Phys. Earth Planet. Int*., **172**, 67–73.

Funamori, N., Yagi, T., Uchida T., (1994), Deviatoric stress measurement under uniaxial compression by a powder x-ray diffraction method, *J. Appl. Phys.*, **75**, 4327–4331.

Gotou, H., Yagi, T., Frost, D.J., and Rubie, D.C., (2006), Opposed-anvil-type high-pressure and high-temperature apparatus using sintered diamond, *Rev. Sci. Instrum.*, **77**, 035113.

Hammersley, A.P., (1998), Fit2d: V9.129 reference manual v3.1, Internal Rep. ESRF98HA01, ESRF, Grendole, France.

Hilairet, N., Reynard, B., Wang, Y., Daniel, I., Merkel, S., Nishiyama, N., Petitgirard S., (2007), High-pressure creep of serpentine, interseismic deformation, and initiation of subduction, *Science*, **318**, 1910–1912, doi:10.1126/science.1148494.

Karato, S., Weidner, D., (2008), Laboratory studies of rheological properties of minerals under deep mantle conditions, *Elements*, **4**, 191–196, doi:10.2113/gselements.4.3.191.

Kawazoe, T., Karato, S., Otsuka, K., Jing, Z., Mookherjee, M., (2008), Shear deformation of olivine under deep upper mantle conditions using a rotational Drickamer apparatus (RDA), *Phys. Earth Planet. Inter.*, **174**, 128–137.

Li, L., Raterron, P., Weidner, D., Chen, J., (2003), Olivine flow mechanisms at 8 GPa, *Phys. Earth Planet. Int*., **138**, 113–129.

Li, L., Weidner, D., Raterron, P., Chen, J., Vaughan, M., Mei, S., Durham, W., (2006), Deformation of olivine at mantle pressure using the D-DIA, *Eur. J. Mineral*., **18**, 7–19.

Merkel, S., Tome, C., Wenk, H-R., (2009a), Modeling analysis of the influence of plasticity on high pressure deformation of hcp-Co, *Phys. Rev., B*, **79**, 064110, doi:10.1103/PhysRevB.79.064110.

Merkel, S., (2009b), This volume.

Miyagi, L., Nishiyama, N., Wang, Y., Kubo, A., West, D.V., Cava, R.J., Duffy, T., Wenk, H-R., (2008), Deformation and texture development in $CaIrO_3$ post-perovskite phase up to 6 GPa and 1300 K, *Earth Planet. Sci. Lett*., **268**, 515–525.

Nishihara, Y., (2007), High-pressure and high-temperature deformation experiments using Kawai-type apparatus for triaxial deformation (KATD), Annual report of research for the evolving Earth and planets, Tokyo Institute of Technology, pp. 37–40.

Nishihara, Y., Tinker, D., Xu, Y., Jing, Z., Matsukage, K.N., Karato, S., (2008a), Plastic deformation of wadsleyite and olivine at high-pressure and high-temperature using a rotational Drickamer apparatus (RDA), *Phys. Earth Planet. Inter*., **170**, 156–169.

Nishihara, Y., (2008b), Recent technical developments of high-pressure deformation experiments (in Japanese with English abstract), *Rev. High Press. Sci. Technol.*, **18**(3), 223–229.

Nishiyama, N., Wang, Y., Rivers, M.L., Sutton, S.R., Cookson, D., (2007), Rheology of ε-iron up to 19 GPa and 600 K in the D-DIA, *Geophys. Res. Lett*., **34**, L23304, doi:10.1029/2007GL031431.

Nishiyama, N., Wang, Y., Uchida, T., Irifune, T., Rivers, M., Sutton, S.R., (2005), Pressure and strain dependence on the strength of sintered polycrystalline Mg_2SiO_4 ringwoodite, *Geophys. Res. Lett.*, **32**, L04307, doi:10.1029/2004GL022141.

Nishiyama, N., Wang, Y., Sanehira, T., Irifune, T., Rivers, M., (2008), Development of the Multi-anvil assembly 6-6 for DIA and D-DIA type high pressure apparatus, *High Press. Res*., **28**, 307–314.

Nishiyama, N., Wang, Y., Irifune, T., Sanehira, T., Rivers, M.L., Sutton, S.R., Cookson, D., (2009), Development of a combination of a Drickamer apparatus and monochromatic X-rays for stress and strain measurements under high pressure, *J. Synchtr. Rad*., **16**(6), doi:10.1107/S0909049509033342.

Raterron, P., Chen, J., Li, L., Weidner, D., Cordier, P., (2007), Pressure-induced slip-system transition in forsterite: single-crystal rheological properties at mantle pressure and temperature, *Am. Mineral.*, **92**, 1436–1445.

Singh, A.K., (1993), The lattice strains in a specimen (cubic system) compressed nonhydrostatically in an opposed anvil device, *J. Appl. Phys.*, **73**, 4278–4286.

Singh, A.K., Balasingh, C., (1994), The lattice strains in a specimen (hexagonal system) compressed nonhydrostatically in an opposed anvil high pressure setup, *J. Appl. Phys.*, **75** (1994) 4956–4962.

Uchida, T., Funamori, N., Yagi, T., (1996), Lattice strains in crystals under uniaxial stress field, *J. Appl. Phys*., **80**, 739–746.

Uchida, T., Wang, Y., Rivers, M.L., Sutton, S.R., (2004), Yield strength and strain hardening of MgO up to 8 GPa measured in the deformation-DIA with monochromatic X-ray diffraction, *Earth Planet. Sci. Lett.*, **226**, 117–126.

Uchida, T., Wang, Y., Rivers, M., Sutton, S., (2005), Stress and strain measurements of polycrystalline materials under controlled deformation using monochromatic synchrotron radiation. In: *Advances in High-Pressure Technology for Geophysical Application*, edited by J. Chen, Y. Wang, T. Duffy, G. Shen, L. Dobrzhinetskaya, Elsevier, Amsterdam, pp. 137–165.

Wang, Y., Durham, W.B., Getting, I.C., Weidner, D.J., (2003), The deformation DIA: a new apparatus for high temperature triaxial deformation to pressures up to 15 GPa, *Rev. Sci. Instrum*., **74**, 3002–3011.

Wang, Y., (2009), Large volume presses for high-pressure studies using synchrotron radiation, This volume.

Weidner, D.J., Li, L., Davis, M., and Chen, J., (2004), Effect of plasticity on elastic modulus measurements. *Geophys. Res. Lett.*, **31**, doi:10.1029/2003GL019090.

Wenk, H-R., Ischia, G., Nishiyama, N., Wang, Y., Uchida, T., (2005), Texture development and deformation mechanisms in ringwoodite, *Phys. Earth Planet. Int.*, **152**, 191–199.

Xu, Y., Nishihara,Y., Karato, S., (2005), Development of a rotational Drickamer apparatus for large-strain deformation experiments under deep Earth conditions. In: *Frontiers in High-Pressure Research: Applications to Geophysics*, edited by J. Chen, Y. Wang, T.S. Duffy, G. Shen, and L.F. Dobrzhinetskaya, Elsevier, Amsterdam, pp. 167–182.

Yamazaki, D., Karato, S., (2001), High pressure rotational deformation apparatus to 15 GPa, *Rev. Sci. Instrum.*, **72**, 4207–4211.

RADIAL DIFFRACTION IN THE DIAMOND ANVIL CELL: METHODS AND APPLICATIONS

SEBASTIEN MERKEL*
Laboratoire de Unité Matériaux et Transformations, Université Lille 1, CNRS, 59655 Villeneuve d'Ascq, France

Abstract Radial diffraction in the diamond anvil cell is a relevant technique for the study of plastic behavior of materials under high pressure. In this geometry, incident x-rays are perpendicular to the compression direction and we study the distortion of the diffraction rings, as well as variations of diffraction intensities with orientation. Plastic deformation induces local stress heterogeneities that are not properly accounted for in theories relying on elasticity only. Here, I show how those experiments coupled to numerical plasticity models can be used to extract important information, such as the identification of microscopic deformation mechanisms, a measure of the average stress supported by the sample, and a quantification of local stresses.

Keywords: Radial diffraction, texture, plasticity, stress, lattice preferred orientations

1. Introduction

Radial diffraction in the diamond anvil cell was first developed for the study of elastic properties (*Mao et al.*, 1996, 1998; *Singh et al.*, 1998). It gave rise to controversies as the elastic moduli deduced from this method did not agree with other techniques (*Duffy et al.*, 1999; *Weidner et al.*, 2004; *Antonangeli et al.*, 2006). On the other hand, the technique has been very successful for the study of plastic behavior of polycrystals (*Wenk et al.*, 2000, 2006; *Merkel et al.*, 2002, 2006a).

In general, diamond anvil cell experiments use the transparency of diamond for spectroscopy, diffraction, and other measurements. In this conventional geometry, and for diffraction experiments, the incoming x-ray

* E-mail: sebastien.merkel@univ-lille1.fr

E. Boldyreva and P. Dera (eds.), *High-Pressure Crystallography: From Fundamental Phenomena to Technological Applications*, DOI 10.1007/978-90-481-9258-8_10,

beam is parallel to the compression direction, and the results are sufficient for many studies. In the radial geometry, the incoming x-ray beam is perpendicular to the compression direction and diffraction spectra arise from lattice planes having many orientations relative to the compression. Elastic deformation supported by the sample can be seen from the distortion of the Debye rings that become elliptic. Plastic deformation is visible through the variations of diffraction intensities with orientations, which indicate lattice preferred orientations.

Here, I will start by briefly introducing the technique. In the second part, I will show how it can be used to study lattice preferred orientations in polycrystals and deduce microscopic deformation mechanisms controlling the plastic behavior of the sample. In the last section, I will discuss the issue of stress analysis and show how measured d-spacings are largely influenced by effects of plasticity.

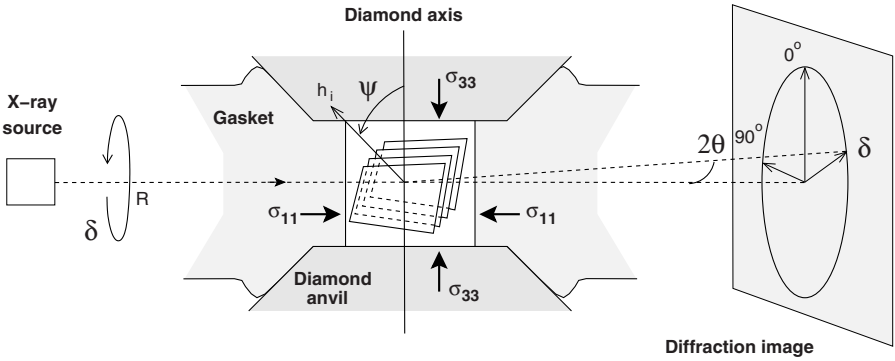

Figure 1. Radial Diffraction using monochromatic beam. The sample is confined under non-hydrostatic stress. σ_{33} and σ_{11} are the axial stress imposed by the diamonds and the radial stress imposed by the gasket, respectively. The incoming beam is sent through the gasket and diffraction data is collected on an area detector perpendicular to the beam. Positions and intensities of diffraction are analyzed as a function of the azimuth angle δ on the imaging plate, from which we calculate the angle ψ between the maximum stress direction and the normal to the diffracting plane.

2. Experimental Technique

2.1. SETUP

In opposed anvil experiments, the maximal stress axis is aligned parallel to the axis of the anvils. Here, we want to study the variation of the diffraction spectra with the orientation of the diffracting plane in the stress field. Therefore, diffraction has to be performed in a radial geometry, with the incoming x-ray beam perpendicular to the compression direction (Figure 1).

This technique was first introduced by *Kinsland and Bassett* (1976) and further developed in the last 10 years (*e.g. Mao et al*., 1996, 1998; *Merkel et al.*, 2002).

If the stress is axisymmetric around the anvil axis, one can find the angle ψ between the diffracting plane normal and the load direction using

$$\cos\psi = \cos\delta\cos\theta,$$

where δ is the azimuth on the image plate and θ the diffraction angle.

Note that axial symmetry is not mandatory. Effects of non axial stresses on measured d-spacings can be deconvoluted (*Merkel*, 2006). Moreover, axial symmetry of plastic deformation can be verified when analyzing lattice preferred orientations in the MAUD software (*Miyagi et al.*, 2006; *Speziale et al.*, 2006).

2.2. X-RAY TRANSPARENT GASKET

Gaskets for radial diffraction experiment should be x-ray transparent. Several techniques have been developed, such as

- Removing the gasket and use the sample itself as containing material (*Kinsland and Bassett*, 1976)
- Using a mixture of amorphous boron and epoxy (*Mao et al.*, 1996)
- Using beryllium (*Hemley et al.*, 1997)
- Using a kapton ring surrounding an amorphous boron and epoxy insert (*Merkel and Yagi*, 2005)

At the moment, beryllium gaskets are the only solution for experiments above 60 GPa or on fluid samples. However, Be gaskets are not fully transparent and diffraction from Be can hide that of the sample. Moreover, some laboratories restrict the use of Be because of the health risks associated with Be powders. For experiments below 60 GPa and on solid materials, kapton, amorphous boron, and epoxy gaskets are the easiest and most reliable solution.

3. Lattice Preferred Orientations

Orientations of crystallites that constitute a polycrystal are rarely random and those preferred orientations have important implications for the macroscopic properties of the material. In general, lattice preferred orientations result from plastic deformation, and in particular, activation of mechanisms such as slip or twinning. If one knows the texture of a polycrystal, average properties such as elasticity can be calculated. Moreover, a comparison

between experimentally observed textures and results of plasticity numerical models can be used to determine the microscopic mechanisms controlling the plastic behavior of the material (*e.g. Wenk et al.*, 2006).

Texture in the sample can be represented by an orientation distribution function (ODF). This function is used to estimate anisotropic physical properties of polycrystals (*Kocks et al.*, 1998). It represents the probability for finding a crystal orientation, and it is normalized such that an aggregate with a random orientation distribution has a probability of one for all orientations. If preferred orientation is present, some orientations have probabilities higher than 1 and others lower than 1.

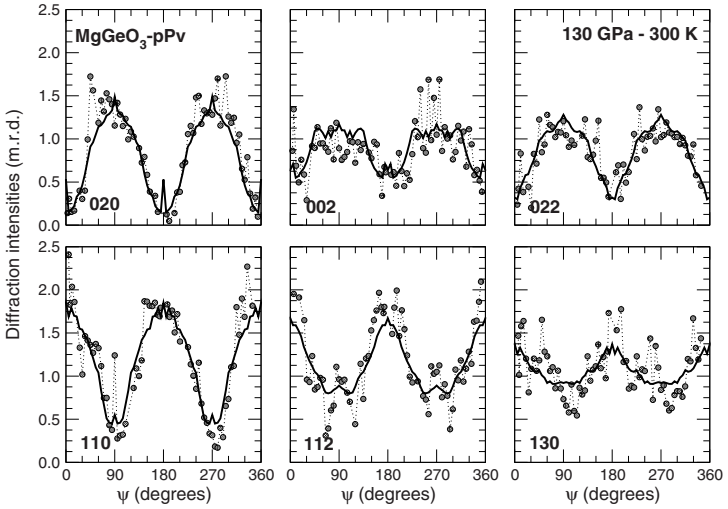

Figure 2. Diffraction intensities versus ψ for a sample of $MgGeO_3$ post-perovskite after deformation (*Merkel et al.*, 2006a). Circles indicate intensities measured experimentally while thick solid lines are recalculated from the ODF. Diffraction data were measured in-situ at 130 GPa for the 020, 002, 022, 110, 112, and 130 diffraction lines of $MgGeO_3$-pPv. Experimental data have been scaled to match those recalculated from the ODF, expressed in m.r.d.

The ODF is calculated from the variations of diffraction intensities with orientation using tomographic algorithms such as WIMV in the BEARTEX package (*Wenk et al.*, 1998) or E-WIMV in the Rietveld analysis software MAUD (*Lutterotti et al.*, 1999). For instance, Figure 2 presents the variations of diffraction intensities as a function of ψ for a sample of $MgGeO_3$ post-perovskite. Data were collected at 130 GPa in a radial geometry, using a beryllium gasket, and we used WIMV in BEARTEX to fit an ODF to the measured diffraction intensities for 020, 002, 022, 110, 112, and 130 assuming a cylindrical symmetry around the compression direction (*Merkel et al.*, 2006a). In WIMW, the diffraction intensities are simulated from the ODF

and compared to the experimental measurements until the agreement is satisfactory.

The ODF fitted to the experiment can then be compared to results of plasticity numerical models. Development of lattice preferred orientations depends on the deformation geometry and the microscopic deformation mechanisms activated in the polycrystal. A comparison between experimental textures and results of simulations can be used to identify the mechanisms activated in the experiment. In general, those simulations use the Los Alamos code VPSC (Visco-Plastic Self-Consistent, *Lebensohn and Tomé*, 1994). The aggregate is represented as a discrete number of orientations and treats each orientation as a viscoplastic inclusion in a homogeneous matrix that has the average properties of the polycrystal and can be used for texture simulations. Starting with an initial distribution of crystallite orientations and assuming deformation by slip and twinning, we can simulate a deformation path by enforcing incremental deformation steps. As deformation proceeds, crystals deform and rotate to generate preferred orientation. In VPSC calculations, the elastic response of the polycrystal is neglected, but grain rotations are properly accounted for, and this code has been used multiple times to model and understand textures obtained in radial diffraction experiments (*Wenk et al.*, 2006).

Figure 3, for instance, shows the orientations deduced for the sample of $MgGeO_3$ at 130 GPa along with results of VPSC calculations assuming slip along (100), (010), (001) and a combination of (100) and (110). Simulations that favor slip along (100), (110), or a combination of the two best match those obtained experimentally (*Merkel et al.*, 2006a).

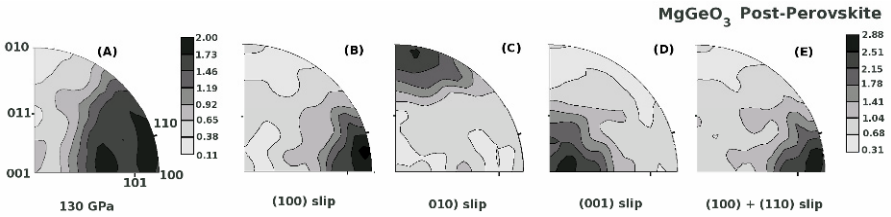

Figure 3. Inverse pole figures of the compression direction illustrating lattice preferred orientations in $MgGeO_3$ deduced from the experimental data (A) or (B, C, D, E) simulated in VPSC after 20% axial compression using models that favor slip along (100), (010), (001) and a combination of (100) and (110). Equal area projection. Linear contours expressed in m.r.d.

This technique has been applied to numerous studies under pressure (see *Wenk et al.*, 2006 for a review). Also, note that the E-WIMW algorithm in MAUD can be used to assess the hypothesis of cylindrical symmetry of texture around the compression direction (*Miyagi et al.*, 2006) and even

analyze textures for samples that did not deform in this geometry, after gasket failure for instance (see *Speziale et al.*, 2006).

4. Stress and Elasticity

4.1. EXPERIMENTAL OBSERVATIONS

Elastic deformations supported by the sample appear as sinusoidal variations of measured d-spacings as a function of ψ. Low d-spacings correspond to planes that are perpendicular to the compression direction (e.g. ψ = 0°), large d-spacings correspond to planes that are parallel to the compression direction (e.g. ψ = 90°). Interpretation of those variations of d-spacings with orientation has given rise to controversies in the litterature (*Weidner et al.*, 2004; *Antonangelli et al.*, 2006) and has now been solved, which will be described later.

Numerous experiments (see *Singh et al.*, 1998; *Duffy et al.*, 1999; *Merkel et al.*, 2002; *Kavner*, 2007; *Weinberger et al.*, 2008) have shown that measured d-spacings vary linearly with $(1 - 3\cos^2\psi)$ and that d-spacings measured at ψ = 54.7° (or $1 - 3\cos^2\psi = 0$) correspond to those expected under hydrostatic conditions. We introduce the lattice strain parameter Q using

$$\varepsilon(hkl,\psi) = \frac{d_m(hkl,\psi) - d_P(hkl)}{d_P(hkl)} = Q\left(1 - 3\cos^2\psi\right)$$

where $d_m(hkl,\psi)$ is the measured d-spacing for the *hkl* line at ψ, $d_P(hkl)$ is the d-spacing under equivalent hydrostatic pressure *P*, and $Q(hkl)$ the lattice strain parameter.

The value of $Q(hkl)$ indicates the amplitude of elastic deformations for the *hkl* diffraction line. It is linked to the differential stress *t*, the single crystal elastic moduli C_{ijkl}, and the plastic deformation applied to the sample.

Figure 4, for instance, presents the d-spacings extracted from data on hcp-Co at 42.6 GPa from *Merkel et al.* (2006b). The measured strains $\varepsilon = (d_m - d_p)/d_p$ are nearly linear with $(1 - 3\cos^2\psi)$. Therefore, approximation of the experimental data using the lattice strain parameter $Q(hkl)$ is relevant in this case.

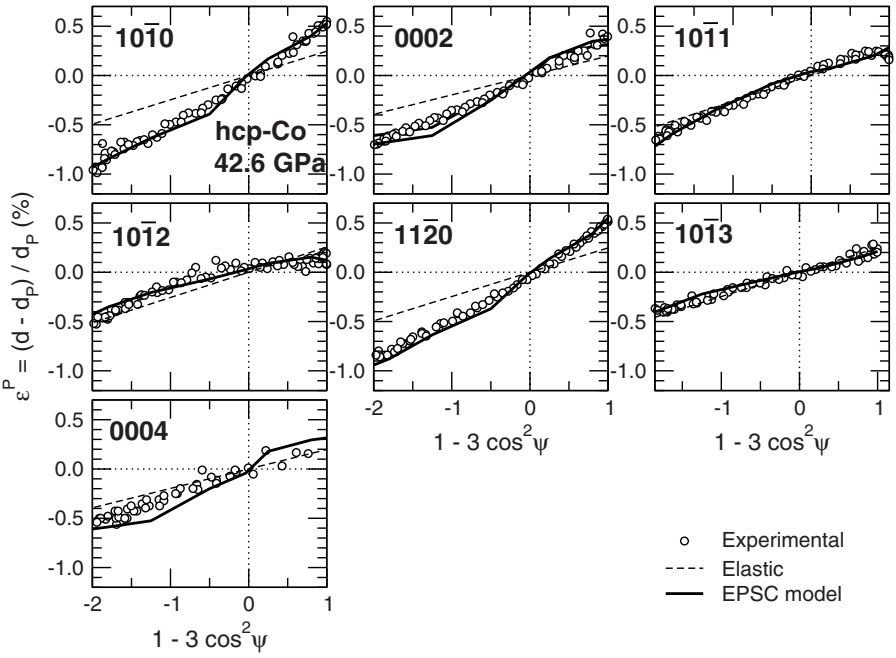

Figure 4. d-Spacings measured in hcp-Co at 42.6 GPa (*Merkel et al.*, 2006b) as a function of $(1 - 3\cos 2\psi)$. Circles are experimental data. Dashed lines are deduced from an elastic model (*Singh et al.*, 1998) assuming a differential stress of 4 GPa and the elastic moduli of *Antonangeli et al.* (2004). Solid lines are results of recent elasto-plastic models (*Merkel et al.*, 2009).

4.2. THE ELASTIC MODEL

The geometry of the diamond anvil cell defines an axial stress field with the main axis of the stress tensor aligned with the compression direction. Therefore, the stress tensor can be expressed as

$$\sigma = \begin{bmatrix} P & 0 & 0 \\ 0 & P & 0 \\ 0 & 0 & P \end{bmatrix} + \begin{bmatrix} -t/3 & 0 & 0 \\ 0 & -t/3 & 0 \\ 0 & 0 & 2t/3 \end{bmatrix}$$

where P is the hydrostatic pressure and t the differential stress.

For polycrystals, a diffraction line is the sum of the contributions of all crystallites in correct reflection position, *i.e.* those for which the normal to the *(hkl)* plane is parallel to the diffraction vector. For each crystallite, d-spacings depend on the local stress applied to the crystallite and its elastic properties; the measured d-spacing is the arithmetic mean of all those d-spacings.

Theories have been developed to relate single crystal elastic moduli C_{ijkl}, average differential stress t, and the measured d-spacings. Most rely on elasticity and assume that either stress, strain or a combination of both is continuous within the polycrystal. Moreover, if one assumes that the polycrystal is free of lattice preferred orientations, the lattice strain parameter *Q(hkl)* can be related to the average differential stress and the single crystal elastic moduli (*Singh et al.*, 1998). In this case, it can also be shown that

$$t \approx 6G < Q(hkl) >$$

where G is the shear modulus of the aggregate.

Elastic theories that do include effects of lattice preferred orientations have been developed as well (*Matthies et al.*, 2001). In this case, one can not define the lattice strain parameter *Q(hkl)* and measured d-spacings are not linear with $(1 - 3\cos^2\psi)$. Measured d-spacings can still be related to the average differential stress and single crystal elastic moduli. However, effects of lattice preferred orientations in the elastic theory are small and can be hard to distinguish experimentally.

4.3. LIMITATIONS OF THE ELASTIC MODEL

Very rapidly, it was found that the elastic model was not appropriate. In particular, elastic moduli deduced using this technique for ε-Fe were inconsistent between experiments (*Mao et al.*, 1998, 2008; *Merkel et al.*, 2005). This was confirmed by extensive work on hcp-Co that demonstrated that stresses or elastic moduli deduced using the elastic model are not consistent with those measured with other techniques (*Merkel et al.*, 2006b; *Antonangeli et al.*, 2006).

Limitations of the elastic model appear in different forms. If one tries to use radial diffraction to study elastic moduli, the parameters obtained may not agree with those obtained using other methods. This theory is also used for analyzing the stress state in samples plastically deformed under high pressure. In this case, the limitations of the elastic model will appear as inconsistencies in the measured stresses (*Weidner et al.*, 2004; *Merkel et al.*, 2006b).

Figure 4, for instance, shows the results of the elastic model for hcp-Co at 42.6 GPa assuming a differential stress of 4 GPa. They agree with the experimental measurements for some diffraction lines, but underestimate variations of d-spacings for lines such as 0002. Stresses deduced using the elastic model will depend on the diffraction line used for the analysis.

4.4. ELASTO-PLASTIC MODEL

The limitations of the elastic model can be overcome using elasto-plastic models, as demonstrated by works on MgO (*Weidner et al.*, 2004; *Li et al.*, 2004), quartz (*Burnley and Zhang*, 2008), and hcp-Co (*Merkel et al.*, 2009).

Similarly to VPSC models, self-consistent elasto-plastic (EPSC) models represent the aggregate as a discrete collection of orientations with associated volume fractions. The latter are chosen such as to reproduce the initial texture of the aggregate. EPSC treats each orientation as an ellipsoidal elastoplastic inclusion embedded within a homogeneous elastoplastic effective medium with anisotropic properties characteristic of the textured aggregate. The external boundary conditions (stress and strain) are fulfilled on average by the elastic and plastic deformations at the grain level. The self-consistent approach explicitly captures the fact that soft-oriented grains tend to yield at lower stresses and transfer load to plastically hard-oriented grains, which remain elastic up to rather large stress.

Those models use known values of single crystal elastic moduli, the average deformation applied to the polycrystal, and critical resolved shear stresses (CRSS) for each microscopic deformation mechanism. Simulated microscopic deformations are compared to experimental measurements by identifying which orientations contribute to the diffraction and calculating the corresponding average d-spacings.

For the case of hcp-Co, for instance, we have been able to fully interpret the data that had been previously collected (*Merkel et al*., 2009). Figure 5 shows the distribution of stress in the polycrystal after 17% axial compression, corresponding to a pressure of 46.2 GPa. Those calculations were performed assuming a plasticity model including basal and prismatic slip combined with compressive twinning. Plastic deformation induces large stress heterogeneities within the sample. Elastic models always neglect this phenomenon and, as shown in Figure 5, this not appropriate for samples undergoing plastic deformation.

Results of EPSC models are important as they allow a measure of the true stress applied to the sample. Moreover, a comparison between measurements in radial diffraction and EPSC models allows the identification of deformation mechanisms controlling the plastic behavior of the polycrystal and their mechanical properties such as CRSS values and hardening coefficients.

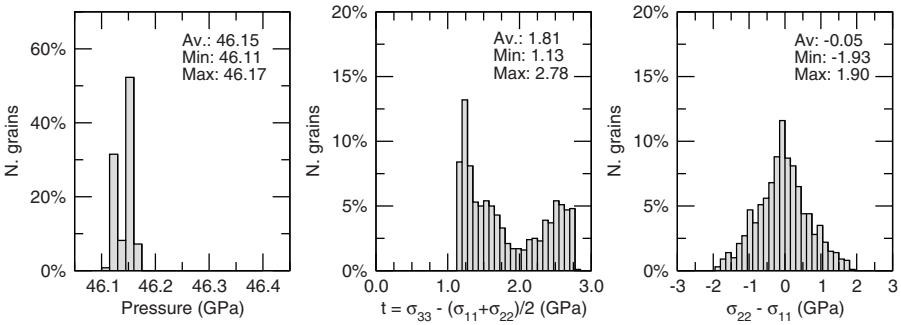

Figure 5. Histograms of stress distribution within the grains of a polycrystal of hcp-Co plastically deformed up to 46.2 GPa (*Merkel et al.*, 2009). Those results were obtained in a EPSC model including basal slip, prismatic slip, and compressive twinning.

5. Conclusions

Radial diffraction is a useful method for the investigation of plastic behavior under high pressure. Variations of diffraction intensities with orientation can be used to assess lattice preferred orientations within the sample which, in turn, can be compared to results of numerical plasticity models for the identification of microscopic mechanisms that control the plastic behavior.

Variations of measured d-spacings with orientation can be compared to results of elasto-plastic models. They allow a measure of the true stress applied to the sample, the identification and characterization of microscopic deformation mechanisms, and a quantification of local stress heterogeneities within the sample.

Local stress heterogeneities induced by plastic deformation are not properly accounted for in models based on elasticity only. Those models always assume some continuity of stress or strain and are not relevant for materials undergoing plastic deformation.

References

Antonangeli, D., M. Krisch, G. Fiquet, D. L. Farber, C. M. Aracne, J. Badro, F. Occelli, and H. Requardt, 2004, Elasticity of Cobalt at High pressure studied by inelastic x-ray scattering, *Phys. Rev. Lett*. **93**, 215505.

Antonangeli, D., S. Merkel, and D. L. Farber, 2006, Elastic anisotropy in hcp metals at high pressure and the sound wave anisotropy of the Earth's inner core, *Geophys. Res. Lett*. **33**, L24303.

Burnley, P. C., and D. Zhang, 2008, Interpreting in situ x-ray diffraction data from high pressure deformation experiments using elastic-plastic self-consistent models: an example using quartz, *J. Phys.: Condens. Matter* **20**, 285201.

Duffy, T. S., G. Shen, D. L. Heinz, J. Shu, Y. Ma, H. K. Mao, R. J. Hemley, and A. K. Singh 1999, Lattice strains in gold and rhenium under non-hydrostatic compression to 37 GPa, *Phys. Rev. B* **60**, 15063–15073.

Hemley, R. J., H. K. Mao, G. Shen, J. Badro, P. Gillet, M. Hanfland, and D. Häusermann, 1997, X-Ray imaging of stress and strain of diamond, iron, and tungsten at megabar pressures, *Science* **276**, 1242–1245.

Kavner, A., 2007, Garnet yield strength at high pressures and implications for upper mantle and transition zone rheology, *J. Geophys. Res*. **112**, B12207.

Kinsland, G. L., and W. A. Bassett, 1976, Modification of the diamond anvil cell for the measuring strain and the strength of materials at pressures up to 300 kilobar, *Rev. Sci. Instrum*. **47**, 130–132.

Kocks, U. F., C. Tomé, and H. R. Wenk, 1998, Texture and Anisotropy: Preferred Orientations and their Effects on Material Properties, Cambridge University Press, Cambridge.

Lebensohn, R. A., and C. N. Tomé, 1994, A self-consistent visco-plastic model: calculation of rolling textures of anisotropic materials, *Mater. Sci. Eng. A* **175**, 71–82.

Li, L., D. J. Weidner, J. Chen, M. T. Vaughan, M. Davis, and W. B. Durham, 2004, X-ray strain analysis at high pressure: Effect of plastic deformation in MgO, *J. Appl. Phys*. **95**, 8357–8365.

Lutterotti, L., S. Matthies, and H. R. Wenk, 1999, MAUD: a friendly Java program for materials analysis using diffraction, *IUCr: Newslett. CPD* **21**, 14–15.

Mao, H. K., J. Shu, Y. Fei, J. Hu, and R. J. Hemley, 1996, The wüstite enigma, *Phys. Earth Planet. Int*. **96**, 135–145.

Mao, H. K., J. Shu, G. Shen, R. J. Hemley, B. Li, and A. K. Singh, 1998, Elasticity and rheology of iron above 220 GPa and the nature of the Earth's inner core, *Nature* **396**, 741–743.

Mao, W. L., V. V. Struzhkin, A. Q. R. Baron, S. Tsutsui, C. E. Tommaseo, H.-R. Wenk, M. Y. Hu, P. Chow, W. Sturhahn, J. Shu, R. J. Hemley, D. L. Heinz, and H. K. Mao, 2008, Experimental determination of the elasticity of iron at high pressure, *J. Geophys. Res*. **113**, B09213.

Matthies, S., H. G. Priesmeyer, and M. R. Daymond, 2001, On the diffractive determination of single-crystal elastic constants using polycrystalline samples, *J. Appl. Cryst*. **34**, 585–601

Merkel, S., H. R. Wenk, J. Shu, G. Shen, P. Gillet, H. K. Mao, and R. J. Hemley, 2002, Deformation of polycrystalline MgO at pressures of the lower mantle, *J. Geophys. Res*. **107**, 2271.

Merkel, S., and T. Yagi, 2005, X-ray transparent gasket for diamond anvil cell high pressure experiments, *Rev. Sci. Instrum*. **76**, 046109.

Merkel, S., J. Shu, P. Gillet, H. Mao, and R. Hemley, 2005, X-ray diffraction study of the single crystal elastic moduli of ε-Fe up to 30 GPa, *J. Geophys. Res*. **110**, B05201.

Merkel, S., 2006, X-ray diffraction evaluation of stress in high pressure deformation experiments, *J. Phys.: Condens. Matter* **18**, S949–S962.

Merkel, S., A. Kubo, L. Miyagi, S. Speziale, T. S. Duffy, H.-K. Mao, and H.-R. Wenk, 2006a, Plastic deformation of $MgGeO_3$ post-perovskite at lower mantle pressures, *Science* **311**, 644–646.

Merkel, S., N. Miyajima, D. Antonangeli, G. Fiquet, and T. Yagi, 2006b, Lattice preferred orientation and stress in polycrystalline hcp-Co plastically deformed under high pressure, *J. Appl. Phys*. **100**, 023510.

Merkel, S., C. Tomé, and H.-R. Wenk, 2009, A modeling analysis of the influence of plasticity on high pressure deformation of hcp-Co, *Phys. Rev. B* **79**, 064110.

Miyagi, L., S. Merkel, T. Yagi, N. Sata, Y. Ohishi, and H. R. Wenk, 2006, Quantitative Rietveld texture analysis of $CaSiO_3$ perovskite deformed in a diamond anvil cell, *J. Phys.: Condens. Matter* **18**, S995–S1005.

Singh, A. K., C. Balasingh, H. K. Mao, R. J. Hemley, and J. Shu, 1998, Analysis of lattice strains measured under non-hydrostatic pressure, *J. Appl. Phys*. **83**, 7567–7575.

Speziale, S., I. Lonardelli, L. Miyagi, J. Pehl, C. E. Tommaseo, and H. R. Wenk, 2006, Deformation experiments in the diamond-anvil cell: texture in copper to 30 GPa, *J. Phys.: Condens. Matter* **18**, S1007–S1020.

Weidner, D. J., L. Li, M. Davis, and J. Chen, 2004, Effect of plasticity on elastic modulus measurements, *Geophys. Res. Lett*. **31**, L06621.

Weinberger, M. B., S. H. Tolbert, and A. Kavner, 2008, Osmium metal studied under high pressure and nonhydrostatic Stress, *Phys. Rev. Lett.* **100**, 045506.

Wenk, H. R., S. Matthies, J. Donovan, and D. Chateigner, 1998, BEARTEX: a Windows-based program system for quantitative texture analysis, *J. Appl. Cryst*. **31**, 262–269.

Wenk, H. R., S. Matthies, R. J. Hemley, H. K. Mao, and J. Shu, 2000, The plastic deformation of iron at pressures of the Earth's inner core, *Nature* **405**, 1044–1047.

Wenk, H. R., I. Lonardelli, S. Merkel, L. Miyagi, J. Pehl, S. Speziale, and C. E. Tommaseo, 2006, Deformation textures produced in diamond anvil experiments, analyzed in radial diffraction geometry, *J. Phys.: Condens. Matter* **18**, S933–S947.

REDUCTION AND ANALYSIS OF TWO-DIMENSIONAL DIFFRACTION DATA INCLUDING TEXTURE ANALYSIS

SVEN C. VOGEL*
LANSCE, Los Alamos National Laboratory, NM 87545, USA

Abstract This chapter provides a commented list of references which the author considers useful for diffraction data analysis such as references relating to Rietveld analysis. In particular, references relating to the analysis of two-dimensional detector data such as image plates or CCDs are given. Literature dealing with texture analysis and interpretation as well as web links for software and online tutorials are also provided.

Keywords: Diffraction data analysis, Rietveld refinement, texture analysis

1. Introduction

The purpose of this chapter is to point the novice or intermediate level diffractionist into the direction of tutorials, software and literature that the author found useful for his own work or training of LANSCE users over the past decade. Specific attention is paid to the data reduction and analysis of two-dimensional detector systems such as image plates and CCD detectors, but information relating to the analysis of general diffraction data such as X-ray or neutron diffraction data using single peak or full pattern Rietveld analysis is also provided. Naturally, the information offered here is biased by the opinions and limited by the experience of the author. However, the hope is that the information is still useful for the reader and saves some time searching for appropriate literature.

* E-mail: sven@lanl.gov

E. Boldyreva and P. Dera (eds.), *High-Pressure Crystallography: From Fundamental Phenomena to Technological Applications*, DOI 10.1007/978-90-481-9258-8_11,

2. Data Reduction for Two-Dimensional Detector Data

Two-dimensional X-ray diffraction data has been analyzed since the "invention" of X-ray powder diffraction by Debye and Scherrer in 1916 in Germany. Image plates and other 2D X-ray detectors became standard equipment since the mid 1990s (*e.g. Amemiya*, 1995; *He*, 2003). The combination of these detectors with state-of-the-art synchrotron sources and sophisticated data analysis software running on fast computers has pushed the limits of X-ray powder diffraction. Nowadays, even the crystal structure solution and refinement of hen egg white lysozyme from 30 s exposure time at a synchrotron (*Von Dreele*, 2006) or a full texture analysis from a single shot (*Ischia et al.*, 2005) has become possible.

The quasi-standard for real-time analysis at the beamline and data reduction (i.e. conversion of two-dimensional detector data to 2θ scans) of two-dimensional detector data is Fit2D.[1] While it is very robust, allows to perform the geometry calibration (*i.e.* sample detector distance, detector tilt and tilt angle), can be automated, allows for a lot of corrections (flat-field (*Moy et al.*, 1996), dark current subtraction, spatial distortion (*Hammersley et al.*, 1994), decay (*Hammersley et al.*, 1995), *etc.*) and conversions of different data formats, the author of this chapter found that it cannot fulfill

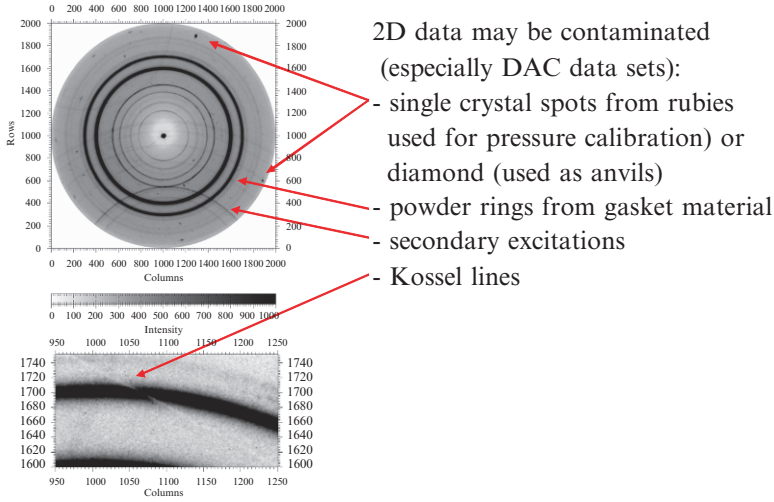

Figure 1. Examples of contaminations two-dimensional datasets.

[1] http://www.esrf.eu/computing/scientific/FIT2D/

all needs and he started the development of his own software Two2One to fill the gaps left by Fit2D. Two2One can for instance quite reliably detect and mask single crystal spots, Kossel lines and other outliers (*Vogel*, 2001; *Vogel et al.*, 2002; *Vogel and Knorr*, 2005), which can obscure integrated diffraction data (*Loveday et al.*, 1990; *Okada and Iwasaki*, 1980) (see Fig. 1 The software also assigns intensity uncertainties to each 2θ bin during integration of two-dimensional data into a conventional 2θ scan, that take into account that data at larger 2θ (larger radius) were measured more frequently. While both Fit2D and Two2One assign

$$\bar{I} = \sum_{i=1}^{N} I_i / N \tag{1}$$

as the intensity for a bin at a given 2θ with bin width Δ2θ (N = number of points with $2\Theta - \frac{1}{2}\Delta\Theta < 2\Theta_i \leq 2\Theta + \frac{1}{2}\Delta\Theta$) during integration, Fit2D outputs the result, e.g. in GSAS data format, without an uncertainty, leading GSAS to assume a Poisson error as uncertainty:

$$w_i = \sqrt{\bar{I}} \tag{2}$$

Alternatives were suggested by *Chall et al.* (2000)

$$w_i = \sqrt{\bar{I}} / N \tag{3}$$

(implemented in Two2One) and *Von Dreele* (2007)

$$w_i = \tan^2(2\theta) / 0.01\ \mathrm{I} \tag{4}$$

A thorough comparison of the effect of the first two schemes is given in (*Vogel*, 2001). Two2One is still developed, for instance it was recently expanded to determine strain information from radiography images (*Vogel et al.*, 2007). It is available upon request from the author (sven@lanl.gov). Other software similar to Fit2D (*i.e.* useful for geometry calibration) and Two2One are Powder3D IP (*Rajiv et al.*, 2007), MAUD,[2] DataSqueeze,[3] and XRD2DScan.[4]

[2] http://www.ing.unitn.it/~maud/

[3] http://www.datasqueezesoftware.com/, 50/100 USD acad./comm

[4] http://www.ugr.es/~anava/xrd2dscan.htm, , 400/800 Euros acad./comm

3. Rietveld Analysis of Diffraction Data

The Rietveld method was invented by Hugo Rietveld in the late 1960s to circumvent limitations for crystal structure refinement resulting from peak overlap in neutron diffraction data (*Rietveld*, 1969). The method has been refined since and has become the quasi-standard for neutron, x-ray and synchrotron powder diffraction data analysis.

3.1. GENERAL POWDER DIFFRACTION RESOURCES

The International Tables of Crystallography[5] are still fundamental for many crystal structure related problems. The Bilbao Crystallographic Server[6] hosts online crystallography utilities such as reflection conditions or group/ subgroup relations. General x-ray and neutron powder diffraction related issues were covered in the IUCr Commission on Powder Diffraction (CPD) newsletter,[7] which seems to have ceased, but the old editions, available online free of charge, still contain a vast body of powder diffraction related topics. An excellent and reasonably priced introduction to neutron diffraction is Wenk's "Neutron Scattering in Earth Sciences" (*Wenk*, 2006). The website also hosts presentations given by many of the co-authors of Wenk's book. An extensive review on the topic of powder diffraction was given by *Langford and Louër* (1996). Finally, many codes are available to plot the fruits of the labor of crystal structure refinements. The author mostly uses the Mercury code which is freely available in a limited but still very useful version for many operating systems.[8]

3.2. GENERAL RIETVELD RESOURCES

Many Rietveld and related codes (e.g. data conversion, structure plotting etc.) are available free of charge from the CCP14 website.[9] The same site hosts a great number of tutorials and short recipes on the usage of many of those programs. In particular the GSAS package (*Larson and Von Dreele*, 2004) contains an extensive manual with a detailed description of the mathematics and ~100 pages of tutorials. It is probably fair to say that the

[5] International Tables for Crystallography, Springer; 5th revised ed. 2002. Corr. 2nd printing edition (March 31, 2002)
[6] http://www.cryst.ehu.es/
[7] http://www.fkf.mpg.de/cpd/html/body_newsletter.html
[8] http://www.ccdc.cam.ac.uk/products/mercury/
[9] http://ccp14.sims.nrc.ca/ and other mirrors

big players in the field, *i.e.* to most frequently used codes are BGMN (commercial), FullProf (free), GSAS (free), MAUD (free), RIETAN (free), and Topas (commercial) (apologies for any omitted code). A great starting point for Rietveld analysis are the Rietveld refinement guidelines (*McCusker et al.*, 1999) or the much more extensive book by *Young* (1995). Excellent online Rietveld tutorials are provided by the Advanced Photon Source.[10]

3.3. MORE SPECIFIC RESOURCES

While "a Rietveld refinement is never perfected, merely abandoned",[11] the user needs to have an idea of how to judge the product of the refinement. Some excellent insight on the meaning of the numerical ***goodness-of-fit*** indicators produced by Rietveld programs is given by *Cox and Papoular* (1996) and *Toby* (2006). The bottom-line here is that the inspection of the measured data together with fit and difference curve in conjunction with an assessment of the crystal chemistry (*i.e.* bond length etc.) (*Kaduk*, 2007) is the only way to ensure that a "good" refinement was achieved; the "condensation" of all this information into two or three numbers is merely an indicator to monitor the progression of the refinement. The so-called ***normal probability plots***, available for instance in GSAS, allow in some cases to pin-point where data reduction and refinement problems are, e.g. over- or underestimation of the uncertainties of data points (*e.g. Abrahams and Keve*, 1971; see also special chapter in the International Tables).

Besides crystal structure refinement, ***quantitative phase analysis*** may be the objective of a diffraction experiment. The papers by *Madsen et al.* (2001) and *Toraya* (2000) provide a good overview and possible pitfalls. Especially at synchrotron and neutron sources, ***parametric studies***, *i.e.* investigations of changes of phase composition, crystal structures etc. as a function of an external parameter (temperature, pressure, stress *etc.*) play an important role. Besides the quickly arising issues of automated data analysis, *Stinton and Evans* (2007) suggested to integrate the external parameter into the Rietveld refinement. Since neutron diffraction was mentioned, some fundamental differences between constant wavelength X-ray as well as neutron data on one side and pulsed ***neutron time-of-flight*** data on the other side are explained in a classic work by *Von Dreele et al.* (1982). For some crystal structure related problems, a ***combined neutron/ X-ray data refinement*** might be the only way to obtain a valid crystal structure (making use of the different scattering power for neutrons and

[10] http://www.aps.anl.gov/Xray_Science_Division/Powder_Diffraction_Crystallography/
[11] Peter Stephens

X-rays of the same element). One of the first applications of this technique, using the GSAS code, is the refinement of the crystal structure of the high T_C superconductor $YBa_2Cu_3O_{7-x}$ (*Williams et al.*, 1988). Two sources the author found very valuable to understand and interpret ***thermal motion parameters***: The paper by *Kuhs* (1992) and the book "Thermal Vibrations in Crystallography" by *Willis and Pryor* (1975), which is unfortunately out of print and only available in well equipped libraries. Occasionally, the reliable determination of ***site occupancies*** is of concern. *Heuer* (2001) applied the lower order truncation method, proposed originally for single crystal structure determination, to Rietveld refinements and could greatly improve the reliability of these parameters. The paper by *Almer et al.* (2003) on ***strain and texture*** analysis of metal nitride coatings on TiN and CrN using an APS beamline serves as a good example for ***engineering applications*** of synchrotrons. While some Rietveld codes provide features to derive ***particle size and strain*** information from diffraction data (see tutorial on the MAUD website), this kind of profile analysis is more frequently performed from single peak fit analysis rather than full-pattern Rietveld analysis (*Ungár et al.*, 2001; *Balzar et al.*, 2004) or even combinations of both approaches (*Palosz et al.*, 2002; *Palosz et al.*, 2005). Beyond structure *refinement* with the Rietveld method, it is also possible with modern computers to *determine* crystal structures *ab initio* from powder diffraction data. Le Bail compiled many related resources[12] (the website also provides access to the Rietveld mailing list, including the archives, a very useful resource for the powder diffractionist). Finally, although a special topic for neutron diffraction, the possibility of Rietveld refinements of the ***magnetic structure*** (*Robinson et al.*, 1995) and in particular the tutorial provided by *Cui et al.* (2006) is worth mentioning.

4. Texture Analysis

Quantitative[13] texture analysis is concerned with the determination of the orientation distribution function (ODF) of a sample and was introduced into Rietveld refinements by *Von Dreele* (1997). The ODF describes the probabilities of crystal orientations (described in the sample coordinate system) for a given sample. An excellent textbook describing the basics of texture research (measurement and representation of the ODF, examples of texture for metals, alloys, rocks and ceramics, modeling of textures etc.) was written by *Kocks et al.* (2008). While the direct inspection of the ODF

[12] http://www.cristal.org/

[13] Not to be confused with "preferred orientation correction"!

is probably done only by texture experts, inspection of pole figures derived from the ODF is becoming more and more frequent for powder diffraction users. Pole figures are plots of the probability of a given crystallographic direction, *e.g.* 0001 in a hexagonal crystal system, for any sample direction. Pole figures are typically equal area projections, but occasionally also stereographic projections. Consequently, inverse pole figures are plots of the probability to find for a given sample direction, *e.g.* a compression axis, any crystal direction. The packages popLA (free) (*Kallend et al.*, 1991a, b) and BEARTEX (commercial) (*Wenk et al.*, 1998) are useful utilities for determination, processing and plotting of texture data.

The only non-commercial Rietveld codes capable of texture analysis to the author's knowledge are GSAS and MAUD. While GSAS is limited to the spherical harmonics representation of the ODF, MAUD has spherical harmonics, exponential spherical harmonics, and the so-called WIMV algorithm implemented. The spherical harmonics description of the ODF has the disadvantage that for sharper textures the weaker parts of the orientation space are dominated by oscillations or even unphysical negative orientation probabilities. These artifacts are similar to oscillations occurring when describing for instance a rectangle function with a finite number of terms in a Fourier series. While the exponential spherical harmonics description circumvents elegantly the negative probabilities, only the WIMV method provides positive definite orientation probabilities (see *e.g. Matthies et al.*, 2005 for a critical comparison of these methods).

However, in practice frequently only a single sample orientation is measured, precluding the application of the WIMV method, and one has to rely on the interpolating (exponential) spherical harmonics method. While this may be insufficient for a thorough quantitative texture analysis, it might well be sufficient to estimate the type and strength of the texture (depending on the number of available reflections and number of phases in the pattern). For example, in a high pressure experiment, it might be possible to calculate texture patterns during pressurizing and determine the onset of plastic deformation due to major deviatoric stresses from changes in the pole figures.

An excellent tutorial for texture analysis with MAUD from two-dimensional diffraction data is provided by Sébastien Merkel,[14] who is also the author of several papers on high pressure deformation (*Matthies et al.*, 2001; *Merkel*, 2004, 2005, 2006). Investigations of active deformation mechanism at high pressures are an evolving field with only few instruments available. The paper by *Wenk et al.* (2005) may serve as an example

[14] http://merkel.zoneo.net/RDX

on how deformation mechanisms, *i.e.* active deformation modes, can be determined from high pressure texture measurements. A glimpse at the complexities of the deconvolution of hydrostatic pressure and deviatoric stress from radial diffraction data, taking into account the pressure dependence of single crystal elastic constants, and the possible solution of this problem by elasto-plastic self-consistent deformation modeling is available in the papers by *Burnley and Zhang* (2008) and especially by *Merkel et al.* (2009).

5. Summary

While the bibliography for this contribution has to be incomplete (apologies to the people neglected!), it is still hoped that this compilation turns out to be useful and provides a basis for a journey in the fascinating world of powder diffraction.

ACKNOWLEDGEMENTS

I am indebted to a large number of people who contributed in one way or another to this work. In alphabetical sequence, I specifically wish to thank Davor Balzar, Joel Bernier, Lars Ehm, Karsten Knorr, Luca Lutterotti, Sébastien Merkel, Bob Von Dreele, and Rudy Wenk. Finally, I wish to thank the organizers of the high pressure crystallography school 2009 in Erice, Italy, for inviting me and stimulating this work.

References

Abrahams S.C., E. T. Keve, Normal probability plot analysis of error in measured and derived quantities and standard deviations, Acta Crystallogr. A, 27, 157–65 (1971).

Almer J., U. Lienert, R. L. Peng, C. Schlauer, M. Odén, Strain and texture analysis of coatings using high-energy x-rays, J. Appl. Phys., 94, 697 (2003).

Amemiya Y., Imaging plates for use with synchrotron radiation, J. Synchrotron Rad., 2, 13–21 (1995).

Balzar D., N. Audebrand, M. R. Daymond, A. Fitch, A. Hewat, J. I. Langford, A. Le Bail, D. Louër, O. Masson, C. N. McCowan, N. C. Popa, P.W. Stephens, B. H. Toby, Size–strain line-broadening analysis of the ceria round-robin sample, J. Appl. Cryst., 37, 911–924 (2004).

Burnley P. C., D. Zhang, Interpreting in situ x-ray diffraction data from high pressure deformation experiments using elastic–plastic self-consistent models: an example using quartz, J. Phys.: Condens. Matter, 20, 285201 (2008).

Chall M., K. Knorr, L. Ehm, W. Depmeier, Estimating intensity errors of powder diffraction data from area detectors, High Press. Res., 17, 315–323 (2000).

Cox D. E., R. J. Papoular, Structure refinements with synchrotron data: R-factors, errors and significance tests, Mat. Sci. For., 228–231, 233–238 (1996).

Cui J., Q. Huang, B. H. Toby, Magnetic structure refinement with neutron powder diffraction data using GSAS: a tutorial, Powder Diffract., 21, 71–79 (March 2006).

Graham W. Stinton, S. O. John, Evans: parametric Rietveld refinement, J. Appl. Cryst., 40, 87–95 (2007).

Hammersley A. P., et al., Calibration and correction of spatial distortions in 2D detector systems, Nucl. Instr. Meth., A346, 312–321 (1994).

Hammersley A. P., et al., Calibration and correction of distortions in 2D detector systems, Rev. Sci. Instr., 66, 2729–2733 (1995).

He B. B., Introduction to two-dimensional X-ray diffraction, Powder Diffract., 18, 71–85 (2003).

Heuer M., The determination of site occupancies using a new strategy in Rietveld refinements, J. Appl. Cryst., 34, 271–279 (2001).

Ischia G., H.-R. Wenk, L. Lutterotti, F. Berberich, quantitative Rietveld texture analysis of zirconium from single synchrotron diffraction images, J. Appl. Cryst., 38, 377–380 (2005).

Kaduk J. A., Chemical reasonableness in Rietveld analysis; organics, Powder Diffract., 22, 74–82 (2007).

Kallend J. S., U. Kocks, A. D. Rollett, H. -R. Wenk, Operational texture analysis, Mater. Sci. Eng. A, 132, 1–11 (1991a).

Kallend J. S., U. F. Kocks, A. D. Rollett, H. -R. Wenk, popLA – an integrated software system for texture analysis, Text. Microstruct., 14–18, 1203–1208 (1991b).

Kocks U. F., C. N. Tomé, H. -R. Wenk, Texture and Anisotropy, Cambridge University Press, Cambridge (2008).

Kuhs W. F., Generalized atomic displacements in crystallographic structure analysis, Acta Cryst., A48, 80–98 (1992).

Langford J. I., D. Louër, Powder diffraction, Rep. Prog. Phys., 59, 131–234 (1996).

Larson A. C., R.B. Von Dreele, General structure analysis system (GSAS), Los Alamos National Laboratory Report LAUR 86-748 (2004).

Loveday J. S., et al., The effect of diffraction by the diamonds of a diamond-anvil cell on single-crystal sample intensities, J. Appl. Cryst., 23, 392–396 (1990).

Madsen I. C., Nicola V. Y. Scarlett, Lachlan M. D., Cranswick and Thaung Lwin, Outcomes of the International Union of Crystallography Commission on Powder Diffraction Round Robin on Quantitative Phase Analysis: Samples 1a to 1h, J. Appl. Cryst., 34, 409–426, (2001).

Matthies S., J. Pehl, H. -R. Wenk, L. Lutterotti, S. C. Vogel, Quantitative texture analysis with the HIPPO neutron TOF diffractometer, J. Appl. Cryst., 38, 462–475 (2005).

Matthies S., S. Merkel, H. R. Wenk, R. J. Hemley, H. K. Mao, Effects of texture on the determination of elasticity of polycrystalline e-iron from diffraction measurements, Earth Planet. Sci. Lett., 194, 201–212 (2001).

Merkel S., The mantle deformed, Nature, 428, 812 (2004).

Merkel S., X-ray diffraction evaluation of stress in high pressure deformation experiments, J. Phys.: Condens. Matter, 18, S949–S962 (2006).

Merkel S., J. Shu, P. Gillet, H. K. Mao, R. J. Hemley, X-ray diffraction study of the single-crystal elastic moduli of ε-Fe up to 30 GPa, J. Geophys. Res., 110, B05201 (2005).

Merkel S., A. Kubo, L. Miyagi, S. Speziale, T. S. Duffy, H.K. Mao, H. -R. Wenk, Plastic deformation of $MgGeO_3$ post-perovskite at lower mantle pressures, Science, 311, 644 (2006).

Merkel S., C. Tomé, H. R. Wenk, Modeling analysis of the influence of plasticity on high pressure deformation of hcp-Co, Phys. Rev. B, 79, 064110 (2009).

McCusker L. B., R. B. Von Dreele, D. E. Cox, D. Louer, P. Scardi, Rietveld refinement guidelines, J. Appl. Cryst., 32, 36–50 (1999).

Moy J. -P., et al., A novel technique for accurate intensity calibration of area x-ray detectors at almost arbitrary energy, J. Syn. Rad., 3, 1–5 (1996).

Okada M., H. Iwasaki, X-ray diamond anvil cell and Pseudo-Kossel line pattern, Phys. Stat. Sol. A, 58, 623–628 (1980).

Palosz B., E. Grzanka, S. Gierlotka, S. Stel'makh, R. Pielaszek, U. Bismayer, J. Neuefeind, H. -P. Weber, Th. Proffen, R. Von Dreele, W. Palosz, Analysis of short and long range atomic order in nanocrystalline diamonds with application of powder diffractometry, Z. Kristallogr., 217, 497–509 (2002).

Palosz B., E. Grzanka, C. Pantea, T. W. Zerda, Y. Wang, J. Gubicza, T. Ungár, Microstructure of nanocrystalline diamond powders studied by powder diffractometry, J. Appl. Phys., 97, 064316 (2005).

Rajiv P., B. Hinrichsen, R. Dinnebier, M. Jansen, M. Joswig, Automatic calibration of powder diffraction experiments using two-dimensional detectors, Powder Diffract., 22, 3 (2007), free software, available from the authors of this paper.

Rietveld H. M., A profile refinement method for nuclear and magnetic structures, J. Appl. Cryst., 2, 65 (1969).

Robinson, R. A., A. C. Lawson, A. C. Larson, R. B. Von Dreele, J. A. Goldstone, Rietveld refinement of magnetic structures from pulsed-neutron-source powder-diffraction data, Physica B, 213–214, 985–989 (1 Aug. 1995).

Toby B. H., R factors in Rietveld analysis: how good is good enough? Powder Diffract., 21(1), 67–70 (March 2006).

Toraya H., Estimation of statistical uncertainties in quantitative phase analysis using the Rietveld method and the whole-powder-pattern decomposition method, J. Appl. Cryst., 33, 1324–1328 (2000).

Ungár T., J. Gubicza, G. Ribárik, A. Borbély, Crystallite size distribution and dislocation structure determined by diffraction profile analysis: principles and practical application to cubic and hexagonal crystals, J. Appl. Cryst., 34, 298–310 (2001).

Vogel S., High-pressure and texture measurements with an imaging plate, Diplomarbeit am Institut für Geowissenschaften - Mineralogie - Christian-Albrechts-Universität zu Kiel (2001) (available upon request from sven@lanl.gov).

Vogel S., L. Ehm, K. Knorr, G. Braun, Automated processing of 2D powder diffraction data, Adv. X-Ray Anal., 45, 31–33 (2002).

Vogel S., K. Knorr, IUCr CPD Newsletter, 32, 23 (2005).

Vogel S. C., H. Reiche, D.W. Brown, High pressure deformation study of zirconium, Powder Diffract., 22, 113 (2007).

Von Dreele R. B., Quantitative texture analysis by Rietveld refinement, J. Appl. Cryst., 30, 517–525 (1997).

Von Dreele R. B., J. Appl. Cryst. 40, 133–143 (2006).

Von Dreele R. B., Multipattern Rietveld refinement of protein powder data: an approach to higher resolution, J. Appl. Cryst., 40, 133–143 (2007).

Von Dreele R. B., J. D. Jorgensen, C. G. Windsor, Rietveld refinement with spallation neutron powder diffraction data, J. Appl. Cryst., 15, 581–589 (1982).

Wenk H-R (ed.) Neutron Scattering in Earth Sciences. Reviews in Mineralogy and Geochemistry 63 (2006), Mineralogical Society of America, Chantilly, VA. http://www.minsocam.org/MSA/Rim/Rim63.html (has lots of presentation for download).

Wenk H. -R., G. Ischia, N. Nishiyama, Y. Wang, T. Uchida, Texture development and deformation mechanisms in ringwoodite, Phys. Earth Planet. Int., 152, 191–199 (2005).

Wenk H. -R., S. Matthies, J. Donovan, D. Chateigner, BEARTEX: a Windows-based program system for quantitative texture analysis, J. Appl. Cryst., 31, 262–269 (1998).

Williams A., G. H. Kwei, R. B. Von Dreele, A. C. Larson, I. D. Raistrick, D. L. Bish, Joint X-ray and neutron refinement of the structure of superconducting YBa2Cu3O7-x: precision structure, anisotropic thermal parameters, strain, and cation disorder, Phys. Rev. B, 37(13), 7960–7962 (1988).

Willis, B. T. M., A. W. Pryor, Thermal Vibrations in Crystallography, Cambridge University Press, London (1975).

Young R. A. (ed.), The Rietveld Method (International Union of Crystallography Monographs on Crystallography 5). Oxford University Press, Oxford; new edition (February 21, 1995).

EQUATIONS OF STATE AND THEIR APPLICATIONS IN GEOSCIENCES

TIZIANA BOFFA BALLARAN*
Bayerisches Geoinstitut, Universitaet Bayreuth, 95440 Bayreuth, Germany

Abstract This lecture is an attempt to give an overview of the equations of state (EoS) commonly used to fit *P–V* data in geosciences and to discuss their assumptions. It is limited to static data (i.e. data obtained by squeezing a sample between pistons or anvils and measuring the associated change in volume). The various details of how to determine the parameters of an EoS from experimental data and of the best fitting procedure are discussed extensively in *Angel* (2000) and will be the subject of a workshop.

1. Equations of State

An EoS describes a physical system with a relation between its thermodynamic quantities, such as pressure, temperature, density, entropy, specific heat, *etc.* The best known EoS is of course the one for ideal gases:

$$PV = \mathrm{n}RT \tag{1}$$

which is considered the beginning of thermodynamics and statistical mechanics. Especially at high pressures and at low temperatures, however, real gases deviate from the perfect gas law and Eq (1) has been modified according to different assumptions in order to better describe the real gas behaviour. For solids and liquids, temperature has a minor effect on the *P–V* relationship and it is normally introduced as a thermal expansion correction to a chosen isothermal equation of state. There are several excellent reviews of the various EoS that have been proposed and used to describe the behaviour of condensed matter, see for example *Stacey et al.* (1981), *Anderson* (1995), *Holzapfel* (2001).

* E-mail: Tiziana.boffa-ballaran@uni-bayreuth.de

E. Boldyreva and P. Dera (eds.), *High-Pressure Crystallography: From Fundamental Phenomena to Technological Applications*, DOI 10.1007/978-90-481-9258-8_12,

At low pressures the P–V relationship of a solid may be represented in terms of Hooke's law where the applied stress is the change in hydrostatic pressure ΔP and the resulting strain is the fractional volume change $\Delta V/V$. The bulk modulus or incompressibility is the coefficient that scales strain to stress:

$$\Delta P = -K\frac{\Delta V}{V} \tag{2}$$

This relationship is valid only for pressure ranges much smaller than K, since due to inter-atomic repulsions a solid becomes stiffer with increasing pressure and, hence, large compressions require an expression for which the bulk modulus increases with pressure.

The simplest relationship satisfying the requirement of increasing stiffness with pressure is given by:

$$K=K_0+K_0'P \tag{3}$$

where K_0 is the bulk modulus at room pressure and $K_0'=(\mathrm{d}K/\mathrm{d}P)_{P=0}$ is the pressure derivative of K and is assumed to be independent of pressure. This is referred by *Murnaghan* (1951) as the "integrated linear theory". For pressures in the range $0 < P < K_0/2$ this approximation is reasonable for many materials.

These simple relationships illustrate an important point, *i.e.* that P–V data are usually represented by "parametric" EoS forms which use temperature dependent parameters V_0, K_0, K_0' and K_0'', etc. for the volume, bulk modulus and its pressure derivatives, respectively (the index 0 indicates that these values refer to room pressure).

1.1. EQUATION OF STATE BASED ON THE FINITE STRAIN THEORY

The classical theory of infinitesimal elasticity is based on two assumptions: (1) the strains are uniquely determined by the stresses and are reversible, and (2) the strains are so small that their squares and products are negligible. In finite strain theory, the first assumption is retained, but the restriction to small strains is removed (*Birch*, 1938). A theoretical treatment of finite strains was given first by *Love* (1927), but practical expressions for finite strain were developed by *Murnhagan* (1951) and applied to the Earth by *Birch* (1952). Since the finite strain is defined by the change in distance between two neighboring points during deformation, a reference state needs to be defined. In the Lagrangian formulation the strain is defined relative to the unstrained state (*i.e.* the volume at room pressure), whereas in the Eulerian formulation the strained state (*i.e.* the volume at the final compression) is used as reference state. The two schemes yield definitions

of strain that are equivalent for infinitesimal strain but different for finite strains. Other formulations are of course possible as we will see in section 1.1.2. It is worth stressing that all finite strain theories are empirical in the sense of having plausible analytical forms that appear to follow the trend of observation once the EoS parameters (V_0, K_0 and its pressure derivatives) are properly adjusted to suit the behaviour of different materials. Any analytical form will of course fit a given set of P–V data if sufficient adjustable parameters are allowed. However, as it is the case of any fit procedure, the EoS which uses the fewest parameters to achieve a particular precision of fit will be favored.

1.1.1. *Birch–Murnaghan EoS*

The most widely used isothermal EoS in Geoscience is the Birch-Murnaghan EoS, because it satisfies the criteria outlined above. In spite of the fact that (and I cite directly from *Anderson*, 1995) "the long use and wide application of this EoS has engendered for it a certain authority in the literature, nevertheless, like all other isothermal EoS's, it is based on an unproven assumption. In this case, the EoS rests on the assumption of Eulerian strain". The derivation of such equation from the finite strain theory is given not only in the original papers (see for example *Birch*, 1947) but also in several other texts (*i.e. Stacey et al.*, 1981; *Poirier*, 2000) and it will not be repeated here. It is based upon the assumption that the Helmholtz free energy of a solid can be expressed as a Taylor expansion of the Eulerian finite strain ε, or better of a quantity f which is the negative of ε in order to deal with positive strain in compression:

$$f = -\varepsilon = \frac{1}{2}\left[\left(\frac{V}{V_0}\right)^{-2/3} - 1\right] \tag{4}$$

The choice of Eulerian strain has been ascribed by *Birch* (1952) to the fact that the expansion of the free energy was more strongly convergent than that obtained from an expansion of the Lagrangian finite strain. The fourth-order EoS has the form:

$$P = 3K_0 f(1+2f)^{5/2}\left(1+\frac{3}{2}(K_0'-4)f+\frac{3}{2}\left(K_0K_0''+(K_0'-4)(K_0'-3)+\frac{35}{9}\right)f^2\right) \tag{5}$$

By substituting f and doing successive differentiation (*Stacey et al.*, 1981) we obtain:

$$P = \frac{3}{2} K_0 \left((V/V_0)^{-7/3} - (V/V_0)^{-5/3} \right)$$
$$\left\{ 1 + \frac{3}{4}(K_0' - 4)\left((V/V_0)^{-2/3} - 1 \right) + \frac{3}{8}\left(K_0 K_0'' + (K_0' - 4)(K_0' - 3) + \frac{35}{9} \right)\left((V/V_0)^{-2/3} - 1 \right)^2 \right\} \quad (6)$$

$$K = K_0 (V/V_0)^{-5/3}$$
$$\left\{ 1 + \left(\frac{3}{2} K_0' - \frac{5}{2} \right)\left((V/V_0)^{-2/3} - 1 \right) + \frac{9}{8}\left(K_0 K_0'' + K_0'(K_0' - 4) + \frac{35}{9} \right)\left((V/V_0)^{-2/3} - 1 \right)^2 \right\} \quad (7)$$

$$K' = K_0' + \frac{3}{2} K_0 K_0'' \left((V/V_0)^{-2/3} - 1 \right) \quad (8)$$

The derivation of these equations involves a number of implicit assumptions (a part from the fundamental assumption of Eulerian strain) about the properties of solids under compression. First of all it is strictly valid for isotropic or cubic materials (*Birch*, 1947), second it implies that the solid under compression is homogeneously strained *i.e.* that all part of its structure compress at the same rate. This is clearly far from reality in the case of those materials which contain different type of bonds between atoms as is the case of many silicates (*Angel and Ross*, 1996) or even worse for molecular crystals which have groups of atoms strongly bonded kept together by very weak interactions. Moreover, it is assumed that the EoS parameters are continuously differentiable with respect to pressure (an assumption made for all finite strain EoS) which means that the EoS cannot describe the behaviour of a material through a high-pressure phase transformation. Finally, the free energy Taylor expansion of the BM-EoS is very often truncated either at the second (K_0' has an implied value of 4) or at the third order (with an implied negative value of K_0") depending on the accuracy of the data and this implicitly assumes that higher order terms are considerably small compared to the lowest-order terms.

1.1.2. *Logarithmic Equation of State*

If, instead of choosing as reference state either the undeformed or the deformed state, one chooses to define an increment of strain $d\varepsilon$ corresponding to the increase or decrease by dl of the length l of a sample experiencing extension or compression, the total finite strain or Hencky strain experienced by a material which changes its length from l_0 to l is:

$$\varepsilon_H = \int_{l_0}^{l} d\varepsilon_H = \ln \frac{l}{l_0} \quad (9)$$

A logarithmic EoS can be derived from a Taylor expansion of the free energy in terms of the Hencky strain whose third-order form is (*Poirier*, 2000):

$$P = K_0 \frac{\rho}{\rho_0} \ln \frac{\rho}{\rho_0} \left[1 + \left(\frac{K_0' - 2}{2} \right) \ln \frac{\rho}{\rho_0} \right] \tag{10}$$

which for $K_0' = 2$ reduces to the simple second-order expression (*Poirier and Tarantola*, 1998):

$$P = K_0 \frac{\rho}{\rho_0} \ln \frac{\rho}{\rho_0} \tag{11}$$

1.2. EQUATIONS OF STATE BASED ON INTERATOMIC POTENTIAL

An alternative approach of deriving EoS is to propose a form of interatomic potential which defines the mutual forces between atoms in the crystal so that density can be calculated as a function of pressure. The atomic potentials used, however, are just as empirical as the strain equations described above. *Stacey et al.*, (1981) and *Anderson* (1995) give an extensive review of EoS derived from several different atomic potential. Here, I will describe two of the commonly used.

1.2.1. *Born-Mie Potential*

The potential function studied first by G. Mie has the form:

$$E(r) = -\frac{a}{r^m} + \frac{b}{r^n} \tag{12}$$

where the interatomic potential $E(r)$ is expressed in terms of long-range attractive and short-range repulsive forces, i.e. $n > m$. Adjusting a and b to obtain $r = r_0$ and $K = K_0$ at $P = 0$, the following free energy expression is obtained (*Poirier*, 2000):

$$F(V) = \frac{9K_0V_0}{n-m} \left[-\frac{1}{m} \left(\frac{V_0}{V} \right)^{-m/3} + \frac{1}{n} \left(\frac{V_0}{V} \right)^{-n/3} \right] \tag{13}$$

and:

$$P = \frac{3K_0}{n-m} \left[\left(\frac{V_0}{V} \right)^{1+n/3} - \left(\frac{V_0}{V} \right)^{1+m/3} \right] \tag{14}$$

with

$$K_0' = \frac{1}{3}(m+n+6) \tag{15}$$

$$K_0 K_0'' = -\frac{1}{9}(m+3)(n+3) \tag{16}$$

Specific values of m and n have been used by different authors (*Stacey et al.*, 1981). In the simple case of ionic crystals (Born potential) m is equal to 1 and the potential curve is asymmetric resulting in anharmonic oscillations. In the special case of $m = 2$ and $n = 4$ expression (14) coincides with the second order BM-EoS.

1.2.2. *Vinet EoS*

This equation:

$$P = 3K_0\left(\frac{V}{V_0}\right)^{-2/3}\left[1-\left(\frac{V_0}{V}\right)^{1/3}\right]\exp\left\{\frac{3}{2}(K_0'-1)\left[1-\left(\frac{V_0}{V}\right)^{1/3}\right]\right\} \tag{17}$$

(see derivation in *Vinet et al.*, 1987, 1989 and in *Poirier*, 2000) has a special interest because it gives good results for very compressible solids and at very large pressure. It is derived from a Morse potential and has the implied value for K_0" of:

$$K_0 K_0'' = -\left[\left(\frac{K_0'}{2}\right)^2 + \frac{K_0'}{2} - \frac{19}{36}\right] \tag{18}$$

Note however that such EoS is not intended for material with significant degree of structural freedom such as bond-bending.

1.3. THERMAL EQUATIONS OF STATE

There is a number of EoS which can be used to treat high-temperature and high-pressure data. Details of their derivations and their limits can be found in *Duffy and Wang* (1998) and *Poirier* (2000). Here we limit the discussion to consider the high-temperature Birch–Murnaghan EoS which is a relatively simple approach but is sufficient for fitting most of the *P–V–T* data collected up to 1,000 K. The zero pressure parameters are (as in the case of expression (6)) V_{T0}, K_{T0} and K_{T0}' and refer to an initial high-temperature state, *i.e.* the compression curve is considered as isotherms at a given high-temperature and different isotherms (one for every T data set)

are considered in the fitting procedure. The high-temperature values of the volume and bulk modulus are given by:

$$V(T) = V_0(T_0)\exp\int_{T_0}^{T}\alpha(T)dT \tag{19}$$

$$K(T) = K_0(T_0) + \left(\frac{\partial K}{\partial T}\right)_P (T - T_0) \tag{20}$$

where T_0 is the reference temperature (usually 298 K) and both thermal expansion $\alpha(T) = a + bT$ and bulk modulus are considered to vary linearly with T. Given the uncertainties on most of the P–V–T data, it is usually assumed that K' does not vary with T and its value is fixed to 4; however, if the data are particularly accurate, it is possible to use a variable K' associated with each isothermal EoS.

2. Comparison Between EoS

In spite of its number of assumptions, the most widely used EoS in the Geoscience community is the BM-EoS (second or third order depending on the accuracy of the data). *Poirier* (2000) has shown that the third-order BM-EoS gives practically the same result as the logharitmic and the Vinet EoS at relatively low pressures or at any pressure for K_0' = 3.5.

As a practical example I have refitted single-crystal *P–V* data of an $MgSiO_3$ perovskite containing a small amount of Al and Fe (*Saikia et al.*, 2008) using a second and a third-order BM, a third-order logarithmic and a third-order Vinet EoS. The resulting EoS parameters from the fitting of the *P–V* data using the three different EoS are reported in Table 1. As expected all three third-order EoS give the same results given that the *P–V* data represent a small compression, the only difference being the implied value of K_0". The requirements of having few adjustable parameters and of following the trend of the experimental data appear therefore fulfilled by all three EoS and the choice of using a BM-Eos instead of any of the other two as done by *Saikia et al.* (1998) is a matter of common use.

TABLE 1. EoS parameters resulting from the fitting of the P–V data of sample $Fe^{3+}_{0.03}$-$Al_{0.05}$ (From *Saikia et al*., 2008)

EoS	V_0	K_0	K_0'	K_0" (implied)
BM II order	163.673 (7)	247.4 (7)	4 (implied)	–0.0157
BM III order	163.681 (9)	243 (3)	5.0 (7)	–0.0247
Logarithmic	163.681 (9)	243 (3)	5.1 (7)	–0.0579
Vinet	163.681 (9)	243 (3)	5.1 (7)	–0.0351
Ono et al., 2004	164.24 (fixed)	272 (8)	4 (fixed)	

If these EoS parameters, however, are used to extrapolate the compressibility behaviour of perovskite to pressures far beyond the experimental range studied (*i.e.* to the Earth's lower mantle conditions), a significant difference among the three predictions is visible (Figure 1) and the third-order BM-EoS suggests the smallest compressibility of perovskite.

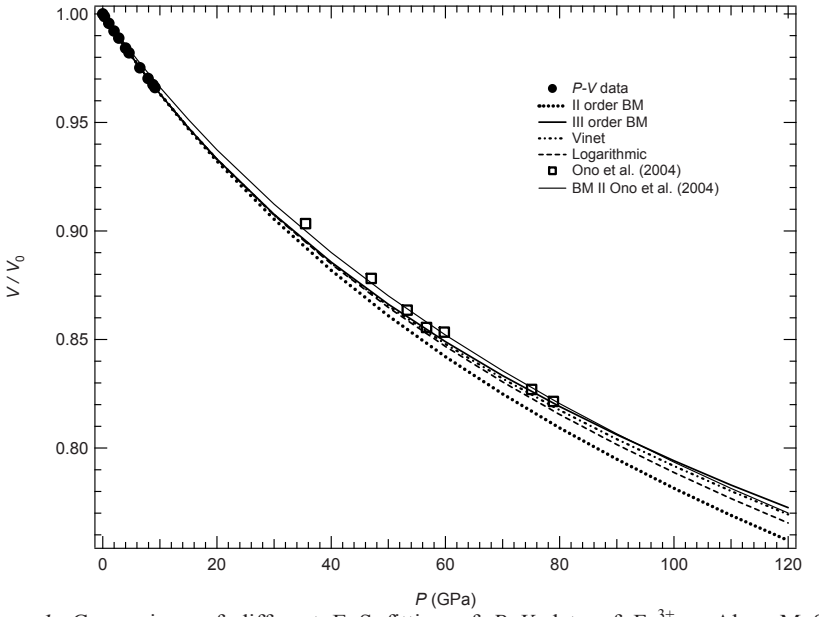

Figure 1. Comparison of different EoS fitting of *P–V* data of $Fe^{3+}_{0.03}$–$Al_{0.05}$ $MgSiO_3$ perovskite (*Saikia et al.*, 2008). At high pressures the different Eos define different trends in spite of resulting in the same EoS parameters at room pressure.

Note that none of the extrapolation fits the high-pressure data collected for a perovskite of similar composition (*Ono et al.*, 2004), although, at least for the highest-pressures data points the third-order BM-EoS seems the best solution. Few points need to be stressed here. Single-crystal x-ray diffraction data are usually collected using *in-house* facilities and are

limited to low pressures (<10 GPa). The precision and accuracy of the data collected is such that not only K_0 and K_0' can be refined, but also subtle changes in compression behaviour can be detected. However, as we have seen above, extrapolations at pressures of the Earth's interior depend on the chosen EoS formalism. In the other hand, powder diffraction data can be collected at megabar pressures using synchrotron facilities, but their scatter is such that very often only a second-order BM Eos can be used. As a result very often the room pressure bulk modulus values reported in the two different types of studies may differ quite significantly. In situations where compression data are available only at very high-pressure it is advisable to employ EoS parameters for which the reference is not at zero pressure but at the pressure of the first volume measurement.

3. Pressure Determination

Not only will the uncertainties in the volume measurements but also those in the pressure determination influence the accuracy and precision of the EoS parameters. For single-crystal x-ray diffraction experiments up to 10 GPa, *Angel et al.* (1997) suggest to use as pressure internal standard an oriented single-crystal of quartz for which they have determined an accurate BM-EoS. This results in a precision of the pressure determination of 0.009 GPa at 9 GPa, which is a considerable improvement with respect to the pressure determination by means of the ruby fluorescence technique. However, for room *T* high-pressure experiments which exceed 10 GPa, the pressure-induced wavelength shift of the ruby fluorescence spectrum is at the moment the easiest solution. Note, however, that the wavelength shift depends not only on the absolute pressure, but also on the pressure medium used, and therefore the correct calibration of the ruby shift need to be used. Three calibration are available, one for non-hydrostatic media as NaCl or LiF (*Mao et al.*, 1978), one for quasi-hydrostatic media as Ar (*Mao et al.*, 1986) and recently one for He pressure medium (*Jacobsen et al.*, 2008). As an alternative to ruby, MgO is sometime used as internal standard in high-pressure powder diffraction experiment since its EoS has been better and better refined over the years.

In high-pressure high-temperature experiments, unfortunately, the precision of pressure determination is limited. The ruby fluorescence shift has been calibrated up to 15 GPa and 600°C by *Rekhi et al.* (1999) and its extrapolation at higher pressures and temperatures is commonly used in spectroscopic experiments. In diffraction experiments the unit-cell lattice parameters of a metal (for example gold) are used to determine the pressure

at temperatures. However, in both cases the uncertainties can be up to 1–2 GPa at very high-pressures and moderate temperatures.

References

Anderson, O. L., 1995, *Equations of State of Solids for Geophysics and Ceramic Science.* Oxford University Press, Oxford.

Angel, R. J., 2000, Equations of state. In R. M. Hazen and R. T. Downs (eds.), High-pressure and high-temperature crystal chemistry, MSA Rev. Mineral., **41:**35–60.

Angel, R. J., and Ross, N. L., 1996, Compression mechanism and equations of state. *Phil. Trans. R. Soc. Lond.*, **354:**1449–1459.

Angel, R. J., Allan, D. R., Miletich, R., and Finger, L. W., 1997, The use of quartz as an internal pressure standard in high pressure crystallography. *J. Appl. Crystallogr.*, **30:**461–466.

Birch, F., 1938, The effect of pressure upon the elastic parameters of isotropic solids, according to Murnaghan's theory of finite strain. *J. Appl. Phys.*, **9:**279–288.

Birch, F., 1947, Finite elastic strain of cubic crystals. *Phys. Rev.*, **71:**809–824.

Birch, F., 1952, Elasticity and constitution of the earth's interior. *J. Geophys. Res.*, **57:**227–286.

Duffy, T. S., and Wang, Y., 1998, Pressure-volume-temperature equations of state. In R. J Hemley. (ed.), Ultrahigh-pressure mineralogy: physics and *c*hemistry of the Earth's deep interior, MSA Rev. Mineral., **37:**425–457.

Holzapfel, W. B., 2001, Equations of state for solids under strong compression. *Z. Kristallogr.*, **216:**473–488.

Jacobsen, S. D., Holl, C. M., Adams, K. A., Fischer, R. A., Martin, E. S., Bina, C. R., Lin, J.-F., Prakapenka, V. B., Kubo, A., and Dera P., 2008, Compression of single-crystal magnesium oxide to 118 Gpa and a ruby pressure gauge for helium pressure media. *Am. Mineral.*, **93:**1823–1828.

Love, A. E. H., 1927, *A Treatise of the Mathematical Theory of Elasticity*. Fourth edition, Cambridge University Press, Cambridge.

Mao, H.-K., Bell, P. M., Shaner, J., and Steinberg, D., 1978, Specific volume measurements of Cu, Mo, Pd and Au and calibration of the ruby R_1 fluorescence pressure gauge from 0.06 to 1 Mbar. *J. Appl. Phys.*, **49:**3276–3283.

Mao, H.-K., Xu, J., and Bell, P. M., 1986, Calibration of the ruby pressure gauge to 800 kbar under quasi-hydrostatic conditions. *J. Geophys. Res.*, **91:**4673–4676.

Murnaghan, F. D., 1951, *Finite Deformation of an Elastic Solid*. Wiley, New York.

Ono, S., Kikegawa, T., and Iizuka, T., 2004, The equation of state of orthorhombic perovskite in a peridotitic mantle composition to 80 GPa: implications for chemical composition of the lower mantle. *Phys. Earth Planet. Int.*, **145:**9–17.

Poirier, J.-P., 2000, *Introduction to the Physics of the Earth Interior*. Second edition. Cambridge University Press, Cambridge.

Poirier, J. P., and Tarantola, A., 1998, A logarithmic equation of state, *Phys. Earth Planet. Int.*, **109:**1–8.

Rekhi, S., Dubrovinsky, L. S., and Saxena, S. K., 1999, Temperature-induced ruby fluorescence shifts up to a pressure of 15 GPa in an externally heated diamond anvil cell. *High Temp. – High Press.*, **31:**299–305.

Saikia, A., Boffa Ballaran, T., and Frost, D. J., 2008, The effect of Fe and Al substitution on the compressibility of $MgSiO_3$ perovskite determined through single–crystal X-ray diffraction. *Phys. Earth Planet. Int.*, **173:**153–161.

Stacey, F. D., Brennan, B. J., and Irvine, R. D., 1981, Finite strain theories and comparison with sismological data. *Geophys Surv.*, **4:**189–232.

Vinet, P., Ferrante, J., Rose, J. H., and Smith, J. R., 1987, Compressibility of solids. *J. Geophys. Res.*, **92:**9319–9325.

Vinet, P., Rose, J. H., Ferrante, J., and Smith, J. R., 1989, Universal features of the equation of state of solids. *J. Phys: Condens. Matter*, **1:**1941–1963.

ANISOTROPIC COMPRESSION. WHAT CAN IT TEACH US ABOUT INTERMOLECULAR INTERACTIONS?

ELENA BOLDYREVA*
REC-008 Novosibirsk State University, Institute of Solid State Chemistry and Mechanochemistry SB RAS, Novosibirsk, ul. Kutateladze, 18, 630128, Russia

Abstract The effect of pressure on solids is often discussed in terms of bulk compressibility. At the same time, for any solids with the crystal structures, the symmetry of which is lower than cubic, it is not sufficient to describe the bulk compressibility alone, since the structural distortion is anisotropic – i.e. depends on the crystallographic direction. The lecture gives a comprehensive introduction into the techniques of studying the strain anisotropy based on diffraction experiments, and illustrates, how the knowledge of the anisotropy of lattice strain may assist in understanding the intermolecular interactions in crystals.

Keywords: Lattice strain, anisotropy, intermolecular interactions, molecular crystals, hydrogen bonds

1. Strain Tensor and Strain Ellipsoid

1.1. GENERAL DEFINITIONS

Strain of a solid can be characterized by a tensor [e_{ij}], which is calculated as:

$$e_{ij} = \frac{\partial u_i}{\partial x_j} \qquad (i, j = 1,2,3), \tag{1}$$

where u_i – is the shift of a point with x_j coordinates. The components e_{11}, e_{22}, e_{33} characterize the expansion (contraction) per length unit in the directions $0x_1$, $0x_2$, $0x_3$, respectively; e_{12} – rotation along $0x_3$ in the direction

*E-mail: eboldyreva@yahoo.com

E. Boldyreva and P. Dera (eds.), *High-Pressure Crystallography: From Fundamental Phenomena to Technological Applications*, DOI 10.1007/978-90-481-9258-8_13,

of the linear element parallel to $0x_2$, etc. If a solid rotates without any deformation, the corresponding $[e_{ij}]$ tensor is antisymmetric. In general, the contribution of rotation into the deformation of a solid can be eliminated, so that any symmetric part of the $[e_{ij}]$ tensor is considered.

Strain tensor $[\varepsilon_{ij}]$ is defined as the symmetric part of $[e_{ij}]$ with components $\varepsilon_{ij} = ½(e_{ij} + e_{ji})$, or:

$$\begin{bmatrix} \varepsilon_{11} & \varepsilon_{12} & \varepsilon_{13} \\ \varepsilon_{21} & \varepsilon_{22} & \varepsilon_{23} \\ \varepsilon_{31} & \varepsilon_{32} & \varepsilon_{33} \end{bmatrix} = \begin{bmatrix} e_{11} & \frac{1}{2}(e_{12}+e_{21}) & \frac{1}{2}(e_{13}+e_{31}) \\ \frac{1}{2}(e_{12}+e_{21}) & e_{22} & \frac{1}{2}(e_{23}+e_{32}) \\ \frac{1}{2}(e_{13}+e_{31}) & \frac{1}{2}(e_{23}+e_{32}) & e_{33} \end{bmatrix}, \qquad (2)$$

where the diagonal terms describe the deformation of expansion (contraction), and the non-diagonal terms – the shear deformation. The tensor can be diagonalized to its principal axes (the three directions that remain normal to each other on deformation):

$$\begin{bmatrix} \varepsilon_1 & 0 & 0 \\ 0 & \varepsilon_2 & 0 \\ 0 & 0 & \varepsilon_3 \end{bmatrix}, \qquad (3)$$

where ε_1, ε_2, ε_3 – the principal strain.

For a uniform three-dimensional strain a shift of a point, which is due to the pure deformation, can be defined as $\boldsymbol{u}_i = \varepsilon_{ij}x_j$. On deformation, a vector $\boldsymbol{l}$ changes both its length and direction. The shift of the end of this vector is: $\boldsymbol{u}_i = \varepsilon_{ij}l_j$. Linear strain in an arbitrary direction $\boldsymbol{l}$ is equal to the projection of $\boldsymbol{u}$ on $\boldsymbol{l}$, and can be expressed as:

$$\varepsilon = \varepsilon_1 l_1^2 + \varepsilon_2 l_2^2 + \varepsilon_3 l_3^2. \qquad (4)$$

As a result of strain, a sphere transforms into an ellipsoid, which is termed *strain ellipsoid*, and its surface (*deformation surface*) can be described by the equation:

$$\frac{x_1^2}{(1+\varepsilon_1)^2} + \frac{x_2^2}{(1+\varepsilon_2)^2} + \frac{x_3^2}{(1+\varepsilon_3)^2} = 1, \qquad (5)$$

where ε_1, ε_2, ε_3 – linear strain along the principal axes; x_1, x_2, x_3 – coordinates of a point at the deformation surface.

Linear strain in a certain direction, ε, can be calculated as:

$$\frac{\cos\varphi_1^2}{(1+\varepsilon_1)^2}+\frac{\cos\varphi_2^2}{(1+\varepsilon_2)^2}+\frac{\cos\varphi_3^2}{(1+\varepsilon_3)^2}=\frac{1}{(1+\varepsilon)^2}, \quad (6)$$

where φ_1, φ_2, φ_3 – direction cosines between the direction and the principal axes 1, 2, 3 of strain ellipsoid.

The magnitudes of strain in different directions can be visualized in the following ways:

1. A solid having spherical shape (radius = 1) will change shape to an ellipsoid, and sections of this ellipsoid by selected planes can be plotted. The strain ellipsoid is always a real ellipsoid, and its projections are always ellipses.
2. One can plot the *representation quadric*, which is described by the equation:

$$\varepsilon_1 x_1^2 + \varepsilon_2 x_2^2 + \varepsilon_3 x_3^2 = C, \quad (7)$$

where $C = \pm 1$.

The length of any radius vector leading to the surface of the quadric represents the reciprocal of the square root of linear strain along that direction. If all the ε_i are positive, $C = 1$, and the quadric is represented by an ellipsoid, whose semiaxes have lengths equal to $1/\sqrt{\varepsilon_i}$. If all the ε_i are negative, then C is set equal to -1, and the quadric is again a real ellipsoid. If the ε_i have different signs, the quadric is a hyperboloid. The asymptotic cone represents directions along which no strain occurs. If one of the ε_i is negative, then, if C is chosen as +1, the hyperboloid has one (belt-like) sheet and the squares of reciprocal lengths of radius vectors leading to points on this sheet represent positive strain along the particular directions. Along directions where the hyperboloid has no real values, strain is negative. To visualize these, C is set to -1. The resulting hyperboloid has two (cap-like) sheets, and r^{-2} represents the amount of contraction along the particular direction. If two of the ε_i are negative, the situation is complementary to the previous case.
3. The magnitude of strain in a certain direction can be plotted as a radius vector. If spherical coordinates (φ, θ) are used to specify the direction, the length of **r** is:

$$|\mathbf{r}| = (\alpha_1\cos^2\varphi + \alpha_2\sin^2\varphi)\sin^2\theta + \alpha_3\cos^2\theta \quad (8)$$

Sections through this representation surface are called *polar diagrams*.

1.2. RELATION TO CRYSTAL SYMMETRY

For an isotropic action on a solid, such as isotropic heating, or hydrostatic compression, *Neumann's principle* is valid, according to which the symmetry group of a physical property must include the symmetry elements of the crystal point group, i.e. the symmetry of a physical property must be higher than or equal to the symmetry of the crystal structure. This principle imposes restrictions on the possible orientations of the principal axes of the strain tensor and of the relative values ε_i, if the crystal symmetry is different from triclinic (Table 1). For example, a sphere made from a single crystal with tetragonal symmetry may not transform into a general ellipsoid, but either into a rotation ellipsoid with the rotation axis parallel to the fourfold symmetry axis, or to a sphere.

TABLE 1. Anisotropy of strain related to crystal symmetry

Crystal system	Strain ellipsoid	Orientation
Cubic	Sphere	Any
Tetragonal Trigonal Hexagonal	Rotation Ellipsoid	one of the axes $\parallel$ 4 $\parallel$ 3 $\parallel$ 6
Orthorhombic	Ellipsoid	All the three axes $\parallel$ 2 ($\perp$ m)
Monoclinic		An axis $\parallel$ 2 ($\perp$ m)
Triclinic		Any

At the same time, one cannot predict from considering the crystal symmetry only, if the structure should expand or compress along a principal axis, and how much linear strain along the principal axes should actually differ. For example, when a crystal of $[Co(NH_3)_5NO_2]Cl(NO_3)$ is subject to hydrostatic pressure, it *compresses* most along the crystallographic ***c*** direction, and the same structure *expands* most of all in the same direction, if the strain is induced by homogeneous substitution of some of the cations with N-coordinated nitro-group for the cations with O-coordinated ligands (*substitution, or composition strain*).

1.3. CALCULATION FROM EXPERIMENTAL DATA

The formalism described above can be applied to any solid with anisotropic properties, not necessarily to a crystal. The medium can be approximated as continuous, so that the strain is considered at a macroscopic level, and no changes in the interatomic distances are discussed. In this case, to calculate the strain tensor, one would need to carry out *dilatometric* measurements, i.e. to measure linear dimensions of the solid in several directions (using, for example, optical interferometry, pushrod dilatometry, or electrical capacity measurements). For the crystalline solids, an alternative to the dilatometry is X-ray diffraction at variable temperatures (thermal expansion) or pressures (hydrostatic compression), that gives the information on the changes in the d_{hkl} distances *vs* T (P). The strain tensor can be calculated either from these changes in the d_{hkl} values directly, or from the values of cell parameters a, b, c, α, β, γ. Several computing programs based on either of these two principles are available. The direct approach (based on the d_{hkl} values) is advantageous for reasons of the propagation of errors.

2. Intermolecular Interactions

2.1. APPROACHES TO DESCRIBE INTERMOLECULAR INTERACTIONS

Modern quantum chemistry *ab initio* approaches operate with *electron density distribution* and do not require a consideration of individual chemical bonds. High-precision X-ray diffraction analysis provides direct experimental information on the distribution of the electron density in the crystals. Still, chemists continue using such terms as covalent bonds and non-covalent interactions, hydrogen bonds, π–π interactions, stacking interactions, halogen-halogen bonds, multi-center bonds, dispersive interactions, van der Waals forces, etc. The reason for this is not the "mental inertia". Considering interactions of various types, chemists learnt to be quite efficient in designing not only ever more complex molecules and molecular complexes, but also large molecular assemblies, including two-dimensional layers and three-dimensional crystals. The same "qualitative", "chemical" approach is often much more efficient for understanding and really predicting structure-properties relations, than a sophisticated *ab initio* "physical" calculation.

Within the "chemical approach", intermolecular interactions can be classified as directional and non-directional, specific and non-specific, saturated and not saturated. One can characterize them by the geometrical parameters (the distances between the atoms involved in the intermolecular bond or an interatomic contact, the angles between the vectors connecting atoms in the intermolecular bond, deviations of a group of atom involved in

an intermolecular interaction from planarity) and by their energies. The geometrical information is provided by diffraction techniques, and the data on the energy of interactions are usually obtained from vibrational spectroscopy. More rarely, one uses the data on the heat capacity, dissolution heat, sublimation and melting temperatures. Electron charge density analysis of the high-precision diffraction data is one of the options when studying the energy of intermolecular interactions. It is also quite common to make conclusions on the relative energies of different interactions on the basis of the statistical analysis of the geometrical parameters retrieved from the structural databases for series of related structures.

2.2. ANISOTROPY OF STRAIN AND ANISOTROPY OF INTERACTIONS – ANISOTROPY OF STRAIN ON COOLING

The anisotropy of interactions in a crystal structure accounts for the anisotropy of strain. This has been realized long ago in relation to the anisotropy of thermal expansion. The anharmonicities of the interatomic potentials gain importance with increasing vibration amplitudes of the atoms. Since, at a given temperature, weakly bonded atoms oscillate with larger amplitudes, they contribute to a larger extent to thermal expansion in comparison with stronger bonds. Compressibility and thermal expansion can be thus assumed to be a rough measure of the interatomic and intermolecular forces. At the same time, it is important to remember, that linear strain in a certain direction should not necessarily be correlated straightforwardly with the change in the interatomic distances in the same direction, especially if the crystal is heterodesmic, i.e. several types of bonds are present. For example, in a molecular crystal, the changes in the intramolecular distances between the atoms linked by covalent bonds can be negligible, whereas the distances in the intermolecular contacts can make the main contribution into the strain value. There are also examples, when all the contacts (both intra- and intermolecular) shorten, but the structure expands in a certain direction, because the molecular conformation changes (molecular fragments rotate with respect to each other, a molecule stretches because torsion and valence angles change).

Many attempts have been made to correlate the anisotropy of thermal expansion with the crystal structures. Ubbelohde and co-workers were probably the first to correlate the anisotropy of thermal expansion of molecular crystals to the different strength of hydrogen bonds in different directions. Moreover, they have suggested to use the data on the anisotropy of thermal expansion of hydrogen-bonded crystals, to prove the existence of hydrogen bonds and to locate the hydrogen atoms in the structure.

The following generalizations can be found, e.g. in the International Tables of Crystallography:

1. Covalent bonds are associated with very small thermal expansions, whereas van der Waals bonds give rise to large thermal expansions. In accordance with their relatively high elastic stiffness, hydrogen bonds, especially short hydrogen bonds, lead to relatively small thermal expansions.
2. In layer-like structures, the maximum thermal expansion occurs normal to the layers.
3. Thermal expansion decreases when the density of weak bonds decreases: therefore, expansion is greater for crystals with small molecules (many van der Waals contacts per volume) than for their larger homologues.

In several publications it has been shown that short hydrogen bonds expand on heating, whereas the long ones – contract, so that the direction of maximum thermal expansion coincides with the direction of strong hydrogen bonds. Opposite effects have been also observed.

These rules are not a dogma, and there are many exceptions to them, since the anisotropy of thermal expansion observed for a real heterodesmic crystal results from a complex interplay between expansion and compression of many different contacts, rotations of molecular fragments and molecules as a whole, stretching of molecules due to the angular changes, and changes in the molecular conformations. However, most of the attempts to correlate the anisotropy of thermal expansion and the anisotropy of the intermolecular interactions are empirical; even for the simplest possible systems theoretical modeling remains a serious problem.

2.3. ANISOTROPY OF STRAIN WITH INCREASING PRESSURE

2.3.1. *General Notes*

Hydrostatic pressure is also a scalar action, and a formal description of the anisotropy of strain on compression is the same as that of the compression on cooling. For the simplest isotropic systems a Grueneisen relation links thermal expansion and isothermal compressibility:

$$\beta = \bar{\gamma} \frac{\kappa c^V}{V}, \tag{9}$$

where κ – is the volume thermal expansion, β – the isothermal compressibility, c – the specific heat, V – the volume, and $\bar{\gamma}$ – the Grueneisen parameter averaged over all the vibrational modes. For anisotropic media,

$\Delta V/V$ is replaced by the strain u_{kl} and κ^{-1} is replaced by the stiffness tensor c_{ijkl}, so that the Grueneisen parameter becomes a second rank tensor γ_{ij}:

$$\gamma_{ij} = \frac{V}{c^V} c^T_{ijkl} \alpha_{kl}, \tag{10}$$

where α_{kl} is the thermal expansion tensor.

Another way of comparing the structural strain induced in the same structure on cooling and with increasing pressure is to compare the anisotropy of strain on two actions and try to correlate it with the anisotropy of intermolecular interactions in the crystal. Systematic studies of the anisotropy of strain on hydrostatic compression within the limits of stability of the same polymorph, when no phase transitions occur, can be successfully applied, in order to:

(a) Correlate lattice strain and changes in the intermolecular contacts
(b) Estimate relative strength of different intermolecular interactions
(c) Distinguish between attraction and repulsion

This approach has been suggested in the 1990s, applied to Co(III) coordination compounds, then to molecular crystals, including pharmaceuticals, such as paracetamol or phenacetine, and is being actively developed ever since for various systems. Several methods of visualizing the anisotropy of structural strain at the microscopic level (the changes in the interatomic distances and intermolecular contacts) are being used in the literature, including plots of the interatomic distances and their changes versus pressure, or the analysis of Hirshfeld surfaces. Sections of strain ellipsoid or polar diagrams are plotted in relation to the fragments of crystal structures in different projects, or simply the directions of principal axes of strain tensor are shown.

2.3.2. *Pressure-Induced Strain in the Crystalline Amino Acids*

Crystals of amino acids can be considered as models for peptide chains. The main structure-forming unit in these crystals is a head to tail chain, in which amino-group, NH_3^+, of one zwitter-ionic molecule is linked via bifurcated NH…O hydrogen bond to the carboxy-group, COO^-, of another zwitter-ion. These chains are very robust and are preserved not only during the continuous compression on cooling or under pressure, but also during the phase transitions.

Although bulk compressibility in the crystals of various amino acids studied up to now is approximately the same, the anisotropy of strain is different, and reflects the difference in the interactions involving the side chains. The values of linear strain in the crystalline aminoacids are of the same order of magnitude as those measured for proteins.

For the same amino acid, several polymorphs can show pronounced differences in their response to variations in pressure. For example, the simplest amino acid, glycine, $^{+}NH_3–CH_2–COO^{-}$, is known since the 1960s to exist at ambient conditions as three polymorphs – the α-form ($P2_1/n$), the β-form ($P2_1$), and the γ-form ($P3_1$).

As could be expected, the lowest compressibility in all the three structures has been observed along the head to tail chains. Less obvious was the result of a comparison of the compression of the layered polymorphs (α- and β-forms): the structure of the β-polymorph was the most compressible normal to the layers, and the structure of the α-polymorph – within a layer, in the direction of the NH…O hydrogen bonds. Two more layered polymorphs have been obtained at high pressure – the β'-polymorph (from the β-form reversibly at 0.76 GPa), and the δ-polymorph (from the γ-polymorph irreversibly at about 3.5 GPa). The largest compression of the β'-polymorph was observed normal to the layers, the compressibility of the δ-polymorph normal to the plane and within a plane was the same. In the structures of the β- and β'-polymorphs, the zwitter-ions are linked into the three-dimensional network by hydrogen bonds, which act as springs, making the structures compressible normal to the layers. In the α- and in the δ-polymorphs the layers are further linked into double bands by NH…O hydrogen bonds, so that only CH…HC and CH…O the interactions between the layers are present. The difference in the anisotropy of strain of these two polymorphs gives insight into the relative contributions of these two types of contacts in the stability and in the dynamics of the structures.

2.3.3. *Pressure-Induced Strain in the Polymorphs of Paracetamol*

Another example illustrates some other aspects of the studies of the anisotropy of pressure-induced strain in molecular crystals. Paracetamol – a common drug – is known to exist at ambient conditions as two polymorphs, which differ in their bioavailability, solubility, and stability on storage. The orthorhombic form (metastable at ambient conditions) shows a better pharmaco-kinetics, but has an obvious disadvantage as compared to the monoclinic form: it cannot be compressed into tablets without additives – excipients. The reason was sought in different compressibility of the two forms, but our studies have shown, that the bulk compressibility of the two forms is the same, and it is the anisotropy of strain that differs.

The anisotropy of strain is related not only to the compression of the hydrogen-bond network, but also to the continuous changes in the molecular conformations (flattening with increasing pressure). The monoclinic and the orthorhombic polymorphs of paracetamol are built from similar molecular chains linked by –OH…O=C– and –NH…OH hydrogen bonds. These chains,

in turn, form layers, pleated in the monoclinic polymorph, and flat in the orthorhombic form. When pressure increases, the NH…O and the OH…O hydrogen bonds are compressed in both the polymorphs, but since the molecular chains within the layers are packed differently, the layers in the monoclinic form expand in some directions and compress in the other, whereas the layers in the orthorhombic polymorph compress isotropically. Vibrational spectroscopy provides further information on the different effect of pressure on the two types of the hydrogen bonds: the OH…O and the NH…O. Although the two types of the bonds shorten similarly under pressure, this shortening is accompanied by blue and red frequency shifts, respectively, indicating at the opposite energy changes. The reason is that the OH-group donates a hydrogen to the –C=O group, but simultaneously accepts another hydrogen from the NH-group, and the resulting shift in the ν_{OH} frequency results from an interplay of these two processes having opposing effects.

2.3.4. *A Comparison of the Anisotropy of Strain with Increasing Pressure and on Cooling – Prospects for Using the Experimental Analysis of the Anisotropy of Strain for Improving the Intermolecular Potentials*

Both cooling and increasing pressure result in the volume reduction; however, the anisotropy of strain induced by these two scalar actions is often very different. It is not easy at this stage to interpret the observed pronounced difference but very qualitatively, at a very simple half-intuitive empirical level. Whereas the anharmonicity of vibrations accounts for the anisotropy of thermal expansion, the anisotropy of compression with increasing pressure is determined to a larger extent by the way, in which it is easier for the structure to “squeeze out” the “empty space”, to pack the molecules and other chemical species more efficiently. The experimental data on the changes in the cell parameters resulting from a complex interplay of the changes in many local interatomic contacts on variations of temperature and pressure provide a unique information for testing and improving atom-atom potentials used for the simulations of crystal structures and polymorph prediction, which are so important, e.g. for the research and development of drugs. Research in this direction awaits those who take this challenge. The results of the first trial attempts are promising.

3. Conclusion

A decade ago there were only a very few people, who were interested in systematic studies of the anisotropy of pressure-induced lattice strain as a tool of achieving a better understanding of the intermolecular interactions in

molecular crystals. Today the activity in this field has grown enormously. The research of the strain in the crystals under hydrostatic conditions is being complemented by the studies of the deformation of molecular crystals induced by other types of mechanical action. Sometimes, even a mere observation of a crystal touched by a pin, or a squeezer, provides the insight into the nature of the intermolecular interactions in the structure, as has been demonstrated in recent work by Desiraju and his colleagues (see Reddy, C.M., Padmanabhan, K.A., Desiraju, G.R., Structure–property correlations in bending and brittle organic crystals, Cryst. Growth Des. 6 (12), pp. 2720–2731 (2006) as an example). The following conclusions can be made based on the studies of pressure-induced strain in crystals:

1. Compression of solids with the symmetry lower than cubic, even under hydrostatic conditions, is anisotropic and should be described by strain tensor, visualized as strain ellipsoid, a quadric, or a polar diagram.
2. The analysis of the anisotropy of strain provides information on the anisotropy of intermolecular interactions.
3. Comparing the anisotropy of pressure-induced strain in the polymorphs in the series of chemically related compounds, in the chiral and racemic forms, as well as comparing strain on cooling and on hydrostatic pressure is especially helpful.

4. Further Reading

4.1. GENERAL DEFINITIONS AND FORMALISM

Nye, J.F., Physical Properties of Crystals: Their Representation by Tensors and Matrices, Oxford Science Publications, first edition 1957, reprinted with corrections many times after that.

International Tables for Crystallography, Volume D, Physical Properties of Crystals, First on-line edition 2006.

4.2. CALCULATING STRAIN TENSOR FROM EXPERIMENTAL DATA

Hazen, R.M., & Finger, L.W., 1982, Comparative Crystal Chemistry. Temperature, Pressure, Composition and the Variation of Crystal Structure, Wiley: London.

Jessen, S.M., & Kueppers, H., 1991, The precision of thermal expansion tensors of triclinic and monoclinic crystals, *J. Appl. Cryst*., **24**, 239–242.

4.3. INTERMOLCULAR INTERACTIONS

Pauling, L., 1939, The Nature of the Chemical Bond, Cornell University Press: Ithaca, New York.

Jeffrey, G.A., & Saenger, W., 1991, Hydrogen Bonding in Biological Structures, Springer Verlag: Berlin.

Jeffrey, G.A., 1997, An Introduction to Hydrogen Bonding: Oxford University Press: New York.

Desiraju, G.R., & T. Steiner, The Weak Hydrogen Bond, Oxford Science Publications: Oxford, first edition 1999, revised later editions available.

4.4. REVIEW PAPERS (WITH EXTENSIVE REFERENCES THEREIN)

Boldyreva, E.V., 1994, Intramolecular linkage isomerization in the crystals of some Co(III) – ammine complexes: a link between inorganic and organic solid state chemistry, Mol. Cryst. Liq. Cryst. Inc. Non-Lin. Opt., 242: 17–52.

Boldyreva, E.V., 1996, Homogeneous solid state reactions, In: Reactivity of Solids. Past, Present, Future, IUPAC Series "Chemistry in the 21st Century", Ed. V. Boldyrev, Blackwells: Oxford, pp.141–184.

Boldyreva, E.V., & Boldyrev, V.V. (Eds.), 1999, Reactivity of Molecular Solids, Molecular Solid State Series, V. 3, Wiley: Chichester.

Boldyreva, E.V., 2001, Structural aspects of intramolecular solid-state linkage isomerization in Co(III) pentaammine nitro/nitrito complexes, J. Coord. Chem., 27(5): 1–28.

Boldyreva, E.V., 2003, Anisotropy of pressure-induced structural distortion of molecular crystals, J. Mol. Struct., 647(1–3): 159–179.

Boldyreva, E.V., 2004, High pressure and supramolecular systems, Russ. Chem. Bull., 53(7): 1315–1324.

Boldyreva, E.V., 2004, High-pressure induced structural changes in molecular crystals preserving the space group symmetry: anisotropic distortion/isosymmetric polymorphism, Cryst. Eng., 6(4): 235–254.

Boldyreva, E.V., 2004, High-pressure studies of the hydrogen bond networks in molecular crystals, J. Mol. Struct., 700(1–3): 151–155.

Boldyreva, E.V., 2004, Molecules in strained environment, in High-Pressure Crystallography, Eds. A. Katrusiak & P.F. McMillan, Kluwer: Dordrecht, pp. 495–512.

Boldyreva, E.V., et al., 2004, Variable-temperature and variable-pressure studies of small-molecule organic crystals, Arkivoc, XII: 128–155.

Boldyreva, E.V., 2007, Crystalline amino acids – a link between chemistry, materials science and biology, In: Models, Mysteries, and Magic of Molecules, Eds. J.C.A. Boeyens & J.F. Ogilvie, Springer Verlag, Berlin, pp. 169–194.

Boldyreva, E.V., 2007, High-pressure polymorphs of molecular solids: when are they formed, and when are they not? Some examples of the role of kinetic control, crystal growth and design, 7(9): 1662–1668.

Boldyreva, E.V., 2007, High-Pressure Studies of Crystalline Amino Acids and Simple Peptides/Proceedings of the IV-th International Conference on High Pressures in Biosciences and Biotechnology, Presented by J-STAGE, Tsukuba, Japan, September, 25th–26th 2006; Abe F., Suzuki, A. Eds; Japan Science and Technology Agency: Saitama, Japan, 1(1): 28–46.

Boldyreva, E.V., et al., 2008, Pressure-induced phase transitions in organic molecular crystals: a combination of X-ray single-crystal and powder diffraction, Raman and IR-spectroscopy, J. Phys. Conf. Ser., 121: 022023.

Boldyreva, E.V., 2008, High-pressure diffraction studies of molecular organic solids. A personal view, Acta Crystallogr. A., 64(1): 218–231.

Boldyreva, E.V., 2009, Combined X-ray diffraction and Raman spectroscopy studies of phase transitions in crystalline amino acids at low temperatures and high pressures. Selected examples, Phase Trans., 82 (4): 303–321.

HIGH-PRESSURE STRUCTURAL EVOLUTION OF MOLECULAR CRYSTALS

NICOLA CASATI*
Dipartimento di Chimica Strutturale e Stereochimica Inorganica, Università degli Studi di Milano, via Venezian 21, 20133 Milano, Italy

Abstract Careful High Pressure single crystal experiments enable the study of subtle modifications in intramolecular bond distances. This in turn allows an "inherent structure correlation" analysis, effectively showing the pressure evolution of selected chemical features and their potential energy surface. Techniques and results are discussed with oxalic acid as a case study.

Keywords: Single crystal x-ray diffraction, high pressure, crystallography, phase transition, structural changes, hydrogen bond

1. Introduction

1.1. MOLECULAR CRYSTALS

Molecular crystals are characterized by two different kinds of interactions. On one hand, there are strong intramolecular bonds that define the connectivity of the molecule. These bonds are extremely rigid and their geometric features such as distances and valence angles, as well as their strength, are predictable and in most cases tabulated (torsion angles are, on the contrary, more flexible). On the other hand, interactions between neighbor molecules are usually weak, and not only their features cannot be predicted easily but, as the large polymorphism observed suggests, there can be many different and almost isoenergetic ways of arranging molecules together. There are of course exceptions, like soft intramolecular bonds, such as metal–metal or metal–ligand in organometallics, or strong intermolecular interactions, such as hydrogen or halogen bonds. Nevertheless, the dual

* E-mail: nicasati@yahoo.it

E. Boldyreva and P. Dera (eds.), *High-Pressure Crystallography: From Fundamental Phenomena to Technological Applications*, DOI 10.1007/978-90-481-9258-8_14,

nature of molecular crystals has prompted the discussion of their characteristics and behavior (as already implied) in terms of molecule (or molecular fragment) and surroundings, enabling the crystallographer to focus on either of them.

Single crystal high-pressure (HP) studies on this kind of materials have been growing quickly in the last decade both because of the availability of better equipment and techniques for their implementation and because of the interesting effects that HP triggers. The energetics involved with the pressures commonly achieved (around 10 GPa) is quite large and gives rise to many phase transitions and a large polymorphism (see as examples *Boldyreva*, 2004, 2007, 2008; *Moggach et al.*, 2008). Techniques to obtain single crystals from liquids have also demonstrated the possibility to obtain different polymorphs with respect to the low-temperature grown ones (*Allan et al.*, 1998 and many other papers, also in this book). Recently HP polymorphs were also recovered at ambient pressure (*Oswald et al.*, 2009), making it an even more appealing field of research. HP structural characterization of these species is, nevertheless, still in its infancy as the number of molecules studied up to now is relatively small, especially if compared with the ones that can be found in the structural databases. Techniques and machinery are also still improving. The quality of the structural characterizations is still poorer than at ambient conditions due to the absorption and scattering of the cell elements and to the shading of its body, which restricts the reciprocal space that can be probed. Molecular crystals, moreover, are usually weakly diffracting as a result of the weak internal order and the presence of light elements (often oxygen being the heaviest atom). As a consequence, the majority of the HP molecular studies focus on the intermolecular features i.e. on the polymorphism and phase transitions, with intramolecular variations mainly restricted to torsion angles. Indeed, to stabilize the refinements, in many cases bond distances are even fixed and covalent bond variations have been analyzed in few cases only, when phase transitions dictate a variation of the bond order (*Katrusiak*, 1990), or when exceptionally good data could be obtained with special techniques (*Boldyreva et al.*, 1998; *Dziubek and Katrusiak*, 2004).

1.2. HYDROGEN BOND

Given its central role in various aspects of chemistry and biochemistry, it is of no surprise that a number of studies have been dedicated to hydrogen bond, including some of the pioneering high pressure experiments on molecular crystals (*Katrusiak*, 1990; *Katrusiak and Nelmes*, 1986). Indeed pressure, in strong hydrogen bonded systems, has been shown to prompt large deformations of their potential energy surface. Among the other

observed effects are phase transitions involving ordering-disordering of the hydrogen site (*Katrusiak and Nelmes*, 1986), molecular rearrangement following a proton transfer (*Katrusiak*, 1990), as well as the extreme case of total equalization of donor-H and acceptor-H distances (*Hemley et al.*, 1987). While these studies permit the experimental evidence of extreme behavior, a different way to follow hydrogen bond features has been applied by *Steiner and Saenger* (1994) using structure correlation analysis. It involves the statistical analysis of a large number of high quality independent structure determinations, assuming that the structural features of a molecular fragment in different environments are a good representation of its potential energy surface. The authors explicitly warn against any kind of extrapolation, given the uncertainty and variability of the population used. Following the evolution in a single structure of such a fragment as a function of a strong perturbation (or at least strong enough to produce measurable structural variations) would be another way to probe its potential energy surface, in a sort of "inherent structural correlation". In addition, it would not bear the problems connected with the variance of a large population thus allowing some kind of extrapolation. Temperature variation, despite the rather small perturbation it triggers, has been successfully used to study proton shifts (*Wilson*, 2001; *Martins et al.*, 2009) On the other hand HP would be the ideal perturbation, as the energetic variations it involves are large, the measurement of structural modification is indeed possible, but usually neither very precise, nor accurate. Experiments have to be designed and conducted carefully, in order to obtain the quality data required for meaningful results. These should in turn permit the exploration of areas of the potential energy surface not available with traditional techniques.

2. Achieving High Quality Data on Oxalic Acid Di-hydrate: A Case Study

Needless to say, that the first and the most important step of any crystallographic experiment, including HP ones, is the choice of well-sized, highly diffracting, twin-free and optically perfect crystals. Crystals cut from a larger samples may have some points of fragility and should be avoided, if possible, in HP experiments. In addition to these features the orientation, in which we want to mount the crystals, is critical for non-cubic systems. Monoaxial crystals should of course be mounted with the axis parallel to the culet, but for systems with lower symmetry there are orientations that will enable us to better determine the parameters we are interested in, depending on their main direction in the unit cell and on the crystal metrics. Oxalic acid di-hydrate crystallizes in the monoclinic $P2_1/n$ space symmetry group. The di-acid is on an inversion centre and makes strong hydrogen bonds with

two water molecules. The aim of the study was to observe modifications in the C–O and C=O bonds that could provide an insight into any kind of movement of the hydrogen (not locatable with x-rays) (*Casati et al.*, 2009). To achieve, on these bonds, a precision (which is a normal output of the refinement) and an accuracy (that can be tested reasonably on the room pressure data collected in the DAC and assuming the ambient pressure structure determined outside the cell as the true value) comparable with the expected deformations, a single crystal experiment proved to be insufficient and two crystals were mounted at the same time. They were carefully checked for defects with a polarizing microscope, checked for diffraction quality, indexed and mounted on pre-oriented faces, in such a way to probe partially the same part of the Ewald sphere (necessary for accurate scaling), but mainly to obtain information in directions normal to each other, thus improving the data collection completeness and data/parameter ratio. Full description of the crystal size and faces, useful for an accurate determination of the absorption, was done before sealing the DAC with a pentane/isopentane 1:1 mixture, which was used because of the slow reaction occurring between methanol and the sample.

While many different techniques can be found in literature (*Budzianowski and Katrusiak*, 2004; *Dawson et al.*, 2004), an experimentalist should always take into consideration the uniqueness of the instrumentation he can use and the target of his studies. Point detectors, although rapidly disappearing from most chemical crystallography laboratories, have still some advantages in HP experiments. The possibility of applying long distance extra slits cutting the scattering from the cell body, effectively improves the signal/noise ratio (*Boldyreva et al*., 1998). Nevertheless, accurate studies can be done also with CCD detectors: a Bruker diffractometer equipped with an APEX-II detector was used for these studies. For 3-circles diffractometers the collection on different sides of the DAC may provide the variation of the missing χ cradle, and indeed two sides of a triangular Merrill-Basset type DAC have been measured, to improve completeness and redundancy (necessary for a good statistical outlier rejection). During the integration, the effective area of the CCD (where diffraction is not shaded by the DAC body), the overlap with diamond or the second crystals' reflections, as well as the area covered by the [1 0 1] ring from the Be backing plates were all taken into account, to avoid the inclusion of badly biased reflections (and to avoid their influence on the integration of neighbor reflections) (*Angel*, 2004). Absorption from the cell was treated analytically using Absorb6.1 (*Angel*, 2004) while the crystal absorption was performed empirically (*Siemens*, 1996). Careful analysis of the data showed few areas of integration, close to the DAC border, where reflections had intensities systematically lower than other equivalents. These areas had to be rejected. Reflections with intensities

higher than their equivalents and laying on Be rings were inspected and, in some cases, rejected (the spotty nature of the Be rings and the problems it causes can, anyway, be avoided with modern Be-free backing plates and diamonds) (*Ahsbahs*, 2004; *Boehler*, 2006; *Sowa and Ahsbahs*, 2006). Refinements were then finally giving the desired quality data, except for the highest pressure value where, due to the failure of one crystal, data have a poorer accuracy and precision.

3. Structural Evolution at HP

3.1. OXALIC ACID DI-HYDRATE

The structure of oxalic acid di-hydrate, which, as mentioned, crystallizes in the $P2_1/n$ space symmetry group, is dominated by hydrogen bonds. The acid is on an inversion center and makes two strong hydrogen bonds with symmetry equivalent water molecules (O_1---O_w ~ 2.50 Å, see Figure 1). These, in turn, make longer hydrogen bonds to carbonyl oxygens of neighbor acid molecules (O_w---O_2 ~ 2.80 Å, see Figure 1). This network of hydrogen bonds extends mainly in the *c* direction while in the *b* one molecules are stacked on top of each other.

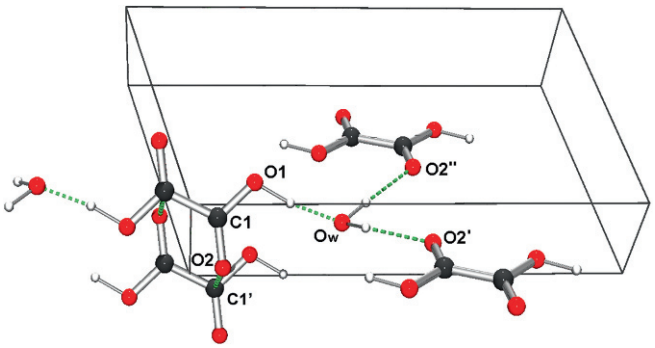

Figure 1. Hydrogen bond and stacking interactions in oxalic acid di-hydrate structure.

As pressure is raised, the different nature and strength of interactions give rise to an anisotropic compression and, not surprisingly, the most compressed direction is the one corresponding to the weakest interaction, namely *b*, while the most stiff one corresponds to *c*. Despite being the strongest intermolecular interaction, even the O_1---O_w distance decreases to 2.429(4) Å at 3.6 GPa, entering the range of the shortest hydrogen bonds observed. According to the structural correlation showed by *Steiner and Saenger* (1994), this should be a sign of a partial migration of the hydrogen

from the donor to the acceptor. As hydrogens cannot be precisely located with x-rays, we tried to analyse the evolution of the C–O and C=O bonds. As the acidic hydrogen is progressively donated, one would expect the single bond to slightly contract while the double one should slightly increase its value. As shown in Figure 2, not only is this tendency towards a symmetrization predicted by periodic DFT calculations, but is also well observed in experimental data.

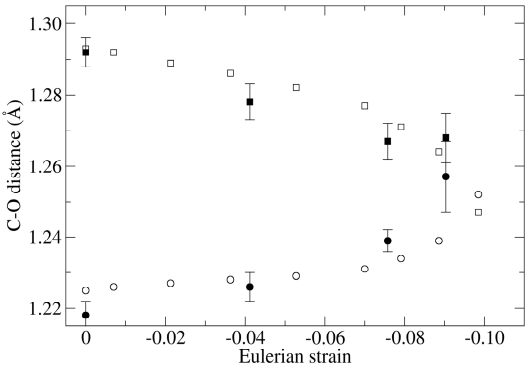

Figure 2. Experimental (filed symbols) and calculated (empty symbols) C=O and C–O distances plotted versus the Eulerian strain $\varepsilon = 0.5(1 - V_0/V)^{2/3}$.

Calculated distances for the acidic hydrogen show a total transfer of the proton at the last pressure and an equalization of the two carbon oxygen distances, which indeed seems to be confirmed by the experiments. Despite the lower quality of the last data point, the experimental values fit well in a structural correlation analysis performed on the best structures present in the Cambridge Structural Database (Figure 3). This confirms the general

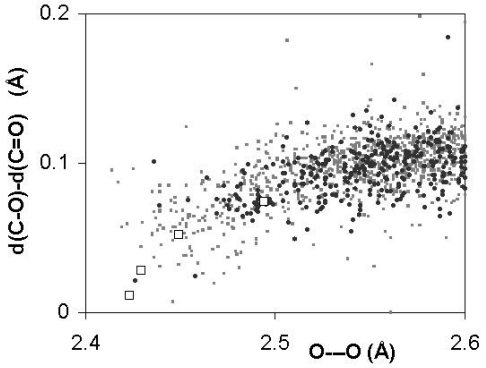

Figure 3. Difference of C–O and C=O distances plotted versus O---O separation for reported data (empty squares) and structures present in the CSD. Darker spots represent fragments with water as the acceptor.

validity of the approach and, when acceptors are restricted to water molecules, it shows also the potential of probing areas of the intermolecular fragment, which are not otherwise available.

To better clarify the hydrogen positions and to confirm the total migration of the acidic hydrogen, effectively resulting in an oxalate/hydronium ionic crystal, neutron diffraction experiments have also been carried out at ISIS facility on a powder sample of perdeuterated oxalic acid di-hydrate. Despite an isotopic effect could be expected, it was not found to be detectable in our experiments. The values of the O_1–D_1 and D_1--O_w distances, as resulting from Rietveld refinements at the reported pressures, are shown in Table 1. They confirm the total transfer of the proton from the acid to the water, depicting a solid-state acid–base reaction, as well as supporting further the x-ray diffraction trend observed.

TABLE 1. Evolution of the hydrogen distances with pressure in perdeuterated oxalic acid di-hydrate (neutron data)

Pressure(Gpa)	O1–H1 (Å)	H1–O_w (Å)
1.81	1.058	1.467
4.33	1.195	1.289
6.09	1.304	1.174

3.2. POTASSIUM BINOXALATE

KHC_2O_4 crystallizes as well in the monoclinic $P2_1/c$ spacegroup with infinite chains of binoxalate intercalated to potassium counter-ions (Figure 4).

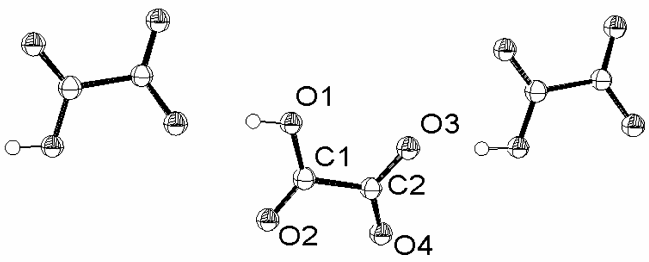

Figure 4. Chains of binoxalate ions. Potassium omitted for clarity.

Increasing pressure has a large effect on all the cation–anion distances, with a sharp decrease of the oxygen polyhedra around the K atom. The O1---O3 distance experiences also a large contraction, from 2.522(7) to

2.443(4) Å. Despite the distance not being as short as in oxalic acid, some slight structural variations can be expected. In this case, anyway, the eventual proton transfer would simply lead to the inversion of the molecule and, in the absence of other intermolecular interactions, is not predicted. Nevertheless, rather than an equalization of C1–O1 and C1–O2 distances the equalization of "tail" and "head", i.e. of C1–O1 with C2–O3 and of C1–O2 with C2–O4 would be expected. The evolution of the different C-O distances, shown in Figure 5, despite not being as clear as for oxalic acid, follows this simple scheme underlying a potential symmetrization of the hydrogen bond at higher pressure.

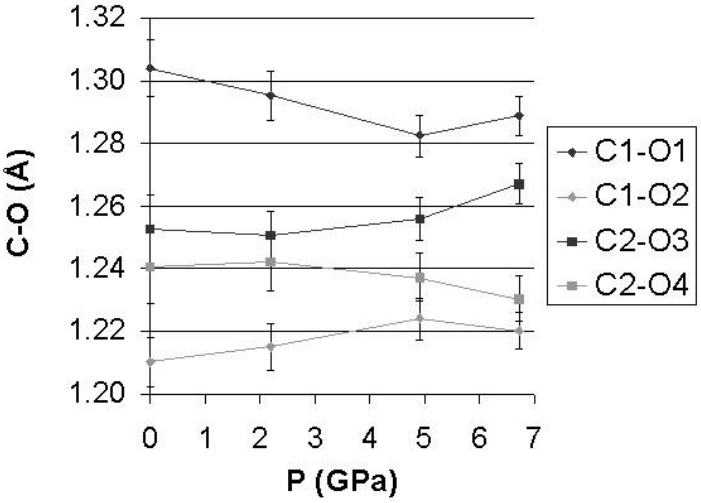

Figure 5. C–O distances in the binoxalate ion as a function of pressure.

4. Conclusion

The large energies involved in HP experiments allow the access to a large portion of the potential energy surface in molecular or intermolecular moieties. It is currently possible to characterize structurally, using laboratory equipment, the subtle modifications of intramolecular bonds at high pressure, which have been in many cases considered rigid. This enables the development of an "inherent structural correlation". As shown by oxalic acid di-hydrate this kind of evolutionary study fits well with the normal structure correlation analysis while pushing its boundaries further. It also enables a direct study of the evolution of an intermolecular fragment, perfectly describing the solid-state acid/base reaction between oxalic acid and water.

References

Ahsbahs, H., 2004, New pressure cell for single-crystal X-ray investigations on diffractometers with area detectors, *Z. Krist.* **219**(6): 305–308.

Allan, D.R., Clark, S.J., Brugmans, M.J.P., Ackland, G.J., Vos, W.L., 1998, Structure of crystalline methanol at high pressure. *Phys. Rev. B* **58**(18): R11809–R11812.

Angel, R.J., 2004, Absorption corrections for diamond-anvil pressure cells implemented in the software package Absorb6.0. *J. Appl. Cryst.* **37**(3): 486–492.

Boehler, R., 2006, New diamond cell for single-crystal X-ray diffraction. *Rev. Sci. Instr.* **77**(11), 115103/1–115103/3.

Boldyreva, E.V., 2004, High-pressure-induced structural changes in molecular crystals preserving the space group symmetry: anisotropic distortion/isosymmetric polymorphism, *Cryst. Eng.* **6**(4): 235–254.

Boldyreva, E.V., 2007, High-pressure polymorphs of molecular solids: when are they formed, and when are they not? Some examples of the role of kinetic control, *Cryst. Growth Des.* **7**(9): 1662–1668.

Boldyreva, E.V., 2008, High-pressure diffraction studies of molecular organic solids. A personal view, *Acta Cryst. A*. **64**(1): 218–231.

Boldyreva, E.V., Naumov, D.Y., Ahsbahs, H., 1998, Distortion of crystal structures of some Co^{III} ammine complexes. III. Distortion of crystal structure of $[Co(NH_3)_5NO_2]Cl_2$ at hydrostatic pressures up to 3.5, *Acta Cryst.* B **54**(6): 798–808.

Budzianowski, A., Katrusiak, A., 2004, High-pressure crystallographic experiments with a CCD-detector. *NATO Sci. Ser., II: Mathematics, Physics and Chemistry*, **140** (High-Pressure Crystallography): 101–112.

Casati, N., Macchi, P., Sironi, A., 2007, Improving the quality of diamond anvil cell data collected on an area detector by shading individual diamond overlaps, *J. Appl. Cryst.* **40**(3): 628–630.

Casati, N., Macchi, P., Sironi, A., 2009, Hydrogen migration in oxalic acid di-hydrate at high pressure? *Chem. Comm.* **19**: 2679–2681.

Dawson, A., Allan, D.R., Parsons, S., Ruf, M., 2004, Use of a CCD diffractometer in crystal structure determinations at high pressure. *J. Appl. Cryst.* **37**(3): 410–416.

Dziubek, K.F., Katrusiak, A., 2004, Compression of intermolecular interactions in CS_2 crystal, *J. Phys. Chem. B* **108**(50): 19089–19092.

Hemley, R.J., Jephcoat, A.P., Mao, H.K., Zha, C.S., Finger, L.W., Cox, D.E., 1987, Static compression of H_2O-ice to 128 GPa (1.28 Mbar), *Nature.* **330**(6150): 737–740.

Katrusiak, A., 1990, High-pressure X-ray diffraction study on the structure and phase transition of 1,3-cyclohexanedione crystals, *Acta Cryst. B***46**: 246–256.

Katrusiak, A., Nelmes, R.J., 1986, On the pressure dependence of the crystal structure of squaric acid ($H_2C_4O_4$). *J. Phys. C: Solid State Physics*. **19**(32): L765–L772.

Martins, D.M.S., Middlemiss, D.S., Pulham, C.R., Wilson, C.C., Weller, M.T, Henry, P.F., Shankland, N., Shankland, K., Marshall, W.G., Ibberson, R.M., Knight, K., Moggach, S., Brunelli, M., Morrison, C.A., 2009, Temperature- and pressure-induced proton transfer in the 1:1 adduct formed between squaric acid and 4,4'-bipyridine, *J. Am. Chem. Soc.*, **131**: 3884–3893.

Moggach, S.A., Parsons, S., Wood, P.A., 2008, High-pressure polymorphism in amino acids, *Cryst. Rev.* **14**(2): 143–184.

Oswald, I.D.H., Chataigner, I., Elphick, S., Fabbiani, F.P.A., Lennie, A.R., Maddaluno, J., Marshall, W.G., Prior, T.J., Pulham, C.R., Smith, R.I., 2009, Putting pressure on elusive polymorphs and solvates, *Cryst. Eng. Comm.* **11**(2): 359–366.

Siemens, 1996, SADABS. Siemens Industrial Automation Inc., Madison, Wisconsin, USA.
Sowa, H., Ahsbahs, H., 2006, High-pressure X-ray investigation of zincite ZnO single crystals using diamond anvils with an improved shape, *J. Appl. Cryst.* **39**(2): 169–175.
Steiner, T., Saenger, W., 1994, Lengthening of the covalent O-H bond in O-HO hydrogen bonds re-examined from low-temperature neutron diffraction data of organic compounds. *Acta Cryst.* **B50**(3): 348–57.
Wilson, C., 2009, Migration of the proton in the strong O-H---O hydrogen bond in urea-phosphoric acid (1/1). *Acta Cryst.* **B57**: 435–439 (2001).

INTRODUCTION INTO THE THEORY OF PHASE TRANSITIONS

VLADIMIR DMITRIEV*
SNBL at ESRF, BP220, 38043 Grenoble, France

Abstract Symmetry-based consideration introduces basic concepts of the theory of phase transitions. We show a background for different classifications of phase transitions and specify its terminology.

Keywords: Phase transition, symmetry, order parameter, transformation mechanism, thermodynamics, phase diagram

Phase transitions constitute an important topic in condense matter science. Working in its different domains researchers observe, analyze, and describe different manifestations of phase transformations. Basic principles and terminology of the theory of phase transitions form a unifying platform for the specific studies. This chapter aims to clarify the symmetry and thermodynamic origins of the rules and classifications existing in the field.

1. Phase Transition

1.1. PHASE

A phase is a region of space (a thermodynamic system), throughout which all physical properties of a material are essentially uniform. The phase space can refer to the space that is parameterized by the *macroscopic* states of the system, such as pressure, temperature, etc.

1.2. PHASE DIAGRAM

1.2.1. *Free Energy*

In thermodynamics, a system is characterized in any point of the phase space (in fact, at certain thermodynamic conditions) by its *free energy:*

*E-mail: dmitriev@esrf.fr

E. Boldyreva and P. Dera (eds.), *High-Pressure Crystallography: From Fundamental Phenomena to Technological Applications*, DOI 10.1007/978-90-481-9258-8_15,

$$F=<E>-TS=-k_BT\cdot lnZ=-k_BT\cdot ln\int \exp\left\{-\tfrac{1}{T}E(q)\right\}d\Gamma\ . \qquad (1)$$

In Eq (1) k_B denotes the Bolzmann constant, Z is the partition function, and the integral is taken over phase space. In the phenomenological approach suggested by L. Landau, degrees of freedom q are segregated into two groups: (a) few *critical* (non-equilibrium) degrees responsible for the symmetry breaking, and (b) remaining equilibrium variables inducing no singularities in energy. The free energy, therefore, reads:

$$F=-k_BT\cdot ln\int \exp\left\{-\tfrac{1}{T}\left[E_0(q)+E_1(q,\eta)\right]\right\}d\Gamma=F_0(P,T,...)+F_L(P,T,\eta). \qquad (2)$$

F_L in Eq (2) is a variational free energy and not an equilibrium energy, since it is calculated for an arbitrary *order parameter* η. The equilibrium free energy of the system is $F_L^{eq}(P,T)=F(P,T,\eta_0)$ where η_0 is found as a result of minimization of $\partial F_L(\eta)/\partial\eta = 0$. The Landau free energy is, therefore, an incomplete (partly integrated) thermodynamic potential.

1.2.2. *Phenomenological Approach*

Thus the phenomenological Landau theory of phase transitions defines two basic concepts: the *order parameter* (OP) and the *variational* (non-equilibrium) *free energy*. From the symmetry properties of these two quantities, it is possible to infer, on the one hand, a certain number of observable symmetry characteristics of the system. On the other hand, macroscopic quantities can be classified as function of their symmetries with respect to the order parameter. From this can be deduced a classification of the type of anomalous behavior induced by the occurrence of the phase transition.

In its classical form, the theory suggests the occurrence of a symmetry relationship between the two phases surrounding the transition, i.e. there is a specific correspondence between the symmetry elements of the two phases. The lower symmetry structure (symmetry G_d) is considered as a slightly distorted reference one, termed the parent structure (G_0). Hence, the increment of probability density in a crystal at a phase transition can be expanded using $\phi_{ki}(\boldsymbol{r})$ basis functions of a relevant irreducible representation of the G_0 space group:

$$\Delta\rho(\boldsymbol{r}) = \rho_d(\boldsymbol{r})-\rho_0(\boldsymbol{r})=\boldsymbol{\Sigma}\eta_{ki}\phi_{ki}(\boldsymbol{r}), \qquad (3)$$

where η_{ki} are the order parameter (OP) components and $\boldsymbol{k}$ is the reciprocal space vector. It is worth underlining that Eq (3) is an expansion in a basis but not in a series that allows η_{ki} to be non-small, as it simply characterizes a contribution ("weight") of each symmetry coordinate in the total structure distortion. Scalar order parameter components η_{ki} and normalized basis functions $\phi_{ki}(\boldsymbol{r})$ have identical symmetry properties and span the same

irreducible representation of the space group G_0. Either of the two sets, therefore, can be used as variational parameters for the non-equilibrium energy. It is convenient for η_{ki} to play the role: $F_L = F_L(P,T,\eta)$. The symmetry properties of $\Delta\rho$ determine the form of the non-equilibrium variational energy F_L.

In order to determine the stable distorted phases, one needs to minimize the Landau potential with respect to the OP components:

$$\partial F(P,T,\eta_{ki})/\partial\eta_{ki}=0. \tag{4}$$

The stability domains of the corresponding phases are determined by the inequalities

$$\partial^2 F(P,T,\eta_{ki})/\partial\eta_{ki}^2\geq 0. \tag{5}$$

Although the general form of the Landau potential $F_L(P,T,\eta_i)$ is entirely determined by the symmetry of the order parameter, the equilibrium values of the order parameter components, as functions of the phenomenological coefficients depend on the specific model chosen for F_L.

1.2.3. *Phase Diagram*

In physics, a phase space is a space representing all possible states of a system. Each possible state of the system corresponds to one unique point in the phase space. In phase space, every degree of freedom or parameter of the system is represented as an axis of a multidimensional space. For every possible state of the system, or allowed combination of values of the system's parameters, a point is plotted in the multidimensional space. The phase space can refer to the space that is parameterized by the *macroscopic* states of the system, such as pressure, temperature, etc. For instance, one can view pressure-volume diagrams or entropy–temperature diagrams describing part of this phase space.

In order to display all principal features of the phase diagram: critical lines, special points etc., we consider a canonical example of the six-degree expansion in the order-parameter components:

$$F_L(P,T,\eta)=a_1\eta^2+a_2\eta^4+a_3\eta^6, \tag{6}$$

which describes both second- and first-order phase transitions. The phase diagram corresponding to the potential (6) is shown in Figure 1. It is mapped onto the plane of the phenomenological parameters a_i, which can be transformed, by a linear transformation $a_i(P,T) = \alpha_i(P - P_0)+\beta_i(T - T_0)$, to the conventional thermodynamic (P,T) space.

On the phase diagram of Figure 1 one finds *stability limit lines* corresponding to the equality $\partial^2 F(P,T,\eta_{ki})/\partial\eta_{ki}^2 = 0$ in Eq (5), and the *transition lines* corresponding to the equality of the equilibrium energies $F_I = F_{II}$. The

main distinctive properties of the first-order transformation regime are: (i) the coexistence of the two phases I and II; (ii) a discontinuous jump of the order parameter at the transition point. The consequences are the existence of a latent heat and specific discontinuities for the related physical quantities. The second-order transformations occur at the points of the coincidence of the stability limits for the phases I and II. The line of first-order transitions goes over the second-order transition line at the tricritical point Tr located at the origin ($a_1 = a_2 = 0$).

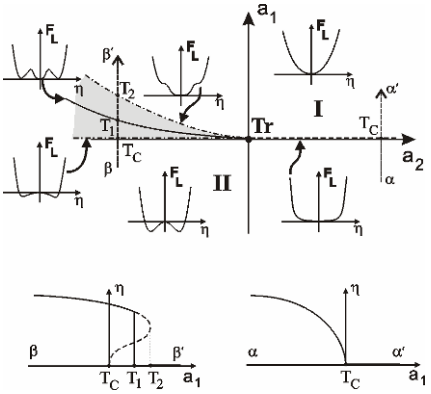

Figure 1. Phase diagram corresponding to the potential (6). Full, dashed, and dashed-dotted lines are, respectively, first-order, second-order, and limit of stability lines. The tricritical point Tr separates the second-order transition line $T = T_C$ ($a_2 > 0$) from the first-order transition line $T = T_1$ ($a_2 < 0$). Shadowed zone is the phase I–II coexistence region. The curves $F_L(\eta)$ are shown in significant regions and on lines of the phase diagram. Lower panels show the functional form of the order parameter for different transformation regimes.

1.2.4. *Multiphase Point: Phase Rule*

Multiphase points exist on the phase diagrams of elements, alloys and compounds. Gibbs' phase rule provides, in general, the number of degrees of freedom (control variables: pressure, temperature, concentration, etc.) for a system, which can be arbitrarily varied without destroying the equilibrium. The Gibbs' rule forbids, in particular, the coexistence of more than three phases of a given compound at one (P, T) point.

The phase rule stems from a pure mathematical restriction when one considers a system consisting of different π phases in contact. In general, each phase contains all substances, in which all phases are independent: no structure links are considered. The number of independent components in the system is C. Then each phase is described by its pressure, temperature and chemical potential μ. In the general case, if P and T are the common

pressure and temperature, the phase equilibrium condition will be that all chemical potentials are equal to each other:

$$\mu_i^I = \mu_i^{II} = ... = \mu_i^{\pi} \quad (i = 1 \div C). \tag{7}$$

Each of these potentials μ_i^{π} is a function of $C + 1$ independent variables: P, T, and C-1 concentrations. Hence, the number of unknowns is $2 + \pi(C - 1)$. To have solutions, the number of equations must not be greater than the number of unknowns, i.e. $C(\pi - 1) \leq 2 + \pi(C - 1)$, or $\pi \leq C + 2$, which is called the phase rule. The number of variables which can be arbitrarily varied is called the number of *thermodynamic degrees of freedom (f)* of the system. The phase rule may be written:

$$f = C + 2 - \pi. \tag{8}$$

Thus, when a one-component system ($C = 1$) is considered, the number of *independent* phases, π, that exist in contact on the phase diagram cannot exceed three. However, the Gibbs' phase rule still holds when all phases merging at the triple point are assumed to be *independent*, i.e. *no parent phase* and *no order parameters* are defined. The phenomenological approach, introducing the latter, increases the number of equations by adding the equations of state (4). This increases, in turn, the number of variables which can be arbitrarily varied, and allows, therefore, the existence of N-phase point * –s–* (N > 3) on phase diagrams.

2. Classifications of Phase Transitions

2.1. THERMODYNAMIC: EHRENFEST CLASSIFICATION

The most general characteristic of a phase transition is its "order": this basic thermodynamic classification considers the thermodynamic potential (free energy) and its derivative at the transition. If first derivations of F exhibit jump singularities there, the transition is classified as *first order* (*discontinuous*). If first derivatives are continuous but second ones are singular, we have a *second-order* (*continuous*) transition. Although the Ehrenfest scheme is an inaccurate method of classifying phase transitions, it is still in use. Its main weakness is in its "mean-field" character – it is inaccurate in the vicinity of phase transitions, as it neglects the role of critical thermodynamic fluctuations. However, in general, at a first-order transition there is no diverging correlation length and therefore, no critical phenomena is to be expected. Moreover, for structural phase transitions the crucial role of fluctuations has also been shown to be of importance in the extremely limited vicinity of the point of continuous phase transition.

2.2. SYMMETRY CRITERIA

In the Section 1.2.2 we showed that the increment of probability density in a crystal at a phase transition can be described in terms of basis functions $\phi_{ki}(\boldsymbol{r})$ of certain irreducible representations of the parent G_0 space group [see Eq (3)]. The basis functions $\phi_{ki}(\boldsymbol{r})$ are Bloch-type functions consisting of a plane wave envelop function $exp\{i\boldsymbol{kr}\}$ multiplied by a periodic function $U_{ki}(\boldsymbol{r})$:

$$\phi_{ki}(\boldsymbol{r}) = e^{i\boldsymbol{kr}} \cdot U_{ki}(\boldsymbol{r}), \tag{9}$$

where $U_{ki}(\boldsymbol{r})$ has the period of the crystal lattice with $U_{ki}(\boldsymbol{r}) = U_{ki}(\boldsymbol{r} + \boldsymbol{T})$. The exponential functions from Eq (9) constitute the basis for an irreducible representation of the subgroup of translations of G_0. $U_{ki}(\boldsymbol{r})$ does the same for representations of the "little" group $G_{\boldsymbol{k}}$ of the relevant vector $\boldsymbol{k}$ of the reciprocal space.

Hence, the symmetry related classification distinguishes between (i) translation symmetry breaking, and (ii) the change of the total symmetry characterized by a space group.

2.2.1. *Translation Symmetry*

In analyzing the translation properties of a phase G_d that arises as a result of the G_0–G_d phase transition, it suffices to consider an expansion of the G_d density function in the form:

$$\rho(\boldsymbol{T}_j) = \Sigma_j e^{i\boldsymbol{k}_j\boldsymbol{T}_j}\rho_j(0), \tag{10}$$

where the summation is performed over all the arms $\boldsymbol{k}_1 \ldots \boldsymbol{k}_j$ of the reciprocal space vector star $\{\boldsymbol{k}\}$. This equation relates the density in the jth crystal unit cell to the density $\Sigma_j\rho_j(0)$ in the zero cell, and it is a direct consequence of (3). The unit cell vectors $\boldsymbol{T}_d$ of a distorted, low-symmetry structure are determined from the condition that the density function $\rho(\boldsymbol{T}_j)$ is invariant under all translations of the new phase G_d. Using Eq (3) one obtains:

$$e^{i\boldsymbol{k}_j\boldsymbol{T}_d} = 1. \tag{11}$$

Two possibilities exist: (i) we consider OPs with zero $\boldsymbol{k}$-vector (Γ-point of the corresponding Brillouin zone). Then there is no change of translational symmetry at the transition. In this case the transition is called *equitranslational* or *ferrodistortive*. (ii) If $\boldsymbol{k} \neq 0$, Eq (11) defines new lattice vectors which are linear combinations of the parent phase basis vectors. In this case we call the transition *non-equitranslational* or *antiferrodistortive*.

2.2.2. *Total Symmetry*

The total symmetry change is considered only in a symmetry-based definition of the reconstructive phase transformation. The latter is identified as a one breaking the group-subgroup relationship between structures adjusting the transformation point. In contrast, it is worth considering here transitions without changing the space group of the structure – *isosymmetric* transformations. Two transformation types can be distinguished for this case: (i) *isostructural* transformations, and (ii) *anti-isostructural* ones.

2.2.2.a. Isostructural Phase Transition

A Landau type theoretical approach to isotructural transitions is known to deal with a single-component order parameter spanning the *totally symmetrical* (*identity*) irreducible representation of the parent phase space group. A scalar (isotropic) physical quantity, such as volume or density deviation, perfectly fits this role.

The non-equilibrium energy (Landau potential) associated with the simplest model of an isostructural phase transition has the form (*Kuznetsov et al.*, 2003):

$$F(\eta)=b_1\eta+b_2\eta^2+b_3\eta^3+\eta^4, \tag{12}$$

where η is the totally symmetrical (non-symmetry breaking) order parameter, and b_i are phenomenological parameters. The change of variables $\eta = \Delta - b_3/4$ and following elimination of the equilibrium part of the energy transforms Eq (12) into the normal form:

$$F(\Delta)=a_1\Delta+a_2\Delta^2+\Delta^4, \tag{13}$$

where $a_1 = b_1 - b_2b_3/2 + b_3^3/8$, and $a_2 = b_2 - 3b_3^2/8$. Minimization of the potential $F(\Delta)$ with respect to the order parameter Δ yields an equation of state as follows:

$$\partial F/\partial\Delta = a_1 + 2a_2\Delta + 4\Delta^3=0. \tag{14}$$

The Landau potential (13) coincides with one of the *elementary catastrophes*, namely, the *cusp* catastrophe, and its mathematical aspects were studied comprehensively in the framework of the mathematical catastrophe theory. The equilibrium values of the order parameter Δ are the solutions of the equation of state (14). Because this is a cubic equation it has either one or three real roots, and only these have a physical meaning. The number of roots is determined by the determinant $D = 8a_2^3 + 27a_1^2$. If $D \le 0$ there are three real roots:

$$\Delta_1 = 2\rho\cdot\cos(\phi/3),\ \Delta_{2,3}=2\rho\cdot\cos\{(\pi \pm \phi)/3\};\ \ \rho = sgn[a_1(a_2/6)^{1/2}], \tag{15}$$

two ($\Delta_{2,3}$) corresponding to minima of the Landau potential and one (Δ_1) corresponding to a maximum; otherwise there is only one (Δ_1) corresponding to a minimum. Figure 2 illustrates this by a three-dimensional diagram of the equilibrium surface (14) and its projection on the a_1–a_2 plane. One can see that smooth variations in a_1 and a_2 almost always produce a smooth variation in Δ. The only exceptions occur when the system crosses the energy equality (isostructural first-order phase transition) line $F(\Delta_2) = F(\Delta_3)$, i.e. $a_1 = 0$. In this point it jumps to the other sheet corresponding to the other energy minimum ($\Delta_2 \leftrightarrow \Delta_3$). This brings about a sudden change in Δ. The projection of the folds in the equilibrium surface onto the a_1–a_2 plane ($D = 0$, $a_2 = 3a_1^{2/3}/2$) are the stability limit lines for the corresponding states (Figure 2). The variation regime in Δ can be changed smoothly from discontinuous to continuous by varying the a_2 parameter from negative to positive sign. The change of regime occurs at $a_2 = 0$, i.e. at the critical point, K, of the liquid-gas type (Figure 2).

Two phases adjacent to the transition line are "qualitatively" identical but "quantitatively" distinct. Closely associated with isostructural phase transition is a supercritical "*crossover*" ($a_2 > 0$) in which thermal expansion or pressure compressibility, for example, vary non-monotonically. However, and it is worth underlining, such behavior cannot be assigned to a continuous regime of the isostructural transformation as no transformation occurs. There are neither two distinguishable states, nor two energy minima which could be linked by a phase transition.

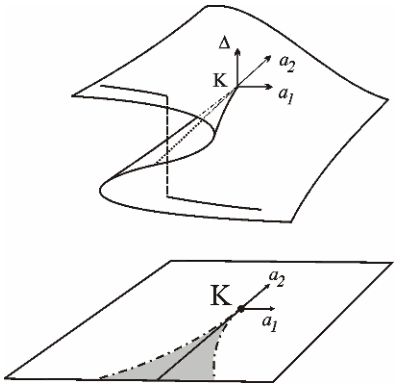

Figure 2. Equilibrium surface corresponding to Eq. (14), and its projection onto the a_1-a_2 plane. Dashed-dotted lines are stability limit lines, solid line – the first-order isostructural phase transition line. K is the critical end-point. Shadowed zone is the phase coexistence region.

2.2.2.b. Anti-Isostructural Phase Transition

The symmetry of the order-parameter (i.e. the equilibrium relationship between the OP components) remains unchanged between two isostructural phases. In contrast, for *anti-isostructural* transitions, though the space groups of the phases are the same, the *sign* of the order-parameter components changes from one phase to another. Thus, the two phases can be distinguished qualitatively and no critical end-point will be found on a first-order transition line of anti-isostructural transition. For instance, in the In-Pb alloys the two tetragonal phases correspond to opposite signs of the experimentally measured strain $\varepsilon_1 = (c_t/a_t - 1) = (e_{xx} + e_{yy} - 2e_{zz})$, where a_t and c_t are the tetragonal parameters (Figure 3). In terms of the spontaneous strain tensor components one has $e_{zz} > e_{xx} = e_{yy}$ in one phase, compared to $e_{zz} < e_{xx} = e_{yy}$ in the other phase (*Dmitriev et al.,* 2007).

The corresponding Landau potential is a function of a two-component order parameter and contains, in contrast to Eq (6), odd-degree terms:

$$F_L = a_1(\eta_1^2 + \eta_2^2) + a_2(\eta_1^3 - 3\eta_1\eta_2^2) + a_3(\eta_1^4 + \eta_2^4) + \ldots \qquad (16)$$

The phase diagram for the model (16) is shown in Figure 3. Two low-symmetry phases I and II with identical symmetry are associated with opposite value of the equilibrium order-parameter components, i.e. phases are anti-isostructural. The *Landau point* L ending a line of first-order transitions, separating two anti-isostructural phases, is an isolated point of a second-order phase transition.

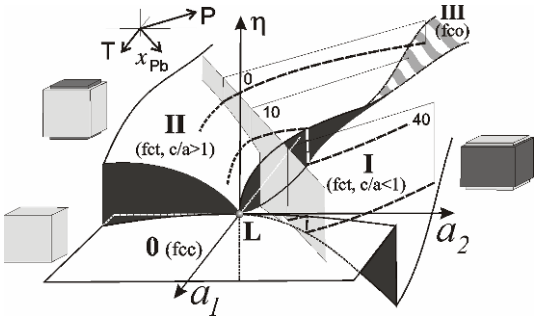

Figure 3. Equilibrium phase diagram corresponding to the thermodynamic potential (16), in the (a_1, a_2, η) space. Grayish plane is an ambient isobaric plane. Vertical planes are (η, P) isothermal sections corresponding to $In_{1-x}Pb_x$ with different Pb content. Dashed lines in the planes show order parameter $\eta = (c/a\text{-}1)$ as a function of pressure. The numbers indicate the atomic percentage of lead. L is a Landau point.

2.3. MICROSCOPIC MECHANISM

A phase transition from the parent phase gives rise to a state, which at microscopic level may be specified by the occurrence of a spontaneous tensorial property on each atom position. In group-theoretical terms, it means that a representation relevant to the order parameter is the direct product of three representations: the representation of the subgroup of translations, a permutation representation, and the representation operating with components of the tensor which specifies the microscopic mechanism of the phase transition. Variation of a scalar (zero-rank tensor) results in the *ordering*-type phase transition characterized by a change in the relative probability for different atoms of occupying certain crystallographic positions. In the case of *displacive*-type phase transitions a polar displacement vector (first-rank tensor) is assigned to an atom. The assignment of an axial vector (pseudovector) yields a static magnetic moment in a *magnetic* phase transition.

2.4. MACROSCOPIC PROPERTIES

General classification can be formulated in terms of the level of the point symmetry. In the general case, the point group of one phase (the ferroic phase) is a strict subgroup of the other one (the parent phase). The transition is then classified as *ferroic*. At a ferroic transition components of certain macroscopic tensor acquire nonzero values in the low-symmetry phase. If two point groups are identical, the corresponding transition is classified as *non-ferroic*.

The lowering of point-group symmetry at ferroic phase transitions is accompanied by an increased number of independent components of some property tensors, i.e. the appearance of spontaneous tensor components, which equal zero in the parent phase and nonzero in the ferroic phase. In the case of equitranslational (ferrodistortive) phase transitions the symmetry of the corresponding tensor may be identical to the symmetry of the primary (symmetry-breaking) order parameter. Then, if the primary OP transforms as a vector, the equitranslational phase transition is called a *proper ferroelectric* transition. Similarly, if the primary OP transforms as components of a symmetric second-rank tensor, the corresponding principal tensor parameter is a spontaneous strain and the equitranslational phase transition is called *proper ferroelastic*.

The property tensor components (secondary OP) may transform as a symmetric square $[\tau_i]^2$ of the primary order parameter belonging to a non-central point of the Brillouin zone of the parent crystal lattice. The corresponding non-equitranslational phase transition is called *improper*.

References

Dmitriev, V., Chernyshov, D., Filinchuk, Y., and Degtyareva, V., 2007, Anti-isostructural phases and anomalous thermoelasticity in In-based alloys: Synchrotron x-ray diffraction experiments and unified phenomenological model. Phys. Rev. B. 75: 024111.

Kuznetsov, A., Dmitriev, V., Bandilet, O., and Weber, H.P., 2003, High-temperature fcc phase of Pr: negative thermal expansion and intermediate valence state, Phys. Rev. B 68: 064109.

Suggested Reading

Izyumov, Yu., and Syromyatnikov, V., 1990, *Phase Transitions and Crystal Symmetry,* Kluwer, Dordrecht.

Landau, L.D., and Lifshitz, E.M., 1980, *Statistical Physics. Part 1*, Pergamon, Oxford.

Toledano, P., and Dmitriev, V., 1996, *Reconstructive Phase Transitions in Crystals and Quasicrystals*, World Scientific, Singapore.

PHASE TRANSITIONS IN AB SYSTEMS. SYMMETRY ASPECTS

HEIDRUN SOWA*
GZG Abt. Kristallographie, Georg-August-Universität Göttingen, Goldschmidtstr. 1, 37077 Göttingen, Germany

Abstract Possible pathways for pressure-induced reconstructive phase transitions in AB compounds can be derived if a common subgroup of the space groups of the phases before and after the phase transformation is found, which allows a deformation of one structure type into the other. An energetically favoured path avoids the breaking of bonds. Therefore, the concept of sphere packings enables to find suitable transition mechanisms. This is exemplarily shown for a transition path from the zinc-blende- to the NaCl-structure type.

Keywords: Reconstructive phase transitions, group – subgroup relations, orientation relations

1. Introduction

The understanding of the mechanisms of phase transformations is a challenging problem in crystal chemistry. Displacive transitions involve only small displacements of the atoms and can be described by means of group theory because the symmetry groups of the phases before and after the phase transition show group – subgroup relations. Reconstructive phase transitions are accompanied by large volume discontinuities, often the coordination numbers of the atoms change and it is assumed that a huge reorganization of the atomic arrangement takes place involving the breaking of bonds and formation of new ones. The symmetries of the phases do not show group – subgroup relations. Since many years, attempts have been made to understand the nature of the underlying transition mechanisms. For several compounds, models have been derived that involve cooperative shifts of the atoms while

*E-mail: Heidrun.Sowa@geo.uni-goettingen.de

E. Boldyreva and P. Dera (eds.), *High-Pressure Crystallography: From Fundamental Phenomena to Technological Applications*, DOI 10.1007/978-90-481-9258-8_16,

the metrics change simultaneously (e.g., *Christy,* 1993; *Dmitriev et al.*, 1988; *Dmitriev and Tolédano*, 1996; *Shôji*, 1931).

2. Pressure-Induced Phase Transitions in AB Compounds

The pressure-induced phase transitions in AB compounds are usually termed reconstructive. Up to now, mainly the transformations between the structure types of NaCl and CsCl, zinc-blende and NaCl and wurtzite and NaCl have been investigated. Based on experimental results, on geometrical considerations or on molecular dynamics simulations, possible atomic movements leading from one structure type to the other were described in a very illustrative way (e.g. NaCl↔CsCl: *Buerger*, 1951; *Hyde and O'Keeffe*, 1973; *Shôji*, 1931; *Watanabe et al.*, 1977; zinc-blende↔NaCl: *Miao et al.*, 2003; *Shimojo et al.*, 2000; wurtzite↔NaCl: *Corll*, 1967; *Knudson et al.*, 1999; *Miao et al.*, 2003; *Sharma and Gupta*, 1998; *Shimojo et al.*, 2004; *Tolbert and Alivisatos*, 1995; *Wickham et al.*, 2000). If structural relationships between the phases before and after the transition are present, it should be possible to describe the transition by means of group theory. *Christy* (1993), for instance, pointed out that the shortest transformation pathway may be found by considering shared structural features of the two phases and the lattice modes that preserve these features while changing the rest of the structure. He specified the space groups of possible intermediate states, for example, for the transitions between the NaCl and the CsCl type. More effective than such an intuitive search for common structural characteristics is another method for the derivation of possible transition paths: a transition mechanism can be modelled if a common subgroup of the space groups of the phases before and after the phase transformation is found, which allows a deformation of one structure type into the other. Such a consideration is closely related to the analysis of corresponding lattice modes, but shared structural features must not be known. Various mechanisms have been derived in this way for the transitions from the NaCl to the CsCl type (*Sowa*, 2000a, 2003; *Stokes et al.*, 2004; *Tolédano et al.*, 2003), from the zinc-blende to the NaCl type (*Blanco et al.*, 2000; *Catti*, 2001, 2002; *Hatch et al.*, 2005; *Perez-Mato et al.*, 2003; *Sowa*, 2000b, 2003; *Wilson et al.*, 2002;) and from the wurtzite to the NaCl type (*Limpijumnong and Lambrecht*, 2001; *Sowa*, 2001, 2005a; *Stokes et al.*, 2007; *Wilson and Madden*, 2002).

However, it is not sufficient to derive the common subgroups. Since there are a large number of such subgroups, additional criteria must be chosen to find proper transition pathways. This may be, for instance, energy calculations, maximal distances for the atomic movements or restrictions for the size change of the unit cell etc. (e.g. *Cai et al.*, 2007; *Hatch et al.*,

2005; *Stokes et al*., 2004, 2007). *Capillas et al*. (2007) searched only for high-symmetry paths and restricted the number of possible pathways by limiting the values for the lattice strain and the atomic displacements.

One example for a procedure of deriving transition mechanisms is given in the following section.

3. Pressure-Induced Phase Transitions from the Zinc-Blende to the NaCl Type

The transition from the zinc-blende to the NaCl type is a good example for showing how difficult it is to find unchanged structural features common in the starting and in the final phase even in simple compounds:

Zinc-blende crystallizes in the cubic space group $F\bar{4}3m$. The atoms are located at Wyckoff positions 4(*a*) 0,0,0 and 4(*c*) $^1/_4,^1/_4,^1/_4$ (Figure 1a). After the pressure-induced phase transition a NaCl-type modification becomes stable. It is also cubic, space group $Fm\bar{3}m$. The atoms occupy the positions 4(*a*) 0,0,0 and 4(*b*) $^1/_2,^1/_2,^1/_2$ (Figure 1b).

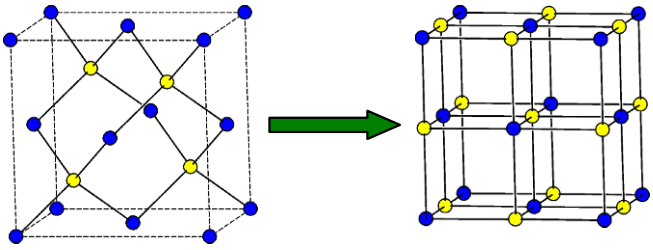

Figure 1. (a) Zinc-blende-type structure, (b) NaCl-type structure.

In crystal structures of both types, the cations as well as the anions form cubic face-centred lattices that are shifted against each other by a vector $(^1/_4,^1/_4,^1/_4)$ in the case of the zinc-blende type, and by a vector $(^1/_2,^1/_2,^1/_2)$ in the case of the NaCl type. For obvious reasons a transition mechanism may be suggested that implies a movement of the entire cation substructure

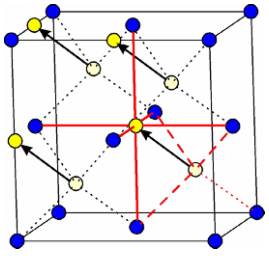

Figure 2. Transition path from zinc-blende to NaCl type via an intermediate state with symmetry $R3m$.

against the anion substructure along one of the ⟨111⟩ directions. Then, the intermediate phase would have the symmetry $R3m$ (Figure 2). However, the consequence of such a mechanism would be the breaking of one bond per atom. Therefore, the energy barrier for the corresponding atomic motions may be too high.

In deriving common subgroups of $F4\,3\,m$ and $Fm\bar{3}\,m$ *Hatch et al*. (2005) found 925 possible transitions pathways, but only eight of them are energetically favorable. *Capillas et al*. (2007) got six common subgroups with maximum symmetry, by restricting the number of atoms per unit cell in the subgroups.

Transition mechanisms may be also derived by using the concept of sphere packings (*Sowa*, 2000a, b, 2001, 2003, 2005a). A sphere packing is an arrangement of spheres with the symmetry of a space group, where any two spheres are connected by a chain of spheres with mutual contact. This means, that there are not only closest sphere packings, but also a large number of those with lower contact numbers. Unfortunately, not all of them are already known. Up to now, all cubic, tetragonal, trigonal, hexagonal, triclinic and part of the orthorhombic ones have been derived (see *e.g*., *Fischer et al*., 2006, Sowa & Fischer, 2010 and references therein).

Energetically favorable is a pathway that does not imply the breaking of bonds. Therefore, possible transition mechanisms may be found if the starting structure can be described by means of a sphere packing and if this sphere packing can be deformed into the final structure without losing sphere contacts.

A zinc-blende-type structure may be described as a heterogeneous (consisting of different kinds of atoms) sphere packing with four contacts per sphere. Since it is easier to investigate homogeneous sphere packings that contain only one type of sphere (all spheres are symmetrically equivalent), we replace the different atoms by like ones. The resulting structure with space group $Fd\bar{3}\,m$ belongs to the diamond type. It corresponds to a homogenous sphere packing of type 4/6/c1 (*cf*. *Fischer*, 1973). Replacing the atoms in a NaCl-type structure leads to an arrangement corresponding to a cubic primitive lattice and a sphere packing of type 6/4/c1 with space group $Pm\bar{3}\,m$ with a lattice parameter a which is half as long as that of $Fm\bar{3}\,m$. Now, starting from $Fd\bar{3}\,m$ the symmetry has to be reduced until it is possible to deform a sphere packing of type 4/6/c1 into one of type 6/4/c1 without losing any sphere contacts. This is possible, for instance, in space group *Imma* that is a subgroup of $Fd\bar{3}\,m$ as well as of $Pm\bar{3}\,m$ (Figure 3). Starting from space group $Fd\bar{3}\,m$ symmetry reduction leads *via* the translational equivalent subgroup $I4_1/amd$ of $Fd\bar{3}\,m$ to the translational equivalent subgroup *Imma* of $I4_1/amd$. In the standard setting of *Imma* (origin 1) the origin of the unit cell is shifted by a vector $(0,-{}^1/_4,-{}^1/_8)$

relative to that of $I4_1/amd$. Starting from space group $Pm\bar{3}m$ removing of the threefold axes leads to the translational equivalent subgroup $P4/mmm$. Maintaining the diagonal mirror planes, the translational equivalent subgroup $Cmmm$ of $P4/mmm$ with $\mathbf{a}' = \mathbf{a} - \mathbf{b}$, $\mathbf{b}' = \mathbf{a} + \mathbf{b}$ and $\mathbf{c}' = \mathbf{c}$ is obtained. Further symmetry reduction results in the class equivalent subgroup with doubled c lattice parameter $Imam$ of $Cmmm$. In order to get the standard setting of $Imma$ the second and the third lattice parameters have to be interchanged and an origin shift by a vector $(0,-^1/_4,0)$ is necessary. The diamond configuration occurs as a limiting form within Wyckoff position 4(e) $0,^1/_4,z$; with $z = ^1/_8$ and $a/b = 1$ and $c/b = \sqrt{2}$ whereas a cubic primitive arrangement is obtained with $z = 0$ and $a/b = c/b = ^1/_2\sqrt{2}$ (*Fischer et al*., 2006).

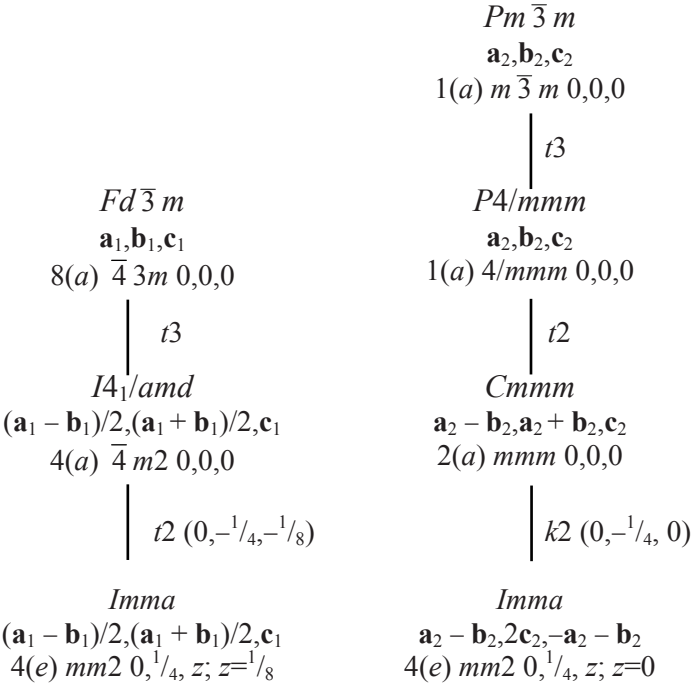

Figure 3. Symmetry relations between a diamond configuration and a cubic primitive lattice.

The analogous symmetry reductions for the binary compounds can be made in subgroups of index 2 of the space groups mentioned above (Figure 4). Symmetry reduction for zinc-blende-type structures leads from $F\bar{4}3m$ via $I\bar{4}m2$ to $Imm2$, for NaCl-type structures from $Fm\bar{3}m$ via $I4/mmm$ and $Immm$ to $Imm2$. The ideal zinc-blende-type arrangement is obtained if the Wyckoff positions 2(a) 0,0,z with $z = 0$ and 2(b) $0,^1/_2,z$ with $z = ^1/_4$ are occupied and $a/b = 1$ and $c/b = \sqrt{2}$. The undistorted NaCl type occurs if

the atoms are located at 2(*a*) 0,0,*z* with *z* = 0 and 2(*b*) 0,½,*z* with z = 0 and *a*/*b* = *c*/*b* = $^1/_2\sqrt{2}$.

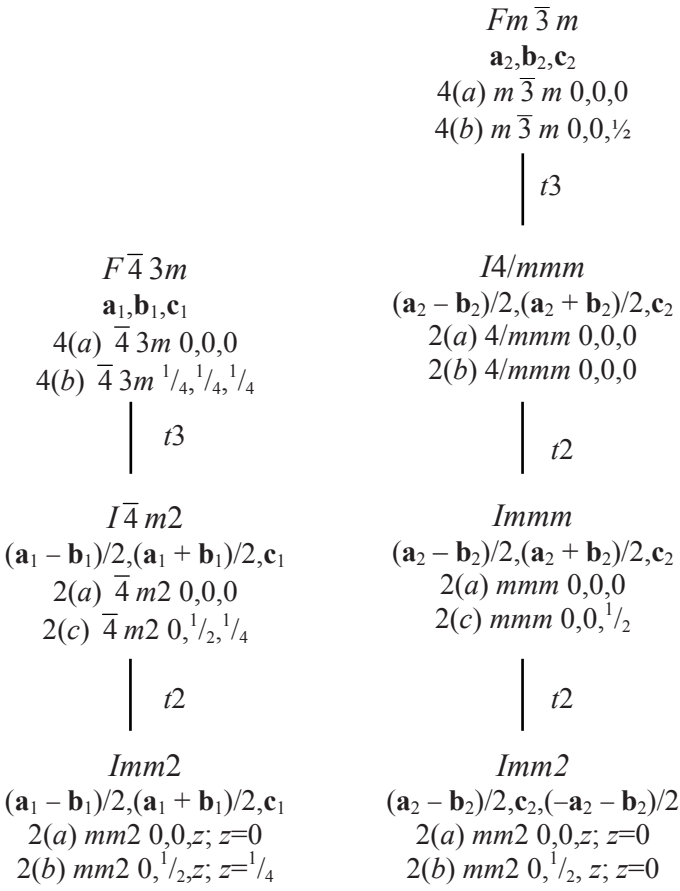

Figure 4. Symmetry relations between the zinc-blende and the NaCl- structure type.

In *Imma* 4(*e*) a sphere packing of type 4/6/*c*1 (diamond configuration) may be deformed in such a way that a cubic primitive lattice is formed. The sphere packing condition can easily be determined as shown in Figure 5 for the transition between zinc-blende and NaCl-type structures: there are two symmetrically different kinds of distances between the central atom and its neighbors. A and B atoms have to remain equidistant during the deformation. C atoms enter the coordination sphere in the NaCl type.

Figure 6 shows the atomic movements during the transition: cations and anions have to be shifted against each other by one eighth of the *c* lattice parameter. This means that the whole cation substructure is shifted by a vector (0,0,$^1/_4$) against the whole anion substructure along $[001]_{ZnS}$.

The orientation relation between the unit cells of the zinc-blende and the NaCl type can directly be seen in the group – subgroup diagrams, as illustrated in Figure 7: $[001]_{Zns}$ is parallel to $[\bar{1}\,\bar{1}\,0]_{NaCl}$ and. $[110]_{Zns}$ is parallel to $[001]_{NaCl}$. Simultaneously to the atomic movements, the metrics of the unit cell are changed (Figure 7). For ideal sphere packings the structure shrinks by about 39% along $[001]_{Zns}$, and by about 13% along $[1\,\bar{1}\,0]_{ZnS}$, while along $[110]_{ZnS}$ an elongation by about 22% takes place.

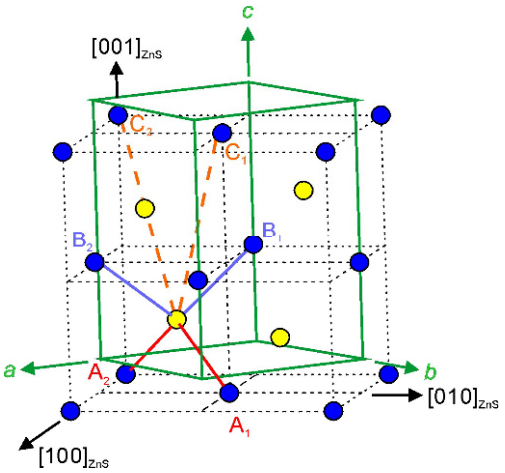

Imm2

centre: $^1/_2,0,z$

neighbours:
A_1: $^1/_2,^1/_2,-z$
A_2: $^1/_2,-^1/_2,-z$
B_1: $0,0,-z+^1/_2$
B_2: $1,0,-z+^1/_2$

Distances:
$d_A^2 = {}^1/_4 b^2 + 4z^2c^2$
$d_B^2 = {}^1/_4 a^2 + 4z^2c^2 - 2zc^2 + {}^1/_4 c^2$

Sphere packing condition: $d_A^2 = d_B^2 \rightarrow z = {}^1/_8(a^2/c^2 - b^2/c^2 + 1)$

Figure 5. Deriving the sphere-packing condition.

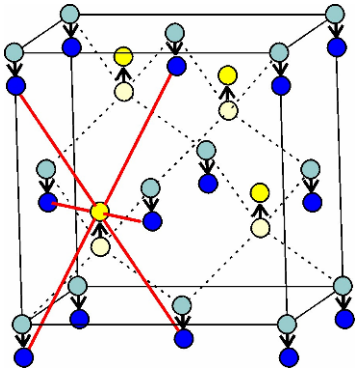

Figure 6. Transition path from zinc-blende to NaCl type *via* an intermediate state with symmetry *Imm*2.

However, one has to keep in mind that the distances between the nearest neighbors are not exactly maintained during the transition but become slightly longer. Moreover, the sphere packing with four contacts has two degrees of freedom in *Imma* 4(*e*). Therefore, the true transition path between zinc-blende- and NaCl-type structures *via Imm*2 cannot be determined geometrically, but, in addition, energy calculations are necessary.

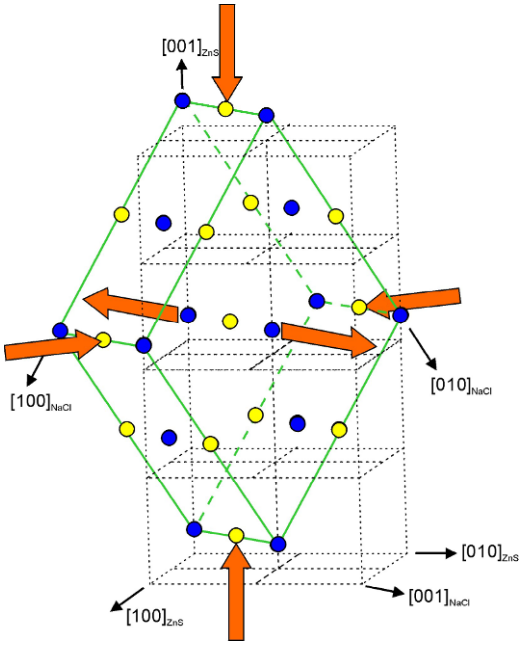

Figure 7. Orientation relations and metrical changes between zinc-blende and NaCl types according to the transition path *via Imm*2. Arrows indicate the directions of contraction or elongation.

Is there an experimental evidence of the proposed path for pressure-induced phase transitions in zinc-blende-type compounds? Up to now, there are relatively few experiments that deal with orientation relations between the phases before and after a phase transition in AB compounds. Most of the studies have been performed on the transition between the NaCl and the CsCl type (*e.g.* references in *Sowa*, 2000a). There are only few experiments on the transition between the zinc-blende and the NaCl type (*Sowa*, 2005b, 2007). The analysis is complicated because single crystals are commonly destroyed during the transformation. In addition, the obtained powders of the high-pressure phases show strong preferred orientation. In AgI the corresponding transition according to the mechanism mentioned above is favourable from an energetical point of view (*Catti*, 2005) but it could be excluded owing to the observed orientation relations (*Sowa*, 2007). For

CdTe (*Sowa*, 2005b) another mechanism, which has also been derived by sphere packing considerations (*Sowa*, 2003), probably takes place.

References

Blanco, M.A., Recio, J.M., Costales, A., & Pandey, R., 2000, Transition path for the B3⇔B1 phase transformation in semiconductors. *Phys. Rev. B* **62**: R10599–R10602.

Buerger, J., 1951, *Phase Transformations in Solids*, edited by R. Smoluchowski, J.E. Mayers, and W.A. Weyl. Wiley, New York, pp. 183–211.

Cai, J., Chen, N., & Wang, H., 2007, Atomistic study of the pressure-induced phase-transition mechanism in GaAs by Möbius inversion potentials. *J. Phys. Chem. Solids* **68**: 445–457.

Capillas, C., Perez-Mato, J.M., & Aroyo, M.I., 2007, Maximal symmetry transition paths for reconstructive phase transitions. *J. Phys.: Condens. Matter* **19**: 275203.

Catti, M., 2001, Orthorhombic intermediate state in the zinc blende to rocksalt transformation path of SiC at high pressure. *Phys. Rev. Lett.* **87**: 35504.

Catti, M., 2002, Reply to the comment on "Orthorhombic intermediate state in the zinc blende to rocksalt transformation path of SiC at high pressure". *Phys. Rev. Lett*. **88**: 189602.

Catti, M., 2005, Kinetic mechanisms of the pressure-driven phase transitions of AgI. *Phys. Rev. B* **72**: 064105.

Christy, A.G., 1993, Multistage diffusionsless pathways for reconstructive phase transitions: Application to binary compounds and calcium carbonate. *Acta Crystallogr. B.* **49**: 987–996.

Corll, J.A., 1967, Effect of pressure on the elastic parameters and structure of CdS. *Phys. Rev*. **157**: 623–626.

Dmitriev, V.P., Rochal, S.B., Gufan, Yu.M., & Tolédano, P., 1988, Definition of a transcendental order parameter for reconstructive phase transitions. *Phys. Rev. Lett*. **60**: 1958–1961.

Dmitriev, V.P., & Tolédano, P., 1996, *Reconstructive phase transitions in crystals and quasicrystals*. World Scientific Publishing Company, Singapore.

Fischer, W., 1973, Existenzbedingungen homogener Kugelpackungen zu kubischen Gitterkomplexen mit weniger als drei Freiheitsgraden. *Z. Kristallogr*. **138**: 129–146.

Fischer, W., Sowa, H., & Koch, E., 2006, Orthorhombic sphere packings. I. Invariant and univariant lattice complexes. *Acta Cryst. A*. **62**: 413–418.

Hatch, D.M., Stokes, H.T., Dong, J., Gunter, J., Wang, H., & Lewis, J.P., 2005, Bilayer sliding mechanism for the zinc-blende to rocksalt transition in SiC. *Phys. Rev. B.* **71**: 184109.

Hyde, B.G., & O'Keeffe, M., 1973, On mechanisms of the B1 ↔ B2 structural transformation. In: *Phase Transitions*, edited by L. E. Cross. Pergamon, Oxford, pp. 345–349.

Knudson, M.D., Gupta, Y.M., & Kunz, A.B., 1999, Transformation mechanism for the pressure-induced phase transition in shocked CdS. *Phys. Rev. B.* **59**: 11704–11715.

Limpijumnong, S., & Lambrecht, W.R.L., 2001, Homogeneous strain deformation path for the wurtzite to rocksalt high-pressure phase transition in GaN. *Phys. Rev. Lett*. **86**: 91–94.

Miao, M.S., & Lambrecht, W.R.L., 2003, Unified path for high-pressure transitions of SiC polytypes to the rocksalt structure. *Phys. Rev. B.* **68**: 092103.

Perez-Mato, J.M., Aroyo, M., Capillas, C., Blaha, P., & Schwarz, K., 2003, Comment on Orthorhombic intermediate state in the zinc blende to rocksalt transformation path of SiC at high pressure. *Phys. Rev. Lett*. **90**: 49603.

Sharma, S.M., & Gupta, Y.M., 1998, Wurtzite-to-rocksalt structural transformation in cadmium sulphide shocked along the a axis. *Phys. Rev. B* **58**: 5964–5971.

Shimojo, F., Ebbsjö, I., Kalia, R.K., Nakano, A., Rino, J.P., & Vashishta, P., 2000, Molecular dynamics simulation of structural transformation in silicon carbide under pressure. *Phys. Rev. Lett*. **84**: 3338–3341.

Shimojo, F., Kodiyalam, S., Ebbsjö, I., Kalia, R.K., Nakano, A., Vashishta, P., 2004, Atomistic mechanism for wurtzite-to-rocksalt structural transformation in cadmium selenide under pressure. *Phys. Rev. B* **70**: 184111.

Shôji, H., 1931, Geometrische Beziehungen unter den Strukturen der Modifikationen einer Substanz. *Z. Kristallogr*. 77: 381–410.

Sowa, H., 2000a, The NaCl to CsCl type phase transition discussed on the basis of the *cP* to *cI* deormation with the symmetry *Cmcm* 4(*c*) *m*2*m*. *Acta Cryst. A***56**: 288–299.

Sowa, H., 2000b, A transition path from the zinc-blende to the NaCl type. *Z. Kristallogr*. **215**: 335–342.

Sowa, H., 2001, On the transition from the wurtzite to the NaCl type. *Acta Cryst. A* **57**: 176–182.

Sowa, H., 2003, Relations between the zinc-blende and the NaCl type. *Acta Cryst. A* **59**: 266–272.

Sowa, H., 2005a, A transition path for the pressure induced wurtzite- to NaCl-type transformation described in $Pna2_1$. *Acta Cryst. A* **61**: 325–330.

Sowa, H., 2005b, Orientation relations between zincblende-, cinnabar- and NaCl-type phases of CdTe under high pressure. *J. Appl. Cryst.* **38**: 537–543.

Sowa, H., 2007, Orientation relations between four phases of AgI. *Z. Kristallogr*. 222: 89–94.

Sowa, H., & Fischer, W., 2010, Orthorhombic sphere packings III. Trivariant lattice complexes of space groups with mirror symmetry. *Acta Cryst. A*. **66**: 292–300.

Stokes, H.T., Gunter, J., Hatch, D.M., Dong, J., Wang, H., & Lewis, J.P., 2007, Bilayer sliding mechanism for the wurtzite-to-rocksalt transition. *Phys. Rev. B* **76**: 012102.

Stokes, H.T., Hatch, D.M., Dong, J., & Lewis, J.P., 2004, Mechanisms for the reconstructive phase transition between the B1 and B2 structure types in NaCl and PbS. *Phys. Rev. B*. **69**: 174111.

Stokes, H.T., & Hatch, D.M., 2002, Procedure for obtaining microscopic mechanisms of reconstructive phase transitions in crystalline solids. *Phys. Rev. B* **65**: 144114.

Tolbert, S.H., & Alivisatos, A.P., 1995, The wurtzite to rock salt structural transformation in CdSe nanocrystals under high pressure. *J. Chem. Phys*. **102**: 4642–4656.

Tolédano, P., Knorr, K., Ehm, L., & Depmeier, W., 2003, Phenomenological theory of the reconstructive phase transition between the NaCl and CsCl structure types. *Phys. Rev. B* **67**: 144106.

Watanabe, M, Tokonami, M., & Morimoto, N., 1977, The transition mechanism between the CsCl-type and NaCl-type structures in CsCl. *Acta Cryst. A* **33**: 294–298.

Wickham, J.N., Herhold, A.B., & Alivisatos, A.P., 2000, Shape change as an indicator of mechanism in the high-pressure structural transformations of CdSe nanocrystals. *Phys. Rev. Lett*. **84**: 923–926.

Wilson, M., Hutchinson, F., & Madden, P.A., 2002, Simulation of pressure-driven phase transitions from tetrahedral crystal structures. *Phys. Rev. B* **65**: 094109.

Wilson, M., & Madden, P.A., 2002, Transformations between tetrahedrally and octahedrally coordinated crystals: the wurtzite → rocksalt and blende → rocksalt mechanisms. *J. Phys.: Condens. Matter* **14**: 4629–4643.

THE CHARM OF SUBTLE H-BONDS TRANSFORMATIONS

Specific Features of Hydrogen-Bonds at Increased Pressure

ANDRZEJ KATRUSIAK*
Faculty of Chemistry, Adam Mickiewicz University, Grunwaldzka 6, 60-780 Poznań

Keywords: Molecular crystals, phase transitions, polymorphism, in-situ crystallization, hydrogen bonds, interatomic interactions

1. Introduction

The human presence and activities on Earth is mainly confined to the temperature range of few hundred kelvin and pressure range of few tenth of a GPa (at explosions). Therefore most of chemical and materials-sciences knowledge has been determined experimentally at these thermodynamic conditions. A more general knowledge is advantageous, as it allows one to extend the understanding of physical and chemical phenomena to any conditions. Actually, the normal conditions are quite unique in Universe – usually temperature and pressure are much lower or much higher outside the biosphere of Earth.

Hydrogen bonds are abundant in Nature and they are essential for the properties of water and most substances of biological importance, cellulose, proteins, DNA strands, or pharmaceutical drugs. Hydrogen bonds are present in numerous minerals in the Earth crust, in water aggregates of water vapour, and in the tiny droplets or ice particles in the clouds. Just like other types of interactions – van der Waals, electrostatic or metallic forces – hydrogen bonds shape the properties of substances, the ability of molecules to form aggregates, to associate with the molecules of other substances, and generally the physical and chemical properties of hydrogen-bonded materials. It is due to hydrogen bonds that new branches of chemical sciences have developed, such as supramolecular chemistry or the chemistry of inclusion compounds. In the physical sciences there are several long-studied problems related to hydrogen bonding, such as the transformations of water and ice (*Franks*, 1972; *Kuhs and Lehmann*, 1986; *Nylud and Tsironis*, 1991; *Ohimine and Saito*, 1999) or the paraelectric-ferroelectric phase transition in the KH_2PO_4

*E-mail: katran@amu.edu.pl

E. Boldyreva and P. Dera (eds.), *High-Pressure Crystallography: From Fundamental Phenomena to Technological Applications*, DOI 10.1007/978-90-481-9258-8_17,

and KH_2PO_4-type crystals (*Hollander et al.*, 1977; *McMillan et al.*, 1982; *Nelmes*, 1987; *Poprawski and Dziedzic*, 1988; *Poprawski et al.*, 1979; *Samara and Semmingsen*, 1979; *Semmingsen et al.*, 1977; *Yasuda et al.*, 1978). For a detailed comprehension of the properties of hydrogen-bonded substances it is essential that the structural transformations of hydrogen bonds are classified and understood. Hydrogen bonds are different from other intermolecular interactions because they are directional, and because they involve at least three atoms: the H-atom donor, the H-atom, and the H-atom acceptor. Moreover, there is a considerable variety of different types of hydrogen bonds, between different H-donors and H-acceptors, or those involving two, or more interacting groups, in different environments. The hydrogen bonds can transform in very different ways: they can be bent, broken, formed, the H-atom can be moved to the other side of the H-bond or can become disordered dynamically; the ionic contribution to the H-bond energy can be reduced or increased. The energy of formation of hydrogen bonds is comparable to the energy of thermal vibrations at room temperature. Thus the dynamic hydrogen-bond transformations apply to all biosphere and to all living organisms, where the H-bonds can be transformed – including their breaking and formation – many times as the elements of the physical or chemical transformations of the system. In principle the same general rules should apply to hydro-thermal deposits, or to dense atmospheres of large planets. The dynamics of hydrogen bonds involve momentary squeezing and stretching of hydrogen bonds, which can be modelled by studies of the hydrogen bonds at varied temperatures and high pressures. The principles of the hydrogen-bond transformations revealed in the studies on simple systems, can be further generalized and applied to more complex crystals, and even to non-crystalline substances: clusters of hydrogen-bonded molecules in vapour, liquids, colloids, biological systems, or even to the living tissue.

General rules describing the transformations of hydrogen bonds can be formulated for structures undergoing continuous or discontinuous phase transitions. Naturally, apart from the hydrogen bonds there are others interactions and transformations, which influence the properties of substances. However the rules describing the temperature and pressure dependence of the hydrogen bonds can be applied for predicting subtle structural transformations, and for understanding the properties of the hydrogen-bonded crystals.

2. Transformations of Crystals

Structures of all substances transform at varied thermodynamic conditions. In principle these transformations may proceed continuously without phase transitions, or anomalously when a phase transition takes place and the substance transforms from one phase into another.

Monotonic changes in crystal structures are usually considered to be predictable: most crystals with few exceptions expand with increasing temperature, and so most of intermolecular interactions are expected to become longer. The rare exceptions to this are intensively studied – not only because of their exceptionality, but also due to their manifold technical applications. The pressure dependence of crystals is less complicated than temperature dependence in that dV/dp is inevitably positive for the systems in equilibrium. Although most of interactions in a pressurised crystal are squeezed, the behaviour of individual interactions cannot be generalized. In particular a hydrogen bond, or indeed any interatomic distance within a compressed structure, may become shorter or longer over a range of pressure (*Putkonen et al.*, 1985; *Boldyreva et al.*, 1998). Competition between interactions in a structure may result in the compression of weaker interactions and the stretching of the stronger hydrogen bonds, in accordance with the le Chatelier principle.

There are many different types of phase transitions and they are classified in various ways (*Herbstein*, 1996; *Klamut et al.*, 1979). Solid-state to solid-state phase transitions are usually classified into continuous and non-continuous ones (Fisher's classification), or second-order and first order transitions (Ehrenfest's classification), respectively.

Continuous phase transitions are described by Landau's theory, the group-subgroup relation connects the symmetries of the transforming phases, the Gibbs free energy is a continuous function through T_c, no hysteresis or latent heat are observed, and there are no discontinuous changes in either unit-cell parameters or volume. The Landau type of phase transitions also includes these of discontinuous phase transitions, for which the group-subgroup relations combine the symmetries of the transforming phases. In such cases the phase transitions often are considered as possessing a mixed character with continuous and discontinuous contributions.

A large group of phase transitions is discontinuous, and no symmetry relations connect the transforming phases. At T_c discontinuities occur in the unit-cell dimensions, different Gibbs free-energy functions describe the phases, and a hysteresis and latent heat accompany the transformations. The absence of symmetry relations between the transforming phases implies that there is also the possibility that symmetry does not change. The phase transitions preserving translational and space-group symmetries are termed *isostructural phase transitions*. The isostructural phase transitions are relatively infrequent, and in most cases they are induced by collapses of low symmetry structures at low temperatures (e.g. due to the elimination of dynamical disorder) (*Katrusiak*, 1991), or at high pressure (*Allan et al.*, 1994; *Katrusiak*, 1990).

Apart from the intermolecular interactions, pressure and temperature can affect the structure of molecules in crystals. In particular, flexible molecules are prone to conformational and other chemical transformations. The possible changes may involve conformations of molecular rings, rotations of moieties about single bonds (*Boldyreva et al.*, 2000; *Budzianowski and Katrusiak*, 2002; *Bujak et al.*, 2008; *Gajda and Katrusiak*, 2008; *Hazen et al.*, 1987), formation of H-tautomers, dynamic or static disordering of molecules or their moieties, charge transfers *etc*. Such transformations of molecular structure, as well as stoichiometry changes occurring when compounds become unstable at certain thermodynamic conditions, will be neglected in the further discussion.

3. Structure–Property Relations for H-bonds at Phase Transitions

Certain types of hydrogen-bond transformations can be related to the specific types of phase transitions. It is very unlikely that the H-transfers transforming OH···O hydrogen bonds in one ordered structure, into O···HO bonds in its other ordered phase would proceed as a continuous phase transition, while the dynamic H-disordering is a common feature of Landau-type transformations. The dynamic H-disordering can be related to specific properties of the transforming structures: to the dimensions of the hydrogen bond (*Katrusiak*, 1993), anomalous thermal expansion of the crystal at T_c (*Katrusiak*, 1993), temperature of the transition (*Katrusiak*, 1995, 1996a), or to the occurrence of the tricritical point of pressure and temperature, where the first-order contribution to the character of the phase transition disappears (*Katrusiak*, 1996a).

4. H-site – Structure Coupling

It can be generally stated that the H-site in a hydrogen bond is in some way coupled to the arrangement of molecules or ions. For the –OH···O= hydrogen bonds this coupling occurs through the electronic structure of the H-donor and H-acceptor groups. In this case the H-donor is in the sp^3 hybridisation, and the H-acceptor is in the sp^2 hybridization. The different directions of the H-bond formation favoured by the H-donor and acceptor groups have some effect on the orientation of the hydrogen-bonded molecules in the crystal structure, as illustrated in Figure 1. The H-transfer reverses the hybridizations, and also changes the favoured directions for the formation of the hydrogen bond.

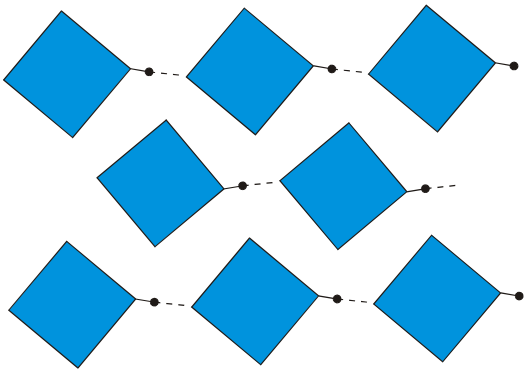

Figure 1. A schematic representation of a ferroelectric phase of a hydrogen-bonded crystal. Molecules are represented as square blocks, hydrogen atoms as small circles, H-donor bonds to hydrogen atoms as lines, and the hydrogen bonds to the H-acceptors as dashed lines. The effect of different hybridization of the H-donor and H-acceptor groups (note the acute and obtuse angles formed by the H-bonds with the sides of the blocks) on the orientation of the molecules has been strongly enhanced for clarity.

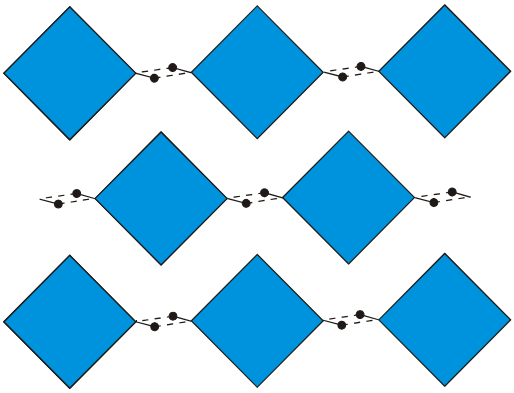

Figure 2. A block scheme of the paraelectric phase transformed from the ferroelectric hydrogen-bonded crystal structure presented in Figure 1. The hydrogen atoms are disordered each in two symmetry-equivalent positions – thus each of the circles represents a site half-occupied by the hydrogen atom. In the paraelectric phase the crystal acquires the symmetry relating the sites of the disordered H-atoms, and also the molecules represented here as square blocks become symmetric.

Thus the directionality of the hydrogen bonds plays the crucial role for such an H-transfer, and it also involves small rotations of the heavy hydrogen-bonded groups (in this paper all the atoms or groups different from H-atoms will be termed ‘heavy’ ones). Similarly, the dynamical H-disordering changes somewhat the orientation of the hydrogen-bonded groups (compare Figures 1 and 2). Consequently, the phase transitions involving the H-disordering in

the –OH···O= hydrogen bonds usually have a significant contribution of atomic displacements. These displacements introduce characteristic features to the thermodynamic character of the phase transitions, and can be shown to be the main causes of the anomalous volume change of the crystal at T_c. The anomalous volume change (ΔV) of the crystal at the phase transition is characteristic of the 1st-order phase transitions. The H-atom disordering induces strains to the hydrogen bond. In consequence, the O-H···O angle become sharpened and the O···O' distance shorter, as explained in Figure 3. This O···O' distance shortening can be precisely predicted and calculated (*Katrusiak*, 1993), and it contributes to the volume change at T_c (*Katrusiak*, 1995). The volume change observed in the prototypical KH_2PO_4 ferroelectric crystal (often denoted as KDP) as the function of pressure and temperature is shown in Figure 4. When the pressure increases the T_c decreases, and also ΔV becomes smaller (*Kobayashi et al.*, 1970). At the tricritical point ΔV becomes equal zero, and the phase transition becomes purely continuous. This tricritical point occurs at 0.28 GPa and 106 K for the KDP crystal. Similar behaviour is common for all the crystals of the KDP-type. These thermodynamical features of the KDP crystal can be related to the changes in the dimensions of the hydrogen bond in the KDP structure (*Katrusiak*, 2001).

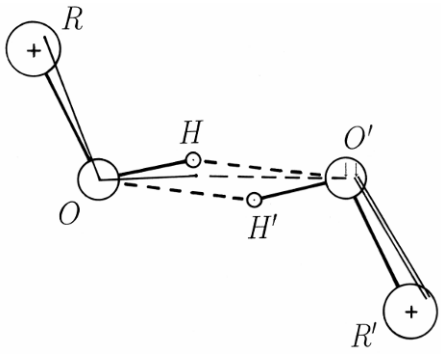

Figure 3. Geometric effects of the H-atom disordering on the structure of a hydrogen bond at the ferroelectric (H-ordered – thin lines) to paraelectric (H-disordered – thick lines) phase transition (compare Figures 1 and 2). The single and double thin lines represent single and double bonds in the ferroelectric phase, respectively. In the paraelectric phase the hydrogen atoms are disordered each in two symmetry-equivalent positions – thus each of the circles represents a site half-occupied by the hydrogen atom. The H-disordering induces strain sharpening the O–H···O angle shortening the O···O' distance in the paraelectric phase, as indicated by two small vertical arrows within the circle representing the atom O'. The magnitudes of the O–H···O' angle sharpening and the O···O' distance shortening have been somewhat enhanced for clarity.

Also in other types of hydrogen bonds the H-transfers or H-disordering are in some ways coupled to the structural arrangements of the hydrogen-bonded units. For example, the hydrogen bonds between hydroxyl groups are strongly coupled to the arrangement of the molecules (*Katrusiak*, 1998). Similar relations apply to water molecules in ices and water clusters (*Katrusiak*, 1996b). It should be stressed, that for the structural considerations the mechanism of how the H-atom transfers to the other side of the hydrogen bond is of secondary importance, but it is the actual state of the H-atom in the hydrogen bond before and after the transformation that matters. Thus, the H-atom can be ordered or disordered; or the H-atom can be located: (i) on the 'left', or (ii) on the 'right' side of the hydrogen bond. It does not matter for these considerations if the H-atom actually jumps form one oxygen atom to the other, or if the hydroxyl groups rotate and in this way induce the disorder.

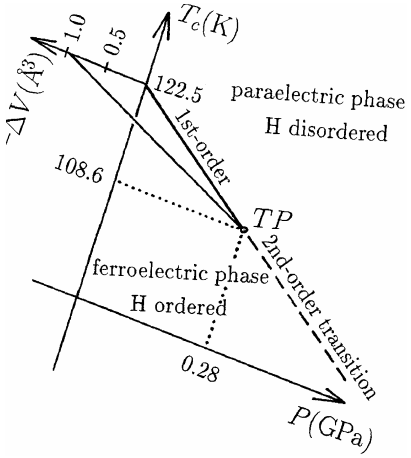

Figure 4. Changes of volume, temperature and pressure about the ferroelectric-paraelectric phase transition in the KH_2PO_4 crystal. The tricritical point (*TP*) occurs at 108.6 K and 0.28 GPa. At ambient pressure at T_c = 122.5 K the volume changes by ca. 1.0 Å^3. The negative sign of ΔV in the plot indicates that the volume decreases when the crystal is heated to the paraelectric phase.

The coupling between the H-site and molecular arrangement applies also to other than OH···O bonds. The analogous coupling was described for the NH^+···N bonds. It is characteristic, that the coupling in molecular crystals involves the hybridization of the H-donor and H-acceptor atoms, while in ionic crystals these are the ionic displacements that are coupled to the proton sites (*Katrusiak*, 1999). This coupling mechanism may be considered responsible for the existence of NH^+···N bonded ferroelectrics (*Katrusiak and Szafranski*, 1999), in certain respects analogous to the KDP-type ferroelectric

crystals. The specific structural features of the $NH^+\cdots N$ bonds lead to the formation of defects in the linear aggregates (Figure 6) and to unprecedented anisotropic relaxor properties of the compounds.

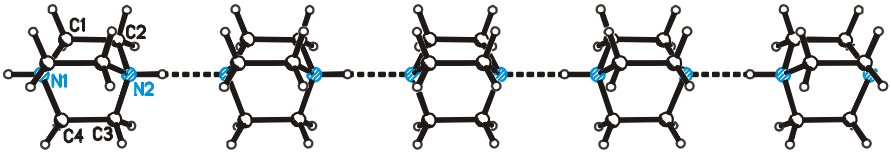

Figure 5. A chain fragment of NH^+- - N bonded dabco cations, as present in the dabco monosalts. The proton-site defects lead to the chain-polarisation defects and exceptional dielectric properties of the crystals (*Budzianowski et al.*, 2008; *Szafranski and Katrusiak*, 2008).

5. Conclusions

In most cases it is possible to predict fine anomalous effects in compressibility or thermal expansion of hydrogen-bonded solids. These predictions are not only qualitative, but also quantitative. For example it is possible to determine with accuracy the tricritical point for KDP-type ferroelectrics, or to evaluate the temperatures of the paraelectric-ferroelectric phase transitions from the structural data. This information often cannot be measured experimentally at ambient pressures, as transition temperatures may exceed the melting points of the crystals. Also other properties of substances may be rationalised by transformations of their hydrogen-bonded structures (*Katrusiak*, 1996b). The structural properties of hydrogen bonds have been successfully applied for engineering the ferroelectric crystals of very strong polarisation and relaxor behaviour (*Szafranski and Katrusiak*, *2008*). The crystal of dabcoHI is the first $NH^+\cdots N$ bonded relaxor, and the first stoichiometric (not doped) compound of these properties. Owing to the specific network of hydrogen bonds, it also exhibits the unique property of anisotropic relaxor response, along the $NH^+\cdots N$ bonded chains. Thus, it appears that structural transformations of hydrogen bonds, often regarded as weak and complex interactions difficult for theoretical description, can be successfully predicted for various substances and at varied thermodynamic conditions. This information can be further applied for understanding the behaviour and properties of any materials with hydrogen-bonded aggregates in their structure. The understanding of the structure–property relations for hydrogen-bonded crystals can also prove useful for validating results of structural analysis. Positions of hydrogen atoms are not always determined precisely by x-ray diffraction methods, and in dubious cases the geometrical features of hydrogen bonds, in particular orientations of the hydrogen-bonded molecules or ions, can be used to verify the interpretation of the diffraction data.

References

Allan, D.R., Loveday, J.S., Nelmes, R.J., and Thomas, P.A., 1994, A high-pressure structural study of potassium titanyl phosphate (KTP) up to 5GPa, *J. Phys. Condensed Matter*. **4**: 2747–2760.

Boldyreva, E.V., Naumov, D.Yu., and Ahsbahs, H., 1998, Distortion of crystal structures of some Co^{III} ammine complexes. III. Distortion of crystal structure of $[Co(NH_3)_5NO_2]Cl_2$ at hydrostatic pressures up to 3.5 GPa, *Acta Cryst. B*. **54**: 798–808.

Boldyreva, E.V., Shakhtshneider, T.P., Vasilchenko, M.A., Ahsbahs, H., and Uchtmann H., 2000, Anisotropic crystal structure distortion of the monoclinic polymorph of acetaminophen at high hydrostatic pressure, *Acta Cryst. B*. **56**: 299–309.

Budzianowski, A., and Katrusiak, A., 2002, Coupling of the lactone-ring conformation with crystal symmetry in 6-hydroxy-4,4,5,7,8-pentamethyl-3,4-dihydrocoumarin, *Acta Cryst. B*. **58**: 125–133.

Budzianowski, A., Katrusiak, A., and Szafrański, M., 2008, Anomalous protonic-glass evolution from ordered phase in NH···N hydrogen-bonded dabcoHBF$_4$ ferroelectric, *J. Phys. Chem. B*. **112**: 16619–16625.

Bujak, M., Podsiadło, M., and Katrusiak, A., 2008, Energetics of conformational conversion between 1,1,2-trichloroethane polymorphs, *Chem. Commun*.: 4439–4441.

Franks, F. (Ed.), 1972, *Water A Comprehensive Treatise*, Plenum Press, New York/London.

Gajda, R., and Katrusiak, A., 2008, Pressure-freezing with conformational conversion of 3-aminopropan-1-ol molecules, *Acta Cryst. B*. **64**: 476–482.

Hazen, R.M., Hoering, Th.C., and Hofmeister, A.M., 1987, Compressibility and high-pressure phase transition of a metalloporphyrin: (5,10,15,20-ttetraphenyl-21H,23H-porphinato)cobalt (II), *J. Phys. Chem*. **91**: 5042–5045.

Herbstein, F.H., 1996, Some applications of thermodynamics in crystal chemistry, *J. Mol. Struct*. **374**: 111–128.

Hollander, F.J., Semmingsen, D., and Koetzle, T.F., 1977, The molecular and crystal structure of squaric acid (3,4-dihydroxy-3-cyclobutene-1,2-dione) at 121°C: A neutron diffraction study, *J. Chem. Phys*. **67**: 4825–4831.

Katrusiak, A., 1995, Coupling of displacive and order-disorder transformations in hydrogen-bonded ferroelectrics, *Phys. Rev. B*. **51**: 589–592.

Katrusiak, A., 1990, High-pressure X-ray diffraction study on the structure and phase transition of 1,3-cyclohexanedione crystals, *Acta Cryst*. *B*. **46**: 246–256.

Katrusiak, A., 1991, Structure and phase transition of 1,3-cyclohexanedione crystals as a function of temperature, *Acta Cryst. B*. **47**: 873–879.

Katrusiak, A., 1993, Geometric effects of H-atom disordering in hydrogen-bonded ferroelectrics, *Phys. Rev. B* **48**: 2992–3002; Stereochemistry and transformation of –OH···O= hydrogen bonds. Part I. Polymorphism and phase transition of 1,3-cyclohexanedione crystals, *J. Mol. Struct*. **269**: 329–354.

Katrusiak, A., 1996a, Macroscopic and structural effects of hydrogen-bond transformations, *Crystallogr. Rev*. **5**: 133–180.

Katrusiak, A., 1996b, Rigid H_2O molecule model of anomalous thermal expansion of ice, *Phys. Rev. Lett*. **77**: 4366–4369.

Katrusiak, A., 1996c, Stereochemistry and transformation of –OH···O= hydrogen bonds. Part II. Evaluation of T_c in hydrogen-bonded ferroelectrics from structural data, *J. Mol. Struct*. **374**: 177–189.

Katrusiak, A., 1996d, Structural origin of tricritical point in KDP-type ferroelectrics, *Ferroelectrics* **188**: 5–10.

Katrusiak, A., 1998, Modelling hydrogen-bonded crystal structures beyond resolution of diffraction methods, *Pol. J. Chem*. **72**: 449–459.

Katrusiak, A., 1999, Stereochemistry and transformations of NH···N hydrogen bonds. Part~I. Structural preferences for the H-site, *J. Mol*. *Struct.* **474**: 125–133.

Katrusiak, A., 2001, Pressure-induced H-transfers in the networks of hydrogen bonds, in H. D. Hochheimer, B. Kuchta, P. K. Dorhout and J. F. Yarger (eds.) *Frontiers of High Pressure Research II Application of High Pressure to Low-Dimensional Novel Electronic Materials*, Kluwer, Dordrecht, pp. 73–85.

Katrusiak, A., and Szafrański, M., 1999, Ferroelectricity in NH···N hydrogen-bonded crystals, *Phys. Rev. Lett*. **82**: 576–579.

Klamut, J., Durczewski, K., and Sznajd, J., 1979, *Wstęp do fizyki przejść fazowych*, Ossolineum, Wrocław. [in Polish].

Kobayashi, J., Uesu, Y., Mizutani, I., and Enomoto, Y., 1970, X-ray study on thermal expansion of ferroelectric KH_2PO_4, *Physica Stat. Solidi (a)* **3**: 63–69.

Kuhs, W.F., and Lehmann, M.S., 1986, The structure of ice-Ih, *Water Sci. Rev*. **2**: 1–65.

McMullan, R. K., Thomas, R., and Nagle, J. F., 1982, Structures of the paraelectric and ferroelectric phases of $NaD_3(SeO_3)_2$ by neutron diffraction: a vertex model for the ordered ferroelectric state, *J. Chem. Phys.* **77**: 537–547.

Nelmes, R.J., 1987, Structural studies of KDP and KDP-type transition by neutron and X-ray diffraction: 1970–1985, *Ferroelectrics* **71**: 87–123.

Nylud, E.S., and Tsironis, G.P., 1991, Evidence for solitons in hydrogen-bonded systems, *Phys. Rev. Lett*. **66**: 1886–1889.

Ohimine, I., and Saito, Sh., 1999, Water dynamics: fluctuation, relaxation, and chemical reactions in hydrogen bond network rearrangement, *Acc. Chem. Res*. **32**: 741–749.

Poprawski, R., and Dziedzic, J., 1988, Hydrostatic pressure influence on phase transitions in rubidium hydrogen selenate crystals, *Solid State Commun*., **66**: 1257–1260.

Poprawski, R., Mróz, J., Czapla, Z., and Sobczyk, L., 1979, Ferroelectric properties and domain structure in $RbHSeO_4$ crystals, *Acta Phys. Polon. A*. **55**: 641–646.

Putkonen, M.-L., Feld, R., Vettier, C., and Lehmann, M.S., 1985, Powder neutron diffraction analysis of the hydrogen bonding in deutero-oxalic acid dihydrate at high pressures, *Acta Cryst. B*. **41**: 77–79.

Samara, G. A., and Semmingsen, D., 1979, Effects of pressure on the dielectric properties and phase transition of the 2-D antiferroelectric squaric acid ($H_2C_4O_4$ and $D_2C_4O_4$), *J. Chem. Phys*. **71**: 1401–1407.

Semmingsen, D., Hollander, F.J., and Koetzle, T.F., 1977, A neutron diffraction study of squaric acid (3,4-dihydroxy-3-cyclobutene-1,2-dione), *J. Chem. Phys*. **66**: 4405–4412.

Szafrański, M., and Katrusiak, A., 2008, Giant dielectric anisotropy and relaxor ferroelectricity induced by proton transfers in NH^+···N-bonded supramolecular aggregates, *J. Phys. Chem. B*. **112**: 6779–6785.

Szafrański, M., Katrusiak, A., and McIntyre, G.J., 2002, Ferroelectric order of parallel bistable hydrogen bonds, *Phys. Rev. Lett*. **89**: 215507-1-4.

Yasuda, N., Okamoto, M., Shimizu, H., Fujimoto, S., Yoshino, K., and Inuishi, Y., 1978, Pressure-induced antiferroelectricity in ferroelectric CsH_2PO_4, *Phys. Rev. Lett*. **41**: 1311–1314.

CARRIER BANDWIDTH PHYSICAL PHENOMENA IN STRONGLY CORRELATED MAGNETIC OXIDES: LESSONS FROM NEUTRON DIFFRACTION AT HIGH PRESSURES

DENIS P. KOZLENKO*
Frank Laboratory of Neutron Physics, Joint Institute for Nuclear Research, 141980 Dubna, Russia

Abstract A review of investigations of high-pressure effects on the crystal and magnetic structure of complex manganese and cobalt oxides $R_{1-x}A_xMO_3$ (A – rare earth, A – alkaline earth elements) performed by neutron diffraction is presented. A rich variety of magnetic state modifications at high pressure was observed in complex manganese oxides. In cobalt oxides application of high pressure induces spin changes, affecting physical properties. The observed phenomena are discussed in the framework of existing theoretical concepts.

Keywords: Strongly correlated electronic systems, transition metal oxides, phase transitions, magnetic phenomena, spin state, neutron diffraction, high pressure

1. Introduction

The complex manganese and cobalt oxides $R_{1-x}A_xMO_{3-d}$ (A – rare earth, A – alkaline earth elements, M – Mn or Co) with perovskite-like crystal structures exhibit spectacular phenomena which are extensively studied at present time – colossal magnetoresistance, insulator-metal transition, orbital and charge ordering, spin state modifications and spin state ordering, and variable magnetic structures (*Dagotto et al.*, 2001; *Kozlenko and Savenko*, 2006; *Tokura*, 2000). These phenomena occur due to a strong correlation of magnetic, electronic, and transport properties of these compounds. Potential technological applications of such materials and nanostructures on their basis can be highly diversified and extremely effective, for example, as

* E-mail: denk@nf.jinr.ru

E. Boldyreva and P. Dera (eds.), *High-Pressure Crystallography: From Fundamental Phenomena to Technological Applications*, DOI 10.1007/978-90-481-9258-8_18,

magnetoresistive heads for data recording and reading, electrodes for solid oxide fuel cell elements, etc. (*Dagotto et al*., 2001; *Kozlenko and Savenko*, 2006; *Tokura*, 2000).

The undoped $RMnO_3$ manganites, containing only Mn^{3+} ions are insulators and have, as a rule, orthorhombic crystal structure (space group *Pnma*) and an A-type antiferromagnetic (AFM) ground state. The injection of additional carriers due to doping with alkaline-earth elements gives rise to two competing interactions in $R_{1-x}A_xMnO_3$ ($R_{1-x}A_x[(Mn^{3+})_{1-x}(Mn^{4+})_x]O_3$) manganites – double exchange (Figure 1) associated with the kinetic energy gain due to the hopping of delocalized e_g electrons in the Mn^{3+}-O^{2-}-Mn^{4+} chains, which favors the ferromagnetic (FM) ordering of Mn magnetic moments, and antiferromagnetic superexchange between Mn magnetic moments formed by localized t_{2g} electrons (*Dagotto et al.*, 2001; *Kaplan and Mahanti*, 1999; *Kozlenko and Savenko*, 2006; *Tokura*, 2000).

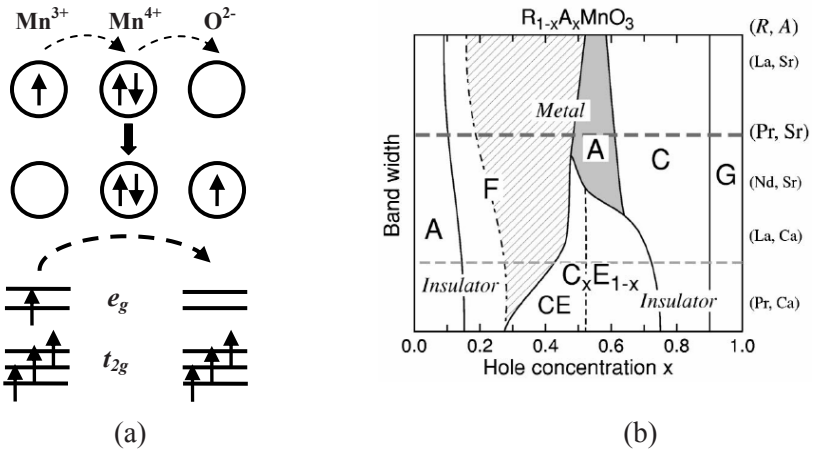

Figure 1. (a) – The double exchange mechanism, (b) – the schematic generalized phase diagram of manganites.

At concentrations $0.2 < x < 0.5$, double exchange is, as a rule, the dominant interaction, which leads to transition from the paramagnetic insulating state to the ferromagnetic (FM) metallic state at a Curie temperature approximately equal to the insulator–metal transition temperature $T_C \approx T_{IM}$ in many manganites. The temperatures T_C, T_{IM} reach a maximum at an optimal doping level of $x \sim 0.3$. In the framework of the double-exchange model, the magnetic and transport properties of manganites having a ferromagnetic metallic state are determined by the carrier bandwidth W and $T_C \approx T_{IM} \propto W$ within the approximation of strong intra-atomic exchange interaction ($J_H >> W$) (*Dagotto et al.*, 2001; *Kaplan and Mahanti*, 1999;

Kozlenko and Savenko, 2006; *Tokura*, 2000). When oxygen octahedra exhibit no Jahn–Teller distortions, the carrier bandwidth is determined by the hopping integral of e_g electrons in Mn^{3+}–O^{2-}–Mn^{4+} chains. In this case, it depends on the mean value of the Mn–O bond length l and on the Mn–O–Mn angle φ as $W = W_0 \sim \cos^2\varphi / l^{3.5}$ (*Harrison*, 1980; *Kozlenko and Savenko*, 2006). The occurrence of static cooperative Jahn–Teller distortions of oxygen octahedra due to the presence of Mn^{3+} ions with a single e_g electron leads to the formation of polarons and to an effective change in the bandwidth $W \sim W_0 \exp(-\gamma E_{JT}/\hbar\omega)$, where E_{JT} is the polaron binding energy, ω is the characteristic frequency of the phonon modes corresponding to vibrations of oxygen octahedra, and $0 < \gamma < 1$ the electron–phonon coupling parameter. With decreasing concentration of Jahn–Teller Mn^{3+} ions, the AFM super-exchange between Mn magnetic moments formed by localized t_{2g} electrons becomes the dominant magnetic interaction at $x > 0.5$.

With increasing x in the range $0.5 < x < 1$, the character of the magnetic ground state in the $La_{1-x}Sr_xMnO_3$, $Pr_{1-x}Sr_xMnO_3$ and $Nd_{1-x}Sr_xMnO_3$ varies in the following common sequence: FM (metallic) → A-type AFM (metallic) → C-type AFM (insulating) → G-type AFM (insulating). When the Mn^{3+}: Mn^{4+} ratio in $La_{1-x}Ca_xMnO_3$, $Pr_{1-x}Ca_xMnO_3$, $Nd_{1-x}Ca_xMnO_3$, and $Nd_{1-x}Sr_xMnO_3$ manganites with a smaller mean radius of the A cation r_A(a smaller charge carrier bandwidth W) is close to the perfect 0.5:0.5, an AFM state of the so-called CE type with the charge and e_g orbital ordering of the Mn^{3+} and Mn^{4+} ions is observed (*Dagotto et al.*, 2001; *Kaplan and Mahanti*, 1999; *Kozlenko and Savenko*, 2006; *Tokura*, 2000). These ions form two magnetic sublattices with the propagation vectors $q_1 = (0\ 0\ 1/2)$ and $q_2 = (1/2\ 0\ 1/2)$.

The great variety of magnetic states observed in doped manganites reflects the strong dependence of the balance between various factors (FM and AFM competing exchange interactions, electron–phonon coupling, and orbital degrees of freedom) on the interatomic distances Mn–O and angles Mn–O–Mn and on the strength of the static cooperative distortion of oxygen octahedra. A schematic, generalized, phase diagram of manganites (*Kajimoto et al.*, 2002; *Kozlenko and Savenko*, 2006) is shown in Figure 1.

The unique feature of cobalt oxides, making them distinctive from manganites or cuprates, is a spin degree of freedom of Co^{3+} ions. Depending on the delicate balance of comparable values of intra-atomic exchange energy (JH) and crystal field splitting (ΔCF), low spin LS (t_{2g}^6, S = 0), intermediate spin IS ($t_{2g}^5 e_g^1$, S = 1) or high spin HS ($t_{2g}^4 e_g^2$, S = 2) states can be realized. In perovskite-like cobaltites $RCoO_3$ (R – rare earth element) a thermally induced LS-IS/HS crossover leads to a change of the ground state from low temperature nonmagnetic to high temperature paramagnetic at $T \approx$ 100-800 K (R = La–Y), followed by the semiconductor–metal phase

transition at T = 500–820 K (La–Y) (*Knižek et al.*, 2005; *Raccah and Goodenough*, 1967). Upon substitution of rare earth R by alkali earth A element, a ferromagnetic (FM) ground state is stabilized in $R_{1-x}A_xCoO_3$ compounds for x > 0.18 (*Kreiner et al.*, 2004). Recent experimental investigations have shown that the balance between different spin states in $R_{1-x}Sr_xCoO_3$ for Co^{3+} ions in octahedral coordination and physical properties of these compounds can be strongly changed by application of high pressure (*Golosova et al.*, 2006; *Kozlenko et al.*, 2007; *Lengsdorf et al.*, 2004).

In a comparison to other experimental methods, the application of high pressure is a direct method of controlled variation of magnetic interactions by means of variation of interatomic distances and angles. Structural investigations at high pressure provide a unique opportunity for studying the interplay of the changes in the crystal structure parameters, interatomic distances, and angles with the modification of the magnetic structure and macroscopic (magnetic and transport) properties, which is necessary to understand the nature and mechanism of physical phenomena observed in complex systems. The neutron diffraction is the best method for studying the crystal and magnetic structure of materials containing light atoms, like oxygen, while the techniques of neutron experiments over a sufficiently wide range of pressures (0–10 GPa and higher) have been developed quite recently.

In the present lecture, the systematic investigations of the crystal and magnetic structure of complex manganese and cobalt oxides $R_{1-x}A_xMO_3$ at high pressures by neutron diffraction method are reviewed. A special attention is given to the analysis of correlations between structural changes and the relevant modifications of magnetic ordering, macroscopic physical properties and comparison of experimental results with theory predictions.

2. Experimental Technique

Neutron diffraction experiments were performed on the DN-12 spectrometer (*Kozlenko et al.*, 2005) of the IBR-2 pulsed high-flux reactor (Frank Laboratory of Neutron Physics, JINR, Dubna) using high-pressure sapphire anvil cells (*Glazkov and Goncharenko*, 1991) in the range of high external pressures up to 5 GPa and temperatures of 10–300 K. The diffraction spectra were measured at the scattering angles $2\theta = 90°$ and 45.5°. For these scattering angles, the diffractometer resolution at the wavelength $\lambda = 2$ A was $\Delta d/d = 0.015$ and 0.025, respectively. The characteristic measurement time of one spectrum was 20 h. The volume of the samples under study was $V \sim 2.5$ mm^3. The pressure in the cell was measured by the ruby fluorescence technique. The diffraction data were analyzed by the Rietveld method.

In addition, a number of experiments were performed on the G6.1 diffractometer at the stationary Orphee reactor (Laboratoire Leon Brillouin, France) using a high-pressure sapphire anvil cell and on the Pearl/HiPr diffractometer at the ISIS pulsed neutron source (Rutherford Appleton Laboratory, United Kingdom) using Paris–Edinburgh high-pressure cells with tungsten carbide anvils in the range of pressures up to 10 GPa.

3. $Pr_{1-x}Sr_xMnO_3$ Compounds

The $Pr_{1-x}Sr_xMnO_3$ manganites at ambient conditions are paramagnetic insulators and exhibit several structural phases: orthorhombic crystal structures of *Pnma* symmetry at $x < 0.42$ and *Imma* one at $0.42 \le x < 0.48$; a tetragonal structure of *I*4/*mcm* symmetry at $0.48 \le x \le 0.8$, and an ideal perovskite-like cubic structure of $Pm\bar{3}m$ symmetry at $x > 0.8$ (*Kozlenko and Savenko*, 2006). The type of the magnetic ground state in the low-temperature region changes as FM (metallic, $0.25 < x < 0.5$), A-type AFM (metallic, $0.5 < x < 0.6$), C-type AFM (insulating, $0.6 < x < 0.9$), G-type AFM (insulating, $x > 0.9$).

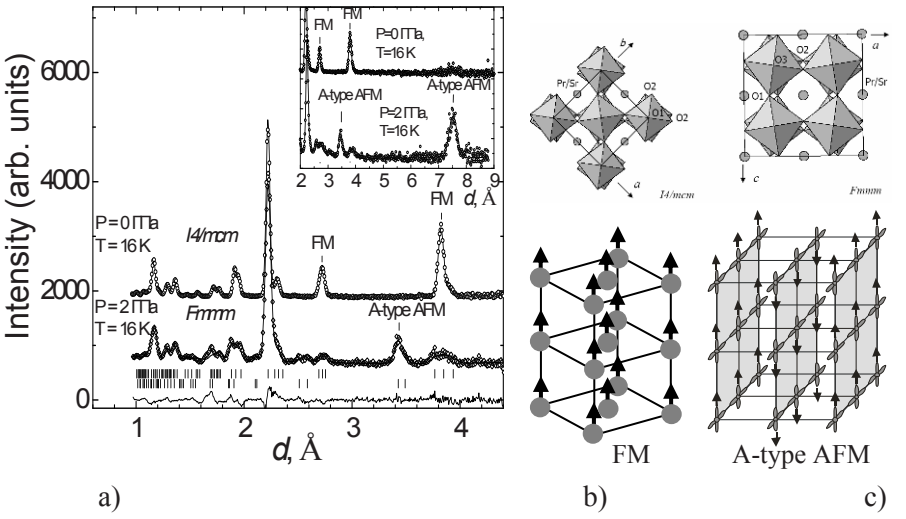

Figure 2. (a) Neutron diffraction patterns of $Pr_{0.52}Sr_{0.48}MnO_3$, measured at selected pressures and temperatures and processed by Rietveld method; (b) tetragonal crystal structure of the *I4/mcm* symmetry and the corresponding FM magnetic structure; (c) orthorhombic crystal structure of the *Fmmm* symmetry and the corresponding A-type AFM magnetic structure.

Neutron diffraction patterns of the $Pr_{0.52}Sr_{0.48}MnO_3$ manganite measured at various pressures and T = 16 K are shown in Figure 2. At ambient pressure and $T < T_C$ = 265 K, a magnetic contribution to the intensities of the (110)/(002) and (200)/(112) nuclear reflections located at $d_{hkl} \approx 3.86$ and

2.73 Å was observed (Figure 2), which pointed to the occurrence of a ferromagnetic (FM) state. The Mn magnetic moments with values 3.60(5) μ_B at T = 16 K are oriented along the tetragonal c-axis. At P = 2 GPa on cooling below $T_N \approx 250$ K, some splitting of diffraction peaks in d-spacing regions 1.8–2 Å and 3.7–3.95 Å is evident (Figure 2). In addition, new magnetic lines at d = 7.53 and 3.44 Å appear, indicating an onset of the new AFM state. The data analysis shows that observed modifications of diffraction patterns correspond to the pressure-induced onset of the A-type AFM state (Figure 2), which is accompanied by the structural phase transformation from the tetragonal crystal structure of *I4/mcm* symmetry to the orthorhombic structure of *Fmmm* symmetry. No ferromagnetic contribution to diffraction patterns is found.

In $Pr_{0.44}Sr_{0.56}MnO_3$ at ambient pressure the transition from the paramagnetic tetragonal *I4/mcm* phase to the A-type AFM orthorhombic *Fmmm* phase occurs directly at T_N = 220 K. Under high pressure P = 1.9 GPa, the Néel temperature remains practically unchanged (T_N (A-type) ~ 220 K) but with further temperature decrease at $T < T_{N2}$ = 125 K an additional purely magnetic line at d = 5.4 Å appears and some other diffraction peaks in the d-spacing region 1.8–2 Å are changed notably in intensity (Figure 3). This observation may be attributed to the onset of the C-type AFM state (Figure 3) with the tetragonal *I4/mcm* structure.

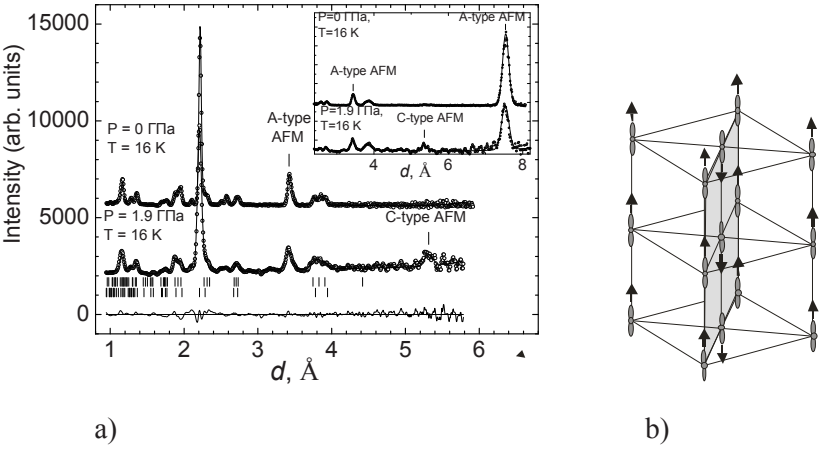

Figure 3. (a) Neutron diffraction patterns of $Pr_{0.44}Sr_{0.56}MnO_3$, measured at selected pressures and temperatures and processed by the Rietveld method; (b) the C-type AFM tetragonal magnetic structure.

The $Pr_{0.15}Sr_{0.85}MnO_3$ compound at ambient conditions has a cubic perovskite structure. With decreasing temperature, a C-type AFM tetragonal *I4/mcm* phase arises at $T_N = 290$ K. This AFM state remains stable at high pressures to 4 GPa, and T_N only slightly depends on pressure.

The observed changes in the magnetic state of $Pr_{1-x}Sr_xMnO_3$ manganites at high pressure can be analyzed using the theoretical considerations of the phase diagram for concentrations $x > 0.5$ obtained from analysis of the Hamiltonian for the simple cubic perovskite unit cell ($a_p \times a_p \times a_p$) of the following form (*Pai*, 2001):

$$H = J_{AF}\sum_{<ij>}\vec{S}_i\vec{S}_j - J_H\sum_{i,\alpha,\mu,\mu'}\vec{S}_i\cdot c^{\dagger}_{i\alpha\mu}\vec{\sigma}_{\mu\mu'}c_{i\alpha\mu'} - \sum_{<ij>,\mu}t^{\alpha\beta}_{ij}c^{\dagger}_{i\alpha\mu}c_{j\beta\mu}.$$

Here, the first term describes the superexchange AFM interaction between localized t_{2g} spins $\vec{S}_i$ and $\vec{S}_j$ of Mn ions at the nearest neighbor sites i and j, the second term corresponds to the intra-atomic exchange interaction between delocalized e_g electrons and t_{2g} spins, and the third term describes the kinetic energy of e_g-electron hopping in Mn^{3+}-O^{2-}-Mn^{4+} chains. Indices $\alpha(\beta)$ correspond to $d(3z^2 - r^2)$ and $d(x^2 - y^2)$ e_g orbitals, indices $\mu(\mu')$ correspond to spin projections +1/2 and –1/2, $\vec{\sigma}_{\mu\mu'}$ are the Pauli matrices, $t^{\alpha\beta}_{ij} = t<i\alpha/j\beta>$ is the hopping integral of e_g electrons between the nearest neighbor Mn sites through oxygen p orbitals, and is the creation operator of an electron with spin projection μ and orbital type α at site i. Because the hopping integral $t \sim W \sim l^{-3.5}$ and the superexchange coupling constant $J_{AF} \sim t^4 \sim l^{-14}$ depend differently on the Mn–O bond length l (*Harrison*, 1980; *Kozlenko and Savenko*, 2006), the action of high pressure will result in an increase in the parameter $J_{AF}S^2/t \sim l^{-10.5}$. Following the theoretical phase diagram (*Pai*, 2001), one can expect that an increase in high pressure and in the parameter $J_{AF}S^2/t$ should lead to the following changes in the magnetic state: FM → A-type AFM → C-type AFM in manganites with $x \sim 0.5$–0.55 and C-type AFM → G-type AFM in manganites with $x > 0.8$. The pressure dependences of this parameter for $Pr_{1-x}Sr_xMnO_3$ can be obtained from the known pressure dependences of the Mn–O bond lengths. For $Pr_{0.52}Sr_{0.48}MnO_3$ the calculated pressure value of the FM – A-type AFM phase transition is $P_{F-A} \approx 0.9$ GPa, in accordance with the experiment (*Kozlenko & Savenko*, 2006). For $Pr_{0.44}Sr_{0.56}MnO_3$, the calculated pressure value of the A-type AFM – C-type AFM phase transition is $P_{A-C} \approx 4.7$ GPa, which is somewhat larger in comparison with the experimental observation (*Kozlenko and Savenko*, 2006). For $Pr_{0.15}Sr_{0.85}MnO_3$, the estimated pressure $P_{C-G} \sim 14$ GPa for the possible transition from the C-type AFM phase to the G-type AFM phase considerably exceeds the maximum pressure obtained in the experiments.

4. $La_{1-x}Ca_xMnO_3$ and $La_{1-x}Sr_xMnO_3$ Compounds

The $La_{1-x}Ca_xMnO_3$ manganites crystallize in the orthorhombic crystal structure of *Pnma* symmetry. For Ca concentrations $x = 0.18–0.5$ a transition from the paramagnetic insulating phase to the metallic FM phase occurs on cooling (*Dagotto et al.*, 2001; *Kozlenko and Savenko*, 2006; *Tokura*, 2000). At $x = 0.5–0.75$, insulating AFM states of different symmetries arise (CE-type for $x \sim 1/2$, Wigner crystal for x ~2/3), whose distinctive feature is the spatial charge ordering of Mn^{3+}: Mn^{4+} ions. At $x > 0.75$, the C-type AFM state is observed, which coexists with the G-type AFM state at $x > 0.8$. Studies of the magnetic and transport properties of optimally doped $La_{1-x}Ca_xMnO_3$ manganites with $x \sim 0.3$ revealed anomalously high pressure coefficients of nearly coinciding Curie temperature and the insulator–metal (IM) transition temperature $dT_C(T_{IM})/dP \sim 20$ K/GPa in the range of relatively low pressures below 1–2 GPa and a strong decrease in dT_{IM}/dP in the region of higher pressures ($P > 6$ GPa) to ~ 2 K/GPa (*Postorino et al.*, 2003). The large values of $dT_C(T_{IM})/dP$ in the moderate pressure range was assumed to be a consequence of electron–phonon coupling effects associated with the static cooperative distortion of MnO_6 octahedra and resulting in an effective change in the carrier bandwidth.

The phase diagram of $La_{1-x}Sr_xMnO_3$ manganites is rather similar to that of $Pr_{1-x}Sr_xMnO_3$ one (*Dagotto et al.*, 2001; *Kaplan and Mahanti*, 1999; *Kozlenko and Savenko*, 2006; *Tokura*, 2000). The distinctive feature of $La_{1-x}Sr_xMnO_3$ is the presence of the rhombohedral structural phase of $R\bar{3}c$ symmetry for $x = 0.14–0.5$ having a metallic FM ground state. The static cooperative Jahn–Teller distortion is forbidden by symmetry in this phase. Therefore, a comparison of high-pressure effects on the crystal and magnetic structure of the $La_{1-x}Ca_xMnO_3$ and $La_{1-x}Sr_xMnO_3$ manganites with close values of x provides an opportunity to clarify a role of electron–phonon coupling effects in the pressure behavior of T_C (T_{IM}).

In neutron diffraction patterns of $La_{0.75}Ca_{0.25}MnO_3$ below $T_C = 240$ K at ambient pressure a magnetic contribution to the intensity of nuclear reflections (101)/(020) and (200)/(002)/(121) located at $d_{hkl} = 3.88$ and 2.75 Å was observed, indicating the occurrence of a ferromagnetic state. The Mn magnetic moments have values 3.29(5) μ_B at $T = 12$ K and they are located in the (*ac*) planes. At $P = 1.5$ GPa, new magnetic reflections at $d_{hkl} = 7.47$ and 3.44 Å were observed below $T_N \approx 150$ K. An analysis of the diffraction data showed that these reflections correspond to the formation of an A-type AFM state. Both FM and A-type AFM phases coexist at high pressures and their volume fractions are 70% and 30% at $P = 4.5$ GPa. From the temperature dependences of magnetic moments the pressure coefficient value $dT_C/dP = 12$ K/GPa was obtained.

With increasing pressure, an anisotropic compression of the non-equivalent Mn–O bonds is observed, resulting in an uniaxial compression of the oxygen octahedra along the *b*-axis. Such an anisotropic compression leads to a predominant population of the $d(x^2–z^2)$ e_g orbitals of Mn ions and decrease in the exchange integral between nearest neighbors in the direction of uniaxial compression. These factors create favorable conditions for the formation of the A-type AFM state (*Kozlenko and Savenko*, 2006).

In $La_{0.7}Sr_{0.3}MnO_3$ compound the rhombohedral crystal structure and the FM metallic ground state remain stable at high pressures to 6 GPa. The pressure coefficient dT_C/dP = +5.3 K/GPa is substantially smaller in comparison with $La_{0.75}Ca_{0.25}MnO_3$. Using the obtained structural parameters at high pressure, one can calculate a contribution from variation of interatomic distances and angles to T_C (T_{IM}) values using the expression $T_C \approx T_{IM} \propto W \sim \cos^2\varphi / l^{3.5}$ discussed in Section 1. For $La_{0.7}Sr_{0.3}MnO_3$ the calculated value $(dT_C/dP)_S$ = 3.12 K/GPa is close to the experimental one dT_C/dP = 5.3 K/GPa, whereas the value calculated for $La_{0.75}Ca_{0.25}MnO_3$ $(dT_C/dP)_S \approx 2$ K/GPa is significantly smaller than the experimental one dT_C/dP = 12 K/GPa. The difference between $(dT_C/dP)_S$ and dT_C/dP in the case of $La_{0.75}Ca_{0.25}MnO_3$ is due to the contribution from electron–phonon coupling associated with the static cooperative Jahn–Teller distortion of oxygen octahedra, which is missing for $La_{0.7}Sr_{0.3}MnO_3$. Using the pressure behavior of the conductivity activation energy (known from literature) and vibrational modes of oxygen octahedra, one can estimate more accurately the value $(dT_C/dP)_{calc} \approx 18$ K/GPa, comparable with the experimental one dT_C/dP, using the expression $W \sim W_0 \exp(-\gamma E_{JT}/\hbar\omega)$, discussed in Section 1. Neutron diffraction studies of the crystal and magnetic structure of $La_{0.5}Ca_{0.5}MnO_3$ showed that the charge and orbitally ordered CE-type AFM state is retained in the range of pressures up to 6 GPa and the magnetic ordering temperature increases with dT_N/dP = 4 K/GPa (*Kozlenko and Savenko*, 2006). For $La_{0.33}Ca_{0.67}MnO_3$, the charge and orbitally ordered Wigner crystal-type AFM state is remarkably unstable at high pressures and rapidly suppressed in the favour of the C-type AFM state (*Kozlenko and Savenko*, 2006).

5. $La_{1-x}Sr_xCoO_3$ Compounds

The $LaCoO_3$ compound crystallizes in the rhombohedral structure of $R\bar{3}c$ symmetry. At low temperature $LaCoO_3$ is a nonmagnetic semiconductor with a ground state of Co^{3+} ions of a low-spin (LS) configuration (t_{2g}^6, S = 0). As temperature increases, a sharp anomaly in the magnetic susceptibility corresponding to the appearance of the paramagnetic state was observed at $T \sim 100$ K and a gradual semiconductor–metal (S–M) transition accompanied

by another broad anomaly in the magnetic susceptibility occurs at $T \sim 500$ K. Both susceptibility anomalies are also associated with the anomalies in the thermal lattice expansion (*Knižek et al.*, 2005; *Kozlenko et al.*, 2007; *Kreiner et al.*, 2004; *Raccah and Goodenough*, 1967). The anomalous part of the thermal unit cell volume expansion $Q = (V - V_T)/V_T$ obtained from neutron diffraction data at different pressures, where V_T described the normal thermal expansion due to phonons (*Radaelli and Cheong*, 2002) is shown in Figure 4. The presence of two correlated anomalies can be explained quite naturally if two successive changes of the spin state of Co^{3+}, to intermediate spin state IS ($t_{2g}^5 e_g^1$, $S = 1$) and high spin (HS) ($t_{2g}^4 e_g^2$, $S = 2$) state, occur. In the three-level LS-IS-HS model (Figure 4) $Q = Q_1 x_1 + Q_2 x_2$, where x_1 and x_2 are the populations corresponding to IS and HS thermally excited states of the Co^{3+} ions (*Kozlenko et al.*, 2007). The coefficients Q_1 and Q_2 are related to the change of the equilibrium unit cell volume due to the change of the spin state, IS and HS. The populations of the IS and HS states are determined by the degeneracy factors and LS–IS and LS–HS energy splittings as $x_{1,2} = \nu_{1,2}\exp(-E_{1,2}/k_BT)/(1+\nu_1\exp(-E_1/k_BT) + \nu_2\exp(-E_2/k_BT))$. From the fitting of $Q(T)$ data measured at different pressures it was found that both LS–IS and LS–HS energy splittings increase substantially under high pressure (Figure 4) with $d\ln E_1/dP = 0.37$ GPa^{-1} and $d\ln E_2/dP = 0.23$ GPa^{-1}.

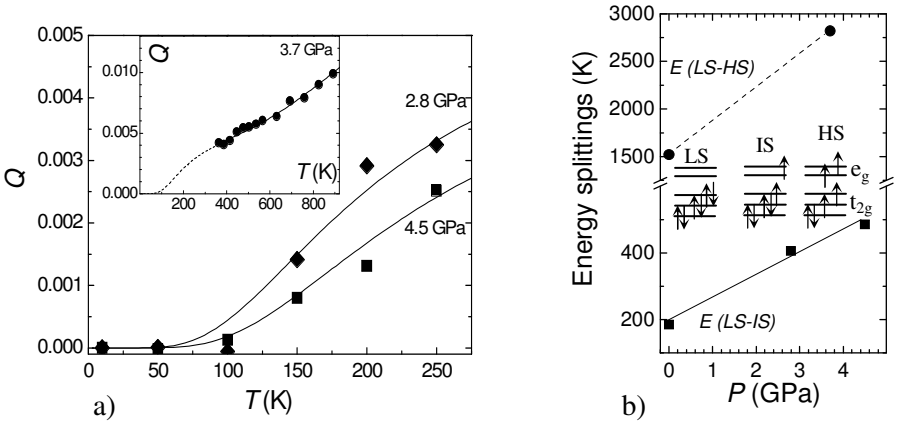

Figure 4. (a) The anomalous part of the thermal volume expansion of $LaCoO_3$ at selected temperatures fitted by the LS-IS-HS model; (b) LS-IS and LS-HS energy splittings as functions of pressure; insert shows electronic configuration of LS, IS and HS states of Co^{3+}.

Upon substitution of rare earth R by alkali earth A element, a ferromagnetic metallic ground state is stabilized in $R_{1-x}A_xCoO_3$ compounds for $x > 0.18$ (*Kriener et al.*, 2004). The $La_{0.7}Sr_{0.3}CoO_3$ compound is isostructural to parent $LaCoO_3$ and have the Curie temperature value $T_C = 205$ K. From the

neutron diffraction data it was found that the magnetic moment per Co atom at T = 12 K decreases from 1.7 to 1.4 μ_B, while T_C decreases to 170 K in 0–4.2 GPa pressure range (*Golosova et al.*, 2006). The observed FM state suppression is caused by a gradual spin state change of Co^{3+} ions from IS (S = 1) to LS (S = 0).

ACKNOWLEDGEMENTS

The work was supported by RFBR, grant 09-02-00311-a and grant of the President of Russian Federation MD-696.2010.2.

References

Dagotto, E., Hotta, A., Moreo, A., 2001, Colossal magnetoresistant materials: the key role of phase separation. *Phys. Rep*. **344**: 1.

Glazkov, V.P., Goncharenko, I.N., *Fizika I Technika Vysokih Davlenij* 1, 56 (1991) (in Russian).

Golosova, N.O., Kozlenko, D.P., Voronin, V.I., Glazkov, V.P., Savenko, B.N., 2006, The influence of high pressure on the crystal and magnetic structures of the $La_{0.7}Sr_{0.3}CoO_3$ cobaltite. *Phys. Solid State* **48**: 96.

Harrison, W.A., 1980, *The Electronic Structure and Properties of Solids*, Freeman, San Francisco, CA.

Kajimoto, R., Yoshizawa, H., Tomioka, Y., Tokura, Y., 2002, Stripe-type charge ordering in the metallic A-type antiferromagnet $Pr_{0.5}Sr_{0.5}MnO_3$. *Phys. Rev.* B **66**: 180402.

Kaplan, T.A., Mahanti, S.D., Eds., 1999, *Physics of Manganites*, Kluwer/Plenum, New York.

Knížek, K., Jirák, Z., Hejtmánek, J. Veverka, M., Maryško, M., Maris, G., Palstra, T.T.M., 2005, Structural anomalies associated with the electronic and spin transitions in $LnCoO_3$, *Eur. Phys. J.* B **47**: 213.

Kozlenko, D.P., Savenko, B.N., 2006, High-pressure effects on the crystal and magnetic structure of managanites. *Phys. Part. Nuclei.* **37**: S1.

Kozlenko, D.P., Golosova, N.O., Jirák, Z., Dubrovinsky, L.S., Savenko, B.N., Tucker, M.G., Le Godec, Y., and Glazkov, V.P., 2007, Temperature- and pressure-driven spin-state transitions in $LaCoO_3$. *Phys. Rev.* B **75**: 064422.

Kozlenko, D.P., Savenko, B.N., Glazkov, V.P., Somenkov, V.A., 2005, Neutron scattering investigations of structure and dynamics of materials under high pressure at IBR-2 pulsed reactor. *Neutron News* **16**(3): 13.

Kriener, M., Zobel, C., Reichl, A., Baier, J., Cwik, M., Berggold, K., Kierspel, H., Zabara, O., Freimuth, A., Lorenz, T., 2004, Structure, magnetization, and resistivity of $La_{1-x}M_xCoO_3$ (M = Ca, Sr, and Ba). *Phys. Rev.* B **69**: 094417.

Lengsdorf, R., Ait-Tahar, M., Saxena, S.S., Ellerby, M., Khomskii, D.I., Micklitz, H., Lorenz, T., Abd-Elmeguid, M.M., 2004, Pressure-induced insulating state in $(La,Sr)CoO_3$. *Phys. Rev.* B **69**: 140403.

Pai, V.G., 2001, Magnetic phases of electron-doped manganites. *Phys. Rev.* B. **63**: 064431.

Postorino, P., Congeduti, A., Dore, P., Sacchetti, A., Gorelli, F., Ulivi, L., Kumar, A., Sarma, D.D., 2003, Pressure tuning of electron-phonon coupling: the insulator to metal transition in manganites. *Phys. Rev. Lett.* **91**: 175501.

Radaelli, P.G., Cheong, S.-W., 2002, Structural phenomena associated with the spin-state transition in $LaCoO_3$. *Phys. Rev.* B **66**, 094408.

Raccah, P.M., Goodenough, J.B., 1967, First-order localized-electron collective-electron transition in $LaCoO_3$. *Phys. Rev.* **155**: 932.

Tokura, Y., (Ed.), 2000, *Colossal Magnetoresistance Oxides*, Gordon & Breach, New York.

JAHN–TELLER SYSTEMS AT HIGH PRESSURE

FERNANDO RODRIGUEZ*
MALTA Consolider Team, DCITIMAC, Facultad de Ciencias, Universidad de Cantabria, 39005 Santander, Spain

Abstract Structural studies of Jahn–Teller (JT) systems involving transition metal ions often require using complementary spectroscopic techniques in order to complete an adequate characterization. X-ray absorption and diffraction though standard techniques for structural studies in concentrated materials are not well suited to investigate diluted or structurally subtle JT compounds. In this work we analyze the usefulness of optical spectroscopy to investigate structural properties of JT systems involving both diluted and concentrated compounds that are difficult to extract from diffraction experiments. Moreover, in some cases, the usage of different experimental techniques is crucial to obtain reliable conclusions. Some Mn^{3+}, Ni^{3+} and Co^{3+} systems with perovskite structure will be presented and analyzed as an illustration.

Keywords: Jahn–Teller effect, Spin state, Mn^{3+}; Co^{3+}, High-pressure absorption

1. Introduction

Jahn–Teller (JT) systems of transition-metal (TM) ions like $Cu^{2+}(d^9)$, $Fe^{2+}(d^6)$, $Cr^{2+}(d^4)$, $Ni^{3+}(d^7$; LS), $Co^{3+}(d^6)$ and $Mn^{3+}(d^4)$ are interesting systems in perovskite oxides AMO_3 or fluorides AMF_n (n = 3,4). The electrical, optical and magnetic properties of these materials are often strongly correlated due to the interplay between spin state, orbital ordering and JT distortion of the TM ions. The compounds $LaCoO_3$ (*Imada et al.*, 1998), $YNiO_3$ (*Garcia-Muñoz et al.*, 2004), $(Mg,Fe)SiO_3$ (*Burns*, 1993), K_2CuF_4 (*Ishizuka et al.*, 1998; *Valiente and Rodríguez*, 1999), $CsMnF_4$ (*Aguado et al.*, 2007), are illustrative examples. High-spin (HS) to low-spin (LS) phenomena; metal–insulator transitions; ferromagnetic-antiferromagnetic transitions are volume-dependent

*E-mail: fernando.rodriguez@unican.es

E. Boldyreva and P. Dera (eds.), *High-Pressure Crystallography: From Fundamental Phenomena to Technological Applications*, DOI 10.1007/978-90-481-9258-8_19,

properties related to these materials that can be modified by application of external pressure.

The knowledge and comprehension of these strongly correlated phenomena require a characterization of the crystal structure in connection to the electronic structure and associated properties. However the structural characterization is not an easy task on dealing with TM ions showing distorted coordination polyhedra by the JT effect. The detection of such distortions from diffraction techniques can be difficult since the structural information is usually hidden in antiferrodistortive type ordering or twining. In addition, XRD powder diagrams often exhibit intensity deviations due to preferential orientation that can hinder analysis. The $LaMnO_3$, $LaCoO_3$ and $LaNiO_3$ are clear examples of this behaviour.

Optical spectroscopy, particularly crystal-field spectroscopy, has been shown to be an efficient probe for revealing not only the JT distortion around the TM ion but also to estimate the associated distortion in terms of TM–X bond distances or the corresponding normal coordinates (*Aguado et al.*, 2003, 2007; *Reinen et al.*, 2007; *Rodriguez and Aguado*, 2003; *Valiente and Rodríguez*, 1999). Nevertheless, structural estimates of the JT distortion require correlation studies between the d-orbital splitting related to the JT effect and the distortion measured by x-ray diffraction (XRD) in reference compounds. The crystal-field spectrum (absorption, excitation or emission spectra) of TM ions usually provides information on d-d electronic transitions and, hence, the JT splitting associated with either the parent octahedral t_{2g} or e_g orbitals, denoted by Δ_t and Δ_e, respectively. An account of these splittings and their dependence with the corresponding crystal-field distortions of D_{4h} or D_{2h} symmetry is given elsewhere (*Aguado et al.*, 2003, 2007; *Rodríguez and Aguado*, 2003; *Valiente and Rodríguez*, 1999). The crucial point to achieve such correlation is to find structurally characterized compound series, the optical spectra of which can be obtained under different pressure and temperature conditions. In particular, the variation of the optical spectra with volume requires the use of Diamond Anvil Cells specially adapted for optical spectroscopy techniques (IIa diamonds, easy adaptation to cryostats and microscope devices; time-resolved spectroscopy in case of photoluminescence studies, etc. (*Hernández and Rodríguez*, 2003; *Hernández et al.*, 2007).

The aim of this chapter is to illustrate that optical spectroscopy can be a useful tool to deal with structural studies in systems under pressure, where standard XRD or XAS techniques are unable to solve the problem. In particular, crystal-field spectroscopy of TM ions and their variation with pressure can provide valuable information on the local symmetry and bond distances associated the JT distortion of TM ions introduced either as a crystal constituent or as an impurity.

2. Experimental Techniques

In this work three different systems are investigated. Firstly, we deal with the Mn^{3+} compound series A_nMnF_{3+n} (A: Na, K, Tl, Cs; n = 1–3) where Mn^{3+} shows a E⊗e JT distortion, the degree of which increases with the crystal dimensionality n = 3(isolated MnF_6^{3-})→2(chains)→1(layers) (*Aguado and Rodríguez*, 2003; *Rodríguez and Aguado*, 2003). Secondly, we explore the optical properties of fluorides and oxides having TM ions exhibiting a T⊗e JT effect. CoF_3 or $La(Al,Co)O_3$ and Al_2O_3: Ti^{3+} with d^6 and d^1 electronic configuration, are model crystals (*Garcia-Revilla et al.*, 2002; *Sanz-Ortiz et al.*, 2008a, b, 2009). Thirdly, we study the optical spectra of TM ions having an orbital singlet ground state like Cr^{3+} in the cubic elpasolite Rb_2KCrF_6 (*Hernández et al.*, 2008).

Optical absorption experiments under pressure as well as time-resolved spectroscopy were done using the experimental setup described in Figure 1. Details on experimental setups for optical absorption (OA) as well as luminescence and time resolved spectroscopy using high-pressure techniques are reported elsewhere (*Moral and Rodriguez*, 1995; *Hernandez et al.*, 2003, 2008; *Rodriguez-Lazcano et al.*, 2009). The setup performance for obtaining suitable OA spectra is illustrated through Figures 2–5. In all cases, the pressure was determined through the R-line shift of ruby chips introduced in the hydrostatic cavity.

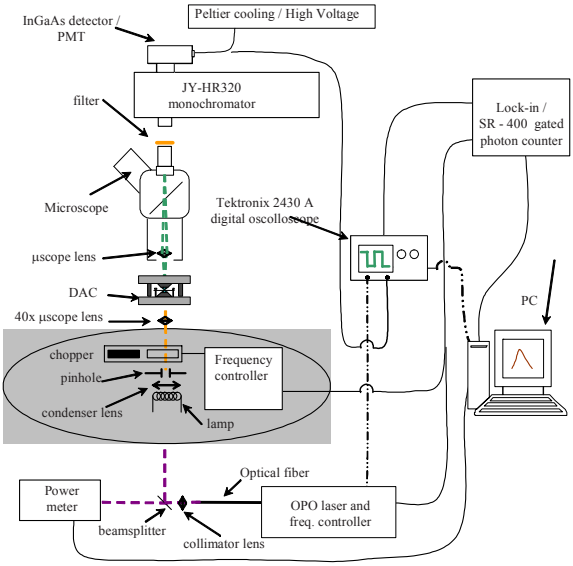

Figure 1. Experimental setup for optical absorption and time-resolved spectroscopy employed in high-pressure experiments. Excitation in the 407–2,400 nm range is provided by a OPO laser.

CoF_3 was obtained from Sigma-Aldrich; Co-doped $LaAlO_3$ crystals were synthesized following the procedures described elsewhere (*Sanz-Ortiz et al.*, 2008). Due to the high reactivity of CoF_3 in air, silicone oil and paraffin, special care was paid for handling and loading the diamond anvil cell (DAC) in argon atmosphere using a glove box.

The optical spectra of Co-doped $LaAlO_3$ were obtained using a Cary 6000i spectrophotometer operating directly in reflectance mode and in absorption mode, using KBr-diluted sample pellets (12.5% mol) in the latter case. The absorption spectra of CoF_3 were directly obtained by compacting CoF_3 powders in the DAC together with several Ruby chips homogeneously distributed in the gasket hole. This procedure guarantees a full absorption measurement of the sample. The experimental setup is a home-made single-beam microspectrometer (Nikon microscope with an output optical fibre attached to a Chromex H-500 monochromator), using a SR440 lock-in amplifier and suitable Hamamatsu InGaAs and R928 photomultiplier detectors for synchronous detection (Figure 1).

3. Results and Discussion

3.1. JAHN–TELLER SYSTEMS

Throughout this manuscript we refer to JT systems, when a compound has a TM ion with an orbitally degenerate ground state in octahedral (sixfold) coordination. Under such circumstances, any crystal-field distortion of either tetragonal (Q_θ), or rhombic (Q_ε) symmetry splits the electronic ground state leaving the centre of gravity of the parent octahedral e_g and t_{2g} orbitals unchanged. Such a distortion leads to a gain of the total energy of the system. If this occurs, we say that there is an electron-lattice (or electron-vibration) coupling between the electronic ground state and the crystal-field distortion of e_g symmetry (Q_θ, Q_ε) yielding a low-symmetry distortion equilibrium geometry beyond O_h. This is known as JT effect and the associated distortion as JT distortion. Details are given elsewhere (*Aguado et al.*, 2003, 2007; *Rodríguez and Aguado*, 2003; *Sanz-Ortiz and Rodríguez*, 2009).

If we denote the electron-lattice coupling by A and the effective force constant related to the low-symmetry distortion Q by k, then the energy as a function of Q and the corresponding equilibrium geometry (or JT distortion) at the energy minimum are given by:

$$E(Q) = E_{Oh} - AQ + \tfrac{1}{2}\, kQ^2 \quad (1)$$

$$Q_{eq} = A/k \quad (2)$$

E_{Oh} and Q_{eq} are the energy of the undistorted O_h system and the equilibrium JT distortion, respectively. The JT energy, which is defined by the energy gain with respect to O_h, is given by:

$$E_{JT} = E(Q_{eq}) - E_{Oh} = -\tfrac{1}{2}\, kQ_{eq}^{\,2} = -\tfrac{1}{2}\, AQ_{eq} \qquad (3)$$

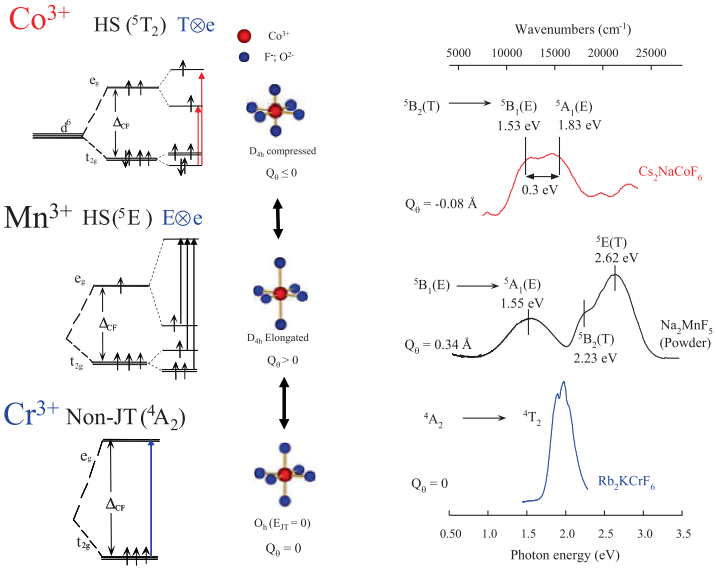

Figure 2. Optical absorption spectra of different transition-metal ions in fluorides showing different degrees of Jahn–Teller distortions ($\rho \approx Q_{\theta}$.) determined from x-ray diffraction. The corresponding one-electron energy level diagrams and observed electronic transitions are indicated.

The TM ions whose JT effect is related to twofold orbitally degenerate electronic states (E symmetry) are known as E⊗e JT systems, whereas those associated with threefold orbitally degenerate electronic states (T symmetry) are T⊗e JT systems. In E⊗e (*Rodríguez and Aguado*, 2003), the JT energy is related in first order approximation to the splitting of the one-electron e_g orbitals (Δ_e) by $E_{JT} = \frac{1}{4}\, \Delta_e$ (Figure 2).

On dealing with JT systems optical spectroscopy can provide directly the splittings of the $e_g(\Delta_e)$ and $t_{2g}(\Delta_t)$ orbitals due to the JT effect from optical spectra and hence the corresponding JT energy as well as the relationship between Δ_e and Δ_t or, equivalently, the associated A_e and A_t electron-lattice coupling parameters (*Hitchman*, 1994; *Reinen and Atanasov*, 1991; *Reinen et al.*, 2007; *Rodríguez and Aguado*, 2003; *Sanz-Ortiz and Rodríguez*, 2009). The crucial point to obtain structural information from optical spectroscopy

in JT systems is to establish correlations between Δ_e and Δ_t and the corresponding JT distortion; i.e. Q_θ and Q_ε at the equilibrium geometry.

In this chapter we investigate the electronic structure of Mn^{3+} and Co^{3+} and their relation with their JT distortion as typical examples of E⊗e and T⊗e JT systems, respectively (*Reinen et al.*, 2007; *Rodríguez and Aguado*, 2003; *Sanz-Ortiz et al.*, 2009). For illustration purposes, Figure 2 shows the absorption spectra corresponding to trivalent transition-metal ions exhibiting JT distortions of T⊗e (Cs_2NaCoF_6) (*Reinen et al.*, 2007) and E⊗e (Na_2MnF_5) (*Rodríguez and Aguado*, 2003), as well as others having regular octahedron coordination (Rb_2KCrF_6) (*Hernández et al.*, 2008). Note that depending on the strength of the JT distortion the main absorption band, involving electronic transitions between the octahedral e_g and t_{2g} orbitals, splits in a different way. The spectra clearly show how the strength of JT effect influences the crystal-field splitting Δ_e and Δ_t. In Co^{3+} (T⊗e) the observed splitting is related to Δ_e by the equilibrium geometry imposed by the JT effect of the electronic ground state of T symmetry (T⊗e). However Δ_e in Mn^{3+} (Na_2MnF_5) is four times larger than in Co^{3+} reflecting the bigger JT distortion associated with an electronic ground state of E symmetry (E⊗e). In other words, the JT electron-lattice coupling associated with e_g orbitals is stronger than that of t_{2g} orbitals. Although it is well known that e_g orbitals give rise to a stronger JT effect than t_{2g} in O_h TM ions, the spectra of Figure 2 provide a direct confirmation of this phenomenon. Furthermore optical spectroscopy permits to elucidate the strength of the JT effect as well as to distinguish TM ions without JT effect; i.e. in an orbital singlet ground state like Cr^{3+} ($^4A_2$), the spectrum consists of a single $e_g \rightarrow t_{2g}$ transition within O_h. The structure observed in the absorption band of Cr^{3+} is not related to a d-splitting but Fano resonances between different excited states (*Hernández et al.*, 2008). At the end of the chapter the interplay between spin state and JT effect in connection with the spin crossover pressure is discussed in terms of crystal-field models following the procedure established elsewhere for Mn^{3+} and Ni^{3+} (*Aguado et al.*, 2007; *Oelkrug*, 1971; *Sanz-Ortiz et al.*, 2008, 2009). In what follows we deal with correlations between Δ_e and Δ_t and corresponding JT distortion studied by optical spectroscopy using a selected compound series of Mn^{3+} and Co^{3+}.

3.1.1. *E⊗e Jahn–Teller Systems of Mn^{3+}*

It is worth noting that the largest d-splitting exhibited by the spectra of Figure 2 corresponds to Mn^{3+} (Na_2MnF_5). It means that the JT effect associated with e_g electrons is significant stronger than that produced by t_{2g} electrons. In fact, for strong E⊗e JT coupling systems like Na_2MnF_5, the spectrum consists of three bands located nearby the optical range at 1.55, 2.23 and 2.62 eV consistently with a distortion, $Q_\theta = 0.34$ Å (*Aguado et al.*,

2003). As indicated in Figure 2, they correspond to spin-allowed electronic transitions between one-electron e_g and t_{2g} orbitals split both by the octahedral crystal-field and the low-symmetry distortion. A complete account of structural correlations carried out in Mn^{3+} by optical spectroscopy is given in (*Rodríguez and Aguado*, 2003). According to the JT theory, the stabilization energy is ¼ the e_g splitting: $E_{JT} = ¼\Delta_e$, which is 0.39 eV/Mn^{3+} for Na_2MnF_5 (Δ_e = 1.55 eV). Interestingly, the optical spectrum provides also the t_{2g} splitting, Δ_t, for the same JT distortion imposed by the equilibrium geometry due to the E⊗e JT effect in Na_2MnF_5. The measured value, Δ_t = 0.39 eV, is obtained from the two absorption bands at higher energy and is approximately ¼Δ_e. Though similar, in general, Δ_t must not be identified with E_{JT} in E⊗e.

Figure 3 shows the optical spectra of different Mn^{3+} fluorides, the distortion of which is known from XRD (*Rodríguez and Aguado*, 2003). This series allows us to establish correlations between Δ_e and Δ_t, and the JT distortion through the normal coordinate Q_θ (the rhombic distortion is $Q_\varepsilon \approx 0$ in the compound series). In terms of the axial (R_{ax}) and equatorial (R_{eq}) bond distances of the elongated MnF_6^{3-} octahedron, Q_θ is defined as $Q_\theta = 2/\sqrt{3}\,(R_{ax} - R_{eq})$.

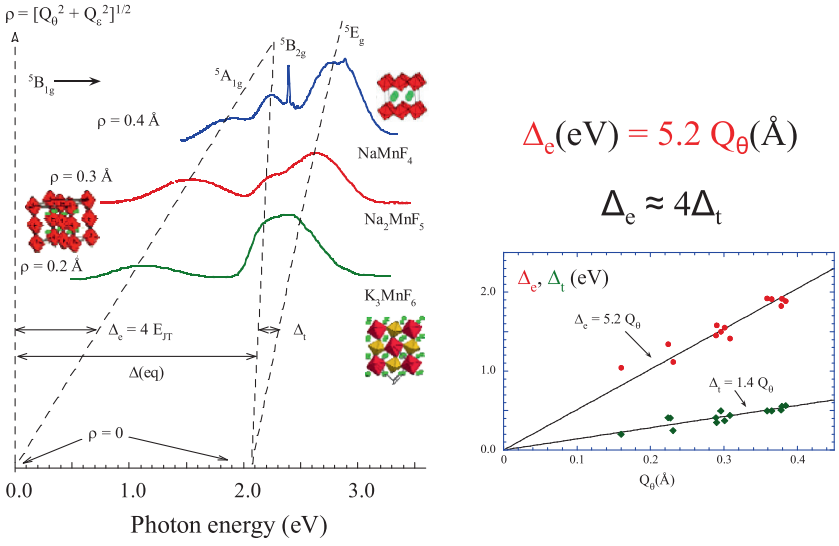

Figure 3. Optical absorption spectra of 0D, 1D and 2D Mn^{3+} fluorides displaying Jahn–Teller distortions of nearly D_{4h} symmetry ($\rho \approx Q_\theta$.). The tetragonal splittings, Δ_e and Δ_t, increase linearly with Q_θ. The unit cell of each crystal is represented near the spectrum.

It must be noted from Figure 3, that both Δ_e and Δ_t increase linearly with the JT distortion Q_θ, according to equations:

$$\Delta_e(\text{eV}) = 5.2\ Q_\theta(\text{Å}) \qquad \text{and} \qquad \Delta_t(\text{eV}) = 1.4\ Q_\theta(\text{Å}) \tag{4}$$

The ratio $\Delta_e/\Delta_t \approx 4$ shows that for a given Q_θ distortion the splitting of e_g is four times larger than the t_{2g} splitting, thus confirming the stronger coupling of the e_g electrons in the JT effect of octahedral TM complexes. These correlations are important for dealing with Mn^{3+} impurities in fluorides and oxides since an estimate of the local distortion Q_θ or, more precisely, $\rho = [Q_\theta^2 + Q_\varepsilon^2]^{1/2}$ (to include an eventual rhombic distortion) can be obtained from their optical spectra. Interestingly, such a correlation seems also to apply for Mn^{3+} in epidote with $\Delta_e = 1.5$ eV for $\rho = 0.28$ Å (*Burns*, 1993), and, as shown below, is also obeyed for Co^{3+} in fluorides (Figure 4) (*Reinen et al.*, 2007).

3.1.2. *T⊗e Jahn–Teller Systems of Co^{3+}*

The situation for Co^{3+} (T⊗e) is quite different. The one-electron energy diagram is basically the same as E⊗e but the T⊗e distortion is smaller due to the weaker electron-lattice coupling. The first transition energy in d^6 corresponds to Δ_t and the difference between the other two transitions, which are the ones usually observed in the VIS-NIR range, gives directly Δ_e. Figure 4 shows the absorption spectra of Co^{3+}-doped $LaAlO_3$ and CoF_3 adapted from (*Sanz-Ortiz et al.*, 2008). For comparison purposes, the spectra of Cs_2NaCoF_6 and $CsCoF_4$ taken from (*Reinen et al.*, 2007) are included. All spectra show one absorption band with two components located at 1.53 and 1.83 eV in Cs_2NaCoF_6 (*Reinen et al.*, 2007), 1.39 and 1.81 eV in Li_3CoF_6 (*Allen and Warren*, 1971), 1.17 and 2.18 eV in $CsCoF_4$ (*Reinen et al.*, 2007), and 1.45 and 1.89 eV in CoF_3 (*Sanz-Ortiz et al.*, 2008). The absorption bands are related to crystal-field transitions of Co^{3+} from the HS ground state ($^5T_2$) to the excited state ^5E split by the T⊗e JT distortion. In fact, the splitting of the absorption band for Cs_2NaCoF_6 and $CsCoF_4$ is $\Delta_e = 0.3$ and 1.0 eV, respectively (Figure 4). These splittings are approximately 1/5 and 2/3 of Δ_e for Mn^{3+} in Na_2MnF_5. If we compare Δ_e for Cs_2NaCoF_6 and $CsCoF_4$ with $NaMnF_4$ these factors reduce to 1/6 and 1/2 (*Rodríguez and Aguado*, 2003), thus indicating that distortions are significantly smaller in Co^{3+}, as corresponds to the weaker T⊗e JT effect (*Reinen et al.*, 2007; *Sanz-Ortiz*, 2008). Q_θ (and ρ) values determined by x-ray diffraction (*Reinen et al.*, 2007; *Lacorre et al.*, 1989) in Cs_2NaCoF_6 and $CsCoF_4$ are –0.08 and –0.18 Å, respectively, in agreement with their corresponding Δ_e values and the structural correlations established for Mn^{3+} in fluorides (*Rodríguez and Aguado*, 2003). Therefore the relation between the JT distortion, $\rho = [Q_\theta^2 + Q_\varepsilon^2]^{1/2}$, and the tetragonal splitting Δ_e, given by

the equation: Δ_e(eV) = 5.1 ρ(Å) applies also for Co^{3+} fluorides and Mn^{3+} in epidote (ρ = 0.28 Å) (*Burns*, 1993; *Sanz-Ortiz et al.*, 2008, 2009). Hence their absorption spectra provide the type of the JT effect (E⊗e or T⊗e) and its strength from Δ_e. It must be noted that in CrF_6^{3-} (Figure 2) the first absorption band does not show any structure related to the JT effect as corresponds to an orbital singlet ground state ($^4A_2$) with ρ = 0 Å. In this case the transition energy gives directly the crystal-field energy: Δ_{CF} = 1.9 eV for $R_{Cr\text{-}F}$ = 1.89 Å (*Hernández et al.*, 2008).

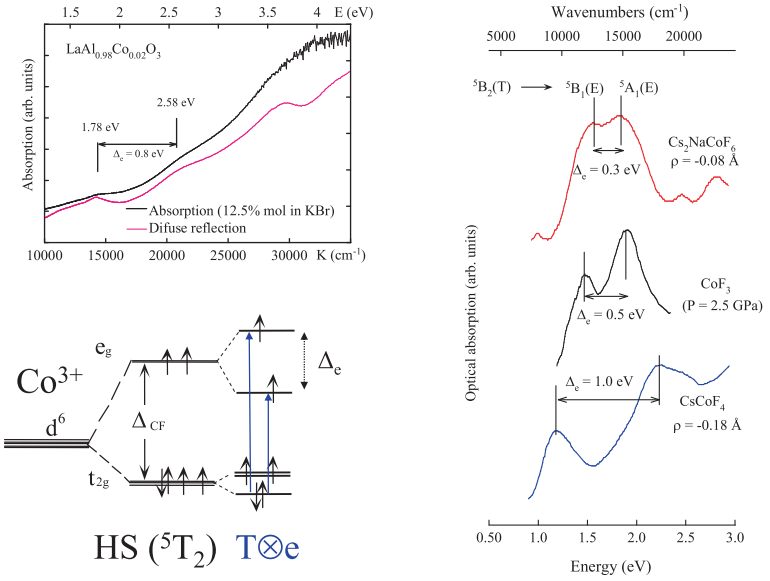

Figure 4. Optical absorption spectrum of Co^{3+}-doped $LaAlO_3$ at ambient conditions (left) and those of Cs_2NaCoF_6 (*Reinen et al.*, 2007), $CsCoF_4$ (*Allen and Warren*, 1971) and CoF_3 (*Sanz-Ortiz et al.*, 2008) (right). The arrows in the one-electron level diagram indicate the observed transitions.

Note that the splitting in CoF_3 (Δ_e = 0.45 eV) is similar to that measured in Li_3CoF_6 (0.42 eV) (*Allen and Warren*, 1971) or Cs_2NaCoF_6 (0.30 eV) but lower than in $CsCoF_4$ (1.01 eV) (*Reinen et al.*, 2007). From these correlations we conclude that the CoF_3 spectrum is consistent with a HS ground state ($^5T_2$) which experiences a significant T⊗e JT effect yielding a e_g-splitting Δ_e similar to that attained in other HS Co^{3+} fluorides. From Δ_e, we estimate that the JT distortion ρ is about 0.09 Å; i.e. the bond distance difference ($\Delta R = R_{eq} - R_{ax}$) in the compressed CoF_6^{3-} complex will be about 0.08 Å. It must be pointed out that Co^{3+} distortion has not been reported for CoF_3 from XRD that provides an unique Co-F distance, R = 1.89 Å.

However EXAFS experiments on CoF_3 were not able to resolved this local structure, although a fit with two (3 + 3) F shells around Co provided Co–F distances of 1.85(1) and 1.91(1) Å (*Hector et al.*, 1998). This example justifies the usefulness of optical spectroscopy as a complementary tool for obtaining local structural information.

A similar absorption spectrum is observed in Co^{3+}-doped $LaAlO_3$ at ambient conditions (*Sanz-Ortiz et al.*, 2008) as is shown in Figure 4. Its absorption bands appear at 1.74 and 2.52 eV, being consistent with $\Delta_e = 0.8$ eV and $\Delta_{CF} = 2.1$ eV (*Sanz-Ortiz et al.*, 2008). Interestingly, the crystal-field Δ_{CF} reveals that the system is beyond the spin-transition crossover (1.8 eV) (*Gütlich and Goodwin*, 2004; *Sanz-Ortiz et al.*, 2008), and thus the electronic ground state must correspond to the LS $^1A_1$ state as was confirmed by magnetic measurements (*Sanz-Ortiz et al.*, 2008). Co^{3+} is non magnetic (LS: S = 0) at low temperature and its magnetic moment increases with temperature due to thermal population of either the intermediate spin state (S = 1) or the high spin state (S = 2) or both IS and HS states. A similar behaviour was observed in the neat compound $LaCoO_3$ (*Kozlenko et al.*, 2007; *Ropka and Radwanski*, 2003; *Vankó et al.*, 2006). Nevertheless, the spectroscopic data in the diluted compound suggest that the thermally populated state corresponds to the HS state ($^5T_2$). Therefore the present results indicate that the HS state lies above the LS state, in agreement with conclusions given elsewhere (*Sanz-Ortiz et al.*, 2008). High-resolution XRD experiments were performed in order to prove the involvement of IS state in the magnetic properties of $LaCoO_3$ by measuring the distortion of the CoO_6 octahedron due to the E⊗e JT effect associated with IS state (^3T) (*Maris et al.*, 2003). It is shown that CoO_6 exhibits a slight distortion with three different Co–O bond distances: 1.87, 1.93 and 1.99 Å at T = 300 K. In terms of the tetragonal, Q_θ, and rhombic, Q_ε, normal coordinates, related to E⊗e JT effect, it corresponds to $\rho = 0.12$ Å. From the measured Δ_e for $LaAlO_3$: Co^{3+} we estimate a distortion $\rho = 0.15$ Å for Co^{3+}, which is similar to that found for the pure $LaCoO_3$ by XRD. In either case, such distortions seem to be very small for being due to a E⊗e JT effect if we take into account that Mn^{3+} distortions in E⊗e systems like $LaMnO_3$ correspond to four short Mn-O distances of 1.94 Å and two long Mn-O distances of 2.18 Å ($\rho \approx Q_\theta = 0.28$ Å) (*Haverkort et al.*, 2006; *Ramos et al.*, 2007).

3.1.3. *High Spin to Low Spin Phenomena in Jahn–Teller Systems*

The interplay between spin state and JT effect has been recently discussed in order to understand the crystal-field strength requirements to induce spin crossover in Mn^{3+}, Ni^{3+} or Co^{3+} (isoelectronic of Fe^{2+}) (*Goncharov et al.*, 2006). In addition, there is some controversy about the existence of IS (S = 1) in $Co^{3+}(3d^6)$ around the S = 0 ($^1A_1$) to S = 2 ($^5T_2$) spin crossover transition.

The observation of magnetic moments with values $\mu_{eff} > 0$ for T > 0 K that increase with temperature in Co^{3+}-oxides (*Imada et al.*, 1998) has been explained in terms a mixture of either IS and LS states around the spin transition, or of HS and LS states, which actually corresponds to S = 1 or S = 2 and S = 0 spin states in thermal equilibrium, respectively (*Haverkort et al.*, 2006; *Imada et al.*, 1998; *Maris et al.*, 2003; *Vankó et al.*, 2006).

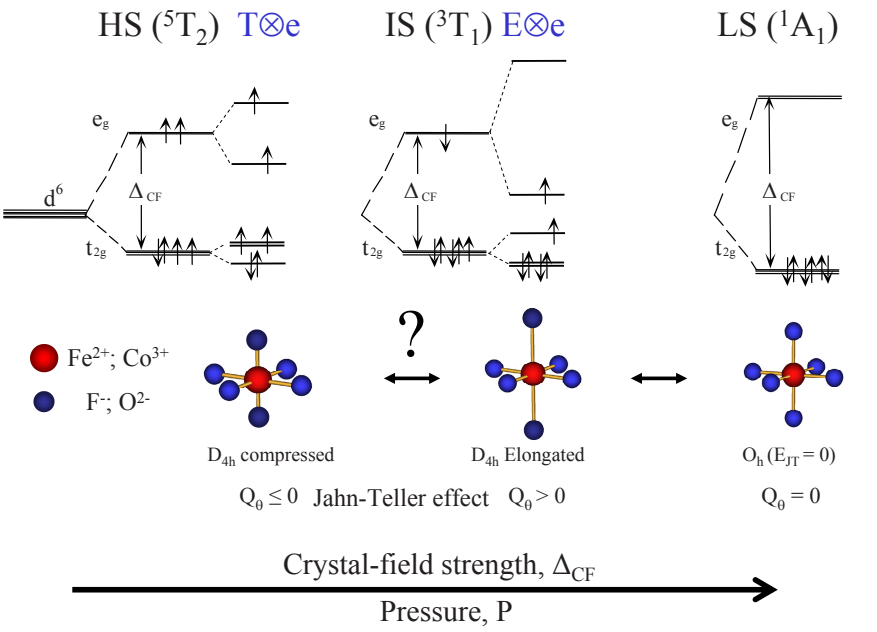

Figure 5. Energy level diagrams corresponding to the three possible spin-state electronic configurations in Co^{3+}. The expected evolution with pressure is indicated.

Figure 5 shows the three possible spin states for Co^{3+} and the corresponding one-electron level diagram taking into account the strength of the JT effect associated with each state. We aim to discuss how the crystal-field spectra and, particularly, the orbital splitting related to the JT distortion for different electronic ground states (weak T⊗e for HS ($^5T_2$) and strong E⊗e (plus T⊗e) for the supposedly low-lying first-excited state IS ($^3T_{1,2}$)) can help to distinguish between such spin states.

Concerning $Ni^{3+}(d^7)$ and $Mn^{3+}(d^4)$, the JT effect favours stabilization of LS and HS, respectively (*Sanz-Ortiz et al.*, 2008). While Ni^{3+} exhibits a LS state in $(RE)NiO_3$ perovskites at ambient pressure (*Garcia-Muñoz et al.*, 2004), Mn^{3+} shows a HS state, the crystal field required to stabilize the LS being stronger than that expected on the basis of the Tanabe-Sugano

diagram (*Sugano et al.*, 1970) by the JT energy (*Aguado et al.*, 2007). The opposite occurs for Ni^{3+} (*Aguado et al.*, 2007; *Oelkrug*, 1971; *Sanz-Ortiz et al.*, 2008; *Sugano et al.*, 1970). Figure 6 illustrates this behaviour. The variation of the optical spectra of $CsMnF_4$ with pressure gives clear evidence a HS-LS transition around 40 GPa (*Aguado et al.*, 2007). The optical spectrum transforms from a typical JT-related three broad-band structure with HS ground state to a single broad-band spectrum characteristic of Mn^{3+} LS. Interestingly, such a spin crossover is induced after the JT distortion is released by applying pressure.

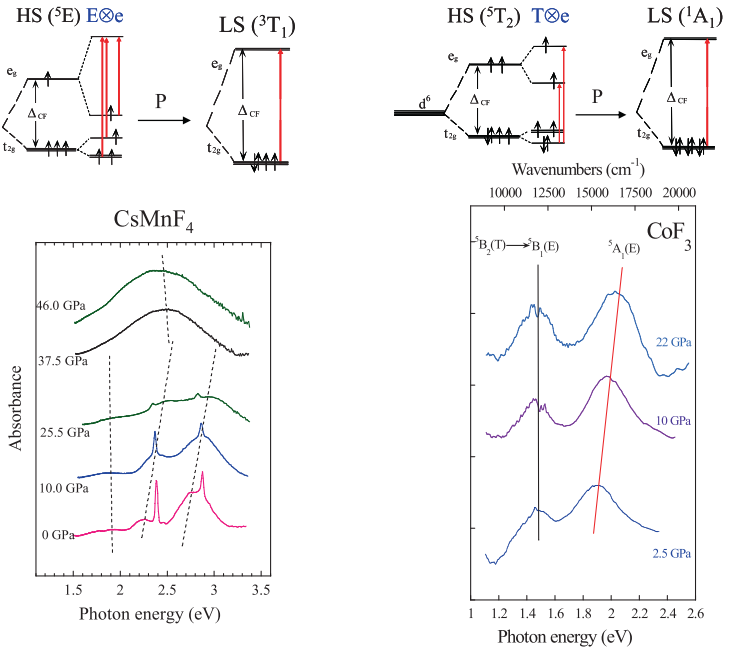

Figure 6. Variation of the absorption spectra of $CsMnF_4$ (*left*) and CoF_3 (*right*) with pressure at room temperature along the spin crossover transition. The schematic energy level diagram showing the change of electronic configuration in each transition is indicated above.

In the case of Co^{3+}, insulating oxides and fluorides are attractive systems for elucidating the controversy of how spin crossover transitions involve IS state prior to LS state. In fact, these compounds have crystal-field values Δ_{CF} for Co^{3+} at, or nearly below, the spin crossover transition ($^5T_2 \leftrightarrow {}^1A_1$): Δ_{CF} = 2.1 eV (*Burns*, 1993) and 1.7 eV (*Reinen et al.*, 2007), respectively. According to the Tanabe-Sugano diagram for $Co^{3+}(3d^6)$, the crossover crystal field is Δ_{SCO} = 1.9 eV as derived from the optical spectra (*Burns*, 1993; *Reinen et al.*, 2007; *Sanz-Ortiz et al.*, 2008; *Sugano et al.*, 1970). Magnetic

measurements and x-ray emission spectroscopy (XES) performed on CoF_3 and $LaCoO_3$ clearly indicate that the low temperature ground state corresponds to high spin (S = 2) (*Gütlich and Goodwin*, 2004) and low spin (S = 0) (*Gütlich and Goodwin*, 2004; *Sanz-Ortiz et al.*, 2008; *Vankó et al.*, 2006), respectively. XES was employed to explore the increase of spin with temperature in $LaCoO_3$ as a probe for IS (*Vankó et al.*, 2006). However, the proof of IS on the basis of a S = 1 state in Boltzmann equilibrium with a S = 0 state, as deduced from magnetic measurements (*Kozlenko et al.*, 2007), is doubtful since the magnetic data can also be interpreted in terms of the $^5T_2$ HS state split by the spin-orbit and trigonal crystal field in $LaCoO_3$ (*Ropka and Radwanski*, 2003).

The variation of the CoF_3 spectra with pressure through the spin-crossover transition clarifies this behaviour. Figure 6 shows the pressure dependence of the absorption spectra of CoF_3 in the 0–20 GPa range (*Sanz-Ortiz et al.*, 2008). We detect a JT-related splitting (Δ_e) in the explored pressure range. The band at 1.45 eV practically does not shift with pressure, thus indicating that not only Δ_{CF} but also Δ_e increase with pressure. This result is not surprising since Δ_e can increase with pressure even if the JT distortion, ρ, decreases (*Aguado et al.*, 2003). In CoF_3, Δ_e and Δ_{CF} increase as 9 and 5 meV/GPa, respectively, but the high-energy band increases above 10 GPa suggesting that the HS-LS crossover already occurred around this pressure (*San-Ortiz et al.*, 2008). These spectroscopic results confirm the pressure stability of the JT distortion in Mn^{3+} (E⊗e) and Co^{3+} (T⊗e) in fluorides as well as the pressure-induced HS-LS crossover transition.

4. Conclusions

In conclusion, this chapter illustrates the usefulness of optical spectroscopy to characterize JT systems of TM ions through their e_g and t_{2g} splittings under high-pressure conditions. The optical spectra can be used as efficient probes to follow variations of electronic structure with pressure and, eventually, the local structure around the TM octahedron. Structural correlations provide information on the JT energy and the associated electron-lattice couplings. The knowledge of these values allows us to extract complementary structural information about TM ion from the optical spectra. In particular, this information is crucial when standard XRD or XAS techniques are not efficient for such purposes due to structural constraints (antiferrodistortive structure, twining, preferential orientation, etc.), or because we are dealing with diluted JT systems.

ACKNOWLEDGEMENTS

I wish to thank Dr. Fernando Aguado and Dr. Marta N. Sanz-Ortiz for collaboration. Some material presented here belongs to the Jahn–Teller chapters of their respective doctoral thesis. Financial support from the Spanish Ministerio de Ciencia e Innovación (Project No MAT2008-06873-C02-01) and MALTA INGENIO-CONSOLIDER 2010 (Ref. CDS2007-0045) is acknowledged.

References

Aguado, F., Rodríguez, F., and Núñez, P., 2007, Pressure-induced Jahn-Teller suppression and simultaneous high-spin to low-spin transition in the layered perovskite $CsMnF_4$, *Phys. Rev. B*. **76:** 094417.

Aguado, F., Rodriguez, F., and Núñez, P., 2003, Pressure effects on $NaMnF_4$: Structural correlations and Jahn-Teller effect from crystal-field spectroscopy, *Phys. Rev.* **B 67:** 205101.

Allen, G.C., and Warren, K.D., 1971, The electronic spectra of the hexafluoro complexes of the first transition series, *Struct. Bond.* **9:** 49.

Burns, R.G., 1993, *Mineralogical applications of crystal field theory*, Cambridge University Press, Cambridge.

Garcia-Muñoz, J.L., Amboage, M., Hanfland, M., Alonso, J.A., Martínez-Lope, M.J., and Mortimer, R., 2004, Pressure-induced melting of charge-order in the self-doped Mott insulator $YNiO_3$, *Phys. Rev. B* **69:** 094106.

Garcia-Revilla, S., Rodriguez, F., Valiente, R., and Pollnau, M., 2002, Optical spectroscopy of Al_2O_3:Ti^{3+} single crystal under hydrostatic pressure. The influence on the Jahn–Teller coupling, *J. Phys. Cond. Matter* **14:** 447.

Goncharov, A.F., Struzhkin, V.V., and Jacobsen, S.D., 2006, Reduced radiative conductivity of low-spin (Mg,Fe)O in the lower mantle, *Science* **312:** 1205.

Gütlich, P., and Goodwin, H.A., 2004, *Spin Crossover in Transition Metal Compounds II*, Springer, Heidelberg.

Haverkort, M.W., Hu, Z., Cezar, J.C., Burnus, T., Hartmann, H., Reuther, M., Zobel, C., Lorenz, T., Tanaka, A., Brookes, N.B., Hsieh, H.-H., Lin, H.-J., Chen, C.-T., and Tjeng, H.L., 2006, Spin state transition in $LaCoO_3$ studied using Soft X-ray absorption spectroscopy and magnetic circular dichroism, *Phys. Rev. Lett.* **97:** 176405.

Hector, A.L., Hope, E.G., Levason, W., and Weller, M.T., 1998, The mixed valence structure of R-NiF_3, *Z. Anorg. Allg. Chem.* **624:** 1982.

Hernández, I., and Rodríguez, F., 2003, Pressure-induced photoluminescence in Mn^{2+}-doped SrF_2 and BaF_2 fluorites, *Phys. Rev. B* **67:** 012101.

Hernández, I., Rodríguez, F., and Hochheimer, H.D., 2007, Pressure-induced two-color photoluminescence in MnF_2 at room temperature, *Phys. Rev. Lett.* **99:** 027403.

Hernandez, I., Rodríguez, F., and Tressaud, A., 2008, Optical properties of the $(CrF_6)^{3-}$ complex in A_2BMF_6:Cr^{3+} elpasolite crystals: variation with M-F bond distance and hydrostatic pressure, *Inorg. Chem.* **47:** 10288.

Hitchman, M.A., 1994, The influence of vibronic coupling on the spectroscopic properties and stereochemistry of simple 4- and 6-coordinate copper (II) complexes, *Comments Inorg. Chem.* **15:** 197.

Imada, M., Fujimori, A., and Yoshinori, T., 1998, Metal-insulator transitions, *Rev. Mod. Phys.* **70:** 1039.

Ishizuka, M., Terai, M., Hidaka, M., Endo, S., Yamada, I., and Shimomura, O., 1998, Pressure-induced structural phase transition in two-dimensional Heisenberg ferromagnet K_2CuF_4, *Phys. Rev. B* **57:** 64.

Kozlenko, D.P., Golosova, N.O., Jirák, Z., Dubrovinsky, L.S., Savenko, B.N., Tucker, M.G., Le Godec, Y., Glazkov, V.P., 2007, Temperature- and pressure-driven spin-state transitions in $LaCoO_3$, *Phys. Rev. B* **75:** 064422.

Lacorre, P., Pannetier, J., Averdunk, F., Hoppe, R., Ferey, G., 1989, Crystal and magnetic structures of $LiCoF_4$: the first compound with a dirutile structure, *J. Sol. St. Chem.* **79:** 1.

Maris, G., Ren, Y., Volotchaev, V., Zobel, C., Lorenz, T., and Palstra, T.T.M., 2003, Evidence for orbital ordering in $LaCoO_3$, *Phys. Rev. B* **67:** 224423.

Moral, B.A., and Rodríguez, F., 1995, New double-beam spectrometer for microsamples. Application to hydrostatic pressure experiments, *Rev. Sci. Inst.* **66:** 5178.

Oelkrug, D., 1971, Absorption spectra and ligand field parameters of tetragonal 3d-transition metal fluorides, *Struct. Bond.* **9:** 1.

Ramos, A.Y., Tolentino, H C.N., Souza-Neto, N.M., Itié, J.P., Morales, L., and Caneiro, A., 2007, Stability of Jahn-Teller distortion in $LaMnO_3$ under pressure: An X-ray absorption study, *Phys. Rev. B* **75:** 052103.

Reinen, D., and Atanasov, M., 1991, The Jahn-Teller effect and vibronic coupling in transition metal chemistry, *Magn. Res. Rev.* **15:** 167.

Reinen, D., Atanasov, M., and Köhler, P., 2007, The Jahn-Teller effect in octahedral T Ground states – an experimental and DFT study on $M^{III}X_6$ polyhedra [M^{III}: Ti, V, Co; X: Cl, F] in various solids, *J. Mol. Struct.* **838:** 151.

Rodríguez, F., and Aguado, F., 2003, Correlations between structure and optical properties in Jahn–Teller Mn^{3+} fluorides: A study of $TlMnF_4$ and $NaMnF_4$ under pressure, *J. Chem. Phys.* **118:** 10867.

Rodríguez-Lazcano, Y., Nataf, L., and Rodríguez, F., 2009, Electronic structure and luminescence of $[(CH_3)_4N]_2MnX_4$ (X=Cl,Br) crystals at high pressures by time-resolved spectroscopy: Pressure effects on the Mn-Mn exchange coupling, *Phys. Rev. B* **80:** 085115.

Ropka, Z., and Radwanski, R.J., 2003, ^{5}D term origin of the excited triplet in $LaCoO_3$, *Phys. Rev. B* **67:** 172401.

Sanz-Ortiz, M.N., Rodríguez, F., and Demazeau, G., 2008, Spin transition in Co^{3+} by optical absorption and time-resolved spectroscopy under pressure: an appraisal of the different spin states, *High Press. Res.* **28:** 571.

Sanz-Ortiz, M.N., Rodríguez, F., Baranov, A., and Demazeau, G., 2008, Synthesis under pressure and characterizations through optical spectroscopy of Jahn-Teller cations (LS Ni^{3+}, IS Co^{3+}) as probes diluted in a perovskite matrix, *J. Phys. Conf. Ser.* **121:** 092003.

Sanz-Ortiz, M.N., and Rodríguez, F., 2009, Photoluminescence properties of Jahn-Teller transition-metal ions, *J. Chem. Phys.* **131:** 124512.

Sugano, S., Tanabe, Y., and Kamimura, H., 1970, *Multiplets of transition-metal ions in solids*, Academic, New York.

Valiente, R., and Rodríguez, F., 1999, Electron-phonon coupling in charge-transfer and crystal-field states of Jahn-Teller $CuCl_6^{4-}$ systems, *Phys. Rev. B* **60:** 9423.

Vankó, G., Rueff, J.P., Mattila, A., Németh, Z., and Shukla, A., 2006, Temperature- and pressure-induced spin-state transitions in $LaCoO_3$, *Phys. Rev. B* **73:** 024424.

EFFECT OF SPIN TRANSITIONS IN IRON ON STRUCTURE AND PROPERTIES OF MANTLE MINERALS

LEONID DUBROVINSKY*[1], OLGA NARYGINA[1], INNOKENTY KANTOR[2]
[1]*Universität Bayreuth, Bayreuth, Germany,*
[2]*CARS, University of Chicago, USA*

Abstract Iron is an important element in Earth lower mantle minerals. At conditions of the deep Earth's interior iron ions could undergo high-to-low spin crossover. We discuss evolution of the spin state of iron in ferropericlase (Mg,Fe)O, silicate perovskite and garnet (Mg,Fe)SiO_3 at high pressures and temperatures.

Keywords: Iron, spin state, pressure, ferropericlase, silicate perovskite

1. Introduction

The main iron-bearing minerals in the Earth (olivine and its high-pressure modifications, pyroxenes, ferropericlase and silicate perovskite) contain iron in a high-spin state at ambient conditions. However, high pressure in the Earth's interior could induce a spin-pairing transition in all these materials, which can have a significant effect on the properties of corresponding phases. Possible iron spin crossover in the main lower-mantle phases silicate perovskite, majorite, and ferropericlase has been a subject of numerous experimental and theoretical studies. Here we present and discuss some results concerning spin crossover in the most abundant minerals in the Earth's lower mantle containing low-spin iron.

* E-mail: Leonid.Dubrovinsky@uni-bayreuth.de

E. Boldyreva and P. Dera (eds.), *High-Pressure Crystallography: From Fundamental Phenomena to Technological Applications*, DOI 10.1007/978-90-481-9258-8_20,

2. Iron in Octahedral Environment in Ferropericlase

Iron, being a transition metal with uncompleted d-electron shell, can exist in different spin states. The Fe^{2+} ion has a $3d^6$ electronic configuration, and six electrons are distributed over five d-orbitals. For a free ion all of these orbitals have equal energy. In a ligand field of octahedral symmetry the degeneracy is removed, and orbitals are split into two E_g orbitals with higher energy and three T_{2g} levels with lower energy, which are separated by an amount Δ_O (the subscript "O" stands for octahedral splitting). We will use the Δ_O notation for the octahedral crystal field splitting in order to distinguish from the Mössbauer quadrupole splitting Δ. Electronic occupation of d-orbitals depends on the magnitude of Δ_O. In a weak field Δ_O is small, and the energy gain from unpaired electrons overcomes the crystal-field splitting and a high-spin configuration with four unpaired electrons exists (Figure 1a). In a strong field Δ_O is higher with respect to the electron-pairing energy and electrons occupy lower-energy levels. This state is called low-spin and has no unpaired electrons (Figure 1b).

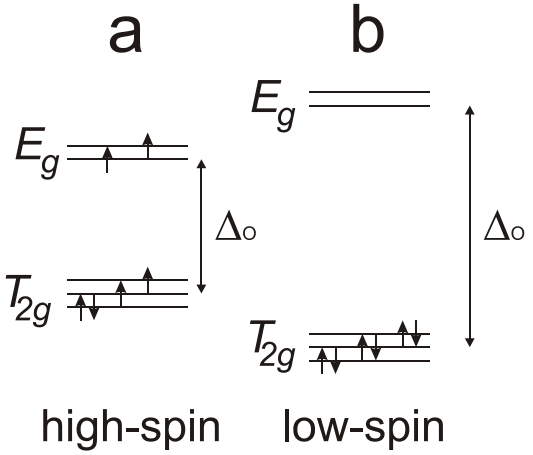

Figure 1. Energy levels of Fe^{2+} in an octahedral field. (a) Weak field (high-spin state) and (b) strong ligand field (low-spin state).

The crystal-field splitting describes the d-electron energy levels only in a pure ionic state. The ligand field theory expresses the energy levels of a partly filled d-shell in terms of two types of parameters: the orbital energy differences Δ_O and the integrals of interelectronic repulsion. These integrals are described by the empirical Racah parameters, and the resulting energy levels (known as Tanabe-Sugano diagrams) are quite complex for a Fe^{2+} octahedral compound. Racah parameters reflect the degree of metal-ligand bond covalency, and a low-spin state could be stabilised even with a small

value of Δ_O in the case of strongly covalent chemical bonding. Both crystal-field splitting and Racah parameters depend on thermodynamic parameters, and the spin state of iron can be changed by varying temperature or pressure. Such a transition is known as a spin transition or spin crossover and occurs in many metal-organic and other compounds. Physical properties can change dramatically upon spin crossover. Sometimes there is a strong density change (by a few percent), optical property changes, and even structural transitions caused by iron spin crossover. In low-spin Fe^{2+} there are no unpaired electrons and magnetic moments, and hence transformation to the low-spin state causes also a loss of magnetism.

3. Iron in Silicate Peroskite and Majorite

$(Mg,Fe)(Si,Al)O_3$ perovskite phase has an orthorhombic structure, with Si or Al in nearly symmetrical octahedral "B-site" (colored in green in Figure 2a) and Mg^{2+} or Fe^{2+} in more distorted eightfold to 12-fold coordinated "A-site" (*Horiuchi et al.*, 1987; *McCammon et al.*, 1992). At ambient conditions A–O distances range from 2.02 to 2.43 Å with average value 2.21 Å. Certain amount of Fe^{3+} can also probably occupy the smaller octahedral site (*McCammon et al.*, 1992, 1998; *Jephcoat et al.*, 1999). Physical properties (elasticity, thermal and electrical conductivity, *etc.*) of silicate perovskite is believed to be influenced by the electronic state of iron at high pressures and temperatures (*Badro et al.*, 2004; *McCammon et al.*, 2008; *Goncharov et al.*, 2008; *Keppler et al.*, 2009).

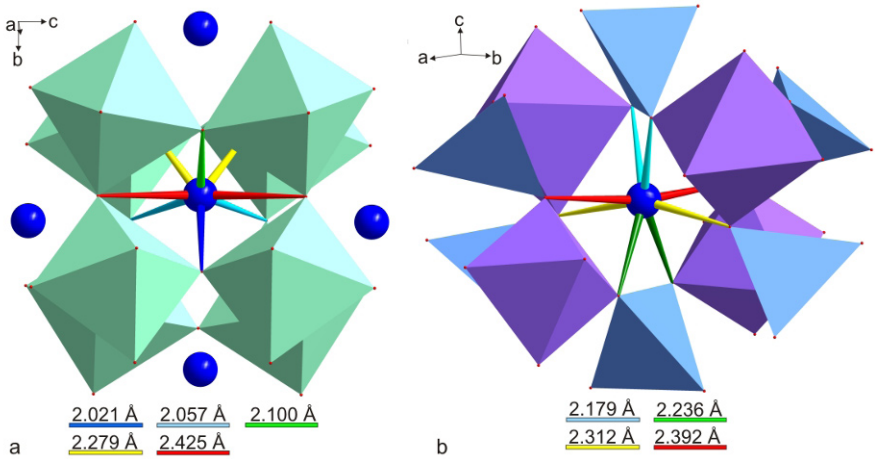

Figure 2. Coordination environment of ferrous iron (large solid blue spheres) in the perovskite (a) and garnet (b) structures. Green octahedra and blue tetrahedra represent the oxygen environment of Si, and the purple octahedra represent the Mg/Si site in the garnet structure.

$(Mg,Fe)SiO_3$ majorite has a tetragonal structure, with Mg^{2+} and Fe^{2+} cations in the dodecahedral (or distorted cubic) site and Si in the octahedral (colored in purple in Figure 2b) and tetrahedral (colored in blue in Figure 2b) sites; a small amount of Fe^{3+} can also occupy the octahedral site. The addition of Al to the end member tetragonal $MgSiO_3$ majorite stabilizes cubic symmetry (*Hatch and Ghose*, 1989). At ambient conditions interatomic distances in dodecahedral position range from 2.18 to 2.39 Å with the average value 2.28 Å. Since the silicate garnet and perovskite structures have clear similarities in environment of Fe^{2+} located in 8-coordinated position, one can expect analogies in the iron behaviour in these two minerals.

4. Spin Crossover in Ferropericalse

On compression of ferropericlase samples with different compositions at ambient temperature the low-spin component gradually increases with increasing pressure, and the amount of the high-spin component decreases accordingly (Figures 3 and 4). The high-spin and low-spin fractions were calculated from the absorption areas of the subspectral components, assuming equal Debye–Waller factors of the HS and LS Fe ions. In fact this is not true, but this difference is usually neglected. The studied samples were highly enriched with the ^{57}Fe isotope and the effective Mössbauer thickness was much higher than ideal. The high thickness of the absorber results in significant internal multiple absorption, which could significantly distort the relative areas of the two subspectral components in the mixed spin region. Thickness corrections can be accounted for using a full transmission integral calculation. We used NORMOS software (a commercially available fitting program written by R.A. Brand and distributed by Wissenschaftliche Elektronik GmbH, Germany) to perform simultaneous full transmission integral calculations and non-linear least-squares spectrum fitting. The thickness of the source is also higher than in conventional experiments due to the higher concentration of ^{57}Co in a point source, but thickness effects in the source are much smaller compared to those in the absorber. The relative subspectral components areas are not significantly affected by thickness effects – no more than 10–15%.

The range over which high- and low-spin states coexist is remarkable: for the Fe5 sample it is about 30 GPa, and more than 50 GPa for the Fe20 sample (Figures 3 and 4). Such a broad region of spin crossover cannot be attributed to pressure gradients in the DAC. With several small ruby chips placed in different parts of the sample chamber, pressure gradients could be measured and were not higher than 5–7 GPa.

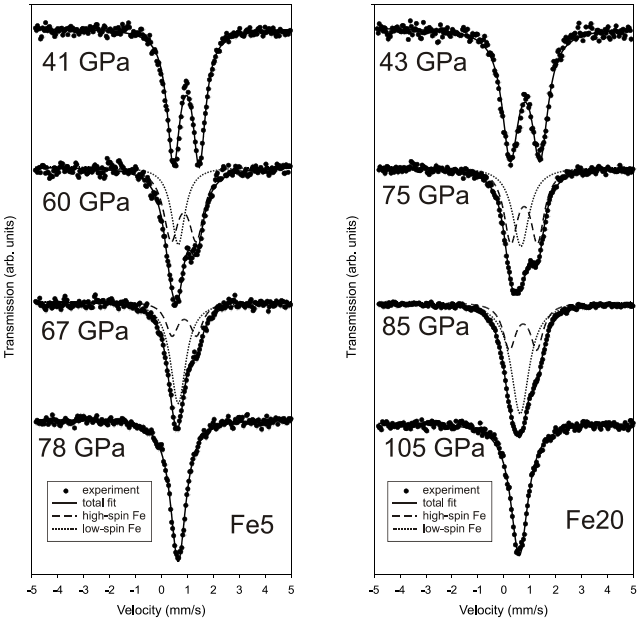

Figure 3. Room temperature Mössbauer spectra of Fe5 (*left*) and Fe20 (*right*) ferropericlase samples upon spin crossover. Dashed lines show the high-spin component and dotted lines show the low-spin component in the spectra.

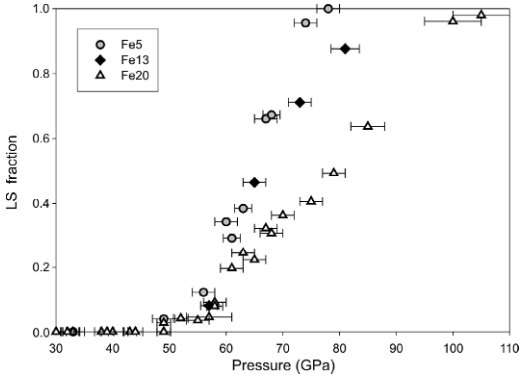

Figure 4. Low-spin fraction in ferropericlase as a function of pressure at room temperature. Circles, diamonds and triangles are for Fe5, Fe13, and Fe20 samples, respectively.

In order to understand these results on spin crossover in ferropericlase, a brief digression into the physics of this phenomenon in general should be made. Spin crossover in ferropericlase is often discussed in terms of a phase transition. A number of studies are focused on a determination of the volume (density) collapse, and the magnitude of seismic wave velocity discontinuity associated with the spin transition. The question of whether it is a first- or a second-order transition is also discussed (*Lin et al.*, 2005;

Speziale et al., 2005; *Tsuchiya et al.*, 2006; *Sturhahn et al.*, 2006). However, spin crossover is not necessarily a phase transition. In order to apply a thermodynamic theory of phase transitions, there should be two distinct phases – a high-spin and a low-spin phase. In the case of two or more possible different states of an atom (in this case high- or low-spin electronic configuration), all the states have always (at any finite temperature) a certain non-zero probability. Every energy level or quantum state of an atom is populated, as described by the Boltzmann thermal population function. This means that in any Fe^{2+} compound and under any thermodynamic conditions, there are some iron ions in a high-spin and some in a low-spin state. Usually, one state is dominating and the other state has negligible population, and a compound is considered to be either high- or low-spin. However, there can be a continuous change in spin probability between these two states. The term "spin crossover" reflects this particular idea: at some particular *P,T*-conditions the low-spin probability and the high-spin probabilities are equal. Different molecules or ions within the same crystal exist in different spin states while the crystal is still a single phase (*Bolvin and Kahn*, 1995). When both spin states of iron coexist in significant amounts in a single crystal, they cannot be considered as two distinct phases. However, the physical properties and chemical bonding in high- and low-spin Fe compounds can be significantly different, giving rise to a real phase transition. If any structural changes occur upon spin crossover, it should be described as a phase transition. In case if there is a volume discontinuity or changes in symmetry of a crystal, spin crossover can be described in terms of a phase transition.

Our experimental observations allow the interpretation of spin changes in ferropericlase at high pressure as a spin crossover without phase transition.

5. (Fe,Mg)SiO_3 Majorite

Let us now consider in details the high pressure and temperature behavior of eight-coordinated $^{[8]}Fe^{2+}$ in majorite and then compare it with that one of the high-QS component in perovskite.

In general the value of quadrupole splitting is determined by two factors: (i) lattice contribution, which is proportional to the electrical field gradient (EFG) produced by the charge distribution surrounding the absorbing nucleus which is normally negligible and does not vary significantly with pressure and temperature) and (ii) valence contribution, which is proportional to the EFG produced by the electrons distributed over the valence energy levels, associated with the absorbing nucleus; therefore the valence contribution to

the quadrupole splitting (QS) value is temperature and pressure dependent (*Ingalls*, 1964).

In the case of Fe^{2+} in majorite, the valence contribution to the EFG is determined by the Boltzmann distribution of six 3d-electrons over the five 3d levels, which are split into two levels with lower energy, e_g, and three levels of higher energy, t_{2g}, that are separated by the crystal field splitting energy – Δ_C (*Burns*, 1970).

The lower energy levels correspond to the d_z^2 and $d_{x^2-y^2}$ electronic orbitals and the high energy levels correspond to the d_{xy}, d_{yz}, d_{xz} orbitals. If the d_z^2 and $d_{x^2-y^2}$ orbitals are equally populated, the magnitude of their contributions to the EFG would be the same, but opposite in sign. Consequently their total contribution to the EFG would be zero. The same is true in the case of the three t_{2g} orbitals.

According to the Boltzmann distribution $n_i = n_0 \cdot \exp^{-\frac{\Delta_i}{kT}}$, where Δ_i is the energy of the ith state and n_0 is a normalization constant, the values of Δ_i and therefore the population of energy levels depend on crystal field splitting (Δ_C) and spin pairing energy (SPE), as well as on temperature. The relative magnitudes of Δ_C and SPE determine which spin configuration occurs. Depending on the relation between these two values one of the spin configurations is stable.

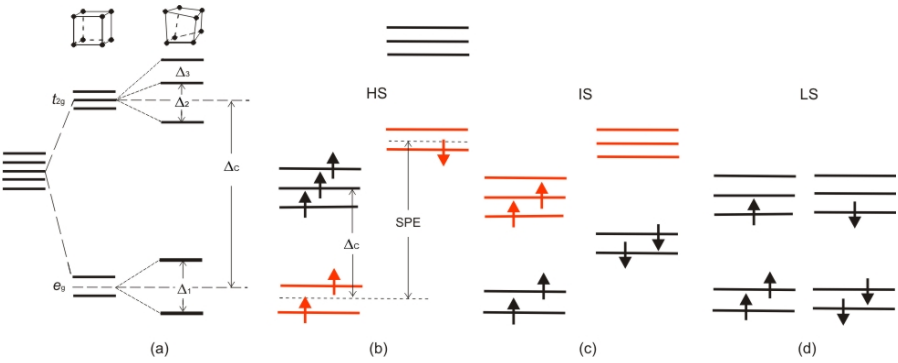

Figure 5. Splitting of Fe^{2+} energy levels (a) and possible spin state configurations (b, c, d) in a distorted cubic field (modified after *Burns*, 1993). The energy levels that predominantly contribute to EFG for a certain spin configuration are highlighted in red.

In the case of high spin $^{[8]}Fe^{2+}$ in majorite (SPE >> Δ_C), five 3d electrons occupy each of the five levels and the last sixth electron pairs with the one occupying the lowest energy level (Figure 5). For this configuration only e_g orbitals contribute to the EFG, because the t_{2g} orbitals are equally populated and compensate each other. Consequently the value of QS in this case is mainly determined by the energy difference between e_g levels – Δ_1 (defined in

Figure 5). Note that the larger the difference and the lower the temperature, the higher the quadrupole splitting will be. The value of Δ_1 in this particular case (HS $^{[8]}Fe^{2+}$ in majorite) can be estimated through the temperature dependence of quadrupole splitting, as was shown by *Huggins* (1975). Based on the *Ingalls* model (1964), *Huggins* (1975) derived the following simple expression for the variation of quadrupole splitting (QS) with temperature (T), for the case of ferrous iron in garnet:

$$QS(T) = (QS(0) + F_{lat})\left(\frac{1 - e^{-\delta_1/kT}}{1 + e^{-\delta_1/kT}}\right) - F_{lat}, \quad (1)$$

where QS(0) is the quadrupole splitting (in mm/s) at 0K, Δ_1 is the separation of e_g levels (in J), k is Boltzmann's constant and F_{lat} is the lattice contribution (in mm/s) to the quadrupole splitting.

Applying this formula to our variable temperature data for majorite and assuming $F_{lat} = 0$ (Huggins, 1975), we obtained the results that at 20 GPa Δ_1 is 1,500(50) cm^{-1} and 1680(70) cm^{-1} for ferrous iron in $^{57}Fe_{0.18}Mg_{0.82}SiO_3$ and $^{57}Fe_{0.11}Mg_{0.89}SiO_3$, respectively.

Consequently, in the case of majorite we can account for the high value of QS (about 3.6–3.7mm/s) as a consequence of the large splitting between the lower energy levels e_g.

6. (Fe,Mg)SiO_3 Perovskite

As a first approximation the energy diagram for $^{[8–12]}Fe^{2+}$ in silicate perovskite is similar to that for $^{[8]}Fe^{2+}$ in majorite (Figure 5), hence we can interpret the origin of the high QS-component in the Mössbauer spectrum of silicate perovskite in the framework of the same theoretical model that was used for majorite. If we consider the pressure and temperature dependence of central shift CS and QS of the high-QS and $^{[8]}Fe^{2+}$ components, they have the same trend without any abrupt changes. However the relative areas of the two components behave very differently at high pressure and temperature. In the case of majorite the amount of $^{[8]}Fe^{2+}$ almost does not change with pressure and temperature within the range of uncertainty, while in the case of perovskite we clearly observe an increase of the relative area of the high-QS component with pressure and temperature. Therefore, we suggest that the origin of the high-QS component in perovskite is different from that of majorite.

In order to understand the origin of the high QS-component we come back to the energy diagram for ferrous iron in a distorted cubic site (Figure 5) to explore possible spin configurations. As already mentioned, the stability of a particular spin configuration is determined by the relation between

crystal field splitting (Δ_C) and spin pairing energy (SPE). If SPE exceeds Δ_C HS state is stable (Figure 5) and only e_g orbitals contribute to the EFG and therefore to the QS value. With increasing pressure Δ_C increases, while SPE remains the same (*Sherman*, 1988) and when at a certain point Δ_C becomes higher than SPE, the intermediate-spin state (IS) becomes energy favorable: the two lower levels are completely populated by four 3d-electrons and the other two valence electrons occupy two of the three upper levels (Figure 5). Hence in this case the EFG (and consequently the value of QS) is determined by the population of t_{2g} orbitals. Finally, with the further increase of Δ_C and decrease of SPE low-spin state (LS) becomes energy favorable: all valence electrons are spin-paired and the EFG is equal to zero and does not contribute to the QS value (Figure 5).

According to *Keppler et al.* (1994) in the case of $^{[8-12]}Fe^{2+}$ in perovskite the energy difference between t_{2g} levels is much higher than between e_g levels, the crossover from HS to IS would cause an increase of quadrupole splitting. This is what is experimentally observed, hence we propose that the high QS of IS $^{[8-12]}Fe^{2+}$ in perovskite (about 4 mm/s) implies that $\Delta_3 >> \Delta_2$ (defined in Figure 5).

References

Badro J, Rueff J-P, Vankó G, Monaco G, Fiquet G and Guyot F (2004) Electronic transitions in perovskite: Possible non-convecting layers in the lower mantle. Science 305:383–386.

Bolvin H and Kahn O (1995) Ising model for low-spin high-spin transitions in molecular compounds; within and beyond the mean-field approximation. Chem Phys 192:295–305.

Burns RG (1970) Mineralogical Applications of Crystal Field. Cambridge University Press, Cambridge.

Goncharov AF, Haugen BD, Struzhkin VV, Beck P and Jacobsen S (2008) Radiative conductivity in the Earth's lower mantle. Nature 456:231–234.

Hatch DM and Ghose S (1989) Symmetry analysis of the phase transition and twinning in $MgSiO_3$ garnet: Implications to mantle mineralogy. Am Mineral 74:1221–1224.

Horiuchi H, Ito E and Weidner DJ (1987) Perovskite-type $MgSiO_3$: Single-crystal X-ray diffraction study. Am Mineral 72:357–360.

Huggins FE (1975) The 3d levels of ferrous iron in silicate garnets. Am Mineral 60:316–319.

Ingalls R (1964) Electric-field gradient tensor in ferrous compounds. Phys Rev 133A:787–795.

Jepchoat AP, Hriljac JA, McCammon CA, O'Neill HStS, Rubie DC and Finger LW (1999) High-resolution X-ray powder diffraction and Rietveld refinement of two $(Mg_{0.95}Fe_{0.05})SiO_3$ perovskite samples synthesized under different oxygen fugacity conditions. Am Mineral 8:214–220.

Keppler H, McCammon CA and Rubie DC (1994) Crystal-field and charge-transfer spectra of $(Mg,Fe)SiO_3$ perovskite. Am Mineral 79:1215–1218.

Keppler H, Dubrovinsky LS, Narygina OV and Kantor I (2009) Optical absorption and radiative thermal conductivity of silicate perovskite to 125 gigapascals. Science 322:1529–1532.

Lin JF, Struzhkin VV, Jacobsen SD, Hu MY, Chow P, Kung J, Liu H, Mao HK and Hemley RJ (2005) Spin transition of iron in magnesiowüstite in the Earth's lower mantle. Nature 436:377–380.

McCammon CA, Rubie DC, Ross II CR, Sieifert F and O'Neill HStC (1992) Mössbauer spectra of $^{57}Fe_{0.05}Mg_{0.95}SiO_3$ perovskite at 80 and 298 K. Am Mineral 77:894–897.

McCammon CA (1998) The crystal chemistry of ferric iron in $Fe_{0.05}Mg_{0.95}SiO_3$ perovskite as determined by Mössbauer spectroscopy in the temperature range 80–293 K. Phys Chem Minerals 25:292–300.

McCammon CA, Kantor IYu, Narygina OV, Rouquette J, Ponkratz U, Sergueev I, Mezouar M, Prakapenka V and Dubrovinsky LS (2008) Exceptional stability of intermediate-spin ferrous iron in lower mantle perovskite. Nature Geosci 1:684–687.

Sherman DM (1988) Structural and Magnetic Phase Transitions in Minerals, Advances in Physical Geochemistry. Ghose S, Coey JMD and Salje E. Springer (ed) New York 7:113–128.

Speziale S, Milner A, Lee VE, Clark SM, Pasternak MP, and Jeanloz R (2005) Iron spin transition in Earth's mantle. Proc Natl Acad Sci U S A 102:17918–17922.

Sturhahn W, Jackson JM and Lin J-F (2006) The spin state of iron in minerals of Earth's lower mantle. Geophys Res Lett 32: L12307.

Tsuchiya T, Wentzcovitch RM, da Silva CRS and de Gironcoli S (2006) Spin transition in magnesiowüstite in earth's lower mantle. Phys Rev Lett 96: 198501.

BORON AND BORON-RICH SOLIDS AT HIGH PRESSURES

ALAIN POLIAN*, SERGEY V. OVSYANNIKOV,
MICHEL GAUTHIER, PASCAL MUNSCH,
JEAN-CLAUDE CHERVIN, GILLES LEMARCHAND
Institut de Minéralogie et de Physique des Milieux Condensés, CNRS, Université Pierre et Marie Curie Paris 6, 140 rue de Lourmel, 75015 Paris, France

Abstract Boron seems to be the indispensable ingredient to obtain materials with high hardness. It exists under many different structures. The simplest member of the family, α-boron is based on an arrangement of slightly distorted B_{12} icosahedra in a rhombohedral unit cell. $B_{12}X_2$ compounds, with X = O, P, As, are based on the α-boron structure, with the X atoms in the inter-icosahedra space. The stability of α-boron has been studied by x-ray diffraction and Raman scattering up to 100 GPa, showing no sign of phase transformation, and by Raman scattering for $B_{12}P_2$ and $B_{12}As_2$ with the observation of phase transformation in the 80 GPa range.

Keywords: Very hard compounds, boron compounds, x-ray diffraction, Raman scattering

1. Introduction

Elemental boron and boron-rich solids have many applications in research and industry. In particular, boron seems to be a key element to obtain compounds with high hardness, and a less sensitivity to oxidation than carbon. In the last 20 years, no less that 16 international symposia were entirely dedicated to the results obtained on these compounds (*Gurin and Korsukova*, 2004; *Emin et al.*, 1991). Boron has the second most complicated structure among the elements (*Donohue*, 1974), after sulphur. At ambient conditions, it exists in various complex crystal structures, all dominated by the icosahedral B_{12} cluster. These icosahedra can be interlinked by strong covalent bonds in

* E-mail: Alain.Polian@pmc.jussieu.fr

E. Boldyreva and P. Dera (eds.), *High-Pressure Crystallography: From Fundamental Phenomena to Technological Applications*, DOI 10.1007/978-90-481-9258-8_21,

different ways to form several polymorphs, such as the α-rhombohedral B_{12}, (α-B_{12}, 12 atoms *i.e.* one icosahedron in the unit cell), or β-rhombohedral B_{105} (105 atoms in the unit cell), the most common of these compounds, both belonging to the same space group $R\bar{3}m$. Superconductivity has been recently found in β-boron (*Eremets et al.*, 2001), which has stimulated theoretical calculations (*Papaconstantopoulos and Mehl*, 2002; *Calandra et al.*, 2004; *Ma et al.*, 2004). Very recently (*Oganov et al.*, 2008), a new polymorph of boron, ionic γ-boron with 28 atoms in the unit cell has been synthesized at high pressure and high temperature, again based on icosahedra.

The pressure dependence of the vibrational properties of α-boron were measured by Raman scattering at ambient temperature up to 30 GPa and compared with *ab initio* lattice dynamics calculations (*Vast et al.*, 1997). This enabled an unambiguous assignment of all the features, including the remarkably narrow mode at 524 cm^{-1}, attributed to a highly harmonic librational mode of the icosahedron. Since then, two papers have dealt with high-pressure structural properties of β-boron; the first one to 30 GPa (*Ma et al.*, 2003) and the second to 100 GPa (*Sanz et al.*, 2002). In this last paper, the authors claim a pressure-induced amorphisation around 100 GPa, and discussed the relative stability of the intra- and inter-icosahedral bonds.

Few experimental works were published on the properties of α-boron. It is only very recently (*Kaneshige et al.*, 2007; *Fujii et al.*, 2007) that new results were obtained, both on powder samples. The first one presented studies of conductivity up to 112 GPa without any pressure transmitting medium (PTM) and Raman scattering up to 80 GPa using Daphne oil as a PTM, the second one (*Fujii et al.*, 2007) on x-ray diffraction up to 106 GPa and Raman scattering up to 75 GPa. We have recently measured the equation of state of α-boron up to 100 GPa on a single crystal, and measured also the Raman scattering (*Polian et al.*, 2008). These results show that the structure is stable up to this pressure, and the lowest frequency E_g mode (524 cm^{-1}) decreases from 20 GPa up.

Calculations predict that the structure of α-B_{12} is stable in the 210 (*Mailhiot et al.*, 1990) – 270 (*Zhao and Lu*, 2002) GPa range, which would make it the most stable elemental structure. Nevertheless, recently, new *ab initio* calculations (*Häussermann et al.*, 2003) have predicted a structural change α-B_{12} → α-Ga-type boron phase accompanied by a non-metal–metal transition at a pressure of about 74 GPa, in agreement with a fully unconstrained variable-cell evolutionary simulations at 100 GPa (*Oganov et al.*, 2008). These predictions need to be clarified and confirmed, and the hypothetical high-pressure structure (fcc (*Mailhiot et al.*, 1999) or bct (*Zhao and Lu*, 2002)) has to be possibly determined.

$B_{12}P_2$ and $B_{12}As_2$ have the same structure as α-B_{12}, with the pnictogen atoms in inter-icosahedral positions, hence modifying the inter-icosahedral interaction, but leaving almost unchanged the intra-icosahedral one. Not only will their study shed light on the pure α-boron properties, but they may serve as prototype for the very hard boron based compounds. Hence, the stability of their structure is interesting and important to establish. The scientific information concerning the structural and vibrational properties of $B_{12}P_2$ and $B_{12}As_2$ is extremely poor: nothing about the first one and only one publication on the second one by Raman scattering up to 15 GPa (*Pomeroy et al.*, 2004).

In the present paper, we will present new results obtained on $B_{12}P_2$ and $B_{12}As_2$ by Raman scattering measurements up to 110 GPa, showing the possibility of a phase transformation around 80 GPa. These results will be compared with those obtained on α-boron.

2. Experimental

All the samples used in the present study were provided by T.L. Aselage, from Sandia Laboratories, Albuquerque, NM (USA). The microcrystalline samples of α-B_{12} were single crystals prepared by recrystallization from solution of isothermal saturation of molten palladium–boron alloys, using a vapour source of boron. Single crystals of $B_{12}P_2$ and $B_{12}As_2$ were grown by a top-seeded solution technique at 1,260°C using molten nickel as a solvent (*Yang and Aselage*, 1995).

We used a membrane diamond cell (*Le Toullec et al.*, 1998; *Chervin et al*., 1995), with bevelled diamond anvils whose culet was 300 μm for the bevel and 100 μm for the center. The gasket was made of rhenium, with an initial thickness of 20 μm. The sample, 10 × 10 × 3 μm^3 was placed together with a ruby sphere (*Chervin et al.*, 2001) 3 μm in diameter at the center of the 50 μm of diameter hole. The pressure transmitting medium was neon, loaded at high pressure (*Couzinet et al.*, 2003). The pressure was measured *in situ* by the ruby fluorescence (*Mao et al.*, 1986), the equation of state of neon (*Hemley et al.*, 1989) or in Raman scattering by the pressure dependence of the first order Raman line of the diamond anvil tip (*Baer et al.*, 2008).

Raman scattering experiments were performed on a Jobin-Yvon T64000 triple monochromator spectrometer, with 100 mW of the 514.5 nm line of an Ar^+ laser.

X-ray diffraction experiments were performed at the ID27 beamlines of the ESRF, in Grenoble (France). The wavelength was 0.3738 Å (33.2 keV). The spot was focussed down to 5 × 5 Fm, and the cell was rotated between

−17° and +17° in order to increase the number of diffraction spots. The detector was a MAR 345 Image plate. The spectra were analysed using the Fit2d software (*Hammersley*, 1995).

3. Experimental Results

α-Boron, $B_{12}As_2$ and $B_{12}P_2$ belong to the same space group, $R\bar{3}m$, and are based on the same icosahedra, the boron compounds having just two pnictogen atoms inserted in the inter-icosahedral space (Figure 1).

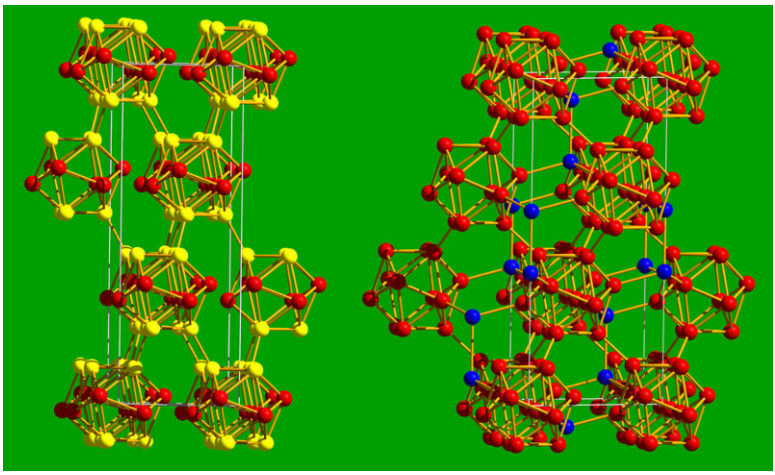

Figure 1. Structure of α-boron (*left*): yellow atoms are at polar positions, and red ones at equatorial positions; structure of $B_{12}X_2$ (*right*): red atoms are boron, and blue ones the phosphorus or arsenic atoms.

3.1. α-BORON

3.1.1. *Structural Properties*

The structural properties of α-boron were measured by x-ray diffraction up to 100 GPa. In Figure 2, they are compared with unpublished results by *Fujii et al.* (2007), and results on β-boron (*Sanz et al.,* 2002). From these data, the equation of state was deduced, and the bulk modulus is $B_0 = 207.1 \pm 12.8$ GPa, and a $B' = 4.2 \pm 0.3$. This is in fairly good agreement with previous results, both experimental and theoretical. Moreover, no sign of phase transformation or amorphisation is observable from our results.

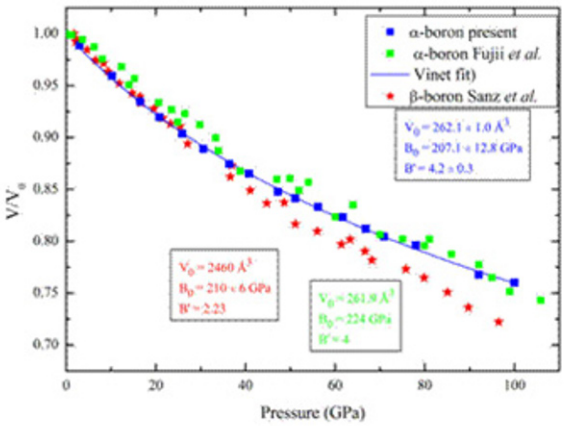

Figure 2. Experimental equation of stats of α-boron compared with other studies on α- and β-boron.

3.1.2. *Raman Scattering*

At the Γ point, the modes decompose as:

$$4\ A_{1g} + 2\ A_{2g} + 6\ E_g + 2\ A_{1u} + 4\ A_{2u} + 6\ E_u$$

where $1A_{1u} + 1E_u$ are acoustic modes, $3\ A_{1u} + 5E_u$ are infrared active and $4\ A_{1g} + 6\ E_g$ are Raman active.

All the Raman active modes have been observed and followed as a function of pressure up to 100 GPa (Figure 3). Again, as in the case of the x-ray diffraction results, there is no sign of approach of a phase transformation. The frequency decrease of the 524 cm^{-1} mode might indicate a "pre-destabilization" of the structure. Nevertheless, there is no broadening of this mode in the "softening" pressure range.

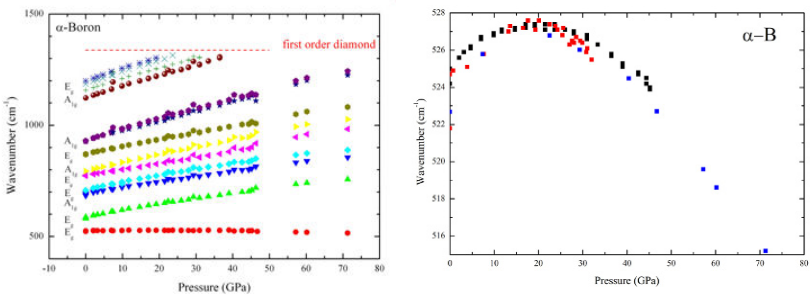

Figure 3. Pressure dependence of the Raman lines of α-boron. Right: detail of the 524 cm^{-1} mode pressure dependence.

3.1.3. *$B_{12}P_2$ and $B_{12}As_2$*

In these two compounds, there are 14 atoms in the unit cell, and therefore 42 modes of vibration, whose irreducible representations are:

$$5\ A_{1g},\ 2\ A_{2g},\ 7\ E_g,\ 2\ A_{1u},\ 5\ A_{2u},\ 7\ E_u.$$

The Raman active modes are 5 A1g and 7 Eg i.e. 12 different frequencies corresponding to 19 degrees of freedom.

Until now, only one study was performed on $B_{12}X_2$ under pressure, on $B_{12}As_2$ up to 15 GPa (*Pomeroy et al.*, 2004). In this paper, the authors could measure the pressure dependence of 11 vibrational modes from the 12 allowed, and deduced their Grüneisen parameters.

A typical spectrum obtained at ambient conditions is shown in Figure 4.

We performed several experiments, each time with neon as a pressure transmitting medium, and with small pieces of both compounds. The results are shown in Figures 5 and 6. In $B_{12}P_2$, there is a good agreement with the

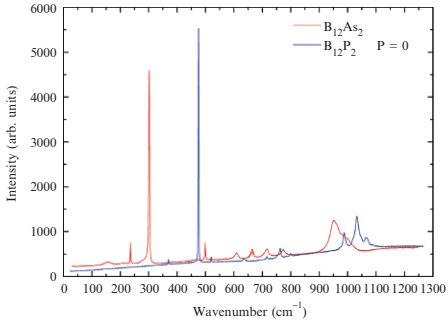

Figure 4. Raman spectra both samples at ambient pressure.

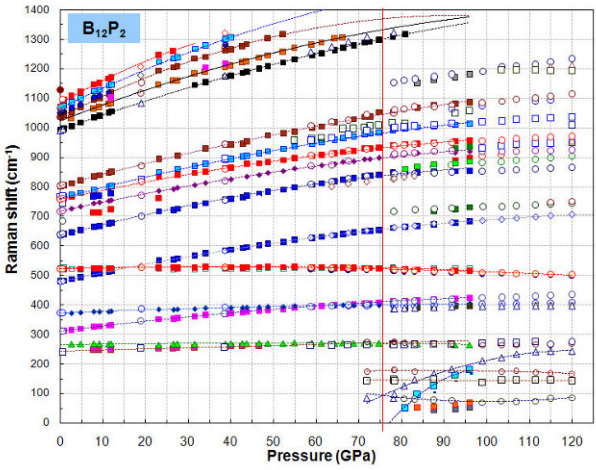

Figure 5. Pressure dependence of the observed Raman active mode in $B_{12}P_2$.

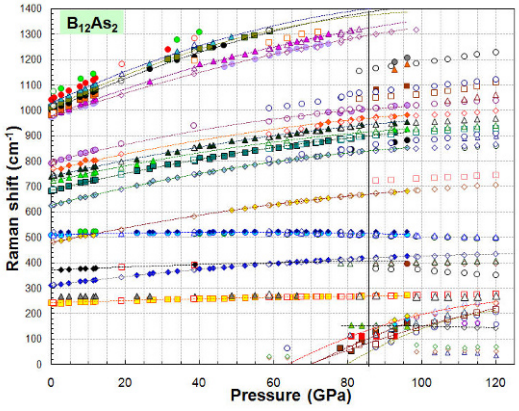

Figure 6. Pressure dependence of the observed Raman active modes in $B_{12}As_2$.

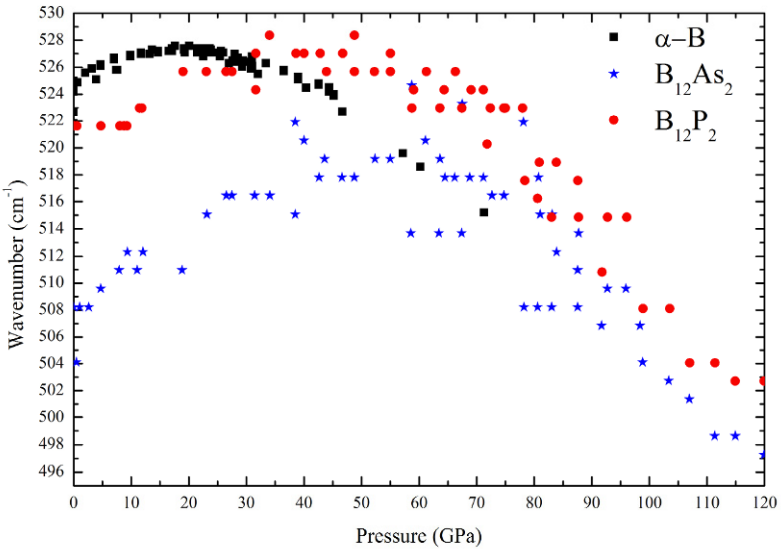

Figure 7. Comparison of the pressure dependence of the librational modes in α-boron, $B_{12}P_2$ and $B_{12}As_2$.

previous data obtained up to 15 GPa (*Pomeroy et al.*, 2004), and the results obtained in $B_{12}As_2$ are consistent with $B_{12}P_2$, with a shift to lower frequencies due to the mass difference between arsenic and phosphorus.

The most interesting result deduced from the experiments shown in Figures 5 and 6 is the appearance of new peaks around 70–75 GPa in $B_{12}P_2$, and 80–85 GPa in $B_{12}As_2$. From these results it seems to be clear that the general structure of both crystals is preserved, in the sense that the vibrations typical of the B_{12} icosahedron is preserved, as can be deduced from Figure 7, which do not present any disappearance, nor discontinuity up to the highest

pressure reached. This is a clear proof of the stability of this structure. Moreover, as the Raman spectra clearly show, there is no amorphisation up to 120 GPa, in contrast with what happens in β-boron around 100 GPa (*Sanz et al.*, 2002).

Another interesting result presented in Figure 7 is the comparison of the pressure dependence of the icosahedron librational mode in the three studied compounds. Like in pure boron, this mode in both $B_{12}P_2$ and $B_{12}A_2$ present first a hardening with pressure followed by a softening. The frequency maximum is reached around 20 GPa in the case of pure boron, whereas it lays more around 50 GPa for the two other compounds. In all cases, and within the accuracy of the measurements, the behaviour of this mode in the three compounds seems to converge at high pressure. Such a behaviour may be the sign of an approaching phase transformation in which the icosahedra would be destroyed, but it is still just a hypothesis that has to be confirmed both by *ab initio* calculations and by measurements at higher pressure.

4. Conclusions

In this paper we report x-ray diffraction and Raman measurements on pure α-boron and $B_{12}P_2$ and $B_{12}As_2$ up to 120 GPa. These crystals, all build on the same icosahedra of boron atoms, are very hard materials, and the present study proves that they are also very stable compounds against pressure in the pnictides compounds, the intericosahedral chain seems to destabilize the low pressure structure, but preserving the existence of the icosahedra. The phase transformation occurs around 70–75 GPa in the crystal with phosphorus, and 80–85 GPa in that with arsenic.

References

Baer B.J., M.E. Chang, W.J. Evans, J. Appl. Phys. **104**, 034504 (2008).
Calandra M., N. Vast, F. Mauri, Phys. Rev. **B69**, 224505 (2004).
Chervin J.C., B. Canny, J.M. Besson, P. Pruzan, Rev. Sci Instrum. **66**, 2595 (1995).
Chervin J.C., B. Canny, M. Mancinelli, High Press. Res. **21**, 305 (2001).
Couzinet B., N. Dahan, G. Hamel, J.C. Chervin. High Press. Res **23**, 409 (2003).
Donohue J., The Structures of The Elements, Wiley, New York (1974).
Emin D., T. Aselage, A.C. Switendick, B. Morosin, C.L. Beckel (Eds.) *Boron-Rich Solids*, AIP Conference Proceedings vol 231, New York (1991).
Eremets E.I., V.V. Struzhkin, H.K. Mao, R.J. Hemley, Science **293**, 272 (2001).
Fujii Y., Mori Y., Nishii T., Fujii A., Hyodo H., Takarabe K., Kimura K., 21th AIRAPT Conference, 2007.

Hammersley A.P., ESRF Internal Report, EXP/AH/9501,FIT2D V6.4 Reference Manual V1.18 (1995).
Häussermann U., S.I. Simak, R. Ahuja, B. Johansson, Phys. Rev. Lett. **90**, 065701 (2003).
Hemley R.J., C.S. Zha, A.P. Jephcoat, H.K. Mao, L.W. Finger, Phys. Rev. **B39**, 11820 (1989).
Gurin V., M. Korsukova (Eds.) Boron, borides and related compounds, Proc. 14th International Symposium on Boron, Borides and Related Compounds, J. Sol. St. Chem. **177**, 381–631 (2004).
Kaneshige M., Hirayama S., Yabuushi T., Matsuoka T., Shimizu K., Mita Y., Hyodo H., Kimura K., J. Phys. Soc. Jpn., **76**, Suppl. A, 19 (2007).
Le Toullec R., J.P. Pinceaux, P. Loubeyre, High Press. Res. **1**, 77 (1988).
Ma Y., J.S. Tse, D.D. Klug, R. Ahuja, Phys. Rev. **B70**, 214107 (2004).
Ma Y., C.T. Prewitt, G. Zou, H.K. Mao, R.J. Hemley, Phys. Rev. **B67**, 174116 (2003).
Mailhiot C., J.B. Grant, A.K. McMahan, Phys. Rev. **B42**, 9033 (1990).
Mao H.K., J. Xu, P.M. Bell, J. Geophys. Res. **91**, 4673 (1986).
Oganov A.R., J. Chen, C. Gatti, Y. Ma, Y. Ma, C.W. Glass, Z. Liu, T. Yu, O.O. Kurakevych, V.L. Solozhenko, Nature **457**, 863 (2009).
Papaconstantopoulos D.A., M.J. Mehl, Phys. Rev. **B65**, 172510 (2002).
Polian A., J.C. Chervin, P. Munsch, M. Gauthier, J. Phys. Conf. **121**, 042017 (2008).
Pomeroy J.W., M. Kuball, H. Hubel, N.W.A. van Uden, D.J. Dunstan, R. Nagarajan, J.H. Edgar, J. Appl. Phys. **96**, 910 (2004).
Sanz D.N., P. Loubeyre, M. Mezouar, Phys. Rev. Lett. **89**, 245901 (2002).
Vast N., S. Baroni, G. Zerah, J.M. Besson, A. Polian, M. Grimsditch, J.C. Chervin, Phys. Rev. Lett. **78**, 693 (1997).
Yang P, T.L. Aselage, Powder Diffr. **10**, 263 (1995).
Zarechnaya E.Y., L. Dubrovinsky, N. Dubrovinskaia, N. Miyajima, Y. Filinchuk, D. Chernyshov, V. Dmitriev, Sci. Technol. Adv. Mater. **9**, 044209 (2008).
Zhao J., J.P. Lu, Phys. Rev. **B66**, 092101 (2002).

NON-MOLECULAR CARBON DIOXIDE AT HIGH PRESSURE

MARIO SANTORO[1,2*]
[1]*LENS, European Laboratory for Non-linear Spectroscopy, Sesto Fiorentino, Firenze, Italy,* [2]*IPCF-CNR, UOS, c/o Universit`a di Roma "La Sapienza," Rome, Italy*

Abstract A brief review on the high pressure, non-molecular phases of CO_2, which have been all discovered along the present decade, will be presented. It includes references to experimental studies, based on the XRD and optical spectroscopy techniques coupled to the diamond anvil cell (DAC), and to *ab initio* simulation studies. The matter is still under strong debate, and many open issues are left on the high pressure-high temperature phase diagram of this important substance.

Keywords: Carbon dioxide, high pressure, x-ray diffraction, optical spectroscopy

1. Introduction

The high-pressure phase/kinetic diagram of carbon dioxide includes up to seven solid phases and an amorphous form (*Giordano and Datchi*, 2007; *Iota et al.*, 2007; *Santoro and Gorelli*, 2006) (Figure 1). Although CO_2 is a very simple molecule, the solid–solid phase transitions in this system are affected by extremely large metastabilities, which prevented to identify the true phase boundaries above 10–15 GPa. In this pressure range strikingly different kinetic boundaries have been found in the various studies, depending on the different P–T paths and analysis techniques. It is remarkable that beyond the well known phase I (dry ice) all the other transformations, including the high P–T decomposition of CO_2 into carbon and oxygen (*Tschauner et al.*, 2001), have been discovered, along the past two decades, by means of optical spectroscopy. Experimental and *ab initio* computational studies have been showing that all the phases below 30 GPa are molecular crystals (*Santoro and Gorelli*, 2006). We point out that a special discussion

* E-mail: santoro@lens.unifi.it

E. Boldyreva and P. Dera (eds.), *High-Pressure Crystallography: From Fundamental Phenomena to Technological Applications*, DOI 10.1007/978-90-481-9258-8_22,

has been devoted through the recent years to phases II and IV, which where supposed to exhibit intermediate character between molecular and non-molecular, extended solids, based on the x-ray diffraction (XRD) investigation (*Park et al.*, 2003; *Yoo et al.*, 2002). This view has been challenged by an optical spectroscopy study, where it was shown that the vibrational pattern of these phases is only slightly perturbed with respect to phase I (*Gorelli et al.*, 2004). Also, the equation of state (EOS) of these crystals closely resembles the high-pressure extrapolation of the EOS of phase I (*Santoro and Gorelli*, 2006). Computational studies have been showing that the intermediate structures proposed by the XRD investigation are largely unstable, and that indeed both phases II and IV are strictly molecular crystals (*Bonev et al.*, 2003). To my opinion, the most striking high-pressure phenomenon which has been found in CO_2 so far is the reversible transformation to non-molecular, extended solids above 30 GPa, where the thermodynamic phase boundaries are severely confused. This confusion is most likely to be due to the energetic competition of many extended, meta-stable structures, as can be inferred from the results of *ab initio* calculations. Below we consider the non-molecular phases V (Section 2) and VI (Section 4), and on the non-molecular form a-carbonia (Section 3).

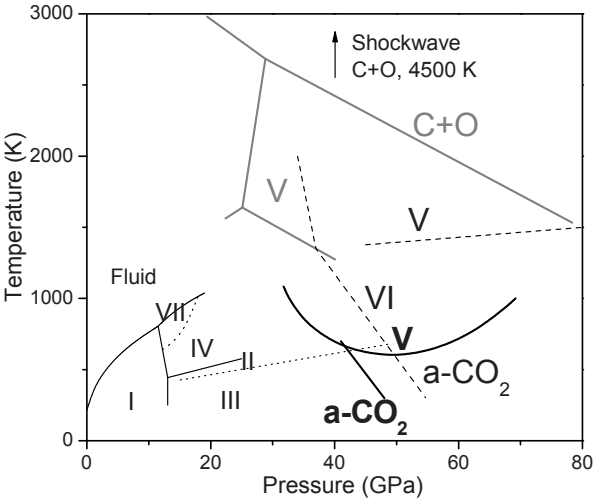

Figure 1. High-pressure phase/kinetic diagram of CO_2 (*Giordano and Datchi*, 2007; *Iota et al.*, 2007; *Santoro and Gorelli*, 2006). Continuous lines below 25 GPa are phase boundaries. Dotted lines below 30 GPa and 1,000 K: kinetic boundaries for forming phase IV from VII, and II from III. Lines above 25 GPa: kinetic boundaries for forming the non-molecular phases V and VI, the form a-CO_2, and the dissociated material, C+O, from molecular CO_2 (dashed (*Iota et al.*, 2007), thick grey (*Tschauner et al.*, 2001), and thick black lines (*Javier et al.*, 2008; *Santoro et al.*, 2004, 2006) correspond to different studies).

2. Phase V

The discovery of non-molecular, crystalline carbon dioxide, indicated as phase V, was achieved by means of Raman spectroscopy (*Iota et al.*, 1999). In fact, the CO_2 in the starting molecular phase III was laser-heated to 1,800 K at about 40 GPa, and then the Raman spectrum of the transformed material quenched to room temperature was measured. The vibrational data identified this phase as an extended solid with carbon–oxygen single bonds, similar to the quartz polymorph of SiO_2. In this picture, the carbon atom is tetrahedrally coordinated by oxygen atoms, forming a three-dimensional network of corner shearing CO_4 tetrahedra. The main point supporting the analogy between phase V and quartz was the sharp peak observed at about 800 cm^{-1} (40 GPa), which was assigned to the symmetric, inter-tetrahedral stretching of C–O–C single bonds. The Raman spectrum of CO_2-V was subsequently confirmed by other experimental investigations (*Santoro et al.*, 2004), where *in situ* Raman measurements on the laser heated DAC have unveiled that the transformation of CO_2 into phase V occurs at temperatures as low as 600 K at about 50 GPa. Only one XRD study has been performed and published on phase V so far (*Yoo et al.*, 1999), showing that this material is indeed made of CO_4 tetrahedral units arranged in an orthorhombic, trydimite-like structure (space group $P2_12_12_1$), as shown in Figure 2. Large volume changes are associated with the III to V transition, equal to 15.3% (12.6%) at 40 (60) GPa. Also, phase V was found to exhibit a very high bulk modulus, equal to 365 GPa, which is higher than that of all the SiO_2 crystals.

Theoretical studies based on *ab initio* calculations have been predicting the tetrahedral structure of phase V (*Dong et al.*, 2000a, b; *Holm et al.*, 2000; *Serra et al.*, 1999). On the other hand, a tetragonal, β-cristobalite arrangement of the CO_4 units resulted to be the most stable structure among a variety of investigated crystals, including different types of trydimite, quartz, coesite, chalcopyrite, and crystobalite (*Dong et al.*, 2000a, b); specifically, β-cristobalite is much more stable than the trydimite structures by at least 0.2 eV/CO_2 (binding energy), corresponding to about 2,400 K. Also, the predicted bulk modulus for a variety of tetrahedrally coordinated phases ranges between 1/2 and 1/3 of the measured one (*Dong et al.*, 2000a, *Serra et al.*, 1999). The β-cristobalite and trydimite structures are very similar. In fact, tetrahedral carbon atoms form a hexagonal network in tridymite and a diamond network in β-cristobalite. In Figure 2, the XRD patterns of the simulated $P2_12_12_1$ and β-cristobalite structures are compared to the experimental XRD pattern of phase V. It is clear that the simulated $P2_12_12_1$ crystal

exhibits diffraction peaks rather different from those of the experimental sample. The XRD pattern of the simulated β-cristobalite crystal only shows three peaks between 5 and 14 degrees because of the high symmetry of this structure, which is even less compatible with the experimental data. On the other hand, the Raman spectrum of the simulated β-cristobalite CO_2 was found to reproduce fairly well the most intense experimental Raman peaks of phase V (*Santoro and Gorelli*, 2006).

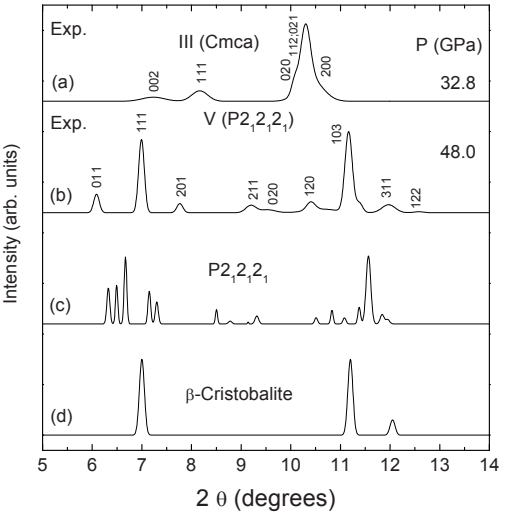

Figure 2. X-ray diffraction patterns of solid CO_2 at high pressures and room temperature (λ = 0.3738 Å). (a), (b): measured patterns of molecular phase III and non-molecular phase V, respectively (*Yoo et al.*, 1999); (c), (d) patterns of simulated, non-molecular $P2_12_12_1$ and β-cristobalite CO_2, respectively (*Dong et al.*, 2000a). The patterns have been analytically reproduced. Miller indices (*hkl*) are indicated for phases III and V.

It appears that a lot of work has still to be done for reconciling the experimental and *ab initio* computational findings and definitely solving the structure of CO_2-V. Surely, additional experimental XRD data should be provided. It could be that Raman spectroscopy is not suitable for discriminating between different tetrahedral structures. The IR absorption spectrum should also be investigated, for providing additional constrains to the interpretation of XRD data. Finally, it should be considered whether the experimental samples of CO_2-V could actually be made of a metastable mixture of different tetrahedral phases, such as trydimite, cristobalite and/or other structures. Indeed, energetically disfavoured phases could be produced in the experimental samples, instead of (or together with) the thermodynamically stable phase, for kinetic reasons, which in turn makes the investigation of the high-pressure phase diagram of CO_2 rather difficult.

3. Amorphous Carbonia

Recently, the non-molecular, extended, glassy form of carbon dioxide, which was predicted to exist by *Serra et al.* (1999) was experimentally discovered (*Santoro et al.*, 2006), and its structure was resolved by means of optical spectroscopy (*Javier et al.*, 2008). The IR spectrum of the new material (a-carbonia, or a-CO_2) exhibits three prominent, broad bands: A, B, and C (Figure 3).

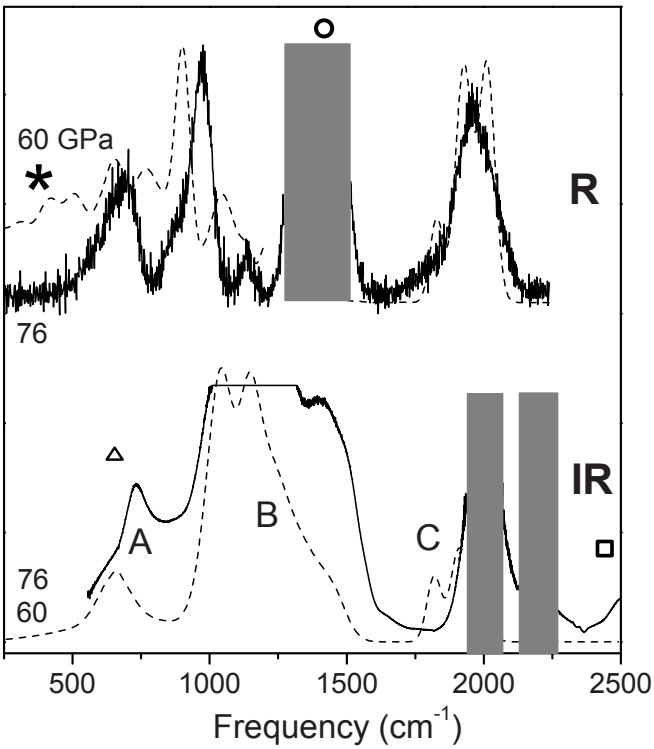

Figure 3. Room T experimental (continuous lines) and theoretically predicted (dashed lines) Raman (R) and IR (IR) spectra of a-CO_2 (*Javier et al.*, 2008; *Santoro et al.*, 2006). Symbols: approximate frequency of the lattice phonons (star) and the internal modes (open triangle, dot and square) of molecular, solid CO_2. Blocks: frequency ranges of diamond bands. The absorption of band B is partially saturated.

Based on the comparison between the experimental and the *ab initio* calculated spectra, one can conclude that the main contributions to band B is made by the antisymmetric C–O–C stretching modes of silica-like CO_4 units. Also, the band C is entirely due to the stretching mode of the carbonyl (C=O) units of partially reacted sites, where carbon is in a threefold coordination. The picture is that of an extended, three-dimensional network

of interconnected CO_4 and CO_3 unites, where the amount of silica-like sites is equal to about 60%. This picture is also supported by the comparison of the experimental and theoretical Raman spectra (Figure 3), which leads to interpreting the broad peak around 900 cm^{-1} as due essentially to the symmetric C–O–C stretching mode of the CO_4 coordination sites, while the broad peak at about 2,000 cm^{-1} is entirely due to the carbon-oxygen stretching mode of the CO_3 sites, similarly to case of the IR spectrum. Carbon in a higher coordination, five and/or six, was ruled out in a-carbonia, at variance with the case of silicon in dense SiO_2 structures. Indeed, the transformation to sixfold coordinated carbon dioxide is predicted to occur in the multi-megabar pressure range (*Holm et al.*, 2000; *Lee et al.*, 2009). Enthalpic considerations suggested that a-carbonia is a metastable intermediate state of the transformation of molecular CO_2 into fully tetrahedral phases.

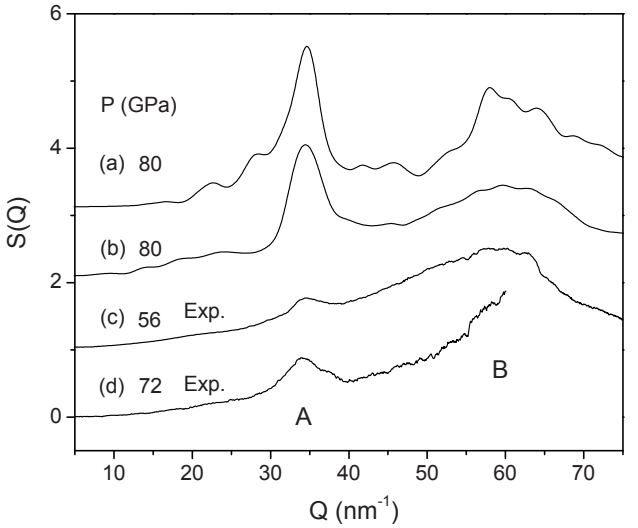

Figure 4. Static structure factor, S(Q), of a-CO_2 (*Santoro et al.*, *2006*). (a) and (b): theoretical S(Q) for CO_4 and higher (up to octahedral) carbon coordination, respectively. (c) and (d): temperature quenched samples synthesized along different P–T paths.

The amorphous, extended character of a-carbonia was also suggested by the XRD (Figure 4) (*Santoro et al.*, 2006). The static structure factor of the this material, S(Q), where Q is the exchanged wave-vector, was measured. The S(Q) is dominated by a broad peak centred around 34 nm^{-1} (peak A), which corresponds to a length scale $2\pi/Q \approx 1.85$ Å, and a much broader peak around 58 nm^{-1} (peak B). The S(Q) was also measured upon decreasing pressure, showing a positive pressure shift of peak A ($\Delta Q = 1.63$ nm^{-1} for $\Delta P = 50$ GPa), consistent with pressure-induced densification. The pressure

shift is, however, very small and parallels that of the strongest CO_2-V Bragg peak, suggesting that the two materials have similar and very small compressibility. In the Figure 4 the theoretical S(Q), calculated on an extended, amorphous structure obtained in a previous first-principles molecular dynamics simulation at 100 GPa (*Serra et al.*, 1999) is shown. The simulated structure is fully tetrahedral, and the sample contains a small number of unsaturated bonds, indicating incomplete polymerization. The theoretical S(Q) reproduces both the experimental peak A, which is mainly contributed by the correlation between nearest neighbour oxygen atoms, and peak B, although peak A exhibits a higher intensity in the theoretical pattern. However, similar agreement with the measured S(Q) can be obtained by considering a theoretical sample containing carbon in higher coordination (see caption to Figure 4). In this case the S(Q) was obtained by classical molecular dynamic simulations of a-SiO_2, brought to 28 GPa, which was found to contain similar proportions of four-, five-, and sixfold coordinated Si, by scaling its volume to that of simulated a-CO_2, and by artificially replacing the atomic form factor of Si with that of C. The similarity between the structure factors calculated with different local environments (from tetrahedral to octahedral) shows that the measured structure factor cannot be used to discriminate between differently coordinated local atomic environments. We note that there are technical limitations in the measurements of the S(Q) which make the experimental, quantitative investigation on the local structure of a-carbonia difficult. In fact, the XRD measurements are extremely challenging on this low Z, amorphous material, which only exhibits a very weak, diffuse x-ray scattering signal. This signal is superimposed to a huge background, 15–20 times stronger, due to the Compton scattering from diamond anvils. When such an intense background is subtracted, relevant errors can be introduced in the determination of the S(Q). The accessible Q range is then limited to 70–80 nm^{-1} by the DAC aperture, which severely limits the achieving of quantitative information on the microscopic structure in the 1 Å length scale. Therefore, the determination of the local structure of a-carbonia represents one important case when optical spectroscopy, instead of XRD, is the crucial route to solve the problem.

4. Phase VI

Another non-molecular, crystalline phase, CO_2-VI, was recently found, in coexistence with a-CO_2 (*Iota et al.*, 2007) (Figure 5). The Raman spectrum of this phase mixture exhibited three new sharp lines, with the strongest one at about 1,020 cm^{-1}, superimposed to the broad bands of a-carbonia. Although CO_2-VI was identified as an extended structure of carbon in

sixfold coordination, subsequent *ab initio* calculations have been showing that non-molecular, octahedral crystals of CO_2 are mechanically unstable at the experimental conditions, decomposing into molecular CO_2 (*Javier et al.*, 2008). One also tried to use the calculations, to identify the actual structure of CO_2-VI on the basis of hypothetical, crystalline structures which include both CO_4 and CO_3 coordination sites, similarly to a-carbonia. These crystals, which are meta-stable in the P–T range of phase VI, exhibit layered structures and differ from each other in the relative amounts of π and σ bonded oxygen atoms. The main (noncarbonylic) Raman peak of the predicted crystals, whose origin can be traced to the stretching of C–O single bonds, lies close to the observed main peak of phase VI, while its precise frequency depends strongly on the local environment. It was then concluded that the structure of CO_2-VI could, indeed, consist of some combination of CO_3 and CO_4 sites. Another study based on *ab initio* calculations have found hypothetical, meta-stable, layered structures composed of a two-dimensional network of corner-sharing CO_4 tetrahedra (*Togo et al.*, 2008).

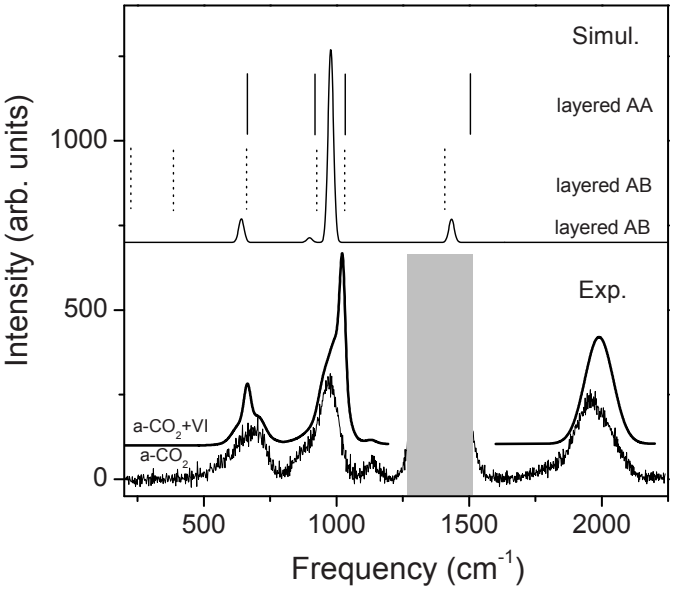

Figure 5. Raman spectra of phase VI and a-carbonia. Bottom part: experimental spectra of a-carbonia at 76 GPa (continuous line), as in Figure 3, and mixed a-carbonia/phaseVI at 60 GPa analytically reproduced from (*Iota et al.*, 2007) (thick, continuous line). In the upper part there are spectra of simulated samples at 60 GPa: AB layered, CO_4 structures (spectrum (*Lee et al.*, 2009), dotted vertical sticks (*Togo et al.*, 2008)), and AA layered, CO_4 structure (continuous vertical sticks (*Togo et al.*, 2008)). Block: frequency range of the diamond band.

Indeed two such crystals, with strongly competing energies, and AA and AB stacking of the layers, respectively, have been obtained as the result of geometrically, likely transition pathways derived from the dynamical instability of the molecular crystals under pressures. The most intense peaks of phase VI remarkably agree with the calculated Raman frequencies for these crystals (Figure 5), thereby providing and alternative, and more convincing route for determining the structure of this phase. In two subsequent studies, based on *ab initio* calculations, the CO_4 crystal with AB layer stacking has been again found by means of a similar procedure, and both Raman intensities and frequencies have been calculated (*Lee et al.*, 2009; *Sun et al.*, 2009). It results that the experimental spectrum is fairly well reproduced by the calculations, as reported in Figure 5. We note that the calculated XRD patterns of the simulated, layered structures do not agree with the experimental one (*Iota et al.*, 2007), which in turn seems to cast a shadow on the interpretation of experimental data. It is likely to be the case that the overall quality of the measured XRD patterns is affected by the incomplete transformation of CO_2 into the non-molecular phase. It surely appears that additional XRD-based investigations are required for definite assessing the structure of phase VI.

5. Conclusions

I hope that the findings presented here make it clear, that the research on non-molecular CO_2 is an exciting and a rapidly developing topic, of great interest for both fundamental physics and chemistry. Many issues have still to be definitely addressed, such as: (i) the thermodynamically stable phase in the P–T range where a so-called "phase V" is experimentally observed, (ii) the kind of non-molecular solid or of phase mixture of non-molecular solids, which actually characterize the experimentally observed "phase V", (iii) the structure of phase VI, (iv) the thermodynamic phase boundaries delimiting the non-molecular phases, (v) the possible existence of non-molecular, melted CO_2, (vi) the phase diagram of non-molecular CO_2 in the multimegabar range. All these problems could be solved only if experiments an *ab initio* calculations are combined. I think, that the rich, intriguing complexity emerging from the high-pressure transformations of the simple CO_2 molecules deserves a lot of investigations in the future.

ACKNOWLEDGEMENTS

My research at LENS is supported by the European Union under Contract RII3-CT2003-506350, and by "Firenze Hydrolab" through a grant by Ente Cassa di Risparmio di Firenze.

References

Bonev, S.A., Gygi, F., Ogitsu, T., and Galli G., 2003, High pressure molecular phases of solid carbon dioxide, *Phys. Rev. Lett.* **91**(6): 065501.

Dong, J., John, J., Tomfohr, K., Sankey, O.F., Leinenweber, K., Somayazulu, M., and McMillan, P.F., 2000a, Investigation of hardness in tetrahedrally bonded nonmolecular CO_2 solids by density-functional theory, *Phys. Rev. B* **62**(22): 14685–14689.

Dong, J., Tomfohr, J.K., and Sankey, O.F., 2000b, Rigid intertetrahedron angular interaction of nonmolecular carbon dioxide solids, *Phys. Rev. B.* **61**(9): 5967–5971.

Giordano, V.M., and Datchi, F., 2007, Molecular carbon dioxide at high pressure and high temperature, *Eur. Phys. Lett.* **77**(4): 46002–46007.

Gorelli, F.A., Giordano, V.M., Salvi, P.R., and Bini, R., 2004, Linear carbon dioxide in the high-pressure high-temperature crystalline phase, *Phys. Rev. Lett.* **93**(20): 205503.

Holm, B., Ahuja, R., Belonoshko, A., and Johansson, B., 2000, Theoretical investigation of high pressure phases of carbon dioxide, *Phys. Rev. Lett.* **85**(6): 1258–1261.

Iota, V., Yoo, C.S., and Cynn, H., 1999, Quartzlike carbon dioxide: an optically nonlinear extended solid at high pressures and temperatures, *Science* **283**(5407): 1510–1513.

Iota, V., Yoo, C.S., Klepeis, J.H., Jenei, Z., Evans, W., and Cynn, H., 2007, Six-fold coordinated carbon dioxide VI, *Nat. Mat.* **6**: 34–38.

Javier, J.A., Rousseau, R., Santoro, M., Gorelli, F. and Scandolo S., 2008, Mixed threefold and fourfold carbon coordination in compressed CO_2, *Phys. Rev. Lett.* **100:** 163002.

Lee, M.S., Montoya, J.A., and Scandolo, S., 2009, Thermodynamic stability of layered structures in compressed CO_2, *Phys. Rev. B* **79**(14): 144102.

Park, J.H., Yoo, C.S., Iota, V., Cynn, H., Nicol, M.F., and LeBihan, T., 2003, Crystal structure of bent carbon dioxide phase IV, *Phys. Rev. B* **68**(1): 014107.

Santoro, M., Gorelli F.A., Bini R., Ruocco G., Scandolo S., and Crichton W.A., 2006, Amorphous silica-like carbon dioxide, *Nature* **441**, 857–860.

Santoro, M., Lin, J.F., Mao, H.K., and Hemley, R.J., 2004, *In situ* high P–T Raman spectroscopy and laser heating of carbon dioxide, *J. Chem. Phys.* **121**(6): 2780–2787.

Santoro, M., and Gorelli, F.A., 2006, High pressure solid state chemistry of carbon dioxide, *Chem. Soc. Rev.* **35**(10): 918–931

Serra, S., Cavazzoni, C., Chiarotti, G.L., Scandolo, S., Tosatti, E., 1999, Pressure induced solid carbonates from molecular CO_2 by computer simulation, *Science* **284**(5415): 788–790.

Sun, J., Klug, D.D., Martoňák, R., Montoya, J.A., Lee, M.-S., Scandolo, S. and Tosatti, E., 2009, High-pressure polymeric phases of carbon dioxide, *Proc. Natl. Acad. Sci. USA* **10**: 6077–6081.

Togo, A., Fumiyasu, O., and Tanaka, I., 2008, Transition pathway of CO_2 crystals under high pressures, *Phys. Rev. B* **77**: 184101.

Tschauner, O., Mao, H.K., and Hemley, R.J. 2001, New transformations of CO_2 at high pressures and temperatures, *Phys. Rev. Lett.* **87**(7): 075701.

Yoo, C.S., Cynn, H., Gygi, F., Galli, G., Iota, V., Nicol, M., Carlson, S., Häusermann, D., and Mailhiot, C., 1999, Crystal structure of carbon dioxide at high pressure: "superhard" polymeric carbon dioxide, *Phys. Rev. Lett.* **83**(26): 5527–5530.

Yoo, C.S., Kohlmann, H., Cynn, H., Nicol, M.F., Iota, V., and LeBihan, T., 2002, Crystal structure of pseudo-six-fold carbon dioxide phase II at high pressures and temperatures, *Phys. Rev. B* **65**(10): 104103.

SIMPLE METALS AT HIGH PRESSURES

OLGA DEGTYAREVA*
Centre for Science at Extreme Conditions and School of Physics, the University of Edinburgh, United Kingdom

Abstract In this lecture we review high-pressure phase transition sequences exhibited by simple elements, looking at the examples of the main group I, II, IV, V, and VI elements. General trends are established by analyzing the changes in coordination number on compression. Experimentally found phase transitions and crystal structures are discussed with a brief description of the present theoretical picture.

Keywords: Simple elements, incommensurate crystal structure, phase stability

1. Introduction

Most of the metallic elements crystallize in the closely-packed atomic arrangements, body-centered cubic (bcc), face-centered cubic (fcc) and hexagonal close-packed (hcp) (*Young*, 1991). The main group IV, V, VI and VII semimetals and non-metals crystallize in open packed structures following the 8-N coordination rule. According to this rule, a structure is formed with a coordination number (i.e. the number of nearest neighbors) equal to 8-N, where N is the group number in the periodic table of elements. As a rule of thumb, most elements in the middle of the periodic table (the so-called transition metals), that crystallize in the closely-packed structures (see crosses in Figure 1), show no structural transitions or transition to other closely-packed structures. For example, Au transforms from fcc to hcp at pressures of 240 GPa and high temperatures (*Dubrovinsky et al.*, 2007). Most elements from the left and from the right of the periodic table (so-called simple or *sp*-elements) undergo on compression a series of structural phase transitions that show diverse and sometimes unexpectedly complex behavior. The non-metallic elements from the main group IV, V, and VI on the

* E-mail: O.Degtyareva@ed.ac.uk

E. Boldyreva and P. Dera (eds.), *High-Pressure Crystallography: From Fundamental Phenomena to Technological Applications*, DOI 10.1007/978-90-481-9258-8_23,

right of the periodic table having large initial atomic volume compared to the transition metals are strongly compressed under pressure, showing a transition to a metallic state with closely-packed structures (see naughts changing to crosses in Figures 1a and b). The main group I and II elements (the alkali and alkali-earth elements) on the left of the periodic table crystallize in closely-packed structures, however under pressure show anomalous behavior transforming to open packed structures (see crosses changing to naughts in Figures 1a and b). In comparison to the transition metals, they have very large initial atomic volumes that decrease drastically on pressure increase while the elements undergo transitions in atomic and electronic structure.

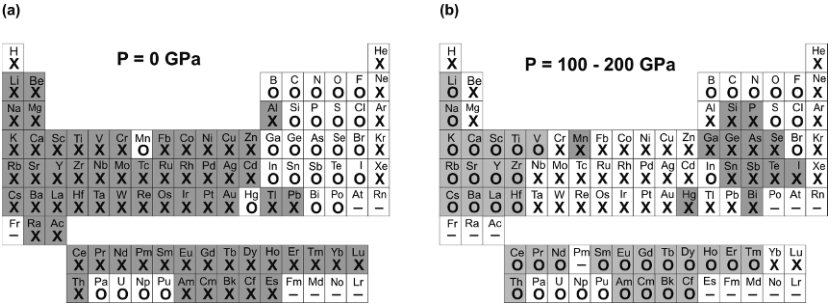

Figure 1. Periodic table with crystal structures of elements (a) at ambient pressure and (b) high pressure of 100–200 GPa (modified from *Young*, 1991). Crosses denote the closely-packed structures, such as body-centered cubic (bcc), face-centered cubic (fcc) and hexagonal close-packed (hcp) structures. Naughts denote open packed and distorted structures. In (b), data are taken from the papers discussed in the text. In (a), the closely-packed structures (crosses) are highlighted, in (b), the changes from crosses to naughts and from naughts to crosses are highlighted.

The high-pressure behavior of elements is described in several reviews, some of the recent being: (*Degtyareva*, 2006; *McMahon and Nelmes*, 2006; *Schwarz*, 2004; *Tonkov and Ponyatovsky*, 2005). In the present lecture we focus on the experimentally found transitions in atomic structure in the main group I, II, IV, V and VI elements with the emphasis on the most recent results reported in years 2006–2009. The lanthanide and actinide elements, although showing lots of changes from crosses to naughts in Figure 1, are not discussed in this lecture. An interested reader is refereed to the review by *Tonkov and Ponyatovsky* (2005) and the recent experimental reports on the phase transitions from close-packed to distorted structures in lanthanides (see e.g. *Cunningham et al.*, 2007; *Errandonea et al.*, 2007; *Pravica et al.*, 2007; *Shen et al.*, 2007).

2. Phase Transitions Under High Pressure

2.1. GROUP-IV ELEMENTS

The semiconducting elements Si and Ge crystallize in a diamond-type structure with the coordination number equal 4, according to the 8-N rule. On pressure increase they transform to a β-Sn structure (white tin), while this transition occurs in Sn at ambient pressure on temperature increase (Table 1) (see (*Schwarz*, 2004 and references therein). On further pressure increase, Si and Ge transform to an orthorhombic structure with four atoms in the unit cell (Pearson notation (*Pearson*, 1967) *oI*4, where "o" stands for orthorhombic, "I" for body-centered, "4" for the number of atoms in the unit cell). The *oI*4 phase transforms to a simple hexagonal structure (sh, Pearson notation *hP*1). All these structures are very simple containing a small number of atoms in the unit cell. Then on further pressure increase, both Si and Ge transform to a crystal structure with an unexpectedly complex arrangement of atoms, with 16 atoms in the orthorhombic unit cell (Pearson notation *oC*16) occupying two different atomic sites 8*d* and 8*f* of the space group *Cmca*.

This phase has long been known to exist in Si, however it was solved only relatively recently: its solution is reported in the year 1999 (*Hanfland et al.*, 1999); the same structure was reported for a high-pressure phase of Cs in 1998 (*Schwarz et al.*, 1998). These experimental studies took advantage of the new 2D image plate techniques that became available at the beginning of 1990s. These publications reported the first structure solution of a complex phase in a simple element and marked a new era of pressure-induced complexity of simple elements. Reports of many other complex structures started to follow. Apart from Si and Ge, the *oC*16 structure has been reported for the alkali metals Cs (as mentioned above) and Rb (Section 2.4), a high-pressure high-temperature modification of Bi, Bi-IV, as well as for Bi–In, Bi–Pb and Bi–Sn alloys, where a site-ordering was observed (see (*Degtyareva et al.*, 2003) and references therein). The fact that this complex structure appears under pressure in alkali metals as well as in polyvalent metals and alloys deserves special attention, as discussed in (*Degtyareva*, 2006).

On further pressure increase, the *oC*16 structure transforms to hcp in both Si and Ge, and further to fcc in Si. Thus, a complete phase transition sequence is observed from an open-packed semiconducting structure of a diamond-type to a metallic close-packed structures hcp and fcc. The coordination number increases gradually with pressure increase from 4 in the diamond-type structure to 6 in β-Sn, to 8 in simple hexagonal, to 10–11 in *oC*16 and finally to 12 in hcp and fcc. The packing density increases from 0.34 in diamond structure to 0.55 in β-Sn, to 0.6 in simple hexagonal

TABLE 1. Sequences of structural transformations on pressure increase for group IV elements. The numbers above the arrows show the transition pressures in GPa. The crystal structures of the phases are denoted with their Pearson symbols, apart from the most common metallic structures bcc, fcc and hcp.

Si	12 13 16 38 42 80 *cF*8 → β-Sn, *tI* 4 → *oI* 4 → *hP*1 → *oC*16 → hcp → fcc < 250 GPa Diamond white tin
Ge	11 75 85 102 160 *cF*8 → β-Sn, *tI* 4 → *oI* 4 → *hP*1 → *oC*16 → hcp < 180 GPa Diamond white tin
Sn	0 8 45 *cF*8 → β-Sn, *tI* 4 → *tI*2 → bcc < 120 GPa Diamond white tin
Pb	13 110 fcc → hcp → bcc < 270 GPa

to 0.74 in hcp and fcc, the highest packing density for the regular spheres. The complex *oC*16 structure plays an important role in this transition sequence providing an atomic arrangement with coordination number 10–11, intermediate between those of open-packed and close-packed structures. The complex atomic arrangement of the *oC*16 phase, a nearly-free electron metal in the case of Si and Ge, provides a reduction of the electronic energy, which reduces the total structure energy (see for example *Degtyareva*, 2000).

2.2. GROUP-V ELEMENTS

2.2.1. *Arsenic, Antimony and Bismuth*

At ambient pressure, the group-V elements As, Sb and Bi crystallize in a rhombohedral As-type structure with two atoms in the unit cell (Pearson notation *hR*2), space group *R*-3*m* (Figure 2, left). Under pressure these elements show a similar phase-transition sequence, as summarized in Table 2. Arsenic transforms from the *hR*2 phase to a simple cubic (sc) structure with one atom per unit cell (Pearson notation *cP*1). The sc structure is stable up to 48 GPa, where it transforms to As-III, which has a monoclinic host–guest structure (*Degtyareva et al.*, 2004 a, b). For Sb, the *hR*2 structure approaches the sc structure on compression, but before it is reached, Sb transform to a monoclinic host–guest structure at 8.0 GPa, followed by a tetragonal host–guest structure at 8.6 GPa (*Degtyareva et al.*, 2004 a, b; *Schwarz et al.*, 2003). For Bi, the *hR*2 structure also approaches sc under pressure but transforms at 2.55 GPa to Bi-II, which has a monoclinic structure with four atoms in the unit cell (Pearson notation *mC*4). This

structure is unique amongst the elements but can be considered as a distorted sc structure. Bi-II has a very narrow stability range, and it transforms at 2.69 GPa to the tetragonal host–guest structure of Bi-III (*McMahon et al.*, 2000a) (Figure 2, middle). At higher pressures, the host–guest structures of As, Sb and Bi all transform to a bcc phase (Figure 2, right). This is the current end member of the known high-pressure structural sequences of these elements (Table 2).

The host–guest structure of group-V elements comprises a body-centered tetragonal (monoclinic) host framework, in which host atoms stack in such a way as to create channels along c-axis. Within these channels lie chains of atoms that form a body-centered tetragonal (monoclinic) guest structure. The host and guest structures are incommensurate with each other along their common c axis, with $c_H/c_G \sim 1.31$. There is a non-integer number of atoms (10.62 in total) in the host unit cell. Both host and guest structures are modulated along the c-axis, as shown from the recent single-crystal study of the Bi-III structure (*McMahon et al.*, 2007a).

A crystallographic description of such host–guest phases requires an application of a four-dimensional superspace formalism (see Section 3.1). The superspace group for the Bi-III structure is $I'4/mcm(00\gamma)0000$, where γ is the (incommensurate) ratio of the *c*-axis lattice parameters of the host and guest structures, c_H/c_G, and I' is the centering (½ ½ ½ ½) in superspace.

The coordination number increases under pressure from 3 in the *hR*2 (As-type) structure to 6 in the simple cubic structure of As or 7 in the *mC*4 structure of Bi, to 9 to 10 for the host–guest structure and finally to 14 (= 8 + 6) in the ultimate bcc structure. The complex atomic arrangement of the modulated host–guest structure (coordination number 9 for the host atoms and 10 for the guest atoms) plays a role of an intermediate step between the open packed semi-metallic As-type structure and metallic closely-packed bcc structure.

TABLE 2. Sequences of structural transformations on pressure increase for group-V elements. The numbers above the arrows show the transition pressures in GPa.

P	5 10 103 137 260 *oC*8 → *hR*2 → *cP*1 → inc. mod. → *hP*1 → bcc < 280 GPa
As	25 48 97 *hR*2 → *cP*1 → monocl. h-g → bcc < 122 GPa
Sb	8.0 8.6 28 *hR*2 → monocl. h-g → tetr. h-g → bcc < 65 GPa
Bi	2.5 2.7 7.7 *hR*2 → *mC*4 → tetr. h-g → bcc < 220 GPa → *oC*16 (>483K) →

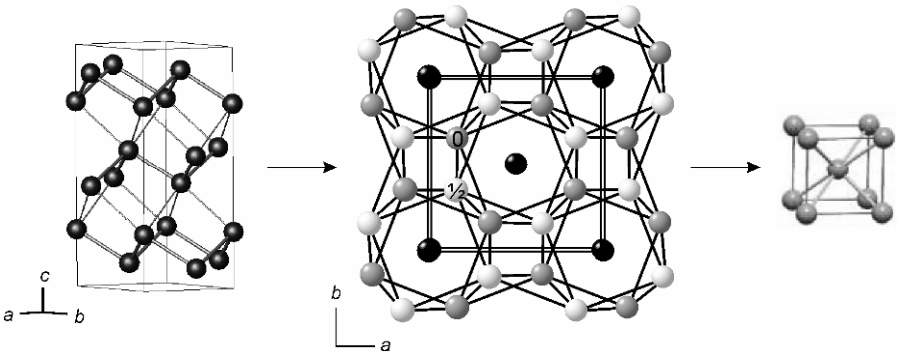

Figure 2. The crystal structure of group-V elements: (*left*) As-type (*hR*2), (*middle*) host–guest structure, and (*right*) bcc.

2.2.2. *Phosphorus*

The lighter group-V element phosphorus forms the As-type (*hR*2) structure only under pressure, above 5 GPa (Table 2), and at 10 GPa transforms to the simple cubic structure, similar to arsenic. Despite of its low packing density, the simple cubic structure is stable in phosphorus over a very wide pressure range up to 103 GPa. It has been long know that on further pressure increase, the simple cubic structure transforms to a simple hexagonal structure via a complex phase (*Akahama et al.*, 1999) that has remained unsolved until recently. Amongst several suggestions, a host–guest structure of Ba-IV type (similar to Bi-III) has been proposed as a candidate for this intermediate phase from the theoretical calculations (*Ehlers and Christensen*, 2004). We know, however, that the coordination number of the Bi-III host–guest structure is 9–10, which is too high for an intermediate phase between simple cubic (coordination number 6) and simple hexagonal phase (coordination number 8). It is only recently that metadynamic calculations (*Ishikawa et al.*, 2006) revealed a modulated atomic structure, while the subsequent experiment demonstrated an incommensurate nature of the modulation (*Fujihisa et al.*, 2007) with a coordination number equal to 6. The simple hexagonal structure is shown to transform to bcc at 260 GPa (*Akahama et al.*, 2000).

2.3. GROUP-VI ELEMENTS

Elemental sulphur, a yellow insulating mineral, is composed of crown-like 8-member ring molecules that form a complex crystal structure. Compression has a dramatic effect on these molecules: they break apart forming various chain and ring structures on pressure increase (*Degtyareva et al.*, 2007a and references therein). Sulphur becomes metallic and superconducting above 90 GPa with Tc = 10 K (*Struzhkin et al.*, 1997) forming an incommensurately

modulated crystal structure at 300 K (Figure 3) (*Degtyareva et al.*, 2005; *Hejny et al.*, 2005). The structure is described by a four-dimensional superspace group $I'2/m(0\beta0)s0$, and is the same as found earlier in the heavier group-VI elements Se and Te (see *McMahon and Nelmes*, 2006 and references therein).

This incommensurately modulated structure forms on pressure increase between the chain structures of S, Se and Te with the two nearest neighbors (according to the 8-N coordination rule) and the β–Po structure (found at high temperature in Te and at room temperature in Se and S) with the coordination number 6 + 2. In Se and Te, the β–Po structure is known to transform to bcc on pressure increase with coordination number 8 + 6 (see *McMahon and Nelmes*, 2006 and references therein). The interatomic distances in the modulated structure are also modulated and give an effective coordination number of 6 (2 + 2 + 2), thus being an intermediate step in the structural sequence from (molecular) chain to the typical metallic structures that shows an increase in coordination number and packing density. For the analysis of the pressure effect on the interatomic distances and coordination number in Se, see (*Degtyareva et al.*, 2005).

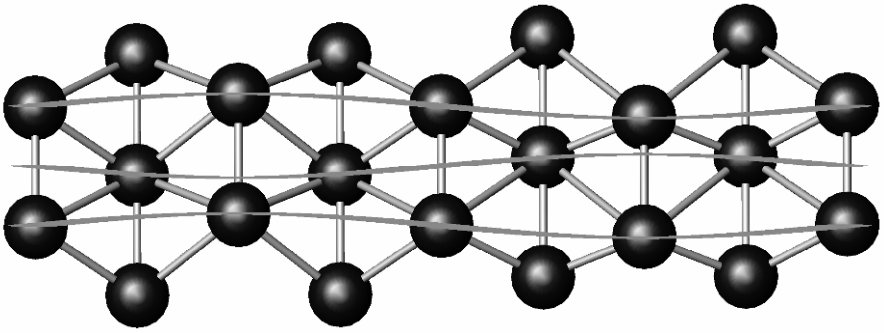

Figure 3. Crystal structure of the high-pressure phase of sulfur, S-IV, that is incommensurately modulated (commensurate approximant is shown in projection down the monoclinic a-axis) (From *Degtyareva et al.*, 2007b).

2.4. GROUP-I ELEMENTS (ALKALI METALS)

On the example of the transition sequences of the group IV, V, and VI elements, we have learned that the covalent and molecular structures respond to high pressure by increasing the coordination number and packing density, transforming to metallic state. Complex crystal structures appear on pressure increase as an intermediate step toward the closely-packed structures. Now to the question "what structures are expected in elements under high pressure" one could intuitively answer "the closely-packed structures".

However, the experimental studies on alkali and alkali-earth metals have shown that for them the close-packed structure is not close enough. Now we look at the "non-simple behaviour of simple metals at high pressure" (*Maksimov et al.*, 2005).

2.4.1. *Results from Experimental Work*

The alkali metals are considered as textbook examples of nearly-free electron metals at ambient conditions. They crystallize in a highly symmetric and closely-packed body-centred cubic (bcc) structure. On pressure increase, the bcc structure transforms to another close-packed structure, face-centred cubic (fcc), and then to unexpectedly complex low-symmetry structures (Figure 4) (see reviews *Degtyareva*, 2006; *McMahon and Nelmes*, 2006; *Schwarz*, 2004; *Syassen*, 2002).

TABLE 3. Sequences of structural transformations on pressure increase for group I elements. The numbers above the arrows show the transition pressures in GPa. "H- g" stands for a host–guest structure, "dhcp" for a double hexagonal close-packed structure.

Li	7.5 39 42 bcc → fcc → *hR*1 → *cI* 16 < 50GPa
Na	65 104 117 125 180 bcc → fcc → *cI* 16 → *oP*8 → h-g → *hP*4 < 200 GPa
K	11.6 20 54 90 96 bcc → fcc → h-g → *oP*8 → *tI*4 → *oC*16 < 112 GPa
Rb	7 13 17 20 48 bcc → fcc → *oC*52 → h-g → *tI* 4 → *oC*16 < 70 GPa
Cs	2.4 4.2 4.3 12 72 bcc → fcc → *oC*84 → *tI* 4 → *oC*16 → dhcp < 223 GPa

Lithium and sodium adopt a complex cubic structure with 16 atoms in the unit cell (Pearson symbol *cI*16) at around 40 GPa (*Hanfland et al.*, 2000) and at 104 GPa (*McMahon et al.*, 2007b; *Syassen*, 2002), respectively (Table 3). On further compression the *cI*16 phase of Na transforms at 118 GPa to an orthorhombic structure with eight atoms in the unit cell (*oP*8) (*Gregoryanz et al.*, 2008), a novel structure-type for an element. At 125 GPa, the *oP*8 phase transforms to an incommensurate host–guest structure (*Gregoryanz et al.*, 2008; *Lundegaard et al.*, 2009a) with the same 16-atom tetragonal host structure observed previously in K and Rb (*McMahon et al.*, 2001, 2006a). Melting line of Na showed a peculiar behavior (*Gregoryanz et al.*, 2005) with a bend-over at 31 GPa and 1,000 K that reached its minimum of room temperature at 118 GPa. Numerous complex phases with large unit cells were discovered in the vicinity of the melting line minimum

(*Gregoryanz et al.*, 2008). The most recent experimental work on Na reported quite an astonishing result that above 180 GPa sodium becomes optically transparent and insulating; complementary theoretical calculations proposed for this phase a hexagonal structure with four atoms in the unit cell, *hP*4 (*Ma et al.*, 2009). At the same time, a publication appeared on a pressure-induced metal to semiconductor transition in Li (*Matsuoka and Shimizu*, 2009) at pressures near 80 GPa, the experimental determination of the corresponding crystal structures however has not yet been reported.

Heavier alkali metals, K, Rb, and Cs, have been long known to assume complex crystal structures under pressure above the stability region of fcc, at much lower pressures than in Li and Na (Figure 4, Table 3). These include orthorhombic structures *oC*52 in Rb and *oC*84 in Cs, a host–guest structure in K and Rb, tetragonal *tI*4 and an orthorhombic *oC*16 structures in Rb and Cs. A very recent high-pressure study on K reported an observation of an *oP*8 structure, similar to that in Na, and the *tI*4 and *oC*16 structures, same as known for Rb and Cs (*Lundegaard et al.*, 2009b).

The phase transitions from fcc to complex structures in all alkali metals are accompanied by a decrease in symmetry, coordination number and packing density. A subsequent increase in coordination number is observed at the transition to the *oC*16 in Rb and Cs and to the double hexagonal close-packed (dhcp) structure in Cs.

2.4.2. *Results from Theoretical Work*

The appearance of some of the complex structures in the heaviest alkali metals Rb and Cs is suggested to be connected to an electronic s to d transfer (see review (*Maksimov et al.*, 2005) and references therein). The transition from fcc to complex phases at high pressures in Li and Na is explained with an *s*-to-*p* band overlap (*Christensen and Novikov*, 2001; *Hanfland et al.*, 2000). However, the observation of a large number of structural transformations and a variety of structural types in alkali metals under pressure require consideration of other factors that might be responsible for the formation of these phases. Hume-Rothery effect has been suggested as a stabilization mechanism for the *cI*16, *oC*52 and *oC*84 structures (*Degtyareva*, 2006). This model explains the appearance of the complex structures as a result of lowering the electronic energy and thus the total energy of the crystal structure due to a formation of additional planes in a Brillouin–Jones zone in a close contact with the Fermi surface. The electronic contribution into total energy becomes more important on compression, adding significantly to the stabilization of the *cI*16 and related phases.

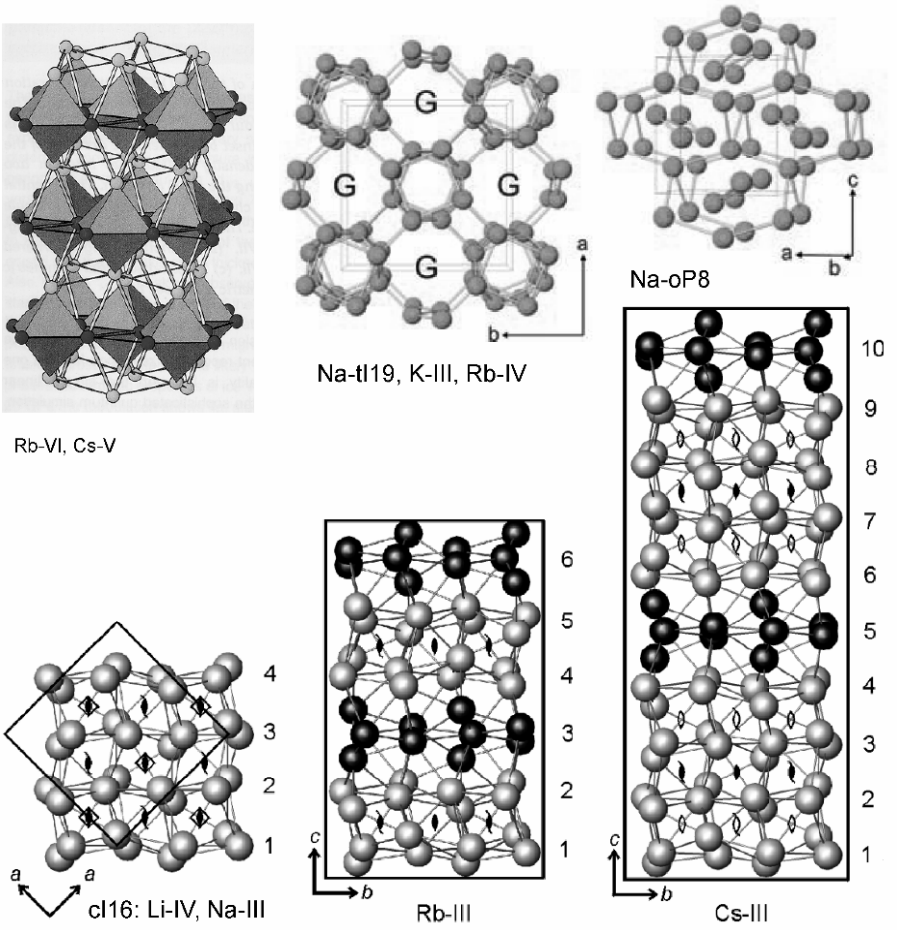

Figure 4. Complex crystal structures of alkali metals forming at high pressure. For the host–guest structure of Na, K and Rb, "G" marks channels occupied by chains of guest atoms, different arrangements are found in different elements.

At higher pressures in the post-*cI*16 region, the density of Li and Na is so high ($\rho/\rho_0 \approx 4$ for Na) that the atomic cores are beginning to touch (*Katsnelson et al.*, 2000; *Neaton and Ashcroft*, 1999, 2001) and new physical phenomena come into play. For both Li and Na, theoretical calculations find that electrons localize in the interstitial regions of the structures (*Christensen and Novikov*, 2001; *Ma et al.*, 2008; *Neaton and Ashcroft*, 1999, 2001, *Rousseau et al.*, 2005; *Zhou et al.*, 2009). These computational studies have suggested several crystal structures for the post-*cI*16 regime in Li and Na, with the most recent reports (*Pickard and Needs*, 2009; *Yao et al.*, 2009a) predicting low-coordinated structures for dense Li containing 24 atoms in the unit cell. The crystal structures uncovered by experimental work,

however, turn out to be quite different from the prediction, containing a much larger number of atoms in the unit cell (*Gregoryanz et al.*, 2008, 2009). There is an alternative view suggesting that the dense phases of alkali metals undergo partial core ionization and attain valence greater than one as, for example, described for *tI*4 and *oC*16 structures of Rb and Cs and *oP*8 structure of Na (*Degtyareva,* 2006; *Degtyareva and Degtyareva*, 2009).

2.5. GROUP-II ELEMENTS (ALKALI-EARTH METALS)

The alkali-earth metals, Ca and Sr, crystallize at ambient conditions in the close-packed face-centered cubic (fcc) structure, both transforming to the body-centered cubic (bcc) structure under pressure. The heavier group-II element Ba has a body-centered cubic (bcc) structure already at ambient pressure at room temperature forming the fcc phase at high temperatures. These three elements showed a surprising and puzzling behavior under pressure, transforming from closely-packed to low-coordinated structures with a reduction of packing density – not the behavior one would intuitively expect on compression.

First we discuss Ca with its simple cubic structure and peculiar Ca-IV and Ca-V phases. Then we talk about Sr and Ba and their host–guest structure which discovery marked a new era of incommensurate crystal structures of elements.

TABLE 4. Sequences of structural transformations on pressure increase for group V elements. The numbers above the arrows show the transition pressures in GPa.

Ca	$\overset{20}{\text{fcc}} \rightarrow \overset{32}{\text{bcc}} \rightarrow \overset{113}{cP1} \rightarrow \overset{139}{tP8} \rightarrow oC8 < 154$ GPa
Sr	$\overset{3.5}{\text{fcc}} \rightarrow \overset{27}{\text{bcc}} \rightarrow \overset{35}{\beta\text{-Sn}, tI4} \rightarrow \overset{49}{mI12} \rightarrow \text{h-g} < 117$ GPa
Ba	$\overset{5.5}{\text{bcc}} \rightarrow \overset{12}{\text{hcp}} \rightarrow \overset{45}{\text{h-g}} \rightarrow \text{hcp} < 105$ GPa

2.5.1. *Calcium*

Calcium transforms from fcc to bcc at 20 GPa, and at higher pressure of 32 GPa to a simple cubic structure (sc, *cP*1) (*Olijnyk and Holzapfel*, 1984). The transition from bcc to sc in Ca occurs with a decrease in packing density and coordination number: it changes from 14 (8 + 6) in bcc down to 6 in sc phase. The simple cubic structure is stable in Ca in a very large pressure range from 32 to 113 GPa (Table 4). Above this pressure, complex

structures are observed: Ca IV stable between 113 and 139 GPa and Ca-V stable above this pressure. Their crystal structures have only recently been identified experimentally: Ca-IV has a primitive orthorhombic structure with eight atoms in the unit cell (*oP*8), space group $P4_12_12$; Ca-V has a C-centered orthorhombic structure with eight atoms in the unit cell (*oC*8), space group *Cmca* (*Fujihisa et al.*, 2008). They were confirmed to be identical to the theoretical models that were predicted recently (*Ishikawa et al.*, 2008a). The structures of Ca-IV and V have a complex atomic coordination with seven nearest neighbors. These structures have never been seen before in other alkaline-earth metals or in other elements.

Interestingly, the simple cubic phase in calcium presents serious theoretical problems. For instance, recent calculations revealed that it is mechanically unstable in the corresponding pressure range (*Gao et al.*, 2008; *Teweldeberhan and Bonev*, 2008), prompting further calculations that tried to reconcile the theory and experiment (*Errea et al.*, 2008). The most recent experimental study on Ca was devoted to checking the stability of the simple cubic structure (*Gu et al.*, 2009). Subsequent resent theoretical work found that the simple cubic phase is indeed stable if calculated at 300 K while it transformed to another structure at lower temperatures (*Yao et al.*, 2009b). Generally, phase transitions in alkali-earth metals are attributed to an *s* to *d* electronic transfer (see review *Maksimov et al.*, 2005), with an alternative explanation suggesting that Ca in the simple cubic structure attains a valence greater than two (*Degtyareva*, 2006).

2.5.2. *Strontium and Barium*

The discovery of the host–guest structure in Ba in 1999 (*Nelmes et al.*, 1999) and subsequently in Sr (*McMahon et al.*, 2000b) marked a beginning of a new era in the high-pressure crystallography of elements. This type of structure has not been observed before in any other element and has not been expected either. The finding was quite astonishing and hard to comprehend but now the existence of the host–guest structure in elemental metals is generally accepted and it is a widely spread phenomenon at high-pressure.

Between 35 and 49 GPa before the transformation to the host–guest structure, strontium shows a unique and peculiar structure (Sr-IV). It is body-centered monoclinic, space group *Ia*, with 12 atoms in the unit cell, and can be viewed as a helical distortion of the tetragonal β-tin structure (Sr-III), in which atoms lying in (straight) chains along the Sr-III c-axis displaced to form helical chains (*Bovornratanaraks et al.*, 2006). The existence of the β-Sn structure in Sr in the pressure range 26–35 GPa is very peculiar, it has never been found in any other alkaline-earth metal, but is known to be a stable phase of group-IV elements (see Section 2.1). The

stability of the β-Sn in Sr received a very limited attention, and similar to the simple cubic structure of Ca, presents difficulties for theoretical calculations (*Phusittrakool et al.*, 2008).

Analyzing the changes in coordination number in Sr under pressure, we can see a dramatic decrease from 14 (8 + 6) in bcc down to 6 (2 + 4) in β-Sn and *mI*12 structures. There is a reversed increase in coordination number at the following transition to the host–guest structure with further pressure increase: the coordination number is 9–10 (this number is given in analogy with the Bi-III host–guest structure, however single crystal structure refinement of atomic modulations is required for a determination of the exact number). Similar reversed increase in coordination number was shown for alkali metals Rb and Cs.

3. Some Remaining Questions and Summary

3.1. GENERAL POINTS

Simple elements exhibit numerous phase transformations under pressure, forming complex crystal structures, often incommensurate, also called aperiodic. Incommensurate structures found in elements up until the year 2004 are summarized in (*McMahon and Nelmes*, 2004a) with subsequent findings described in the review (*McMahon and Nelmes*, 2006). A higher-dimensional formalism is needed for the crystallographic description of the incommensurate structures of elements. Explanation of the meaning of the superspace group symbols can be found, for example, in (*Janssen et al.*, 2004). A detailed crystallographic description of the host–guest structures in group-V elements is presented in (*Degtyareva et al.*, 2004b), while general higher-dimensional superspace formalism is outlined in (*van Smaalen*, 1995; *van Smaalen*, 2007). References (*van Smaalen*, 2004) and (*Petrıcek and Dusek*, 2004) give an elementary introduction to superspace crystallography with some examples. A very detailed and accessible description "for pedestrians" of this crystallographic formalism applied to host–guest (composite) structures is given in (*Sun et al.*, 2007).

The numerous structural transitions in simple elements described above are accompanied by marked changes in the physical properties. As was already mentioned, initially insulating sulphur becomes superconducting at around 90 GPa (*Struzhkin et al.*, 1997), while sodium, initially a free-electron metal, turns into optically transparent insulator at around 200 GPa (*Ma et al.*, 2009). Calcium becomes an element with the highest *T*c among all pressure-induced superconductors, with the critical temperature reaching 25 K at 161 GPa in the complex Ca-V phase (*Yabuuchi et al.*, 2006). The

correlation between the resistivity, superconductivity and crystal structure in simple elements is discussed in the review (*Degtyareva*, 2006).

3.2. HOST–GUEST STRUCTURES

The discovery of incommensurate host–guest structures in elemental metals under pressure has demonstrated unexpected structural complexity in compressed solids, and has challenged theories of condensed matter. First found in the group-II elements Ba and Sr (*McMahon et al.*, 2000b; *Nelmes et al.*, 1999), the host–guest structure is also shown to form at high pressures in the group-I elements Rb (*McMahon et al.*, 2001), K (*McMahon et al.*, 2006a), and Na (*Lundegaard et al.*, 2009a) the group-V elements Bi, Sb and As (*Degtyareva et al.*, 2004 a, b; *McMahon et al.*, 2000a; *Schwarz et al.*, 2003) and in the transition metal Sc (*McMahon et al.*, 2006b) Interestingly, the same host structure is found for the group-II and group-V elements and the transition metal Sc, while another type of host structure is observed for group-I elements. Guest structure in all elements forms chains of atoms that are correlated in various crystal structures or show a disorder between chains.

In the group-V elements, the host–guest structure plays a role of an intermediate step between the semi-metallic open packed and metallic closely-packed structures, while in group-I and II elements a more intricate picture of changes in electronic structure emerges. Such complex atomic arrangement provides a minimization of the electronic energy reducing the overall structural energy.

Several interesting phenomena have been observed in these elemental host–guest structures since their discovery in 1999, including atomic modulation of the host and guest components (*McMahon et al.*, 2007a), incommensurate-to-incommensurate phase transitions (*Degtyareva et al.*, 2004a), and ‘melting’ of the guest chains (*McMahon and Nelmes*, 2004b). An effect of site ordering has been studied on Bi–Sb binary alloys (*Haussermann et al.*, 2004), which showed the formation of a site-disordered incommensurate host–guest structure. First-principles calculations have been performed on the host–guest structures of group II and V elements (*Haussermann et al.*, 2002; *Ormeci and Rosner*, 2004; *Reed and Ackland*, 2000) and more recently of the group-I element Na (*Ma et al.*, 2009; *Lazicki et al.*, 2009) and transition metal Sc (*Arapan et al.*, 2009; *Ormeci et al.*, 2006), using commensurate approximants to describe their electronic structure. For the group-V elements, these calculations revealed that the electronic structure of the host–guest phases is intermediate between that of low pressure semimetallic phases and the high-pressure metallic bcc phase (*Haussermann et al.*, 2002), in accord with our conclusions of Section 2.2.1 based on the analysis of the coordination number.

To better understand their properties, experimental techniques other than X-ray diffraction are being applied to the high-pressure host–guest structures of elements, such as Raman scattering (*Degtyareva et al.*, 2007c; *Wang et al.*, 2006) and inelastic X-ray scattering (*Loa et al.*, 2007).

3.3. INCOMMENSURATELY MODULATED STRUCTURES

Pressure-induced incommensurately modulated structures have been discovered in elements in the year 2003 simultaneously and independently in the high-pressure phases of group-VI element Te and group-VII element iodine (see review *McMahon and Nelmes*, 2006 and references therein). Since then, the incommensurately modulated structures have been found in Se, S and P and suggested in Br, displaying great structural diversity. The group VII element iodine (and probably bromine) form a *Fmm*2(α00)0s0 modulated structure (*Kume et al.*, 2005; *Takemura et al.*, 2003), the group-VI elements Te, Se and S adopt *I*'2/*m*(0β0)s0 structure (*Hejny and McMahon*, 2003; *McMahon and Nelmes*, 2006), the group-V element phosphorus has a *Cmmm*(00γ)*s*00 modulated structure (*Fujihisa et al.*, 2007). Additionally, a long-period structure of a high-pressure phase of Ga, Ga-II (*Degtyareva et al.*, 2004c), was interpreted as a commensurately modulated *Fddd*(00γ)0*s*0 structure (*Perez-Mato et al.*, 2006). At ambient pressure, a modulated structure is known only in one element: uranium.

Theoretical calculations were performed on the modulated structures of phosphorus, sulphur and iodine, using commensurate approximants, to study the electronic origins of the formation of these structures (*Degtyareva et al.,* 2007b; *Ishikawa et al.*, 2008b; *Marqués et al.*, 2008). A charge-density wave instability is found to be responsible for the structural modulation in sulphur, in competition with the superconducting state (*Degtyareva et al.*, 2007b). An inelastic X-ray scattering technique was applied to the incommensurately modulated phase of Te and found a phonon softening associated with the structural modulation, while complementary theoretical calculations found a Fermi surface nesting within this phase (*Loa et al.*, 2009).

4. Conclusions

The discussed phase transitions in the simple elements revealed the following trends. On pressure increase, the group IV, V, VI and VII elements tend to undergo phase transformations from non-metallic open-packed to metallic closely packed structures with an increase in coordination number and packing density, passing through some very complex atomic arrangements

including incommensurate structures. The group I and II elements, the alkali and alkali-earth metals, that form closely-packed structures at ambient pressure, reveal surprisingly complex behavior under pressure, exhibiting structures with very large number of atoms in the unit cell owing it to the complicated changes in their electronic structure.

ACKNOWLEDGEMENTS

The support from the Royal Society is greatly acknowledged. The author would like to thank Valentina Degtyareva for fruitful discussions.

References

Akahama, Y., Kobayashi, M., and Kawamura, H., 1999, Simple-cubic–simple-hexagonal transition in phosphorus under pressure, *Phys. Rev. B.* **59**: 8520.

Akahama, Y., Kawamura H., Carlson, S., Le Bihan, T., and Haüsermann, D., 2000, Structural stability and equation of state of simple-hexagonal phosphorus to 280 GPa: Phase transition at 262 GPa, *Phys. Rev. B.* **61**: 3139.

Arapan, S., Skorodumova, N.V., and Ahuja, R., 2009, Determination of the structural parameters of an incommensurate phase from first principles: the case of Sc-II, *Phys. Rev. Lett.* **102**: 085701.

Bovornratanaraks, T., Allan, D.R., Belmonte, S.A., McMahon, M.I., and Nelmes, R.J., 2006, Complex monoclinic superstructure in Sr-IV, *Phys. Rev. B.* **73**: 144112.

Christensen, N.E. and Novikov, D.L., 2001, High-pressure phases of the light alkali metals, *Sol. State Comm*. **119**: 477.

Cunningham, N.C., Qiu W., Hope, K.M., Liermann, H.-P., and Vohra, Y.K., 2007, Symmetry lowering under high pressure: Structural evidence for *f*-shell delocalization in heavy rare earth metal terbium, *Phys. Rev. B.* **76**: 212101.

Degtyareva, O., McMahon, M.I., and Nelmes, R.J., 2004a, Pressure-induced incommensurate-to-incommensurate phase transition in antimony, *Phys. Rev. B*. **70**: 184119.

Degtyareva, O., McMahon, M.I., and Nelmes, R.J., 2004b, High-pressure structural studies of group-15 elements, *High Pressure Res*. **24**: 319–356.

Degtyareva, O., McMahon, M.I., Allan, D.R., and Nelmes, R.J., 2004c, Structural complexity in gallium under high pressure: relation to alkali elements, *Phys. Rev. Lett.* **93**: 205502.

Degtyareva, O., Gregoryanz, E., Somayazulu, M., Mao, H-k., and Hemley, R.J., 2005, Crystal structure of the superconducting phases of S and Se, *Phys. Rev. B.* **71**: 214104.

Degtyareva, O., Hernández, E.R., Serrano, J., Somayazulu, M., Mao, H-k., Gregoryanz, E., and Hemley, R.J., 2007a, Vibrational dynamics and stability of the high-pressure chain and ring phases in S and Se, *J. Chem. Phys.* **126**: 084503.

Degtyareva, O., Magnitskaya, M.V., Kohanoff, J., Profeta, G., Scandolo, S., Hanfland, M., McMahon, M.I., and Gregoryanz, E., 2007b, Competition of charge-density waves and superconductivity in sulfur, *Phys. Rev. Lett.* **99**: 155505.

Degtyareva, O., Struzhkin, V.V., and Hemley, R.J., 2007c, High-pressure Raman spectroscopy of antimony: As-type, incommensurate host–guest, and bcc phases, *Solid State Commun.* **141**: 164.

Degtyareva, V.F., 2000, Crystal structure of a high-pressure phase in Bi-based alloys related to Si VI, *Phys. Rev. B* **62**: 9.

Degtyareva, V.F., 2006, Simple metals at high pressures: the Fermi sphere – Brillouin zone interaction model, *Phys. Usp.* **49**: 369–388.

Degtyareva, V.F. and Degtyareva, O., 2009, Structure stability in the simple element sodium under pressure, *New J. Phys.* **11**: 063037.

Degtyareva, V.F., Degtyareva, O., and Allan, D.R., 2003, Ordered Si-VI-type crystal structure in BiSn alloy under high pressure, *Phys. Rev. B* **67**: 212105.

Dubrovinsky, L., Dubrovinskaia, N., Crichton, W.A., Mikhaylushkin, A.S., Simak, S.I., Abrikosov, I.A., de Almeida, J.S., Ahuja, R., Luo, W., and Johansson, B., 2007, Noblest of all metals is structurally unstable at high pressure, *Phys. Rev. Lett.* **98**: 045503.

Ehlers, F.J.H. and Christensen, N.E., 2004, Phosphorus Ba-IV-type under pressure: structure as a candidate for P-IV, *Phys. Rev. B.* **69**: 214112.

Errandonea, D., Boehler, R., Schwager, B., and Meoua,r M., 2007, Structural studies of gadolinium at high pressure and temperature, *Phys. Rev. B* **75**: 014103.

Errea, I., Martinez-Canales, M., Oganov, A.R., and Bergara, A., 2008, Fermi surface nesting and phonon instabilities in simple cubic calcium, *High Pressure Res*. **28**: 443–448.

Fujihisa, H., Akahama, Y., Kawamura, H., Ohishi, Y., Gotoh, Y., Yamawaki, H., Sakashita, M., Takeya, S., and Honda K., 2007, Incommensurate structure of phosphorus phase IV, *Phys. Rev. Lett.* **98**: 175501.

Fujihisa, H., Nakamoto, Y., Shimizu, K., Yabuuchi, T., and Gotoh, Y., 2008, Crystal structures of calcium IV and V under high pressure, *Phys. Rev. Lett.* **101**: 095503.

Gao, G., Xie, Y., Cui, T., Ma, Y., Zhang, L., and Zou, G., 2008, Electronic structures, lattice dynamics, and electron–phonon coupling of simple cubic Ca under pressure, *Solid State Commun.* **146**: 181.

Gregoryanz, E., Degtyareva, O., Somayazulu, M., Mao, H-k., and Hemley, R.J., 2005, Melting of dense sodium, *Phys. Rev. Lett.* **94**: 185502.

Gregoryanz, E., Lundegaard, L.F., McMahon, M.I., Guillaume, C., Nelmes, R.J., and Mezouar, M., 2008, Structural diversity of sodium, *Science* **320**: 1054.

Gregoryanz, E., Guillaume, C., Lundegaard, L., Degtyareva, O., McMahon, M.I., Nelmes, R.J., Sinogeikin, S., and Guthrie, M., 2009, On the structures of the dense alkali metals, *Talk at the SMEC Conference*, Miami-Western Caribbean, March 28–April 2.

Gu, Q.F., Krauss, G., Grin, Yu., and Steurer, W., 2009, Experimental confirmation of the stability and chemical bonding analysis of the high-pressure phases Ca-I, II, and III at pressures up to 52 GPa, *Phys. Rev. B* **79**: 134121.

Hanfland, M., Schwarz, U., Syassen, K., and Takemura, K., 1999, Crystal structure of the high-pressure phase silicon VI, *Phys. Rev. Lett.* **82**: 1197.

Hanfland, M., Syassen, K., Christensen, N.E., and Novikov, D.L., 2000, New high-pressure phases of lithium, *Nature* **408**: 174.

Häussermann, U., Söderberg, K., and Norrestam, R., 2002, Comparative study of the high-pressure behavior of As, Sb, and Bi, *J. Am. Chem. Soc.* **124**: 15359.

Häussermann, U., Degtyareva, O., Mikhaylushkin, A.S., Söderberg, K., Simak, S.I., McMahon, M.I., Nelmes, R.J., and Norrestam, R., 2004, $Bi_{1-x}Sb_x$ under high pressure: effect of alloying on the incommensurate Bi-III type composite structure, *Phys. Rev. B*. **69**: 134203.

Hejny, C., Lundegaard, L.F., Falconi, S., McMahon, M.I., and Hanfland, M., 2005, Incommensurate sulfur above 100 GPa, *Phys. Rev. B.* **71**: 020101(R).

Hejny, C. and McMahon, M. I., 2003, Large structural modulations in incommensurate Te-III and Se-IV, *Phys. Rev. Lett.* **91**: 215502.

Ishikawa, T., Nagara, H., Kusakabe, K., and Suzuki, N., 2006, Determining the structure of phosphorus in phase IV, *Phys. Rev. Lett.* **96**: 095502.

Ishikawa, T., Ichikawa, A., Nagara,H., Geshi, M., Kusakabe, K., and Suzuki, N., 2008a, Theoretical study of the structure of calcium in phases IV and V via *ab initio* metadynamics simulation, *Phys. Rev. B.* **77**: 020101(R).

Ishikawa, T., Nagara, H., Mukose, K., Kusakabe, K., Miyagi, H., and Suzuki, N., 2008b, Charge-density waves, incommensurate modulations and superconductivity in phosphorus and iodine, *High Press. Res.,* **28**: 459–467.

Janssen, T., Janner, A., Looijenga-Vos, A., and de Wolf, P.M., 2004, Incommensurate and commensurate modulated structures, in *International Tables for Crystallography, Vol. C Mathematical, Physical and Chemical Tables*, 3rd ed. edited by E. Prince, (Springer), Sec. 9.8.

Katsnelson, M.I., Sinko, G.V., Smirnov, N.A., Trefilov, A.V., and Khromov, K.Yu., 2000, Structure, elastic moduli, and thermodynamics of sodium and potassium at ultrahigh pressures, *Phys. Rev. B.* **61**: 14420.

Kume, T., Hiraoka, T., Ohya, Y., Sasaki, S., and Shimizu, H., 2005, High pressure Raman study of bromine and iodine: soft phonon in the incommensurate phase, *Phys. Rev. Lett.* **94**: 065506.

Lazicki, A., Goncharov, A.F., Struzhkin, V.V., Cohen, R.E., Liu Z., Gregoryanz, E., Guillaume, C., Mao, H.-K. and Russell J. Hemley, 2009, Anomalous optical and electronic properties of dense sodium, *PNAS* **106**: 6525–6528.

Loa, I., Lundegaard, L.F., McMahon, M.I., Evans, S.R., Bossak, A., and Krisch, M., 2007, Lattice dynamics of incommensurate composite Rb-IV and a realization of the monatomic linear chain model, *Phys. Rev. Lett.* **99:** 035501.

Loa, I., McMahon, M. I., and Bosak, A., 2009, Origin of the incommensurate modulation in Te-III and Fermi-surface nesting in a simple metal, *Phys. Rev. Lett.* **102**: 035501.

Lundegaard, L.F., Gregoryanz, E., McMahon, M.I., Guillaume, C., Loa, I., and Nelmes, R.J., 2009a, Single-crystal studies of incommensurate Na to 1.5 Mbar, *Phys. Rev. B.* **79**: 064105.

Lundegaard, L.F., Marqués, M., Stinton, G., Ackland, G.J., Nelmes, R.J., and McMahon, M.I., 2009b, Observation of the *oP*8 crystal structure in potassium at high pressure, *Phys. Rev. B.* **80**: 020101(R).

Ma, Y., Oganov, A.R., and Xie, Y., 2008, High-pressure structures of lithium, potassium, and rubidium predicted by an *ab initio* evolutionary algorithm, *Phys. Rev. B* **78**: 014102.

Ma, Y., Eremets, M., Oganov, A.R., Xie, Y., Trojan, I., Medvedev, S, Lyakhov, A.O., Valle, M. and Prakapenka, V., 2009, Transparent dense sodium, *Nature* **458**: 192.

Maksimov, E.G., Magnitskaya, M.V., and Fortov, V.E., 2005, Non-simple behavior of simple metals at high pressure, *Phys. Usp.* **48**: 761.

Marqués, M., Ackland, G.J., Lundegaard, L.F., Falconi, S., Hejny, C., McMahon, M.I., Contreras-García, J., and Hanfland, M., 2008, Origin of incommensurate modulations in the high-pressure phosphorus IV phase, *Phys. Rev B.* **78**: 054120.

Matsuoka, T. and Shimizu, K., 2009, Direct observation of a pressure-induced metal-to-semiconductor transition in lithium, *Nature* **458**: 186.

McMahon, M.I. and Nelmes, R.J., 2006, High-pressure structures and phase transformations in elemental metals, *Chem. Soc. Rev.* **35**: 943–963.

McMahon, M.I., Degtyareva, O., and Nelmes, R.J., 2000a, Ba-IV-type incommensurate crystal structure in group-V metals, *Phys. Rev. Lett.* **85**: 4896.

McMahon, M.I., Bovornratanaraks, T., Allan, D.R., Belmonte, S.A., and Nelmes, R.J., 2000b, Observation of the incommensurate barium-IV structure in strontium phase V, *Phys. Rev. B.* **61:** 3135.

McMahon, M.I., Rekhi, S., and Nelmes, R.J., 2001, Pressure dependent incommensuration in Rb-IV, *Phys. Rev. Lett.* **87:** 055501.

McMahon, M.I. and Nelmes, R.J., 2004a, Incommensurate crystal structures in the elements at high pressure, *Z. Kristallogr.* **219**: 742–748.

McMahon, M.I. and Nelmes, R.J. 2004b, Chain "melting" in the composite Rb-IV structure, *Phys. Rev. Lett.* **93**: 055501.

McMahon, M.I., Nelmes, R.J., Schwarz, U., Syassen, K., 2006a, Composite incommensurate K-III and a commensurate form: study of a high-pressure phase of potassium, *Phys. Rev. B.* **74**: 140102(R).

McMahon, M.I., Lundegaard, L.F., Hejny, C., Falconi, S., and Nelmes, R.J., 2006b, Different incommensurate composite crystal structure for Sc-II, *Phys. Rev. B.* **73**: 134102.

McMahon, M.I., Degtyareva, O., Nelmes, R.J., van Smaalen, S. and Palatinus, L., 2007a, Incommensurate modulations of Bi-III and Sb-II, *Phys. Rev. B.* **75**: 184114.

McMahon, M.I, Gregoryanz, E., Lundegaard, L.F., Loa I., Guillaume, C., Nelmes, R.J., Kleppe, A.K., Amboage, M., Wilhelm, H., and Jephcoat, A.P., 2007b, *Proc. Natl. Acad. Sci. U.S.A.* **104**: 17297.

Neaton, J.B. and Ashcroft, N.W., 1999, Pairing in dense lithium, *Nature* **400**: 141.

Neaton J.B. and Ashcroft N.W., 2001, On the constitution of sodium at higher densities, *Phys. Rev. Lett.* **86**: 2830.

Nelmes, R.J., Allan, D.R., McMahon, M.I., and Belmonte, S.A., 1999, Self-hosting incommensurate structure of barium IV, *Phys. Rev. Lett.* **83**: 4081.

Olijnyk, H. and Holzapfel, W.B., 1984, Phase-transitions in alkaline-earth metals under pressure, *Phys. Lett. A.* **100**: 191.

Ormeci, A. and Rosner, H., 2004, Electronic structure and bonding in antimony and its high pressure phases, *Z. Kristallogr.* **219**: 370.

Ormeci, A., Koepernik, K., and Rosner, H., 2006, First-principles electronic structure study of Sc-II, *Phys. Rev. B.* **74**: 104119.

Pearson, W.B., 1967, *Handbook of Lattice Spacings and Structures of Metals*, Pergamon Press, Oxford.

Perez-Mato, J.M., Elcoro, L., Aroyo, M.I., Katzke, H., Tolédano, P., and Izaola, Z., 2006, Apparently complex high-pressure phase of gallium as a simple modulated structure, *Phys. Rev. Lett.* **97**: 115501.

Petrıcek, V. and Dusek, M., 2004, Methods of structural analysis and computer program JANA2000, *Z. Kristallogr.* **219**: 692–700.

Phusittrakool, A., Bovornratanaraks, T., Ahuja, R., and Pinsook, U., 2008, High pressure structural phase transitions in Sr from *ab initio* calculations, *Phys. Rev. B* **77**: 174118.

Pickard, C.J. and Needs, R.J., 2009, Dense low-coordination phases of lithium, *Phys. Rev. Lett.* **102:** 146401.

Pravica, M., Quine, Z., and Romano, E., 2007, X-ray diffraction study of elemental thulium at pressures up to 86 GPa, *Phys. Rev. B.* **74**: 104107.

Reed, S.K. and Ackland, G.J., 2000, Theoretical and computational study of high pressure structures in barium, *Phys. Rev. Lett.* **84**: 5580.

Rousseau, R., Uehara, K., Klug, D.D., and Tse, J.S., 2005, Phase stability and broken-symmetry transition of elemental lithium up to 140 GPa, *ChemPhysChem* **6**: 1703.

Schwartz, U., 2004, Metallic high-pressure modifications of main group elements, *Z. Kristallogr.* **219**: 376-390.

Schwarz, U., Takemura, K., Hanfland, M., and Syassen, K., 1998, Crystal structure of cesium-V, *Phys. Rev. Lett.* **81**: 2711.

Schwarz, U., Akselrud, L., Rosner, H., Ormeci, A., and Grin, Yu., 2003, Structure and stability of the modulated phase Sb-II, *Phys. Rev. B* **67**: 214101.

Shen, Y.R., Kumar, R.S., Cornelius, A.L., and Nicol, M.F., 2007, High-pressure structural studies of dysprosium using angle-dispersive x-ray diffraction, *Phys. Rev. B* **75**: 064109.

van Smaalen, S., 1995, Incommensurate crystal structures, *Crystallogr. Rev.* **4**: 79.

van Smaalen, S., 2004, An elementary introduction to superspace crystallography, *Z. Kristallogr.* **219**: 681–691.

van Smaalen, S., 2007, *Incommensurate Crystallography*, Oxford University Press.

Struzhkin, V.V., Hemley, R.J., Mao, H-k., and Timofeev, Y.A., 1997, Superconductivity at 10–17K in compressed sulphur, *Nature* **390**: 382.

Sun, J., Lee, S., and Lin, J., 2007, Four-dimensional space groups for pedestrians: composite structures, *Chem. - Asian J.* **2**: 1204 – 1229.

Syassen, K., 2002, Simple metals at high pressures, in *Proceedings of the International School of Physics "High Pressure Phenomena"*, IOS, Amsterdam, p. 266.

Takemura, K., Kyoko, S., Hiroshi, F., and Onoda, M., 2003, Modulated structure of solid iodine during its molecular dissociation under high pressure, *Nature* **423**: 971.

Teweldeberhan, A.M. and Bonev, S.A., 2008, High-pressure phases of calcium and their finite-temperature phase boundaries, *Phys. Rev. B* **78:** 140101(R).

Tonkov, E.Yu. and Ponyatovsky, E.G., 2005, *Phase Transformations of Elements under High Pressure*, CRC Press, Boca Raton, FL.

Wang, X., Kunc, K., Loa I., Schwarz, U., and Syassen, K., 2006, Effect of pressure on the Raman modes of antimony, *Phys. Rev. B* **74:** 134305.

Yabuuchi, T., Matsuoka, T., Nakamoto, Y., and Shimizu, K., 2006, Superconductivity of Ca exceeding 25K at megabar pressures, *J. Phys. Soc. Jpn.* **75:** 083703.

Yao, Y., Tse, J.S., and Klug, D.D., 2009a, Structures of insulating phases of dense lithium, *Phys. Rev. Lett.* **102**: 115503.

Yao, Y., Klug, D.D., Sun, J., and Martonak, R., 2009b, Structural prediction and phase transformation mechanisms in calcium at high pressure, *Phys. Rev. Lett.* **103**: 055503.

Young, D.A., 1991, *Phase Diagrams of the Elements*, University of California Press, Berkeley, CA.

Zhou, D.W., Bao, G., Ma, Y.M., Cui, T., Liu, B.B., and Zou, G.T., 2009, Peierls transition in sodium under high pressure: a first-principles study, *J. Phys.: Condens. Matter* **21**: 025508.

LIGHT METAL HYDRIDES UNDER NON-AMBIENT CONDITIONS: PROBING CHEMISTRY BY DIFFRACTION?

YAROSLAV FILINCHUK*
Swiss-Norwegian Beam Lines at the European Synchrotron Radiation Facility, BP-220, 38043 Grenoble, France

Abstract Experimental studies of light metal hydrides under variable pressure and temperature are reviewed with an empahsis on the methodological aspects: collecting good quality powder data, solving new structures, relating different polymorphs in an attempt to reveal phase transition mechanisms and the underlying crystal chemistry. Practical recommendations and examples are given.

Keywords: High pressure, synchrotron powder diffraction, structure solution, hydrogen storage, mechanism of phase transition, phase diagram

1. Introduction

Light metal hydrides, such as borohydrides $M(BH_4)_n$, ammonia borane NH_3BH_3 etc. are considered as prospective hydrogen storage materials. Indeed, they can desorb a large quantity of hydrogen (up to 20.8%), that is much higher than traditional transition metal based hydrides, like $LaNi_5H_{5-7}$. However, the decompositon temperatures of borohydrides are usually high and the known compounds do not easily reabsorb hydrogen – thus they lack the reversibility.

Most of the light hydrides are crystalline solids, giving an advantage of using diffraction methods to study their structure and transformations. Diffraction provides an immense ammount of information not only about the structure, but also is more and more frequently used for screening and characterization of new substances, reaction products and intermediates. Detailed diffraction study of a promising material at various temperatures and pressures allows to uncover new polymorphs, follow their structural

* E-mail: Yaroslav.Filinchuk@esrf.fr

E. Boldyreva and P. Dera (eds.), *High-Pressure Crystallography: From Fundamental Phenomena to Technological Applications*, DOI 10.1007/978-90-481-9258-8_24,

evolution and therefore understand the nature of the interactions, or more generally speaking the underlying chemistry of the system. This information is a clue to understanding and maybe even altering the thermodymanic stability and reversibility of hydrides.

This chapter will be mostly focused on the high-pressure studies of the light hydrides. Besides showing how to solve new crystal structures, it is also aiming to give a feeling about how much modern diffraction techniques can go beyond a simple structure characterization. High-pressure characterization of the most revevant hydrides, such as $LiBH_4$ and $Mg(BH_4)_2$ (they release hydrogen at rather high T but show some reversibility) and NH_3BH_3 (releases hydrogen already at 80°C but shows no reversibiliy) is a part of a more common approach, where the changes are monitored under non-ambient conditions – various pressures, temperatures, hydrogen gas loadings or even during reactions with destabilizing agents. Ultimately, by *in-situ* diffraction we can study chemical reactions (for example de- and rehydrogenation) in more practical multicomponent mixtures, approaching the conditions of their anticipated technological use. The design and analysis of such complex systems requires the knowledge of the structure and properties of the fundamental H-rich component under various pressures and temperatures. Thus, bearing in mind the far-reaching research objectives, we will restrict ourselves here to the changes induced in light hydrides by the variation of the thermodynamic parameters, P and T.

2. Optimizing the Data Collection

From the point of view of crystallographic practice, solving and refining a new structure from excellent-quality high-pressure data measured at a synchrotron source is just like treating "bad" powder data, collected at ambient conditions with a standard laboratory source. The use of a small sample contained in a bulky sample environment inevitably reduces the quality of the diffraction data. Such datasets have a limited resolution both in the reciprocal (relatively broad peaks) and in the direct (limited 2θ range) space. Below is the list of tricks aiming to get the best high-pressure diffraction data from light hydrides.

- Most hydrides have relatively simple structures, giving preference to high-intensity medium-resolution area (2D) detectors over the high-resolution ones. The latter are needed only when there is a problem to index peaks of unknown structure or refine an occasionally complex structure, like $Mg(BH_4)_2$ (*Černý et al.*, 2007).

- Substances composed of the light elements give a weak diffraction signal and therefore a lower than usual signal-to-background ratio. The signal is even weaker for small light samples contained in a diamond anvil cell (DAC). Area detectors accumulate extremely high total intensity, thus reducing impact of statistical noise and providing a good time resolution. However, a long exposure time of >10 min. may be necessary to obtain good statistics for the high-angle peaks. For that, the low-background image plate detectors have an advantage over the CCDs.
- All spurious peaks coming from diamond, ruby (used for pressure calibration) etc. should be masked and removed before the integration into a 1D profile. "Cake" option in Fit2D should be used in order to verify the proper detector calibration. Diffraction rings of the sample can be used to determine the coordinates of the $2\theta = 0$ position and the detector tilts. The resulting 1D dataset will have the best resolution, which might be critical on the indexing stage.
- A pattern collected at low pressure, on a phase with a known structure, should be used for refining a "zero shift" value. This parameter has no physical meaning for area detectors, but it corrects for any small remaining calibration errors – this often helps to successfully index peaks of novel high-pressure phases.

On how to collect variable-temperature data at ambient pressure:

- Thin-walled glass capillaries give a relatively high amorphous background and react with some borohydrides at elevated T. A single-crystal sapphire capillary is an option to remove both undesired effects. Strong diffraction spots from the sapphire should be masked.
- In order to remove an uncertainty with non-ideal centering of a capillary, it should be rotated by the same angle and in the same angular range upon each exposure. In this case, the series of powder data collected sequentially at different temperatures will show a consistent (smooth) variation of the cell parameters. It will also allow using the same mask for all 2D images. A gas blower can be set to ramp up the temperature at a constant rate, with an automatic image retaking. This simple procedure reveals all temperature-induced changes in one run!

3. Solving Structures from Powder Diffraction Data

A combination of several programs proved to be very efficient in solving new structures. Their use will be illustrated during two workshops. Here the practical guidelines are given with only one case study, of $LiBH_4$. Thus, this chapter covers partly the lecture and the workshops.

- Input file for indexing in **Dicvol** can be generated and directly called from WinPlotr, a program shell of **FullProf**. Warning: zero shift in Dicvol is defined with the opposite sign to the one in FullProf. Avoid including peaks belonging to other phases: intensity variations for different peaks during heating or upon the compression help to reveal if they belong to the same phase. Be conservative: use only reliable peaks' positions. Indexing should be attempted up to the highest figures of merit (FOM). Other parameters to vary: EPS (expected error of peaks' positions) and the maximum unit cell volume.
- The resulting solutions should be analyzed by making a le Bail fit, also known as "profile matching". The correct cell should not predict too many peaks having zero observed intensity, unless the Bravais lattice is non-primitive. Program **ChekCell** and its subroutine **TrueCell** are the excellent tools for finding higher metric symmetry consistent with the list of indexed peaks, for finding a related supercell that explains extra weak peaks, and for finding a space group by an automated analysis of the systematic absences. The program requires as an input the cell parameters obtained by Dicvol and an extended list of peaks' positions, including the less reliable ones, which might belong to the same phase.
- An elegant trial and error method of structure solution is implemented in the program **FOX**. It works well with moderate-quality datasets, typically obtained at high pressures, where structure solution by direct methods (standard technique for single-crystal data) fails. The profile parameters and data for known secondary phases should be transferred to FOX from the le Bail fit. A few datasets can be used simultaneously.
- The great advantage of the direct space structure solution is the possibility to add our knowledge or expectations of the structural behavior, thus reducing the space of the optimized parameters. The crystal chemistry can be defined in FOX via a set of antibump restraints (minimum distances between atoms of various types) and by defining rigid or semi-rigid bodies. For example, BH_4 groups can be located as complete tetrahedral units, first optimizing only three positional parameters and on the final stage also three orientational parameters. Compared to five independent atoms (15 parameters), this gives a considerable reduction in the number of free parameters. Also, FOX does not require an exact composition: provided the atoms types are correct and given in access to the expected composition, the structure will be solved, and the excess atoms eliminated by using so called "dynamic occupancy correction".
- Once an input file for FOX is generated, structure solution can be easily attempted in different space groups – it is a matter of changing the space group only. With sufficient amount of the empirical information put in, the search limits may be sufficiently narrowed, enabling even the

structure solution in the triclinic space groups. This may allow solving a structure without guessing the space group. The true symmetry can be revealed later by analyzing the resulting "triclinic" structure.

- For the successful structure solution of some new phases forming in DACs, it is essential to model a texture, by including one parameter (March's model) into the global optimization by FOX. Various directions of the preferred orientation should be tested, e.g. for the orthorhombic cell the three main axes should be tested as possible directions. Another approach (*Whitfield*, 2009) does not require an input of the orientation direction when using spherical harmonics preferred orientation correction during the simulated annealing in TOPAS. The remarkable feature of the preferred orientation developing in DACs is the uniform distribution of the diffraction intensities along the Debye rings. In the experimental geometry, where the compression direction coincides with the direction of the primary beam and the area detector is put at $2\theta = 0$ position, the texture appears visually undetectable. Indeed, Figure 1 shows that the powder is averaged by rotation around the axis of the primary beam, thus forming regular powder rings but leaving the perpendicular direction unique. Thus, when all attempts to solve a structure fail, the texture should be assumed *a priori*, making it a part of the globally optimized model (*Filinchuk et al*., 2007). Certainly, this is the option of the last resort.
- A possibly higher crystallographic symmetry of the structure obtained with FOX can be detected in the program **Platon**, using ADDSYM routine. In particular, it enables finding the true symmetry for structures solved in the triclinic space groups. An automatic search for unoccupied voids (CALC VOID) helps to reveal physically unrealistic cavities which usually indicate that some atoms are missing. Once the major part of the structure is identified, the structure can be completed using difference Fourier maps: they can be calculated both in FOX and in FullProf. Amusingly, there are rare cases of truly empty voids in largely ionic borohydrides, see $Mg(BH_4)_2$ as an example (*Filinchuk et al*., 2009).
- Generation of distorted variants of the known structure types can not be considered as an *ab intitio* structure solution, but it is often a way to describe new lower-symmetry derivatives of the known parent structures. For example, an appearance of extra peaks or peaks' splitting upon a phase transition might be explained by a superstructure. The possible superstructures can be generated using group–subgroup relations implemented in **PowderCell**. Small distortions can be introduced manually in the resulting trial models, and the simulated powder patterns can be compared to the experimental ones in order to confirm or reject these variants. Unfortunately, this program does not generate subgroups of the space groups in the non-standard settings – the full list can be found in

the International Tables, volumes A and A1. Sometimes, the symmetry lowering does not proceed via the Γ-point (group–subgroup), but goes via more complicated mechanisms involving other points of the Brillouin zone. Investigating such possibilities requires making a group-theoretical analysis, which can be easier to do employing the **Bilbao Crystallographic Server**.

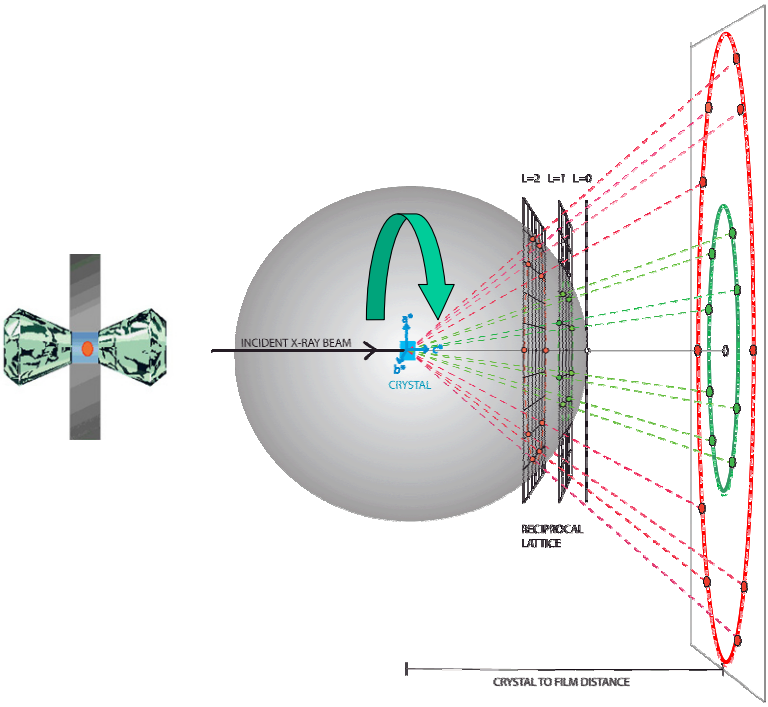

Figure 1. Typical diffraction geometry of the high-pressure experiment in a DAC provides a good powder average by rotation around the axis of the primary beam, forming uniform Debye rings, but leaves the perpendicular direction unique. The texture along this direction is visually undetectable.

- The resulting structure should be finally refined by **Rietveld method**, using, for example, FullProf. A correct weighting scheme should be used in order to obtain unbiased refined parameters. For this, the 2θ – intensity data should be complemented by a third column containing uncertainties of the integrated intensities, σ(I). The resulting large χ^2 values should not come at a surprise, since a statistically small difference between the observed and theoretical patterns cannot be practically achieved in the presence of a vanishingly small noise – any small difference will be considered as statistically significant.

- In cases when a structure shows unexpected features, **DFT calculations** can be used as a part of the structure validation: a DFT-optimization of the experimental structure should converge at nearly the same configuration. Theoretical calculations can also be used to discriminate between a few structures showing a similar fit to the diffraction data: the lowest energy structure is most likely the true one. In is interesting that theoretical predictions of crystal structures of hydrides typically fail. All new compositions and crystal structures have been discovered yet in experiments. Light hydrides seem to be a challenge for theory due to the pronounced rotational dynamics of the light isolated groups, such as BH_4, and the related contribution of the entropy to the total energy. These complications are illustrated by the example of $LiBH_4$ (*Filinchuk et al*., 2008a, c).
- A symmetry-based phenomenological analysis of the structures observed under various P–T conditions helps to understand atomistic mechanisms and thermodynamic aspects of the phase transitions (see *Dmitriev et al*., 2008 as an example). The **symmetry-based analysis** combined with the powder diffraction experiment allows to construct the pressure-temperature phase diagram and even to go beyond making predictions of new possible phases.

4. A Case Study – $LiBH_4$

Theoretical predictions of the high-pressure phases of $LiBH_4$ did not explain the observed powder pattern, collected at 2.4 GPa. None of the known structure types of the ABX_4 family could be matched with our diffraction data, thus the structure had to be solved *ab initio* (Figure 2). The peaks were indexed using Dicvol in a tetragonal cell with $a \sim 3.75$ and $c \sim 6.45$ Å, however the structure could not be solved in any of the tetragonal space groups. It has therefore been solved by global optimization in direct space (program FOX) in the lowest symmetry space group *P*1. Constraints on tetrahedral symmetry of the borohydride anion have been imposed, along with soft "antibump" restraints on Li…H distances. The true symmetry of the resulting structure has been uncovered using Platon software, which suggested a doubled pseudo-tetragonal cell (a,$b \sim 5.30$ and $c \sim 6.45$ Å) and the orthorhombic space group *Ama*2. Thus, it was the pseudo-tetragonal metrics of the orthorhombic structure that made the structure solution so intricate. Fortunately, there was no effect of texture.

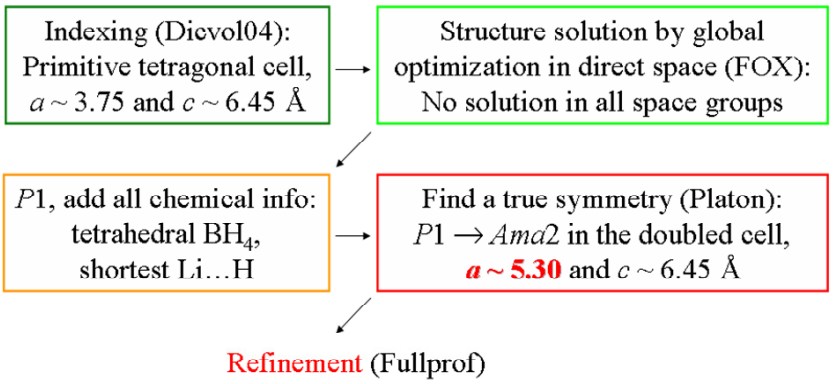

Figure 2. The sequence of steps made for solving the structure of the high-pressure phase of $LiBH_4$ (*Filinchuk et al*., 2008c).

This model was refined by the Rietveld method, keeping the *z*-coordinate for the Li atom fixed to zero (in order to fix the origin of the polar space group). 47 reflections were fitted with 11 intensity-dependent parameters, using eight soft restraints defining an approximately tetrahedral BH_4 geometry. This approach provided a very good fit to the data using a minimal set of reasonable assumptions.

The *Ama*2 phase reveals a new structure type. BH_4 anions form a distorted Cu-type substructure, while Li atoms form a primitive cubic substructure (α-Po-type). The Li and BH_4 sublattices interpenetrate, so that Li atoms occupy tetrahedral voids in the BH_4 network. Most interestingly, the BH_4 anion has a nearly square planar coordination by four Li atoms (Figure 3) – a square coordination of BH_4 anions has no analogues in the crystal chemistry of metal borohydrides (*Filinchuk et al*., 2008b).

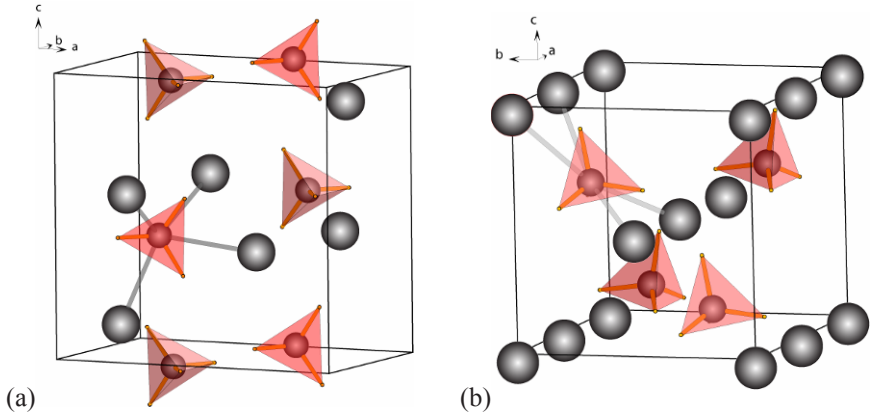

Figure 3. Crystal structures of the $LiBH_4$ phases observed at 0-1 GPa (*left*) and 1-10 GPa (*right*) at ambient temperature. At higher temperatures a hexagonal, and at higher pressures – a cubic phases appear (not shown here).

To validate the structure and gain insight into stability of the novel coordination of BH_4 by metal atoms, the density functional theory (DFT) calculations were employed. The optimized structure is in good agreement with the experimental one: the BH_4 anion fits exactly into the plane of Li neighbors, compared to its small deviation from the plane in the experimental structure. This gives more confidence in the novel planar coordination of the BH_4 unit.

In the *Ama*2 phase, the shortest H…H distance between two neighboring BH_4 anions is 1.87 Å long in the theoretically optimized model, which is even shorter than 1.92 Å obtained from the crystallographic data. These short contacts serve as links within chains formed by borohydride anions, as shown in Figure 4. This geometry is unique, and so short an H…H distance is unprecedented in metal borohydrides. The short inter-anionic contact H…H correlates with the more acute H–B–H angle of ~102° in the DFT-optimized structure (compared with 109.5° for ideal tetrahedral geometry). One can say that the H…H interactions distort the BH_4 anion, and such a distortion is supposed to be a step towards a decomposition of BH_4.

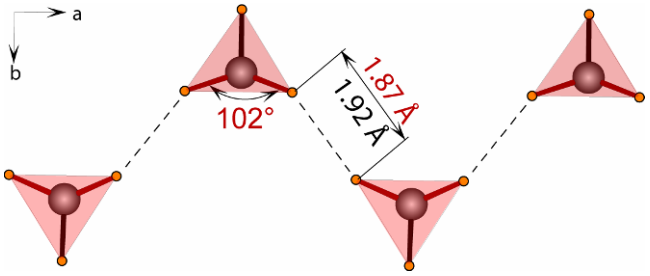

Figure 4. In the *Ama*2 phase of $LiBH_4$ the BH_4 anions are linked by short H…H contacts into chains. These interactions distort the otherwise tetrahedral BH_4 anion.

Short H…H interaction are likely to decrease the activation energy for hydrogen desorption. Thus, this structure may show completely different hydrogen storage properties if stabilized by chemical substitution at ambient pressure. It was suggested that the internal pressure in the structure may be tuned by a partial substitution of lithium by larger cations, or substitution of some BH_4 groups by AlH_4 or halide anions. The resulting $LiBH_4$-based substance with *Ama*2 structure may show more favorable hydrogen storage properties than pure $LiBH_4$ and may turn out to be useful for hydrogen storage applications.

All together, at different P–T conditions, four $LiBH_4$ phases are known: two at ambient and two at high pressure. The low-temperature structure has the *Pnma* symmetry. It transforms into a hexagonal $P6_3mc$ wurtzite-like high-temperature phase at ~380 K. At pressures above 10 GPa a cubic phase

forms. *In situ* synchrotron diffraction serves as an optimal probe to map out the P–T diagram (Figure 5), identify the phases and follow their structural evolution. Such a diagram, with all the supporting information, allows evaluation of fundamental thermodynamic and structural properties of $LiBH_4$.

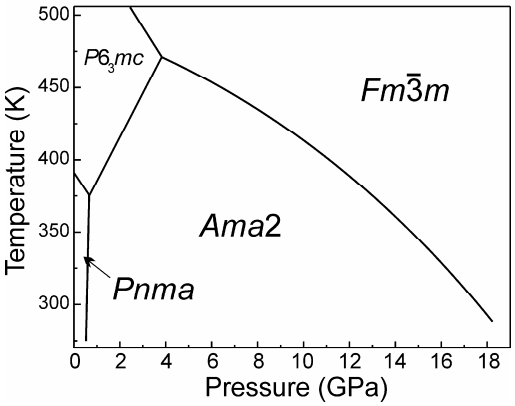

Figure 5. Experimental pressure-temperature phase diagram of $LiBH_4$.

An analysis of symmetry changes and structural deformations, followed by a group theoretical analysis, yields a unified picture of the phase transformations in $LiBH_4$. An existence of cation–anion layers in all four $LiBH_4$ phases is suggested from the phenomenological analysis of mechanisms of phase transitions. A clear evidence for the existence of cation–anion layers is found in the hexagonal phase, where the BH_4 tetrahedron has three short B…Li contacts in the *ab* plane and a long one along the *c* axis. In the *Pnma* phase, these layers are corrugated and the structure is less anisotropic. The layers where Li and BH_4 groups are associated by means of the shorter B…Li contacts can be identified in the (011) plane of the *Ama*2 structure. In the cubic phase, one type of layer is consistent both with geometrical considerations and with the phenomenological model: these are cation–anion layers situated in the (111) plane, similar to those found in the hexagonal phase. Clearly, the formation of layers in the $LiBH_4$ structures is not determined by coordination polyhedra for Li and BH_4 groups, since corresponding coordination numbers and geometries vary with pressure and temperature. Directional interaction of tetrahedral BH_4 with spherical metal atoms explains the relative complexity of $LiBH_4$ structures and of the P–T phase diagram in comparison with NaCl, where both cation and anion are spherical.

References

Černý R., Filinchuk Y., Hagemann H., Yvon K. (2007) *Angew. Chem. Int. Ed*. **46,** 5765.
Dmitriev V., Filinchuk Y., Chernyshov D., Talyzin A.V., Dzwilewski A., Andersson O., Sundqvist B., Kurnosov A. (2008) *Phys. Rev. B* **77**, 174112.
Filinchuk Y., Talyzin A.V., Chernyshov D., Dmitriev V. (2007) *Phys. Rev. B* **76**, 092104.
Filinchuk Y., Černý R., Hagemann H. (2009) *Chem. Mater*. **21**, 925.
Filinchuk Y., Chernyshov D., Černý R. (2008a) *J. Phys. Chem. C* **112**, 10579.
Filinchuk Y., Chernyshov D., Dmitriev V. (2008b) *Z. Kristallogr*. **223**, 649.
Filinchuk Y., Chernyshov D., Nevidomskyy A., Dmitriev V. (2008c) *Angew. Chem. Int. Ed*. **47**, 529.
Whitfield P. S. *J. Appl. Cryst*. **42** (2009) 134.

EVOLUTIONARY CRYSTAL STRUCTURE PREDICTION AND NOVEL HIGH-PRESSURE PHASES

ARTEM R. OGANOV[1,2], YANMING MA[3], ANDRIY O. LYAKHOV[1], MARIO VALLE[4], CARLO GATTI[5]

[1]*Department of Geosciences, Department of Physics and Astronomy, and New York Center for Computational Sciences, State University of New York, Stony Brook, NY 11794-2100, USA*

[2]*Geology Department, Moscow State University, 119992 Moscow, Russia*

[3]*National Lab of Superhard Materials, Jilin University, Changchun 130012, P. R. China*

[4]*Data Analysis and Visualization Group, Swiss National Supercomputing Centre CSCS), Cantonale Galleria 2, 6928 Manno, Switzerland*

[5]*CNR-ISTM, Istituto di Scienze e Tecnologie Molecolari, via Golgi 19, 20133 Milano, Italy*

Abstract Prediction of stable crystal structures at given pressure-temperature conditions, based only on the knowledge of the chemical composition, is a central problem of condensed matter physics. This extremely challenging problem is often termed "crystal structure prediction problem", and recently developed evolutionary algorithm USPEX (Universal Structure Predictor: Evolutionary Xtallography) made an important progress in solving it, enabling efficient and reliable prediction of structures with up to ~40 atoms in the unit cell using *ab initio* methods. Here we review this methodology, as well as recent progress in analyzing energy landscape of solids (which also helps to analyze results of USPEX runs). We show several recent applications – (1) prediction of new high-pressure phases of $CaCO_3$, (2) search for the structure of the polymeric phase of CO_2 ("phase V"), (3) high-pressure phases of oxygen, (4) exploration of possible stable compounds in the Xe–C system at high pressures, (5) exotic high-pressure phases of elements boron and sodium.

* E-mail: artem.oganov@sunysb.edu

E. Boldyreva and P. Dera (eds.), *High-Pressure Crystallography: From Fundamental Phenomena to Technological Applications*, DOI 10.1007/978-90-481-9258-8_25,

1. Introduction

The crystal structure prediction problem occupies a central place in materials design. Solving this problem would also open new ways also for understanding the behaviour of materials at extreme conditions, where experiments are difficult (in some cases, prohibitively difficult).

Often the approach has been to compare the free energies of a number of candidate structures (usually taken from analogous materials, or constructed by chemical intuition). Data mining (*Curtarolo et al*., 2003) efficiently explores databases of known crystal structures and, using correlations between structures adopted by different compounds, indicates a list of likely candidate structures. Problems arise almost every time when a totally unexpected and hitherto unknown structure is stable. A number of simpler intuitive empirical schemes (e.g. structure diagrams, polyhedral clusters – see *Urusov et al*., 1990) have appeared in literature, but their application usually requires a large experimental data set or good understanding of the compound at hand.

Thanks to recent methodological developments, reliable structure prediction can be performed without any prior knowledge or assumptions about the system. Simulated annealing (*Deem and Newsam,* 1989; *Pannetier et al*., 1990; *Boisen et al*., 1994; *Schön and Jansen*, 1996), minima hopping (*Gödecker*, 2004) and metadynamics (*Martonak et al*., 2003, 2005, 2006) have been used with some success. For small systems, even relaxing randomly produced structures can deliver the stable structure (*Pickard and Needs,* 2006). Here we review the evolutionary algorithm USPEX (Universal Structure Predictor: Evolutionary Xtallography) (*Oganov et al*., 2006; *Oganov and Glass*, 2006; *Glass et al*., 2006) and a small selection of the results it has provided so far. Section 2 presents basics of the method, Section 3 shows several interesting test cases (mostly on systems with a known ground state), while a number of applications to systems where the stable structure is unknown are presented in Section 4. This review is an updated version of the previous account of the methodology (*Oganov et al*., 2007).

2. Evolutionary Algorithm USPEX

Several groups attempted the pioneering use of evolutionary algorithms to structure prediction – for crystals (*Bush et al*., 1995; *Woodley*, 2004; *Woodley et al.*, 1999; *Bazterra et al*., 2002), colloids (*Gottwald et al*., 2005) and clusters (*Deaven and Ho*, 1995). The algorithm developed by *Deaven and Ho* (1995) is perhaps especially interesting as some of its features (real-space representation of structures, local optimization and spatial heredity) are similar to the USPEX method. Their algorithm has successfully reproduced

the structure of the C_{60} buckminsterfullerene, but has never been extended to heteroatomic clusters, nor to periodic systems (i.e. crystals). The algorithm of Bush and Woodley (*Bush et al*., 1995; *Woodley*, 2004; *Woodley et al*., 1999) was originally developed for crystals and successfully produced a starting model for solving the structure of Li_3RuO_4 (*Bush et al*., 1995). However, subsequent systematic tests (*Woodley*, 2004; *Woodley et al*., 1999) showed frequent failures even for rather simple systems containing ~10 atoms/cell. Other drawbacks are that this algorithm requires experimental lattice parameters and simulations are very expensive, unless a cheap and crude heuristic expression is used for fitness. Unlike the Deaven-Ho algorithm and USPEX, in this method structures are represented by binary "0/1" strings, there is no local optimization and no spatial heredity.

In USPEX, structures are represented by fractional coordinates for the atoms and lattice vectors. USPEX operates with populations of structures; from them, parent structures are selected. The fitness of structures is the relevant thermodynamic potential derived from *ab initio* total energy calculations. The worst structures of a population are discarded; for the remaining structures the probability of being selected as parent is a function (e.g. linear) of its fitness rank. A new candidate structure is produced from parent structures using one of three operators: (i) heredity, which combines spatially coherent slabs (in terms of fractional coordinates) of two parent structures, while the lattice vectors matrices are weighted averages of the two parent lattice vectors matrices, (ii) permutation (as in *Woodley*, 2004; *Woodley et al*., 1999), which swaps chemical identities in randomly selected pairs of unlike atoms, (iii) lattice mutation, which distorts the cell shape by applying a random symmetric strain matrix. To avoid pathological lattices, all newly produced structures are rescaled to produce a predefined unit cell volume (a reasonable starting value should be supplied in the input, and then allowed to evolve during the run). Heredity enables very broad searches, while preserving already found local fragments of good structures, and introduces ideas of "two-phase" simulations. Permutation facilitates finding the optimal ordering of the atoms; in some situations (for systems with a large range in degree of chemical similarity between different atom types) it may be useful to swap only chemically more similar atoms (e.g. Al–Si in aluminosilicates). Lattice mutation enables better exploration of the neighborhood of parent structures, prevents premature convergence of the lattice, and essentially incorporates the ideas of metadynamics in our search. The action of these variation operators is illustrated in Figures 1 and 2.

Before new candidate structures are relaxed, they are tested against three constraints – first, all interatomic distances must be above the specified minimal values; second, cell angles must be between 60° and 120°; third, all cell lengths must be larger than a specified value (e.g. diameter of the

largest atom). These constraints help to ensure stability of energy calculations and local optimization, and remove only redundant and infeasible regions of configuration space – thus the search is physically unconstrained. If in violation of these constraints, the candidate structure is discarded; otherwise, it is locally optimized (relaxed). Structure relaxations and energy calculations are done by external codes (currently, USPEX is interfaced with VASP (*Kresse and Furthmüller*, 1996), SIESTA (*Soler et al*., 2002), GULP (*Gale*, 2005).

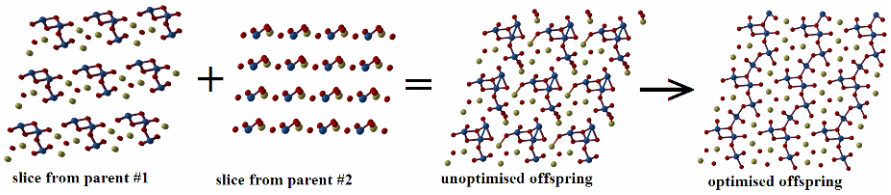

Figure 1. Heredity operator: slices of two parent structures, and the offspring structure before and after local optimization.

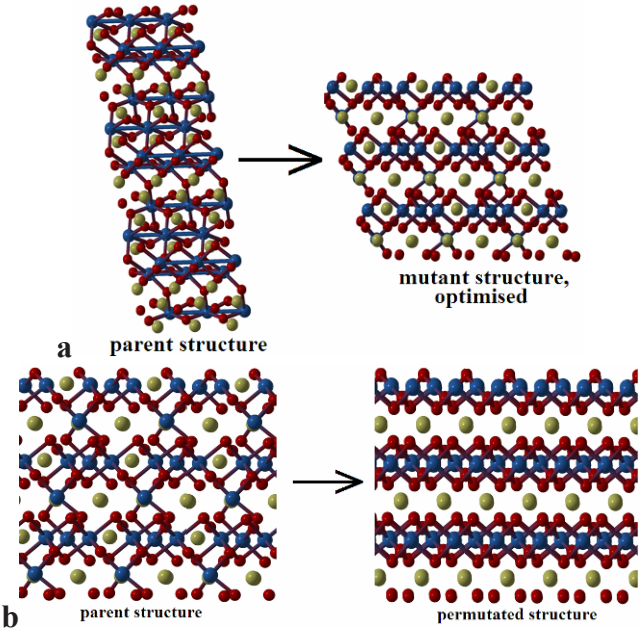

Figure 2. Illustrations of lattice mutation and permutation operators.

The relaxed structures are recorded and used for producing the next generation of structures. A new population of structures is made to contain one or more lowest-enthalpy structures from the previous population and the new structures produced using variation operators. Generation by generation, the above procedure is repeated in a loop.

The first generation usually consists of random structures, but it is possible to include user-specified structures. If lattice parameters are known, runs can be done in the fixed cell, but this is not required and in most cases simulations are done with variable cell shape. We have also improved (*Oganov and Glass*, 2008) the algorithm by more exhaustive removal of lattice redundancies. For more details on the USPEX method, see (*Oganov and Glass*, 2006; *Glass et al*., 2006). A similar evolutionary algorithm was proposed slightly later and independently from us in (*Abraham and Probert*, 2006); this method differs from USPEX in the absence of permutation (i.e. potential problems for binary and more complex compounds), different forms of heredity and mutation, and absence of cell rescaling. We also recently (*Valle and Oganov*, 2008; *Oganov and Valle*, 2009) developed an approach, enabling deeper insight into the performance of structure prediction simulations (e.g. see below on similarity matrices) and into the energy landscape that is being sampled during the simulation.

Why is the USPEX methodology successful? One of the reasons is that local optimization creates chemically reasonable local environments of the atoms. Another reason is that evolutionary pressure (through selection) forces the population to improve from generation to generation. Yet another reason is the choice of variation operators. In heredity, local arrangements of atoms (spatially coherent pieces of structures) are partly preserved and combined. This respects the predominant short-ranged interactions in crystals and exploits information from the current population. For large systems it may be advantageous to combine slabs of several structures. On the other hand, for systems with very few atoms (or molecules) in the unit cell heredity becomes obsolete (in the limit of one atom/unit cell it is completely useless); these cases, however, are trivial for other variation operators and even for local optimization of random structures. As a general note, a successful evolutionary algorithm needs to maintain a balance between the "learning power" and maintaining diversity of the population. Figure 3 illustrates how, without any prior knowledge, a simulation of boron gradually "learned" about B_{12} icosahedra and arrived at the correct ground-state structure.

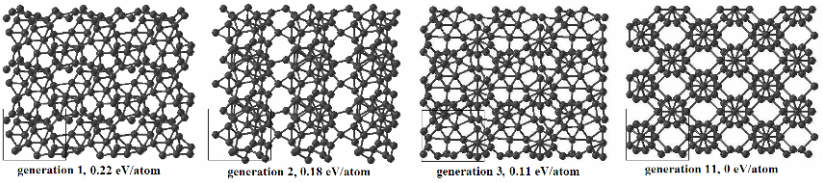

Figure 3. Illustration of an evolutionary search: 24 atoms of boron in a fixed cell. The best structure of the first random generation is 0.22 eV/atom above the ground state and is heavily disordered. In the second generation the best structure already contains an incomplete B_{12} icosahedron, the main building block of the ground-state structure (From (*Oganov et al*., 2009).

Another important reason is that the energy landscapes expected in chemical systems are likely to have an overall "funnel" shape (Figure 3a), where lowest-energy structures are clustered in the same region of configuration (or order parameter) space. In such cases, evolutionary algorithms are particularly powerful: they "zoom in" on the most promising region of configuration space until the global minimum is found. This "zooming in" is enabled by selection of lower-energy structures as parents for the subsequent generation, and by the form of the variational operators.

Actually, it is possible to test the assumption of an overall benign landscape shape using a recent approach (*Oganov and Valle*, 2009) that enables mapping of energy landscapes. If the landscape has one funnel (like in Figure 4a), there will be a direct correlation between the "distance" of all structures from the ground-state structure (this abstract "distance" measures the degree of structural dissimilarity) and the energy relative to the ground state – indeed, in many real systems (for example, GaAs with eight atoms/cell – Figure 4b) such a correlation is found. Even when more than one funnel is present, the number of funnels is usually small (up to three or four). Such situations arise when very different atomic arrangements are energetically competitive, and such systems are particularly challenging as the algorithm may tend to get stuck in one particular funnel. To avoid this, several tools can be used – including dense random or quasirandom sampling (to cover all funnels), tabu lists or special constraint techniques (to deal with each funnel, or a group of funnels, separately).

The energy–distance correlations (Figure 4b) can be regarded as 1D-projections of multidimensional energy landscapes. Projections can, actually, be performed on an arbitrary number of dimensions. Particular visual insight comes from 2D-projections that can be obtained by interpolating and smoothing the 2D-plots presented in (*Oganov and Valle*, 2009). One such depiction of a landscape (for Au_8Pd_4 system) is given in Figure 5.

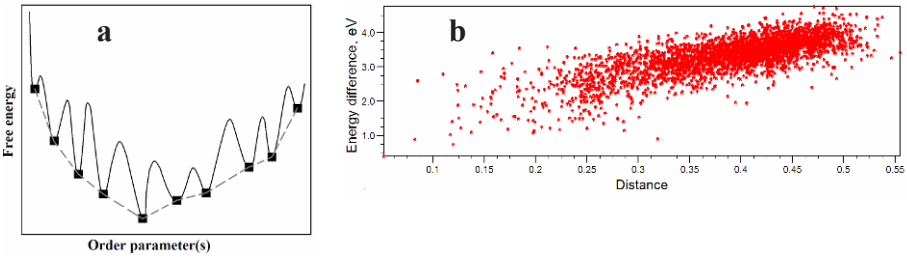

Figure 4. Energy landscapes in chemical systems. (a) A pedagogical cartoon. The original response surface is very "noisy" (i.e. contains very large energy variations, with high barriers between local minima). Local optimization reduces this surface to local minima points (black squares). The reduced response surface (dashed line) is well-behaved and has a simple overall shape. This is one of the reasons why the use of local optimization dramatically improves global optimization (*Glass et al*., 2006) (From *Oganov et al*., 2007). (b) Energy–distance correlation for GaAs (eight atoms/cell). Each point is a locally optimized (i.e. relaxed) structure. The correlation proves that the energy landscape has a simple one-funneled topology (From *Oganov and Valle*, 2009).

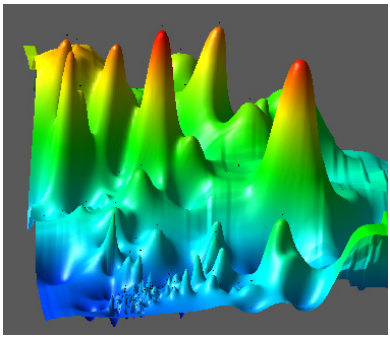

Figure 5. 2D-representation of the energy landscape of Au_8Pd_4 system using method presented in (*Oganov and Valle*, 2009). The surface has the same meaning as the dashed line in Figure 4a – it is an interpolation between the points of local minima. Clearly, there is one energy funnel (blue region), which corresponds to different Au–Pd orderings of the underlying fcc-structure.

The overall landscape shape (Figures 4 and 5) implies that, *en route* to the global minimum some of the low-energy metastable minima can be discovered. This is important; as such phases are often interesting as well. Furthermore, metastable structures found during evolutionary simulations provide a deep insight into the structural chemistry of the studied compound. Thus, evolutionary simulations provide three major results – (1) the ground-state structure; (2) a set of low-energy metastable structures; (3) detailed information on the chemical regime of the compound.

3. Tests of the Algorithm

To measure the strengths and weaknesses of the algorithm, we consider several issues: (i) efficiency of finding the global minimum, in particular relative to a simple well-defined search method, the random sampling;

(ii) size of systems that can be studied in practice; (iii) how fast the diversity decreases along the evolutionary trajectory.

A number of successful tests have been reported in (*Oganov and Glass*, 2006; *Glass et al*., 2006; *Martonak et al*., 2007; *Oganov and Glass*, 2008; *Oganov et al*., 2007). The largest successful test is for a Lennard-Jones crystal with 128 atoms in the (super)cell with variable-cell structure search, which has correctly identified hcp structure as the ground state within three generations (each consisting of only ten structures). For larger Lennard-Jones systems (256 and 512 atoms/cell) we found an energetically very slightly less favorable fcc structure.

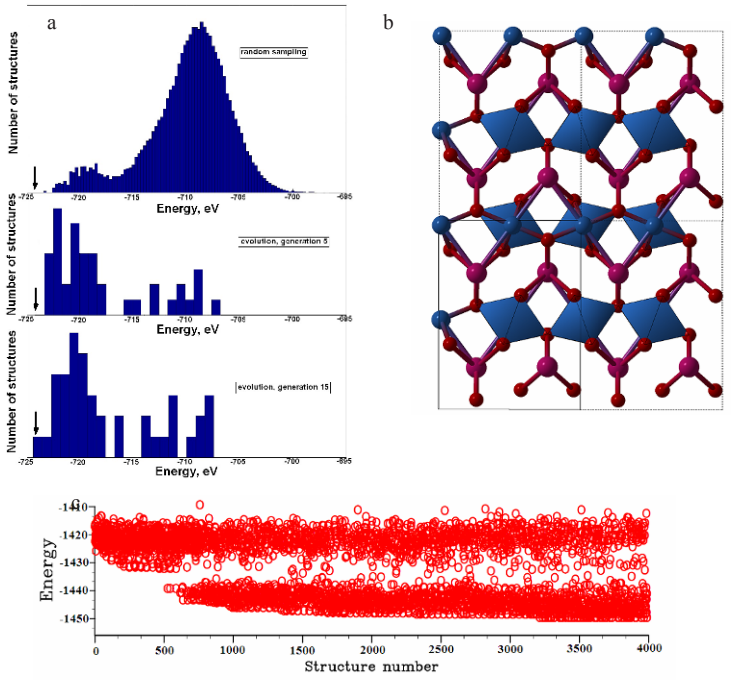

Figure 6. Evolutionary prediction of the structure of $MgSiO_3$ post-perovskite using the experimental cell parameters for (a) 40-atom (*Martonak et al*., 2007) and (b) 80-atom (*Oganov and Glass*, 2008) supercells. In both cases, each generation consisted of 41 structures. Panel (a) compares densities of states of optimized structures generated randomly (top) and in the evolutionary run. Random sampling did not find the correct structure within 1.2×10^5 steps, whereas in the evolutionary simulation shown it was found within 15 generations (i.e. 600 local optimizations). Arrows mark the ground-state energy. Panel (b) shows the energies of structures along the evolutionary trajectory for the 80-atom run; the structure of post-perovskite was obtained within ~3,200 local optimizations. One can see that the density of sampling low-energy structures increases during the simulation.

The largest test for a chemically complex system is the prediction of the structure of $MgSiO_3$ post-perovskite (*Oganov and Ono*, 2004; *Murakami et al.*, 2004) using a relatively large 80-atom supercell (with fixed supercell parameters) and an empirical potential (*Murakami et al.*, 2004) describing interatomic interactions within a partially ionic model. Local optimization and energy calculations were done using the GULP code (*Gale,* 2005). Previously (*Martonak et al.*, 2007) we have shown that already in a 40-atom supercell this test is unfeasible using the simple random sampling (with local optimization): the correct structure was not produced even after 1.2×10^5 random attempts, but was found with 600–950 local optimizations of structures produced by USPEX. With 80 atoms/cell the problem becomes much more complicated (one expects an exponential increase of complexity with system size), but even in this case we correctly produced the post-perovskite structure in a reasonable number (~3,200) of local optimizations – see Figure 6.

Figure 7 shows variable-cell *ab initio* results for $MgSiO_3$ at the pressure of 120 GPa. Several runs with somewhat different parameters (but within a reasonable range) have been performed and all produced the correct ground-state structure of post-perovskite. The number of local optimizations performed before this structure was found ranged in different runs between 120 and 390; the longest run is shown in Figure 7.

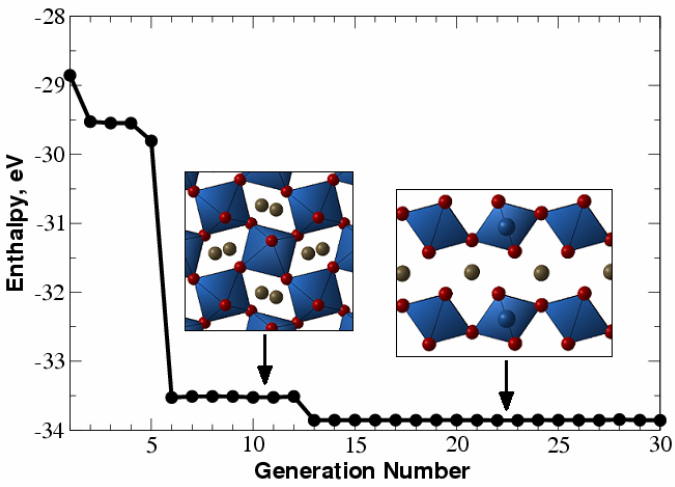

Figure 7. Evolutionary structure search for $MgSiO_3$ at 120 GPa. Evolution of the lowest enthalpy is shown as a function of the generation (insets show the structures of perovskite and post-perovskite phases) (From *Oganov and Glass*, 2006).

An example of a very simple test, variable-cell *ab initio* structure search for GaAs with eight atoms/cell (*Oganov et al*., 2007), is given in Figure 8. The ground-state structure for systems of such size can be found even by local optimization of a reasonable number of randomly produced structures. The density of states of relaxed random structures (Figure 8a), obtained from 3,000 random structures, has a characteristic multimodal shape, which seems to be a general feature of energy landscapes. The stable zincblende structure has the abundance of ~0.2%, i.e. finding it with random search would on average take ~500 local optimizations. In evolutionary simulations (Figure 8b) it can be found within three generations, or just 30 structure relaxations. Similarity matrices for random (Figure 8c) and evolutionary (Figure 8c) searches clearly reveal a strong increase of structure similarity (i.e. decrease of diversity, which can be quantified using the approach (*Valle and Oganov*, 2008; *Oganov and Valle*, 2009) along the evolutionary run, after finding the global minimum. Even in this extreme case a significant number of dissimilar structures are produced long after the global minimum is found.

Au_8Pd_4 (12 atoms/cell) is an unusual system, where a number of different ordered decorations of the fcc structure have competitive energies. The ground state of this system is unknown, but was investigated in several computational studies (*Curtarolo et al*., 2005; *Sluiter et al*., 2006; *Barabash et al*., 2006; *Oganov et al*., 2007). Assuming that the ground-state structure should be an ordered variant of the cubic close-packed ("fcc") structure and using the cluster expansion technique with parameters calibrated on a set of *ab initio* energies, *Barabash et al.* (2006) suggested that there are two energetically nearly degenerate structures (Figure 9c, d). Our calculations found a new ground-state structure (Figure 9b) that has been overlooked by the previous cluster-expansion study (*Barabash et al*., 2006) and turned out to be ~0.1 meV/atom lower in energy than the previously known lowest-energy structures (Figure 9c, d). Examination of all the produced structures shows that most of them are different ordering schemes of the fcc-structure and the energy differences are in most cases very small (Figure 9a).

Periodic boundary conditions suppress decomposition, but when a compound is extremely unstable against decomposition, phase separation can be observed in USPEX simulations. Actually, this happens rather frequently in explorations of hypothetical compositions. A clear example is given by the Cu–C system, which does not have any stable compounds. The tendency to unmixing in this system is very strong and even simulations on small cells show clear separation into layers of fcc-structured Cu and layers of graphite (Figure 10). When the tendency to unmixing is not so large, simulations on small unit cells may find metastable "mixed" structures. Such structures have the lowest thermodynamic potential only at the given

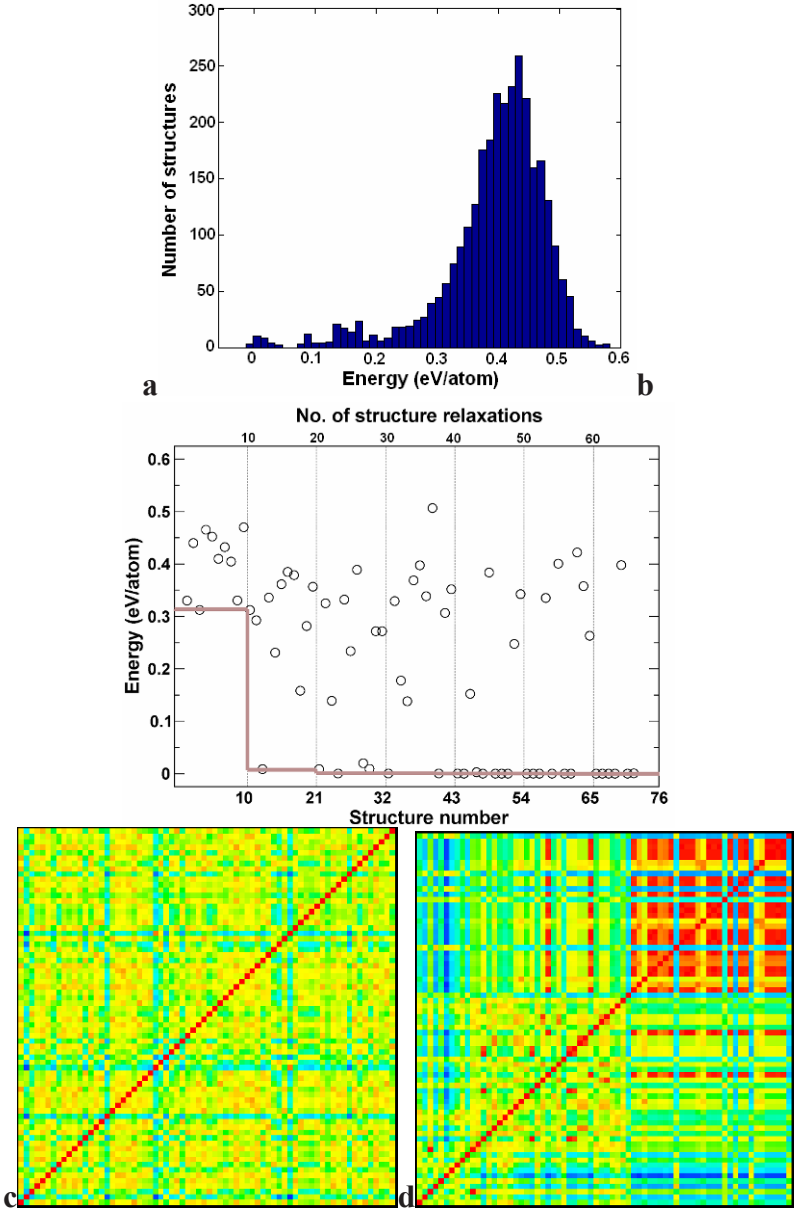

Figure 8. Structure prediction for GaAs (eight atoms/cell): (a) energy distribution for relaxed random structures, (b) progress of an evolutionary simulation (thin vertical lines show generations of structures, and the grey line shows the lowest energy as a function of generation), (c–d) similarity matrices (dimension 70 × 70) for the random and evolutionary searches, respectively. All energies are relative to the ground-state structure. The evolutionary simulation used a population of 10 structures. Calculations are performed within the GGA (*Perdew et al*., 1996) (From *Oganov et al*., 2007).

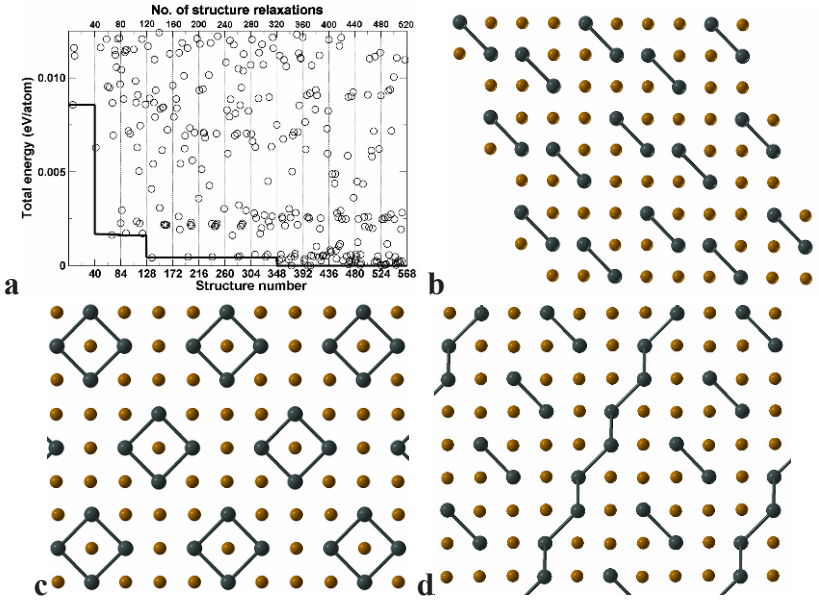

Figure 9. Evolutionary structure search for Au_8Pd_4. (a) evolution of the total energies (only the lowest-energy part is shown for clarity), (b) the lowest-energy structure found in our evolutionary simulation, (c–d) – the lowest-energy structures found by cluster expansion in *Barabash et al.* (2006) (structures No. 4905 and No. 4557, respectively, in the search catalogue of *Barabash et al*., 2006). Energies are given relative to the ground state.

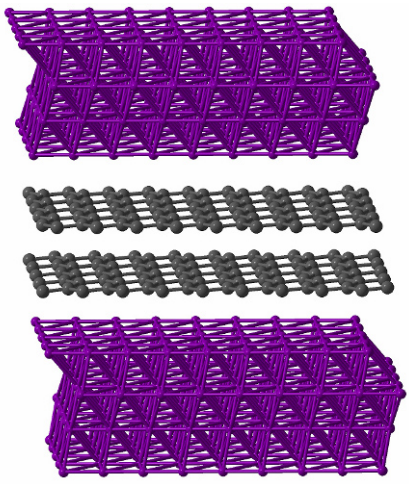

Figure 10. Lowest-energy structure of Cu2C with 12 atoms/cell at 1 atm.

number of atoms in the unit cell; increasing the cell size would lead to phase separation. In the Cu–C system, phase separation is evident already at very small system sizes (Figure 10).

4. Some Applications of the Method

In this section we will review some new insight that has been obtained using our method (see also *Oganov and Glass*, 2006). All structure predictions described here were performed within the generalized gradient approximation (GGA (*Perdew et al*., 1996)) and the PAW method (*Blöchl*, 1994; *Kresse and Joubert*, 1999), using VASP code (*Kresse and Furthmüller*, 1996) for local optimization and total energy calculations. The predicted structures correspond to the global minimum of the approximate free energy surface. For systems where the chosen level of approximation (GGA in cases considered below) is adequate, this corresponds to the experimentally observed structure. Where this is not the case, results of global optimization are invaluable for appraising the accuracy of the approximations.

$CaCO_3$ polymorphs. High-pressure behavior of carbonates is very important for the global geochemical carbon cycle, as high-pressure carbonates of Mg and Ca are expected to contain most of the Earth's oxidized carbon. For $CaCO_3$, there is a well-known transition from calcite to aragonite at ~2 GPa, followed by a transition to a post-aragonite phase at ~40 GPa (*Ono et al*., 2005), the structure of which was solved (*Oganov et al*., 2006) using USPEX, and the predicted structure matched the experimental x-ray diffraction pattern well. Furthermore, we have predicted (*Oganov et al*., 2006) that above 137 GPa a new phase, with space group $C222_1$ and containing chains of carbonate tetrahedra, becomes stable. Recently this prediction was verified by experiments (*Ono et al*., 2007) at pressures above 130 GPa. We note that both post-aragonite and the $C222_1$ structure (Figure 11) belong to new structure types and it would not be possible to find them by analogy with any known structures.

The presence of tetrahedral carbonate-ions at very high pressures invites an analogy with silicates, but the analogy is limited. In silicates, the inter-tetrahedral angle Si–O–Si is extremely flexible (*Lasaga and Gibbs*, 1987), which is one of the reasons for the enormous diversity of silicate structure types. Figure 12 shows the variation of the energy as a function of the Si–O–Si angle in the model $H_6Si_2O_6$ molecule – method borrowed from (*Lasaga and Gibbs*, 1987). One can see only a shallow minimum at $\angle(\mathrm{Si-O-Si})$ = 135°, but a deep minimum at $\angle(C-\mathrm{O}-C)$ = 124° with steep energy variations for $H_6C_2O_7$ (Figure 12). This suggests a much more limited structural variety of metacarbonates, compared to silicates. In both $CaCO_3$ and CO_2 the $\angle(C-\mathrm{O}-C)$ angles are close to 124° in a wide pressure range.

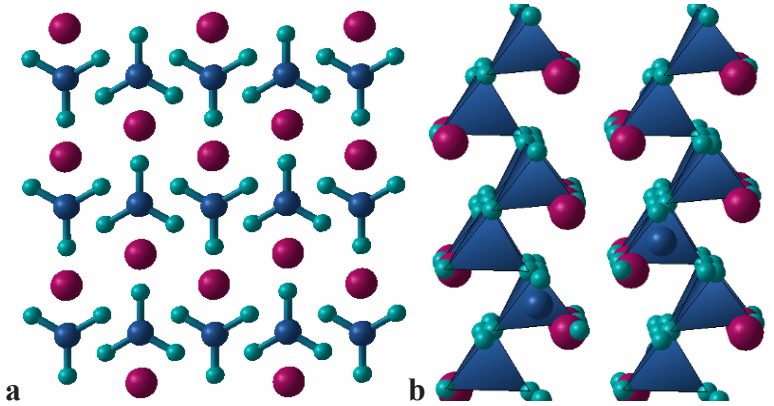

Figure 11. $CaCO_3$ at high pressure. (a) structure of post-aragonite phase, (b) $C222_1$ phase.

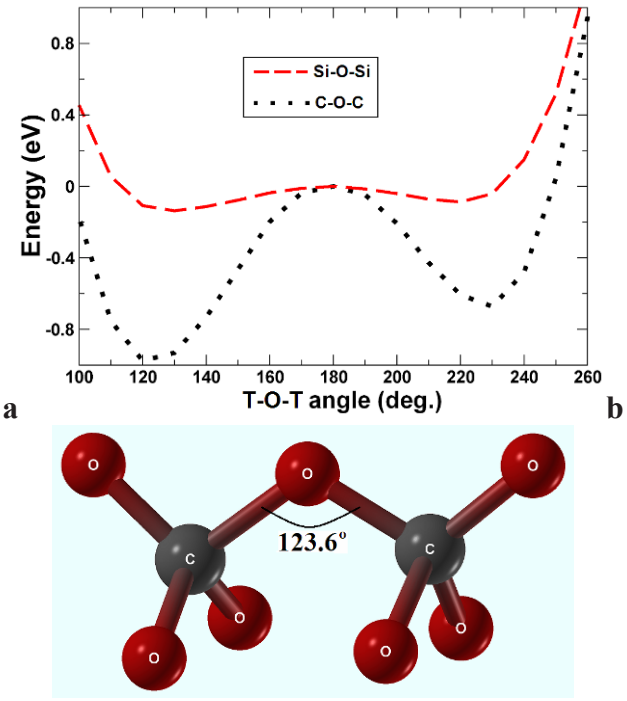

Figure 12. Energy variation as a function of the T–O–T angle (red dashed line – T = Si, black dotted line – T = C). Calculations were performed on $H_6T_2O_7$ molecules; at each angle all T–O distances and O–T–O valence angles were optimized. Optimum angle C–O–C = 124°, Si–O–Si = 135°. These calculations were performed with SIESTA code (*Soler et al*., 2002) using the GGA functional (*Perdew et al*., 1996), norm-conserving pseudopotentials and a double-ζ basis set with a single polarization function for each atom.

Polymeric phase of CO_2 (*Oganov et al.*, 2008). High-pressure behaviour of CO_2 is still controversial (*Bonev et al.*, 2003). It is known that above ~20 GPa a non-molecular phase (called phase V, *Yoo et al.*, 1999) with tetrahedrally coordinated carbon atoms becomes stable, but its structure is still under debate: in the first experimental study (*Yoo et al.*, 1999) a trydimite structure was proposed, but later theoretical works found it to be unstable (even not metastable) and much less favourable than the β-cristobalite structure (*Holm et al.*, 2000; *Dong et al.*, 2000). At the same time, it was not possible to rule out possible existence of even more stable structures. We have performed (*Oganov et al.*, 2008, 2007) evolutionary structure searches at 50 GPa, 100 GPa and 150 GPa for systems with six, nine, 12, 18 and 24 atoms/cell. At all these pressures we confirmed stability of the β-cristobalite structure (Figures 13 and 14), thus suggesting an experimental re-investigation of phase V of carbon dioxide. CO_2-V is stable against decomposition into diamond and oxygen (the enthalpy of decomposition is very large and increases from 3.3 to 3.8 eV between 50 and 200 GPa).

At lower pressures, between 8.9 and 18.9 GPa, the $P\frac{4_2}{m}nm$ phase (see *Bonev et al.*, 2003 for details) is stable, and at even lower pressures (0–8.9 GPa) the *Pa*3 structure is stable (Figure 13). The *Pa*3-$P\frac{4_2}{m}nm$ transition pressure calculated here (8.9 GPa) is consistent with experiment and previous calculation (*Bonev et al.*, 2003).

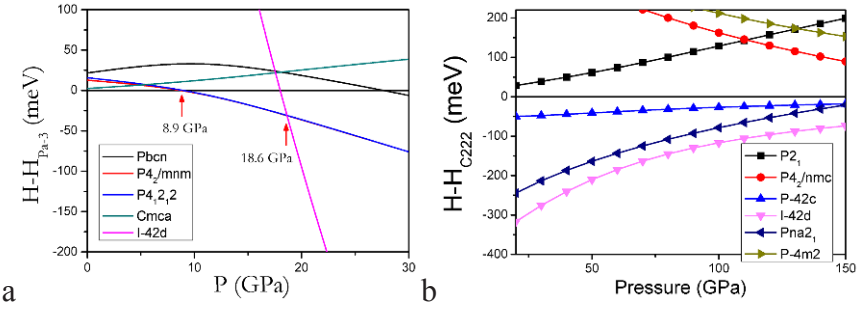

Figure 13. Enthalpies of candidate forms of CO2: (a) in the low-pressure region, relative to the molecular Pa3 structure, (b) in the high-pressure region, relative to the non-molecular C222 structure (From *Oganov et al.*, 2008).

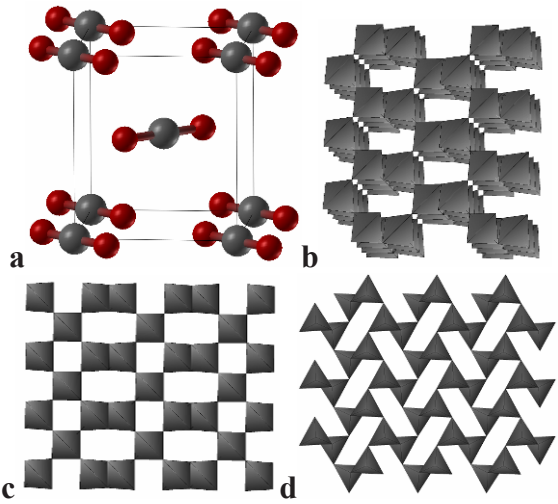

Figure 14. CO2 structures: (a) molecular $P\frac{4_2}{m}nm$ structure, stable at lower pressures than CO2-V, (b) polymeric β-cristobalite-type form of CO_2, suggested to be the structure of phase V and showing carbonate tetrahedra. Structural parameters at 100 GPa: space group $I\bar{4}2d$, a = b = 3.2906 Å, c = 6.0349 Å, C(0.5; 0; 0.25), O(0.2739; 0.25; 0.125), (c) polymeric C222 structure, (d) metastable polymeric $Pna2_1$ structure (From *Oganov et al*., 2008).

Semiconducting and metallic phases of solid oxygen: unusual molecular associations. The red ε-phase of oxygen, stable in the pressure range 8–96 GPa, was discovered in 1979 (*Nicol et al*., 1979), but its structure was solved only in 2006 (*Lundegaard et al*., 2006; *Fujihisa et al*., 2006). The metallic (superconducting at very low temperatures (*Shimizu et al*., 1998)) ζ-phase, stable above 96 GPa, was discovered in 1995 (*Akahama et al*., 1995), and its structure also remained controversial for a long time. Neutron diffraction showed (*Goncharenko*, 2005) that already in the ε-phase (at 8 GPa) there is no long-range magnetic order and likely even no local moments. The disappearance of magnetism is a consequence of increasing overlap of molecular orbitals with increasing pressure. Ultimately, orbital overlap leads to metallization. To understand high-pressure chemistry of oxygen, we performed extensive structure searches at pressures between 25 and 500 GPa (*Oganov and Glass*, 2006; *Ma et al*., 2007), taking into account only non-magnetic solutions.

At 25 GPa we found two particularly interesting structures – one consisting of zigzag chains of O_2 molecules (*Cmcm* structure of *Neaton and Ashcroft*, 2002; *Oganov and Glass*, 2006, see Figure 15b) and one with more complex chains of molecules (see Figure 15c). These have strong similarities

with the experimentally observed structure (*Lundegaard et al*., 2006; *Fujihisa et al*., 2006, see Figure 15a) consisting of O_8 clusters: all of these structures are molecular, and in all of them each molecule is connected with two other molecules, at distances of ~2.1–2.2 Å (the intermolecular distance is ~1.2 Å). The *Cmcm* structure, first suggested in *Neaton and Ashcroft* (2002), is the true GGA ground state, but it differs from experiment; as Figure 16a shows, its enthalpy is ~10 meV/atom lower than for the experimentally found structure (Figure 15a). Metastability of the experimentally studied structure cannot yet be ruled out, but it seems likely that this discrepancy is due to deficiencies of the GGA. The $(O_2)_4$ clusters are held together by weak intermolecular covalent bonds: each O_2 molecule has two unpaired electrons occupying two molecular π^*-orbitals, and sharing these electrons with neighboring molecules creates two intermolecular bonds per molecule and a non-magnetic ground state (*Ma et al*., 2007; *Steudel and Wong*, 2007). It is well known that DFT-GGA does not perform well for stretched covalent bonds, the root of the problem being in the locality of the exchange-correlation hole in DFT-GGA, whereas the true exchange-correlation hole in such cases is highly delocalized. At high pressure, intermolecular distances decrease, intermolecular bonds become more similar to normal covalent bonds and the true exchange-correlation hole becomes more localized. Therefore, we can apply the GGA with greater confidence for the prediction of the structure of the metallic ζ-phase.

For the ζ-phase, evolutionary simulations at 130 and 250 GPa uncovered two interesting structures with space groups *C*2/*m* and *C*2/*c* (*Ma et al.*, 2007). These have very similar enthalpies (Figure 15a); the *C*2/*m* structure is slightly lower in enthalpy and matches experimental x-ray diffraction and Raman spectroscopy data very well, better than the *C*2/*c* structure (*Ma et al*., 2007). Recently (*Weck et al.*, 2009) our predicted *C*2/*m* structure of ζ-oxygen was experimentally confirmed. Both structures contain well-defined O_2 molecules; our simulations show that oxygen remains a molecular solid at least up to 500 GPa. Phonon dispersion curves of the *C*2/*m* structure (Figure 15b–d) contain clearly separated molecular vibrons and show that the structure is dynamically stable (Figure 16), except at 110 GPa, where we see tiny imaginary frequencies in the Γ-V direction, close to the Brillouin zone centre. Such soft modes may result in small-amplitude long-wavelength modulations of the structure at very low temperatures.

The ε-ξ transition is isosymmetric, which implies that it is first-order at low temperatures but can become fully continuous above some critical temperature (*Christy,* 1995). Given the small volume discontinuity upon transition and small hysteresis (one can obtain the *C*2/*m* structure of the ξ-phase by simple overcompression of the ε-O_8 structure, ~5 GPa above the thermodynamic transition pressure), one can expect this critical temperature

to be rather low. We note that within the GGA the ε-ξ transition is predicted to occur at 45 GPa (Figure 16), much lower than the experimental transition pressure (96 GPa). This has two explanations – (i) as the GGA is expected to perform better for the metallic ζ-phase than for the semiconducting ε-O_8 phase, the enthalpy differences are expected to suffer from non-cancelling errors, (ii) since the ε-ξ transition is not only structural, but also electronic (insulator–metal transition), one might expect metallization at lower pressures than in experiment. Typically, density functional calculations overstabilize metallic states relative to insulating ones, and this is exactly what we observe in oxygen.

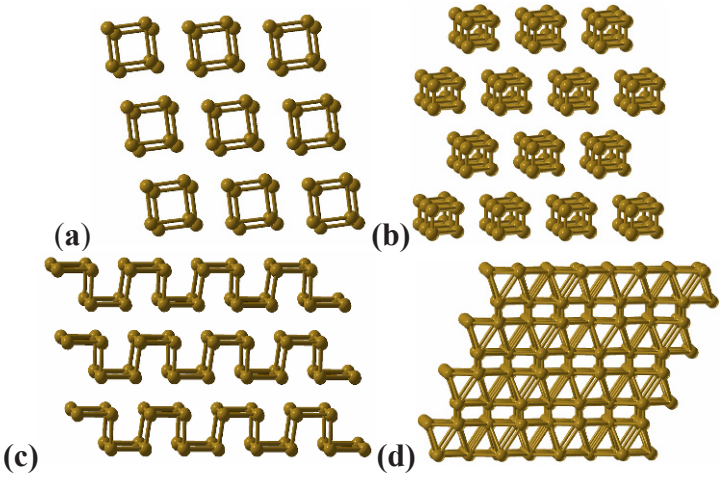

Figure 15. High-pressure structures of oxygen: (a) experimentally found ε-O_8 structure at 17.5 GPa (*Lundegaard et al.*, 2006), (b) Cmcm chain structure (*Neaton and Ashcroft*, 2002; *Oganov and Glass*, 2006), (c) metastable *P*1 chain structure at 25 GPa (*Oganov and Glass*, 2006), (d) C2/m structure of the ζ-phase at 130 GPa (*Ma et al*., 2007). Contacts up to 2.2 Å are shown as bonds (From *Oganov et al*., 2007).

Reactivity of noble gases: are Xe-C compounds possible at high pressure? Inducing major changes in the electronic structure of atoms, high pressure may also change their reactivity. For instance, noble (i.e. largely unreactive) metal platinum under pressure easily forms carbide PtC (*Ono et al*., 2005; *Oganov and Ono*, 2004) and dinitride PtN_2 (*Gregoryanz et al.*, 2004). One should not confuse chemical reactivity with propensity to phase transitions: recently (*Dubrovinsky et al*., 2007) it was groundlessly concluded that gold loses its "nobility" at 240 GPa, when it undergoes an fcc–hcp structural transition. Structural transitions and reactivity are not linked, however: in spite of becoming reactive, Pt does not change its fcc structure, and Cu (not a noble metal by any standards) is only known in one crystalline phase with the fcc structure.

An interesting question is whether noble gases become reactive. Indeed, it was observed that a few percent Xe can be incorporated in quartz (SiO_2) at elevated pressures and high temperatures (*Sanloup et al*., 2005). A possibility has been suggested (*Grochala et al*., 2007) that stable Xe–C compounds may be stable at high pressure; indeed, carbon and xenon have similar valence orbital energies (*cf*. ionization potentials of 12.13 and 11.26 eV for Xe and C, respectively) and one expects that pressure would make Xe more reactive (*Sanloup et al*., 2005). We did simulations at 200 GPa, i.e. above the metallization pressure of Xe (132 GPa; *Goettel et al*., 1989), when its closed electronic shells are strongly perturbed. These calculations were done within the GGA (*Perdew et al*., 1996) and on cells containing up to 14 atoms/cell. At this pressure all Xe carbides are extremely unstable (Figure 17) and their structures show clear separation into close-packed Xe layers (i.e. fragments of the elemental Xe structure) and 3,4-connected carbon layers (intermediate between graphite and diamond). The only exception is the 3D-clathrate structure of XeC_8. The observed layering is consistent with the instability to decomposition. Although Xe carbides are unstable at 200 GPa, already at that pressure we observe considerable bonding Xe–C interactions and the effect of Xe on the carbon sublattice is far beyond simple mechanistic size factor – the carbon layers adopt unusual and exciting configurations that may be prepared in the laboratory under certain conditions.

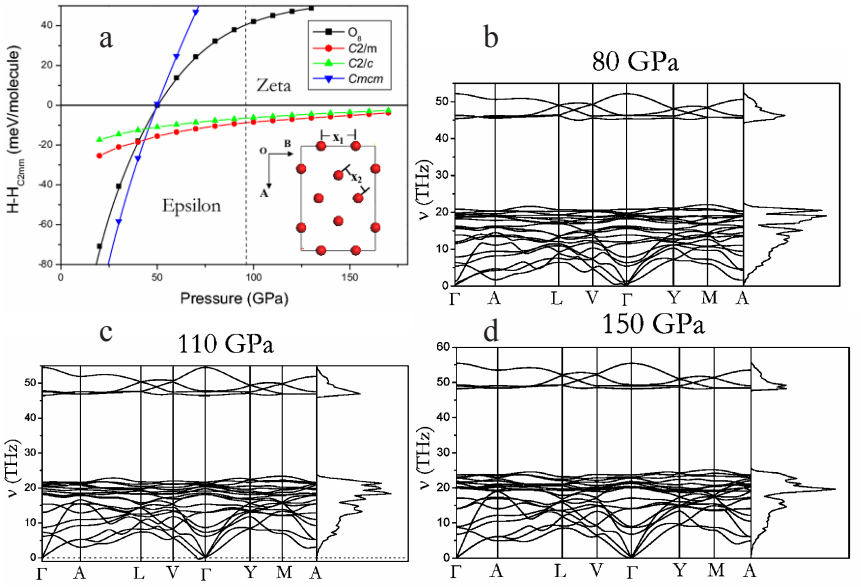

Figure 16. High-pressure phases of oxygen: (a) enthalpies (relative to the C2mm structure of *Serra et al.*, 1998) of several possible structures as a function of pressure (from *Ma et al.*, 2007) of several possible structures, (b-d) phonon dispersion curves and densities of states of the C2/m ζ-phase at three pressures. From (*Oganov et al.*, 2007).

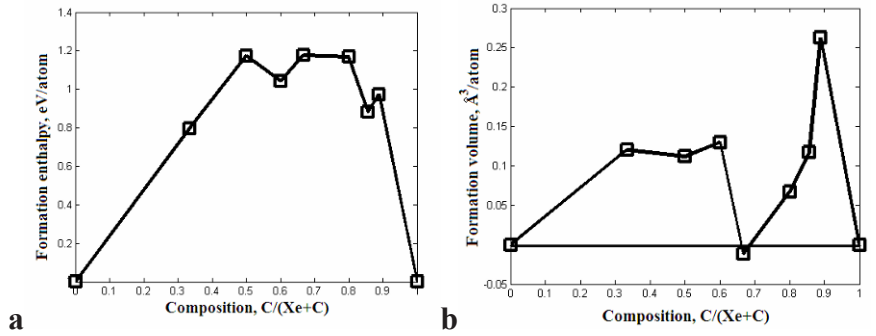

Figure 17. Predicted enthalpy (a) and volume (b) of formation of Xe–C compounds at 200 GPa. The compounds shown are Xe (hcp), Xe_2C, XeC, Xe_2C_3, XeC_2, XeC_4, XeC_6, XeC_8, C(diamond). Note that XeC_2 has a small negative volume of formation and might become stable at much higher pressures (From *Oganov et al*., 2007).

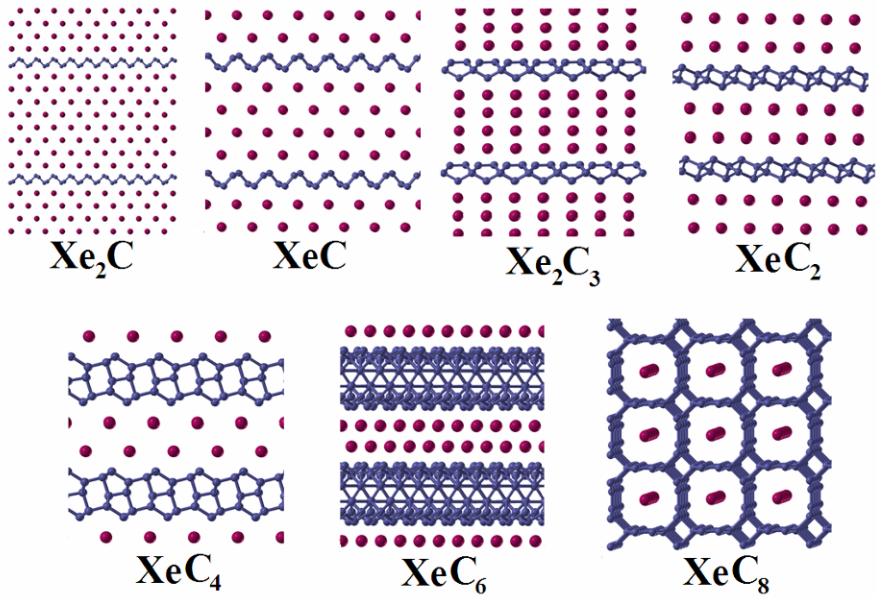

Figure 18. Predicted structures of Xe_2C, XeC, Xe_2C_3, XeC_2, XeC_4, XeC_6, XeC_8 at 200 GPa (From *Oganov et al*., 2007).

Boron: novel phase with a partially ionic character. Boron is perhaps the most enigmatic element: at least 16 phases were reported in the literature, but most are believed or suspected to be compounds (rather than forms of the pure element), and until recently the phase diagram was unknown. Following experimental findings of J. Chen and V.L. Solozhenko

(both arrived independently at the same conclusions in early 2004) of a new phase at pressures above 10 GPa and temperatures of 1,800–2,400 K, whose structure could not be determined from experimental data alone, we found the structure using USPEX. We named this phase γ-B_{28} (because it contains 28 atoms/cell). Its structure has space group *Pnnm* and is comprised of icosahedral B_{12} clusters and B_2 pairs in a NaCl-type arrangement. This phase is stable between 19 and 89 GPa, and exhibits sizable charge transfer from B_2 pairs to B_{12} clusters, quite unexpected for a pure element. Details are given in (*Oganov et al*., 2009) and Figures 19 and 20. Figure 21 shows a comparison of theoretical and experimental X-ray powder diffraction profiles.

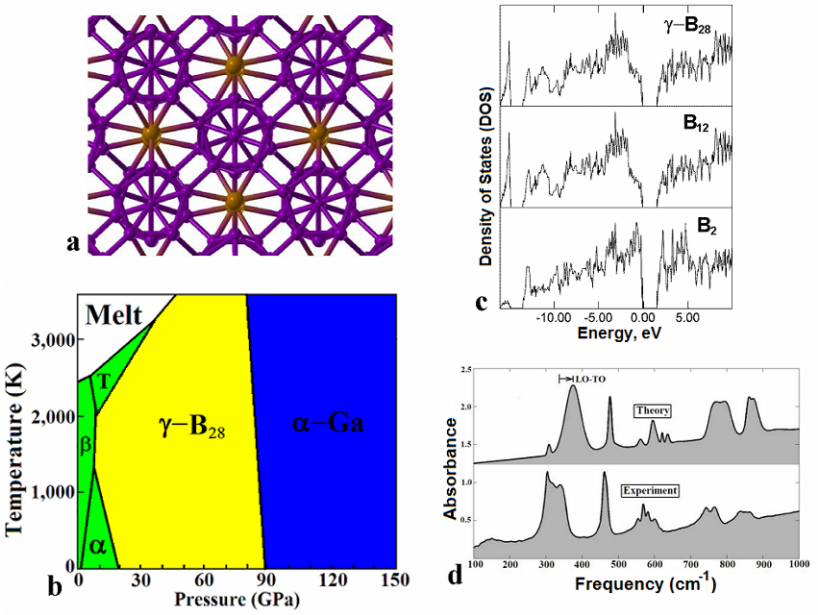

Figure 19. Boron: (a) structure of γ-B_{28} (B_{12} icosahedra are shown in blue, B_2 pairs – in orange). (b) phase diagram of boron, showing a wide stability field of γ-B_{28}. (c) electronic DOS and its projections onto B_{12} and B_2 units (all DOSs are normalized per atom), (d) comparison of theoretical and experimental IR spectra. IR spectra indicate the presence of non-zero Born charges on atoms (From *Oganov et al*., 2009).

γ-B_{28} can be represented as a "boron boride" $(B_2)^{\delta+}(B_{12})^{\delta-}$; although the exact value of the charge transfer δ depends on the definition of an atomic charge, for all definitions that we used the qualitative picture is the same. Perhaps the most reliable definition of a charge, due to *Bader* (1990), gives δ~0.5 (*Oganov et al*., 2009). We have recently found that (based on the similarity of synthesis conditions and many diffraction peaks) the same high-pressure boron phase may have been observed by Wentorf in 1965 (*Wentorf*, 1965),

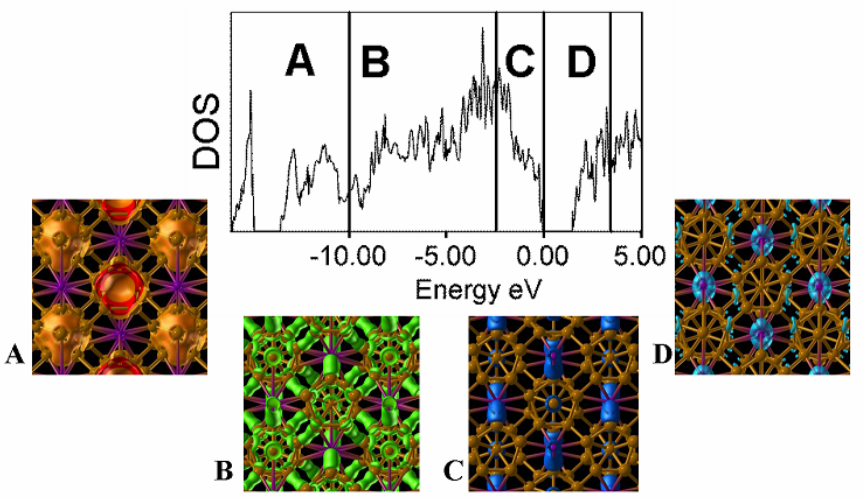

Figure 20. γ-B_{28}: total electronic DOS and energy-decomposed electron densities. Lowest-energy valence electrons are localized predominantly by the B_{12} icosahedra, while top of the valence band and bottom of the conduction band (i.e. holes) are localized on the B_2 pairs. This is consistent with atom-projected DOSs (Figure 19c) and the picture of charge transfer $B_2 \rightarrow B_{12}$.

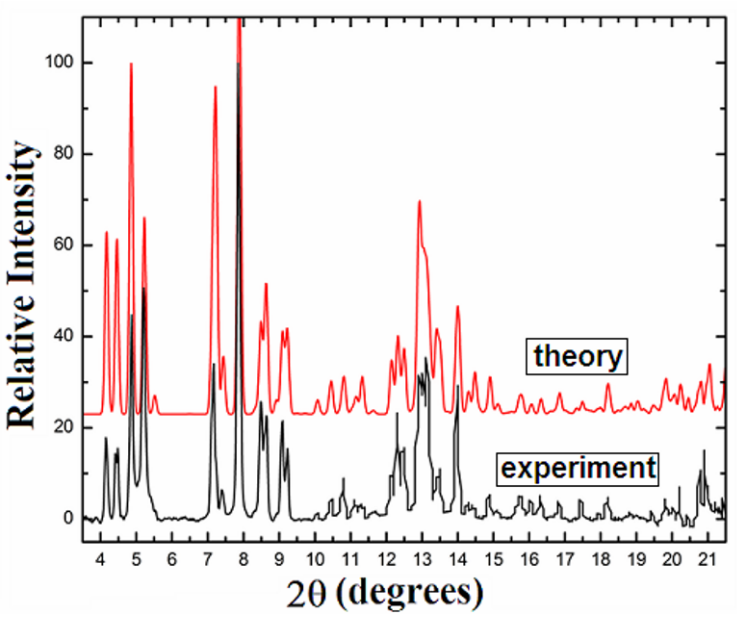

Figure 21. Comparison of theoretical and experimental X-ray powder diffraction profiles of γ-B_{28}. X-ray wavelength λ = 0.31851 Å (From *Oganov et al.*, 2009).

though Wentorf's material was generally not believed to be pure boron (due to the extreme sensitivity of boron to impurities and lack of chemical analysis or structure determination in *Wentorf* (1965)) and its diffraction pattern was

deleted from Powder Diffraction File database. γ-B_{28} is structurally related to several compounds – for instance, B_6P (*Amberger and Rauh*, 1974) or $B_{13}C_2$ (*Kwei and Morosin*, 1996)), where the two sublattices are occupied by different chemical species (instead of interstitial B_2 pairs there are P atoms or C–B–C groups, respectively). The concept of charge transfer in this phase follows naturally from its atomic and electronic structure (e.g. Figure 20); yet, without presenting valid evidence, Dubrovinskaia and Dubrovinsky (see their chapter in this volume) incorrectly claimed chemical bonding to be purely covalent in this material (see our criticisms in *Oganov et al*., 2009a). Significant charge transfer can be found in other elemental solids, and observations of dielectric dispersion (*Tsagareishvili et al*., 2009), equivalent to LO–TO splitting, suggest it for β-B_{106}. The nature of the effect is possibly similar to γ-B_{28}. Detailed microscopic understanding of charge transfer in β-B_{106} would require detailed knowledge of its structure, and reliable structural models of β-B_{106} finally begin to emerge from computational studies (*van Setten et al*., 2007; *Ogitsu et al*., 2009). It is worth mentioning that γ-B_{28} is a superhard phase, with a measured Vickers hardness of 50 GPa (*Solozhenko et al*., 2008), which puts it among half a dozen hardest materials known to date.

Sodium: a metal that goes transparent under pressure. A sequence of recent discoveries demonstrated that sodium, a simple s-element at normal conditions, behaves in highly non-trivial ways under pressure. The discovery of an incommensurate host–guest structure (*Hanfland et al*., 2002), followed by finding of several complex structures (*Gregoryanz et al*., 2008) in the range of pressures corresponding to the minimum of the melting curve (*Gregoryanz et al*., 2005), and the very existence of that extremely deep minimum in the melting curve at about 110 GPa and 300 K – all this evidence pointed to some unusual changes in the physics of sodium. Later it was also shown that the incommensurate host-guest structure is a 1D-metal (*Lazicki et al*., 2009), where conductivity is primarily due to chains of atoms in the guest sublattice. Yet another unusual phenomenon was predicted using USPEX and later (but within the same paper (*Ma et al*., 2009)) verified experimentally: on further compression sodium becomes a wide-gap insulator! This happens at ~190 GPa, and Figure 22 shows the crystal structure of the insulating "hP4" phase, its enthalpy relative to other structures, and the electronic structure. The structure can be described as a double hexagonal close-packed (dhcp) structure, squeezed by a factor of >2 along the *c*-axis, as a result of which sodium atoms have sixfold coordination. There are two inequivalent Na positions: Na1 and Na2, which have the octahedral and trigonal-prismatic coordination, and the hP4 structure can be described as the elemental analog of the NiAs structure type (the same way as diamond is the elemental analog of the zincblende structure type). Calculations suggest that sodium is no longer an s-element; instead, the outermost valence electron has significant

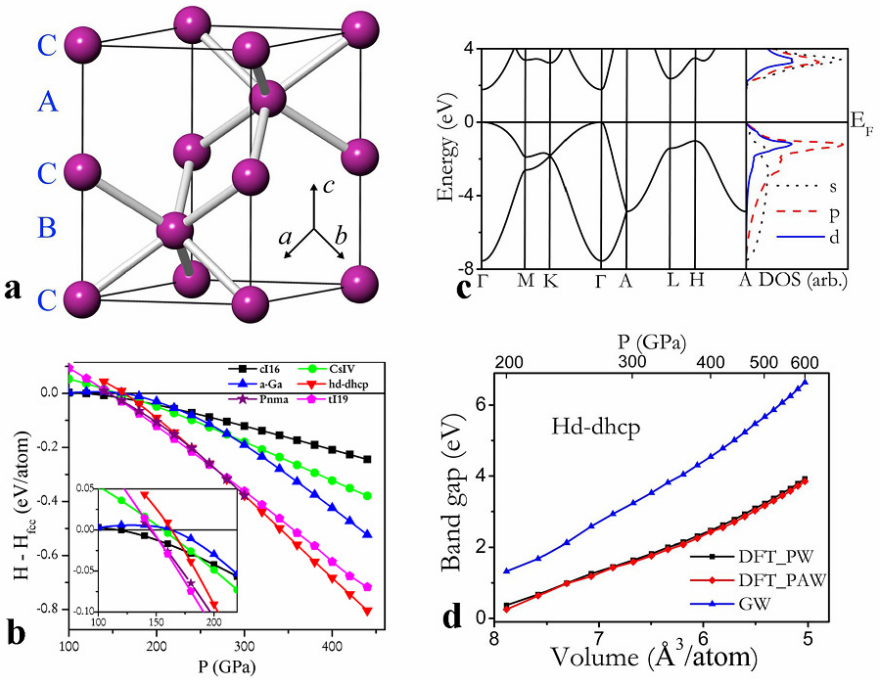

Figure 22. Summary on the hP4 phase of sodium: (a) its crystal structure, (b) enthalpies of competing high-pressure phases (relative to the fcc structure), (c) band structure, (d) pressure dependence of the band gap, indicating rapid increase of the band gap on compression (From *Ma et al.*, 2009).

s-, p- and d-characters (Figure 22c). Compressed sodium can be considered as a transition metal, because of its significant d-character.

The band gap is direct, and increases with pressure. At 200 GPa the bandgap calculated with the GW approximation (known to give rather accurate results) is 1.3 eV, and increases to 6.5 eV at 600 GPa. These predictions implied that above 200 GPa sodium will be red and transparent, and at ~300 GPa it will become colorless and transparent (like wide-gap insulators). This has indeed been confirmed in experiments of M.I. Eremets (*Ma et al*., 2009), see Figure 23. The insulating behavior is explained by the extreme localization of the valence electrons in the interstices of the structure, i.e. in the "empty" space (Figure 24). These areas of localization are characterized by surprisingly high values of the electron localization function (nearly 1.0) and maxima of the total electron density. The number of such maxima is half the number of sodium atoms, and therefore in a simple model we can consider Na atoms as completely ionized (Na^+), and interstitial maxima as containing one electron pair. The hP4 structure can also be described as a Ni_2In-type structure, where Na atoms occupy positions of

Ni atoms, and interstitial electron pairs in hP4-Na sit on the same positions as In atoms in Ni_2In. At first counterintuitively, the degree of localization of the interstitial electron pairs increases with pressure, explaining the increase of the band gap (Figure 22d). hP4-Na can be described as an electride, i.e. an ionic "compound" formed by ionic cores and localized interstitial electron pairs. The very fact that sodium, one of the best and simplest metals, under pressure becomes a transparent insulator with localized valence electrons, is remarkable and forces one to reconsider classical ideas of chemistry.

Interstitial charge localization can be described in terms of (s)-p-d orbital hybridizations, and its origins are in the exclusionary effect of the ionic cores on valence electrons: valence electrons, feeling repulsion from the core electrons, are forced into the interstitial regions at pressures when atomic cores begin to overlap (*Neaton and Ashcroft*, 1999).

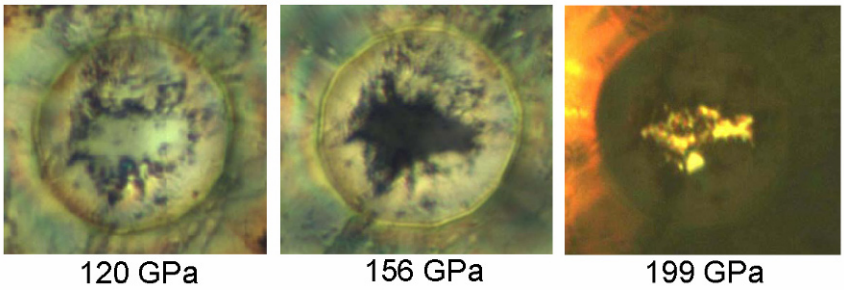

Figure 23. Photographs of sodium samples under pressure. At 120 GPa the sample is metallic and highly reflective, at 156 GPa the reflectivity is very low, and at 199 GPa the sample is transparent (From *Ma et al*., 2009).

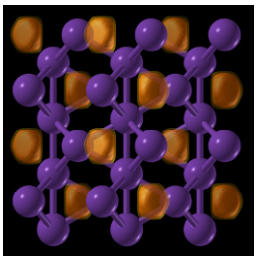

Figure 24. Crystal structure and electron localization function (orange isosurfaces – lowest contour 0.82) of the hP4 phase of sodium at 300 GPa. Interstitial electron localization is clearly seen.

5. Conclusions

Evolutionary algorithms, based on physically motivated forms of variation operators and local optimization, are a powerful tool enabling reliable and efficient prediction of stable crystal structures. This method has a wide field

of applications in computational materials design (where experiments are time-consuming and expensive) and in studies of matter at extreme conditions (where experiments are very difficult or sometimes beyond the limits of feasibility).

One of the current limitations is the accuracy of today's *ab initio* simulations; this is particularly critical for strongly correlated and for van der Waals systems. Note, however, that the method itself does not make any assumptions about the way energies are calculated and can be used in conjunction with any method that is able to provide total energies. Most of practical calculations are done at T = 0 K, but temperature can be included as long as the free energy can be calculated efficiently. Difficult cases are aperiodic and disordered systems (for which only the lowest-energy periodic approximants and ordered structures can be predicted at this moment).

We are suggesting USPEX as the method of choice for crystal structure prediction of systems with up to ~50 atoms/cell, where no information (or just the lattice parameters) is available. Above 50–100 atoms/cell runs become expensive (although still feasible), eventually necessitating the use of other ideas within USPEX or another approach, due to the 'curse of dimensionality'. There is hope of enabling structure prediction for very large (>200 atoms/cell) systems. The extension of the method to molecular systems (i.e. handling whole molecules, rather than individual atoms) is already available. The first successful step has been made (*Schönborn et al.*, 2009) in adapting USPEX to clusters. Similar extensions, which are relatively straightforward, still need to be done for surfaces and interfaces. One other important problem is the simultaneous prediction of all stable stoichiometries and structures (in a given range of compositions). A pioneering study (*Jóhannesson et al*., 2002) succeeded in predicting stable stoichiometries of alloys within a given structure type. The first steps in simultaneous prediction of structure and stoichiometry have recently been made (*Wang et al*., 2008).

USPEX has been applied to many important problems. Apart from the applications described above, several noteworthy results have been published by us recently. These include the high-pressure post-magnesite phases of $MgCO_3$ (*Oganov et al*., 2008), polymeric phases of nitrogen (*Ma et al*., 2009a), superconducting phases of silane (SiH_4) (*Martinez-Canales et al*., 2009) and germane (GeH_4) (*Gao et al*., 2008), the latter predicted to have a remarkably high T_C = 64 K (*Gao et al*., 2008). Its ability to predict not only the ground states, but also low-energy metastable structures has led to the finding (*Oganov and Glass,* 2006) of an interesting metastable structure of carbon, which has recently been shown (*Li et al*., 2009) to match the observed properties of the so-called "superhard graphite", a material scratching on diamond and formed by metastable room-temperature compression of

graphite beyond 15 GPa (*Mao et al*., 2003). One expects many more applications to follow, both in high-pressure research and in materials design.

ACKNOWLEDGEMENTS

ARO thanks R. Hoffmann, W. Grochala, R.J. Hemley and R.M. Hazen for exciting discussions. ARO also gratefully acknowledges financial support from the Research Foundation of Stony Brook University and from Intel Corporation. YM's work is supported by the China 973 Program under Grant No. 2005CB724400, the National Natural Science Foundation of China under grant No. 10874054, the NSAF of China under Grant No. 10676011, and the 2007 Cheung Kong Scholars Programme of China. We acknowledge support from the National Science Foundation of China for the Research Fellowship for International Young Scientists (grant No. 10910263) and thank the Joint Supercomputer Center (Russian Academy of Sciences, Moscow) and CSCS (Manno) for providing supercomputer time. USPEX code is available on request from ARO.

References

Abraham N.L., Probert M.I.J. (2006). A periodic genetic algorithm with real-space representation for crystal structures and polymorph prediction. *Phys. Rev.* **B73**, art. 224104.

Akahama Y., Kawamura H., Hausermann D., Hanfland M., Shimomura O. (1995). New high-pressure structural transition of oxygen at 96 GPa associated with metallization in a molecular solid. *Phys. Rev. Lett.* **74**, 4690–4693.

Amberger E., Rauh P.A. (1974). Structur des borreichen Borphosphids. *Acta Cryst.* **B30**, 2549–2553.

Bader (1990). *Atoms in Molecules. A Quantum Theory*. Oxford University Press: Oxford, 438 pp.

Barabash S.V., Blum V., Muller S., Zunger A. (2006). Prediction of unusual stable ordered structures of Au-Pd alloys via a first-principles cluster expansion. *Phys. Rev.* **B74**, art. 035108.

Bazterra V.E., Ferraro M.B., Facelli J.C. (2002). Modified genetic algorithm to model crystal structures. I. Benzene, naphthalene and anthracene. *J. Chem. Phys.* **116**, 5984–5991.

Blöchl P.E. (1994). Projector augmented-wave method. *Phys. Rev.* **B50**, 17953–17979.

Boisen M.B., Gibbs G.V., Bukowinski M.S.T. (1994). Framework silica structures generated using simulated annealing with a potential energy function based on an $H_6Si_2O_7$ molecule. *Phys. Chem. Miner.* **21**, 269–284.

Bonev S.A., Gygi F., Ogitsu T., Galli G. (2003). High-pressure molecular phases of solid carbon dioxide. *Phys. Rev. Lett.* **91**, 065501.

Bush T.S., Catlow C.R.A., Battle P.D. (1995). Evolutionary programming techniques for predicting inorganic crystal structures. *J. Mater. Chem.* **5**, 1269–1272.

Christy A.G. (1995). Isosymmetric structural phase transitions: phenomenology and examples. *Acta Cryst.* **B51**, 753–757.

Curtarolo S., Morgan D., Ceder G. (2005). Accuracy of *ab initio* methods in predicting the crystal structures of metals: a review of 80 binary alloys. *CALPHAD: Comput. Coupling Phase Diagrams Thermochem.* **29**, 163–211.

Curtarolo S., Morgan D., Persson K., Rodgers J., Ceder G. (2003). Predicting crystal structures with data mining of quantum calculations. *Phys. Rev. Lett.* **91**, art. 135503.

Deaven D.M., Ho K.M. (1995). Molecular geometry optimization with a genetic algorithm. *Phys. Rev. Lett.* **75**, 288–291.

Deem M.W., Newsam, J.M. (1989). Determination of 4-connected framework crystal structures by simulated annealing. *Nature* **342**, 260–262.

Dong J.J., Tomfohr J.K., Sankey O.F., Leinenweber K., Somayazulu M., McMillan P.F. (2000). Investigation of hardness in tetrahedrally bonded nonmolecular CO_2 solids by density-functional theory. *Phys. Rev.* **B62**, 14685–14689.

Dubrovinsky L., Dubrovinskaia N., Crichton W.A., Mikhailushkin A.S., Simak S.I., Abrikosov I.A., de Almeida J.S., Ahuja R., Luo W., Johansson B. (2007). Noblest of all metals is structurally unstable at high pressure. *Phys. Rev. Lett.* **98**, 045503.

Fujihisa H., Akahama Y., Kawamura H., Ohishi Y., Shimomura O., Yamawaki H., Sakashita M., Gotoh Y., Takeya S., Honda K. (2006). O_8 cluster structure of the epsilon phase of solid oxygen. *Phys. Rev. Lett.* **97**, art. 085503.

Gale J.D. (2005). GULP: Capabilities and prospects. *Z. Krist.* 220, 552–554.

Gao G., Oganov A.R., Bergara A., Martinez-Canalez M., Cui T., Iitaka T., Ma Y., Zou G. (2008). Superconducting high pressure phase of germane. *Phys. Rev. Lett.* **101**, 107002.

Glass C.W., Oganov A.R., Hansen N. (2006). USPEX – evolutionary crystal structure prediction. *Comp. Phys. Comm.* **175**, 713–720.

Goettel K.A., Eggert J.H., Silvera I.F., Moss W.C. (1989). Optical evidence for the metallization of xenon at 132(5) GPa. *Phys. Rev. Lett.* **62**, 665–668.

Goncharenko I.N. (2005). Evidence for a magnetic collapse in the epsilon phase of solid oxygen. *Phys. Rev. Lett.* **94**, art. 205701.

Gottwald D., Kahl G., Likos C.N. (2005). Predicting equilibrium structures in freezing processes. *J. Chem. Phys.* **122**, art. 204503.

Gödecker S. (2004) Minima hopping: an efficient search method for the global minimum of the potential energy surface of complex molecular systems. *J. Chem. Phys.* **120**, 9911–9917.

Gregoryanz, E., Degtyareva, O., Somayazulu, M., Hemley, R.J., Mao, H.K. (2005). Melting of dense sodium. *Phys. Rev. Lett.* **94**, 185502.

Gregoryanz E., Lundegaard L.F., McMahon M.I., Guillaume C., Nelmes R.J., Mezouar M. (2008). Structural diversity of sodium. *Science* **320**, 1054–1057.

Gregoryanz E., Sanloup C., Somayazulu M., Badro J., Fiquet G., Mao H.K., Hemley R.J. (2004). Synthesis and characterization of a binary noble metal nitride. *Nat. Mater.* **3**, 294–297.

Grochala W. (2007). Atypical compounds of gases, which have been called 'noble'. *Chem. Soc. Rev.* **36**, 1632–1655.

Hanfland M., Syassen K., Loa I., Christensen N.E., Novikov D.L. (2002). Na at megabar pressures. Poster at 2002 High Pressure Gordon Conference.

Holm B., Ahuja R., Belonoshko A., Johansson B. (2000). Theoretical investigation of high pressure phases of carbon dioxide. *Phys. Rev. Lett.* **85**, 1258–1261.

Jóhannesson G.H., Bligaard T., Ruban A.V., Skriver H.L., Jacobsen K.W., Nørskov J.K. (2002). Combined electronic structure and evolutionary search approach to materials design. *Phys. Rev. Lett.* **88**, art. 255506.

Kresse G., Furthmüller J. (1996). Efficient iterative schemes for *ab initio* total-energy calculations using a plane wave basis set. *Phys. Rev.* **B54**, 11169–11186.

Kresse G., Joubert D. (1999). From ultrasoft pseudopotentials to the projector augmented-wave method. *Phys. Rev.* **B59**, 1758–1775.

Kwei G.H., Morosin B. (1996). Structures of the boron-rich boron carbides from neutron powder diffraction: implications for the nature of the inter-icosahedral chains. *J. Phys. Chem.* **100**, 8031–8039.

Lasaga A.C., Gibbs G.V. (1987). Applications of quantum-mechanical potential surfaces to mineral physics calculations. *Phys. Chem. Minerals* **14**, 107–117.

Lazicki A., Goncharov A.F., Struzhkin V.V., Cohen R.E., Liu Z., Gregoryanz E., Guillaume C., Mao H.K., Hemley R.J. (2009). Anomalous optical and electronic properties of dense sodium. *Proc. Natl. Acad. Sci.* **106**, 6525–6528.

Li Q., Oganov A.R., Wang H., Wang H., Xu Y., Cui T., Ma Y., Mao H.-K., Zou G. (2009). Superhard monoclinic polymorph of carbon. *Phys. Rev. Lett.* **102**, 175506.

Lundegaard L.F., Weck G., McMahon M.I., Desgreniers S., Loubeyre P. (2006). Observation of an O_8 molecular lattice in the epsilon phase of solid oxygen. *Nature* **443**, 201–204.

Ma Y., Eremets M.I., Oganov A.R., Xie Y., Trojan I., Medvedev S., Lyakhov A.O., Valle M., Prakapenka V. (2009). Transparent dense sodium. *Nature* **458**, 182–185.

Ma Y.-M., Oganov A.R., Glass C.W. (2007). Structure of the metallic ζ-phase of oxygen and isosymmetric nature of the ε-ζ phase transition: *ab initio* simulations. *Phys. Rev.* **B76**, art. 064101.

Ma Y., Oganov A.R., Xie Y., Li Z., Kotakoski J. (2009a). Novel high pressure structures of polymeric nitrogen. *Phys. Rev. Lett.* **102**, 065501.

Ma Y., Wang Y., Oganov A.R. (2009). Absence of superconductivity in the novel high-pressure polymorph of MgB_2. *Phys. Rev.* **B79**, 054101.

Mao W.L., Mao H.K., Eng P.J., Trainor T.P., Newville M., Kao C.C., Heinz D.L., Shu J., Meng Y., Hemley R.J. (2003). Bonding changes in compressed superhard graphite. *Science* **302**, 425–427.

Martinez-Canales M., Oganov A.R., Lyakhov A., Ma Y., Bergara A. (2009). Novel structures of silane under pressure. P*hys. Rev. Lett.* **102**, 087005.

Martoňák R., Donadio D., Oganov A.R., Parrinello M. (2006). Crystal structure transformations in SiO_2 from classical and *ab initio* metadynamics. *Nature Materials* **5**, 623–626.

Martoňák R., Donadio D., Oganov A.R., Parrinello M. (2007). 4- to 6- coordinated silica: transformation pathways from metadynamics. *Phys. Rev.* **B76**, 014120.

Martonak R., Laio A., Bernasconi M., Ceriani C., Raiteri P., Zipoli F., and Parrinello M. (2005). Simulation of structural phase transitions by metadynamics. *Z. Krist.* **220**, 489–498.

Martonak R., Laio A., Parrinello M. (2003). Predicting crystal structures: the Parrinello-Rahman method revisited. *Phys. Rev. Lett*, **90**, 075503.

Martonak R., Oganov A.R., Glass C.W. (2007). Crystal structure prediction and simulations of structural transformations: metadynamics and evolutionary algorithms. *Phase Transitions* **80**, 277–298.

Murakami, M., Hirose, K., Kawamura, K., Sata, N., Ohishi, Y. (2004). Post-perovskite phase transition in $MgSiO_3$. *Science* **307**, 855–858.

Neaton J.B., Ashcroft N.W. (1999). Pairing in dense lithium. *Nature* **400**, 141–144.

Neaton J.B., Ashcroft N.W. (2002). Low-energy linear structures in dense oxygen: implications for the epsilon phase. *Phys. Rev. Lett.* **88**, 205503.

Nicol M., Hirsch K.R., Holzapfel W.B. (1979). Oxygen phase equilibria near 298 K. *Chem. Phys. Lett.* 68, 49–52.

Oganov A.R., Chen J., Gatti C., Ma Y.-Z., Ma Y.-M., Glass C.W., Liu Z., Yu T., Kurakevych O.O., Solozhenko V.L. (2009). Ionic high-pressure form of elemental boron. *Nature* **457,** 863–867.

Oganov A.R., Glass C.W. (2006). Crystal structure prediction using *ab initio* evolutionary techniques: principles and applications. *J. Chem. Phys.* **124**, art. 244704.

Oganov A.R., Glass C.W. (2008). Evolutionary crystal structure prediction as a tool in materials design. *J. Phys.: Cond. Mattter* **20**, art. 064210.

Oganov A.R., Glass C.W., Ono S. (2006). High-pressure phases of $CaCO_3$: crystal structure prediction and experiment. *Earth Planet. Sci. Lett.* **241**, 95–103.

Oganov A.R., Ma Y., Glass C.W., Valle M. (2007). Evolutionary crystal structure prediction: overview of the USPEX method and some of its applications. *Psi-k Newsletter*, issue 84, Highlight of the Month, 142–171.

Oganov A.R., Martoňák R., Laio A., Raiteri P., Parrinello M. (2005). Anisotropy of Earth's D" layer and stacking faults in the $MgSiO_3$ post-perovskite phase. *Nature* **438**, 1142–1144.

Oganov, A.R., Ono, S. (2004). Theoretical and experimental evidence for a post-perovskite phase of $MgSiO_3$ in Earth's D" layer. *Nature* **430**, 445–448.

Oganov A.R., Ono S., Ma Y., Glass C.W., Garcia A. (2008). Novel high-pressure structures of $MgCO_3$, $CaCO_3$ and CO_2 and their role in the Earth's lower mantle. *Earth Planet. Sci. Lett.* **273**, 38–47.

Oganov A.R., Solozhenko V.L., Kurakevych O.O., Gatti C., Ma Y., Chen J., Liu Z., Hemley R.J. (2009a). Comment on "Superhard semiconducting optically transparent high pressure phase of boron", http://arxiv.org/abs/0908.2126

Oganov A.R., Valle M. (2009). How to quantify energy landscapes of solids. *J. Chem. Phys.* **130**, 104504.

Ogitsu T., Gygi F., Reed J., Motome Y., Schwegler E., Galli G. (2009). Imperfect Crystal and Unusual Semiconductor: boron, a Frustrated Element. *J. Am. Chem. Soc.* **131**, 1903–1909.

Ono S., Kikegawa T., Ohishi Y. (2005). A high-pressure and high-temperature synthesis of platinum carbide. Sol. St. Comm**.** **133**, 55–59.

Ono S., Kikegawa T., Ohishi Y. (2007). High-pressure phase transition of $CaCO_3$. *Am. Mineral*. **92**, 1246–1249.

Ono S., Kikegawa T., Ohishi Y., Tsuchiya J. (2005). Post-aragonite phase transformation in $CaCO_3$ at 40 GPa, *Am. Mineral.* **90**, 667–671.

Ono S., Oganov A.R., Brodholt J.P., Vocadlo L., Wood I.G., Glass C.W., Côté A.S., Price G.D. (2007). High-pressure phase transformations of FeS: novel phases at conditions of planetary cores. *Earth Planet. Sci. Lett.* **272**, 481–487.

Pannetier J., Bassasalsina J., Rodriguez-Carva jal J., Caignaert V. (1990) Prediction of crystal structures from crystal chemistry rules by simulated annealing. *Nature*, **346**, 343–345.

Perdew J.P., Burke K., Ernzerhof M. (1996). Generalized gradient approximation made simple. *Phys. Rev. Lett.* **77**, 3865–3868.

Pickard C.J., Needs R.J. (2006). High-pressure phases of silane. *Phys. Rev. Lett.* **97**, art. 045504.

Sanloup C., Schmidt B.C., Perez E.M.C., Jambon A., Gregoryanz E., Mezouar M. (2005). Retention of xenon in quartz and Earth's missing xenon. Science **310**, 1174–1177.

Schönborn S., Goedecker S., Roy S., Oganov A.R. (2009). The performance of minima hopping and evolutionary algorithms for cluster structure prediction. *J. Chem. Phys.* **130**, 144108.

Schön J.C., Jansen M. (1996) First step towards planning of syntheses in solid-state chemistry: determination of promising structure candidates by global optimization. *Angew. Chem. – Int. Ed*. **35**, 1287–1304.

Serra S., Chiarotti G., Scandolo S., Tosatti E. (1998). Pressure-induced magnetic collapse and metallization of molecular oxygen: the ζ-O_2 phase. *Phys. Rev. Lett.* **80**, 5160–5163.

Shimizu K., Suhara K., Ikumo M., Eremets M.I., Amaya K. (1998). Superconductivity in oxygen. Nature **393**, 767–769.

Sluiter M.H.F., Colinet C., Pasturel A. (2006). *Ab initio* calculation of phase stability in Au-Pd and Ag-Pt alloys. *Phys. Rev.* **B73**, 174204.

Soler J.M., Artacho E., Gale J.D., Garcia A., Junquera J., Ordejon P., Sanchez-Portal D. (2002). The SIESTA method for *ab initio* order-N materials simulation. *J. Phys.: Condens. Matter* **14**, 2745–2779.

Solozhenko V.L., Kurakevych O.O., Oganov A.R. (2008). On the hardness of a new boron phase, orthorhombic γ-B_{28}. *J. Superhard Mater.* **30**, 428–429.

Steudel R., Wong M.W. (2007). Dark-red O_8 molecules in solid oxygen: rhomboid clusters, not S_8-like rings. *Angew. Chem. Int. Ed.* **46**, 1768–1771.

Tsagareishvili O.A., Chkhartishvili L.S., Gabunia D.L. (2009). Apparent low-frequency charge capacitance of semiconducting boron. *Semiconductors* **43**, 14–20.

Urusov V.S., Dubrovinskaya N.A., Dubrovinsky L.S. (1990). Generation of likely crystal structures of minerals. Moscow State University Press, Moscow.

Valle M. (2005). STM3: a chemistry visualization platform. *Z. Krist.* **220**, 585–588.

Valle M., Oganov A.R. (2008). Crystal structure classifier for an evolutionary algorithm structure predictor. *IEEE Symposium on Visual Analytics Science and Technology* (October 21–23, Columbus, OH), pp. 11–18.

van Setten M.J., Uijttewaal M.A., de Wijs G.A., de Groot R.A. (2007) Thermodynamic stability of boron: The role of defects and zero point motion. *J. Am. Chem. Soc*. 129, 2458–2465.

Wang Y, Oganov AR (2008) Research on the evolutionary prediction of very complex crystal structures. IEEE Computational Intelligence Society Walter Karplus. Summer Research Grant 2008 Final Report. http://www.ieee-cis.org/_files/EAC_Research_2008_Report_WangYanchao.pdf

Weck G., Desgreniers S., Loubeyre P., Mezouar M. (2009). Single-crystal structural characterization of the metallic phase of oxygen. *Phys. Rev. Lett*. 102, 255503.

Wentorf, R.H. (1965) Boron: another form. *Science* **147**, 49–50.

Woodley S.M. (2004). Prediction of crystal structures using evolutionary algorithms and related techniques. S*truct. Bond.* **110**, 95–132.

Woodley S.M., Battle P.D., Gale J.D., Catlow C.R.A. (1999). The prediction of inorganic crystal structures using a genetic algorithm and energy minimization. *Phys. Chem. Chem. Phys.* **1**, 2535–2542.

Yoo C.S., Cynn H., Gygi F., Galli G., Iota V., Nicol M., Carlson S., Hausermann D., Mailhiot C. (1999). Crystal structure of carbon dioxide at high pressure: "Superhard" polymeric carbon dioxide. *Phys. Rev. Lett.* **83**, 5527–5530.

AB INITIO QUANTUM CHEMISTRY AND SEMI-EMPIRICAL DESCRIPTION OF SOLID STATE PHASES UNDER HIGH PRESSURE: CHEMICAL APPLICATIONS

PIERO MACCHI*
Laboratory of Chemical Crystallography,
Department of Chemistry and Biochemistry,
University of Bern, Switzerland

Abstract There is nowadays a consensus that the structures of crystals at high pressure provide useful chemical information, at least in three important fields: (a) discoveries of new polymorphs and mechanisms of solid-solid transitions or high-pressure crystallizations; (b) intra- and inter-molecular bonding as a function of the external stress; (c) structure-property correlation. While experimental evidence is vital at high pressure, there is an increasing need of support from theoretical work, in particular for predicting new phases and their structure, for explaining the mechanisms of phase transformations and for computing and predicting the material properties. In this chapter, a brief survey of quantum mechanical descriptions of the solid state is given, summarizing the state of the art in the field and the potential developments. Some examples will illustrate the successful synergy between theory and experiment in studies on molecular crystals at high pressure.

Keywords: *Ab initio* calculations, quantum chemistry, semi-empirical modeling, high pressure

1. Introduction

Historically, high-pressure crystallographic studies have been carried out mainly to investigate minerals, elemental or simple inorganic solids and ices. These studies are related to topics in geology and mineralogy and their

*E-mail: piero.macchi@dcb.unibe.ch

E. Boldyreva and P. Dera (eds.), *High-Pressure Crystallography: From Fundamental Phenomena to Technological Applications*, DOI 10.1007/978-90-481-9258-8_26,

major goal is simulating the environment effects at conditions of the earth mantle. For this reason, very high-pressure regimes are typically sampled.

Beside some pioneering studies on organic solids at high pressures, (*Bridgman*, 1931; *Vereschagin and Kabalkina*, 1979) these works remained quite isolated for many years. However, in the last 2 decades, the number of publications dealing with the effects of hydrostatic pressure on small-molecule organic or metallorganic crystals (in the range 0.1–10 GPa) has rapidly grown (*Boldyreva*, 2008).

Applications to chemistry are extremely interesting and recent experimental works have attracted the attention of the scientific community. The most important areas are:

1. *Search of new polymorphs*: the discovery of new solid-state phases of molecules is extremely important (for example, because of the potential applications in material science or because of the different uses as pharmaceuticals).
2. *Investigation of chemical bonding*: structural chemistry has always been intimately connected with chemical bonding analysis. Experimental crystal structures in highly modified environment could shed more light on intra- and inter-molecular interactions.
3. *Structure–property correlation*: tightly connected with structural chemistry is also the materials engineering, which rationalizes the production of a specific property. The possibility to vary molecular and supra-molecular structures provides useful information.

Some recent works demonstrate the potential of x-ray (or neutron) diffraction at high pressure, providing new fundamental understanding in chemistry. *Eremets et al.* (2004) discovered a covalent solid phase of nitrogen after transformation of the triply bonded N_2 molecules into a polymer of single-bonded N atoms. *Oganov et al.* (2009) reported on a new high-pressure phase of boron, characterized by segregation of partially ionic moieties, although some other work criticized this conclusion (*Zarechnaya et al.*, 2009). A clear view is now presented by *Oganov et al*. (2009b).

Many applications also deal with molecular electronics and pharmaceuticals. For example, Boldyreva carried out several investigations on high-pressure structures of amino-acids (*Boldyreva*, 2007 a, b, c; 2008, 2009), pharmaceuticals (*Boldyreva et al.*, 2000, 2002, 2006b), hydrogen bonded aggregates (*Boldyreva et al.*, 2004) and simple inorganic solids (*Boldyreva et al.*, 2006a). Parsons investigated the polymorphism of many simple organic molecules: very recent is the discovery of isotopic polymorphism in deuterated pyridine (*Crawford et al.*, 2009), whereas previous studies were mainly concerned with polymorphism in molecular crystals of alcohols (*Ibberson et al.*, 2008) and amino-acids (*Johnstone et al.*, 2008). Studies on hydrogen-bonded (HB) molecules have been reported by *Katrusiak* (1990):

the investigated systems are characterized by pseudosymmetric double-well potentials, giving sudden phase transitions. Katrusiak has more recently characterized high-pressure phases of halo–alkanes (*Olejniczak et al.*, 2008).

Some of the technical developments that brought to these exciting experimental results have been recently summarized (*Katrusiak*, 2008). These new potentialities of experimental crystallography urge more sophisicated and accurate predictions of the solid-state structures. The progresses in this field allow nowadays to use first principle calculations to predict structures, stability ranges (hence phase diagrams) and properties of crystals at various thermodynamic conditions. Of course, different levels of approximations are possible depending on the size and the complexity of the problems. In this chapter, the focus is mainly on molecular crystals and their chemical applications. While more accurate work is possible on phases with smaller crystal unit cell volumes, such as minerals and small inorganic compounds, organic and organo-metallic molecular crystals are very demanding in terms of computational costs, because of the high dimensionality of the conformational space and therefore the inherent time consuming determination of a molecular wave function within periodic boundary conditions. Anyway, some works have demonstrated the possible use of theoretical approaches to model high-pressure solid state phases of molecular crystals. Theoretical predictions might complement experimental observations in several ways, which are briefly summarized in the following:

1. *Accurate molecular geometries*: organic compounds, characterized by light scattering atoms, are challenging x-ray diffraction studies at experimental high pressure conditions, like crystal structure determinations were at ambient conditions in the early days of Crystallography, when atomic distances (crucial to understand the stereochemistry) could be refined with low precision only and hydrogen atoms were, in general, not visible. Therefore, *ab initio* molecular geometry optimizations in the solid state (carried out using information on crystal cell volumes from x-ray diffraction) might be important because they could give accurate bond distances and allow to locate H atoms precisely.
2. *Prediction of phase transitions*: a full investigation of the whole phase diagram is more difficult with the increasing size of the molecule. However, by selecting useful internal coordinates, it is possible to investigate the stability of a given phase against breaking of some symmetry element as a function of pressure.
3. *Material properties*: the behavior of a molecular crystal upon interaction with light, heat, current etc. depends on the properties of the singular molecular constituents and on the way these are arranged, *i.e.* on the molecular packing. Changes of pressure might induce variations in the properties. Interestingly, more information would become available, if

we could discriminate between changes due to the individual constituents and those due to the molecular aggregation.

As it is clear from these applications, a theoretical study of a molecular crystal might be undertaken with different perspectives, which also means that different level of approximations can be adopted.

2. Molecular Quantum Mechanics: A Brief Survey

The *ab initio* calculations of the relative stabilities of isomers of gas-phase molecules is one of the outstanding scientific achievements of the twentieth century. Nowadays, it is possible to predict not only molecular geometries, but also reaction mechanisms. The most popular quantum mechanical methods propose approximate solutions to the Schrödinger's equation for the electrons (under the Born–Oppenheimer approximation, which allows treating the nuclear coordinates as parameters):

$$\mathbf{H}_{el}\psi_{el} = \mathrm{E}_{el}\,\psi_{el} \tag{1}$$

where $\mathbf{H}_{el}$ is the Hamiltonian operator which contains terms describing the electronic kinetic energy and electron-electron and nuclear–electron interaction energies; Ψ_{el} is the electronic wave function of the n electrons of the molecule and E_{el} is the total electronic energy of the system. Ψ_{el} might have several forms. The most adopted (in chemistry) is a combination of Slater determinants of molecular orbitals (MO, φ), each obtained from a linear combination of atomic orbital (LCAO, χ) functions (typically a set of Gaussian-type basis functions that simulate the radial behavior of atomic Slater orbitals). Depending on the approximations applied to elements of the Hamiltonian, the number of Slater determinants and the completeness of the basis used to compute Ψ_{el}, the theoretical description can be more or less accurate. A Hamiltonian applied on a single Slater determinant wave function necessarily describes each electron in the effective (static) field of the nuclei and the remaining electrons (ignoring electron correlation phenomena). This is the Hartree–Fock (HF) method, which returns a wave function through a self-consistent field (SCF) procedure (taking advantage of the variational nature of this problem).

The HF solution of the Schrödinger's equation is not sufficiently accurate, in general, and geometry optimizations based on minimum HF energy criterion are highly unsatisfactory. Only wave functions computed including (at least some) electron correlation allow accurate calculations of the electronic energy, hence of the molecular geometry. This, however, requires computing many more electronic configurations (hence more Slater determinants). A full configuration interaction wave function is very expensive and several

intermediate degrees of approximations can be used instead (selecting only some sensible electronic configurations among all the possible ones). Post-HF methods provide more satisfactory energies, better equilibrium geometries and vibrational frequencies, more accurate interaction energies, more accurate molecular properties, *etc*. Unfortunately, their cost is quite large. For this reason, the alternative approach provided by the Density Functional Theory (DFT) has become extremely popular, despite the inherent loss of a pure *ab initio* approach (because some assumption is needed in the Hamiltonian). The DFT is based on the fundamental theorem of *Hohenberg and Khon* (1964), who demonstrated that the quantum mechanical energy of a system can be expressed in terms of a unique (but unknown) functional of the electron density distribution, $\rho(\mathbf{r})$ (the one electron probability, that can be computed from a molecular wave function). Several possible functionals have been proposed, able to include (some) correlation effects into a single configuration wave function, hence at computational costs no larger than a simple HF wave function. The enormous progresses of DFT methods have produced an increasing number of sophisticated studies. For the purpose of simulating molecule-molecule interactions occurring in the crystals, a limitation of DFT functionals is their failure to describe *dispersive* or London forces. Dispersive forces mainly depend on dynamical effects and would require proper multi-configuration wave functions. However, some recent advances allow to include in the DFT functional a potential taking care of long range dispersion effect (*Grimme*, 2004) (empirically modeled).

The reader is addressed to more specific textbooks for a more detailed presentation of molecular quantum chemistry and the latest developments (see, for example, *Jensen*, 2006).

3. Quantum Chemistry with Periodic Boundary Conditions

3.1. MODELING A PERIODIC SYSTEM

At variance from molecules in the gas phase, the theoretical understanding of the solid-state structures of molecular crystals is much less advanced. This is mostly because simulations in the solid state are more complex and computationally demanding, because the Hamiltonian shall operate on a periodic wave function to model an ideal crystal (*i.e.* an infinite, periodic object). Periodicity of the wave function is typically imposed using Bloch functions:

$$\psi_{el}(\mathbf{k};\mathbf{r}+\mathbf{g}) = \psi_{el}(\mathbf{k};\mathbf{r})\exp(i\mathbf{k}\cdot\mathbf{g}) \tag{2}$$

where the wave vector **k** is used to force a translational periodicity. Many periodic wave functions could be used for this model, for example combination of plane waves

$$\psi_{el}(\mathbf{k};\mathbf{r}) = \sum_{\mathbf{k}'} a(\mathbf{k};\mathbf{k}') \exp(i(\mathbf{k}+\mathbf{k}')\cdot\mathbf{r}) \tag{3}$$

or "crystal orbitals" obtained as linear combination of atomic orbitals (expanded in Gaussian functions), somewhat similarly to MO-LCAO

$$\varphi_i(\mathbf{k};\mathbf{r}) = \sum_{\mathbf{g}} \chi_i(\mathbf{r}-\mathbf{g}) \exp(i\mathbf{k}\cdot\mathbf{g}) \tag{4}$$

Some software (like WIEN2K (*Blaha et al.*, 2001), VASP (*Kresse and Furthmuller*, 1996), CASTEP (*Clark et al.*, 2005)) adopts plane waves. Beside many advantages, they might have the disadvantage that electron density cusps at nuclear positions are poorly described. For this reason, core electron density is often omitted. This implies the usage of effective core potentials (*ecp*) to model the missing core electrons.

The code CRYSTAL06 (*Dovesi et al.*, 2006), instead, is using the LCAO approach, which allows a more accurate treatment of the electron density in the core region. From the chemical point of view, LCAO calculations allow simple interpretation and, for molecular crystals, an immediate comparison with gas phase MO calculations, as the crystal orbitals are somewhat related to molecular orbitals of the isolated molecule. With the LCAO method, *ecp* can also be used, but only with the purpose to reduce the computational costs, for example when dealing with heavy elements like transition metals. Noteworthy, the number of electrons to be excluded from the calculations is crucial for the eventual accuracy of the molecular geometry. Typically, first row transition metals could be modeled using large *ecp* (*i.e.* 18 core electrons are replaced by pseudopotentials) or small *ecp* (ten core electrons being replaced). The former approach does not return accurate geometries, as distances to a metal may be seriously underestimated, although trends along a given pressure gradient might be qualitatively reproduced. Additional problems at high pressure (*i.e.* at smaller crystal volumes) are due to the difficult convergence of a wave function SCF calculations and the possible contamination of spurious electronic states. So far, the most accurate calculations in the solid state have been carried out at DFT level (post-HF corrections have been anticipated but they are much more time consuming and far from common practice, at present).

3.2. SIMULATING THE PRESSURE

Simulations in the gas phase can be carried out neglecting the pressure-volume (PV) component of the free energy (see Eq (5)) and often are not taking into account entropy terms (thus describing the system virtually at T = 0 K). These approximations are however not possible when the purpose of a study is describing the phase diagram of a molecular crystal. In general the total free energy shall be computed:

$$G = U + PV - TS \tag{5}$$

At room pressure conditions, one can still neglect PV and obtain a crystal electronic wave function, which associated energy is sufficiently representative of the free energy of that phase. Some problems could arise by the poor description of *dispersive* forces, which are the major sources of cohesion for molecular crystals of neutral non-polar species at room pressure. The new DFT functionals might overcome these limitations.

The internal energy U in Eq (5) is computed from the electronic energy E_{el} (available after solution of the Schrödinger's equation (1) at the geometry of a local minimum on the electronic energy surface) and from translation, rotational and vibrational thermal energies (computed using "ensemble properties", within a statistical mechanics approach). In practice, the thermal energies are available if the electronic energy surface is investigated not only at the minimum of the energy surface (corresponding to the equilibrium geometry), but also around this point to compute frequencies. This is of course more expensive.

The entropy S also contains contribution from the electronic configuration as well as from vibration, rotations and translations of the system. Proper calculations of the vibrational contributions in the solid state require a full investigation of all the possible wave vectors in the crystals (which implies calculations over the entire first "Brillouin zone" in the reciprocal space). This could represent a bottle-neck in solid state simulations of molecular crystals, especially those of lower symmetry.

In general, U increases exponentially as the volume is contracted, due to increasing molecule-molecule repulsions or, as more physically appropriate, due to the higher energy necessary to confine electrons in smaller volumes. On the other hand, S decreases, because the higher potential associated with a closer packing reduces the freedom of the molecules. As a consequence, the role of the PV energy is basically *stabilizing smaller crystal volumes*, associated with less favorable electronic and entropic terms. Hence, a pressure induced crystal structure allows the visualization of the molecule at values of its internal energy much higher than those of equilibrium geometries at room conditions (and even farther away from the gas phase).

In practice, a crystal structure optimization, at a given pressure and temperature, requires several geometry optimization steps at (constrained) crystal volumes and then the search of a minimum of the free energy. This procedure is clearly time-consuming, therefore *ab initio* simulations of molecular crystals for relatively large molecules are computationally demanding. Some simplification could come if the function E_{el} + PV is minimized instead of G. This means ignoring the effect of temperature (noteworthy even at 0 K a zero point vibration energy can be computed and would change as a function of the pressure; therefore, the approximation introduced above is not only assuming 0 K temperature, but really ignoring *in toto* the thermodynamic variable Temperature). Beside formally inaccurate, E_{el} + PV could be a reasonable function to minimize for a gross search of equilibrium geometries in a phase diagram simulation.

Further simplifications are possible using semi-empirical approaches, instead of proper quantum mechanic treatments. In this case, the exact quantum mechanical potential is replaced by simplified parameterized (atom-atom) potentials, as we will see in the next paragraph.

4. Semi-Empirical Approaches

In quantum chemistry, any replacement of exact terms of the Hamiltonian with approximate ones (often chosen to fit experimental evidence) transforms an *ab initio* treatment into a semi-empirical approach. There are several levels of simplification; the ultimate one is computing the internal energy of the system only from parameterized atom-atom potentials (which are simple functions of the molecular geometry).

At *molecular level*, the force fields shall describe each bond stretching (two atom potentials), bending (three atom potentials) or torsion (four atom potentials). At *supramolecular level*, the force fields account for the *electrostatic* interaction (the columbic energy of two molecular electron density distributions, $\rho(\mathbf{r})$), *polarization* (energy arising from $\rho(\mathbf{r})$ of one molecule polarizing that of another), *dispersion* (due to mutual interaction of excited configurations) and *repulsion* (the energy necessary to host electrons in smaller volumes, a destabilization due to Pauli principle of anti-symmetry for wave functions describing electron motions). *Dispersion* and *repulsion* are typically computed from parameterized atom-atom pair potentials, whereas several methods are possible for *electrostatic* and *polarization* energies (from simple atomic partitioning of the molecular charge to more accurate and exact calculations which account for the anisotropy of the charge density distributions).

All thermodynamic functions can be obtained from semi-empirical calculations, though of course at a much higher level of approximation (typically neglecting the electronic energy contribution). In this context, a notable software is GULP (*Gale*, 2005), originally intended for inorganic phases, but currently working also for molecular crystals and polymers. However, GULP is not using a sophisticated treatment of the electrostatic terms, whereas works by *Gavezzotti* (2004) or by *Volkov et al.* (2004) have demonstrated the superior information obtained computing the "exact" molecule-molecule electrostatic energy (evaluated from a gas phase *ab initio* molecular electron density).

In many cases, the semi empirical approaches are limited to compute the *lattice energy* (*i.e.* the difference in internal energy between the sum of isolated gas phase molecules and the crystal). In fact, intra-molecular terms are ignored (and molecules are then taken as rigid bodies), the computed energy is basically giving the excess (or defect) of internal energy of the crystal respect to a collection of isolated non-interacting molecules (perfect gas). While this approach is very popular (especially among scientists working in crystal structure prediction), it shall be considered that it only gives estimates of the stability of a given phase, because it ignores the proper corrections when going into the gas phase. In addition, PV terms cannot be neglected when simulating a phase at high pressure. Thus, the lattice energy might be used to rank the relative stability of different molecular crystal phases, but it would hardly return any accurate comparison with experimentally measured heats. A more proper way to handle semi-empirical force field in simulations of high-pressure phases is using the crystal enthalpy (i.e. adding PV to the semi-empirical U term) and minimizing this function to optimize the phase structure. A proper combination of molecular and supramolecular force fields could allow acceptable results.

5. Applications

5.1. PHASE TRANSITIONS IN ORGANOMETALLIC MOLECULAR CRYSTALS

An example of pressure induced solid-solid phase transitions in organometallic species is provided by the species $Co_2(CO)_6(XPh_3)_2$ (X = P, As). At high pressure or at low temperature, these molecules undergo a conformation change of the carbonyl ligands about the Co–Co bond from *staggered* to (almost) *eclipsed* (*Casati et al.*, 2005, 2009a). This re-arrangement is accompanied by a solid–solid phase transition (where the R-3 space group is preserved, but the trigonal c axis is doubled).

It is interesting that the very flexible metal–metal bond is initially compressed, then elongated due to the increased intra-carbonyl repulsion and eventually compressed (see Figure 1). Periodic DFT simulations reproduce the thermodynamics of the transformation and predict the distortions produced by the external stress: (*Casati et al.*, 2005) the change of molecular symmetry is induced by the high internal energy raise associated with the staggered carbonyl conformation, which does not allow an efficient packing upon compression. The eclipsed conformer, though less stable in isolation, guarantees a better entanglement of molecules. The flexibility of the Co–Co bond is easily explained by the low stretching frequencies computed for this bond, in the gas phase as well as in the solid state. Thus the energy necessary to rotate the XPh_3 or $Co(CO)_3$ groups is quite similar to that requested to stretch a Co–Co bond.

The compound is relatively large, and it contains some heavier elements (like Co, As or even P). This requires the use of *ecp* in the modeling, therefore theoretical calculations cannot achieve highest accuracy in this case. Nevertheless, the qualitative agreement is quite satisfactory (*Casati et al.*, 2005).

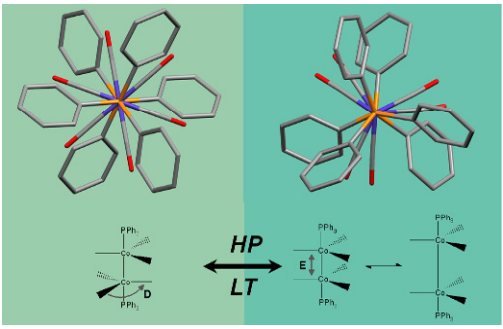

Figure 1. Structural modifications occurring to $Co_2(CO)_6(XPh_3)_2$ at high pressure or low temperature: CO ligands are staggered at room conditions, but almost eclipsed above 4.0 GPa), and consequently Co–Co bond length increases.

5.2. PROTON MIGRATION

X-ray diffraction experiments on oxalic acid di-hydrate ($H_2C_2O_4$•$2H_2O$) (*Casati et al.*, 2009b) reveal a complete symmetrization of the carboxylic group at high pressure. This would indicate the transformation of the acid into a di-anion and the consequent proton transfer to the water molecules (Figure 2). Although the hydrogen atoms cannot be located with the X-ray analysis, periodic DFT calculations in the solid state confirm the migration, in agreement with neutron diffraction (*Casati et al.*, work in progress).

Because the system is sufficiently small, accurate theoretical simulations are possible in this case. Therefore, not only the proton transfer is predicted in a good agreement with the neutron diffraction results, but also the energetic of the system is nicely reproduced. In Figure 3, one can see that the raise of internal energy at high pressure (computed at DFT level) is in close agreement with the work done on the crystal (computed from the experimentally observed strain and pressure).

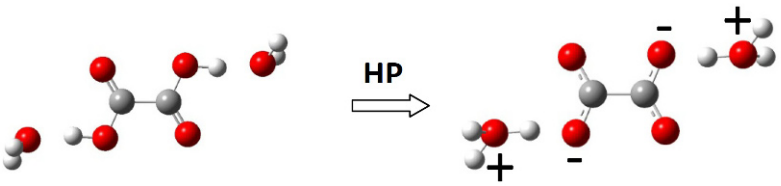

Figure 2. Structural changes in oxalic acid di-hydrate at high pressure.

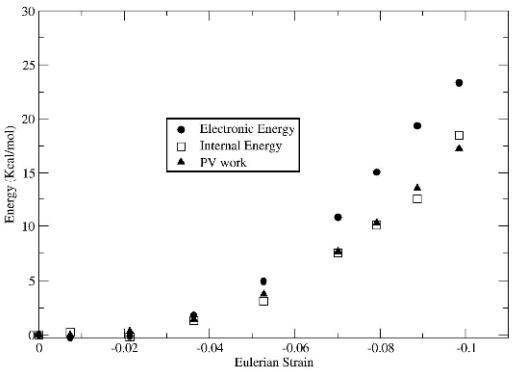

Figure 3. Computed electronic and internal energy for ($H_2C_2O_4$•$2H_2O$) as a function of the Eulerian strain. Experimentally derived PV-work done on the system is also plotted.

5.3. NON-LINEAR OPTIC MATERIALS

Another interesting synergy between theory and experiment is the calculation of material properties, with the aim to establish a relation between the molecular and supra-molecular arrangements and the optic, thermal, electronic or magnetic behavior of an ideal crystal.

One example is here provided by molecular materials having significant second harmonic generation (SHG), a non-linear optic phenomenon. For example, the 4-amino-benzophenone (4-ABP) is a SHG active molecule which crystallizes in the non-centrosymmetric space group $P2_1$ (a necessary condition to obtain SHG also in the crystal). The crystal SHG changes as a function of the pressure. The reasons of this change are not immediately obvious. In fact, they could be due to: (a) different molecular conformations

which a change in the molecular properties; (b) different orientations of the molecules in the solid state, which change the way, in which the macroscopic property is constructed; (c) formation of new intermolecular interactions and mutual polarization of the molecules. To solve this puzzle, it is necessary to tackle the problem at different levels. First, changes in the conformation (see Figure 4) might affect the molecular hyper-polarizability. This can be calculated *ab initio*, simulating the molecule in the gas phase, constraining the conformations at angles observed in the solid state. In fact, a significant increase of the hyperpolarizability is observed as the 4-ABP becomes more planar (as it occurs at high pressure), because of the augmented conjugation between the two aromatic rings.

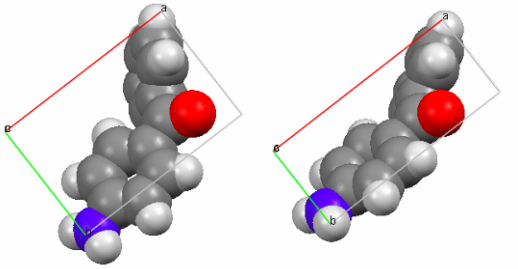

Figure 4. Conformational changes of 4-aminoobenzophenone at high pressure.

To solve the intermolecular conjectures, instead, we have to resort on some semi-empirical modeling. In fact, using time-dependent solution of the Schrödinger equation at semi-empirical level, it was demonstrated (*Nunzi et al.*, 2008) that parallel stacking of aromatic rings (in the so-called J-type aggregation) enhances optical properties of the molecules (and this aggregation is also visible from electronic spectroscopy because of a characteristic absorption band). Interestingly, the 4-ABP is in fact changing the supra-molecular aggregation between room conditions (where no stacking of the aromatic rings is present) and high pressure conditions (where a stacking is formed, after the change of molecular conformation makes this aggregation more likely).

Finally, the crystal SHG shall depend also on the matching between all molecules in the solid state. A very intuitive and simple analysis is given by (*Zhyss and Chemla*, 1987), where the intra-molecular charge transfer vector is used to estimate the relative SHG efficiency as a function of the packing. In the case of 4-ABP, the molecule does not change its orientation in the crystal upon compression, hence the intramolecular charge transfer is also unmodified, therefore, the SHG changes are not due to molecular re-orientation.

6. Conclusions and Outlook

Although studies on molecular crystals at high pressure are yet not so common practice, the theoretical framework nowadays available is sufficient to undertake accurate investigations that could complement the experimental observations. Some examples in this chapter demonstrate the potentiality of theoretical analyses, in particular when information from experiment might be ambiguous (for example to locate Hydrogen atoms, to confirm molecular conformations and to address formation of new chemical bonds). In addition, quantum mechanical treatments could give insight of the mechanisms of pressure induced transformations.

Future applications might be especially devoted to the prediction of crystal properties at non-ambient conditions, which could be important for screening materials of interest, before carrying out highly demanding experimental work.

ACKNOWLEDGEMENTS

The author thanks the Swiss National Science Foundation for financial support (project 200021_126788).

References

Blaha, P., Schwarz, K., Madsen, G.K.H., Kvasnicka, D., and Luitz, J., 2001, *WIEN2K, An Augmented Plane Wave + Local Orbitals Program For Calculating Crystal Properties*, ed. K. Schwarz. Techn. Universitat, Wien, Austria ISBN 3-9501031-1-2.

Boldyreva, E.V., 2004, High-pressure studies of the hydrogen bond networks in molecular crystals, *J. Mol. Struct.* **700**: 151–155.

Boldyreva, E.V., 2008, High-pressure diffraction studies of molecular organic solids. A personal view, *Acta Cryst. A.* **64**: 218–231.

Boldyreva, E.V., Ahsbahs, H., Chernyshev, V.V., Ivashevskaya S.N., and Oganov, A.R., 2006a, Effect of hydrostatic pressure on the crystal structure of sodium oxalate: X-ray diffraction study and ab initio simulations, *Z. Kristallogr.* **221**: 186–197.

Boldyreva, E.V., Dmitriev, V.P., and Hancock, B.C., 2006b, Effect of pressure up to 5.5 GPa on dry powder samples of chlorpropamide form-A, *Int. J. Pharm.* **327**: 51–57.

Boldyreva, E.V., Shakhtshneider, T.P., Vasilchenko, M.A., Ahsbahs, H., and Uchtmann H., 2000, Anisotropic crystal structure distortion of the monoclinic polymorph of acetaminophen at high hydrostatic pressure, *Acta Cryst. B.* **56**: 299–309.

Boldyreva, E.V., 2007a, Crystalline amino acids – a link between chemistry, materials science and biology, In: *Models, Mysteries, and Magic of Molecules*, Eds. Boeyens, J.C.A., Ogilvie, J.F., Springer Verlag, New York, pp. 169–194.

Boldyreva, E.V., 2007b, High-pressure polymorphs of molecular solids: when are they formed, and when are they not? Some examples of the role of kinetic control, *Crystal Growth Des.* **7**(9): 1662–1668.

Boldyreva, E.V., 2007c, High-pressure studies of crystalline amino acids and simple peptides/*Proceedings of the IV-th International Conference on High Pressures in Biosciences and Biotechnology*, Presented by J-STAGE, Tsukuba, Japan, September, 25th–26th, 2006, Eds. Abe F., Suzuki, A., Japan Science and Technology Agency, Saitama, Japan, **1**(1), pp. 28–46.

Boldyreva, E.V., 2009, Combined X-ray diffraction and Raman spectroscopy studies of phase transitions in crystalline amino acids at low temperatures and high pressures. Selected examples, *Phase Transitions*, **82**(4): 303–321.

Bridgman, P.W., 1931, *The Physics of High Pressure*, Bell and Sons., London.

Casati, N., Macchi, P., and Sironi, A., 2005, Staggered to eclipsed conformational rearrangement of $[Co_2(CO)_6(PPh_3)_2]$ in the solid state: an X-ray diffraction study at high pressure and low temperature, *Angew. Chem. Int. Ed.* **44**: 7736–7739.

Casati, N., Macchi, P., and Sironi, A., 2009a, Molecular crystals under high pressure: theoretical and experimental investigations of the solid–solid phase transitions in $[Co_2(CO)_6(XPh_3)_2]$ (X=P, As), *Chemistry, Eur. J.* **15**: 4446–4457.

Casati, N., Macchi, P., and Sironi, A., 2009b, Hydrogen migration in oxalic acid di-hydrate at high pressure?, *Chem. Commun.* **21**: 2679–2681.

Casati, N., Macchi, P., Marshall, W., Sironi, A. submitted for pubblication.

Clark, S.J., Segall, M.D., Pickard, C.J., Hasnip, P.J., Probert, M.J., Refson, K., and Payne, M.C., 2005, First principles methods using CASTEP, *Z. Kristall.* **220**: 567–570.

Crawford, S., Kirchner, M.T., Blaser, D., Boese, R., David, W.I.F., Dawson, A., Gehrke, A., Ibberson, R.M., Marshall, W.G., Parsons, S., Yamamuro, O., 2009, Isotopic Polymorphism in Pyridine, *Angew. Chem. Int. Ed.* **48**: 755–757.

Dovesi, R., Saunders, V.R., Roetti, C., Orlando, R., Zicovich-Wilson, C.M., Pascale, F., Civalleri, B., Doll, K., Harrison, N.M., Bush, I.J., D'Arco, Ph., and Llunell, M., 2006, *CRYSTAL06 User's Manual*, University of Torino, Torino.

Boldyreva, E.V., Shakhtshneider, T.P., Ahsbahs, H., Sowa, H., and Uchtmann, H., 2002, Effect of high pressure on the polymorphs of paracetamol, *J. Therm Anal. Calorim*. **66:** 437–452.

Eremets, M.I., Gavriliuk, A.G., Trojan, I.A., Dzivenko, D.A., and Boehler, R., 2004, Single-bonded cubic form of nitrogen, *Nature Mater.* **3**: 558–563.

Gale, J., 2005, GULP: Capabilities and prospects, *Z. Kristallogr.* **220**: 552–554.

Gavezzotti, A., 2002, Calculation of intermolecular interaction energies by direct numerical integration over electron densities. I. Electrostatic and polarization energies in molecular crystals, *J. Phys. Chem. B.* **106**: 4145–4154.

Grimme, S., 2004, Accurate description of van der Waals complexes by density functional theory including empirical corrections, *J Comput Chem.* **25**: 1463.

Hohenberg, P. and Kohn, W., 1964, Inhomogeneous electron gas, *Phys. Rev.* 136: B864.

Ibberson, R.M., Parsons, S., Allan, D.R., and Bell, A.M., 2008, Polymorphism in cyclohexanol, *Acta Cryst.* **B64**: 573–582.

Jensen, F., 2006, *Introduction to Computational Chemistry*, Wiley-VCH, Weinheim, Germany.

Johnstone, R.D.L., Francis, D., Lennie, A.R., Marshall, W.G., Moggach, S.A., Parsons, S., Pidcock, E., and Warren, J.E., 2008, High-pressure polymorphism in L-serine monohydrate: identification of driving forces in high pressure phase transitions and possible implications for pressure-induced protein denaturation, *CrystEngComm.* 10: 1758–1769.

Katrusiak, A., 1990, High-pressure X-ray-diffraction study on the structure and phase-transition of 1,3-cyclohexanedione crystals, *Acta Cryst. B* **46**: 246–256.

Katrusiak, A., 2008, High-pressure crystallography, *Acta Cryst. A* **64**: 135–148.

Kresse, G. and Furthmuller, J., 1996, Efficiency of *ab initio* total-energy calculations for metals and semiconductors using a plane-wave basis set, *Comput. Mater. Sci.* **6**: 15–50.

Nunzi, F., Fantacci, S., DeAngelis, F., Sgamellotti, A., Cariati, E., Ugo, R., and Macchi, P., 2008, Theoretical investigations of the effects of J-aggregation on the linear and nonlinear optical properties of E-4-(4-Dimethylaminostyryl)-1-methylpyridinium [$DAMS^{+}$], *J. Phys. Chem. C.* **112**: 1213–1226.

Oganov, A.R., Chen, J., Gatti, C., Ma, Y., Ma, Y., Glass, C.W., Liu, Z., Yu, T., Kurakevych, O.O., and Solozhenko, V.L., 2009, Ionic high-pressure form of elemental boron, *Nature* **457**: 863–868.

Oganov, A.R., Solozhenko, V.L., Kurakevych, O.O., Gatti, C., Ma, Y., Chen, J., Liu, Z., Hemley, R.J., (2009b), arXiv: 0908.2126v2

Olejniczak, A., Katrusiak, A., and Vij, A., 2008, High-pressure freezing, crystal structure studies and Si-CF3 bond polarizability of trimethyl(trifluoromethyl)silane *J. Flor. Chem.* **129**: 1090–1095.

Vereschagin, L.F., and Kabalkina, S.S., 1979, X-ray diffraction studies at high pressures, *Nakuka, Moscow.*

Volkov, A., Koritsanszky, T., and Coppens, P., 2004, Combination of the exact potential and multipole methods (EP/MM) for evaluation of intermolecular electrostatic interaction energies with pseudoatom representation of molecular electron densities, *Chem. Phys. Lett.* **391**: 170–175.

Zarechnaya, E.Yu., Dubrovinsky, L., Dubrovinskaia, N., Filinchuk, Y., Chernyshev, D., Dmitriev, V., Miyajima, N., El Goresy, A., Braun, H.F., Van Smaalen, S., Kantor, I., Kantor, A., Prakapenka, V., Hanfland, M., Mikhaylushkin, A.S., Abrikosov, I.A., and Simak, S.I., 2009, Superhard semiconducting optically transparent high pressure phase of Boron *Phys. Rev. Lett.* **102**: 185501-4.

Zyss, J. and Chemla, D.S. (eds) 1987, *Nonlinear Optical Properties of Organic Molecules and Crystals*, Academic, Orlando, **1**: pp. 23–187.

FIRST-PRINCIPLES SIMULATIONS OF ALLOY THERMODYNAMICS IN MEGABAR PRESSURE RANGE

IGOR A. ABRIKOSOV*
Department of Physics, Chemistry and Biology, Linköping University, Sweden

Abstract We outline recent developments of theoretical methodology for first-principles simulations of alloys at high pressure. Particular attention will be paid to the techniques for a treatment of solution phases. Limitations of the present-stage theory are discussed, and a necessity of having a close collaboration between theory and experiment are emphasized. We show several examples where the collaboration leads to new discoveries important for physical and geophysical communities.

Keywords: *Ab initio* simulations, phase stability, alloys; high-pressure

1. Introduction

An interest in studies of the effect of high pressure on the properties of matter is rapidly growing because of several reasons. First, recent experimental advances led to a possibility to reach the multimegabar pressure range, and consequently to change the density of condensed state by up to an order of magnitude. This allows researchers to investigate the most fundamental physical phenomena, such as the metal–insulator transition, quantum states of hydrogen, quantum phase transitions, polymorphism in water, and superconductivity. Second, the high-pressure synthesis allows one to tune the materials properties, and to produce novel materials with special properties, for instance, super-hard materials. This possibility is attractive not only for the physical community, but also for the materials scientists and for solid-state chemists. Third, there is a very large interest and necessity in understanding the structure and composition of the interior of the Earth, as well as other planets, which explains the interest towards

*E-mail: igor.abrikosov@ifm.liu.se

E. Boldyreva and P. Dera (eds.), *High-Pressure Crystallography: From Fundamental Phenomena to Technological Applications*, DOI 10.1007/978-90-481-9258-8_27,

the problem of phase stabilities at high pressure from the geophysical community.

Studies of phase stabilities and phase transformations in solids are of major fundamental and practical interest. Traditionally, in theoretical physics this problem was considered at ambient pressure. However, a possibility to reach multimegabar pressures in experiment puts on the agenda a necessity to developing theoretical tools, which are capable of making predictions and providing an understanding for the experimental observations. In particular, one can clearly see that a new research field is emerging where a combined effect of alloying and compression on the structure and properties of materials is in focus. To understand fundamental properties of alloys under extreme conditions is a challenging problem for the theory.

Indeed, experimental research has been the dominating approach in studying materials. However, at present the electronic structure theory allows one to obtain reliable results for the thermodynamic, mechanical, electrical and magnetic properties of metals, semiconductors or insulators without any adjustable parameters fitted to the experiment (*Martin*, 2004). Of course, until recently this was mostly done for relatively simple systems (for example, a perfectly ordered compound or a completely random alloy). At the same time, we can see today that the first-principles simulations are extended towards more realistic materials, as well as realistic experimental conditions, which are of direct importance for physical and geophysical communities.

2. Thermodynamics Approach to Phase Stabilities

The physical and mechanical properties of materials depend on the chemical content and on the internal structure, which is formed during their manufacturing and service. A straightforward way to describe phase equilibria and to construct phase diagrams is offered within the phenomenological thermodynamics approach. For alloy systems one considers most often temperature-composition phase diagrams at ambient pressure. Thus, one deals with a system in thermal and mechanical contact with a constant-temperature constant-pressure heat bath, whose equilibrium is described by the thermodynamic potential $G = E + PV - TS = H - TS$, where G is the Gibbs free energy, E is the energy of the system, H is the enthalpy, S denotes the entropy, and thermodynamic variables P, V, T represent pressure, volume, and temperature, respectively. During natural processes G decreases and general conditions for equilibrium are represented by its minimum. If phase α transforms into phase β in a pure material at equilibrium transformation temperature T_c, then $G_\alpha = G_\beta$ at T_c. For alloy

solutions, the chemical terms for the free energy are included by adding the chemical potential

$$\mu_I = \left(\frac{\partial G}{\partial n_I} \right)\Bigg|_{T,P,n_J \neq n_I} \tag{1}$$

for each component I, where n_I is the number of moles of component I. At equilibrium, the Gibbs–Duhem relation holds:

$$SdT - VdP + \sum_I n_I \mu_I = 0 \tag{2}$$

For example, in a binary system $A_{1-x}B_x$ it immediately follows that at constant P and T the G curves as a function of an alloy component fraction $x = x_B = n_B/[n_A + n_B]$ for the phases in equilibrium must share a common tangent.

3. First-Principles Approach

In contrast (or perhaps more properly as a complement) to the thermodynamic approach, the first-principles simulations of the phase stability of alloys are based on the atomistic description of the problem. Because the number of particles is of the order of the Avogadro number, the theory must use a statistical approach. The main goal of statistical mechanics is to derive the properties of a macroscopic system from its microscopic properties by averaging over unobservable microscopic coordinates leaving only macroscopic coordinates, say volume, and macroscopic variables, say temperature. This is done by introducing an idea of a statistical ensemble, which can be defined as a large number of replicas of a system, considered all at once, each of which represents a possible state that the real system might be in.

For the phase stability simulations one most often uses the so-called canonical ensemble (CE), which is a statistical ensemble that corresponds to a system in the heat bath (equivalently, to an assembly of identical replicas of a system) subject of constrain by macroscopic parameters T, V, and number of particles N, and with the distribution function given by Boltzmann distribution. The thermodynamic potential, which describes a system at constant temperature and volume is the Helmholtz free energy $F = E - TS$, and general conditions for equilibrium are represented by minimum of F. For the canonical ensemble the Helmholtz free energy is calculated as:

$$F(T,V,N) = -k_B T \ln Z(T,V,N) = -k_B T \ln \left[\sum_{\{R\}} \exp\left(-\frac{E_{\{R\}}}{k_B T} \right) \right] \tag{3}$$

where $Z(T,V,N)$ is the partition function and k_B is the Boltzmann constant. In Eq (3) the sum runs over all possible states $\{R\}$ of the system (for example, if we need to find the lowest energy configuration for $A_{1-x}B_x$ alloy at fixed composition x and underlying crystal lattice, say, bcc, $\{R\}$ represents all possible occupations of the bcc lattice by $(1 - x)N$ A and xN B atoms).

Note that we have used the classical statistical mechanics for our description above, and it is definitely sufficient for most of the problems within the field (some interesting deviations may occur, e.g. while working with hydrogen). However, a determination of energies $E_{\{R\}}$ in Eq (3), generally speaking, requires a solution of a complex many-body quantum mechanical problem for each particular atomic configuration $\{R\}$ of the solution phase $A_{1-x}B_x$. The essence of the alloy theory is to avoid this impossible task, and modern approaches to this problem are discussed below. However, it is still necessary to carry out quantum mechanical calculations for selected configurations $\{R\}$ in order to derive *ab initio* parameters for the models used in subsequent statistical mechanics simulations.

A solution to the quantum mechanical problem is provided by the electronic structure theory, and an excellent summary of it has been recently given by *Martin* (2004). Nowadays, the majority of calculations within the field are carried out in the framework of the density functional theory (DFT). Within the DFT one solves the so-called Kohn–Sham (KS) equations for a system of independent "electrons" (characterized by single-particle wave functions). The essence of the KS theory is that it is constructed in such a way that the density of the independent "electrons" (which we denote as n) obtained from a self-consistent solution of the KS equations is exactly the same as the electron density in the original system of real interacting electrons. However, the accuracy of approximations used within DFT at present does not allow for predictions of thermodynamics parameters with metallurgical accuracy. Indeed, for example, the phase transition temperatures need to be known within 0.5 K, while state-of-the-art DFT simulations predict them with at best 100 K accuracy. Thus, the most promising approach in studies of alloys behavior at extreme conditions combines theoretical simulations and experiment. For example, in studies of the mineralogy and chemistry of the Earth's core, the experiment can reach pressure of about 250 GPa. Verifying an accuracy of theoretical predictions at these conditions increases a reliability of theoretical predictions at the Earth's core pressure (up to 360 GPa).

4. Treatment of Solution Phases

A serious problem with the application of the DFT formalism occurs if a configuration *{R}* of the solution phase $A_{1-x}B_x$ does not have any translational periodicity, which is the most common situation in practice. The point is that in this case group theory, which is the corner stone of the modern electronic structure calculations, cannot be used directly. Below we outline modern approaches for solving the electronic structure problem and calculating the total energy for systems with substitutional disorder.

One obvious way to deal with a disorderd system is to consider its fragment(s), to impose periodic boundary conditions, and to solve the KS problem for such "supercells". A tremendous progress taken place in computer technologies, together with a development of efficient *ab initio* algorithms, makes it nowadays possible to carry out calculations for systems with up to a thousand of atoms. Within this so-called supercell method one can use the codes developed for the periodic solids, and minimize the total energy with respect to the electronic degrees of freedom, as well as with the positions of atoms within the supercell. In many cases this way of simulating the disorder is acceptable for energetic properties. However, it is important to remember that this model is based on the use of translational symmetry, which is absent in real random alloys. Moreover, the choice of a supercell is not a trivial task. The problem is that whether a supercell can be considered as (quasi-)random or not in the total energy calculations is exclusively dictated by the nature of the interatomic interactions in this particular system (*Ruban and Abrikosov*, 2008).

As a matter of fact, *Zunger et al.* (1990) suggested a method for supercells construction using the intelligent design of the atomic distribution within the cell rather than *ad hoc* "flip coin" technique. In their so-called special quasirandom structures (SQS) the atomic correlation functions are required to be the same as in completely random alloys for the first few coordination shells. Of course, the long-range correlation functions in the SQS are non-zero. However, from the discussion presented in (*Ruban and Abrikosov*, 2008) it is obvious, that in order to calculate correctly the total energy of a random structure using the supercell method one needs to satisfy two important conditions: (i) interactions between all the atoms for which correlation functions are nonzero should be negligibly small, and (ii) *vice versa* short-range order parameters should be zero for all the coordination shells for which interactions are nonzero. Since the effective interactions are usually quite long-ranged, these conditions are never satisfied in the supercell calculations exactly. But in many cases the SQS technique gives a reasonable representation of a random alloy due to the fact that the strongest effective interactions are usually present in the nearest neighbor coordination

shells. It is clear, that the quality of an SQS is improving with the number of correlation functions satisfying the second condition. It is also obvious that total energies calculated with supercells, where the correlation functions are not controlled, e.g. with *ad hoc* constructed supercells, may lead to unpredictable results even if one carries out an averaging over several (but still limited) number of different supercells.

As an alternative to the supercell approach one can reconstruct three-dimensional periodicity of the substitutionally disordered system (we need it in any case!) by mapping it onto a suitably chosen ordered lattice of "effective" atoms, which describe the original system on the average. The simplest way here is to apply the mean-filed approximation, which are common in all areas of physics. The basic principle of the method (*Ducastelle*, 1991) is the following: one considers a few degrees of freedom concentrated in a limited region of the space where they are defined, and assumes that their interactions with all the others can be replaced by what is called a mean-field. Averaging out the considered degrees of freedom, one obtains a homogeneous medium, which yields self-consistent relations determining these fields. The mean-field equations are non-linear, and can be difficult to solve, but this non-linearity is the root of the richness of the method.

In terms of the electronic structure problem, one is ultimately interested in processes of electron scattering of the atoms in the system, the so-called multiple-scattering. The simplest mean field method, the coherent potential approximation (CPA), is constructed by placing effective scatterers at the sites of the original system. Scattering properties of these effective atoms have to be determined self-consistently from the condition that the scattering of electrons of the alloy components, embedded in the effective medium as impurities, vanishes on the average. The CPA is currently one of the most popular techniques to deal with substitutional disorder, and it is implemented in several codes (*Abrikosov and Skriver*, 1993; *Ruban and Skriver*, 1999; *Vitos et al*., 2001).

Numerous applications of the CPA show its excellent efficiency and rather high accuracy in the description of electronic and thermodynamic properties of alloys. In particular, an implementation of the CPA within the exact muffin-tin orbital (EMTO) theory (*Vitos et al*., 2001) was used with great success in studies of alloys at extreme conditions (*Dubrovinsky et al*., 2003, 2005, 2007). In particular, in (*Dubrovinsky et al*., 2003) the effect of pressure on the phase stability of Fe–Si alloys was studied by *ab initio* calculation of the mixing enthalpy.

The mixing enthalpy H at pressure P of an alloy with x parts Si is:

$$H_{Fe_{1-x}Si_x} = E_{Fe_{1-x}Si_x}(V^P_{Fe_{1-x}Si_x}) - (1-x)E_{Fe}(V^P_{Fe}) - xE_{Si}(V^P_{Si}) \qquad (4)$$

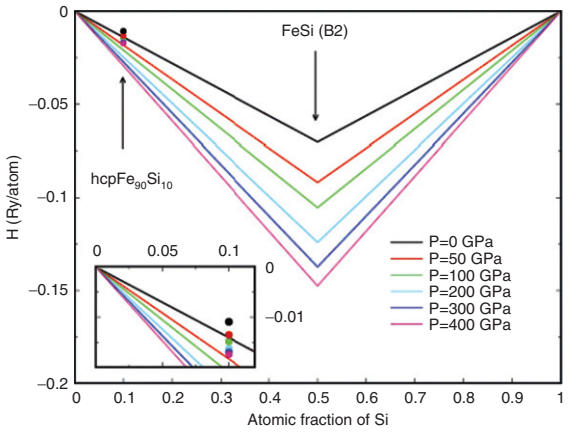

Figure 1. Theoretically determined mixing enthalpies (in Ry/atom) of random *hcp* $Fe_{0.9}Si_{0.1}$ alloy (filled circles) and formation enthalpies (in Ry/atom) of *B2* FeSi compound (atomic fraction of Si equal to 0.5) at different pressures. Increasing pressure corresponds to lines and circles with more negative slope.

Theoretically determined mixing enthalpies of random *hcp* $Fe_{0.9}Si_{0.1}$ alloy and formation enthalpies of *B2* FeSi compound at different pressures are shown in Figure 1. For the mixing enthalpies, the *hcp* phase of Fe and the *fcc* phase of Si were chosen as standard states at all pressures. Mixing enthalpies were also calculated for less concentrated random *hcp* alloys, as well as for *bcc* random alloys (not shown in the figure). The latter were found to transform into the former at pressures close to the *bcc-hcp* transition pressure in the pure Fe. So-called ground state lines connect pure Fe and points corresponding to the formation enthalpies of the B2 compound. The fact that the mixing enthalpy of a random alloy at a given pressure is above the corresponding ground state line indicates its instability with respect to the decomposition into the Si poor *hcp* alloy and *B2* FeSi. From the inset in Figure 1 one can clearly see that this tendency increases with increasing pressure. This effect was confirmed experimentally (*Dubrovinsky et al*., 2003).

Despite the success of the CPA calculations for the Fe–Si alloys, it is important to underline that it gives an approximate, mean-field description of the scattering properties of a system. A way beyond the mean-field theory in total energy calculations for solution phases is associated with the development of so-called *O(N)* methods (*Martin*, 2004). The point is that computational efforts for a conventional electronic structure code scale as N^3 with respect to the number of atoms in a system (or a supercell). In *O(N)* methods the scaling is linear, which allows for simulations of systems with much larger number of atoms. Unfortunately, most of them can not deal with metallic systems. However, the locally self-consistent Green's function

method (LSGF) (*Abrikosov et al*., 1996) has been applied for metals with considerable success.

5. Phase Stabilities at High Pressure: Discussion and Conclusions

A clear necessity to obtaining a fundamental understanding of the phase stability problem led to a substantial theoretical development of the field. Qualitative picture of bonding in metals and alloys has been developing from the early years of the last century, pioneered by the works of Hume-Rothery. These works led to a formulation of three Hume–Rothery rules for primary solid solutions, which can be summarized as follows (*Massalski,* 1996):

(i) The size effect. If difference between the atomic sizes of the component elements forming an alloy exceeds 15%, solid solubility should become restricted.
(ii) The electrochemical effect. Formation of stable intermediate compounds will restrict primary solid solubility.
(iii) The relative valence effect. The extent of solid solubility and the stability of certain intermediate phases (the so-called Hume-Rothery phases) is determined by the electron concentration.

For equilibria involving only solid and liquid phases, the phase boundaries are typically shifted only by the order of a few hundredths of a degree per bar change in P, and therefore the effect of pressure upon the phase diagram is often assumed to be negligible unless the pressure is of the order of hundreds atmospheres. At the same time, a possibility to influence the phase stability by compression follows directly from above mentioned Hume-Rothery rules for primary solid solutions. Indeed, according to the third rule the extent of solid solubility and the stability of the Hume-Rothery phases in metallic systems are determined by the electron concentration, and the latter can be modified by pressure. For instance, in transition and noble metals this occurs due to the charge transfer between *sp*- and *d*- electrons (*Pettifor*, 1995), leading to pressure-induced structural phase transitions even in such stable metals as gold (*Dubrovinsky et al*., 2007). A variation of the electron concentration by a combined effect of alloying and compression may therefore lead to a stabilization of new structures, as compared to ambient or low-pressure regions of phase diagrams. As an example here one can mention the effect of Ni on the high-pressure and high temperature stabilization of the bcc phase of Fe (*Dubrovinsky et al*., 2007) (at ambient pressure Ni has the opposite effect) and the pressure-induced shifting of structural transitions to lower valence electron concentration observed in In–Gd and In–Sn alloys (*Mikhaylushkin et al*., 2005).

It is probably less appreciated that parameters entering the first and the second Hume–Rothery rule can also be affected by pressure. Indeed, if the compressibility of one of the alloy components is quite different form another, the difference between their atomic sizes should vary strongly with pressure, leading to a possibility of the pressure-induced alloying between elements with very low solubility at ambient conditions. This effect was predicted from first-principles for Fe alloys with Mg (*Dubrovinsky et al*., 2005), K (*Lee et al*., 2004), and Xe (*Lee et al*., 2006). For the Fe–Mg alloy the theoretical prediction was confirmed experimentally (*Dubrovinsky et al*., 2005). Also, at high pressure the electrochemical effect can lead to an increase in stability of intermediate compounds, which should further restrict primary solid solubility. This phenomenon was predicted theoretically (see Figure 1) and observed experimentally in Fe–Si alloys (*Dubrovinsky et al*., 2003).

A task of calculating phase diagrams at high pressure may seem to be straightforward, as the techniques discussed above for the simulations of the phase equilibria at ambient pressure should also be applicable for compressed systems. Indeed, first-principles calculations of the pressure dependence of phase equilibria were carried out for, e.g. Al–Li (*Sluiter et al*., 1996) and Ni-Al (*Geng et al*., 2004) systems. In these works the Ising Hamiltonian with pressure (or more correctly volume) dependent interaction parameters determined by the Connolly–Williams procedure was used together with the cluster variation method for the calculations of the corresponding phase diagrams. The theory predicted that the compression up to 5.4 GPa should affect the phase equilibria in Al–Li system as follows (*Sluiter et al*., 1996): the solubility of Li in Al should decrease while the solubility of Al in Li should increase, the equilibrium between the fcc Al-rich solid solution phase and the metastable Al_3Li intermetallic compound should not be affected, and the ordering tendencies at Li-rich end of the phase diagram should be slightly enhanced. In the case of Ni-Al system, the strengthening of the stability of DO_3, B2, and bcc Al phases with pressure increasing to 400 GPa was predicted, as well as parameters of an equation which relates the order-disorder transition temperature to the change of pressure (chosen in the form of Simon equation) were obtained (*Geng et al*., 2004).

However, large class of tasks relevant for practical, e.g. geophysical, applications requires to carrying out simulations at extremely high temperatures. Thus, one must take into consideration non-configurational contributions to the free energy, e.g. the electronic entropy, lattice vibrations and thermal lattice expansion. These are non-trivial problems. In addition, high-pressure crystal structures of the alloy phases and even chemical content of the alloys may not be known, which is often a situation in first-principles modeling of Earth and planetary materials, but sometimes also in

high-pressure materials synthesis. Recent progress in the theoretical treatment of the above mentioned problems was reviewed by *Gillan et al.* (2006). But as a matter of fact, majority of simulations are still carried out for pure elements, or at best for highly diluted systems. Thus, the first-principles description of phase stabilities of alloys at high-pressure is still a challenging problem for the theory.

ACKNOWLEDGEMENTS

We would like to thank the Swedish Research Council (VR), the Swedish Foundation for Strategic Research (SSF) and the Göran Gustafsson Foundation for Research in Natural Sciences and Medicine for financial support.

References

Abrikosov, I.A. and Skriver, H.L., Self-consistent linear-muffin-tin-orbitals coherent-potential technique for bulk and surface calculations: Cu-Ni, Ag-Pd, and Au-Pt random alloys. 1993, *Phys. Rev. B*. **47**: 16532.

Abrikosov I.A., Niklasson A.M.N., Simak S.I., Johansson B., Ruban A.V., and Skriver H.L., 1996, Order- N Green's function technique for local environment effects in alloys. *Phys. Rev. Lett.* **76**: 4203.

Dubrovinsky, L.S., Dubrovinskaia, N.A., Crichton, W.A., Mikhaylushkin, A.S., Simak, S.I., Abrikosov, I.A., de Almeida, J.S., Ahuja, R., Luo, W., and Johansson, B., 2007, Noblest of all metals is structurally unstable at high pressure. *Phys. Rev. Lett*. **98**: 045503.

Dubrovinsky, L., Dubrovinskaia, N., Kantor, I., Crichton, W.A., Dmitriev, V., Prakapenka, V., Shen, G., Vitos, L., Ahuja, R., Johansson, B., and Abrikosov, I.A., 2005, Beating the miscibility barrier between iron group elements and magnesium by high-pressure alloying *Phys. Rev. Lett.* **95**: 245502.

Dubrovinsky, L., Dubrovinskaia, N., Langenhorst, F., Dobson, D., Rubie, D., Gessmann, C., Abrikosov, I.A., Johansson, B., Baykov, V.I., Vitos, L., Le Bihan, T., Crichton, W.A., Dmitriev, V., and Weber, H.-P., 2003, Iron-silica interaction at extreme conditions and the electrically conducting layer at the base of Earth's mantle. *Nature* **422**: 58.

Dubrovinsky, L., Dubrovinskaia, N., Narygina, O., Kuznetzov, A., Prakapenka, V., Vitos, L., Johansson, B., Mikhaylushkin, A.S., Simak, S.I., and Abrikosov, I.A., 2007, Body-centered cubic iron-nickel alloy in earth's core. *Science* **316**: 1880.

Ducastelle, F., 1991, *Order and Phase Stability in Alloys,* North-Holland, Amsterdam.

Geng, H.Y., Chen, N.X., and Sluiter, M.H.F., 2004, First-principles equation of state and phase stability for the Ni-Al system under high pressures. *Phys. Rev. B.* **70**: 094203.

Gillan, M.J., Alfè, D., Brodholt, J., Vočadlo, L., and Price, G.D., 2006, First-principles modelling of Earth and planetary materials at high pressures and temperatures. *Rep. Prog. Phys.* **69**: 2365.

Lee, K.K.M. and Steinle-Neumann, G., 2006, High-pressure alloying of iron and xenon: "Missing" Xe in the Earth's core? *J. Geophys. Res. – Solid Earth*, **111**: B02202.

Lee, K.K.M., Steinle-Neumann, G., and Jeanloz, R., 2004, Ab-initio high-pressure alloying of iron and potassium: Implications for the Earth's core. *Geophys. Res. Lett.* **31**: L11603.

Martin, R.M., 2004, *Electronic Structure. Basic Theory and Practical Methods*, Cambridge University Press, Cambridge.

Massalski, T.B., 1996, Structure and Stability of Alloys, in *Physical Metallurgy*, fourth, revised and enhanced edition, vol. 1, eds. R.W. Cahn and P. Haasent, North-Holland, Amsterdam, pp. 135–204.

Mikhaylushkin, A.S., Simak, S.I., Johansson, B., and Häussermann, U., 2005, Electron-concentration and pressure-induced structural changes in the alloys $In_{1-x}X_x$ (X=Cd,Sn). *Phys. Rev. B.* **72**: 134202.

Pettifor, D.G., 1995, *Bonding and Structures of Molecules and Solids*, Clarendon Press, Oxford.

Ruban, A.V. and Skriver, H.L., 1999, Calculated surface segregation in transition metal alloys. *Comput. Mater. Sci.* **15**: 119.

Ruban, A.V. and Abrikosov, I.A., 2008, Configurational thermodynamics of alloys from first principles: Effective cluster interactions. *Rep. Prog. Phys.* **71**: 046501.

Sluiter, M.H.F., Watanabe, Y., de Fontaine, D., and Kawazoe, Y., 1996, First-principles calculation of the pressure dependence of phase equilibria in the Al-Li system. *Phys. Rev. B.* **53**: 6137.

Vitos, L., Abrikosov, I.A., and Johansson, B., 2001, Anisotropic lattice distortions in random alloys from first-principles theory. *Phys. Rev. Lett*. **87**: 156401.

Zunger, A., Wei, S.H., Ferreira, L.G., and Bernard, J.E., 1990, Special quasirandom structures. *Phys. Rev. Lett.* **65**: 353.

FIRST-PRINCIPLES MOLECULAR DYNAMICS AND APPLICATIONS IN PLANETARY SCIENCE

SANDRO SCANDOLO*
The Abdus Salam International Centre for Theoretical Physics (ICTP), Trieste, Italy, INFM-CNR Democritos National Simulation Center, Trieste, Italy

Abstract I will review some fundamental aspects of atomistic simulations in high-pressure research, including the construction of the interatomic potentials and the basic methods Chto sample the constant-pressure and constant-temperature statistical ensemble. I will also present a couple of examples where such methods have been used to describe materials of planetary interest.

Keywords: *Ab-initio* molecular dynamics, interatomic potentials, phase transitions, planetary science

1. Introduction

Research at high pressure has benefited enormously from methodological developments in the area of atomistic simulations. The properties of materials can change unexpectedly under the application of pressure and temperature and simulations have proven themselves essential in the interpretation of experimental data as well as in the design of new experiments (*Scandolo*, 2002). Simulations are also essential to explore conditions that cannot be reached in the laboratory, such as those that can be found in the interiors of planets, including the Earth (*Oganov et al.*, 2005).

*E-mail: scandolo@ictp.it

E. Boldyreva and P. Dera (eds.), *High-Pressure Crystallography: From Fundamental Phenomena to Technological Applications*, DOI 10.1007/978-90-481-9258-8_28,

2. Methods

2.1. THE INTERATOMIC POTENTIAL

Any theoretical model aimed at predicting or interpreting the structural, mechanical, vibrational, and transport properties of materials under pressure requires the definition of energy at the atomistic level, i.e. of a function of the atomic positions and, in the case of crystalline solids, also of the crystal cell parameters. Energy can be used to determine relative stabilities between crystal structures, to extract thermodynamical data both for solids and for liquids, to calculate vibrational modes, transport coefficients, and several other properties.

2.1.1. *Classical Interatomic Potentials*

Theoretical approaches to the construction of interatomic potentials have been historically based on a "classical" description of the interaction between atoms, where the energy of a material is expressed as a sum of terms describing the mutual interaction between atom pairs. Refinements of these minimal models include the addition of terms describing energetic correlations between three atoms, or four atoms, and so forth. Combined with efficient numerical tools to explore the phase space identified by the structural parameters (cell and internal parameters), such an approach has been very successful in describing the properties of a number of materials at ambient temperature, including phase transitions, sound velocities, Raman and IR frequencies and intensities, etc. Combined with a description of the atomic dynamics based on Newton's equation (so called molecular dynamics) it has allowed the inclusion of temperature effects and the description of phenomena such as melting, thermal transport, high-temperature elasticity, etc. However, a "classical" approach fails in a series of important situations frequently encountered in high-pressure physics. It fails for example in describing phase changes when the bonding properties of the material change substantially, for example due to pressure. It is also unable to provide any information regarding optical, magnetic, electronic transport properties, and in general in all those cases where the electronic states of the material are relevant.

2.1.2. *The "First-Principle" Potential*

A more theoretically sound and general approach to the atomistic description of materials consists of constructing the energy of interaction between atoms starting from the fundamental laws of quantum mechanics, i.e. from the "first principles". Although a first-principle approach is in principle exact, it is still numerically challenging, with present-day computers, to solve it for realistic materials. A series of approximations such as the adiabatic

decoupling of the atomic dynamics from the electronic dynamics, and the introduction of an effective interaction between electrons through density-functional theory, have recently brought first-principle approaches into the realm of computational tools that can effectively describe the properties of realistic materials, at least in those cases where the complexity of the system (measured in terms of the size and time scales required to describe a given property) does not exceed the computational limits set by today's parallel computers. The application of first-principle methods is by now widespread in the fields of condensed matter physics, chemistry, and material science, and has recently become to flourish also in high-pressure physics (see also Piero Macchi's lecture, chapter 26 of this book). Initially restricted to structural optimization of crystal structures, and determination of low temperature phase diagrams, in the last decade methodological advances have allowed first-principle methods to extend their domain of application to finite temperature properties, as well as to address crucial spectroscopic properties such as the magnetic, optical, and vibrational properties thereby allowing a direct comparison with experiments (see also Bjorn Winkler's and Igor Abrikosov's lectures, chapters 27 and 40 of this book).

2.2. EXPLORING THE PHASE SPACE

Once the energy of the system is defined, the next step of a simulation consists in sampling the phase space of the atomic coordinates (and of the cell parameters in the case of crystals) in order to obtain the correct thermodynamic description of the system at the pressure and temperature conditions of interest (*Frenkel and Smit*, 1996). Among the several methods that have been proposed to sample statistical ensembles, molecular dynamics (i.e. integrating Newton's equations until the system is fully equilibrated) stands out for its simplicity. Molecular dynamics also provides atomic trajectories that can be used to extract transport coefficients and vibrational spectra. Molecular dynamics is however limited by the time scales, particularly when large energy barriers separate the initial state from the (often unknown) thermodynamically stable state. Several methods have been developed recently to enhance the search for the thermodynamically stable state, among them the "metadynamics" method, the random search method, and a variant of the genetic algorithm specifically designed for crystals (see Artem Oganov's lecture, chapter 25 of this book).

3. Examples

I will describe a couple of examples of applications of first-principle molecular dynamics to the study of materials of planetary interest. In the first example I will discuss the properties of water and methane, including their mixtures (*Lee and Scandolo*, 2009), at the conditions of the interiors of Uranus and Neptune. I will then describe selected simulations carried out for silica (SiO_2) to unveil the microscopic aspects of its pressure-induced collapse from tetrahedral to higher coordination (*Liang et al.*, 2007).

4. Software

Most of the codes for first-principle calculations are now available free of charge on the net. I will briefly describe one of such codes, developed in cooperation with a team of developers based at the "Democritos" National Simulation Center in Trieste, and available for download at http://www.quantum-espresso.org (*Scandolo et al.*, 2005).

References

Frenkel, D., and Smit, B., 1996, *Understanding Molecular Simulations*, Academic Press, San Diego, CA.

Liang, Y., Miranda, C.R., and Scandolo, S., 2007, Tuning oxygen packing in silica by non-hydrostatic pressure, *Phys. Rev. Lett*. **99**: 215504.

Oganov, A., Price, G.D., and Scandolo, S., 2005, Ab-initio theory of planetary materials, *Z. Krist*. **220**: 531.

Scandolo, S., 2002, First-principles molecular dynamics simulations at high pressure, *Proc. of the International School of Physics "E. Fermi" on "High Pressure Phenomena"*, IOS, Amsterdam, pp. 195–214.

Scandolo, S., Giannozzi, P., Cavazzoni, C., de Gironcoli, S., Pasquarello, A., and Baroni, S., 2005, First-principles codes for computational crystallography in the "Quantum-ESPRESSO" package, *Z. Krist.* **220**: 574.

MOLECULAR ORBITAL APPROACH TO INTERPRET HIGH PRESSURE PHENOMENA – CASE OF ELUSIVE GOLD MONOFLUORIDE*

WOJCIECH GROCHALA[1†], DOMINIK KURZYDŁOWSKI[2]
[1]*University of Warsaw, Interdisciplinary Centre for Mathematical and Computational Modeling, Pawinskiego 5A, 02106 Warsaw Poland.; University of Warsaw, Faculty of Chemistry, Pasteur 1, 02093 Warsaw Poland,* [2]*University of Warsaw, Faculty of Chemistry, Pasteur 1, 02093 Warsaw Poland*

Abstract Usefulness of Molecular Orbital analysis for prediction and interpretation of a variety of high-pressure phenomena will be illustrated for the case of elusive gold monofluoride, Au(I)F.

Keywords: DFT calculations, gold, Molecular Orbital theory, periodic systems, relativistic effects

1. Oh, are these Molecular Orbitals any Good?

The term *"orbital"* was first used in English by great American chemist Robert S. Mulliken in 1925 (see *Mulliken*, 1967 and refs therein) as the unique English translation of Schrödinger's original expression '*Eigenfunktion*'. It has since been equated with the "spatial region" associated with the function. '*Molecular orbitals*' were introduced by Friedrich Hund in a series of papers, which have appeared in 1927 (see *Kutzelnigg*, 1996 and refs therein) and independently by Mulliken in 1928 (*Mulliken*, 1967 and refs therein). The linear combination of atomic orbitals (LCAO) approximation for molecular orbitals from Sir John Lennard-Jones has followed in 1929 (*Kutzelnigg*, 1996 and refs therein).

Usefulness of the Molecular Orbital (MO) scheme for analysis of ambient-pressure phenomena – within either Hartree–Fock or Density Functional

* This work is dedicated to Neil W. Ashcroft, an unusual physicist who loves chemistry and torments his students with the periodic table of elements, in admiration of his contributions to solid state and high pressure science.

† E-mail: wg22@cornell.edu

E. Boldyreva and P. Dera (eds.), *High-Pressure Crystallography: From Fundamental Phenomena to Technological Applications*, DOI 10.1007/978-90-481-9258-8_29,

Theory approaches (*i.e.* Kohn–Sham orbitals) – cannot be overestimated (*Piela*, 2007). An arbitrary selection of seven important reasons for that is given below.

(i) First, the MO analysis helps to rationalize qualitatively the chemical bonding in molecules and solids by identifying orbitals which are bonding, antibonding, or simply non-bonding for every pair of atoms. This enables chemists to support a simplified yet intuitive and very useful description of bonding, where single or multiple bonds (localized between given atoms) and lone pairs are drawn (so called 'dot' or simply 'Lewis model' of 'cubical atoms', where two dots form a solid line) (Figure 1). Such localization makes it in turn possible to consider the VSEPR model and to predict molecular shape without performing any geometry optimizations (*Gillespie and Nyholm*, 1957). The model may be turned quantitative by introduction of various charge or bond population schemes but its strength is precisely in its qualitative part. Ask a chemist to construct an as yet unknown or an exotic molecule for you – he will certainly begin with drawing of a set of Lewis formulas trying to preserve valence octets or doublets around each atom. Remarkably, it is always one of the reasonable Lewis formulas which corresponds to the lowest-energy isomer of a molecule.

(ii) Second, derivation of MOs allows one to visualize frontier orbitals (HOMO and LUMO or SOMO) of any system; these MOs have major impact on system's reactivity and explain the origin of the lowest-lying excited states. The shape of the frontier orbitals determines the placement of donor and acceptor centers of a molecule and thus they allow to understand susceptibility of the molecule towards acid/base and redox reactions. For example, HOMO of an isolated Au(I)F molecule is centered mainly on Au and formed by an axially–symmetric $5d(z^2)$ AO of Au, while LUMO of this molecule is a σ* combination of $6s/6p(z)_{Au}$ and $2s/2p(z)_F$ hybrids (Figure 2). Right below HOMO two degenerate MOs can be seen, constituted from two π* combinations of $5d(xz,yz)_{Au}$ and 2p(x,y) lone pairs on F atom (perpendicular to molecular axis) (some may find it difficult to recognize HOMO–1 as π* judging from the electronic density integrated for two degenerate orthogonal MOs of an axially symmetric AuF molecule).

$$\left|\overline{\underline{\mathbf{F}}}\right|^{-} \; \mathbf{He} \rightarrow \overline{\underline{\mathbf{O}}}\left|\right.$$

Figure 1. One of the few possible Lewis structures of the hypothetical metastable $[FHeO]^{-1}$ anion (*Grochala*, 2009). A total of 16 valence electrons are forced to localize to avoid He's hypervalence.

The shapes of HOMO–1, HOMO and LUMO suggest that AuF molecules should have pronounced tendency towards:

(i) Head-to-tail oligo- or polymerization via HOMO–1/LUMO overlap between adjacent molecules
(ii) Aurophilic interactions via HOMO/LUMO interactions

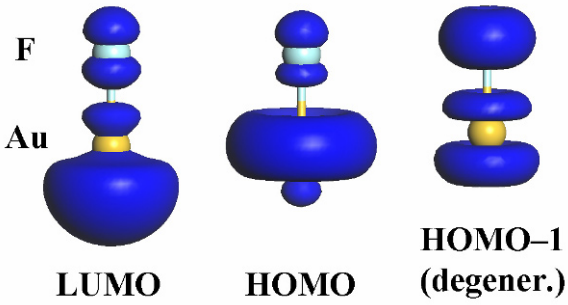

Figure 2. Electron density integrate for the frontier orbitals and HOMO–1 of the AuF molecule in the gas phase at its experimental geometry (*Evans and Gerry*, 2000); periodic DFT GGA/PBE calculations for the molecule in a box; periodic GGA/PBE calculations with the 400 eV cutoff and relativistic Vanderbilt-type pseudopotentials (CASTEP, VASP, PHONON).

Inspecting the electronic population (not shown) one may notice that LUMO has a substantial share from the $5d(z^2)_{Au}$ and $6p(z)_{Au}$ AOs which suggests that there is depopulation of the d set and partial occupation of the nominally empty $6s_{Au}$ orbital. This phenomenon, known also for isoelectronic Pt^0 complexes, comes from strong relativistic stabilization of the 6s orbital and simultaneous destabilization of the 5d one, and it makes Au atom – and less so its monovalent cation – similar to hydrogen atom (see for example *Pyykkö*, 2004).

We will return to the Au(I)F molecule and the MO-based predictions in Section 2.

(iii) Third, MOs give access – via Koopmans theorem – to two important quantitative descriptors of Mulliken electronegativity, χ_M (*Mulliken*, 1934), and Pearson's hardness, η_P (Figure 3) (*Pearson,* 1985). If you consider interaction of two molecules and you would like to know which will be the direction and extent of charge density redistribution upon this interaction, first calculate and compare Mulliken electronegativities of both species – electrons will flow from a less towards a more electronegative species… If you study a certain type of chemical reaction for a set of related molecules and you would like to know which molecule will exhibit the smallest barrier at the reaction pathway, first calculate values of Pearson's hardness – the smallest one will guide you to the most facile reaction…

(iv) Fourth, molecular orbitals are usually constructed by combining AOs or hybrid orbitals from each atom of the molecule, or from other molecular orbitals from groups of atoms. It is usually presumed that this task cannot be made without computer's help. But this is not true. If your system exhibits numerous symmetry elements (which is fortunately quite often the case) it is possible to easily construct your MOs from symmetry–adapted combinations of atomic orbitals (AOs).

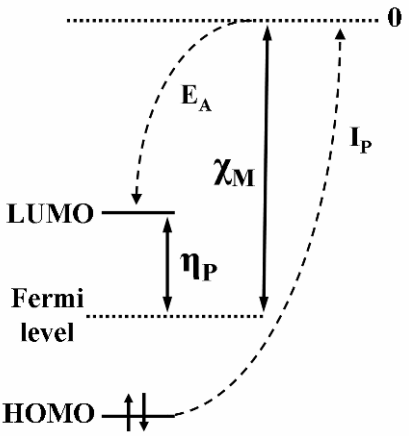

Figure 3. Illustration of Mulliken electronegativity, χ_M, and Pearson's hardness, η_P, for an even–electron system with non-degenerate HOMO. I_P stands for the first ionization potential, E_A for the first electron affinity.

The older author of these lecture notes had great pleasure to spend his first postdoctoral stay in Roald's Hoffmann group at Cornell University, where the MO theory is, so to speak, at home. He has witnessed numerous situations when the group leader (Figure 4) has tought how to step-by-step construct MOs using the symmetry–adapted combinations of AOs for different molecules. It has also happened a few times during the group seminars when a Distinguished Guest spoke about his Very Precise MP4 (or maybe it was Coupled Cluster…?) study for rhenium (cobalt, copper…?) complex with, say, 1,2–diiminetetrachloro… etc. (or do you prefer 1,8–diphosphanaphtalene derivative?) that Roald murmured "ethylene…" and subsequently showed why selected MOs of this complex organometallic species must resemble σ and σ* of C_2H_4 molecule. These "ethylenes", "acetylenes" or "ozones" became proverbial, a vivid testimony to great usefulness of what is now called an *isolobal analogy*.

To sum up – and hopefully encourage younger audience – an approximate shape of MOs of your molecule (obviously, without values of coefficients at AOs) may easily be derived in your brain, no need for calculations here

(please *cf*. also *Hoffmann*, 1998). The effort pays off, since you get immediate access to symmetry conservation rules, and to distinction between symmetry-allowed and forbidden reactions. This knowledge may be subsequently utilized in a broad spectrum of problems, including as demanding ones as catalysis, surface reorganization of solids, etc.

(v) Fifth, the MO treatment is of undisputable historical importance since it laid way to more advanced post-Hartree–Fock quantum mechanical treatments including the configuration–interaction (CI) scheme.

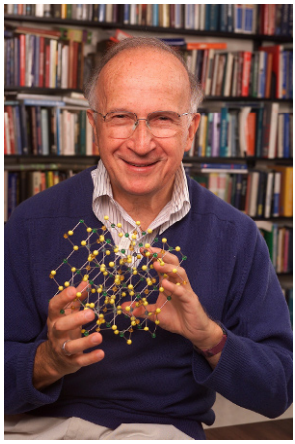

Figure 4. Prof. Roald Hoffmann (Cornell University, Ithaca NY, USA), father of the Extended Hückel Theory, of symmetry selection rules and great master of structures, orbitals, bonds and bands (Photo by G. Hodges, reproduced with permission).

(vi) Sixth, if you would like to understand magnetism and magnetic super-exchange, be it in bi- or poly-nuclear molecules or in extended solids, then better forget about 'through space' interactions and concentrate on 'through bonds' ones (*Hoffmann*, 1998). Drawing orbitals will help you a lot to identify the most efficient super-exchange paths and sometimes also deduce the sign of the super-exchange constants (antiferromagnetic or ferromagnetic coupling?) (*Landrum and Dronskowski*, 2000).

(vii) Seventh, and the last, one may use MO description for all periodic solids, as well. A non-sophisticated procedure, which could be named as 'crystal orbitals from molecular orbitals' or 'from bonds to bands approach', helps to understand origin and features of crystal orbitals (COs) (*Hoffmann*, 1988).

Thus, if the MO description is so useful to describe matter of any degree of complexity at ambient pressure, then why it is not equally popular for the elevated pressure regime? Why in most of theoretical papers discussing

electronic structure of solids one may find just some unreadable *spaghetti*-like images of the band structure…? (The list of such works is so long that we prefer to risk an offence of omission instead of citing of the most representative cases in a long Appendix). And why solid state chemists so seldom try to actually *watch* various contributions to a total electronic density (visualized inside the unit cell) but they prefer to follow physics view of effective electron masses and momentum (in the reciprocal cell)?

The authors of this contribution do not know the answer to these questions, so at least in the next few sections they will attempt to help filling in the invisible gap which separates well-known MOs we draw for matter from the daily ambient-pressure world and those – hardly any different – MOs we might derive for compressed matter at small, moderate or even very high or 'negative' pressures.

2. Towards Genuine Au(I)F in the Solid State as Deduced from Phonon Instabilities of High–Symmetry Polymorphs

2.1. THE TARGET: ELUSIVE Au(I)F IN THE SOLID STATE

It is usually assumed that species exhibiting a closed electronic shell (*i.e* s^2, p^6, d^{10}, f^{14}) are particularly stable. This is the case of inert noble gases (He $1s^2$, Ne $2s^22p^6$, etc.), liquid metallic mercury (Hg $6s^25d^{10}$) and many other isoelectronic species. One might therefore expect that compounds of Au(I) ($5d^{10}$) will also exhibit remarkable stability. Indeed, monovalent gold is known in many binary and multinary compounds such as AuCl, $CsAuCl_2$, AuI, Au_2S, KAuS, etc. However, Au(I)F, the 'simplest' among binary fluorides of gold, has been synthesized in the gas phase only recently, and it has never been obtained in condensed phases (*Saenger and Sun*, 1992; *Schröder et al*., 1994; *Schwerdtfeger et al*., 1994; *Evans and Gerry*, 2000; *Mohr*, 2004). This is in striking contrast with the existence of monofluoride of gold's lighter congener, silver, as well as difluoride of an isoelectronic Hg(II).

So, what is wrong about Au(I)F in the solid state? What are the reasons for its presumed lack of thermodynamic stability? Could it be synthesized at some (P,T) conditions and what crystal structure would it adopt? Could it be brought to ambient conditions (quenched) and would it then be metastable? Antropomorphizing this simple compound we could say that its stubborn 'refusal' to exist at ambient (P,T) conditions and despite efforts of the best pedigree of experimental chemists, has set us on the track of theoretical investigations (*Kurzydłowski and Grochala*, 2008a). The answer to the questions asked above has already been provided (*Kurzydłowski and Grochala*, 2008a), and here we will concentrate only on selected aspects of reasoning and in

particular on rationalization the results of quantum mechanical calculation with the MO theory approach.

2.2. THE METHOD: PHONON INSTABILITIES–BASED COMPUTATIONAL APPROACH TO PREDICT LOWEST ENTHALPY POLYMORPHS

Various high- rate-success methods to predict the lowest-energy isomers (polymorphs) have been described in the literature. Here we would like to choose a simple and intuitive one, which is transplanted from molecular calculations to solids without any modifications. A set of initial guess structures of various symmetries is proposed, geometry of a molecule (unit cell of a crystal) is optimized taking into account the above-mentioned symmetry constraints, and vibrational (phonon) spectrum is then calculated. Detection of imaginary modes indicates that structure is not a real minimum, and subsequent optimization(s) is (are) performed for lower symmetry structures. These new structures are obtained by distorting a higher symmetry structure along the normal vector of the imaginary vibrational mode (which usually lowers the symmetry) and re-optimizing them. At the end all real minima are compared with respect to their energy parameter of choice (energy, free energy, enthalpy, free enthalpy, etc.)

Practice shows that relatively small cut-off values may be used for initial structure screening and phonon calculations. This is important because computational effort and time of calculations may be greatly reduced. This in turn allows for screening of a much richer set of initial structures. In the spirit of this approach initial calculations for Au(I)F have been performed with the cutoff of 400 eV and only after detection of few important local minima (*i.e.* polymorphic forms) these structures were recomputed with the 600 eV cutoff.

Visualization in the unit cell of electronic density integrated over selected crystal orbitals constitutes an essence of the standard MO approach. This feature is not yet available in the very efficient commercial VASP package (Medea) but it has been implemented for some time now in the competitive but numerically less efficient CASTEP (Materials Studio). Sometimes the integration is difficult because single straws of the band structure *maccaroni* cross one another at various k-points and it is impossible to separate two or more contributions of various symmetries. Despite these difficulties, as it will be shown below, it is indeed worth to integrate, visualize and analyze electron density over every particular band of interest.

Unfortunately, the currently existing DFT codes do not permit visualization of the Kohn–Sham orbitals at selected k-points (just their normalized square *i.e.* density); this feature is however available for some EHT programs such as YAEHMOP. Comparison of orbital shapes at various k-points within

a given band is especially important for understanding origin of bands of very large dispersion (which is quite common at high pressures). It is hoped that this severe deficiency will one day be removed from commercial packages thus gaining these products larger solid-state chemistry audience.

2.3. FOLLOW THE CASCADE OF PHONON INSTABILITIES

2.3.1. *Step 1: Starting Point. The NaCl- and CsCl-Type Ionic Structures*

At the beginning let us not care about bonds, orbitals, covalence and VSEPR theory, but let us instead try to think, which structure type could be adopted by Au(I)F if an ionic picture of bonding applied. This attempt is justified because fluorine is indeed the most electronegative amongst all chemical-bond-forming elements, and despite unusually large electronegativity of gold. In other words, let us analyze traditional packing of spheres first.

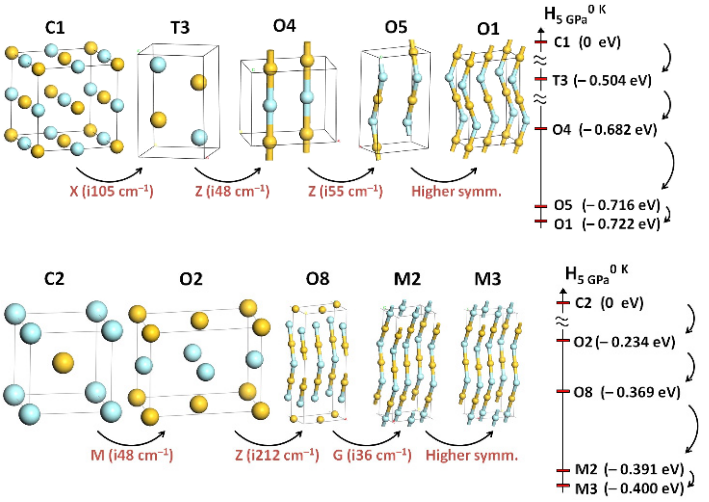

Figure 5. Selected cubic, tetragonal and orthorhombic crystal structures of Au(I)F considered in this study, i.e. Top: from *left* to *right*: a parent ionic one Fm–3m NaCl–type (C1), and four others derived from phonon instabilities: P4/nmm (T3); Pmmn (O4); Pnma (O5); Cmcm (O1), i.e. O5 after symmetry recognition with a restrictive threshold and reoptimization. *Bottom*: from *left* to *right*: a parent ionic one Pm–3m CsCl–type (C2), and four others derived from phonon instabilities: Cmmm (O2); Amm2 (O8); Cm (M2); C2/m (M3), i.e. M2 after symmetrization. Arrows indicate relationship between the parent and the derived structure, and also show which imaginary phonon has been followed. Nomenclature of polymorphs is consistent with that used in (*Kurzydłowski and Grochala*, 2008a). Light/dark balls represent gold/fluorine atoms.

The Pauling radii of Au(I) and of F^{-1} anions are 1.37 Å and 1.36 Å, respectively, which leads to the ratio of 1.01. This number is larger than the borderline value of 0.73 which suggests that 'ionic Au(I)F' should adopt the

CsCl-type structure with Au(I) in an 8-coordinated site (Figure 5) rather than the NaCl-type structure with its 6-coordinated metal site (Figure 5). It will turn out later how far this prediction – which neglects chemical bonding – falls from truth. For didactic purposes we will consider both prototypical high symmetry structure types in this lecture (it is good to start with a less realistic and presumably a higher–energy structure, since there is a larger chance for the appearance of substantial phonon instabilities and thus for a subsequent large energy decrease during re-optimizations…!).

In Figure 5 we also show other possible crystal structures of Au(I)F, which will become of importance at later stages of this analysis. Reader is referred to *Kurzydłowski and Grochala* (2008a) for further details.

2.3.2. *Step 2: Following Phonon Instabilities from the NaCl-Type Structure*

This study is for P = 5 GPa, and not for P = 1 atm since DFT methods incorrectly reproduce weak interactions inevitably present in low-dimensional structures; this indeficiency matters less at elevated pressure. It turns out that Au(I)F optimized at 5 Gpa in the NaCl and CsCl type structures both show few imaginary phonons (Figure 6; for the CsCl-type see Section 2.3.3.). Let us now see where the distortions associated with these phonons will lead us and try to understand how they influence the electronic structure.

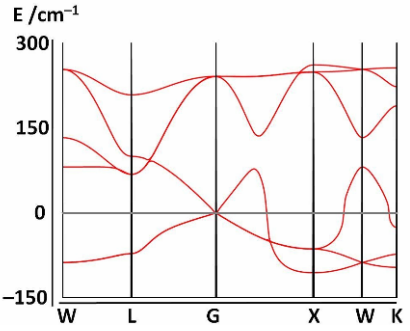

Figure 6. Phonon band structure of AuF in the NaCl–type structure. A triple degeneracy of the imaginary phonon at G(Γ) is testified by splitting of phonon branches, for example between X and W, or between W and L.

The NaCl structure shows three imaginary phonon branches, which are degenerate at Γ (T_{1u} mode). The largest imaginary wavenumber of 105 $cm^{-1}_{(i)}$ is reached at X (½ 0 ½). Following this normal mode yields a tetragonal T3 structure. The T3 structure exhibits two imaginary phonons (not shown), with the largest imaginary wavenumber of 48 $cm^{-1}_{(i)}$ at Z (0 0 ½), leading to an orthorhombic O4 structure. The O4 structure in turn has just one imaginary phonon (not shown) with the largest imaginary wavenumber of 55 $cm^{-1}_{(i)}$

at Z (0 0 ½), leading to another orthorhombic structure, O5. Symmetry recognition with a very restrictive threshold indicates that O5 adopts in fact a C-centered Cmcm unit cell (this structure is called O1, see Section 2.3.4). Here a cascade of phonon instabilities comes to end and O1 is the lowest energy polymorph in this series. More meticulous structural screening, not presented here, suggests that O1 is in fact *the* lowest energy polymorph of Au(I)F at 5 GPa (*Kurzydłowski and Grochala*, 2008a).

Analysis of the electronic band structures of all the polymorphs which appear on the C1→O1 pathway (Figure 7) leads to conclusion that imaginary phonons are strongly coupled to the electronic structure of Au(I)F. The top of the uppermost (unoccupied) band moves progressively to lower energies, from +20.7 eV for C1, via +15.2 eV for T3 and +14.0 eV for O4, down to +13.7 eV for O5 and then +12.6 eV for O1 (see Section 2.3.4 and Figure 10). Simultaneously the bottom of the lowermost occupied band moves from –4.4 eV for C1 to –5.6 eV for O5.

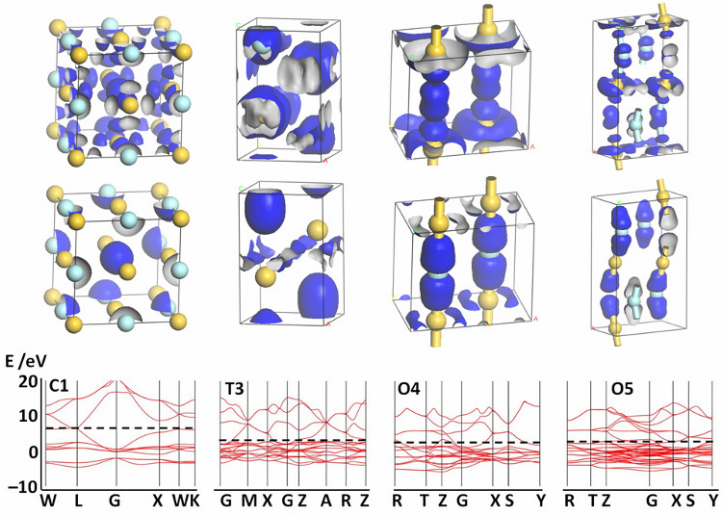

Figure 7. Electronic band structure of AuF in C1 structure, T3 structure, O4 structure, and O5 structure. Note the progressive lowering of the occupied and unoccupied bands from C1 to O5. Electronic density integrated over the lowest occupied and highest unoccupied band (*top*) is presented for every structure at isovalue of 0.02 e $Å^{-3}$. The position of the Fermi level, shown with a dotted line, has not been arbitrarily set to zero. Localized states exhibiting small dispersion (at ca. –23 eV) of a predominant $2s_F$ character have not been shown.

As symmetry is step-by-step decreased by imaginary phonons (cubic → tetragonal → orthorhombic), the unoccupied bands may mix up with the occupied bands, what leads to the energy lowering of the latter. This in turn results in the decrease of the enthalpy per one formula unit (FU) by over –

0.7 eV, which in turn testifies to imaginary character of the phonons. One clearly deals with strong *vibronic instabilities* here.

As these instabilities are followed, substantial modifications to connectivity pattern, chemical bonding – and concomitant reorganizations of the electronic density – take place. Evolution of the coordination sphere of Au(I) in Au(I)F at 5 GPa begins from its 6-coordination in the NaCl–type structure (six equal large bond lengths of 2.44 Å). The first coordination sphere of Au(I) then takes an unusual 1 + 4 + 1 form for the T3 structure (1 × 2.30 Å, 4 × 2.53 Å, 1 × 2.66 Å) and transforms to 2-coordination for the O4 structure (2 × 2.09 Å + secondary bonding). The 2-coordination is preserved for O5 and also for the lowest enthalpy O1 structure (2 × 2.12 Å +4 × 3.00 Å). It might thus be concluded comparing the O1 structure with its parent NaCl-type structure, that two of six Au–F bonds have been strengthened at the expense of the remaining four. Similar plasticity of the first coordination sphere is also known for the species exhibiting the first order (*Gažo et al*., 1976), as well as the second order (*Landrum and Hoffmann*, 1998) Jahn–Teller effect, such as Cu(II) ($3d^9$) or Sb(III) ($5s^2$). Appearance of this phenomenon for Au(I)F is not actually too surprising, if one considers that there is a substantial depopulation of 5d orbital for Au(I), which makes it analogous to Cu(II) (see Section 1).

In the consequence of the bond-localizing distortions the first coordination sphere of relativistic Au(I) adopts its preferred dumbbell shape seen in the $[AuF_2]$ units, which then polymerize to form the 1D infinite $[AuF_{2/2}]$ chains. The dumbbell shape of the $[AuF_2]$ units allows for an efficient s-p-d hybridization at Au atom (*cf.* Figure 7) while bending of the chains at F atoms suggests the exposure of the s-p hybridized lone pairs at F and testifies to marked covalence of the Au–F bonding (vide: VSEPR rules). The resulting O1 structure is similar, but not identical to, that of AuCl. It might be argued that covalence of the Au–F bonds is sufficient to yield directional F–Au–F bonding within the dumbbell, but insufficient to localize electron density even further leading to a crystal structure comprising of weakly interacting AuF molecules (*cf.* crystal structures of related solid HF and IF).

One more structural feature of Au(I)F in the O1 structure immediately attracts attention: the aurophilic interactions. While they are absent for the NaCl–type structure (12 equal secondary Au…Au contacts at 3.32 Å, which is equal to double of the van der Waals radius of Au atom), they are quite pronounced for the O1 structure (2 × 2.82 Å, 4 × 2.87 Å, which may be compared to twice the covalent radius of Au, 2.72 Å).

Summarizing on this section we should add that major leitmotifs detected for the crystal structure of Au(I)F confirm the predictions made from the simplistic MO analysis for an isolated AuF molecule (Section 1).

As we may judge from this example, the orbitals, the orbital-interaction-driven distortions and the covalence of chemical bonds really matter.

2.3.3. *Step 3: Following Phonon Instabilities from the CsCl-Type Structure*

The phonon-instability-driven evolution of Au(I)F in the CsCl-type (C2) structure (Figure 8) is similar to the one described above for the NaCl-type structure; the major difference is that the symmetry lowering leads here directly from the cubic to the orthorhombic Cmmm (O2) structure (Figure 5, Section 2.3.1), skipping the intermediate tetragonal stage. This is followed by distortions yielding structures: Amm2 (O8), Cm (M2), with a consecutive decrease in energy. The M2 structure turns out to be symmetrizable to C2/m (M3). Here imaginary distortions come to end.

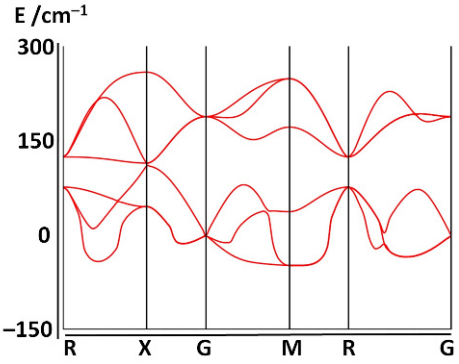

Figure 8. Phonon band structure of AuF in the CsCl–type structure. A triple degeneracy of the imaginary phonon at G (Γ) is testified by splitting of phonon branches, for example between R and X, or between G and M.

It turns out that the M3 structure is quite similar to the O1 one (Figure 5); the main difference is that the $[AuF]_\infty$ chain is bent at every second F atom for the former structure, and at every F atom for the latter one. This is also the reason why the O1 structure is marginally more stable than the M3 one (by < 0.1 eV per AuF). Comparison of the M3 and O1 polymorphs is important because they were obtained from, respectively, NaCl- and CsCl-type precursors with ***significantly*** different topology of heavy Au atoms. In other words our structure-exploring algorithm which follows cascade of phonon instabilities, senses quite well the shape of the complex surface of potential energy of crystalline binary species and it is able to converge to a polymorph exhibiting energy minimum (or nearly so) starting from distinctly different prototypical structures.

2.3.4. *The Final: Phonon and Electronic Band Structure of the most Stable Polymorph of Au(I)F (at 5 GPa)*

Phonon distortions have led us to the lowest-enthalpy O1 polymorph. But what is its electronic structure? Analysis of the electronic band structure of AuF at 5 GPa (Figure 9) suggests that this compound should be semi-metal. Careful analysis of the electronic band structures of C1, T3, O4, O5 and O1 polymorphs show that vibronic distortions progressively remove density of states from the Fermi level leaving off just a little of it in the most stable structure. Apparently, the 'maximum hardness principle' is in operation. However, this result might in fact be an artifact of the DFT methods, which are known to underestimate the band gap. If the top of the 'valence band' moves down with respect to the bottom of the 'conduction band' by ca. 1 eV then the indirect electronic band gap would open and Au(I)F should be considered a semiconductor.

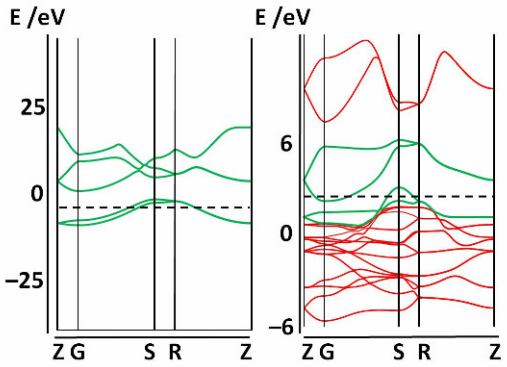

Figure 9. Not every gold fluoride that glitters… Analysis of electronic band structure of AuF at 5 GPa in the lowest-enthalpy O1 structure (*right*) suggests that this compound should be semimetal and exhibit weak metallic luster, but this result might in fact be an artifact of the DFT method (see text). Electronic band structure of a hypothetical O1 unit cell of AuF with all F atoms removed, Au atoms substituted by H atoms and unit cell vectors rescaled so to yield reasonable H…H interactions (*left*).

Due to relativistic nature of the $6s_{Au}$ orbital, which becomes partly populated for Au(I)F, fragments of the band structure of Au(I)F bears strong similarity to that of the similar Cmca cell containing only atomic H instead of Au with all F atoms removed from the cell (Figure 8 and ESI to *Kurzydłowski and Grochala*, 2008a). This resemblance points to a large share of $6s_{Au}$ states to the electronic bands of Au(I)F found in the vicinity of the Fermi level, and it is also consistent with the results of population analysis.

2.3.5. *Structural Transformations of AuF at Negative and Large Positive Pressure Regimes*

As we have seen the MOs and their mutual interactions largely govern structural preferences of AuF in the solid phase at small pressures (~5 GPa). However, very high pressures render less important the MO interactions and atoms' preferences for chemical bond formation and for particular coordination numbers, and this is good packing that matters most (*Grochala et al*., 2007). Indeed, the phase transformations which have been anticipated for Au(I)F involve a transition to the layered T3 structure (at 86 GPa) (*Kurzydlowski and Grochala*, 2008a). Our recent results show, however, that a transition to the CsCl structure will occur at even lower pressure of 42–43 GPa. The coordination number of Au(I) is appreciable at 50 GPa, namely 14, with 8 short Au–F separations of 2.43 Å, and 6 short Au–Au distances of 2.81 Å.

So what is left from MOs of AuF at 0.5 mln atm? The electronic band structure exhibits very broad bands of a typical dispersion of 8–10 eV (not shown), thus pointing to an enormously strong s-p-d mixing. And the compound is metallic, of course. Speaking from the vantage point of molecular orbitals such situation is not too advantageous for our didactic purposes.

And what about the 'negative' pressure regime? Leaving aside the issue of technically feasibility (chemists usually mimic 'negative pressure' by simply diluting or isolating molecules from one another!), it may be anticipated that the O1 structure subjected to negative pressure will at first break its weakest chemical bonds *i.e.* aurophilic interactions, and dissociate into isolated infinite 1D [$AuF_{2/2}$] chains. At subsequent 'decompression' the chains will break down into oligomers and then single AuF molecules (with the CN of Au(I) equal to 1). In this way the entire lifecycle of a molecule transforming into its dense polymeric and simultaneously metallic form – consider, this metamorphosis involves 1-, 2-, 4-, 6-, 8-, 12- or even 13-coordinated Au(I)! – may be directed by changing a single physical parameter: pressure.

2.4. ANOTHER ROUTE TOWARDS AUF – VIA EXOTIC XEAUF – AND AGAIN INSPIRED BY ORBITALS

For strong mixing within the MO manifold the AOs must have comparable energies and similar spatial extent; this enables their good overlap. A comparison of the DFT–derived AO energies for Xe, Au and F immediately suggests that xenon – nominally a 'noble' gas – might form strong bonds to gold, as first suggested in a careful theoretical study (*Pyykkö*, 1995). Thus, one might anticipate that Xe might actually facilitate synthesis of AuF via

formation of a (meta?)stable XeAuF intermediate (*Grochala*, 2007). That this surmise is right has been testified by periodic DFT calculations for XeAuF (*Kurzydłowski and Grochala*, 2008b); the formation of short Xe–Au bonds and further strengthening of Au–F ones, as well as some interesting redox reactions, have been discussed during the lecture.

3. Conclusions

The purpose of this lecture has been to encourage young crystallographers to use the intuitive MO description. We also wanted to demonstrate that there exists a computational procedure which may lead to quite complex lowest energy crystal structure (as exemplified by AuF) even if one starts from some 'simple' *i.e.* high symmetry structure types, remembered by everyone (here, the NaCl-type structure adopted by AgF, a lighter analogue of AuF).

The MO theory is very frequently utilized to analyze bonding in isolated molecules and sometimes also in solids at ambient pressure. It seems natural – and definitely in our own flair – to extend the MO approach to the moderate pressure regime (~1–20 GPa). While this approach has not been pursued so far by too many groups, it has many advantages: the MO theory offers simple explanations without loosing its applicability for most families of solids even if electronic bands gain on dispersion.

References

Evans, C.J., and Gerry, M.C.L., 2000, Confirmation of the existence of gold(I) fluoride, AuF: Microwave spectrum and structure. *J. Am. Chem. Soc.* **122**: 1560.

Gažo, J., Bersuker, I.B., Garaj, J., Kabešová, M., Kohout, J., Langfelderová, H., Melník, M., Serátor, M., and Valach, F., 1976, Plasticity of the coordination sphere of copper(II) complexes, its manifestation and causes. *Coord. Chem. Rev.* **19**: 253.

Gillespie, R. and Nyholm, R. S. 1957, Inorganic stereochemistry. *Quart. Rev.* **11**: 339.

Grochala, W., 2007, Atypical compounds of gases, which have been called 'noble'. *Chem. Soc. Rev.* **36**: 1632.

Grochala, W., 2009, On chemical bonding between helium and oxygen. *Pol. J. Chem.* **83**: 87.

Grochala, W., Feng, J., Hoffmann, R., and Ashcroft, N.W., 2007, The chemical imagination at work in very tight places. *Angew. Chem. Int. Ed. Engl.* **46**: 3620.

Hoffmann, R., 1971, Interaction of orbitals through space and through bonds. *Acc. Chem. Res.* **4**: 1.

Hoffmann, R., 1988, *Solids and Surfaces: A Chemist's View of Bonding in Extended Structures*, VCH, New York.

Hoffmann, R., 1998, Qualitative thinking in the age of modern computational chemistry - or what Lionel Salem knows. *J. Mol. Str. (Theochem)* **424**: 1.

Kurzydłowski, D., and Grochala, W., 2008a, Elusive AuF in the solid state as accessed via high-pressure comproportionation. *Chem. Commun.* 1073.

Kurzydłowski, D., and Grochala, W., 2008b, Xenon as a mediator of chemical reactions? Case of scarce gold monofluoride, AuF, and its adduct with xenon. *Z. Anorg. Allg. Chem.* **634**: 1082.

Kutzelnigg, W., 1996, Friedrich Hund and chemistry. *Angew. Chem.* **35**: 573.

Landrum, G.A., and Dronskowski, R., 2000, The orbital origins of magnetism: from atoms to molecules to ferromagnetic alloys. *Angew. Chem. Int. Ed. Engl.* **39**: 1560.

Landrum, G.A., and Hoffmann, R., 1998, Secondary bonding between chalcogens or pnicogens and halogens. *Angew. Chem. Int. Ed. Engl.* **37**: 1887.

Lennard-Jones, J.E., 1929, The electronic structure of some diatomic molecules. *Trans. Faraday Soc.* **25**: 668.

Mohr, F., 2004, The chemistry of gold-fluoro compounds: A continuing challenge for gold chemists. *Gold Bull.* **37**: 164.

Mulliken, R.S., 1934, A new electroaffinity scale; together with data on valence states and on valence ionization potentials and electron affinities. *J. Chem. Phys.* **2**: 782.

Mulliken, R.S., 1967, Spectroscopy, molecular orbitals, and chemical bonding. *Science.* **3785**: 157.

Pearson, R.G., 1985, Absolute electronegativity and absolute hardness of Lewis acids and bases. *J. Am. Chem. Soc.* **107**: 6081.

Piela, L., 2007, *Ideas of quantum chemistry,* Elsevier, Amsterdam.

Pyykkö, P., 1995, Predicted chemical bonds between rare gases and Au^{+}. *J. Am. Chem. Soc.* **117**: 2067.

Pyykkö, P., 2004, Theoretical chemistry of gold. *Angew. Chem. Int. Ed. Engl.* **43**: 4412.

Saenger, K.L., and Sun, C.P., 1992, Yellow emission bands produced during gold etching in O_2-CF_4 rf glow-discharge plasmas: Evidence for gas-phase AuF. *Phys. Rev. A* **46**: 670.

Schröder, D., Hrušak, J., Tornieporth–Oetting, I.C., Klapoetke T.M., and Schwarz, H., 1994, Neutral gold(I) fluoride does indeed exist. *Angew. Chem., Int. Ed. Engl.* **33**: 212.

Schwerdtfeger, P., McFeaters, J.S., Stephens, R.L., Liddell, M.J., Dolg, M., Hess, B.A. 1994, Can AuF be synthesized? A theoretical study using relativistic configuration interaction and plasma modeling techniques. *Chem. Phys. Lett.* **218**: 362.

HIGH-PRESSURE SYNTHESIS OF MATERIALS

PAUL F. MCMILLAN *
Department of Chemistry, University College London, 20 Gordon St., London WC1H 0AJ, U.K.

Abstract High pressure-high temperature techniques are used to synthesise new solid state compounds and materials that can be developed for technological applications. Laboratory and synchrotron x-ray diffraction and optical spectroscopy are combined with *ab initio* calculations to determine the structures and properties of new materials. We describe recent work on major classes of new materials including boron-rich solids, transition metal nitride superconductors, nitride spinels and light element solids based in the C–N–H system using examples from our own work.

Keywords: Solid state chemistry, new materials, boron-based solids, nitride spinels, nitride superconductors, carbon nitride

1. Introduction

The pioneering research of P.W. Bridgman first led to major developments in high-pressure physics and solid state chemistry. He also investigated materials properties of metals, ceramics and other substances (*Bridgman*, 1931; *McMillan*, 2005). The field of high-pressure research made another leap forward with the invention of the diamond anvil cell that permitted direct observation of samples held under extreme pressures that now extend into the multimegabar range (*Eremets*, 1996; *Holzapfel and Isaacs*, 1997; *Jamieson et al.*, 1959; *Jayaraman*, 1983; *Piermarini*, 2001; *Van Valkenburg*, 1962; *Weir et al.*, 1959). Following the laboratory preparation of diamond (*Bovenkerk et al.*, 1959; *Bundy et al.*, 1995, 1996; *Hazen*, 1999) and the synthesis of cubic boron nitride (c-BN, *Wentorf*, 1957) high-pressure–high-temperature research became an important tool for synthesis and exploration of new materials with potential technological applications (*McMillan*, 2002). Materials

* E-mail: p.f.mcmillan@ucl.ac.uk

E. Boldyreva and P. Dera (eds.), *High-Pressure Crystallography: From Fundamental Phenomena to Technological Applications*, DOI 10.1007/978-90-481-9258-8_30,

investigated include new superhard phases, materials with unusual electronic, magnetic and superconducting properties, structural ceramics and solid state compounds with wide-gap optoelectronic behaviour and catalytic properties. X-ray diffraction carried out in the laboratory on quenched samples or *in situ* at high pressures and high temperatures at synchrotron beamlines is a primary technique for determining the structure and compressibility properties of the new materials, as well as establishing their recovery to ambient conditions. This is complemented by optical techniques including Raman scattering and FTIR or UV-visible spectroscopy. The electrical conductivity and magnetic properties of new materials are investigated *in situ* in the DAC or large volume devices and upon recovery to ambient conditions.

2. New Materials Exploration: High-P,T Strategies

Techniques introduced by Bridgman led to development of new high pressure apparatus generally termed "large volume" devices (*Eremets*, 1996; *Holzapfel and Isaacs*, 1997; *Hazen*, 1999; *Liu and Bassett*, 1986). In particular, the opposed anvil geometry gave rise to the "belt" press used in the synthesis of diamond and to "toroidal" anvil instruments developed in Russia (*Hall*, 1960; *Khvostanstev et al.*, 2004). That work led to the "Paris–Edinburgh" press developed as a portable device for neutron scattering and other experiments at large facilities and in the laboratory (*Besson et al.*, 1992). The piston cylinder apparatus envisaged by Kennedy for diamond synthesis was developed for geological studies and is now used routinely in solid state chemistry and materials investigations (*Hazen*, 1999; *Boyd and England*, 1960; *Coes*, 1955). Modern multi-anvil devices that reach 24 GPa or higher were developed from von Platen's and T. Hall's original designs for diamond production (*Hazen*, 1999; *von Platen*, 1962). These instruments are used in laboratories to investigate the synthesis and recovery to ambient conditions of new solid state compounds and technological materials. Because large press techniques can be scaled up to achieve industrial scale production of important materials following examples of diamond and c-BN, they set a benchmark for advanced materials research. First, new materials must be recoverable to ambient conditions in a useful form. That usually limits the materials applications to powdered polycrystalline samples obtained from high-P,T synthesis or single crystalline materials of high value (*e.g.*, large gem-quality diamonds or substrates for optoelectronic materials; *Sumiya et al.*, 2000; *Krukowski et al.*, 2001). Developing new technologically relevant materials differs from exploratory solid state science in that commercial and environmental considerations must also be taken into account.

The DAC permits direct observation and *in situ* studies of materials under high pressure conditions extending into the multimegabar range. Laser-heating and resistive heating methods permit simultaneous studies under high-P,T conditions, as well as synthesis of new solid state compounds and potentially important technological materials. *In situ* studies during release of pressure allow us to evaluate the recovery of the new compounds to ambient conditions and the evolution of their properties during decompression. Useful strategies for exploration and development of new materials combine *in situ* and high-P,T synthesis studies using DAC and large volume technique with *ab initio* calculations to predict the stability and properties of new phases and interpret experimental results.

X-ray diffraction studies at high pressure lead to determination of the equation of state and the bulk or shear moduli, often used as a guide to identifying materials with high hardness (*He et al.*, 2004; *Brazhkin et al.*, 2002; *Haines et al.*, 2001; *Teter*, 1998; *Veprek*, 1999). Spectroscopy gives information on electronic and phonon structure and measurements of magnetism and electrical conductivity at high P guide formation and recovery of new phases with potentially useful superconducting or multiferroic behaviour by observing the evolution of these properties as a function of the density.

3. Boron-Rich Solids

Elemental boron exhibits structure-property relations and bonding unique within the periodic table. According to traditional valency rules it has three electrons that typically form three covalent bonds resulting in planar molecular units or clusters with pyramidal structures. However these are electron deficient relative to the 8-electron rule and they readily form new compounds or complexes with electron-donating species often resulting in increased coordination of the B atoms or incorporation of "impurity" atoms into boron-rich structures. Motifs based on dodecahedral or icosahedral clusters containing triangular units are common in molecular and solid state boron chemistry. These are generally incompatible with developing long-range translation symmetry and the result is a series of highly complex boron-based structures among the elemental forms and compounds with metals and non-metallic species. The element is available with varying degrees of purity in amorphous or α- or β-structured forms: the β-B_{105} structure is thought to be most thermodynamically stable. Superconductivity has been observed in boron at very high pressure and new high pressure forms have been recognised that have interesting and potentially useful electronic and magnetic properties (*Oganov et al.*, 2009; *Haüssermann et al.*, 2003; *Papaconstantopoulos and Mehl*, 2002; *Eremets et al.*, 2001). Reports of

superconductivity in B-doped diamond are now under investigation (*Yokoya et al.*, 2005; *Dubrovinskaia et al.*, 2006; *Ekimov et al.*, 2006).

The c-BN structure was predicted and synthesised shortly after the first laboratory production of diamond to give rise to a new high-pressure material that has become technologically important (*Wentorf*, 1957). It is second hardest to diamond and is used for cutting and grinding applications: modern research continues to investigate high-P,T syntheses of this phase along with advanced diamond production (*Sumiya et al.*, 2000; *Demazeau et al.*, 1990; *Solozhenko*, 2002b; *Solozhenko et al.*, 2000, 2002a; *Pal'yanov et al.*, 2002; *Sokol et al.*, 2001; *Sung and Tai*, 1997). c-BN is a wide-gap semiconductor with potential applications in high-T electronics and opto-electronics and high-P,T research has succeeded in producing doped single crystals (*Taniguchi et al.*, 2002), as well as of h-BN for UV laser applications (*Watanabe et al.*, 2004). Exploratory high-P,T research to develop new super-hard compounds in the C-B-N system continues and a new ordered cubic compound BC_2N competitive in hardness with c-BN was discovered recently (*Solozhenko et al.,* 2001a, b; *Solozhenko*, 2002a).

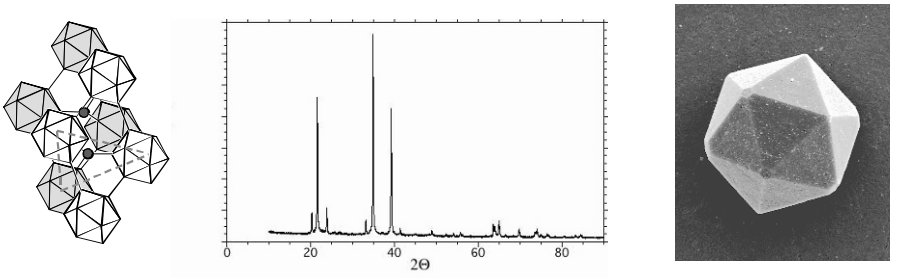

Figure 1. The α-B structure based on B_{12} icosahedra linked by electron-deficient 3-centre B-B bonding readily accepts electron rich species such as O, N, etc. to result in high-hardness semiconducting materials. The result is a rhombohedral ($R\bar{3}m$) structure (XRD shown at centre). High-P,T synthesis results in unusual macroscopic icosahedra formed multiple twinning or by Mackay packing (*Hubert et al.*, 1997, 1998a, b; *McMillan et al.*, 1999).

The α-B structure forms the basis for series of suboxides, subnitrides and other chalcogenide or pnictide compounds (Figure 1). Here electron-rich species such as O, N, P, As occupy trigonal sites between the B_{12} icosahedra. Materials such as B_6O_{1-x} provide high-hardness refractory ceramics (*He et al.*, 2002, 2004; *Hubert et al.*, 1996, 1998a, b; *Lundstrom*, 1997; *Lundstrom and Andreev*, 1996; *Rizzo et al.*, 1962). B_6O is also a wide-gap semiconductor that might be developed for high-T thermoelectric applications. During high-P,T synthesis experiments from B + B_2O_3 mixtures at 3–4 GPa it was discovered that the O content could be increased to near unity ($B_6O_{0.96}$) and the resulting materials formed macroscopic

icosahedral particles up to ~40 μm in diameter (Figure 1) (*Hubert et al.*, 1996, 1998a, b; *McMillan et al.*, 1999). These formed as a result of multiple twinning within the rhombohedral α-B structure. The growth can also be described in terms of Mackay packing, that constitutes a novel space-filling scheme ordering successive layers of B_{12} icosahedra and O atoms in a radial stacking pattern without translational symmetry (*Hubert et al.*, 1998a, b; *McMillan et al.*, 1999). Formation of analogous B_6N was reported from high-P,T synthesis but the results have recently been questioned (*Hubert et al.*, 1997; *Solozhenko et al.*, 2006).

4. Transition Metal Nitrides

Transition metal nitrides, carbides and borides form important refractory materials with high hardness and low compressibility used as abrasives and for structural applications including anvils for high P devices (*Oyama*, 1996; *Toth*, 1971; *Kaner et al.*, 2005). They are generally metallic and members including cubic ε-NbN and hexagonal δ-MoN can achieve high superconducting T_c values (15–17 K; *Chen et al.*, 2004; *Shebanova et al.*, 2006). The hexagonal structures are based on metallic layers with interstitial trigonal prismatic or octahedral sites for the nonmetal species (Figure 2). δ-MoN synthesis from reactions such as $MoCl_5 + NH_3$ results in poorly crystalline material with disordered N atoms and T_c ~5 K (*Lengauer*, 1988). Annealing at high P prevents N_2 loss and leads to N ordering and T_c increases to 12–17 K, comparable with ε-NbN (*Bezinge et al.*, 1987; *Bull et al.*, 2004). The hypothetical cubic compound MoN has been predicted to achieve very high T_c values ranging up to 30 K. However the known cubic phase in the system is non-stoichiometric (γ-Mo_2N) with a rocksalt structure containing 50% vacancies on the anion sites. High P,T experiments including laser-heated DAC and multi anvil syntheses have determined that cubic MoN is unlikely to exist, consistent with theoretical predictions (*Hubert et al.*, 1997, 1998a, b; *McMillan et al.*, 1999; *Machon et al.*, 2006). However, it appears that cubic solid solutions between NbN and MoN_x can be prepared, although the superconducting T_c appears to vanish upon substitution of Mo for Nb. Hexagonal (Mo,Nb)N phases can also be prepared and their T_c values are being studied. This work has now revealed a new oxynitride Mo_3O_2N with T_c ~ 17 K (*Bailey and McMillan*, 2010).

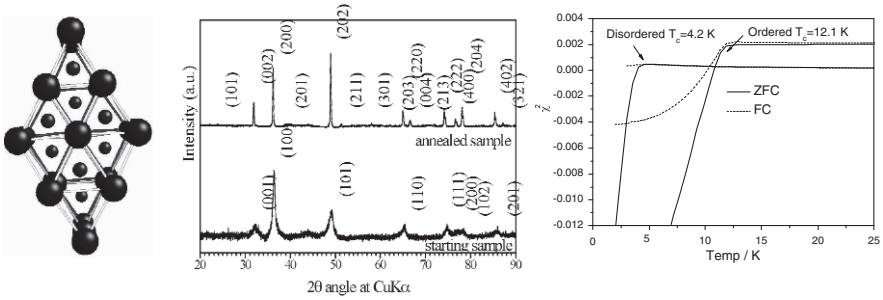

Figure 2. Left: the hexagonal MoN structure. The Mo layers define trigonal prismatic sites for N atoms that are 50% occupied in each layer. Centre: High P annealing results in N ordering and a doubling of the hexagonal unit cell along the *c* axis. SQUID magnetometry results shows the increase in T_c from disordered to ordered MoN (right) (*Bull et al.*, 2004).

5. Spinel Nitrides

The spinel structure is common among oxides, chalcogenides and halides with AB_2X_4 stoichiometry. The type mineral $MgAl_2O_4$ is used as a substrate for the semiconductor industry and in optically transparent and scratch resistant coatings. Transition metal oxide spinels MFe_2O_4 (M = Fe^{2+}, Ni^{2+}, Cu^{2+}, Mn^{2+}, Zn^{2+}, Mg^{2+} *etc.*) are magnetic materials used for information storage and in transformer cores. Other important spinels include cation deficient $Li_{1-x}(Mn,Fe)_2O_4$ used in battery technology and for fuel cells and in catalysis. However, until 1999, no spinels based on the N^{3-} anion had been prepared. In that year, however, reports of spinel-structured γ-Si_3N_4 and γ-Ge_3N_4 synthesised at high-P,T and Sn_3N_4 prepared from SnI_4 in liquid NH_3 appeared (*Leinenweber et al.*, 1999; *Serghiou et al.*, 1999; *Zerr et al.*, 1999; *Scotti et al.*, 1999; *Schnick*, 1999; *Sekine et al.*, 2000). The new nitride spinels have high hardness and low compressibility and they could become useful refractory ceramics for structural and abrasive applications (*Tanaka et al.*, 2002; *Jiang et al.*, 2001, 2002; *Soignard et al.*, 2001). They are also predicted to have wide direct bandgaps that could give rise to novel optoelectronic materials operating in the UV range and high-T semiconductors (*Dong et al.*, 2000; *Leitch et al.*, 2004; *Ching et al.*, 2001a). Now Ga and (Si,Al) oxynitride spinels are available and research is under way to realise the first transition metal containing examples of nitride and oxynitride spinels that are predicted to be stable (*Schwarz et al.*, 2002; *Sekine et al.*, 2001; *Kinski et al.*, 2005; *Soignard et al.*, 2005; *Ching et al.*, 2001b; *Hector et al.*, 2006; *McMillan et al.*, 2007).

6. C–N–H Solids

Since the prediction that dense phases of C_3N_4 might have extremely low compressibility and potentially high hardness (*Cohen*, 1985; *Liu and Cohen*, 1989; *Teter and Hemley*, 1996) there has been intense interest in developing the high-P,T chemistry of carbon nitrides and other materials in the C–N–H system. The original study suggested the new C_3N_4 phase might be isostructural with β-Si_3N_4. Later calculations suggested that other dense phases could also be found in the system, with α- as well as β-Si_3N_4 structures, or structures based on cubic spinel or wurtzite types. Many attempts at synthesis of high-density C_3N_4 compounds have been reported using high-P,T methods or by deposition from the vapour phase but to date the structures and chemical composition of the materials produced have not been fully characterised (*Malkow*, 1996; *Horvath-Bordon et al.*, 2006). In a collaboration with T.U. Darmstadt we used the laser heated DAC to synthesise a new defect-wurtzite (dwur) phase of C_2N_3H ($C_2N_2(NH)$) from dicyandiamide (DCDA) precursor at P>27 GPa (*Horvath-Bordon et al.*, 2007). Dwur-C_2N_3H was recovered to ambient conditions and its structure and composition were determined by electron diffraction and EELS in the TEM along with nano-SIMS and *ab initio* calculations. Recently we obtained an x-ray diffraction pattern for dwur-C_2N_3H following high-P,T DAC synthesis and determined the bulk modulus (K_o~250 GPa) in agreement with *ab initio* calculations (*Salamat et al.*, 2009). The x-ray diffraction results along with Raman scattering indicate that new C–N–H materials remain to be discovered following high-P,T synthesis. Dwur-C_2N_3H can provide a useful precursor to predicted high-density C_3N_4 phases (Figure 3).

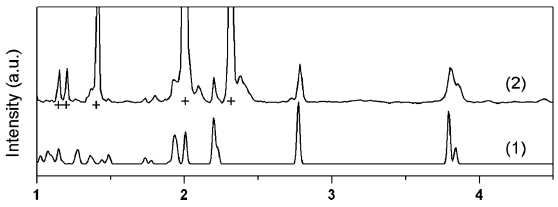

Figure 3. DFT calculated (1) versus experimental (2) XRD pattern for dwur-C_2N_3H obtained using LiF as PTM (*Salamat et al.*, 2009).

7. Summary

High-P,T research including synthesis, *in situ* studies of structure and properties and theoretical calculations is an important component of solid state science with the identification of new phases and compounds and P,T stability relations. The studies also reveal new materials with potentially important technologically relevant properties.

ACKNOWLEDGEMENTS

PFM acknowledges support from EPSRC SRF EP/D07357X and Portfolio grant EP/D504782 (held jointly with C.R.A. Catlow and P. Barnes). The work reported for dwur-C_2N_3H forms part of the Ph.D. research of A. Salamat and K. Woodhead. New data on superconducting MoN and related oxynitride phases were obtained by Dr. E. Bailey at UCL.

References

Bailey E., P. F. McMillan, *J. Mater. Chem*., submitted (2010).
Besson J.-M., G. Hamel, T. Grima, R. J. Nlmes, J. S. Loveday, S. Hull, D. Hausermann, *High Pressure Res,* 8, 625 (1992).
Bezinge A., K. Yvon, J. Muller, W. Lengauer, P. Ettmayer, *Solid State Commun,* 63, 141 (1987).
Bovenkerk H. P., F. P. Bundy, H. T. Hall, H. M. Strong, R. H. Wentorf, *Nature,* 184, 1094 (1959).
Boyd F. R., J. L. England, *J Geophys Res,* 65, 741 (1960).
Brazhkin V. V., A. G. Lyapin, R. J. Hemley, *Phil Mag A,* 82, 231 (2002).
Bridgman P. W., *The Physics of High Pressure* (G Bell and Sons, London, 1931).
Bull C. L., P. F. McMillan, E. Soignard, K. Leinenweber, *J Solid State Chem,* 177, (2004).
Bundy F. P., W. A. Bassett, M. S. Weathers, R. J. Hemley, H.-k. Mao, A. F. Goncharov, *Carbon,* 34, 141 (1996).
Bundy F. P., H. T. Hall, H. M. Strong, R. H. Wentorf, *Nature,* 176, 51 (1955).
Chen X.-J., V. V. Struzhkin, S. Kung, H.-k. Mao, R. J. Hemley, *Phys Rev B,* 70, (2004).
Ching W. Y., S.-D. Mo, L. Ouyang, *Phys Rev B,* 63, 245110 (2001a)
Ching W. Y., S.-D. Mo, I. Tanaka, M. Yoshiya, *Phys Rev B,* 63, 064102 (2001b).
Coes L., *J Am Ceram Soc,* 38, 333 (1955).
Cohen M. L., *Phys Rev B,* 32, 7988 (1985).
Dong J., O. F. Sankey, S. K. Deb, G. H. Wolf, P. F. McMillan, *Phys Rev B,* 61, 11979 (2000).
Dubrovinskaia N., G. Eska, G. A. Sheshin, H. Braun, *J Appl Phys,* 99, 033903 (2006).
Ekimov E. A., V. A. Sidorov, E. D. Bauer, N. N. Mel'nik, N. J. Curro, J. D. Thompson, S. M. Stishov, *Nature,* 428, (2004).
Eremets M., *High Pressure Experimental Methods* (Oxford University Press, Oxford, 1996).
Eremets M. I., V. V. Struzhkin, H. Mao, R. J. Hemley, *Science,* 293, 272 (2001).
Haines J., J. M. Léger, J. Bocqillon, *Ann Rev Mater Sci,* 31, 1 (2001).

Hall H. T., *Rev Sci Instruments,* 31, 125 (1960).
Haüssermann U., S. I. Simak, R. Ahuja, B. Johansson, *Phys Rev Lett,* 90, (2003).
Hazen R. M., *The Diamond Makers* (Cambridge Univ Press, Cambridge, UK, 1999).
He D. W., M. Akaishi, B. L. Scott, Y. Zhao, *J Mater Res,* 17, 284 (2002).
He D., S. Shieh, T. S. Duffy, *Phys Rev B,* 70, 184121 (2004).
Hector A. L., A. W. Jackson, P. F. McMillan, O. Shebanova, *J Solid State Chem,* 179, 1383 (2006).
Holzapfel W. D., N. S. Isaacs, *High-Pressure Techniques in Chemistry and Physics: A Practical Approach* (Oxford University Press, Oxford, 1997).
Horvath-Bordon E., R. Riedel, A. Zerr, P. F. McMillan, G. Auffermann, Y. Prots, R. Kniep, P. Kroll, *Chem Soc Rev,* 35, 987 (2006).
Horvath-Bordon E., R. Riedel, P. F. McMillan, P. Kroll, G. Miehe, P. van Aken, A. Zerr, P. Hoppe, O. Shebanova, I. McLaren, S. Lauterbach, E. Kroke, R. Boehler, *Angew Chem Int Ed,* 46, 1476 (2007).
Hubert H., L. A. J. Garvie, K. Leinenweber, P. Buseck, W. T. Petuskey, P. F. McMillan, 410, 191 (1996).
Hubert H., L. A. J. Garvie, P. R. Buseck, W. T. Petuskey, P. F. McMillan, *J Solid State Chem,* 133, 356 (1997).
Hubert H., B. Devouard, L. A. J. Garvie, M. O'Keeffe, P. R. Buseck, W. T. Petuskey, P. F. McMillan, *Nature,* 391, 376 (1998a).
Hubert H., L. A. J. Garvie, B. Devouard, P. R. Buseck, W. T. Petuskey, P. F. McMillan, *Chem Mater,* 10, 1530 (1998b).
Jamieson J. C., A. W. Lawson, N. D. Nachtrieb, *Rev Sci Instrum,* 30, (1959).
Jayaraman A., *Rev Mod Phys,* 55, 65 (1983).
Jiang J. Z., F. Kragh, D. J. Frost, K. Stahl, H. Lindelov, *J Phys Cond Matter,* 13, L515 (2001).
Jiang J. Z., H. Lindelov, L. Gerward, K. Stahl, J. M. Recio, P. Mori-Sanchez, S. SCarlson, M. Mezouar, E. Dooryhee, A. Fitch, D. J. Frost, *Phys Rev B,* 65, 161202 (2002).
Kaner R. B., J. J. Gilman, S. H. Tolbert, *Science,* 308, 1268 (2005).
Khvostanstev L. G., V. N. Slesarev, V. V. Brazhkin, *High Press Res*, 24, 371 (2004).
Kinski I., G. Miehe, G. Heymann, R. Theissmann, R. Riedel, H. Huppertz, *Z Naturforsch,* 60b, 832 (2005).
Krukowski S., M. Bockowski, B. Lucznik, I. Grzegory, S. Porowski, T. Suski, Z. Romanowski, *J Phys Cond Matter,* 13, 8881 (2001).
Leinenweber K., M. O'Keeffe, M. Somayazulu, H. Hubert, P. F. McMillan, G. H. Wolf, *Chem Eur J,* 5, 3076 (1999).
Leitch S., A. Moewes, L. Ouyang, W. Y. Ching, T. Sekine, *J Phys Cond Matter,* 16, 6469 (2004).
Lengauer W., *J Cryst Growth,* 87, 295 (1988).
Liu L.-G., W. Bassett, *Elements, Oxides, Silicates: High-Pressure Phases with Implications for the Earth's Interior* (Oxford University Press, New York, 1986).
Liu A. L., M. L. Cohen, *Science,* 245, 841 (1989).
Lundstrom T., *J Solid State Chem,* 133, 88 (1997).
Lundstrom T., Y. G. Andreev, *Mater Sci Eng A,* 209, (1996).
Machon D., D. Daisenberger, E. Soignard, G. Shen, T. Kawashima, P. F. McMillan, *Phys Stat Solidi (a),* 203, 831 (2006).
Malkow T., *Mater Sci Eng A,* 302, 309 (1996).
McMillan P. F., *Nature Mater,* 1, (2002).
McMillan P. F., *Nature Mater,* 4, (2005).

McMillan P. F., H. Hubert, A. Chizmeshya, L. A. J. Garvie, W. T. Petuskey, B. Devouard, *J Solid State Chem,* 147, 281 (1999).
McMillan P. F., O. Shebanova, D. Daisenberger, R. Quesada Cabrera, E. Bailey, A. L. Hector, V. Lees, D. Machon, A. Sella, M. Wilson, *Phase Trans,* 80, 1003 (2007).
Oganov A. R., J. Chen, G. C, M. Y, C. W. Glass, Z. Liu, T. Yu, O. O. Kurakevych, V. L. Solozhenko, *Nature,* 457, (2009).
Oyama S. T., *The Chemistry of Transition Metal Carbides and Nitrides* (Blackie Academic, Glasgow, 1996).
Pal'yanov Y. N., A. G. Sokol, Y. M. Borzdov, A. F. Khokhryakov, N. V. Sobolev, *Am Mineral,* 87, 1009 (2002).
Papaconstantopoulos D. A., M. K. Mehl, *Phys Rev B,* 65, 172510 (2002).
Piermarini G. J., *J Res Nat Inst Standards Technol,* 106, 889 (2001).
Rizzo H. F., W. C. Simmons, H. O. Bielstein, *J Electrochem Soc,* 109, 1079 (1962).
Salamat A., K. Woodhead, P. F. McMillan, R. Quesada Cabrera, J.-P. Perrillat, A. Rahman, D. Adriens, F. Cora, *Phys Rev B,* 80, 104106 (2009)
Scotti N., W. Kockelmann, J. Senker, S. Traβel, H. Jacobs, *Z Anorg Allg Chem,* 625, 1435 (1999).
Schnick W., *Angew Chem Int Ed,* 38, 3309 (1999).
Schwarz M., A. Zerr, E. Kroke, G. Miehe, I.-W. Chen, M. Heck, B. Thybusch, B. T. Poe, R. Riedel, *Angew Chem Int Ed,* 41, 788 (2002).
Sekine T., H. He, T. Kobayashi, M. Tansho, K. Kimotot, *Chem Phys Lett,* 344, 395 (2001).
Sekine T., H. He, T. Kobayashi, M. Zhang, F. Xu, *Appl Phys Lett,* 76 (2000).
Serghiou G., G. Miehe, O. Tschauner, A. Zerr, R. Boehler, *J Chem Phys,* 111 (1999).
Shebanova O., P. F. McMillan, E. Soignard, *High Pressure Res,* 26, 87 (2006).
Soignard E., M. Somayazulu, J. Dong, O. F. Sankey, P. F. McMillan, *J Phys Cond Matter,* 13, 557 (2001).
Soignard E., D. Machon, P. F. McMillan, J. Dong, B. Xu, K. Leinenweber, *Chem Mater,* 17, 5465 (2005).
Sokol A. G., Y. N. Pal'yanov, G. A. Pal'yanova, A. F. Khokhryakov, N. V. Sobolev, *Diamond Related Mater,* 10, 2131 (2001).
Solozhenko V. L., *High Pressure Res,* 22, 519 (2002a).
Solozhenko V. L., *Phys Chem Chem Phys,* 4, 1033 (2002b).
Solozhenko V. L., D. Andrault, G. Fiquet, M. Mezouar, D. C. Rubie, *Appl Phys Lett,* 78, 1385 (2001a).
Solozhenko V. L., S. N. Dub, N. Novikov, *Diamond Related Mater,* 10, 2228 (2001b).
Solozhenko V. L., Y. Le Godec, S. Klotz, M. Mezouar, V. Z. Turkevich, J.-M. Besson, *Phys Chem Chem Phys,* 4, 5386 (2002a).
Solozhenko V. L., V. Z. Turkevich, O. O. Kuryakevych, W. A. Crichton, M. Mezouar, *J Phys Chem B,* 106, 6634 (2002b).
Solozhenko V. L., Y. Le Godec, O. O. Kurakevych, *C R Chimie,* 9, 1472 (2006).
Sumiya H., N. Toda, S. Satoh, *New Diamond Frontier Carbon Technol,* 10, 233 (2000).
Sung C.-M., M.-F. Tai, *Int J Refractory Metals Hard Mater,* 15, 237 (1997).
Tanaka I., F. Oba, T. Sekine, E. Ito, A. Kubo, K. Tatsumi, H. Adachi, T. Yamamoto, *J Mater Res,* 17, 731 (2002).
Taniguchi T., T. Teraji, S. Koizumi, K. Watanabe, S. Yamaoka, *Jpn J Appl Phys,* 41, L109 (2002).
Teter D., *Mater Res Soc Bull,* 23, 22 (1998).
Teter D., R. J. Hemley, *Science,* 271 (1996).
Toth L. E., *Transition Metal Carbides and Nitrides* (Academic, New York, 1971).

Van Valkenburg A., *Rev Sci Instrum,* 33 (1962).
Veprek S., *J Vac Sci Technol A,* 17, 2401 (1999).
von Platen B., in: *Modern Very High Pressure Techniques*, ed. R. H. Wentorf (Butterworth, Washington DC, 1962), p. 118.
Watanabe K., T. Taniguchi, H. Kanda, *Nature Materials,* 3 (2004).
Weir C. E., E. R. Lippincott, A. Van Valkenburg, E. N. Bunting, *J Res Nat Bur Standards,* 63A, 55 (1959).
Wentorf R. H., *J Chem Phys,* 26, 956 (1957).
Yokoya T., T. Nakamura, T. Matsushita, T. Muro, Y. Takano, M. Nagao, T. Takenouchi, H. Kawarada, T. Oguchi, *Nature,* 438, 647 (2005).
Zerr A., G. Miehe, G. Serghiou, M. Schwarz, E. Kroke, R. Riedel, H. Fueβ, P. Kroll, R. Boehler, *Nature,* 400 (1999).

HIGH-PRESSURE SYNTHESIS OF NOVEL SUPERHARD PHASES IN THE B–C–N–O SYSTEM

VLADIMIR L. SOLOZHENKO*
LPMTM-CNRS, Institut Galilée, Université Paris Nord 99, av. J. B. Clément, F-93430 Villetaneuse, France

Abstract Recent results on high pressure–high temperature synthesis of new superhard phases in the B–C–N–O system (cubic B–C–N phases, diamond-like BC_5, rhombohedral $B_{13}N_2$, orthorhombic γ-B_{28}, etc.) are briefly reviewed.

Keywords: High-pressure synthesis, superhard phases, B–C–N–O system

1. Introduction

Superhard materials (usually compounds of light elements such as boron, carbon, nitrogen and oxygen) can be defined as having microhardness exceeding 40 GPa. In addition to high hardness, they usually possess other unique properties such as compressional strength, shear resistance, large bulk moduli, high melting temperatures, chemical inertness and high thermal conductivity. This combination of properties makes these materials highly desirable for a number of industrial applications.

Recent achievements in search for new superhard materials indicate that synthesis of phases with hardness exceeding that of diamond (H_V = 115 GPa) is very unlikely. Rather than harder, we should consider the possibility to synthesize materials that are more useful than diamond i.e. thermally and chemically more stable than diamond, and harder than cubic boron nitride (cBN).

Here we briefly review the very recent results on high pressure – high temperature synthesis of novel superhard phases in the B–C–N–O system.

* E-mail: vladimir.solozhenko@univ-paris13.fr

E. Boldyreva and P. Dera (eds.), *High-Pressure Crystallography: From Fundamental Phenomena to Technological Applications*, DOI 10.1007/978-90-481-9258-8_31,

2. New Superhard Diamond-Like Ternary B–C–N Phases

2.1. SYNTHESIS OF CUBIC BC_2N, NOVEL SUPERHARD PHASE

Phase transitions of graphite-like BN–C solid solutions synthesized by simultaneous nitridation of boric acid and carbonization of saccharose in molten urea have been studied up to 30 GPa and 3,000 K using a laser-heated diamond anvil cell and angle-dispersive x-ray diffraction at beamline ID30, European Synchrotron Radiation Facility (*Solozhenko et al.*, 2001a). Novel superhard phase, cubic BC_2N, was synthesized at pressures above 18 GPa and temperatures higher than 2,200 K by direct solid-state phase transition of graphite-like $(BN)_{0.48}C_{0.52}$. The diffraction patterns of *c*-BC_2N exhibit only *111*, *220*, and *311* Bragg lines of the cubic lattice, which correspond to the Fd-3m space group. The absence of the *200* line indicates that the atomic scattering factors of two *fcc* sublattices of the zinc-blende lattice are equal, which is possible only if B, C and N atoms (or B–N and C–C pairs) are uniformly distributed over both sublattices.

Studies of the thermal stability of *c*-BC_2N in the 25–32 GPa pressure range using laser-heated DAC at ID30, ESRF have shown that at temperatures above 2,900 K the phase decomposes to form diamond and cBN (*Solozhenko*, 2002).

The lattice parameter of *c*-BC_2N at ambient conditions is $a = 3.642(2)$ Å (*Solozhenko et al.*, 2001a; *Solozhenko*, 2002), which is larger than those of both diamond (3.5667 Å) and cBN (3.6158 Å). The large deviation of the lattice parameter of cubic BC_2N from the value expected from ideal mixing between diamond and cBN testifies that the synthesized phase is distinct from the so-called "diamond–cBN alloys" reported earlier.

To synthesize macroscopic (~2 mm^3) samples of cubic BC_2N for hardness measurements, etc., we used a 6-8 type multianvil large-volume apparatus at the Bayerisches Geoinstitut (*Solozhenko et al.*, 2001a). The diffraction patterns of the quenched samples showed the presence of a cubic phase with the lattice parameter of 3.640(4) Å which is very close to that of DAC-synthesized *c*-BC_2N. From the full x-ray emission spectra of B, C and N, the stoichiometry of the sample was determined to be $B_{0.4\pm0.1}C_{1.1\pm0.1}N_{0.5\pm0.1}$. Taking into account large errors when analyzing light elements, the phase stoichiometry can be assumed to be BC_2N.

According to the analytical transmission electron microscopy (Philips CM20-FEG) (*Solozhenko*, 2002; *Langenhorst and Solozhenko*, 2002), the grain size of cubic BC_2N ranges from 10 to 30 nm. The largest grains are of a regular cubic or tetrahedral form, while fine grains are of a round form. Selected area electron diffraction patterns exhibit rings corresponding to the *111*, *220* and *311* reflections of the cubic phase. The absence of superstructure

lines points to the statistically uniform distribution of B, C, and N atoms in the crystal lattice. *K*-edge EELS spectra of boron, carbon and nitrogen from different regions of *c*-BC_2N samples were collected with a Gatan PEELS 666 parallel electron spectrometer (*Langenhorst and Solozhenko*, 2002). Presence of characteristic δ* peaks in the electron energy-loss near-edge structure spectra reveals an sp^3 type atomic bonding and gives clear evidence for the formation of diamond-like B–C–N ternary phase. The granular structure of bulk *c*-BC_2N has been investigated by atomic force microscopy. The average size of grains observed in the AFM images was measured to be about 200 nm. The grains have the fine structure that can be attributed to small crystallites of 20-30 nm, which are combined into larger aggregates (*Zinin et al.*, 2005).

A broad Raman band corresponding to sp^3-coordinated atoms (diamond structure) can be seen in spectra of cubic BC_2N excited with UV (λ = 228.9 nm) and visible (λ = 488 nm) lasers (*Hubble et al.*, 2004). Position of the Raman band measured with UV laser excitation was found to be 1324.8(6) cm^{-1} and is consistent with the position of the peak provided by visible laser, 1326.3(19) cm^{-1}. Combining all measurements together gives a mean Raman shift of 1325.7(16) cm^{-1}. This position of the Raman band is located between the Raman peak of diamond and that of cBN and that can be attributed to LO mode of *c*-BC_2N phase. The large width (FWHM is about 25 cm^{-1}) of the observed Raman band most likely reflects random substitution of carbon atoms by boron and nitrogen in the diamond lattice.

The 300-K equation of state of cubic BC_2N was measured to 30 GPa using DAC and angle-dispersive x-ray diffraction at beamline ID30, ESRF (*Solozhenko et al.*, 2001a). The experimental *P–V* data were fitted to the Birch equation of state. The parameters of the fit are B_0 = 282(15) GPa and B_0' = 4.3(1.1), with the zero-pressure cell volume V_0 = 48.49(8) $Å^3$. The bulk modulus of cubic BC_2N is smaller than the 420 GPa value expected for ideal mixing between diamond and cBN and is in agreement with 238 GPa value obtained from Brillouin scattering (*Tkachev et al.*, 2003) (see below).

The thermal stability of cubic BC_2N in a high-purity argon atmosphere at ambient pressure has been studied by x-ray diffraction with synchrotron radiation at LURE. Our findings showed that *c*-BC_2N remains stable up to 1,800 K, and, hence, is characterized by a higher thermal stability than polycrystalline diamond with the same grain size (*V.L. Solozhenko and D. Andrault*, 2009).

Mechanical properties of *c*-BC_2N have been examined using micro- and nanoindentation (*Solozhenko et al.*, 2001a, b). The nanohardness and Young modulus were calculated from the load–displacement curves according to the Oliver–Pharr method. The Vickers (H_V = 76 GPa) and Knoop (H_K = 55 GPa) hardness as well as nanohardness (H_N = 75 GPa) and elastic moduli (*E*, *G*)

of the *c*-BC_2N are intermediate between diamond and cBN that makes the new phase the second hardest known material. The elastic recovery of *c*-BC_2N has been found to be 68% which is higher than the corresponding value for cBN (60%), and is approaching that of diamond (*Solozhenko et al.*, 2001b).

The Brillouin scattering measurements on cubic BC_2N have been successfully performed using the "emulated" platelet scattering geometry (*Tkachev et al.*, 2003). The azimuth dependencies of longitudinal (V_L) and shear (V_S) velocities do not indicate velocity anisotropy and therefore provides evidence that the nanocrystalline cubic BC_2N is elastically isotropic. Using average V_L and V_S values of 13.09 and 8.41 km/s, respectively, we were able to calculated bulk and shear moduli as 259(22) GPa and 238(8) GPa, respectively. The shear modulus value of 447 GPa evaluated from our previous nanohardness measurements (*Solozhenko et al.*, 2001b) is most likely an overestimate due to distinct deformation of the diamond indenter. At the same time, we find good agreement among the obtained bulk modulus and the corresponding value found in our independent compressibility measurements (*Solozhenko et al.*, 2001a).

Thus, the new cubic BC_2N phase has an unusual combination of mechanical properties: its elastic moduli measured by Brillouin scattering and x-ray diffraction are lower than those of cBN, whereas its hardness measured independently by micro- and nanoindentation techniques is higher than that of single-crystal cBN and only slightly lower than that of diamond.

2.2. SHOCK-COMPRESSION SYNTHESIS OF DIAMOND-LIKE BN–C SOLID SOLUTIONS

The shock-compression synthesis of diamond-like B–C–N phases has been done using cylindrical recovery containers with a ring gap that allowed concentration of explosion energy in a given direction and multiple reflection of shock waves at the walls of the container (*Solozhenko*, 2002; *Kurdyumov et al.*, 2000). The incident shock pressures on the samples have been controlled by choosing an explosive (RDX–ANFO or RDX–Nobelit 100 compositions). The use of the special additive that is characterized by a high shock temperature and a high compressibility, allowed a sample heating up to 3,500 K, and its abrupt (~10^8 K/s) cooling in decompression.

Shock compression of graphite-like $(BN)_xC_{1-x}$ ($0.48 \le x \le 0.61$) solid solutions results in formation of diamond-like phases, whose content of the recovered samples drastically increases with pressure and attains 80 wt% at 30 GPa. According to electron microprobe analysis, stoichiometries of synthesized diamond-like phases are $BC_{1.2\pm0.2}N$ and $BC_{0.9\pm0.2}N$ provided that $(BN)_{0.48}C_{0.52}$ and $(BN)_{0.61}C_{0.39}$, respectively, were used as starting materials.

Taking into account considerable errors of determination of light elements, the stoichiometry of both phases might be assumed to be BCN.

X-ray diffraction patterns of diamond-like BCN exhibit *111*, *220* and *311* lines of the cubic lattice while the *200* line is missing. The latter indicates that B, C and N atoms are statistically uniformly distributed over crystal lattice due to extremely high temperatures achieved in our experiments. From the profile analysis of *220* and *311* lines of both cubic BCN phases it follows that the experimentally observed diffraction patterns are attributable to the diamond-like BN–C uniform solid solutions, and not to a mechanical mixture of diamond and cBN (*Kurdyumov et al.*, 2000).

Lattice parameters of *c*-$BC_{1.2\pm0.2}N$ and *c*-$BC_{0.9\pm0.2}N$ have been found to be 3.598(4) and 3.604(4) Å, respectively, and are in a good agreement with corresponding values that should be expected from ideal mixing between diamond and cBN).

According to ATEM studies (*Solozhenko*, 2002; *Langenhorst and Solozhenko*, 2002) a mean grain size of both *c*-BCN phases is about 5 nm. The coarsest grains are of a tetrahedron habit, while fine grains are of a round shape. Selected area electron diffraction patterns are fully consistent with diamond-like BN-C solid solutions. A superstructure was not observed, indicating that B, C and N atoms are randomly distributed in the crystal lattice. The stoichiometry of *c*-BCN phases was estimated from the B*K*, C*K*, and N*K* EELS spectra using calculated partial ionization cross sections, and found to be BCN in both cases (*Langenhorst and Solozhenko*, 2002).

The 300-K equation of state of *c*-$BC_{0.9\pm0.2}N$ was measured up to 45 GPa using DAC and energy-dispersive x-ray diffraction at beamline F3, HASYLAB-DESY (*Solozhenko*, 2002). The experimental *p–V* data were fitted to the Birch–Murnaghan equation of state. The parameters of the fit are $K_0 = 412(9)$ GPa and $K_0' = 4.3(1.1)$. The bulk modulus of *c*-BCN is higher than that of cBN (377 GPa), and is close to the 400 GPa value that should be expected from ideal mixing between diamond and cBN. Thus, the diamond-like BN–C solid solution synthesized in the present work has one of the largest bulk moduli known for any solid, being second only to diamond (446 GPa).

Knoop hardness of bulk *c*-BCN sample sintered from shock-synthesized *c*-$BC_{0.9\pm0.2}N$ powder at high pressures and temperatures makes 52 GPa (*Solozhenko*, 2002) which is only slightly lower than that of cubic BC_2N (*Solozhenko et al.*, 2001a, b).

Thus, shock compression of graphite-like BN–C solid solutions up to 30 GPa and 3,500 K results in a formation of the ideal cubic BN–C solid solution with the stoichiometry close to BCN and statistically uniform atom distribution. This new cubic BCN phase is characterized by the very high values of bulk modulus (412 GPa) and Knoop hardness (52 GPa).

3. New Superhard Binary B–C and B–N Phases

3.1. SYNTHESIS OF DIAMOND-LIKE BC_5

Following the high-pressure synthesis of cubic BC_2N, the second after diamond hardest material, very recently we have synthesized a new superhard phase, diamond-like BC_5 (*d*-BC_5), by direct phase transformation of graphite-like B–C solid solutions at pressures above 25 GPa and temperatures of about 2,200 K using a laser-heated diamond anvil cell at beamline ID27, ESRF (*Solozhenko et al.*, 2009). Structure of the new phase has been studied by angle-dispersive x-ray diffraction with synchrotron radiation, high-resolution transmission electron microscopy and electron energy loss spectroscopy. The lattice parameter of *d*-BC_5 at ambient conditions is $a = 3.635(8)$ Å which is slightly larger than that diamond. Boron and carbon atoms are homogeneously distributed over the crystal lattice not forming superstructures. Among superhard phases, the bulk modulus of *d*-BC_5 ($B_0 = 335(8)$ GPa) is exceeded only by the bulk moduli of diamond and cBN. The phase is metastable in the whole pressure range under study and at high temperatures demonstrates a clear tendency to segregate into carbon and boron carbide, however, at ambient pressure *d*-BC_5 has been found to be more thermally stable than polycrystalline diamond.

Well-sintered millimeter-sized bulks of nanocrystalline diamond-like BC_5, have been synthesized using a T-cup multianvil apparatus combined with a 450-tonne V7 Paris–Edinburgh press and comprehensively studied by various characterization techniques. The results obtained have revealed that the material is identical to *d*-BC_5 synthesized in the DAC experiments. The material is semi-conductive and exhibits extreme hardness ($H_V = 71(8)$ GPa) comparable with that of single-crystal diamond and unusually high for superhard materials fracture toughness ($K_{Ic} = 9.5$ MPa $m^{0.5}$), in combination with high thermal stability (up to 1,900 K) that makes diamond-like BC_5 an exceptional superabrasive (*Solozhenko et al.*, 2007).

3.2. SYNTHESIS OF BORON SUBNITRIDE $B_{13}N_2$

Boron-rich phases of the B–C–N–O system with an α-rhombohedral-boron-like structure (boron carbide B_4C, boron suboxide B_6O, etc.) combine high hardness and wear resistance, chemical inertness, high melting point as well as high cross-section for neutron absorption. Solid-state synthesis of boron subnitride, B_6N, as a result of chemical interaction between boron and boron nitride at 7.5 GPa and ~2,000 K has been previously reported by *Hubert et al*. (1997). However, a critical analysis of the results has shown that the evidence for the formation of boron subnitride with B_6O-like

structure is inconclusive. Recently, we have studied *in situ* the interaction between boron and BN at the same *p–T* conditions using x-ray diffraction with synchrotron radiation (*Solozhenko et al.*, 2006). At 7.4 GPa and 2,000 K the formation of a new phase has not been observed. At the same time, HP–HT treatment has resulted in strong and unpredictable preferred orientation of boron crystallites. This leads to the rise of some weak boron reflections that might be erroneously attributed to the appearance of a new phase. All this has allowed the conclusion that the evidence for the solid-state synthesis of boron subnitride B_6N with B_6O-like structure previously reported in *Hubert et al.* (1997) is completely inconclusive.

Chemical interaction and phase transformations in the B–BN system at pressures up to 5.3 GPa and temperatures up to 2,800 K have been *in situ* studied by x-ray diffraction with synchrotron radiation in MAX80 multianvil high-pressure apparatus at beamline F2.1, HASYLAB-DESY (*Kurakevych and Solozhenko*, 2007; *Solozhenko and Kurakevych*, 2008, 2009). New rhombohedral boron subnitride $B_{13}N_2$ has been synthesized by crystallization from the B-BN melt at 5 GPa. The new phase has been studied by x-ray powder diffraction (conventional and with synchrotron radiation), Raman spectroscopy, high-resolution transmission electron microscopy and electron energy loss spectroscopy. The structure of $B_{13}N_2$ belongs to the *R*-3*m* space group [a = 5.4585(8) Å, c = 12.253(2) Å] and represents a new structural type produced by the distorted B_{12} icosahedra linked together by N–B–N chains and inter-icosahedral B–B bonds (*Kurakevych and Solozhenko*, 2007). The Raman data (*Solozhenko and Kurakevych*, 2008, 2009) are consistent with a fact that the subnitride belongs to a group of boron-rich compounds with structures related to α-rhombohedral boron. The subnitride is an individual compound and not a solid solution, in contrast to boron carbide. The reliable composition of the phase obtained by the refinement of the starting B_4C-like unit cell makes $B_{13}N_2$ (*Kurakevych and Solozhenko*, 2007). The site occupancies of atoms of each type are close to unit, so the synthesized $B_{13}N_2$ phase is stoichiometric. Besides, the formation of two other boron-rich B-N phases denoted as "B_6N" and "$B_{50}N_2$" has been observed (*Solozhenko and Kurakevych*, 2008, 2009). Their structures seem to be much more sophisticated and have not been resolved to present time.

The 300-K equation of state of $B_{13}N_2$ has been measured up to 30 GPa in a Ne pressure medium using a diamond anvil cell and angle-dispersive x-ray diffraction with synchrotron radiation at beamline ID27, ESRF (*Solozhenko and Kurakevych*, 2008, 2009). The value of bulk modulus, B_0 = 200(15) GPa, has been estimated by plotting the normalized pressure versus the Eulerian strain (the B_0' value was fixed to 4).

According to our predictions made in the framework of thermodynamic model of hardness (*Mukhanov et al.*, 2008a, b), the $B_{13}N_2$ subnitride is expected to exhibit extreme hardness of 40 GPa comparable to that of commercial polycrystalline cubic boron nitride.

3.3. SYNTHESIS OF AGGREGATED BORON NITRIDE NANOCOMPOSITES

Unique superhard aggregated boron nitride nanocomposites (ABNNCs) showing the enhancement of hardness up to 100% in comparison with single-crystal cBN have been synthesized by solid-state phase conversion of pyrolytic graphite-like boron nitride at 20 GPa and temperatures of about 1,900 K using a two-stage 6-8 type multianvil system with a Zwick 5,000-ton press at Bayerisches Geoinstitut (*Dubrovinskaya et al.*, 2007). Decrease of the grain size down to 14 nm and simultaneous formation of the two dense BN phases with hexagonal (wBN) and cubic (cBN) structures within the grains at nano- and subnano-level result in enormous mechanical properties enhancement with maximum hardness of 85(5) GPa. The two-time increase of hardness of ABNNC with respect to conventional polycrystalline cBN ($H_V \sim 40$ GPa) can be explained as a result of unique combination of two factors; i.e. (1) nanosize effect, which restricts dislocation propagation through the material, and (2) two-phase composition on nano- and subnanometer scale, which, due to the quantum confinement, should increases hardness of individual crystallites.

Thus, ABNNC is the first non-carbon based bulk material with the value of hardness approaching that of single-crystal diamond. ABNNC has also an unusually high for superhard materials fracture toughness ($K_{Ic} = 15$ MPa $m^{0.5}$) and wear resistance ($W_H = 11$) making it a promising superabrasive. However, low thermal stability of wBN results in relatively low thermal stability of the whole material.

4. Synthesis of Novel Superhard Phases of Pure Elements

4.1. SYNTHESIS OF NANOSTRUCTURED CARBON WITH 'IDEAL' HARDNESS

Phase transformations of fullerite C_{60} at pressures up to 2 GPa and temperatures up to 1,600 K have been studied using quenching experiments in a large-volume piston-cylinder high-pressure apparatus (*Brazhkin et al.*, 2007). New bulk carbon nanomaterial has been synthesized at moderate (0.1–1.5 GPa) pressures. Its structure and properties have been comprehensively studied and it was found that the material is characterized by very high (90%) elastic recovery, fairly high hardness $H \approx 15$ GPa and record values of the

hardness-to-Young-modulus ratio $H/E \approx 0.22$. The observed hardness is close to the 'ideal' limit, which is evidently associated with the nanostructure of the materials that is represented by combination of interlinked curved fragments of C_{60} molecules and nanographite nuclei.

4.2. SYNTHESIS OF NEW BORON PHASE, ORTHORHOMBIC γ-B_{28}

Among the 16 polymorphic modifications of boron mentioned in the literature, only three phases seem to correspond to the pure element, namely, α-B_{12} rhombohedral low-temperature, β-B_{106} rhombohedral high-temperature low-pressure, and t-B_{192} tetragonal high-temperature phases. Very recently, a new high-pressure phase of boron, orthorhombic γ-B_{28}, has been synthesized from highly crystalline β-B_{106} (99.995 at.%) in a multianvil press at pressures from 12 to 20 GPa and temperatures from 1,800 to 2,000 K, and the structure of this phase has been established by *ab initio* calculations and powder x-ray diffraction (*Oganov et al.*, 2009).

Bulk polycrystalline samples of γ-B_{28} have Vickers hardness of 50(11) GPa (*Solozhenko et al.*, 2008), which is markedly higher than the hardness of other boron polymorphs and agrees well with the value of 48.8 GPa that was calculated within the thermodynamic model of hardness (*Mukhanov et al.*, 2008a, b). Thus, new high-pressure phase γ-B_{28} has the highest hardness among the known boron crystalline modifications, which originates from its highest density (2.544 g/cm^3).

Equation of state of γ-B_{28} has been measured in the Ne pressure medium up to 65 GPa at room temperature using a diamond anvil cell and x-ray powder diffraction with synchrotron radiation at beamline ID27, ESRF (*Le Godec et al.*, 2009). A fit of the experimental *p–V* data to the Vinet equation of state yields the values of the bulk modulus, B_0, of 237(5) GPa with the pressure derivative $B_0' = 2.7(3)$ i.e. γ-B_{28} is the least compressible form of elemental boron.

5. Conclusions

All the given examples demonstrate the possibility of synthesis of novel superhard phases using modern high-pressure tools (DAC, multianvil press and shock compression), and the complete recovery of the synthesized products to the ambient conditions, for eventual development as new technological materials.

References

Brazhkin, V.V., Solozhenko, V.L., Bugakov, V.I., Dub, S.N., Kurakevych, O.O., Kondrin, M.V., and Lyapin, A.G., (2007), Bulk nanostructured carbon phases prepared from C_{60}: approaching the 'ideal' hardness, *J. Phys.: Cond. Mat.* 19(23), 236209.

Dubrovinskaya, N., Solozhenko, V.L., Miyajima, N., Dmitriev, V., Kurakevych, O.O., and Dubrovinsky, L., (2007), Superhard nanocomposite of dense polymorphs of boron nitride: Noncarbon material has reached diamond hardness, *Appl. Phys. Lett.* 90(10), 101912.

Hubble, H.W., Kudryashov, I., Solozhenko, V.L., Zinin, P.V., Sharma, S.K., and Ming, L.C., (2004), Raman studies of cubic BC_2N, a new superhard phase, *J. Raman Spectr.* 35(10), 822–825.

Hubert, H., Garvie, L.A.J., Buseck, P.R., Petuskey, W.T., and McMillan, P.F., (1997), High-pressure, high-temperature syntheses in the B–C–N–O system, *J. Solid State Chem.* 133, 356–364.

Kurakevych, O.O., and Solozhenko, V.L., (2007), Rhombohedral boron subnitride, $B_{13}N_2$, by x-ray powder diffraction, *Acta Crystallogr. C* 63(9), i80–i82.

Kurdyumov, A.V., Solozhenko, V.L., Hubaček, M., Borimchuk, N.I., Zelyavskii, W.B., Ostrovskaya, N.F., and Yarosh, V.V., (2000), Shock synthesis of ternary diamond-like phases in the B-C-N system, *Powder Metall. Metal Ceram.* 39(9/100), 467–473.

Langenhorst, F., and Solozhenko, V.L., (2002), ATEM-EELS study of new diamond-like phases of the B-C-N system, *Phys. Chem. Chem. Phys.* 4, 5183–5188.

Le Godec, Y., Kurakevych, O.O., Munsch, P., Garbarino, G., and Solozhenko, V.L., (2009), Equation of state of orthorhombic boron, γ-B_{28}. *Solid State Comm*. 149(33–34), 1356–1358.

Mukhanov, V.A., Kurakevych, O.O., and Solozhenko, V.L., (2008a), Thermodynamic aspects of materials' hardness: prediction of novel superhard high-pressure phases, *High Press. Res.* 28(4), 531–537.

Mukhanov, V.A., Kurakevych, O.O., and Solozhenko, V.L., (2008b), The interrelation between hardness and compressibility of substances and their structure and thermodynamic properties, *J. Superhard Mater.* 30(6), 368–378.

Oganov, A.R., Chen, J., Gatti,C., Ma, Y., Ma, Y., Glass, C.W., Liu, Z., Yu, T., Kurakevych, O.O., and Solozhenko, V.L., (2009), Ionic high-pressure form of elemental boron, *Nature* 457(7231), 863–867.

Solozhenko, V.L., (2002), Synthesis of novel superhard phases in the B-C-N system, *High Press. Res.* 22, 519–524.

Solozhenko, V.L., Andrault, D., Fiquet, G., Mezouar, M., and Rubie, D.C., (2001a), Synthesis of superhard cubic BC_2N, *Appl. Phys. Lett.* 78, 1385–1387.

Solozhenko, V.L., Dub, S.N., and Novikov, N.V., (2001b), Mechanical properties of cubic BC_2N, a new superhard phase, *Diamond Relat. Mater.* 10, 2228–2231.

Solozhenko, V.L., and Kurakevych, O.O., (2008), New boron subnitride $B_{13}N_2$: HP-HT synthesis, structure and equation of state, *J. Phys.: Conf. Ser.* 121, 062001.

Solozhenko, V.L., and Kurakevych, O.O., (2009), Chemical interaction in the B–BN system at high pressures and temperatures. Synthesis of novel boron subnitrides, *J. Solid State Chem.* doi: 10.1016/j.jssc.2009.03.003.

Solozhenko, V.L., Le Godec, Y., and Kurakevych, O.O., (2006), Solid-state synthesis of boron subnitride, B_6N: myth or reality?, *Compt. Rend. Chimie* 9(11–12), 1472–1475.

Solozhenko, V.L., Kurakevych, O.O., Andrault, D., Mezouar, M., and Le Godec, Y. (2007), Patent FR 0702637 Carbure de bore et son procédé de fabrication. – 11/04/2007.

Solozhenko, V.L., Kurakevych, O.O., and Oganov, A.R., (2008), On the hardness of a new boron phase, orthorhombic γ-B_{28}, *J. Superhard Mater.* 30(6), 428–429.

Solozhenko, V.L., Kurakevych, O.O., Andrault, D., Le Godec, Y., and Mezouar, M., (2009), Ultimate metastable solubility of boron in diamond: Synthesis of superhard diamondlike BC_5, *Phys. Rev. Lett.* 102(1), 015506.

Tkachev, S.N., Solozhenko, V.L., Zinin, P.V., Manghnani, M.H. and Ming L.C., (2003), Elastic moduli of the superhard cubic BC_2N phase by Brillouin scattering, *Phys. Rev. B* 68(5), 052104.

Zinin, P.V., Solozhenko, V.L., Malkin, A.J., and Ming, L.C., (2005), Atomic force microscopy studies of cubic BC_2N, a new superhard phase, *J. Mater. Sci.* 40(11), 3009–3011.

SYNTHESIS AND STRUCTURE–PROPERTY RELATIONS OF BINARY TRANSITION METAL CARBIDES AT EXTREME CONDITIONS

B. WINKLER*, A. FRIEDRICH, L. BAYARJARGAL, E.A. JUAREZ-ARELLANO†
Abt. Kristallographie, Inst. f. Geowissenschaften, Goethe University, Altenhoeferallee 1, D-60438 Frankfurt am Main, Germany

Abstract The synthesis of binary transition metal carbides in laser heated diamond anvil cells is discussed. The use of density functional theory calculations to determine structure–property relations is described.

Keywords: Binary transition metal carbides, laser-heated DAC, density functional theory calculations

1. Introduction to Transition Metal Carbides

The carbides of group IV (Ti, Zr, Hf) and group V (V, Nb, Ta) elements have metal-like properties, such as a high thermal and electrical conductivity, they are opaque and have a metallic luster. However, they also have ceramic like properties, such as high melting points, high hardness and large bulk moduli. This combination of properties makes them interesting candidate materials for applications such as coatings and diffusion barriers. Hence, their structure–property relations have been studied extensively, both experimentally and theoretically (*Pierson,* 1996).

These carbides are often termed "interstitial" carbides, as they often show variable stoichiometries which can be described as being due to the insertion of carbon into a sublattice formed by the metal atoms. Most binary transition metal carbides of group IV and V with a carbon:metal ratio of 1:1

* b.winkler@kristall.uni-frankfurt.de
† Now at: CIICAp – UAEM, Av. Universidad 1001, Col. Champila, Cuernavaca, Morelos, Mexico

E. Boldyreva and P. Dera (eds.), *High-Pressure Crystallography: From Fundamental Phenomena to Technological Applications*, DOI 10.1007/978-90-481-9258-8_32,

crystallizes in the NaCl-structure type. Another often encountered structure type is the WC structure (Figure 1).

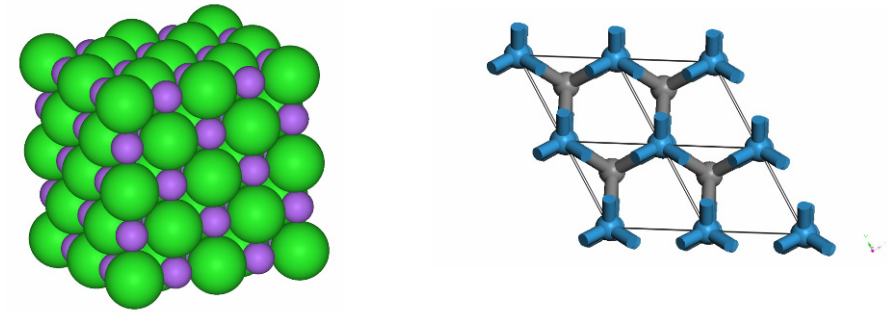

Figure 1. Many binary transition metal carbides crystallize in the NaCl-structure type (*left*). Others, such as MoC and WC crystallize in the WC-structure type (*right*).

The main properties of transition metal carbides of groups IV, V and VI are listed in Table 1. From this table, several common properties and trends can be derived. The ratio of the radius of the carbon atom to that of the metal atom is <0.59, and hence carbon atoms can be incorporated into the interstices formed by a close packing of the metal atoms. The difference in the electronegativities of the carbon and the metal are close to 1.0, and hence the bonding is about 22% ionic (for comparison: in NaCl the difference in electronegativities is 2.2 and the bonding is 67% ionic). In the group IV metal carbides, the melting point of the carbide is nearly twice as high as that of the metal, in the group V metal carbides it is about 1.5 times higher, and in the group VI metal carbides the metals actually have a slightly higher melting temperature than the carbides.

In summary, the fundamental aspects of structure–property relations in binary transition metal carbides of group V and VI elements at ambient pressure are reasonably well understood. It is now of interest to explore their high pressure behavior and to determine, at which (P,T)-conditions carbides from comparatively inert elements, such as those from the platinum group, can be obtained. In a first study, *Ono et al.* (2005) successfully synthesized PtC at pressures above 60 GPa by laser-heating a mixture of the elements. PtC crystallized in the NaCl-structure type, with a lattice parameter of 4.814 Å. The phase was quenchable to ambient conditions.

TABLE 1. Properties of binary transition metal carbides (*Pierson*, 1996)

	Group IV	Group V	Group VI
Period 4	TiC	VC	Cr_3C_2
r_C/r_M	0.526	0.576	0.609
T_M metal [°C]	1660	1890	1865
T_M carbide [°C]	3067	2830	1810
Δ electroneg.	1.0	0.9	0.9
structure type	NaCl	NaCl	
Period 5	ZrC	NbC	β-Mo_2C
r_C/r_M	0.483	0.530	0.556
T_M metal [°C]	1850	1890	2620
T_M carbide [°C]	3420	2830	2520
Δ electroneg.	1.1	0.9	0.7
structure type	NaCl	NaCl	
Period 6	HfC	TaC	WC
r_C/r_M	0.486	0.529	0.553
T_M metal [°C]	2230	2996	3410
T_M carbide [°C]	3928	3950	2870
Δ electroneg.	1.2	1.0	0.8
structure type	NaCl	NaCl	WC

2. Experimental Approach

2.1. GENERAL CONSIDERATIONS

Investigations of the formation of transition metal carbides at high pressure and temperature commence from mixtures of the elements. While fine grained graphite is readily available and an obvious choice as a starting material, the metals are available as foils or powders. The former have the advantage that foils often already have an appropriate thickness. Also, some fine grained metal powders are highly flammable while foils often can be handled outside a glove box. From a practical point of view, it is easier to mix powders of graphite and metal and produce compact samples. There is,

however, clearly a need for new sample preparation techniques to be developed, such as depositing a thick carbon film on a metal foil.

2.2. LASER-HEATED DIAMOND ANVIL CELL EXPERIMENTS

Laser heating of mixtures of graphite and metal is comparatively easy, as both materials absorb radiation over a very wide range of energies. Hence, in contrast to experiments with transparent samples, there is no need to use lasers emitting long wave length radiation, such as CO_2 lasers, but instead the more common Nd:YAG or Nd:YLF lasers can be employed. The sample must be thermally insulated from the diamonds. This can be achieved by either placing a compacted sample on a few grains of material or coating the diamonds, e.g. with NaCl, which can then serve as a pressure medium as well. Due to the strong absorption of the laser radiation by the opaque samples, only moderate laser power (<20 W) is required to achieve bright hot spots. Double sided laser heating is now acknowledged as a prerequisite to minimize thermal gradients.

In situ observations of the reaction require the use of an appropriate experimental facility at a synchrotron. One such station is available at the Advanced Light Source, ALS (Berkeley), where double sided laser heating can be performed at beam line 12.2.2 with fiber lasers. The experimental capabilities are described in detail in *Caldwell et al.* (2007). A number of other experimental stations are available at e.g. the ESRF, the APS and SPring-8. Typically, either image plates or CCDs are employed as detectors.

Depending on the beam line, pressures are determined with either on-line or off-line spectrometers using the ruby fluorescence method and/or from the known equation of state of the pressure transmitting medium, such as NaCl or Ar. Pressures determined independently by ruby fluorescence and an internal standard will typically agree to within 1–2 GPa.

3. Computational Approaches

Density functional theory is currently the method of choice for the calculation of structure–property relations of crystalline materials. As will be discussed in other contributions to this conference, the prediction of unknown phases is a major challenge. For known structures, however, calculations of properties such as the bulk modulus are often straightforward with established packages such as ABINIT, PWSCF, CASTEP or similar codes. Employing codes using plane waves as a basis set in conjunction with pseudopotentials is relatively straightforward, as the numerical convergence only depends on two parameters (*k*-space sampling and number of plane waves) and the error due to the

pseudopotential can be tested by calculating known properties of a range of related structures. The inaccuracies introduced by using one of the approximations for the exchange-correlation energies (e.g. the local density approximation, the generalized gradient approximation or a hybrid functional such as B3LYP) are well controlled. Lattice parameters will generally differ from experimental values by not more than 1–3%, elastic stiffness coefficients of incompressible structures are reproduced to a few GPa, computed band gaps generally have substantial error, while phonon frequencies are correct to within a few cm^{-1}. The application of DFT-based methods to correlated systems, including many iron-containing compounds often requires the use of techniques beyond "standard" DFT, such as LDA/GGA+U. An introduction to DFT calculations is given by *Martin* (2004).

The structural complexity of idealized transition metal carbides is limited, and hence there are very many computational studies aimed at predicting and elucidating the behavior of transition metal carbides at high pressure or investigating the elastic stiffness coefficients (e.g. *Hugosson et al*., 2001; *Lopez de La Torre et al*., 2005)

4. Examples

4.1. TITANIUM CARBIDE

TiC is a typical representative of an interstitial transition metal carbide. Cubic δ-TiC crystallizes in the NaCl-structure type, with space group $Fm\bar{3}m$, and a lattice parameter of $a = 4.327(4)$ Å at ambient conditions. Similarly to most carbides, the structure can accommodate a large concentration of defects on the 'interstitial' carbon positions, leading to substoichiometric TiC_x, with $1 > x > 0.5$. Lattice parameters and physical properties depend on the defect concentration. For example, the lattice parameter for a highly carbon deficient $TiC_{0.5}$ $a = 4.30$ Å (*Pierson,* 1996). Possible ordering schemes of the defects have been discussed in the literature (*Tashmetov et al*., 2002). In a recent in situ neutron scattering study by *Winkler et al.* (2007) only the cubic δ-phase was observed.

The synthesis of TiC at ambient pressure has been studied with various methods (see summary in *Winkler et al*., 2007) and the physical properties of TiC at ambient pressure have been extensively documented (*Pierson*, 1996). An initial study of the high pressure behaviour of TiC has been presented by *Dubrovinskaia et al.* (1999). In that study, a cubic to rhombohedral phase transition was found to occur at around 18 GPa. This was deduced from the observation of a splitting of the cubic (111) reflection. At 1 bar, the (111)-reflection had a FWHM of about 0.03 Å, while the reflection broadens to >0.1 Å at 38 GPa. CsI was employed as a pressure-transmitting medium up

to 18 GPa, while no pressure-transmitting medium was used at higher pressures. Diffractograms were collected with an in-house CCD camera mounted on a rotating anode generator. DFT model calculations, based on the FPLMTO method, were presented by *Dubrovinskaia et al.* (1999) to support their findings, as these calculations showed a lowering of the total energy by a rhombohedral distortion on compression.

In a more recent study (*Winkler et al*., 2008), we investigated the proposed splitting of the cubic (111) and (222) reflections with a higher resolution than was available in the earlier study. We obtained diffraction patterns at higher pressures on heated and annealed samples. After pressurizing the sample to 25 GPa, but before laser heating, NaCl was present in the B1 structure type, ω-Ti and tungsten from the gasket were detectable. After laser heating, NaCl was present both in the B1 and B2 structure type, and the titanium had reacted with the graphite to cubic TiC. Annealing was achieved by scanning the sample from one side with low laser power. This greatly reduced residual strain induced by deviations from hydrostaticity. An enlargement of the regions around the cubic (222) reflections of TiC is shown before and after laser heating in Figure 2.

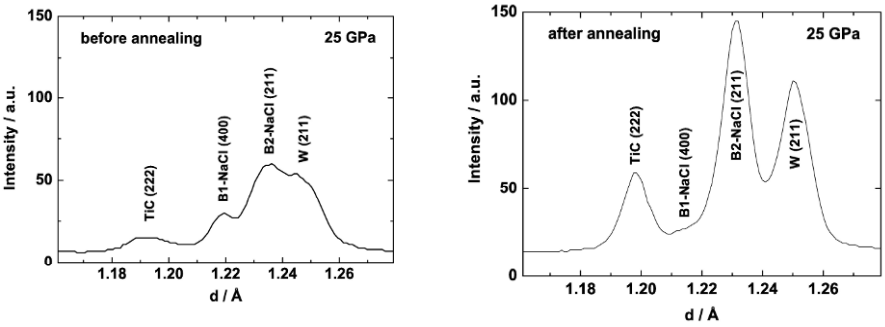

Figure 2. *Left*: Laser-heating a mixture of Ti and graphite, thermally insulated by NaCl, at 25 GPa leads to a mixture of TiC and NaCl, where the B1 and B2 polymorphs coexist at these conditions. *Right*: Annealing with low laser power yields an improved diffraction pattern with sharp reflections. The amount of the B1 polymorph of NaCl is significantly reduced.

The FWHM of the (111) and (222) reflections after annealing were ~0.03 Å, and hence no broadening was detectable. The (111) slightly overlaps with B1-type NaCl-(200), but the non-overlapping (222) also clearly shows no splitting. No further phases were observed on laser-heating at 25 GPa, either on regions of the sample which had been reacted before at lower pressures or on regions in which there was still titanium present. Hence we conclude that the stable carbide phase at these conditions is TiC and that the stability field of TiC extends to at least 2,000 K at 25 GPa.

The lattice parameter of the recovered TiC sample is a(TiC, 1 bar) = 4.3238(6) Å. Fully stoichiometric TiC has a lattice parameter of 4.327 Å and a carbon deficiency causes the lattice parameter to shrink down to 4.30 Å for $TiC_{0.5}$. Hence, the sample synthesized at high (P,T) conditions seems to be fully stoichiometric.

We have shown in an earlier paper (*Winkler et al*., 2007) that a DFT-based model using the generalised gradient approximation, a plane wave basis set and ultrasoft pseudopotentials satisfactorily reproduced structures and properties of titanium and TiC. A comparison with experimental data (*Dodd et al*., 2003) is shown in Table 2.

TABLE 2. Comparison of experimentally determined and computed structural and elastic properties of TiC. μ is the shear stiffness, (values for the Reuss and Voigt shear stiffness are essentially identical). E is Young's modulus, B is the bulk modulus. ν is Poisson's ratio.

	Experimental	Theoretical
a [Å]	4.324	4.333
B [GPa]	232–253	227(1)
μ [GPa]	164–190	168–169
E [GPa]	436–462	419.9
ν	0.17–0.25	0.19

We used commercial and academic versions of CASTEP (*Clark et al*., 2005) for a theoretical investigation of the proposed rhombohedral distortion. Concurrent geometry optimizations of the unit cell and internal co-ordinates were performed so that forces were converged to 0.005 eV/Å and stress residual to 0.005 GPa. Even for pressures as high as 40 GPa, the ground state structure remained cubic and a rhombohedral distortion was always unstable. Hence, the results obtained from experiments and model calculations in the more recent study indicate that TiC does not undergo a structural phase transition up to 25 GPa.

4.2. TANTALUM CARBIDE

The formation of tantalum carbide can be studied in a similar fashion to that of TiC (Figure 3).

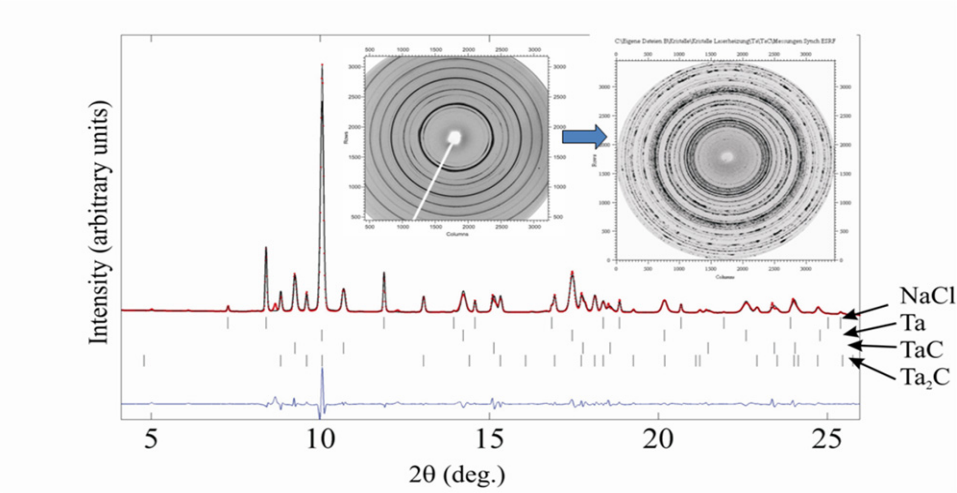

Figure 3. Synthesis of TaC and Ta_2C in a laser-heated diamond anvil cell at 11 GPa.

These reactions are exothermic and this can actually be observed in experiments. Figure 4 shows the measured temperature of the sample while the laser power is increased continuously. At a given (P,T) condition the reaction is triggered and the released heat can be observed. Such experiments can therefore be used to determine the pressure-dependence of the on-set of the reaction.

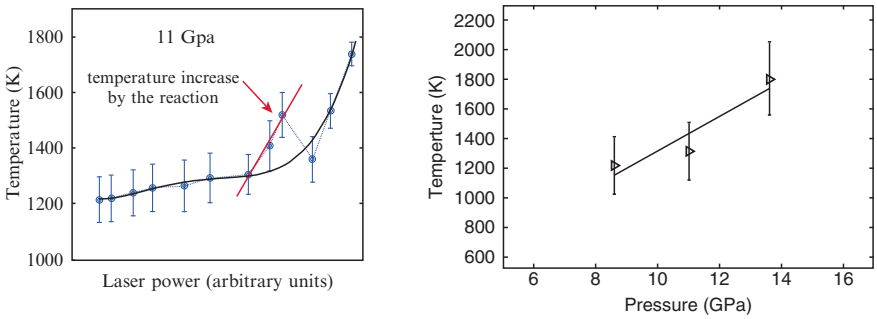

Figure 4. Determination of the pressure-dependence of the exothermic formation of TaC from the elements.

4.3. RHENIUM CARBIDE

In two recent studies (*Juarez-Arellano et al.*, 2008, 2009), we have shown that a rhenium carbide can be synthesized at high (P,T). The experiments again commenced from a mixture of the elements. A typical powder

diffraction pattern is shown in Figure 5. Indexing these patterns is not straightforward as two argon polymorphs coexisted at the synthesis conditions. However, as we were able to outline the (P,T) space in which the new phase was stable, multi-anvil cell experiments, performed by M. Koch-Müller at the GFZ in Potsdam, yielded enough sample to locate the rhenium atoms through a Rietveld refinement. However, it was impossible to locate the light carbon atoms by the Rietveld refinement. Hence, DFT based calculations were used to calculate the relative stabilities of compounds in which the available interstices were filled with carbon atoms. This allowed us to conclude that the new rhenium carbide had a composition Re_2C and is isostructural to MoS_2.

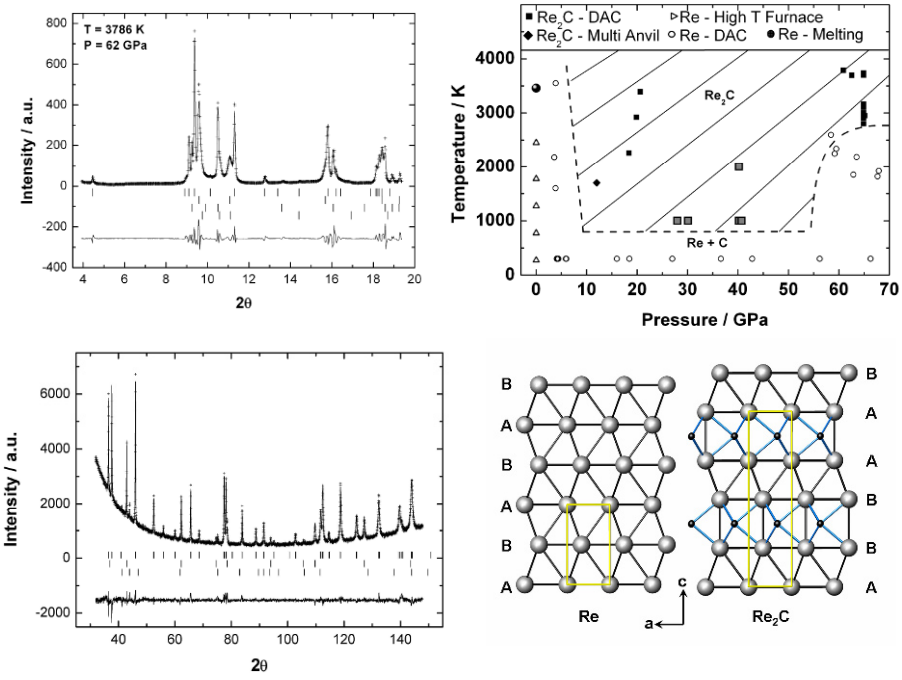

Figure 5. Top left: Powder diffraction pattern of the reacted sample in a DAC at high (P,T). *Top right*: (P,T)-field in which Re_2C can be synthesized. *Lower left*: Powder diffraction pattern and Rietveld refinement of sample synthesized in a multi anvil press. *Lower right*: Structures of Re and Re_2C.

5. Conclusions

The synthesis of binary transition metal carbides from the elements in laser-heated diamond anvil cells offers a route to new compounds with potentially interesting properties. Such experiments may need to be complemented

with model calculations in order to clarify the location of the light carbon atoms when unknown structure types are synthesized. Work aimed at synthesizing further compounds, especially from the period 6 elements, is currently being done.

ACKNOWLEDGEMENT

We are grateful to Monika Koch-Müller at the GFZ Potsdam for performing multi-anvil cell based synthesis, and to Miguel-Avalos-Borja for TEM measurements. Beam time has been provided by the ALS (Berkeley, USA), the ESRF (Grenoble, France) and LANSCE (Los Alamos, USA) and we are grateful for the assistance of the beam line scientists (Simon Clark, Mohamed Mezouar, and Sven Vogel, respectively). The studies have been funded by the DFG (projects Wi1232 within the SPP 1236), the DAAD, and the BMBF.

References

Caldwell, W., Kunz, M., Celestre, R., Domning, E.E., Walter, M.J., Walker, D., Glossinger, J., MacDowell, A.A., Padmore, H.A., Jeanloz, R., and Clark, S.M., (2007), *Nuclear Instruments and Methods in Physics Research*, A 582, 221–225.

Clark, S.J., Segall, M.D., Pickard, C.J., Hasnip, P.J., Probert, M.J., Refson, K., and Payne, M.C., (2005), *Zeitschrift für Kristallographie*, 220, 567–570.

Dodd, S.P., Cankurtaran, M., James, B., (2003), *Journal of Material Science*, 38, 1107–1115.

Dubrovinskaia, N.A., Dubrovinsky, L.S., Saxena, S.K., Ahuja, R., and Johansson, B. (1999), *Journal of Alloys and Compounds,* 289, 24–27.

Hugosson, H.W., Jansson, U., Johansson, B., and Eriksson, O., (2001), *Chemical Physics Letters*, 333, 444–450.

Juarez-Arellano, E.A., Winkler, B., Friedrich, A., Wilson, D.J., Koch-Müller, M., Knorr, K., Vogel, S.C., Wall, J.J., Reiche, H., Crichton, W., Ortega-Aviles, M., and Avalos-Borja, M., (2008), *Zeitschrift für Kristallographie*, 223, 492–501.

Juarez-Arellano, E.A., Winkler, B., Friedrich, A., Bayarjargal, L., Milman, V., Yan, J., and Clark, S.M., (2009), *Journal of Alloys and Compounds*, 481, 577–581.

Lopez de la Torre, L., Winkler, B., Schreuer, J., Knorr, K., and Avalos-Borja, M., (2005), *Solid State Communications*, 134, 245–250.

Martin, R.M., (2004), Electronic Structure: Basic Theory and Methods. Cambridge University Press, Cambridge.

Ono, S., Kikegawa, T., and Ohishi, Y., (2005), A high pressure and high temperature synthesis of platinum carbide, *Solid State Communications*, 133, 55–59.

Pierson, H.O., 1996, Handbook of Refractory Carbides. Noyes Publication, Westwood, NJ.

Tashmetov, M.Y., Em, V.T., Lee, C.H., Shim, H.S., Choi, Y.N., and Lee, J.S., 2002, *Physica B*, 311, 318–325.

Winkler, B., Wilson, D.J., Vogel, S.C., Brown, D.W., Sisneros, T.A., and Milman, V., 2007, *Journal of Alloys and Compounds*, 441, 374–380.

Winkler, B., Juarez-Arellano, E.A., Friedrich, A., Bayarjargal, L., Yan, J., and Clark, S.M., 2009, *Journal of Alloys and Compounds*, 478, 392–397.

HIGH PRESSURE AND SUPERCONDUCTIVITY: INTERCALATED GRAPHITE CaC_6 AS A MODEL SYSTEM

A. GAUZZI[1*], N. BENDIAB[1], M. D'ASTUTO[1], B. CANNY[1], M. CALANDRA[1], F. MAURI[1], G. LOUPIAS[1], S. TAKASHIMA[2], H. TAKAGI[2], N. TAKESHITA[3], C. TERAKURA[3], N. EMERY[4], C. HEROLD[4], PH. LAGRANGE[4], M. HANFLAND[5], M. MEZOUAR[5]

[1]*Institut de Minéralogie et de Physique des Milieux Condensés, Université Pierre et Marie Curie and CNRS, Paris, France*

[2]*Department of Advanced Materials Science, Tokyo University, Japan,* [3]*CERC, National Institute of Advanced Industrial Science and Technology (AIST), Tsukuba, Japan*

[4]*Laboratoire de Chimie du Solide Minéral-UMR 7555, Université Henri Poincaré Nancy I, France*, [5]*European Synchrotron Radiation Facility*

Abstract Superconducting CaC_6 is found to exhibit two important pressure effects: (i) a large *P*-induced T_c enhancement up to 15.1 K at 7.5 GPa, the highest T_c value hitherto reported for graphite intercalated compounds; and (ii) a dramatic T_c drop down to ~3 K at a critical pressure of ~9 GPa suggestive of a structural instability. We show that a combined electrical resistivity and x-ray diffraction study under high pressures provides a comprehensive account of both phenomena within the frame of the BCS theory in terms of a *P*-induced softening of the in-plane Ca mode relevant to the electron–phonon coupling. Our data analysis indicates that, below ~8 GPa, the softening contributes to the T_c enhancement whilst, at higher pressures, it drives the system to a disordered phase presumably characterized by a disordering of the Ca sublattice. Thus, pressure induces a simultaneous order-disorder and lattice-softening phase transition from a good metal phase with high T_c to a bad metal phase with low T_c.

[*]Address : 4, place Jussieu, 75005 Paris, France. E-mail: andrea.gauzzi@upmc.fr

E. Boldyreva and P. Dera (eds.), *High-Pressure Crystallography: From Fundamental Phenomena to Technological Applications*, DOI 10.1007/978-90-481-9258-8_33,

Keywords: Superconductivity, high pressure, graphite intercalated compounds, lattice instability, order-disorder phase transitions

1. Introduction

The recently developed capabilities offered by high-pressure techniques and *ab initio* calculations have lead to important new results in the field of superconductivity (SC). Notable are the discovery of pressure-induced SC in an increasingly large number of simple elements, such as Li (*Shimizu et al*., 2002) and the non-magnetic hexagonal ε-phase of Fe (*Shimizu et al*., 2001), or the prediction of high critical temperatures, $T_c \geq 100$ K, in the hypothetical metallic phase of hydrogen that is expected to be stable at very high pressures, $P \geq 400$ GPa (*Ashcroft*, 1968; *Babaev et al*., 2005). These results may have far-reaching consequences in a variety of fields ranging from cosmology to planetary sciences and materials physics.

For the purpose of the present lecture notes, we restrict ourselves to the effect of pressure-induced enhancement or suppression of superconductivity in conventional Bardeen–Cooper–Schrieffer (BCS) superconductors. We show that this effect may unveil the pairing mechanism and the factors limiting the T_c. As a model system, we focus on the graphite intercalated compound (GIC) CaC_6, which has attracted a great deal of interest owing to the relatively high $T_c = 11.5$ K (*Emery et al*., 2005; *Weller et al*., 2005), as compared to other GICs (*Jishi and Dresselhaus*, 1992). We find that, in this system, a comprehensive description of the effects of pressure on the SC state is achieved within the frame of the BCS theory based on the conventional electron–phonon (e-ph) pairing mechanism. One advantage of the present study as well as of other studies on BCS superconductors is the employment of powerful *ab initio* computational methods like the *Superconducting Density Functional Theory* (SCDFT) (*Lüders et al*., 2005; *Marques et al*., 2005), which enables the reliable *ab initio* computation of all BCS parameters in relatively simple compounds, such as elemental metals (*Marques et al*., 2005; *Profeta et al*., 2006).

In these notes, we shall omit those aspects related to high-pressure studies on superconductors that are complex or controversial. Examples of such advanced topics are the following: (1) The large T_c enhancement under high pressure in some cuprate superconductors, which has lead to the record T_c value of 160 K reported in $HgBa_2Ca_2Cu_3O_8$ (*Gao et al.,* 1994); (2) The competition between superconductivity and other ground states, such as charge and spin density waves (CDW, SDW), in organic compounds (*Jérome,* 1990) and dichalcogenides (*Akrap et al*., 2008, *Morosan et al*., 2006); (3) The use of pressure as a probe of the pairing mechanism in unconventional superconductors, such as the recently discovered Fe-based pnictides (see e.g. *Chen et al.,* 2008; or *Torikachvili et al*., 2008, and refs therein).

Given the tutorial purpose of the present notes, only the main aspects pertaining to the effects of pressure on the structural and superconducting properties of CaC_6 are treated here. The reader is referred to the specialized literature cited in the bibliography section for more details.

2. Transport and Superconducting Properties of CaC_6 at $P = 1$ atm

Graphite intercalated compounds (GICs) (*Dresselhaus and Dresselhaus*, 1981) are interesting since intercalation radically alters the electronic properties of pristine graphite. Depending on the position of the intercalant atom within the van der Waals gap between adjacent graphene layers and on the intercalant concentration, different crystal structures are formed (*Dresselhaus and Dresselhaus*, 1981). For example, the rhombohedral $R\bar{3}m$ structure of CaC_6 (*Emery et al*., 2005) results from the so called $\alpha\beta\gamma$ stacking sequence shown in Figure 1. In the past, intensive efforts were devoted to the search for new superconductors following the hypothesis that the layered structure of GICs may host excitonic superconductivity, according to the idea proposed by *Little* (1964). However, after the first reports on SC GICs in 1965 (*Hannay et al*., 1965), only low T_c values ≤ 5 K have been hitherto reported (*Jishi and Dresselhaus*, 1992). A breakthrough came with the discovery that CaC_6 is superconducting with T_c = 11.5 K (*Emery et al*., 2005; *Weller et al*., 2005), which raised the question of the origin of such unusually high T_c for GICs and stimulated the search of GICs with even higher T_c. For CaC_6, penetration depth measurements (*Lamura et al*., 2006) and *ab initio* calculations (*Calandra and Mauri*, 2005, 2006; *Mazin*, 2005) point at a conventional BCS scenario with an e-ph coupling constant $\lambda \sim 0.83$ and an *s*-wave gap, Δ, with $2\,\Delta/T_c \sim 3.6$. The calculations indicate that Ca intercalation strongly alters the band structure and the phonon modes relevant to λ, contrary to simple rigid band filling.

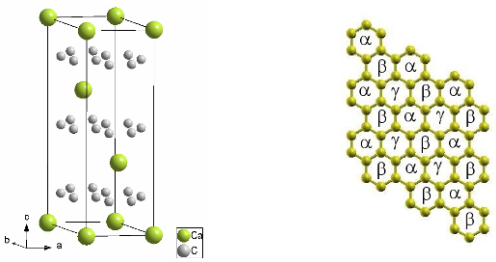

Figure 1. Left: hexagonal cell of $R\bar{3}m$ CaC_6 (*Emery et al*., 2005). The volume of this cell is three times larger than that of the primitive cell, which enables a better visualization of the stacking of the Ca and C layers along the *c*-axis. Right: labeling of intercalant positions. The $R\bar{3}m$ structure of CaC_6 corresponds to the $\alpha\beta\gamma$ stacking sequence.

In order to verify the possibility of raising T_c and to study the role of Ca phonons in the transport and SC properties of CaC_6, we studied the T-dependence of resistivity, $\rho(T)$, of high-quality bulk CaC_6 samples at ambient and high pressure up to 16 GPa. To our knowledge, this is the first study of transport properties on CaC_6. We reproducibly measured three bulk samples of ~1 mm size prepared from oriented pyrolithic graphite (*Emery et al*., 2005) using a dc method in a four-probe bar configuration. Owing to the sample shape and orientation, the in-plane ρ was measured. The ambient pressure results (see also *Gauzzi et al*., 2007) yield low values of room temperature and residual resistivities, $\rho_{300\ K} = 46\ \mu\Omega$ cm and $\rho_0 = 0.8\ \mu\Omega$ cm, respectively, and a large residual resistivity ratio, $RRR = \rho_{300\ K}/\rho_0 = 58$. The T-dependence gradually approaches a linear behavior at high T. This dependence is very different from that of graphite, although the $\rho_{300\ K}$ value is similar (*Klein et al*., 1962; *Primak and Fuchs*, 1954). First, in graphite, RRR is much smaller and ~15 even in best quality samples (*Primak and Fuchs*, 1954; *Soule*, 1958). Second, the T-dependence displays a downward curvature with a characteristic knee at ~140 K. The behavior of CaC_6 is different from that of other GICs as well. K-intercalated compounds display much lower ρ_{300K} ~10 $\mu\Omega$ cm and a sizeable T^2 component (*Potter et al*., 1981). These features indicate that Ca intercalation significantly alters the charge transport in the graphene layers and it does so in a different way as compared to other intercalants. The $\rho(T)$ behavior is consistent with the fact that graphite and other GICs are non superconducting or have much lower T_c. The large RRR of CaC_6 suggests a sizable λ, as discussed below. The picture of nearly-free electrons with dominant e-ph scattering is confirmed by the following analysis of the $\rho(T)$ curve (*Gauzzi et al*., 2007). The curve was fitted using a generalized Bloch–Grüneisen formula (*Grimvall*, 1981) consisting of a discrete decomposition of the $\alpha^2F(\omega)$ Eliashberg function into dispersionless modes (*Lortz et al*., 2005). Two modes with $\omega_1 = 136 \pm 2$ K and $\omega_2 = 600 \pm 5$ K ($\hbar = 1$ and $k_B = 1$) are found to account for our data. Both phonon energies are in excellent agreement with the calculations of *Calandra and Mauri* (2005, 2006), which supports the validity of the present analysis. According to these calculations, the low- (high-) energy mode corresponds to an in-plane Ca (out-of-plane C) mode. The low ρ_0 and the absence of saturation of ρ at high T suggest a small amount of static disorder and a large mean free path, well beyond the Ioffe–Regel limit. We find onset and zero-resistance T_c values of 11.5 and 11.2 K respectively, in agreement with previous magnetization data (*Emery et al*., 2005). In summary, our analysis of the ambient pressure data within the Bloch–Grüneisen model, the agreement between the results of this analysis and the calculations of (*Calandra and Mauri*, 2005, 2006), give evidence of a sizable e-ph scattering associated

with both Ca- and C-modes. This further supports a conventional *s*-wave BCS picture evidenced by the penetration depth study of *Lamura et al.* (2006).

3. Effects of High Pressure on the Transport and Superconducting Properties of Bulk CaC_6

For the high-P measurement of $\rho(T)$, we used a cubic anvil press (*Mori et al*., 2004) enabling hydrostatic conditions up to 16 GPa and down to 2.5 K. The details of the experiment are reported elsewhere (*Gauzzi et al*., 2007). The main results are shown in Figure 2. Two distinct regimes below and above 8 GPa are found. In the former, T_c increases linearly with a large rate ~0.5 K/GPa, in agreement with magnetization data at low pressure (*Kim et al*., 2006; *Smith et al*., 2006), and reaches the maximum of 15.1 K at 7.5 GPa, the largest value hitherto reported for GICs. No discontinuity can be detected in the linear increase. This rules out staging or other transitions below 7.5 GPa, in contrast to superconducting GICs, such as KC_8, RbC_8 and $KHgC_4$, that exhibit an abrupt ~1 K T_c increase in the 1.5–2 GPa range attributed to structural instabilities (*Clarke and Uher*, 1984). One notes that pressure does not affect the qualitative features of the ambient pressure $\rho(T)$ curve. The behavior remains that of a conventional metal with a linear T-dependence at high T and low ρ_0. Note that ρ_0 rapidly increases with P and $\rho_{300\ K}$ and $\partial\rho/\partial T$ increase linearly with P. The above changes of T_c and of the T-dependence of ρ are intrinsic because the pristine T_c value, transition width and the overall T-dependence are recovered after depressurization (data not shown). Extrinsic effects, such as P-induced cracking, may only affect the T-independent contribution to ρ.

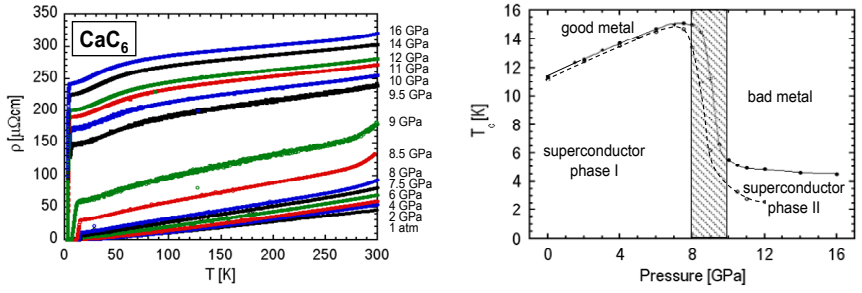

Figure 2. Left: Pressure-dependence of the in-plane ρ. Note the jump of ρ_0 accompanied by a T_c drop above 8 GPa. *Right*: Pressure dependence of T_c. The dashed area denotes the phase instability region. Lines are a guide to the eye. Full and open symbols and full and broken lines refer to onset and offset values, respectively. Different symbols refer to different samples (Data taken from *Gauzzi et al*., 2007).

In order to elucidate the origin of the above *P*-induced changes of T_c and $\rho(T)$, we applied the previous analysis of phonon modes to the data of Figure 2. The fit of the $\rho(T)$ curves up to 8 GPa confirms this softening and also confirms a hardening of the C mode (*Gauzzi et al*., 2007). Between 6 and 7.5 GPa, i.e. near the 8 GPa borderline separating the two transport regimes, both modes exhibit an anomaly. A large frequency jump of the C mode is found at 8 GPa. Thus, at higher *P*, this mode no longer contributes to ρ below 300 K and the Ca mode alone is sufficient to account for the 8.5 GPa data. Since λ scales as the inverse of the average square phonon frequency, the observed T_c enhancement is consistent with the Ca mode softening discussed previously. This argument further supports a BCS picture of e-ph-mediated pairing and the prominent role of Ca in the pairing.

4. High Pressure x-ray Diffraction Study of the Structural Instability

In this section, we address the question of the origin of the structural instability responsible for the large T_c drop and of the concomitant changes of transport properties at ~9 GPa reported above. In order to do this, we have studied the room temperature crystal structure of CaC_6 as a function of pressure from room pressure up to 13 GPa.

4.1. HIGH-PRESSURE X-RAY DIFFRACTION EXPERIMENT

The experiment was carried out at the high-*P* diffraction beamline ID9 of the ESRF. The details of the experiment are reported elsewhere (*Gauzzi et al*., 2008). In summary, a high-quality ~1 mm size bulk sample of CaC_6 was prepared from a platelet of highly oriented pyrolithic graphite, as described elsewhere (*Emery et al*., 2005). A few ~50–100 μm pieces were mounted in two diamond anvil cells (DAC) in the usual opposite anvil configuration. The cells were subsequently charged with high purity helium (sample n. 1) and argon (sample n. 2) used as pressure-transmitting media. The diffraction patterns were measured in the Debye–Scherrer geometry, using a wavelength $\lambda = 0.4133$ Å. For both samples, no significant amount of secondary phases was detected in the sample regions probed by the x-ray beam. In Figure 3, representative diffraction patterns taken on sample n. 1 are shown. The indexation shows that, despite the expected preferential orientation of the sample, reflections with various combinations of h, k and ℓ indices are present. This might be due to the folding of the CaC_6 flakes during sample manipulation. This enabled us to reliably refine the unit cell up to 13 GPa, as described in the next section.

4.2. EXPERIMENTAL AND THEORETICAL EQUATION OF STATE

All of the main Bragg peaks are found to match those of the trigonal $R\bar{3}m$ phase (*Emery et al.*, 2005). The indexation in Figure 3 corresponds to the equivalent hexagonal unit cell with a = 4.330 Å and c = 13.572 Å (*Emery et al.*, 2005) (see Figure 1). The additional features appearing above 9 GPa are discussed later. The result of the refinement and the equation of state are shown in Figure 4. Good refinements were obtained also using the data of samples n. 1 and n. 2 upon depressurization and pressurization, respectively. A comparison of these three data sets shows their reproducibility within the experimental error; no hysteresis was found after depressurization. From the refinement, one notes that both a and c parameters decrease linearly with pressure down to 9 GPa. In this range, a linear regression yields the following: $\partial a/\partial P$= –0.0038 Å/GPa; $\partial c/\partial P$= –0.081 Å/GPa. The c-axis compressibility turns out to be about 20 times larger than the in-plane one, as expected for a layered system. The corresponding compressibility is $\kappa = 1/V_{9\mathrm{GPa}}\partial V/\partial P$ = –0.0082 GPa^{-1}. The above values and the large anisotropy are consistent with previous studies on graphite (*Dresselhaus and Dresselhaus*, 1981) and graphite intercalated compounds with same composition and similar crystal structure, such as LiC_6 (*Clarke and Uher*, 1984). In order to study in detail the P-induced structural changes, the relaxed structure was calculated as a function of P up to 12 GPa using the ESPRESSO DFT code (*Baroni et al.*, 2001), as described elsewhere (*Calandra and Mauri*, 2005, 2006). The results are compared with the experimental data in Figure 4. For $P \leq 9$ GPa, it is noted a good agreement for both a and c parameters, except a slight overestimation of the former.

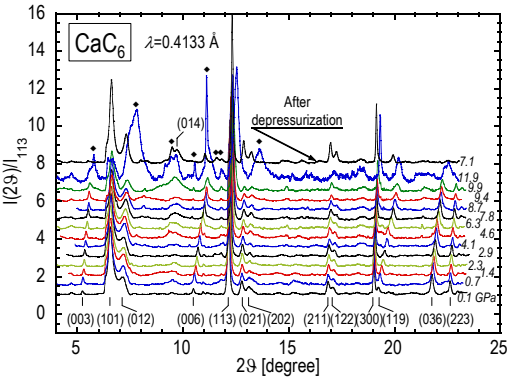

Figure 3. X-ray diffraction patterns of sample n. 1 at different pressures. Intensities are normalized to the maximum intensity of the (113) peak. Bragg indices refer to the hexagonal unit cell of Figure 1. Diamonds mark unindexed peaks and additional broad features appearing above 9 GPa (see text) (Data are taken from *Gauzzi et al.*, 2008).

Notable feature of Figure 4 is a kink at 9 GPa corresponding to a three-times increase of the compressibility, κ, evidencing a second-order phase transition. The kink leads to a discrepancy between experimental and calculated data in the ≥9 GPa range for, in this range, only calculations of volume optimization without structure relaxation were performed. A linear fit of the experimental data in the $P \geq 9$ GPa region yields $\kappa = 1/V_{9\text{GPa}}\partial V/\partial P = -0.0215$ GPa^{-1}, i.e. almost three times larger than in the $P \leq 9$ GPa region. We interpret the kink by noticing that no change of space group symmetry is seen in the diffraction patterns of Figure 3. Thus, the jump of κ suggests a structural change allowed by symmetry leading to a change of electronic structure. The only free parameter of the $R\bar{3}m$ structure is the in-plane x coordinate of the C atom in the hexagonal cell (*International Tables of Crystallography*, *Volume A: Space-group symmetry*, *Ed. T. Hahn*, *Springer Verlag*, *Heidelberg*, 2005). Taking into account the rigidity of the C layers within the plane, the only atomic displacement allowed by symmetry is the off-centering of the Ca atoms with respect to the C layers. At ambient pressure, the Ca atoms are centered with respect to these layers (x = 1/3), whilst the Ca position is (0,0,0) (*Calandra and Mauri*, 2005, 2006), but an off-center in-plane displacement of Ca requires a modest amount of energy due to the soft mode associated with this displacement (*Calandra and Mauri*, 2005, 2006; *Zhang et al*., 2006*)*. This scenario is supported by recent DFT studies at high pressure (*Csànyi et al*., 2007; *Li et al*., 2007).

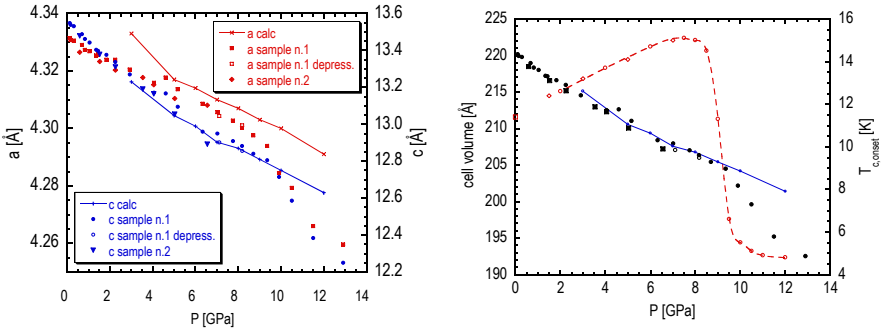

Figure 4. Left: experimental (symbols) and calculated (solid lines) *P*-dependence of the hexagonal *a* and *c* cell parameters. *Right*: *P*-dependence of the cell volume obtained from the data (symbols) and calculations (solid line) of the left panel. The T_c–P data of Figure 2 and (*Gauzzi et al*., 2007) are added to show, that the T_c drop coincides with the compressibility jump at 9 GPa. The broken line is a guide to the eye (Data from *Gauzzi et al*., 2008).

4.3. EVIDENCE OF *P*-INDUCED ORDER-DISORDER PHASE TRANSITION

The peak broadening concomitant to the kink at 9 GPa (see *Gauzzi et al*., 2008 for details) shows that the in-plane displacements of Ca atoms are disordered. This effect is intrinsic, as it turns out to be reversible upon

depressurization. We conclude, that at 9 GPa an order-disorder transition in the Ca sublattice occurs. This transition is explained by the enhanced softening of the in-plane Ca mode under high pressure (*Zhang et al*., 2006). Clearly, beyond a certain point, any in-plane position between adjacent layers would become energetically equivalent owing to the flattening of the potential. This disordering mechanism is consistent with the previous observation of anomalous hardening of the out-of-plane C mode and of bad metallic properties with high ρ_0 values and flat resistivity curves above 8 GPa (*Gauzzi et al*., 2007). *Mutatis mutandis*, an instability of the intercalant sublattice under high pressure was recently reported also in CsC_8 (*Rey et al*., 2008). In addition to the off-centering of the Ca atoms, previous *ab initio* studies (*Csànyi et al*., 2007; *Li et al*., 2007*)* also predict a *P*-induced buckling of the C layers, thus leading to a lowering of the crystal symmetry. Our data do not enable to verify this prediction, for this would require detecting weak extra peaks not visible in our diffraction patterns. Though, an insight into the high-*P* structure is gained by analyzing the new features appearing above 9 GPa, which are intrinsic, as they disappear upon depressurization. A large peak broadening is fully consistent with the above scenario of *P*-induced disorder. Our data also rule out the scenario of staging transitions reported in other GICs (*Fischer and Kim*, 1987).

5. Conclusions

In conclusion, superconducting CaC_6 exhibits a large linear increase of T_c with pressure up to 15.1 K, the largest value hitherto reported for GICs. This increase is accompanied by a softening and a hardening of two dominant Ca and C phonon modes, respectively, which suggests an increase of λ associated with the former mode. The T_c drop at ~8 GPa is concomitant to an anomaly of both modes, which drives the system into a new phase with a low T_c and bad metallic properties. These results support a conventional BCS picture, where Ca plays a dominant role in optimizing the band structure and the phonon-mediated pairing. In order to unveil the structural changes concomitant to this anomaly, we carried out a synchrotron x-ray diffraction under high pressure. Our data analysis shows that the T_c drop and the large increase of resistivity at ~8 GPa is caused by an order-disorder phase transition with no change of space group symmetry, concomitant to a three-times increase of compressibility. Symmetry arguments supported by the above evidence of lattice softening and by *ab initio* calculations suggest that the disorder consists of a random distribution of the Ca atoms between adjacent graphene layers. This is a case of superconductor–superconductor phase transition driven by a simultaneous order-disorder and lattice-softening transition. These results provide a solid frame for understanding the mechanisms limiting T_c in BCS

superconductors. In particular, the large T_c increase suggests that even larger T_c values are possible in GICs by stabilizing the equilibrium positions of the intercalant atoms.

References

Akrap, A., Berger, H., Forró, L., Tutiš, E., Sipos, B., and Kusmartseva, A.F., 2008, From Mott state to superconductivity in 1T-TaS_2, *Nature Mater.* **7**: 960.

Ashcroft, N.W., 1968, Metallic hydrogen: A high-temperature superconductor? *Phys. Rev. Lett*. **21**: 1748.

Babaev, E., Sudbø, A., and Ashcroft N.W., 2005, Observability of a projected new state of matter: a metallic superfluid, *Phys. Rev. Lett.* **95**: 105301.

Baroni, S., de Gironcoli, S., Dal Corso, A., and Giannozzi, P., 2001, Phonons and related crystal properties from density-functional perturbation theory. *Rev. Mod. Phys.* **73**: 515.

Calandra, M., and Mauri, F. 2006, Possibility of superconductivity in graphite intercalated with alkaline earths investigated with density functional theory. Phys. Rev. B**74**: 094507.

Calandra, M., and Mauri, F., 2005, Theoretical Explanation of Superconductivity in C_6Ca. *Phys. Rev. Lett*. **95**: 237002.

Chen, X.H., Wu, T., Wu, G., Liu, R.H., Chen, H., and Fang, D.F., 2008, Superconductivity at 43 K in $SmFeAsO_{1-x}F_x$, *Nature.* **453:** 761–762.

Clarke, R., and Uher C., 1984, High pressure properties of graphite and its intercalation compounds, *Adv. Phys*. **33**: 469–566.

Csànyi, G., Pickard, Ch.J., Simons B.D.., and Needs R.J., 2007, Graphite intercalation compounds under pressure: A first-principles density functional theory study, *Phys. Rev.* B **75**: 085432.

Dresselhaus, M.S., and Dresselhaus G., 1981, Intercalation compounds of graphite, *Adv. Phys*. **30**: 139–326.

Emery, N., Hérold C., and Lagrange Ph., 2005, Structural study and crystal chemistry of the first stage calcium graphite intercalation compound, *J. Solid State Chem*. **178:** 2947–2952.

Emery, N., Hérold, C., D'Astuto, M., Garcia, V., Bellin, Ch., Marêché, J.F., Lagrange, P., Loupias, G., 2005, Superconductivity of Bulk CaC_6, *Phys. Rev. Lett*. **95**: 087003.

Fischer, J. E., and H. J. Kim, 1987, Pressure-induced staging transitions and stage disorder in dilute potassium-graphite intercalation compounds, *Phys. Rev.* B **35**: 6826–6830.

Gao, L., Xue, Y.Y., Chen, F., Xiong, Q., Meng, R.L., Ramirez, D., Chu, C.W., Eggert, J.H., and Mao, H.K., 1994, Superconductivity up to 164 K in $HgBa_2Ca_{m-1}Cu_mO_{2m+2+\delta}$ (m=1, 2, and 3) under quasihydrostatic pressures, *Phys. Rev*. B **50**: 4260–4263.

Gauzzi, A., Bendiab, N., D'Astuto, M., Canny, B., Calandra, M., Mauri, F., Loupias, G., Emety, N., Herold, C., Lagrange, P., Hanfland, M., and Mezouar, M., 2008, Maximum T_c at the verge of a simultaneous order-disorder and lattice-softening transition in superconducting CaC_6, *Phys. Rev.* B **78**: 064506.

Gauzzi, A., Takashima, S., Takeshita, N., Terakura, C., Takagi, H., Emery, N., Hérold, C., Lagrange, P., and Loupias, G., 2007, Enhancement of superconductivity and evidence of structural instability in intercalated graphite CaC_6 under high pressure, *Phys. Rev. Lett.* **98**: 067002.

Grimvall, G., 1981, *The Electron-Phonon Interaction in Metals*, North-Holland, Amsterdam, 304 p.

Hannay, N.B., Geballe, T.H., Matthias, B.T., Andres, K., Schmidt, P., and MacNair, D., 1965, Superconductivity in Graphitic Compounds, *Phys. Rev. Lett*. **14**: 225-226.

Jérome, D., 1990, *Earlier and Recent Aspects of Superconductivity:* Lectures from the international school, Erice, Trapani, Sicily, July 4–16, 1989. J.G. Bednorz, K.A. Müller (eds.), Springer-Verlag, Berlin, New York, 529 p.

Jishi, R.A., and Dresselhaus, M.S., 1992, Superconductivity in graphite intercalation compounds, *Phys. Rev*. B **45**: 12465.

Kim, J.S., Boeri, L., Kremer, R.K., and Razavi, F.S., 2006, Effect of pressure on superconducting Ca-intercalated graphite CaC_6, *Phys. Rev.* B **74**: 214513.

Klein, C.A., Straub, W., and Diefendorf, R.J., 1962, Evidence of single-crystal characteristics in highly annealed pyrolytic graphite, *Phys. Rev.* **125**: 468–470.

Lamura, G., Aurino, M., Cifariello, G., Gennaro Di, Andreone E.A., Emery, N., Hérold, C., Mareche, J.-F., and Lagrange, P., 2006, Experimental evidence of s-wave superconductivity in bulk CaC_6, *Phys. Rev. Lett*. **96**: 107008.

Little, W.A., 1964, Possibility of synthesizing an organic superconductor, *Phys. Rev*. **134**: A1416–A1424.

Lortz, R., Wang, Y., Abe, S., Meingast, C., Paderno, Yu.B., Filippov, V., and Junod, A., 2005, Specific heat, magnetic susceptibility, resistivity and thermal expansion of the superconductor ZrB_{12}, *Phys. Rev*. B **72**: 024547.

Lüders, M., Marques, M.A.L., Lathiotakis, N.N., Floris, A., Profeta, G., Fast, L., Continenza, A., Massidda, S., and Gross, E.K.U., 2005, *Ab initio* theory of superconductivity. I. Density functional formalism and approximate functionals, *Phys. Rev*. B **72**: 024545.

Li, Y., Zhang, L.-J., Cui, T., Liu, Y.-H., Ma, Y.-M., and Zou, G.-T., 2007, First-princiles prediction of high-pressure phase of CaC_6, 2007, *Chin. Phys. Lett*. **24**: 1668–1670.

Marques, M.A.L., Lüders, M., Lathiotakis, N.N., Profeta, G., Floris, A., Fast, L., Continenza, A., Gross, U., and Massidda, S., 2005, *Ab initio* theory of superconductivity. II. Application to elemental metals, *Phys. Rev*. B **72:** 024546.

Mazin, I. I., 2005, Intercalant-driven superconductivity in YbC_6 and CaC_6, *Phys. Rev. Lett.* **95**: 227001.

Mori, N., Takahashi, H., and Takeshita, N., 2004, Low-temperature and high-pressure apparatus developed at ISSP, University of Tokyo, *High Press. Res*. **24**: 225–232.

Morosan, E., Zandbergen, H.W., Dennis, B.S., Bos, J.W.G., Onose, Y., Klimczuk, T., Ramirez, A.P., Ramirez, A.P., Ong, N.P., and Cava, R.J., 2006, Superconductivity in Cu_xTiSe_2, *Nat. Phys*. **2**: 544–550.

Potter, M.E., Johnson, W.D., and Fischer, J.E., 1981, Transport properties of alkali metal-graphite intercalation compounds, *Solid State Comm*. **37**: 713–718.

Primak, W., and Fuchs, L.H., 1954, Electrical conductivities of natural graphite crystals, *Phys. Rev*. **95**: 22–30.

Profeta, G., Franchini, C., Lathiotakis, N.N., Floris, A., Sanna, A., Marques, M.A.L., Lüders, M., Massidda, S., Gross, E.K.U., and Continenza, A., 2006, Superconductivity in lithium, potassium, and aluminum under extreme pressure: a first-principles study. *Phys. Rev. Lett*. **96**: 047003.

Rey, N., Toulemonde, P., Machon, D., Duclaux, L., Le Floch, S., Pischedda, V., Itié, J.P., Flank, A.-M., Lagarde, P., Crichton, W.A., Mezouar, M., Strässle, Th., Sheptyakov, D., Montagnac, G., San-Miguel, A., 2008, High-pressure behavior of CsC_8 graphite intercalation compound: Lattice structures and phase-transition mechanism. *Phys. Rev*. B **77**: 125433.

Shimizu, K., Ishikawa, H., Takao, D., Yagi, T., and Amaya, K., 2002, Superconductivity in compressed Li at 20 K, *Nature* **419**: 597–599.

Shimizu, K., Kimura, T., Furomoto, S., Takeda, K., Kontani, K., Onuki, Y., and Amaya, K., 2001, Superconductivity in the nonmagnetic state of iron under pressure, *Nature* **412**: 316–318.

Smith, R.P., Kusmartseva, A., Ko, Y.T.C., Saxena, S.S., Akrap, A., Forró, L., Laad, M., Weller, Th.E., Ellerby, M., and Skipper, N.T., 2006, Pressure dependence of the superconducting transition temperature in C_6Yb and C_6Ca. *Phys. Rev.* B **74:** 024505.

Soule, D.E., 1958, Magnetic field dependence of the Hall Effect and magnetoresistance in graphite single crystals, *Phys. Rev*. **112:** 698–707.

Torikachvili, M.S., Bud'ko, S.L., Ni, N., and Canfield P.C., 2008, Pressure-induced superconductivity in $CaFe_2As_2$, *Phys. Rev. Lett*. **101:** 057006.

Weller, Th.E., Ellerby, M., Saxena, S.S., Smith, R.P., and Skipper, N.T., 2005, Superconductivity in the intercalated graphite compounds C_6Yb and C_6Ca, *Nature Physics* **1:** 39–41.

Zhang, L., Xie, Y., Cui, T., Li, Y., He, Z., Ma, Y., and Zou, G., 2006, Pressure-induced enhancement of electron-phonon coupling in superconducting CaC_6 from first principles, *Phys. Rev. B* **74:** 184519.

STRUCTURE–PROPERTY RELATIONSHIPS IN NOVEL HIGH PRESSURE SUPERHARD MATERIALS

NATALIA DUBROVINSKAIA[1,*],
LEONID DUBROVINSKY[2]
[1]*Mineralphysik, Institut für Geowissenschaftent, Universität Heidelberg, D-69120 Heidelberg, Germany; Lehrstuhl für Kristallographie, Physikalisches Institut, Universität Bayreuth, D- 95440 Bayreuth, Germany,*
[2]*Bayerisches Geoinstitut, Universität Bayreuth, D-95440 Bayreuth, D- 95440 Bayreuth, Germany*

Abstract Research on novel high-pressure superhard materials (those approaching diamond and cubic boron nitride in hardness) is driven by both scientific and practical objectives: the desire to understand their structure and bonding, which determine the unique properties of these materials, on one hand, and the demand of modern technologies for robust materials with superior properties, on the other. Structure–property relationships in newly synthesised superhard materials, as well as some methodological aspects of their characterisation are in focus of the present paper.

Keywords: Superhard materials, diamond, boron nitride, HP boron, nanocrystalline materials

1. Introduction

Understanding the structure and bonding of inorganic solids is fundamental to being able to explain, model, and predict their properties. This is because the properties of solids are controlled by the structure through interactions between atoms, electrons, defects, elements of microstructure, etc. Structural dependence of functional (thermoelastic, transport, electrical, optical,

* E-mail: Natalia.Dubrovinskaia@geow.uni-heidelberg.de

E. Boldyreva and P. Dera (eds.), *High-Pressure Crystallography: From Fundamental Phenomena to Technological Applications*, DOI 10.1007/978-90-481-9258-8_34,

mechanical) performances of a variety of materials have been extensively investigated. It is important not only for fundamental scientific exploring of the phenomenon of the structure–property relationship, but it also provides clues for design of materials with desired properties. Modern technologies require, among others, such very robust materials for use as abrasives, cutting tools and coatings, where wear prevention, scratch resistance, surface durability and chemical stability are priorities.

Novel superhard materials, such as nanodiamond, nano- and polycrystalline BN, polycrystalline B-doped diamond (Figure 1) and orthorhombic B28 boron are products of the high-pressure synthesis. High pressure is a powerful method for tuning in a controllable and reversible manner the volume of a sample and consequently its properties. High pressure applied to a material can produce structural, electronic and other phase transitions, polymerization, and many other phenomena. Some of them will be considered below.

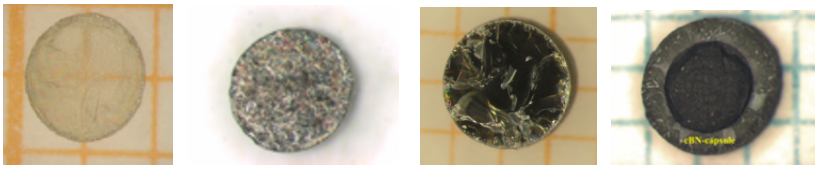

Figure 1. Aggregated diamond nanorods (ADNRs) and nanocrystalline diamond (ND), aggregated boron nitride nanocomposites (ABNNC), polycrystalline boron-doped diamonds (BDDs): Superhard nanocrystalline materials of the technological future?

2. Criteria of "Superhardness" and Hardness Measurements

> *The aim of science is not to open the door to infinite wisdom, but to set a limit to infinite error.*–Bertolt Brech "The Life of Galileo"

Hardness of diamond is measured at 60–120 GPa. As generally agreed in the scientific community, materials with Vickers hardness (Hv) exceeding ~ 40 GPa are considered to be superhard (*Vepřek et al.*, 2000). Until recently among all single phase materials only diamond and cBN were known to be superhard. Extensive research for about the last 2 decades added to this list some other compounds (*McMillan*, 2002), such as, for example, B_6O (*He et al.*, 2002) and BC_2N (*Solozhenko et al.*, 2001) which, however, still have not been synthesized in a quantity sufficient for complete characterization of their mechanical properties and testing their performance compared to that of diamond and cBN.

In the far past, the criteria for hardness measurements were based on a careful comparison and semiquantitative appraisal of materials with respect to each other. The best example of this is the Mohs hardness scale, which categorises materials in terms of their ability to scratch one another, with diamond at the top, with a value of 10. Industrial revolution brought the necessity to quantify the measure of hardness and an indentation technique (1900– Brinell, 1920– Rockwell, 1924– Vickers) was invented. Hardness obtained using this technique varies with the applied load, loading rate, indentor shape and dimensions, the environment and the test temperature (*Morell*, 1987; *Chiang et al.*, 1997). All this complicates the procedure of measurement of hardness, making it sometimes not only science, but art.

Modern indentation techniques for measuring hardness do not differ in principle from that proposed a century ago and invariably involve subjecting a material to relatively high pressures in a localized area, using an indenter that is harder than the substance under test. Hardness can be defined as the resistance of a material to elastic and plastic deformation (*Chiang et al.*, 1997). The latter begins when the shear component of the applied stress exceeds the yield stress (*Cohen*, 1991). For soft materials, plastic deformation can be assumed, and the results easily interpreted. But for hard materials indentation is no longer controlled by plastic deformation alone, and issues such as **brittle cracking** and **deformation of the indenting tip** (*Richter et al.*, 2006) come into play. These effects can change the hardness of a material with load. Attempting to infer the hardness of a material in such instances is, at best, problematic, and at worst, meaningless (*Brazhkin et al.*, 2004). The asymptotic levelling of the hardness-load curve is commonly associated with saturation of population growth of microcracks in brittle materials with increasing load. The community of materials scientists dealing with hard materials strongly recommends that hardness for hard and brittle materials be reported in the **asymptotic-hardness region** with the prerequisite of well-controlled indentation process. Measured **Hv > 120 GPa should not be called "hardness"** (*Brazhkin et al.*, 2004).

Recently it was found that at room temperature graphite undergoes bonding changes under pressure and a phase transition at 17 GPa (*Mao et al.*, 2003). Compressed graphite (*Mao et al.*, 2003) was claimed to be superhard based on its capability of "indenting cubic-diamond single crystals" and forming ring cracks on their surfaces (Figure 2). Unfortunately, this claim is likely incorrect. As early as in 1957 it was shown that "impacters of tungsten carbide and sapphire (*with hardness of about 20 GPa*) as well as diamond have been successfully used to produce ring cracks when pressed against diamond surfaces, thus showing that materials softer than diamond can produce cracks on diamond" (cited from *Berman*, 1965). A comparison

of figures from *Berman*, 1965, (Figure 3), with that from *Mao et al.*, 2003 (Figure 2) gives a clear evidence that one can not *a priori* claim superhardness of compressed graphite synthesized in a diamond anvil cell (DAC). This does not exclude a possibility that it may be superhard, but, if there is no chance to justify the claim by hardness measurements (the substance was observed only in DAC at high pressures and could not be preserved at ambient conditions), one should seriously care about arguments.

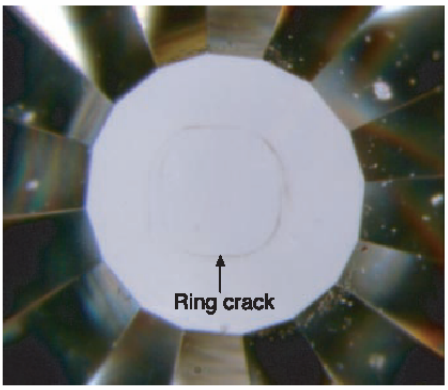

Figure 2. Photomicrograph showing indentation (ring crack) of diamond anvil by the high-pressure form of cold compressed graphite. (From *Mao et al.*, 2003; Reprinted with permission from AAAS).

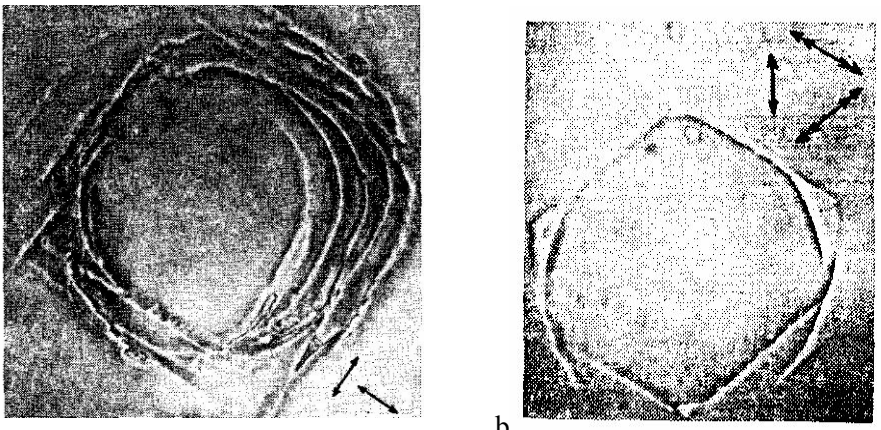

a b

Figure 3. (*a*) Ring crack on a cube face: arrows show <110> directions of traces of (111) planes, x312; (*b*) Ring crack on a dodecahedron face: single arrow shows <110> direction and double arrows show 112 directions of traces of (111) planes, x272 (From *Berman*, 1965; Reprinted with permission from Oxford University Press).

Any claims on synthesis of new superhard materials should be done very accurately in order not to mislead the scientific community and industrialists (especially if prospective applications are foreseen or suggested). Recently synthesised at ambient pressure rhenium diboride ReB_2 (*Chung*

et al., 2007a) was claimed to be superhard. According to the authors, microindentation measurements on ReB_2 indicated Hv of ~48 GPa under an applied load of 0.49 N, and scratch marks left on the diamond surface confirmed its superhard nature. Based on analysis of the measurement technique (hardness was measured at very small loads and reported not in an asymptotic region as recommended for hard materials (*Brazhkin et al.*, 2004) the validity of this claim was questioned (*Dubrovinskaia et al.*, 2007a; *Chung et al.*, 2007b) and it was suggested that rhenium diboride may not be a superhard material (*Dubrovinskaia et al.*, 2007a). In fact, later independent measurements of mechanical properties of ReB_2 (*Qin et al.*, 2008) confirmed that the doubt (*Dubrovinskaia et al.*, 2007a) was true and rhenium diboride is not of superhard nature (Hv = 30 GPa and K_T = 210 GPa) in consistence with properties of OsB_2 (*Cumberland et al.*, 2005; *Gou et al.*, 2006; *Chen et al.*, 2006).

For materials that are purportedly harder than diamond, using relative criteria that are not quantitative or indentation technique that is defined only for materials softer than diamond becomes problematic, which in turn raises the question of what it means – in quantitative terms – for a material to be harder than diamond (*Brazhkin et al.*, 2004). Syntheses of new classes of hard and superhard materials (*McMillan*, 2002) provide new challenges for the measurement of hardness. **Depth sensing nanoindentation** (*Fischer-Cripps*, 2002) differs from impression hardness (Vickers, Brinell and Knoop), where the impressions are first generated using a given load, and then imaged using a microscopy technique. In nanoindentation, load and penetration depths are simultaneously recorded during both loading and unloading, resulting in a load–displacement-diagram. This diagram provides much more information than a microscopy image of the impression since it tells us the "story" of the elastic and plastic deformation with increasing and decreasing load and enables the determination of "hardness" and Young's modulus as a function of the penetration depth (*Oliver and Pharr*, 1992). The results of nanoindentation measurements are dependent on many parameters, so that they must be analysed very critically by specialists in the field to avoid ambiguous claims. So far nanoindentation is not a routine technique, although it has been applied for studies of superhard materials such as hard fullerites, nanodiamonds, ADNRS, synthetic diamond crystals, CVD grown diamond films.

Hardness (and other materials mechanical properties) is strongly influenced by many factors, such as residual stresses, microstructurs, textures, porosity of samples, toughening phases (for non single-component systems), as well as the grain size and structure and composition of grain boundaries, if one considers polycrystalline materials. Below we briefly

overview some of recently synthesized superhard materials and show how the important factors listed above determine their mechanical properties.

3. Novel High-Pressure Superhard Materials

3.1. NANODIAMOND AND AGGREGATED DIAMOND NANORODS (ADNRS)

The beneficial properties of polycrystalline and nanocrystalline diamonds are due to extremely high hardness, the absence of cleavage features, and the high thermal stability of these materials. They can be utilized in industry, if used as abrasion-resistant materials. Until recently nanodiamonds could be synthesized only in form of fine dispersed powders in mixture with many impurities using the shockwave technique. First samples of bulk polycrystalline high-purity diamond were synthesised by *Irifune et al.* (2003) by heating high-purity graphite under static ultra-high pressure. These samples consisted of very fine diamond grains of up to several hundreds of nanometres. In course of our research first nanocrystalline diamond aggregates with crystallite sizes of 5–12 nm (Figure 4) were synthesized using C_{60} and other carbon precursors by their direct solid-state transformation in the diamond stability field (*Dubrovinskaia et al.*, 2004). According to the EELS data, the synthesized materials contain only sp^3-bonded carbon atoms within diamond grains and across all numerous grain boundaries.

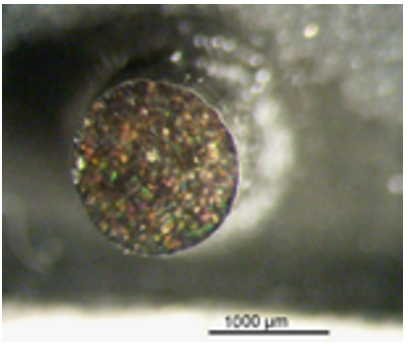

Figure 4. A sample of nanocrystalline diamond aggregate synthesized from C_{60}.

Further investigations showed that varying PT conditions of synthesis one can change not only the size, but also the shape of nanoparticles. In particular, first from C_{60} and then from other carbon precursors aaggregated diamond nanorods (ADNRs) were synthesized at 20(1) GPa and 2200°C (*Dubrovinskaia et al.*, 2005). Individual diamond nanoroads are of 5–20 nm in diameter and longer than 1 μm (Figure 5). The shape of nanocrystals and

arrangement of the nanoparticles (Figure 5) make the ADNRs a unique material with unique properties different from poly-nanocrystalline diamonds synthesised and investigated by Irifune and co-authors (see *Irifune et al.*, 2003; *Sumiya et al.*, 2004; *Sumiya and Irifune*, 2007; *Nakamoto et al.*, 2007 and refs. therein).

a b

Figure 5. Bright-field TEM image of a nanocrystalline aggregate with needle-shaped, elongated crystals (diamond nanorods) (a). The crystals can be longer than 1 μm, whereby their width is only about 20 nm or less. Their random orientation resembles that of needles of a porcupine (b).

The EELS spectra correspond to diamond structure and suggest that carbon atoms near and across the numerous grain boundaries in ADNRs are also sp^3-bonded. The high hardness (measured H_K above 100 GPa) and fracture toughness exceeding that of diamond (*Dubrovinskaia et al.*, 2006a) can possibly be attributed to the random intergrowth of diamond nanorods (Figure 5), zero porosity and suppressed sliding along grain boundaries. The x-ray density of ADNRs (and the density obtained from the measured weight and volume of the sample) is ~0.2–0.4% higher than that of usual diamond. The extremely high isothermal bulk modulus K_T = 491(3) GPa (compare to K_T = 442(4) GPa of diamond) was obtained by *in situ* x-ray diffraction study. Thus, ADNRs is the densest among all carbon materials and it has the lowest compressibility experimentally determined so far (compare with the highest measured K_T: 462 GPa for Os (not confirmed), 420 GPa for WC, 383 GPa for Ir, 380 GPa for cubic BN, 306 GPa for HfN.

3.2. AGGREGATED BORON NITRIDE NANOCOMPOSITES (ABNNC)

High-pressure high-temperature (HPHT) synthesis of cubic boron nitride (cBN) in 1957 opened a field of important technical applications similar to those of diamond (*Wentorf,* 1957). On thermal stability and reaction resistance

cBN is superior to diamond (*Solozhenko and Turkevich*, 1992) (cBN is thermally and chemically stable up to 1,650 K, while diamond only up to 950 K) and due to this cBN can be used for machining hard ferrous steels. However, cBN cannot completely replace diamond, because its hardness is two times lower (hardest single-crystalline cBN has Vickers hardness Hv about 50 GPa, while for single-crystalline diamond this value is about 100 GPa; for commercially used polycrystalline cBN and diamond (PCD), the values are lower (*Dub and Petrusha*, 2006; *Taniguchi et al.*, 1996).

Unique superhard aggregated boron nitride nanocomposites show the enhancement of hardness (reported in the asymptotic-hardness region) up to 100% in comparison with single-crystalline cBN (*Dubrovinskaia et al.*, 2007b). The material is semitransparent in thin pieces. It has a unique Raman spectrum (Figure 6) dominated by broad features centred at ~450 cm^{-1}, ~750 cm^{-1}, and ~1,550 cm^{-1}, which are likely due to scattering by the numerous grain boundaries in the very fine nanocrystalline material, as it was already observed for nanocrystalline diamonds.

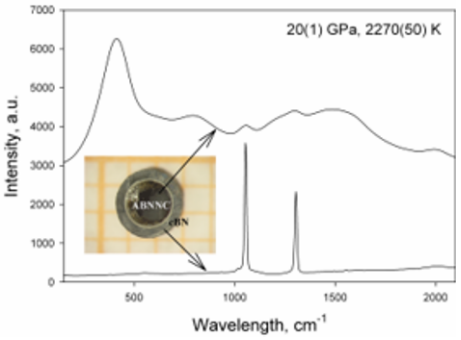

Figure 6. Raman spectra of the materials synthesized simultaneously (in one experimental run) at P = 20(1) GPa and T = 2,270 K from different precursors. A cross-section of the sample chamber after the experiment is shown in the inset. The outer layer of the sample was prepared from hexagonal BN, which transformed to cBN (grey) at HPHT conditions. A central part of the sample, made of pyrolytic p-BN and isolated by a platinum foil, transformed to ABNNC (shining black).

The significant increase of hardness up to 85(5) GPa is due to an interesting arrangement of structural blocks of the material (Figure 7) and to the combination of the Hall–Petch and the quantum confinement effects (on decrease of the grain size down to 14 nm) and simultaneous formation of the two dense BN phases with hexagonal and cubic structures (Figure 7b) within the grains at nano- and subnano-level. Thus, ABNNC is the first non-carbon based bulk material with the value of hardness approaching that of single-crystalline and polycrystalline diamond and aggregated diamond nanorods.

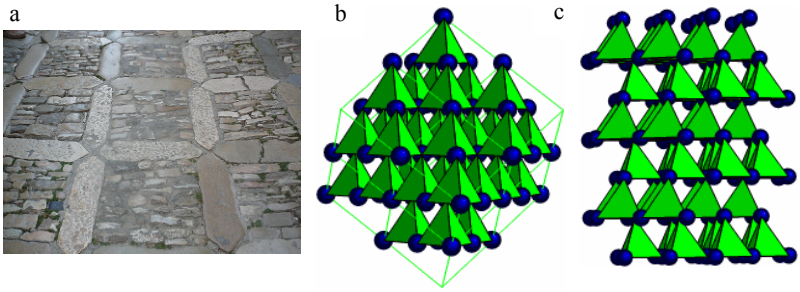

Figure 7. Streetway of the ancient city of Erice (Sicily) (a). It can serve as analogy to the microstructure of ABNNC, which consists of grains of 50–70 nm in size separated by grain boundaries (big blocks of the causeway separated by elongated stones). Each grain in turn consists of intergrown particles of two BN polymorphs, sphalerite (b) and wurzite (c) structured (smaller stones of the causeway filling the big blocks).

3.3. BORON DOPED DIAMOND (BDD)

The basic properties of diamond suggest that it is an ideal material for electronics. It has a wide bandgap (5.5 eV, indirect), high saturated carrier velocities and carrier mobilities (and electrons and holes have similar values), a high electric field breakdown strength, low dielectric constant, high thermal conductivity and high visible-infrared radiation transparency. Many potential applications can, and have been proposed, including high power and high frequency electronic devices.

Pure diamond is an insulator. The *p*-type conductivity occurs for natural diamond only in the very rare type IIb stones, in which boron is the dominant impurity in concentrations below 1 ppm (~$1*10^{-4}$ at.%) (*Tronke,* 2003). Artificially diamond can be doped using a few methods: doping during growth (by high pressure–high temperature (HPHT) method or chemical vapor deposition (CVD) technique); doping by ion implantation; doping by thermal diffusion. So far, the small boron atom seems to be the only efficient dopant atom at all in bulk diamond, which can be incorporated with high reproducibility and high enough concentration to be useful for electronic devices.

The discovery of superconductivity in polycrystalline boron-doped diamond synthesized under high pressure and high temperatures (*Ekimov et al.,* 2004; *Dubrovinskaia et al.*, 2006b) raised a number of questions on the origin of the superconducting state. It was suggested that the heavy boron doping of diamond (exceeding 2.5 at.%) eventually leads to super-conductivity. To justify such statements more detailed information on the microstructure of the composite materials and on the exact boron content in

the diamond grains is needed. For that we used high-resolution transmission electron microscopy (HRTEM) and electron energy loss spectroscopy (EELS). For the studied superconducting BDD samples synthesized at high pressures and high temperatures (bulk B content of 2.6 at.%; Tc onset 2.4 K) the diamond grain sizes are ~1–2 μm with a boron content between 0.2 (2) and 0.5 (1) at.% (*Dubrovinskaia et al.*, 2008). The grains are separated by 10- to 20-nm-thick layers and triangular-shaped pockets of predominantly (at least 95 at. %) amorphous boron (Figure 8). This means that boron has a strong tendency to segregation (also observed for CVD diamonds) and the high values of its bulk concentration in BDD samples reported in literature are not due to the heavy doping, but because of the presence of B-rich impurity phases and amorphous boron in the intergranular space that was impossible to detect in previous investigations. The phase composition of most of the BDD samples described in the literature (*Ekimov et al.*, 2004; *Bustarret et al.*, 2004; *Takano et al.*, 2004; *Umezawa et al.*, 2005; *Sidorov et al.*, 2005; *Dubrovinskaia et al.*, 2006b) has been characterized using only conventional x-ray, which does not allow detecting amorphous B and a small amount of crystalline impurity phases.

Based on the results of our research, we could suggest a few hypotheses for the explanation of the nature of superconductivity in the investigated BDD samples (*Dubrovinskaia et al.*, 2008). One of them was that the intergranular boron-rich material becomes superconducting. In our opinion, this hypothesis is one of most probable, because carbon-doped amorphous boron phase, which is filling all the intergranular space in the polycrystalline samples (Figure 8), forms a continuous net through the whole sample and its amount agrees with the estimations of a superconducting part of the sample based on the heat capacity experimental data. Despite extensive research in the field of superconductive BDD (see recent review in *Nature Materials* by *Blase et al.*, 2009), the problem of the origin of superconductivity has not been resolved yet and the correlation between B content and the transition temperature has not been established, as admitted, because the difficulty to identify boron location in the samples). Only further investigations on the HPHT B-rich B-C phases including HPHT crystalline phases of pure boron can shed light into the nature of superconductivity in BDD.

Investigations of the microstructure of BDDs showed that B tends to escape from the diamond structure and segregates in the intergranular space of polycrystalline samples. Thus, the behavior of boron at HP is worth detailed investigation.

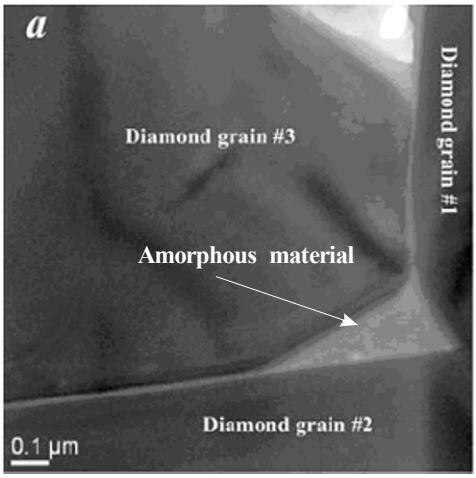

Figure 8. Bright-field TEM image of a BDD polycrystalline sample. The amorphous material constituting the layers along the grain boundaries also fills triangular-shaped pockets at the grain junctions. Electron energy-loss spectra (EELS) at the boron *K* and carbon *K* ionization edges from the pockets and the diamond grains reveal that the pocket material consists of ~95 at.% boron with a small amount (~5–6 at.%) of carbon, while diamond grains are contain less than 0.2 at.% B.

3.4. HIGH SUPERHARD ORTHORHOMBIC BORON (B28)

Pure boron is one of the most enigmatic elements. Boron's three valence electrons are too localized to make it metallic but insufficient in number to form a simple covalent structure. As a compromise, boron atoms form quasimolecular B_{12} icosahedra that become building blocks of boron and boron-rich crystalline phases (*Buschveck*, 1981). Dozens of possible crystalline boron phases have been proposed in literature, but most of them proved to be borides or to be stabilized by small amount of impurities. Only α- (high-temperature form, rhombohedral, 12 atoms per a unit cell) and β-boron (rhombohedral, structure is not fully understood and consists of 105 or 108 atoms in the unit cell) are established as pure boron crystalline forms (see recent review by *Albert and Hillebrecht*, 2009; *Will and Ploog*, 1974; *Brazhkin et al.*, 2004). The existence of "tetragonal boron" as a modification of pure elemental boron, or as boron-rich nitride or carbide has been a subject of controversy (*Naslain*, 1977; *Hoard et al.*, 1970). In addition, elemental boron exists in amorphous forms of different purity prepared by various techniques (*Katada*, 1966; *Gillespie*, 1966). On compression of a β-boron single crystal at room temperature to 100 GPa amorphization was observed (*Sanz et al.*, 2002). Energy-dispersive x-ray powder diffraction experiments in laser-heated diamond anvil cells (DACs) suggest that β-boron is stable up 30 GPa and 3,500 K, and at higher temperatures and pressures a phase transition to the tetragonal "T-192" structure occurs (*Ma et al.*, 2003). Resistivity measurements demonstrate metallization of boron and the occurrence of a superconducting state at about 160 GPa (*Eremets et al.*, 2001). However, the crystal structure of metallic boron is not known. Theoretical studies predict the transformation of α-boron into a phase with the α-Ga

structure, accompanied by an insulator-metal transition (*Häussermann et al.*, 2003). Thus, the behavior of boron at high pressure remains poorly understood.

We have realised experiments on studying the behaviour of pure boron at HP and HT (*Zarechnaya et al.*, 2008, 2009). Experiments in large-volume presses at pressures above 9 GPa and temperatures above 1,500°C starting from boron precursors with purity higher than 99.7% result in formation of an optically homogeneous reddish material. Thus, we confirmed the synthesis of a new boron form reported by R.H. Wentorf in 1965 at pressures above 10 GPa and temperatures above 1,500°C (*Wentorf*, 1965).

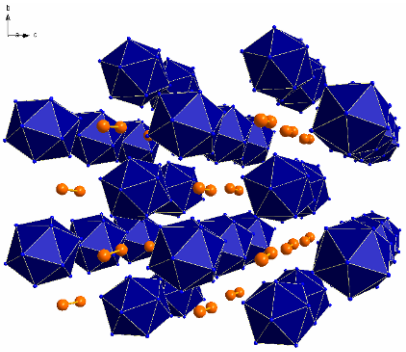

Figure 9. The structure of the HPHT boron phase shown in the *bc* projection.

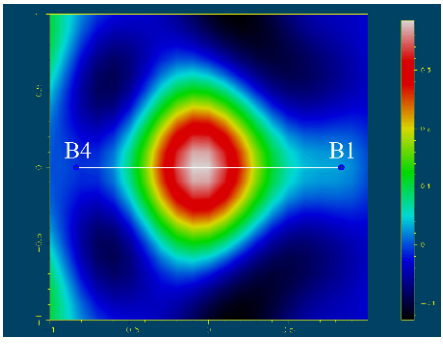

Figure 10. Difference electron density plot around the atoms B1 and B4 extracted from experimental single-crystal x-ray diffraction data. The maximum electron density is centred in the middle of the bond, suggesting covalent bonding between the B_2 dumbbell and the B_{12} icosahedron.

By indexing the powder x-ray diffraction data and using Endeavour© software, the structure of quenched samples was solved in the framework of an orthorhombic unit cell (a = 5.0563(5) Å, b = 5.6126(5) Å, c = 6.9710(7)

Å, V = 197.83(3) Å^3). The suggested structure of the HPHT boron with a space group *Pnnm* contains 28 atoms in a unit cell. The *bc* projection (Figure 9) shows that the structure is built of B_{12} icosahedra linked into a three-dimensional network. Nearly rectangular channels running along the *a* axis are filled with boron chains, composed of B_2 dumbbells and aligned almost parallel to the *a* axis (*Zarechnaya et al.*, 2008).

Our analysis of the type of bonding in B2 was based on theoretical calculations and the difference electron density plots extracted from experimental single-crystal x-ray diffraction data (*Zarechnaya et al.*, 2009). The maximum electron density is centred in the middle of the B–B bond suggesting **covalent** bonding between the B atoms (both within dumbbells and icosahedra, and also between two icosahedra and between dumbbells and icosahedra) in the B28 structure. Indeed, "interstitial charge density is the characteristic feature distinguishing covalent crystals from the other two (molecular and ionic) insulating types" (*Ashcroft and Mermin*, 1976). Recent theoretical studies on the orthorhombic B28 high-pressure phase suggested that the material is an ionic boron boride (*Oganov et al.*, 2009). Our experimental single-crystal structural data (Figure 10) and theoretical results (*Zarechnaya et al.,* 2009) as well as theoretical calculations (*Jiang et al.,* 2009) do not confirm this "ionic" model. Physical properties measured on polycrystalline B28 samples are in good agreement with what could be expected for a compound with strong covalent bonding: B28 has low compressibility (K_{300} = 227(2) GPa; for α-B and β-B reported K_{300} = 185–213 GPa) and very high hardness approaching Hv = 60 GPa.

4. Summary

Exploration and development of superhard materials is a highly multi-disciplinary scientific field with a great potential for applications. Through the synergy of physical, chemical and engineering methods of synthesis and investigations of material properties, we obtained and studied a series of nanocrystalline aggregated diamond and boron nitride materials, as well as polycrystalline boron-doped diamonds and high-pressure boron (the latter also as single crystals). All newly synthesised materials consist of light elements of the B–C–N system and adopt structures with covalent bonding. The hardness of superhard materials has been shown to be influenced not only by their chemistry and structure, but also by the degree of their crystallinity in terms of grain size, grain boundary structure and the composite nature of nano- and polycrystalline aggregates. It was demonstrated that by tuning these factors, there is great potential to vary of technologically important thermoelastic and mechanical properties of superhard materials

such as hardness, fracture toughness, thermal stability and wear resistance, extremely important for their industrial applications.

References

Albert B., Hillebrecht H., Angew. Chem. Int. Ed. 48, 2–31 (2009).

Ashcroft N.W., Mermin N.D., Solid State Physics. Harcourt College Publishers, New York (1976).

Berman R. (ed.), Physical Properties of Diamonds, Clarendon Press, Oxford, 1965.

Blase X., Bustarret E., Chapelier C., Klein T., Marcenat C. *Nat. Mater.* 8, 375–382 (2009).

Brazhkin V., Dubrovinskaia N., Nicol M., Novikov N., Riedel R., Solozhenko V., Zhao Y. *Nat. Mater.* 3, 576–577 (2004).

Brazhkin V.V., Taniguichi T., Akaishi M., Popova S.V., *J. Mater. Res.* 19, 1643 (2004).

Buschveck K.C., Boron Compounds, Elemental Boron and Boron Carbides 13, Gmelin Handbook of Inorganic Chemistry, Springer Verlag, Berlin (1981).

Bustarret E. et al., *Phys. Rev. Lett.* 93, 237005 (2004).

Chen Z.Y., Xiang H.J., Yang J., Hou J.G., Zhu Q., *Phys. Rev. B* 74, 012102 (2006).

Chiang Y., Birnie D.P., Kingery W.D., Physical Ceramics, Wiley, New York/London (1997).

Chung H.Y., Weinberger M.B., Levine J.B., Kavner A., Yang J.M., Tolbert S.H., Kaner R.B., *Science* 316, 436 (2007a).

Chung H.Y., Weinberger M.B., Levine J.B., Cumberland R.W., Kavner A., Yang J.M., Tolbert S.H., Kaner R.B., *Science* 318, 1550d (2007b).

Cohen M.L., *J. Hard Mater.* **2**, 13–27 (1991).

Cumberland R.W., Weinberger M.B., Gilman J.J., Clark S.M., Tolbert S.H., Kaner R.B., *J. Am. Chem. Soc.* 127, 7264 (2005).

Dub S.N., Petrusha I.A., *High Press. Res.* 26, 71 (2006).

Dubrovinskaia N., Dubrovinsky L., Langenhorst F., Jacobsen S., Liebske C., *Diam. Relat. Mater.* 14, 16–22 (2004).

Dubrovinskaia N., Dubrovinsky L., Crichton W., Langenhorst F., Richter A., *Appl. Phys. Lett.* 87, 083106 (2005).

Dubrovinskaia N., Dub S., Dubrovinsky L., *Nano Lett.* 6, 824–826 (2006a).

Dubrovinskaia N., Eska G., Sheshin G. A., Braun H., *J. Appl Phys*., 033903-1-7 (2006b).

Dubrovinskaia N., Dubrovinsky L., Solozhenko V.L., *Science* 318, 1550c (2007a).

Dubrovinskaia N., Solozhenko V. L., Miyajima N., Dmitriev V., Kurakevych O. O., Dubrovinsky L., *Appl. Phys. Lett.* 90, 101912 (2007b).

Dubrovinskaia N., Wirth R., Wosnitza J., Papageorgiou T., Braun H.F., Miyajima N., Dubrovinsky L., *Proc. Natl. Acad. Sci. USA* 105, 33, 11619–11622 (2008).

Ekimov E.A. , Sidorov V.A., Bauer E.D., Mel'nik N.N., Curro N.J., Thompson J.D., Stishov S.M. Nature 428, 542 (2004).

Eremets M.I., Struzhkin V.V., Ho-kwang Mao, Hemley R.J., *Science* 293, 272 (2001).

Fischer-Cripps A.C., Nanoindentation, Springer-Verlag, New York (2002).

Gillespie J.S., *J. Am. Chem. Soc.* 88, 2423 (1966).

Gou H., Hou L., Zhang J., Li H., Sun G., Gao F., *Appl. Phys. Lett.* 88(22), 1904 (2006).

Häussermann U., Simak S.I., Ahuja R., Johansson B., *Phys. Rev. Lett.* 90, 65701 (2003).

He D., Zhao Y., Daemen L., Qian J., Shen T.D., Zerda T.W. *Appl. Phys. Lett.* 81, 643 (2002).

Hoard J.L., Sullenger D.B., Kennard C.H.L., Highes R.E., *J. Solid State Chem.* 1, 268, (1970).
Irifune T., Kurio A., Sakamoto S., Inoue T., Sumiya H., *Nature* (London) 421, 599 (2003).
Jiang C., Lin Z., Zhang J., Zhao Y., *Appl. Phys. Lett.* 94, 191906 (2009).
Katada K., *Jpn. J. Appl. Phys.* 5, 582 (1966).
Ma Y., Prewitt Ch.T., Zou G., Ho-kwang Mao, Hemley R.J., *Phys. Rev. B* 67, 174116 (2003).
Mao W.L., Mao H.-K., Eng P. J., Trainor T.P., Newville M., Kao C.-C., Heinz D.L., J. Shu, Y. Meng, Hemley R. J. *Science* 302, 425–427 (2003).
McMillan P.F., *Nat. Mater.* 1, 19 (2002).
Morell R., Handbook of Properties of Technical and Engineering Ceramics. HMSO books, London (1987).
Nakamoto Y., Sumiya H., Matsuoka T., Shimizu K., Irifune T., Ohishi Y., *Jpn. J. Appl. Phys*., 46, 25, L640–L641 (2007).
Naslain R., Boron and Refractory Borides (Ed.: V. I. Matkovich), Springer Verlag, Berlin (1977).
Oganov A.R., Chen J., Gatti C., Ma Y., Ma Y, Glass C.W., Liu Z., Yu T., Kurakevych O.O., Solozhenko V.L., *Nature* 457, 863 (2009).
Oliver W.C., Pharr G., *J. Mater. Res.* 7, 1562 (1992).
Qin J., He D., Wang J., Fang L., Lei L., Li Y., Hu J., Kou Z., Bi Y., *Adv. Mater*. 20, 4780–4783 (2008).
Richter A., Smith R., Dubrovinskaia N., McGee E., *High Press. Res.* 26, 2, 99–109 (2006).
Sanz D.N., Loubeyre P., Mezouar M., *Phys. Rev. Lett.* 89, 245501 (2002).
Sidorov V.A., Ekimov E.A., Stishov S.M., Bauer E.D., Thompson J.D., *Phys Rev B.* 71, 060502 (2005).
Solozhenko V.L., Turkevich V.Z., *J. Therm. Anal.* 38, 1181 (1992).
Solozhenko V.L., Andrault D., Fiquet G., Mezouar M., Rubie D.C., *Appl. Phys. Lett*. 78, 1385 (2001).
Sumiya H., Irifune T., *J. Mater. Res*., 22, 8 (2007).
Sumiya H., Irifune T., Kurio A., Sakamoto S., Inoue T., *J. Mat. Sci.*, 39, 445–450 (2004).
Takano Y. et al., *Appl. Phys. Lett.* 85, 14, 2851 (2004).
Taniguchi T., Akaishi .M, Yamaoka S., *J. Am. Ceram. Soc. 79*, 547 (1996).
Tronke K., *Semicond. Sci. Technol.* 18, S20 (2003).
Umezawa H. et al., *Z. Anorg. Allg. Chem.* 627, 2100–2104 (2001).
Vepr˘ek S., Zeer A., Riedel R., Handbook of Ceramic Hard Materials (Ed.: R. Riedel), Wiley, Weinheim (2000).
Will G., Ploog K., *Nature* 251, 406 (1974).
Wentorf R.H., *Chem Phys.* 26, 956 (1957).
Wentorf R.H., *Science* 147**,** 49–50 (1965).
Zarechnaya E.Yu., Dubrovinsky L., Dubrovinskaia N., Miyajima N., Filinchuk Y., Chernyshov D., Dmitriev V., *Sci. Technol. Adv. Mater.* 9, 044209 **(**2008).
Zarechnaya E.Yu., Dubrovinsky L., Dubrovinskaia N., Filinchuk Y., Chernyshov D., Dmitriev V., Miyajima N., El Goresy A., Braun H.F., Van Smaalen S., Kantor I., Kantor A., Prakapenka V., Hanfland M. , Mikhaylushkin A.S., Abrikosov I.A., Simak S.I., *Phys. Rev. Lett.* 102, 185501 (2009).

CARBON NANOTUBES UNDER HIGH PRESSURE PROBED BY RESONANCE RAMAN SCATTERING

ALFONSO SAN-MIGUEL[1*], CHRISTOPHE CAILLER[1], DENIS MACHON[1], EDUARDO B. BARROS[2], ACRISIO L. AGUIAR[2], ANTONIO G. SOUZA FILHO[2]
[1]*Laboratoire PMCN, CNRS, UMR 5586, Université Lyon 1, F-69622 Villeurbanne, France,* [2]*Departamento de Física, Universidade Federal do Ceará, C.P. 6030, Fortaleza-CE, CEP 60455-900 Brazil*

Abstract The power of Raman spectroscopy for the study of the high-pressure evolution of carbon nanotubes is shown. After an introduction to carbon nanotubes and its resonance Raman scattering signal, we discuss the high-pressure Raman studies on single-wall carbon nanotubes with particular emphasis on the identification of pressure-induced structural and electronic transitions.

Keywords: High pressure, Raman spectroscopy, carbon nanotubes

1. Introduction

Carbon nanotubes exhibit striking electronic, optical and mechanical properties, which have attracted many research efforts motivated by the discovering of new phenomena as well as by the potential applications. The low dimensionality of these systems leads to interesting optical phenomena, which are associated with the electronic transitions between van Hove singularities in the valence and conduction bands. This leads to the strong resonance Raman scattering phenomena, which strongly couples vibrational and electronic properties in a peculiar way, allowing accessing the electronic properties of the nanotubes through their phonon spectra.

[*]E-mail: alfonso.san.miguel@univ-lyon1.fr

E. Boldyreva and P. Dera (eds.), *High-Pressure Crystallography: From Fundamental Phenomena to Technological Applications*, DOI 10.1007/978-90-481-9258-8_35,

The electronic structure of these materials can be tuned by external variables such as doping, strain, and hydrostatic pressure (*San-Miguel*, 2006; *Souza Filho et al.*, 2005; *Zang et al.*, 2004). Resonance Raman scattering emerges as one of the most appropriate techniques for studying nanotubes under these conditions. In particular, Raman scattering is very powerful for high-pressure studies, because both electronic and structural changes induced by pressure in the nanotubes are well-seen in the vibrational spectra, which are relatively easy to measure, even in the case of isolated nanotubes. Since carbon nanotubes are considered as model systems for nanoscience, high-pressure investigations of these materials are also important for learning about the high pressure effects at the nanoscale, in general.

In this chapter we discuss some aspects of high-pressure effects on vibrational and structural properties of carbon nanotubes. The chapter is organized as follows. In Section 2 we describe the basic structural and electronic properties of carbon nanotubes, including the resonance Raman phenomena in carbon nanotubes. A brief summary of experimental and theoretical results on pressure effects on single-wall carbon nanotubes is given in Section 3 and is followed by the concluding remarks in Section 4.

2. Carbon Nanotubes

A single-wall carbon nanotube is built conceptually by rolling up one individual layer of graphite, called a graphene sheet, thus forming a seamless cylinder, which is one atom in thickness, as schematically shown in Figure 1a. In Figure 1b it is illustrated how a particular nanotube is formed by joining the crystallographically equivalent A to O and B to B' points (*Saito et al.*, 1998). The structure of the carbon nanotube is uniquely defined by the chiral vector that can be represented by taking an integer number of vectors $\mathbf{a_1}$ and $\mathbf{a_2}$ that form the honeycomb lattice (see left panel in Figure 1b). The nanotube structure is then uniquely defined by the *(n,m)* pair or chiral vector. The nanotube formed with the yellow area in Figure 1b is the (4,2) tube, which determines the diameter d_t and the chiral angle θ (helicity) of the molecule. The helicity is related to the direction of the hexagons relative to the nanotube axis. Depending on synthesis conditions carbon nanotubes can be single-walled and multi-walled. Particular kind of multi-walled nanotubes, which can be synthesized with a very good control, are the so-called double-walled carbon nanotubes, which are composed of two concentric single-wall carbon nanotubes.

Regarding the electronic properties, it is remarkable, that the nanotubes can be either metallic or semiconducting, depending only on the geometry, i.e., on the *(n,m)* values. A simple picture states that those tubes, for which the *n–m* is a multiple of 3, are metallic, and otherwise they are semi-

conducting (*Saito et al.*, 1998). The 1D electronic density of states is characterized by the van Hove singularity as is illustrated in Figure 2. For metallic nanotubes (Figure 2a) the Fermi level is populated, while for semiconducting (Figure 2b) nanotubes there is a gap between valence and conduction bands with no density of states. The strong resonance Raman and other optical phenomena are observed when the laser energy used for exciting the spectra matches the electronic transition such that $E_{laser} \sim E_{ii}$. The electronic transition energies values depend both on diameter and helicities, and by changing the laser energy different nanotubes are excited, thus allowing one to selectively probe either metallic or semiconducting tubes in a bundle samples, as is schematically shown in the Kataura plot (Figure 2c). The electronic band structure of graphene is quite peculiar: each *(n,m)* carbon nanotube has a unique set of E_{ii} values, and this allows one to use of Raman spectroscopy, to indentify uniquely the *(n,m)* indices.

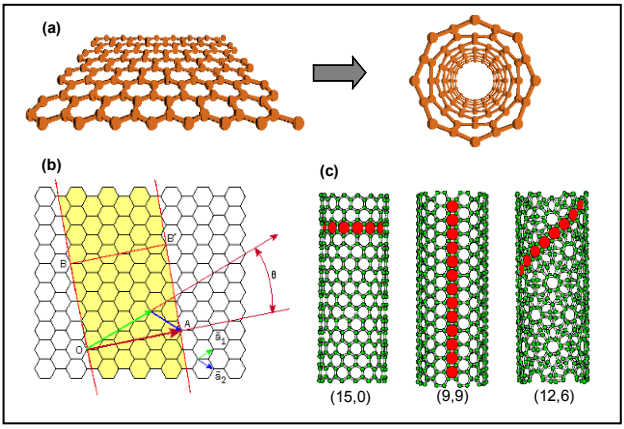

Figure 1. (a) Scheme illustrating how a carbon nanotube is generated from graphene. (b) The definition of chiral vector for the $C_h = 4a_1 + 2a_2 = (4,2)$ nanotube. (c) We show the three types of nanotubes that can be formed with chiral angle $\theta = 0^o$ (15,0) and $\theta = 30^o$ (9,9). An example of nanotubes with $0^o < \theta < 30^o$ is the (12,6) nanotube.

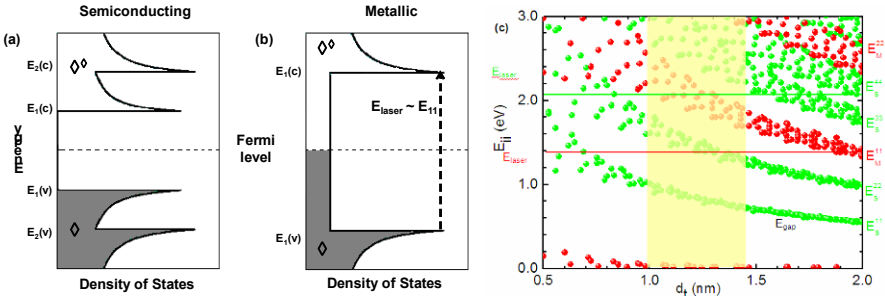

Figure 2. Electronic density of states of (a) semiconducting and (b) metallic single-wall carbon nanotube. c and v mean conduction and valence bands, respectively. In (c) we show the so-called Kataura Plot, which correlates with the electronic transitions energies for both metallic and semiconducting nanotubes as a function of diameter.

2.1. RAMAN SCATTERING IN CARBON NANOTUBES

Two fundamental points are needed for relating the Raman features with the nanotube structure. The first point concerns the electronic–vibrational coupling, whereby the Raman process occurs in a resonance condition and allows one to observe the spectra of a single tube (*Jorio et al.*, 2001). The spectrum observation is possible, when the laser energy matches the transition energy E_{ii}, causing the Raman intensity to be enhanced by some orders of magnitude (*Dresselhaus et al.*, 2002). In the practice most of the nanotube samples are bundle-like, i.e., a collection of tubes with different diameters and helicities. However, for a given laser excitation energy, only some of the nanotubes in the bundle will effectively respond to the excitation, becoming selectively probed within the sample, thanks to the sharp width of the resonant window. The intensity parameter tells us, how close to the E_{ii} value of a given tube the laser energy is. The second fundamental point to consider is the energy of the vibrational modes which manifests in the spectra as several peaks. From the theoretical models it is known, that the frequency of the radial breathing mode (where the atoms vibrate symmetrically relative to the tube axis) is inversely proportional to the tube diameter, and this can be used to identify the tube diameter based on the frequencies of the observed modes. Several papers review the use of Raman spectroscopy for assigning the (*n*,*m*) indexes for carbon nanotubes (*Loa*, 2003; *Shanavas and Sharma*, 2009; *Sluiter et al.*, 2002; *Zang et al.*, 2004).

Raman spectroscopy is a well-established and widely used technique for characterizing carbon nanotubes. This technique allows one to readily probe the structural, vibrational and electronic properties of single-walled, double-walled or multi-walled carbon nanotubes, and it is sensitive to the environment, in which the nanotube resides – isolated, bundled or doped forms, and for samples under extreme conditions as high pressure, for example (*Bandow et al.*, 2000; *Dresselhaus and Eklund*, 2000; *Kukovecz et al.*, 2002; *Rao et al.*, 1997). There are four important Raman spectra features for SWNTs: (i) The radial breathing mode (RBM), in which all carbon atoms vibrate in phase in the radial direction of the nanotube. The frequency ω_{RBM} is related to the nanotube diameter d_t as $\omega_{RBM} \sim 1/d_t$. (ii) The tangential G-band, which is derived from the in-plane Raman-active mode, is present in graphite at 1,580 cm^{-1}. The observed lineshape for a semiconducting SWNT is very distinct from that of a metallic SWNT. Early studies on SWNT bundles using variable Raman excitation uncovered these distinct spectral lineshapes (*Pimenta et al.*, 1998) and provided a clear experimental proof for the predicted electronic structure (*Saito et al.*, 1992). (iii) The disorder-induced D-band, which is associated with any defect that breaks translational symmetry, and (iv) its second-order harmonic, the

G'-band. These latter bands are difficult to be studied in high-pressure set-ups, because their peaks interfere with the very strong Raman peaks (first and second order) from diamonds used in the pressure cell. Other set-ups with moisanite anvils can be used in that case (*del Corro et al.*, 2007).

3. Carbon Nanotubes Under Pressure

Without being exhaustive, there is an important theoretical (*Chan et al.,* 2003; *Chernozatonskii et al.*, 2002; *Elliott et al.*, 2004; *Reich et al.*, 2003; *Shanavas and Sharma*, 2009; *Sluiter and Kawazoe*, 2004; *Sluiter et al.*, 2002; *Zang et al.*, 2004) and experimental (*Caillier et al.*, 2008; *Freire et al.*, 2007; *Ghandour et al.*, 2008; *Kawasaki et al.*, 2004; *Loa*, 2003; *Merlen et al.*, 2005, 2009; *Puech et al.*, 2004; *Rols et al.*, 2001; *Sharma et al.*, 2001; *Thomsen et al.*, 1999; *Venkateswaran et al.*, 2001; *Yao et al.*, 2008) activity on the high pressure evolution of single-wall carbon nanotubes.

Let us first consider the pressure effects on the carbon nanotube electronic structure. Theoretical studies (*Gülseren et al.*, 2002) show, that in the elastic regime, and depending on the tube diameter, a radial deformation in zigzag nanotubes closes the band gap at the Fermi point. In other zigzag SWNTs, the band gap initially increases and then decreases, when strain exceeds a certain threshold value, so that eventually all zigzag tubes will undergo an insulator–metal transition in that regime. In contrast, in metallic nanotubes a radial deformation decreases the density of states at the Fermi level and a metal–semiconductor transition takes place (*Odom et al.*, 1998; *Wildoer et al.*, 1998). High-pressure Raman studies have proved experimentally the strong evolution of the electronic structure of carbon nanotubes. In fact, as explained previously, the Raman spectra of the semiconductor and metallic tubes of similar sizes have distinctive profiles of the G-band related to their different electronic structure. These profiles have been shown to become identical in bundled samples with a narrow tube diameter distribution at pressures above 15 GPa (*Merlen et al.*, 2005) when exciting the sample with two different laser wavelengths. Even if this observation cannot be generalized to all experimental conditions and samples, it shows that the resonance conditions can be strongly modified through pressure application.

In the case of single-wall carbon nanotubes, both theoretical works and experiments agree in pointing out the presence of pressure-induced structural instabilities, which should involve a modification of the nanotube cross-section. Evolution of the C-SWNT cross-section from circular to oval or polygonized followed by a collapse towards “peanut” section or other has been proposed. Most calculations agree on transition pressures scaling as

$1/d^3$, where d is the nanotube diameter, as in continuum medium theory. The scaling fails only for small nanotube diameters well below 1 nm.

The Raman signature associated with the structural changes of single-wall carbon nanotubes is the object of intense debate. Many aspects are related to the difficulties of obtaining a clear image, from which we can cite: (i) the nature of the studied samples, which represent a distribution of diameters and chiralities; (ii) the resonant character of carbon nanotubes, which implies that the tubes being in resonance can evolve with pressure; (iii) the nanostructured character of the samples having all atoms at the surface of the tubes and meaning that all carbon atoms can be in interaction with the pressure-transmitting medium; (iv) the possibility that the pressure-transmitting medium invades the interior of the nanotubes. In early works many of these aspects were not considered, and even the nanotubes size distribution was not reported, making interpretations difficult.

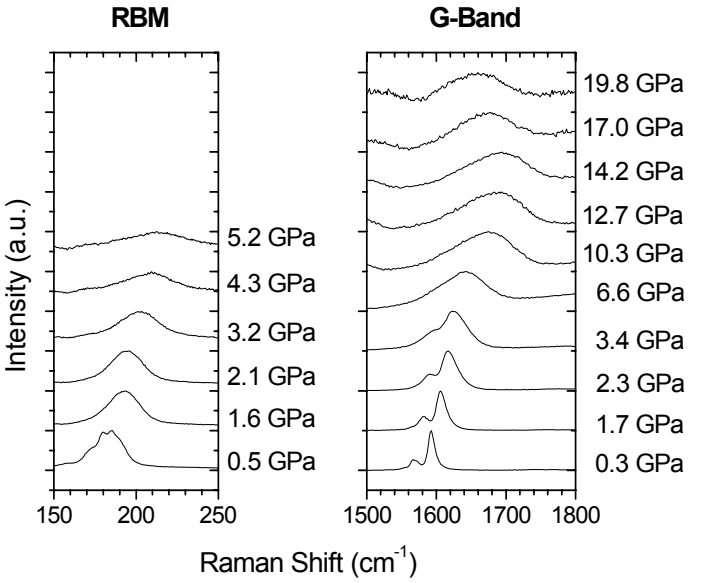

Figure 3. Evolution with pressure of the Raman RBM (*left panel*) and G-band (*right panel*) signal as a function of pressure for bundles of SWNT with a diameter of 1.35 ± 0.1 nm immersed in paraffin oil as pressure transmitting medium.

Both the frequency of the RMB modes and those of the G-band peaks evolve towards higher values under hydrostatic compression (Figure 3). Different changes in the Raman signature of carbon nanotubes related to this evolution have been or are being associated to structural or electronic modifications of carbon nanotubes. The main ones are:

(i) The total or sudden attenuation of the RBM signal
(ii) A discontinuity on the FWHM (full width at half maximum) evolution of the RBM
(iii) A discontinuity on the frequency of the G-band
(iv) A change of slope of the G-band evolution with pressure
(v) A plateau in the G-band pressure evolution eventually followed by a change of sign in the G-band pressure derivative

The observed changes in the Raman signal should be logically related both to the nanotube size, which drives the mechanical transition pressures and to the resonance conditions, which determine the observed Raman signal. In addition to the continuous evolution of resonance conditions with pressure, we shall also consider the discontinuous changes in resonance conditions associated to pressure-induced nanotube cross-section changes.

In the following, we discuss the possible origin of the pressure-induced Raman signal changes. The progressive continuous attenuation of the RBM signal is frequently observed, and, in general, the RBM are difficult to observe at pressures above 5–10 GPa, depending on the experiment. The pressure, at which total RBM attenuation is observed, depends on the resonance conditions, and it is not possible to attribute these pressure values to a nanotube phase transition (*Merlen et al.*, 2005). In fact, strain effects on individual carbon nanotubes have shown the progressive attenuation of the RBM (*Wook Lee et al.*, 2007). Sudden changes in the RBM intensity associated to changes in the G-band evolution have been also reported, which will be discussed later.

In a study of carbon nanotubes filled with fullerenes (systems also called "peapods"), the FWHM of the RBM showed a sudden pressure slope increase from a pressure of 2.5 GPa for carbon nanotubes of 1.45 nm of diameter. The same effect was observed for the same carbon nanotubes without fullerene filling (*Caillier et al.*, 2008). These observations appeared to be independent of the used pressure-transmitting medium. In the case of peapods, the observed change in the RBM evolution was followed at 3.5 GPa by a discontinuity of the pressure evolution of the characteristic Raman peaks of the fullerenes, which could be attributed to tube-fullerene interaction. Then, the RBM FWHM change can be reasonably attributed to a change in the evolution of the nanotube cross-section. An ovalization or a polygonization can be in agreement with several model calculations.

The observed changes in the pressure evolution of the G-band frequency with pressure are of many types, and they can take place, depending on the studies, in some cases at relatively low pressures (between 1 and 2 GPa) or at very high pressures (above 20 GPa) even for samples having, in principle, similar nanotube size distributions. Many possible reasons can

account for such a large scattering of behaviour. It has been recently shown (*Ghandour et al.*, 2008) that sudden decrease of dw_G/dP in the 1 GPa region was dependent on the excitation wavelength corresponding to the tubes of different diameter. On the other side, filling with argon of SWNT lead to a smooth evolution of w_G with pressure up to pressure values of 40 GPa, which could not be only described through a linear evolution (*Merlen et al.*, 2005). Discontinuities on dw_G/dP have been observed in SWNT bundles as in the previously discussed cases, but also in individualized tubes (*Freire et al.*, 2007). In this last case, the (1.34 ± 0.20) nm tubes were solubilised with a surfactant, which allows individualization of the nanotubes from the bundles by sonication. The 3 G-band components of the semiconducting tubes were followed up to 3 GPa. A discontinuity of the G-band pressure slope was observed at 2 GPa independently of the nature of the used surfactant including a change of sign for the slope of the lowest energy component of the G-band. Discontinuous changes in the G-band frequency evolution with pressure have been also observed in SWNT (*Ghandour*, 2009) or in double wall carbon nanotubes (DWNT) (*Puech et al.*, 2008).

The most common explanation of the origin of changes in the G-band or RBM in the low pressure 1–3 GPa region domain are phase transitions associated to the nanotube cross-section modification. Nevertheless, the exact understanding of the underlying reasons of the diversity of such changes, as well as the experimental proof on the nature of these modifications, remain a challenge. The different nature of the tubes (diameter and chirality distributions, presence of defects) associated to the resonant character of the Raman signal are possibly at the heart of such understanding.

The presence of a plateau on the G-band pressure dependence followed by a change of sign in its slope has been observed at higher pressures. In *Caillier et al.* (2008) it was shown, that such a transition is strongly dependent on the nature of the pressure-transmitting medium and can be related to the reversible collapse of the tubes, i.e., to a modification of the cross-section leading to an important proximity between opposite sides of the nanotube walls, in agreement with model calculations. The observed collapse transition could vary for the same system from 12 to almost 30 GPa depending on the pressure-transmitting medium. This scattering of values has been related to the mechanical properties of the nanocomposite system, in which the pressure-transmitting medium (solid at such a pressure!) acts as the matrix. In other cases (*Yao et al.*, 2008), a plateau in the G-band was observed, followed by a positive pressure slope. In that case, a sudden attenuation of the RBM related to the transition was observed. In this last work, calculations correlated this structural transition with a change of the nanotube cross-section from circular to an ellipse-like shape, and then to a flattened oval shape. Again, the nature of the phase

transition taking place at higher pressures and associated to the changes in the G-band evolution needs to be clarified.

Raman spectroscopy constitutes also a valuable tool for the study of the structural evolution of single-wall carbon nanotubes under high-pressure and high-temperature conditions. In fact, the elaboration of diamond has been experimentally performed recently for SWNT (*Merlen et al.*, 2009). The partial graphitization of 1.4 nm SWNT bundles could be readily observed from 12 GPa at 300 K with non-hydrostatic conditions. Total graphitization was observed at 12 GPa and 1,500 K; at about 14.5 GPa and 1,800 K the nanotubes irreversibly transformed into cubic diamond, which could be clearly identified from the characteristic Raman signal.

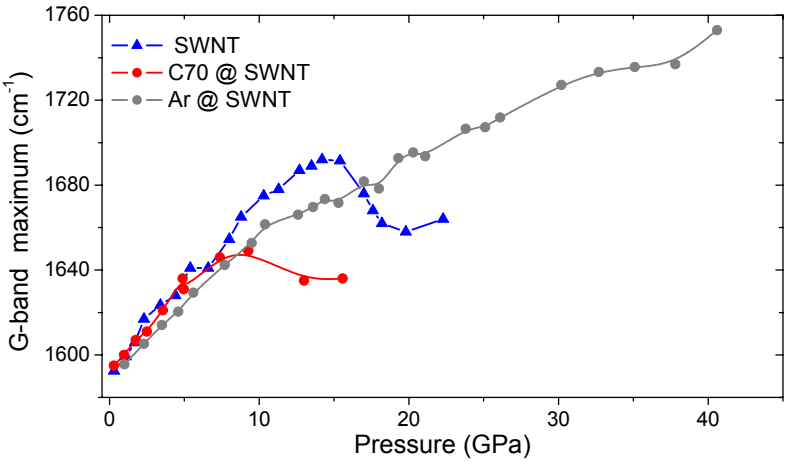

Figure 4. Effect of the homogeneous/inhomogeneous filling of carbon nanotubes on their pressure stability (see text for details). The evolution of the position of the maximum of the Raman G-band is shown for 1.4 nm diameter bundles of SWNT, bundles filled with C_{70} molecules and bundles filled with argon. Lines connecting data points are only guides for the eye.

Filling of carbon nanotubes is of particular interest also as a means to modify their mechanical properties. Recent investigations have shown that the topology of the endohedral filling of carbon nanotubes could determine the stability of the structure towards compression. Filling of carbon nanotubes with C_{70} fullerenes leads to the reduction in the pressure collapse of the structure (*Caillier et al.*, 2008). This is shown in Figure 4, in which the position of the maximum of the Raman G-band of 1.4 nm diameter bundles of SWNT is plotted as a function of pressure. A change in the sign of the pressure derivative of this evolution has been identified as the signature of the nanotubes collapse, which is seen to take place at about 15

GPa for the empty tubes. Filling the nanotubes with C_{70} molecules, which can be considered as a case of inhomogeneous filling, leads to a reduction on the collapse pressure, which can be pointed out at ~ 10 GPa. On the contrary, filling nanotubes with argon molecules, a case of homogeneous filling, leads to push the stability of carbon nanotubes to values beyond 40 GPa. Strain components arising from inhomogeneous filling, could be at the origin of such differences. These observations can be used to alter and improve the compressive mechanical quality of the composites based on the carbon nanotubes by their homogeneous filling.

4. Concluding Remarks

High-pressure Raman experiments in different forms of carbon nanotubes are playing an important role to gain a deeper insight in the high-pressure behaviour of nanomaterials. One important point that needs further investigation is how the evolution of mechanical properties and stability of the nanotube and its chemical interaction with its environment contribute to the evolution of the electronic properties of the nanotube. Up to now these contributions have never been separated, and this led to contradictions between experimental results and theoretical predictions. The knowledge of the two contributions (mechanical and chemical) simultaneously is fundamental in view of the applications of nanotubes, both as sensors in electronic devices and in the reinforcement structures as nanocomposite materials.

References

Bandow, S., Rao, A.M., Sumanasekera, G.U., Eklund, P.C., Kokai, F., Takahashi, K., and Iijima, S., 2000, Evidence for anomalously small charge transfer in doped single-wall carbon nanohorn aggregates with Li, K and Br, *Appl. Phys. A: Mater. Sci. Process.* **71:** 561.

Caillier, C., Machon, D., San-Miguel, A., Arenal, R., Montagnac, G., Cardon, H., Kalbac, M., Zukalova, M., and Kavan, L., 2008, Probing high pressure properties of single wall carbon nanotubes through fullerene encapsulation, *Phys. Rev. B* **77:** 125418.

Chan, S.-P., Yim, W.-L., Gong, X.G., and Liu, Z.-F., 2003, Carbon nanotube bundles under high pressure: Transformation to low-symmetry structures, *Phys. Rev. B* **68:** 07540.

Chernozatonskii, L., Richter, E., and Menon, M., 2002, Crystals of covalently bonded carbon nanotubes: Energetics and electronic structures, *Phys. Rev. B* **65:** 241404(R).

Del Corro, E., Gonzalez, J., Taravillo, M., Flahaut, E., and. Baonza, V.G, 2007, Raman spectra of double-wall carbon nanotubes under extreme uniaxial stress, *Nano Lett.* **8:** 2215.

Dresselhaus, M.S. and Eklund, P.C., 2000, Phonons in carbon nanotubes, *Adv. Phys.* **40:** 705.

Dresselhaus, M.S., Dresselhaus, G., Jorio, A., Souza Filho, A.G., and Saito, R., 2002, Raman spectroscopy on isolated single wall carbon nanotubes, *Carbon* **40:** 2043.

Elliott, J.A., Sandler, J.K.W., Windle, A.H., Young, R.J., Shaffer, M.S., 2004, Collapse of single-wall carbon nanotubes is diameter dependent*, Phys. Rev. Lett*. **92:** 095501.

Freire, P.T.C., Lemos, V., Lima, J.A., Saraiva, G.D., Pizani, P.S., Nascimento, R.O., Ricardo, N.M.P.S., Mendes, J., and Souza, A.G., 2007, Pressure effects on surfactant solubilized single-wall carbon nanotubes, *Phys. Stat. Sol. B* **244:** 105.

Ghandour, A.J., Dunstan, D.J., Sapelkin, A., Proctor, J.E., and Halsall, M.P., 2008, High-pressure Raman response of single-walled carbon nanotubes: Effect of the excitation laser energy, *Phys. Rev. B* **78:** 125420.

Ghandour, A., 2009, *Ph.D. Thesis*, Queen Mary University, London.

Gülseren, O., Yildirim, T., Ciraci, S., and Kilic¸ C., 2002, Reversible band-gap engineering in carbon nanotubes by radial deformation, *Phys. Rev. B* **65:** 155410.

Jorio, A., Saito, R., Hafner, J.H., Lieber, C.M., Hunter, M., McClure, T., Dresselhaus, G., and Dresselhaus, M.S., 2001, Structural (n;m) determination of isolated single-wall carbon nanotubes by resonant Raman scattering, *Phys. Rev. Lett*. **86:** 1118.

Kawasaki, S., Matsuoka, Y., Yao, A., Touhara, H., and Suito, K., 2004, High-pressure behavior of single-walled carbon nanotubes and polymerized fullerenes, *J. Phys. Chem. Sol.* **65:** 327.

Kukovecz, A., Pichler, T., Pfeiffer, R., and Kuzmany, H., 2002, Diameter selective charge transfer in p- and n-doped single wall carbon nanotubes synthesized by the HiPCO method, *Chem. Commun*. **5:** 1730.

Loa, I., Raman spectroscopy on carbon nanotubes at high pressure, *J. Raman Spectrosc*. **34:** 611.

Merlen, A., Bendiab, N., Toulemonde, P., Aouizerat, A., San Miguel, A., Sauvajol, J.-L., Montagnac, G., and Cardon, H., 2005, Resonant Raman spectroscopy of single wall carbon nanotubes under pressure, *P. Petit, Phys. Rev. B* **72:** 035409.

Merlen, A., Toulemonde, P., Le Floch, S., Montagnac, G., Hammouda, T., Marty, O., and San-Miguel, A., 2009, High pressure-high temperature synthesis of diamond from single-wall pristine and iodine doped carbon nanotube bundles, *Carbon* **47:** 1643.

Odom, T.W., Huang, J.-L., Kim, P., and Lieber, C.M., 1998, Atomic structure and electronic properties of single-walled carbon nanotubes, *Nature* **391:** 62.

Pimenta, M.A., Marucci, A., Empedocles, S., Bawendi, M., Hanlon, E.B., Rao, A.M., Eklund, P.C., Smalley, R.E., Dresselhaus, G., and Dresselhaus, M.S., 1998, Raman modes of metallic carbon nanotubes, *Phys. Rev. B* **58:** 16016.

Puech, P., Hubel, H., Dunstan, D.J., Bacsa, R.R., Laurent, C., and Bacsa, W.S., 2004, Discontinuous tangential stress in double-wall carbon nanotubes, *Phys. Rev. Lett*. **93:** 095506.

Puech, P., Ghandour, A., and Sapelkin, A., 2008, Raman G band in double-wall carbon nanotubes combining p doping and high pressure, *Phys. Rev. B* **78:** 045413.

Rao, A.M., Richter, E., Bandow, S., Chase, B., Eklund, P.C., Williams, K.A., Fang, S., Subbaswamy, K.R., Menon, M., Thes, A., Smalley, R.E., Dresselhaus, G., and Dresselhaus, M.S., 1997, Diameter-selective Raman scattering from vibrational modes in carbon nanotubes, *Science* **275:** 187.

Reich, S., Thomsen, C., and Ordejon, P., 2003, Elastic properties and pressure-induced phase transitions of single-walled carbon nanotubes, *Phys. Stat. Sol. B* **235:** 354.

Rols, S., Goncharenko, I.N., Almairac, R., Sauvajol, J.L., and Mirebeau, I., 2001, Polygonization of single-wall carbon nanotube bundles under high pressure*, Phys. Rev. B* **64:** 153401.

Saito, R., Fujita, M., Dresselhaus, G., and Dresselhaus, M.S., 1992, Electronic-structure of chiral graphene tubules, *Appl. Phys. Lett*. **60:** 2204.

Saito, R., Dresselhaus, G., and Dresselhaus, M.S., 1998, *Physical Properties of Carbon Nanotubes,* Imperial College Press, London, p 114.

San-Miguel, A., 2006, Nanomaterials under extreme conditions, *Chem. Soc. Rev*. **35:** 876.

Shanavas, K.V. and Sharma, S.M., 2009, Molecular dynamics simulations of phase transitions in argon-filled single-walled carbon nanotube bundles under high pressure*, Phys. Rev. B* **79:** 155425.

Sharma, S.M., Karmakar, S., Sikka, S.K., Teredesai, P.V., Sood, A.K., Govindaraj, A., and Rao, C.N.R., 2001, Pressure-induced phase transformation and structural resilience of single-wall carbon nanotube bundles, *Phys. Rev. B* **63:** 205417.

Sluiter, M.H.F. and Kawazoe, Y., 2004, Phase diagram of single-wall carbon nanotube crystals under hydrostatic pressure, *Phys. Rev. B* **69:** 224111.

Sluiter, M.H.F., Kumar, V., and Kawazoe, Y., 2002, Symmetry-driven phase transformations in single-wall carbon-nanotube bundles under hydrostatic pressure, *Phys. Rev. B* **65:** 161402(R).

Souza Filho, A.G., Kobayasi, N., Jiang, J., Gruuneis, A., Saito, R., Mendes Filho, J., Samsonidze, G.G., Dresselhaus, G., and Dresselhaus, M.S., 2005, Strain-induced interference effects on the resonance Raman cross section of carbon nanotubes, *Phys. Rev. Lett.* **95:** 217403.

Thomsen, C., Reich, S., Jantoljak, H., Loa, I., Syassen, K., Burghard, M., Duesberg, G.S., and Roth, S., 1999, Raman spectroscopy on single- and multi-walled nanotubes under high pressure, *Appl. Phys. A* **69:** 309.

Venkateswaran, U.D., Brandsen, E.A., Schlecht, U., Rao, A.M., Richter, E., Loa, I., Syassen, K., and Eklund, P.C., 2001, High pressure studies of the Raman-active phonons in carbon nanotubes, *Phys. Stat. Sol. B* **223:** 225.

Wildoer, J.W.G., Venema, L.C., Rinzler, A.G., Smalley, R.E., and Dekker, C., 1998, Electronic structure of atomically resolved carbon nanotubes, *Nature* **391:** 59.

Wook Lee, S., Jeong, G.-H., and Campbell, E.E.B., 2007, In situ Raman measurements of suspended individual single-walled carbon nanotubes under strain, *Nanoletters* **7:** 2590.

Yao, M.G., Wang, Z.G., Liu, B.B., Zou, Y.G., Yu, S.D., Lin, W., Hou, Y.Y., Pan, S.F., Jin, M.X., Zou, B., Cui, T., Zou, G.T., and Sundqvist, B., 2008, Raman signature to identify the structural transition of single-wall carbon nanotubes under high pressure, *Phys. Rev. B* **78:** 205411.

Zang, J., Treibergs, A., Han, Y., and Liu, F., 2004, Geometric constant defining shape transitions of carbon nanotubes under pressure, *Phys. Rev. Lett*. **92:** 105501.

HIGH-PRESSURE STUDIES OF ENERGETIC MATERIALS

COLIN R. PULHAM[1,*], DAVID I. A. MILLAR[1],
AND IAIN D. H. OSWALD[1], WILLIAM G. MARSHALL[2]
[1]*School of Chemistry and Centre for Science at Extreme Conditions, The University of Edinburgh, King's Buildings, West Mains Road, Edinburgh, EH9 3JJ, UK,* [2] *ISIS Neutron and Muon Facility, STFC Rutherford Appleton Laboratory, Harwell Science and Innovation Campus, Didcot, OX11 0QX, UK.*

Abstract High-pressure studies of energetic materials provide valuable information about how these compounds behave under the extreme conditions experienced during detonation. Spectroscopic and diffraction techniques, augmented by computational methods, provide insight into the effects of pressure on intermolecular interactions and phase transitions. Some examples of studies on representative compounds are presented here.

Keywords: Energetic materials, RDX, HMX, CL-20, FOX-7, ammonium perchlorate

1. Introduction to Energetic Materials

Energetic materials are defined as those that release heat and/or gaseous products at a high rate upon stimulus by heat, impact, shock, spark, etc. They can be broadly classified as explosives, propellants, gas generators, and pyrotechnics (*Akhavan*, 2004). These materials are used in a wide variety of applications that include: mining, munitions, rocket motors, space exploration, ejection systems, emergency generation of oxygen in submarines or space vehicles, airbags in automobiles, emergency signaling flares, anti-missile decoy flares, and fireworks. Explosives can be further classified as (a) primary explosives for which a mild impetus leads to a short, strong shock wave, and (b) secondary explosives for which a strong impetus leads to a long-duration shock wave. Primary explosives result in shock waves

* E-mail: C.R.Pulham@ed.ac.uk

E. Boldyreva and P. Dera (eds.), *High-Pressure Crystallography: From Fundamental Phenomena to Technological Applications*, DOI 10.1007/978-90-481-9258-8_36,

that have a strong local effect, but which do much less damage over longer distances and so their main function is to act as an initiator for the detonation of a secondary explosive. Examples of primary explosives include heavy metal compounds such as lead azide [$Pb(N_3)_2$], lead styphnate (lead 2,4,6-trinitroresorcinate), and mercury fulminate [$Hg(ONC)_2$]. These compounds are all very sensitive to friction, impact, and electrical discharge (spark). Once initiated, a secondary explosive liberates a large amount of energy and hence a sustained shock wave that causes more damage at a distance. Examples of secondary explosives include trinitrotoluene (TNT), HMX (1,3,5,7-tetranitro-1,3,5,7-tetrazacyclooctane), and RDX (1,3,5-trinitrohexahydro-1,3,5-triazine). The molecular structures of these compounds are shown in Figure 1.

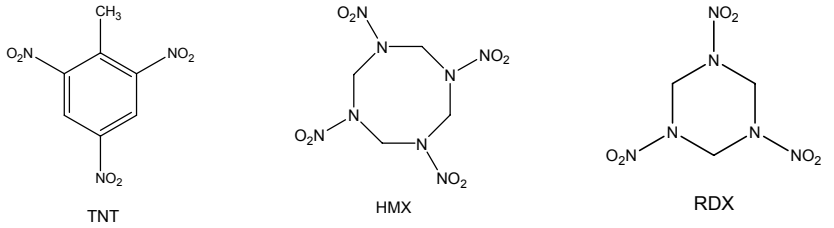

Figure 1. Molecular structures of TNT, HMX, and RDX.

Defining features of these molecules include the presence of oxidizing nitro-groups with an oxidizable hydrocarbon skeleton in close proximity, and a high percentage of oxygen and nitrogen, e.g. the empirical formula for HMX is $C_4H_8N_8O_8$. Explosive decomposition of 1 g HMX according to eq. 1 produces 908 cm^3 gaseous products (measured at STP).

$$C_4H_8N_8O_8 \rightarrow 4CO + 4N_2 + 4H_2O \quad (1)$$

During detonation of an explosive, a high velocity shockwave passes through the material and generates very high pressures and temperatures within the material. For HMX, the limiting detonation velocity is 9,100 m s^{-1} and the detonation pressure is 39 GPa. The performance of energetic materials can depend on a number of factors that include: sensitivity to detonation by stimulus; the rate of the deflagration-to-detonation transition (i.e. a burning reaction that changes to a much faster reaction); the detonation velocity and pressure; the chemical reactivity; the thermal and stability; the crystal density; and crystal morphology. Many of these factors depend on the solid-state structure of the energetic material and hence the performance of the material may be highly dependent on the particular polymorph that is used. The sensitivity of a crystal to shock can depend not only on the orientation of a crystal, but also on which polymorphic form is present. Thus HMX can exist as four crystalline forms (the γ-form is

actually a hydrated form rather than a true polymorph) and the sensitivity to impact is in the order $\delta > \gamma > \alpha > \beta$ (*Palmer and Field,* 1982). Different polymorphs may have substantially different densities; this is important because, to a first approximation, the detonation velocity of an energetic material is proportional to density. Where possible, the densest polymorph of an energetic compound is selected because many applications of energetic materials are volume limited. The crystal morphology of a given polymorph also governs how well the material can be processed and packaged, e.g. prismatic crystals pack more efficiently than crystals with rod, needle, or platelet morphologies. Solid–solid phase transitions in energetic materials are also important because crystals may develop surface and internal defects, and particle size may be reduced. It is generally true that the more defects in a crystalline explosive, the easier it is to initiate, because these defect sites are where explosive reaction is initiated. Thus the sensitivity of an energetic material to initiation is related to the number of defects in a crystal, and indeed a perfect crystal of a high explosive is a very poor explosive. Polymorphism and phase transitions can alter the sensitivity and performance of an energetic material in a complex manner, and since a key requirement for their use is reproducibility in performance, the polymorphic behavior of these materials has been extensively studied and has been summarized by Bernstein in an excellent review (*Bernstein*, 2005). A key priority for NATO munitions and propellants is the desire to reduce the risks of accidental initiation, i.e. there is a strong drive towards the development of what are termed “insensitive munitions”.

2. Why Study Energetic Materials at High Pressure?

A key requirement for energetic materials is the capability to model and understand their characteristics and performance under the extreme conditions of their operation. Hence substantial effort has been expended in studying the properties and chemistry of these compounds at high pressures and/or high temperatures. Comprehensive reviews of experimental and computational methods to characterize decomposition, combustion, and detonation of energetic materials have been published (*Peiris and Piermarini*, 2009; *Politzer and Murray*, 2003; *Shaw et al.*, 2005). Three general methods for the study of these materials at high pressures have been employed; (i) dynamic shock-wave studies, (ii) computational studies, and (iii) direct static compression. Shock-wave studies typically involve the use of a gas gun or explosive charge that fires a high-velocity projectile (velocities up to 8 km s^{-1} are attainable) at the material under study. When the projectile hits its target a shock wave propagates very rapidly through the material

generating pressures in excess of 100 GPa. Shock waves can also be induced by the action of high-power lasers on substrates to produce a high-pressure plasma that either acts directly on the material under study or launches a flyer plate into it. By measuring the propagation speed of the shock-wave front through the material and the jump in particle velocity across the front (i.e. the velocity of the material behind the front if the material ahead of the front is at rest), the relationship between the pressure, volume (or density), and temperature can be determined. Together these constitute the equation of state for the material.

Computational methods are particularly suited to the study of energetic materials since these allow a wide range of pressures and temperatures to be explored relatively easily, and have the potential to provide detailed information about rates and mechanisms of reactions occurring under extreme conditions. For practical reasons such information is often difficult to obtain from experiment. The ultimate aim of such studies is to be able to construct models that accurately predict the performance and characteristics of existing and new energetic materials (see chapter 9 by *Fried et al.* and chapter 11 by Rice in *Shaw et al.*, 2005).

Direct static compression generally involves compression of the sample in a diamond-anvil cell up to pressures of ~50 GPa and temperatures up to 650 K. The sample can then be studied *in situ* using spectroscopic and diffraction methods. Such studies provide direct information about equations of state, anisotropic changes in lattice parameters, the response of intermolecular interactions to pressure, and the identification and characterization of high-pressure polymorphs. In particular, the evolution of crystal structures as a function of pressure provides a means of testing the efficacy of theoretical modeling.

3. Studies of Selected Energetic Materials

3.1. RDX

RDX (1,3,5-trinitrohexahydro-1,3,5-triazine) is a widely used military explosive that can be compounded with mineral jelly or polymers to form plastic explosives such as C4 and PBX compositions. To date, four polymorphic forms have been structurally characterized under a wide range of pressures and temperatures. The structure of the orthorhombic α-form has been determined by both single crystal x-ray and neutron diffraction (*Choi and Prince*, 1972), and shows that the RDX molecule adopts a chair conformation in which two of the nitro-groups are in pseudo-axial positions and the other is in a pseudo-equatorial position – this is denoted as the AAE conformation (see Figure 2). β-RDX was first identified in 1950 by

crystallization from high boiling solvents such as nitrobenzene (*McCrone*, 1950), but on account of its high metastability it has eluded structural characterization until recently (*Millar et al.*, 2009).

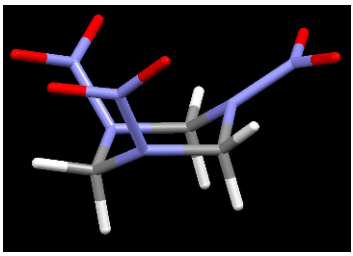

Figure 2. The AAE conformation adopted by α-RDX.

In the crystal structure of the β-form both independent molecules adopt the chair conformation with all nitro groups in axial positions (AAA conformation), resulting in approximate C_{3v} molecular symmetry (*Millar et al.*, 2009).

Compression of the α-form to pressures >3.9 GPa at ambient temperature gives the γ-form. A study using Raman spectroscopy up to 15 GPa proposed that the α→ γ phase transition leads to a rearrangement of the RDX molecules, which in turn significantly changes the intermolecular interaction experienced by the N–O bonds (*Dreger and Gupta*, 2007). The γ-form was recently structurally characterized by single crystal x-ray and neutron powder diffraction and the two independent molecules in the asymmetric unit of this structure adopt different conformations which are best described as AAA and AAI, respectively (see Figure 3), where I denotes an intermediate orientation of the NO_2 group midway between axial and equatorial positions (*Davidson et al.*, 2008).

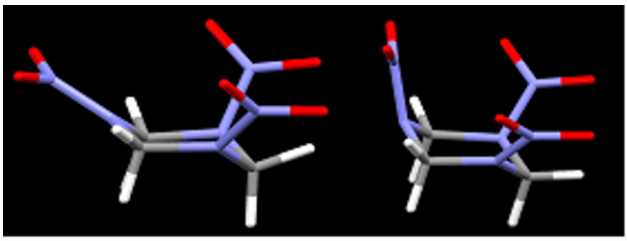

Figure 3. Conformations of the two independent molecules in γ-RDX.

Recent spectroscopic studies have also suggested a further high-pressure form obtained above 17.8 GPa at ambient temperature (*Ciezak et al.*, 2007b; *Ciezak and Jenkins*, 2008), which has been denoted the δ-form, but this has

not been structurally characterized. Two spectroscopic studies of RDX at elevated temperatures and pressures have suggested the presence of yet another form of RDX. *Baer et al.* (1990) observed a transition to a new form at pressures >3.8 GPa and a temperature of 375 K using liquid nitrogen as a pressure-transmitting medium. A later study by *Miller et al.* (1991) using Fluorinert as a pressure-transmitting medium also observed a transition at similar pressures, but at a higher temperature (488 K). Due to similarities in vibrational spectra and the observation that this form persisted on decompression at ambient temperature almost to ambient pressure, both studies concluded that the high-temperature/high-pressure form of RDX is the β-form. More recently, structural characterization of this high-temperature/high-pressure form using single crystal x-ray diffraction and neutron powder diffraction has identified it as ε-RDX in which, like the β-form, all of the nitro-groups are in axial positions (*Millar et al.*, unpublished results).

3.2. HMX

1,3,5,7-tetranitro-1,3,5,7-tetrazacyclooctane or cyclotetramethylene tetranitramine is one of the most widely used secondary explosives. Under ambient conditions, three polymorphs (α, β, and δ) and a hemihydrate are known and have been structurally characterized. Under ambient conditions, the β-form is the most stable. The high-pressure behavior of HMX has been summarized in a study that examined the pressure–volume relationship and Raman spectra of β-HMX under quasi-hydrostatic conditions up to 45 GPa using powder x-ray diffraction and micro-Raman spectroscopy (*Yoo and Cynn*, 1999). The study suggested a phase transition at 12 GPa with no abrupt volume change, and a discontinuous one at 27 GPa with a 4% volume change. X-ray powder diffraction studies have shown that compression of the β-form to 5.8 GPa at temperatures up to 140°C does not result in a phase transition, but on decompression a mixture of the β- and δ-forms is obtained (*Gump and Peiris*, 2005). Using an intermolecular potential developed for nitramines, molecular simulations have reproduced the effects of hydrostatic compression on the crystallographic lattice parameters of β-HMX up to 7.5 GPa (*Sorescu et al.*, 1999). The deflagration rate of HMX has been studied in a diamond-anvil cell over the pressure range 0.7–35 GPa and enhanced rates have been observed at pressures above 10 GPa (*Esposito et al.*, 2003).

3.3. CL-20

CL-20 (or hexanitrohexaazaisowurtzitane or HNIW) is currently the densest and most energetic organic compound that has practical use (see Figure 4

for molecular structure). Four well-characterized forms are known under ambient conditions, one of which (the α-form) is a hemihydrate.

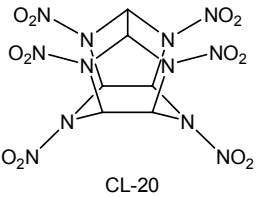

CL-20

Figure 4. Molecular structure of CL-20.

Under ambient conditions the stability sequence is ε > γ > α > β, although the β-form is more dense than the γ-form. In a comprehensive study using optical polarising microscopy and infrared spectroscopy the phase diagram and stability fields have been determined up to 623 K and 14.0 GPa (*Russell et al.*, 1993, and refs therein). The authors identified a new ζ-form that was obtained by compression of the γ-form above 0.7 GPa and demonstrated the different thermal decomposition temperatures associated with the different polymorphs. The high-pressure response of CL-20 has been examined to 27 GPa using vibrational spectroscopy. The results reveal evidence of an ε → γ pressure-induced phase transition between 4.1 and 6.4 GPa and suggest the existence of a γ → ζ transition near 18.7 GPa (*Ciezak et al.*, 2007a). Molecular simulations have successfully reproduced the effects of hydrostatic compression on the crystallographic lattice parameters of the ε-form up to 2.5 GPa (*Sorescu et al.*, 1999).

3.4. FOX-7

FOX-7 (1,1-diamino-2,2-dinitroethene) is a relatively new high explosive with a performance similar to RDX, but with a significantly better stability to heat, friction, and shock (see Figure 5 for molecular structure).

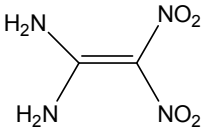

FOX-7

Figure 5. Molecular structure of FOX-7.

The crystal structures of an ambient and two high-temperature forms have been reported (*Bemm and Östmark*, 1998; *Crawford et al.*, 2007; *Evers et al.*, 2004). *Peiris et al.* (2004) have reported Raman and powder

x-ray diffraction studies up to 8.0 GPa to give an equation of state up to 4.2 GPa. Beyond this pressure the authors report that the material becomes amorphous, but it should be noted that these experiments were performed under non-hydrostatic conditions. Our own studies under *hydrostatic* conditions show no sign of amorphisation of a perdeuterated sample. Up to 4.2 GPa, compression of the b-axis is significantly greater than that of the a- and c-axes, reflecting the fact that the b-axis is perpendicular to the zig-zag layers of FOX-7 molecules (see Figure 6) (*Peiris et al.*, 2004).

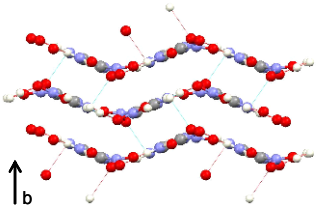

Figure 6. Layers of FOX-7 molecules in crystal structure of α-form.

3.5. AMMONIUM PERCHLORATE

Ammonium perchlorate (AP), $[NH_4]^+[ClO_4]^-$, is an energetic oxidizer that is widely used in solid rocket motors. When mixed with a polymeric binder and aluminium powder it forms a powerful propellant that is used by launch vehicles such as the NASA Shuttle and the ESA Ariane-5. At ambient temperature and pressure, AP adopts an orthorhombic crystal structure in which the NH_4^+ ions rotate freely. On heating to above 511–513 K, a reversible phase transition to a cubic structure has been observed in which there is almost unrestricted rotational reorientation of the perchlorate ions (*Stammler et al.*, 1966), and this transition has also been correlated with sudden changes in the reactivity of the compound (*Bircumshaw and Newman*, 1954). Over the years there has been a range of high-pressure studies on AP, the results of which have not always been consistent. These are summarized in an investigation that used energy-dispersive powder x-ray diffraction and IR and Raman spectroscopy up to a pressure of 5.6 GPa (*Peiris et al.*, 2000, and refs therein). In this study the authors observed one phase transition at about 0.9 GPa, which they attributed to a "freezing" of freely rotating NH_4 units, similar to the effects at low temperature, and a second phase transition near 3.0 GPa. A recent study has identified a pressure-induced phase transition at 4.1 GPa to give a structure in which the ammonium ions and perchlorate ions adopt a more close packed arrangement (see Figure 7) (*Davidson et al.*, 2007).

(a) 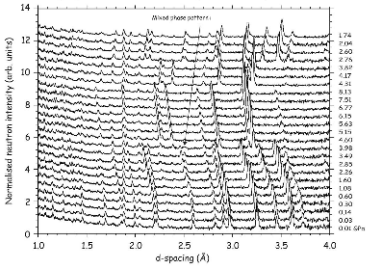

(b) 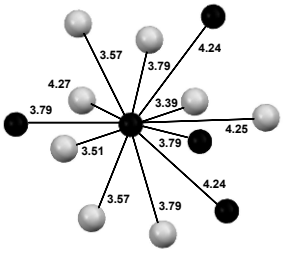

Figure 7. (a) sequence of neutron powder diffraction patterns obtained for ND_4ClO_4 and (b) environment of ammonium ions ion in high-pressure form of AP showing centroids formed by ND_4^+ and ClO_4^- ions (distances in Å).

4. Conclusions

Advances in the techniques for the collection and analysis of high-pressure x-ray and neutron diffraction data now permit the accurate determination of the full crystal structure of energetic materials under extreme conditions. Such information is crucial not only for the effective prediction of their behavior under operational conditions, but also to test the efficacy of theoretical modeling techniques applied to energetic materials. The level of complexity of structures that may be tackled is increasing and hence is opening up opportunities for the study at high pressure of more challenging molecular systems.

ACKNOWLEDGEMENTS

We thank the Defence Science and Technology Laboratory (through A. S. Cumming) and EPSRC for contributions toward a studentship (DIAM), the STFC for the provision of neutron and x-ray beamtime, the Leverhulme Trust for a fellowship (IDHO), and MOD WPE for funding under the terms of contract RD028-06366. We are grateful to D. R. Allan and S. Parsons for their contribution to the development of data collection and analysis strategies, and to A. R. Lennie, J. E. Warren, and D. J. Francis for instrument development at the SRS Daresbury Laboratory and the ISIS Neutron Facility.

References

Akhavan, J., 2004, in *The Chemistry of Explosives*, 2nd edn., Royal Society of Chemistry, Cambridge, UK.

Baer, B. J., Oxley, J., and Nicol, M., 1990, The phase diagram of RDX (hexahydro-1,3,5-trinitro-s-triazine) under hydrostatic pressure, *High Press. Res.*, **2**: 99–108.

Bemm, U., and Östmark, H., 1998, 1,1-Diamino-2,2-dinitroethylene: A novel energetic material with infinite layers in two dimensions, *Acta Cryst. C* **54:** 1997–1999.

Bernstein, J., 2002, in *Polymorphism in Molecular Crystals*, IUCr Monographs on Crystallography, Clarendon Press, Oxford.

Bircumshaw, L.L., and Newman B.H., 1954, The thermal decomposition of ammonium perchlorate. I. Introduction, experimental analysis of gaseous products, and thermal decomposition experiments, *Proc. Roy. Soc. London A*, **227:** 115–132.

Choi, C. S., and Prince, E., 1972, Crystal structure of cyclotrimethylenetrinitramine, *Acta Cryst., B* **28:** 2857–2862.

Ciezak, J.A., Jenkins T.A., and Liu Z., 2007a, Evidence for a high-pressure phase transition of ε- 2,4,6,8,10,12-hexanitrohexaazaisowurtzitane (CL-20) using vibrational spectroscopy, *Propellants, Explos. Pyrotech*., **32:** 472–477.

Ciezak, J.A., Jenkins, T.A., Liu, Z., and Hemley, R.J., 2007b, High pressure Raman spectroscopy of single crystals of hexahydro-1,3,5-trinitro-1,3,5-triazine (RDX), *J. Phys. Chem. A*, **111:** 59–63.

Ciezak, J.A., and Jenkins, T.A., 2008, The low-temperature high-pressure phase diagram of energetic materials: I. hexahydro-1,3,5-trinitro-s-triazine, *Propellants, Explos. Pyrotech.*, **33:** 390–395.

Crawford, M-J., Evers J., Göbel M., Klapötke T.M., Mayer P., Oehlinger G., and Welch J.M., 2007, γ-FOX-7: structure of a high energy density material immediately prior to decomposition, *Propellants, Explos. Pyrotech*., **32:** 478–495.

Davidson, A.J., Allan, D.R., Oswald, I.D.H., Pulham, C.R., Fabbiani, F.P.A., Francis, D.J., Marshall, W.G., Smith R.I., Cumming, A.S., Lennie, A.R., and Prior, T.J., 2007, High-pressure structural studies of energetic ammonium compounds. *Proceedings of the 38th International Annual Conference of ICT: Energetic Materials: Characterisaton and Performance of Advanced Systems,* Karlsruhe, Germany, 26–29 June 2007, 41/1–41/12.

Davidson, A.J., Oswald, I.D.H., Francis, D.J., Lennie, A.R., Marshall, W.G., Millar, D.I.A., Pulham, C.R., Warren, J.E. and Cumming, A.S., 2008, Explosives under pressure – the crystal structure of γ-RDX as determined by high-pressure X-ray and neutron diffraction, *Cryst. Eng. Comm.*, **10:** 162–165.

Dreger, Z.A., and Gupta Y.M., 2007, High pressure Raman spectroscopy of single crystals of hexahydro-1,3,5-trinitro-1,3,5-triazine (RDX), *J. Phys. Chem. B,* **111:** 3893–3903.

Esposito, A.P., Farber, D.L., Reaugh, J.E., and Zaug, J.M., 2003, Reaction propagation rates in HMX at high pressure, *Propellant., Explos., Pyrotech.*, **28:** 83–88.

Evers, J., Klapötke T.M., Mayer P., Oehlinger G., and Welch J., 2006, Alpha- and beta-FOX-7, polymorphs of a high energy density material, studied by x-ray single crystal and powder investigations in the temperature range from 200 to 423 K, *Inorg. Chem*., **45:** 4996–5007.

Gump, J.C., and Peiris, S.M., 2005, Isothermal equations of state of beta-octahydro-1,3,5,7-tetranitro-1,3,5,7-tetrazocine at high temperatures, *J. Appl. Phys*., **97:** 053513–053513/7.

McCrone, W.C., 1950, RDX (Cyclotrimethylenetrinitramine), *Anal. Chem.,* **22:** 954–955.

Millar, D.I.A., Oswald, I.D.H., Francis, D.J., Marshall, W.G., Pulham, C.R., and Cumming A.S., 2009, The crystal structure of β-RDX – an elusive form of an explosive revealed, *Chem. Commun*., **5:** 562–564.

Millar, D.I.A., Oswald, I.D.H., Francis, D.J., Marshall, W.G., Pulham, C.R., and Cumming, A.S., Pressure-cooking of explosives – the crystal structure of ε-RDX as determined by X-ray and neutron diffraction, unpublished results.

Miller, P.J., Block, S., and Piermarini, G.J., 1991, Effects of pressure on the thermal decomposition kinetics, chemical reactivity and phase behavior of RDX, *Combust. Flame*, **83**, 174–184.

Palmer, S.J.P., and Field, J.E., The deformation and fracture of β-HMX, *Proc. R. Soc. London A*, 1982, **383:** 399–407.

Peiris, S.M., and Piermarini, G.J., 2009, *Static Compression of Energetic Materials*, Springer, New York.

Peiris, S.M., Pangilinan G.I., and Russell T.P., 2000, Structural properties of ammonium perchlorate compressed to 5.6 GPa, *J. Phys. Chem. A* **104:** 11188–11193.

Peiris, S.M., Wong, C.P., and Zerilli, F.J., 2004, Equation of state and structural changes in diaminodinitroethylene under compression, *J. Chem. Phys*. **120:** 8060–8066.

Politzer, P., and Murray J.S., 2003, *Energetic Materials: Detonation, Combustion,* Elsevier, Amsterdam.

Russell, T.P., Miller P.J., Piermarini G.J., and Block S., 1993, Pressure/temperature phase diagram of hexanitrohexaazaisowurtzitane, *J. Phys. Chem*., **97**(9): 1993–1997.

Shaw, R.W., Brill, T.B., and Thompson, D.L., (ed), 2005, Overviews of recent research on energetic materials, *Adv.Series Phys. Chem.,* **16**, (World Scientific, Singapore).

Sorescu, D.C., Rice, B.M., and Thompson, D.L., 1999, Theoretical studies of the hydrostatic compression of RDX, HMX, HNIW, and PETN crystals, *J. Phys. Chem*., **103:** 6783–6790.

Stammler, M., Bruenner R., Schmidt W., and Orcutt D., 1966, Rotational polymorphism of methyl-substituted ammonium perchlorates, *Adv. X-ray Anal.,* **9:** 170–189.

Yoo, C.S., and Cynn, H., 1999, Equation of state, phase transition, decomposition of .beta.-HMX (octahydro-1,3,5,7-tetranitro-1,3,5,7-tetrazocine) at high pressures, *J. Phys. Chem*., **111:** 10229–10235.

AMORPHOUS MATERIALS AT HIGH PRESSURE

CHRYSTELE SANLOUP*
CSEC, University of Edinburgh, EH9 3JZ, Edinburgh,
Université Pierre et Marie Curie, 4 place Jussieu,
75252 Paris

Abstract This chapter reviews the different pathways towards high-pressure amorphization, how high-pressure amorphs may be characterized and what are the potential mechanisms causing pressure-induced amorphization and amorphous-amorphous transitions.

Keywords: Amorphs, structure, sulfur, pressure-induced amorphization

1. Introduction

1.1. AMORPHOUS MATERIALS

Amorphous materials are solids that have no long-order range at the atomic scale, a property they share with liquids as non-crystalline materials. There are several ways to synthesize amorphous materials, the most classical being quenching of a liquid which might require ultra-fast quenching techniques, chemical vapor deposition, or destructive methods such as irradiation or ball-milling.

This chapter will focus on amorphous materials synthesized under pressure from an initially solid sample, thereby excluding high P studies of non-crystalline materials synthesized at ambient conditions.

1.2. AMORPHIZATION UNDER PRESSURE

The application of static or dynamic pressures on a crystalline sample can lead to its amorphization. That process is called pressure-induced amorphization (PIA), and can happen upon increasing or releasing pressure (see *Sharma*

* E-mail: chrystele.sanloup@upmc.fr

E. Boldyreva and P. Dera (eds.), *High-Pressure Crystallography: From Fundamental Phenomena to Technological Applications*, DOI 10.1007/978-90-481-9258-8_37,

and Sikka, 1996 for a review) in conjunction with the crossing of a crystalline-crystalline phase transition (Figure 1). Applying pressure (P) on an amorphous material, whether itself formed by PIA or not, can induce an amorphous-amorphous transition (ATT) between a low density amorph (LDA) and a high density amorph (HDA). Such cases of polyamorphism may happen upon P increase or decrease and were for long thought to be restricted to tetrahedral framework materials. But sulfur was recently found to undergo AAT above 65 GPa and other examples are expected to follow with the expansion of the P–T conditions at which non-crystalline materials may now be explored.

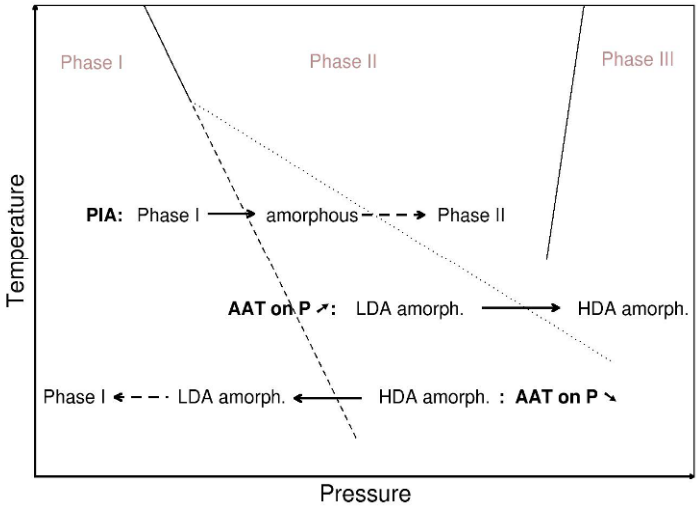

Figure 1. Schematics P-T path towards PIA and AAT. Continuous lines: thermodynamic phase boundaries, dashed arrows indicate potential re-crystallization.

Applied interests mostly reside in the perspective of synthesizing new categories of materials and potentially new nano-materials. The study of high-P amorphs is also largely fuelled by theoretical interests. Among those are the possibility to have first order transitions in non-crystalline materials, and using AAT as proxies for liquid–liquid transitions in the search for second critical points when that lies below the minimum crystallization T.

2. Characterization of Amorphous Materials at High Pressure

2.1. X-RAY AND NEUTRON SCATTERING

By definition, amorphous materials do not have long-range order and are therefore best characterized by diffuse scattering techniques, using either x-ray or neutron sources, giving access to their short-range structure. High-

pressure amorphs can often not be quenched, and if an amorphous material is indeed recovered, it might be different from the form synthesized at high P. Diffuse scattering studies must therefore be conducted *in situ* at high P, which can be challenging as non-crystalline materials are poor scatterers, and their poor signal is convoluted by a strong contribution from the high-pressure cell. The first *in situ* x-ray PIA study was conducted on SnI_4 (*Fujii et al.*, 1985), a material made of heavy, and therefore strongly scattering atoms. For lighter elements and up to very recently, the occurrence of PIA was concluded from the disappearance of crystalline diffraction peaks (*Hemley et al.*, 1988; *Akahama et al.*, 1993) rather than from the appearance of a diffuse signal. However, the latest advancements in synchrotron x-ray radiation techniques have overcome these difficulties and diffuse signals have been observed from amorphous materials as light as CO_2 (*Santoro et al.*, 2006) and nitrogen at 150 GPa (*Gregoryanz et al.*, 2007).

2.2. DENSITY MEASUREMENTS

The collapse of the crystalline structure upon PIA is accompanied by an important volume reduction. Density is therefore a critical property to measure; besides, it is the most direct method to resolve a controversial issue on the nature of AATs, *i.e.* first versus second order transitions? Polyamorphism in ice was first identified by a volume reduction in piston-cylinder experiments (*Mishima et al.*, 1985), the evolution of volume being monitored by the displacement of the piston inside the cylinder. More recent methods allow density measurements on non-crystalline materials up to the megabar range. Briefly, one method is to derive the density from the pair correlation function of the sample, itself extracted from the x-ray diffraction signal (*Eggert et al.*, 2002; *Sanloup et al.*, 2008). Another is based on x-ray absorption (*Sato and Funamori*, 2008). Despite these advancements, it is worth noting that under very high P and unlike structural and spectroscopic studies, density studies of amorphous materials remain a challenge.

2.3. OTHER DIAGNOSTICS

A number of other measurements, not specific to non-crystalline materials, might be usefully conducted on amorphous materials at high P to probe their vibrational (*e.g.* Raman and IR spectroscopies, inelastic scattering) or elastic properties (*e.g.* Brillouin spectroscopy, ultrasonic measurements), and the local structure around specific atoms (*e.g.* x-ray absorption spectroscopy) among others.

2.4. CHARACTERISTICS OF HIGH PRESSURE AMORPHS

In several cases which shall be highlighted here, high-P amorphs have properties that unlike for glasses are crystalline-like and often similar to those of the thermodynamically stable crystalline phase. The most general observation is the sharpness of the diffraction peaks of high-P amorphs compared to that of quenched glasses, indicative of a higher degree of local order. A non-exhaustive list of such crystalline-like properties follows (some examples of materials are given, with the crystalline counterpart when applicable):

- Local structure (LDA H_2O and Ice Ih; a-CO_2[†] and CO_2-V (*Santoro et al.*, 2006); LDA a-S and sulfur S-III, HDA a-S and S-IV (*Sanloup et al.*, 2008); a-ZrW_2O_8 and α -ZrW_2O_8, (*Keen et al.*, 2007); in the case of a-SnI_4, no inference was made on its structure except that it is markedly different from that of the liquid (*Fujii et al.*, 1985).
- Equations of state (HDA a-Si and Si-II (*Daisenberger et al.*, 2007); LDA a-S and S-III, HDA a-S and S-IV (*Sanloup et al.*, 2008), that is again very different from the case of glasses which are more compressible than their crystalline counterparts.
- Vibrational properties as probed by Raman spectroscopy (a-CO_2 and CO_2-V (*Santoro et al.*, 2006))
- T-dependence of the thermal conductivity (LDA H_2O (*Andersson and Suga*, 2002));
- Phonon density of states (LDA H_2O and Ice Ih (*Klug et al.*, 1999)).

Besides, some high-P amorphs preserve the memory of the initial crystallographic orientation, which gives rise to anisotropic properties.

3. Mechanisms of Pressure-Induced Amorphization

3.1. SIMPLE MOLECULAR SYSTEMS

3.1.1. *Cases of Sulfur and Nitrogen*

At least three forms of amorphous sulfur (a-S) have been identified as yet, none of which being stable at ambient P–T conditions. The first one is the ambient P quenched liquid, the two others resulting from PIA and further AAT (*Sanloup et al.*, 2008) at cryogenic T. These high P forms have been synthesized by compressing the molecular from of sulfur stable at ambient conditions (S-I) way out of its stability field. The experimental P–T field of

[†] From here, 'a-X' denotes the amorphous form of X.

a-S extends as T is lowered. Note that sulfur PIA was observed at room T in some works (*Akahama et al.*, 1993; *Luo and Ruoff*, 1993) but not in others which used a hydrostatic transmitting P-medium (*Hejny et al.*, 2005). Upon approaching amorphization, the quality of the diffraction patterns from crystalline S-I becomes poor indicating a largely defective structure; subsequent PIA is accompanied by a 25% density increase (Figure 2, left). a-S re-crystallizes with single-crystal like diffraction patterns upon further P or T increase.

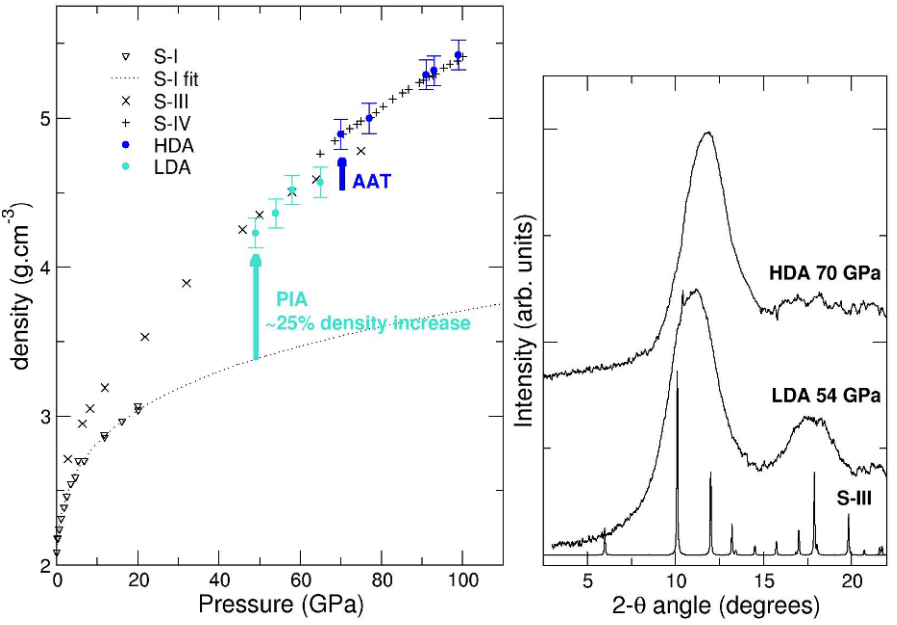

Figure 2. Density of a-S compared to crystalline phases (*right*). X-ray diffraction patterns from HDALDA and the simulated pattern of S-III at 54 GPa.

Nitrogen, an archetypal simple molecular system, was shown to undergo PIA above 140 GPa at room T (*Goncharov et al.*, 2000). a-N is non-molecular, semi-conducting, and transforms into the polymeric cubic-gauche phase upon heating (*Eremets et al.*, 2004). The transition to a-N and back to stable molecular N_2 phases is marked by a large hysteresis (*Eremets et al.*, *2001*; *Gregoryanz et al.*, *2001*); a-N cannot be recovered at ambient P–T conditions.

In both cases, PIA occurs from the compression of a molecular phase, the stable high-P phase being polymeric. Both S_8 rings, the basic unit of sulfur S-I, and triple-bonded N_2 molecules are very hard to break (and to reconstitute), hence their amorphization preempting their transformation to the stable crystalline phase.

3.1.2. *Characteristics of PIA*

The cases of sulfur and nitrogen point out some characteristics of PIA. First, PIA occurs when a parent phase is compressed beyond its thermodynamic stability field as the conversion to the high P crystalline phase is kinetically impeded. It generally occurs at low T which implies non-sufficient thermal energy to provide enough atomic mobility for the crystalline-crystalline phase transition to occur. Second, PIA is the precursor of the phase transformation to the high P crystalline polymorph. Third, PIA is accompanied by a large volume reduction.

3.2. COLD VERSUS MECHANICAL MELTING

PIA was first explained by cold melting (*Mishima et al.*, *1984*), *i.e.* by the crossing of the extended melting curve at high P. Water has a negative melting curve and its pressure extrapolation falls close to the conditions of the observed PIA. A mismatch was later evidenced (*Tse*, *1992*) but the situation is more striking for systems like SiO_2. Cold melting was invoked for the PIA of α-Qz (*Hemley et al.*, *1988*) on the basis of the extrapolation of Qz melting curve to much higher P. The curve flattens at high P, and PIA by cold melting requires further bending at higher P so that the curve becomes negative. However, more recent measurements of SiO_2 melting curve are difficult to reconcile as they require more bending than reasonable. An analysis of various materials undergoing PIA convincingly showed that there is no systematic relation between PIA and melting behavior (*Brazhkin et al.*, *1995*). There is nonetheless a systematic correlation with crystal–crystal transformation just above the amorphization T.

An alternative mechanism to cold melting is mechanical melting, *i.e.* the collapse of the structure due to the development of shear instabilities. Shear instabilities result from a violation of Born stability criteria, those criteria being a function of one or of a combination of elastic moduli. This mechanism has been evidenced in some systems through the measurement of elastic moduli softening (H_2O – *Brazhkin et al.*, 1995; SiO_2 – *Gregoryanz et al.*, 2000) or of phonon softening (H_2O – *Klug et al.*, 1999; *Strässle et al.*, 2004). However, the critical P at which the system will collapse is overestimated if using Born criteria.

3.3. DEFECTS

The cold melting mechanism refers to a homogeneous limit and thus defines an absolute limit for the crystalline structure to persist. The lattice can be destabilized at much lower P if defects are present (*Bustingorry and Jagla*,

2005). Theoretically, that was defended by a thermodynamical analysis showing that the structure collapses for a defect concentration higher than a critical value (*Fecht*, 1992). Experimentally, amorphization of Nb_2O_5 was shown to occur in conjunction with the formation of oxygen defects as the material gets reduced under P (*Serghiou et al.*, 1992). Increasingly defective x-ray diffraction patterns are also commonly observed upon approaching PIA.

3.4. X-RAY AMORPHS: TRUE AMORPHS OR NANO-CRYSTALLITES?

A recurrent question in the PIA literature is whether materials having 'x-ray amorphs' diffraction patterns are truly amorphs or are nano-crystallites, as the crystals might then be to small to be coherent to x-ray wavelengths (*Ivashchenko et al.*, 2007; *Yamanaka et al.*, 1997). As discussed generally before for PIA, the formation of nano-crystallites will result from the crossing of a phase transition at T cold enough to kinetically inhibit their growth (*Bustingorry*, 2005). A Scherrer fit of the x-ray diffraction pattern of LDA sulfur at 54 GPa gives a particle size of approximately 10 Å; a similar size is obtained for LDA ice by fitting neutron diffraction patterns with a crystalline structure (*S. Klotz*, personal communication). In the case of sulfur and water, 10 Å represents roughly three crystallographic cells. That might be a bit too small to define a crystal and consequently consider 'x-ray amorphs' as nano-crystalline materials.

4. Amorphous-Amorphous Transitions

4.1. CASE OF SULFUR

Sulfur LDA and HDA forms share a number of properties with their adjacent crystalline phases, S-III and S-IV (cf. 2.4). The most striking is their undistinguishable equations of state, with a 7% density jump at the transition (Figure 2, left). The local structure of the amorphous forms is also reminiscent of that of the crystalline phases (Figure 2, right) suggesting that both LDA and HDA are polymeric, and upon further P or T increase they re-crystallize into S-III and S-IV phases respectively.

4.2. GENERALIZATION

AAT has been most abundantly studied in the case of water since its discovery by *Mishima et al.* (1985). It is also the most often chosen system for the search a second critical point. Conflicting results have been obtained on several aspects such as the first versus second order nature of the H_2O AAT

(*Klotz et al.*, 2005; *Tulk et al.*, 2002), or the reproducibility of experimental results along a given P–T path. The occurrence of such controversies might not be surprising, given the complexity of the phase diagram of water with no less than ten phases described in the vicinity of the amorphous experimental P–T field. Such a complex phase diagram could also relate to the continuous structural evolution of HDA ice as a function of P (*Saitta et al.*, 2004), and unlike other amorphs, which show a uniform compression or dilatation of their structure. One shall recall here that choice was made in this chapter to exclude the study of non-crystalline materials synthesized at ambient P such as glasses. Those may undergo continuous structural changes, as illustrated by a smooth evolution of coordination numbers (*e.g.* from IV to VI for Ge in GeO_2 glass – *Itié et al.,* 1989; Si in SiO_2 – *Meade et al.*, 1992) accompanied by a continuous density increase (*e.g.* SiO_2 glass, *Sato and Funamori*, 2008), therefore undergoing second order AATs. However, if we discard those 'ambient P amorphous' cases, AAT have been reported to be first order transitions based on the observation of abrupt changes of their properties: Raman signal (Si – *Deb et al.*, 2001), structure (H_2O – *Klotz et al.*, 2005; Si – *Daisenberger et al.*, 2007), volume (H_2O – *Mishima et al.,* 1985; S – *Sanloup et al.*, 2008). Like PIA, AAT occur in conjunction with the conversion to a higher (or lower) P crystalline phase, and the LDA and HDA forms have properties similar to that of the low and high crystalline phases respectively in a number of occurrences (cf. 2.4). Besides, if the crystalline-crystalline phase transition involves a change of the electrical properties like a semi-conductor to metal transition, this is reproduced upon the AAT (Si – *McMillan et al.*, 2005). The crystalline-like properties observed in many high-P amorphs have been taken as an argument against the LDA/HDA transition being taken as a proxy for LDLiquid/HDLiquid transitions (*Tse et al.*, 2005).

5. Conclusions

A variety of materials transforms into amorphs under P as the transition towards a higher (or lower) P crystalline phase is kinetically inhibited due to the lack of thermal energy. Among those amorphous materials, many can not be recovered back to ambient conditions, or are quenched into another amorphous form. Even in the latter case, the pressure variable in P-T-time paths may be usefully tuned to synthesize high quality quenched amorphs (*i.e.* without any crystal) with improved kinetic stability at ambient conditions (*Yu et al.*, 2009). Applied to sulfur or organic compounds, that method is of potential large interest for the polymer industry.

References

Akahama, Y., Kobayashi, M., Kawamura, H., 1993, Pressure-induced structural phase transition in sulfur at 83 GPa, *Phys. Rev. B.* **48**: 6862–6864.

Andersson O., Suga H., 2002, Thermal conductivity of amorphous ices, *Phys. Rev. B.* **65**: 140201.

Brazhkin, V.V., Lyapin, A.G., Stalgorova, O.V., Gromnitskaya, E.L., Popova, S.V., Tsiok, O.B., 1997, On the nature of amorphous-to-amorphous and crystal-to-amorphous transition under high pressure, *J. Non-Cryst. Solids* **212**: 49–54.

Bustingorry S., Jagla E.A., 2005, Pressure-induced amorphization, crystal-crystal transformations, and the memory glass effect in interacting particles in two dimensions, *Phys. Rev. B.* **71**: 224119.

Daisenberger, D., Wilson, M., McMillan, P.F., Quesada Cabrera, R., Wilding, M.C., Machon, D., 2005, High-pressure X-ray scattering and computer simulation studies of density-induced polyamorphism in silicon. *Phys. Rev. B*, **75**: 224118.

Deb, S.K., Wilding, M., Somayazulu, M., McMillan, P.F., 2001, Pressure induced amorphization and an amorphous-amorphous transition in densified porous silicon, *Nature* **414**: 528–530.

Eggert, J.H., Weck, G., Loubeyre, P., Mezouar, M., 2002, Quantitative structure factor and density measurements of high-pressure fluids in diamond-anvil cells by X-ray diffraction: argon and water, *Phys. Rev. B.* **65**: 174105.

Eremets, M.I., Hemley, R.J., Mao, H.-K., Gregoryanz, E., 2001, Semiconducting non-molecular nitrogen up to 240 GPa and its low-pressure stability, *Nature.* **411**: 170–174.

Eremets, M.I., Gavriliuk, A.G., Trojan, I.A., Dzivenko, D.A., Boehler, R., 2004, Single-bonded cubic form of nitrogen, *Nat. Mater*. **3**: 558–563.

Fecht H. J., 1992, Defect-induced melting and solid-state amorphization, *Nature* **356**: 133–135.

Fujii Y., Kowaka, M., Onodera, A., 1985, The pressure-induced metallic amorphous state of SnI_4: I. A novel crystal-to-amorphous transition studied by X-ray scattering, *J. Phys. C: Solid State Phys*. **18**: 789–797.

Goncharov, A.F., Gregoryanz, E., Mao, H.-K., Liu, Z., Hemley, R.J., 2000, Optical evidence for a nonmolecular phase of nitrogen above 150 GPa, *Phys. Rev. Lett*. **85**: 1262–1265.

Gregoryanz, E., Hemley, R.J., Mao, H.-K., Gillet, P., 2000, High-pressure elasticity of α-Quartz: instability and ferroelastic transition, *Phys. Rev. Lett*. **85**: 3117–3120.

Gregoryanz, E., Goncharov, A.F., Hemley, R.J., Mao, H.-K., 2001, High pressure amorphous nitrogen, *Phys. Rev. B.* **64**: 052103.

Gregoryanz, E., Goncharov, A.F., Sanloup, C., Somayazulu, M., Mao, H.-K., Hemley, R.J., 2007, High P-T transformations of nitrogen to 170 GPa, *J. Chem. Phys.* **126**: 184505.

Hejny, C., Lundegaard, L.F., Falconi, S., McMahon, M.I., Hanfland, M., 2005, Incommensurate sulfur above 100 GPa. *Phys. Rev. B.* **71**: 020101.

Hemley, R.J., Jephcoat, A.P., Mao, H.K., Ming, L.C., Manghnani, M.H., 1988, Pressure-induced amorphization of crystalline silica, *Nature* **334**: 52–54.

Itié J.-P., Polian, A., Calas, G., Petiau, J., Fontaine, A., Tolentino, H., 1989, Pressure-induced coordination change in crystalline and vitreous GeO_2, *Phys. Rev. Lett.* **63**: 398–401.

Ivashchenko, V.I., Turchi, P.E.A., Shevchenko, V.I., 2007, Simulations of the mechanical properties of crystalline, nanocrystalline and amorphous SiC and Si, *Phys. Rev. B*. **75**: 085209.

Keen, D.A., Goodwin, A.L., Tucker, M.G., Dove, M.T., Evans, J.S.O., Crichton, W.A., Brunelli, M., 2007, Structural description of pressure-induced amorphization in ZrW_2O_8, *Phys. Rev. Lett*. **98**:225501.

Klotz, S., Strässle, Th., Nelmes, R.J., Loveday, J.S., Hamel, G., Rousse, G., Canny, B., Chervin, J. C., Saitta, A.M., 2005, Nature of the polyamorphic transition in ice under pressure, *Phys. Rev. Lett*. **94**: 025506.

Klug, D.D., Tulk, C.A., Svensson, E.C., Loong, C.-K., 1999, Dynamics and structural details of amorphous phases of ice determined by incoherent inelastic neutron scattering, *Phys. Rev. Lett*. **83**: 2584–2587.

Luo H., Ruoff A.L., 1989, X-ray diffraction study of sulphur to 32 GPa: amorphization at 25 GPa. *Phys. Rev. B*. **48**: 569–572.

McMillan, P.F., Wilson, M., Daisenberger, D., Machon, D., 2005, A density-driven phase transition between semiconducting and metallic polyamorphs of silicon, *Nat. Mater*. **4**: 680–684.

Meade, C., Hemley, R.J., Mao, H.K., 1992, High-pressure X-ray diffraction of SiO_2 glass, *Phys. Rev. Lett*. **69**: 1387–1390.

Mishima, O., Calvert, L.D., Whalley, E., 1984, 'Melting' ice I at 77 K and 10 kbar: a new method of making amorphous solids, *Nature* **310**: 393–395.

Mishima, O., Calvert, L.D., Whalley, E., 1985, An apparently first-order transition between two amorphous phases of ice induced by pressure. *Nature* **314**: 76–78.

Saitta, A.M., Strässle, T., Rousse, G., Hamel, G., Klotz, S., Nelmes, R.J., Loveday, J.S., 2004, High density amorphous ices: disordered water towards close packing, *J. Chem. Phys*. **121**: 8430–8434.

Sanloup, C., Gregoryanz, E., Degtyareva, O., Hanfland, M., 2008, Structural transition in compressed amorphous sulfur, *Phys. Rev. Lett*. **100**: 075701.

Santoro, M., Gorelli, F.A., Bini, R., Ruocco, G., Scandolo, S., Crichton, W.A., 2006, Amorphous silica-like carbon dioxide. *Nature* **441**: 857–860.

Sato, T., Funamori N., 2008, Sixfold-coordinated amorphous polymorph of SiO_2 under high pressure, *Phys. Rev. Lett*. **101**: 255502.

Serghiou G.C., Winters R.R., Hammack W.S., 1992, Pressure-induced amorphization and reduction of T-Nb_2O_5, *Phys. Rev. Lett*. 22: 3311–3314.

Sharma S.M., Sikka S.K., 1996, Pressure induced amorphization of materials, *Progr. Mater. Sci.* **40**: 1–77.

Strässle, Th., Saitta, A.M., Klotz, S., Braden, M., 2004, Phonon dispersion of ice under pressure, *Phys. Rev. Lett*. **93**: 225901.

Tse J.S., 1992, Mechanical instability in ice Ih, A mechanism for pressure-induced amorphization, *J. Chem. Phys*. **96**: 5482–5487.

Tse, J.S., Klug, D.D., Guthrie, M., Tulk, C.A., Benmore, C.J., Urquidi, J., 2005, Investigation of the intermediate- and high-density forms of amorphous ice by molecular dynamics calculations and diffraction experiments, *Phys. Rev. B*. **71**: 214107.

Tulk, C.A., Benmore, C.J., Urquidi, J., Klug, D.D., Neuefeind, J., Tomberli, B., Egelstaff, P.A., 2002, Structure studies of several distinct metastable forms of amorphous ice. Science, **297**: 1320–1323.

Yamanaka, T., Nagai, T., Tsuchiya, T., 1997, Mechanism of pressure-induced amorphization, *Z. Krist*. **212**: 401–410.

Yu, P., Wang, W.H., Wang, R.J., Lin, S.X., Liu, X.R., Hong, S.M., Bai, H.Y., 2009, Understanding exceptional thermodynamic and kinetic stability of amorphous sulfur obtained by rapid compression, *Appl. Phys. Lett*. **94**: 011910.

AMORPHOUS X-RAY DIFFRACTION AT HIGH PRESSURE: POLYAMORPHIC SILICON AND AMYLOID FIBRILS

PAUL F. MCMILLAN*, DOMINIK DAISENBERGER, RAUL QUESADA CABRERA, FILIP MEERSMAN
Department of Chemistry, University College London, 20 Gordon St., London WC1H 0AJ, U.K.
Department of Chemistry, Katholieke Universiteit Leuven, Celestijnenlaan 200 F, B-3001 Leuven, Belgium

Abstract Amorphous x-ray diffraction is used to obtain structural information on amorphous solids and liquids at high pressure as well as other materials without long range crystalline order including biologically important macromolecules and nanomaterials. The intense x-ray beams provided by synchrotron sources are ideal for diffraction studies of noncrystalline materials. We illustrate this with studies of the transition between low- and high-density forms of amorphous Si in the diamond anvil cell at high pressure, and the compressibility of amyloid fibrils.

Keywords: Amorphous x-ray diffraction, amorphous silicon, polyamorphism, amyloid fibrils, protein fibre diffraction

1. Introduction

X-ray diffraction is the primary technique for structure determination of crystalline solids. However, it is equally powerful for studying local and medium range order in amorphous solids or liquids, as well as other materials without perfect crystalline structures including biological macromolecules and nanoparticles (*Fischer et al.*, 2006; *Guinier*, 1994; *Greaves and Sen*, 2007; *Loerting and Giovambattista*, 2006; *Wilding and Benmore*, 2006). The advent of powerful synchrotron sources has revolutionised diffraction studies under extreme conditions of high pressure and high temperature because the

*E-mail: p.f.mcmillan@ucl.ac.uk

E. Boldyreva and P. Dera (eds.), *High-Pressure Crystallography: From Fundamental Phenomena to Technological Applications*, DOI 10.1007/978-90-481-9258-8_38,

intense x-ray beams can easily penetrate the sample environment and high quality data are obtained from very small samples (*Duffy*, 2005). Pioneering studies were conducted in the diamond anvil cell (DAC) and large volume devices at high pressure to study amorphous structures at high pressure (*Imai et al.*, 1996; *Meade et al.*, 1992). Recent studies use the onset of amorphous diffraction to signal melting in materials held under extreme high-P,T conditions (*Dewaele et al.*, 2007). Here we illustrate the application of x-ray amorphous diffraction in the DAC to two current problems in the study of non-crystalline materials at high pressure. The first involves the polyamorphic transition in amorphous silicon, between the low-density semiconducting and a new high density metallic polyamorph (*Daisenberger et al.*, 2007; *Deb et al.*, 2001; *McMillan et al.*, 2007; *Ponyatovsky and Barkalov*, 1992), and the second concerns the structural behaviour of "amyloid" protein and peptide fibrils important in protein misfolding diseases that also have remarkable mechanical properties (*Baldwin et al.*, 2006; *Chiti and Dobson*, 2006; *Dirix et al.*, 2005; *Grudzielanek et al.*, 2006; *Scheibel et al.*, 2003; *Smith et al.*, 2006; *Dobson*, 2003).

2. X-ray Scattering

When a beam of monochromatic x-rays falls onto a thin plate of material the primary beam is attenuated through absorption and scattering effects. In the former an incident x-ray photon is absorbed if the photon energy is close to an atomic absorption edge causing a transition to an excited electronic state: subsequent decay to the ground state results in emission of a photon with lower energy giving rise to fluorescence. Although absorption effects are ignored in most x-ray diffraction experiments these can affect the relative intensities of diffraction features. X-ray diffraction experiments can be designed using wavelengths close to elemental absorption edges to probe site-specific structural features via "anomalous" x-ray scattering techniques (*Fuoss et al.,* 1981). During elastic scattering the incident x-ray photon interacts with a bound electron forming a short-lived electron–photon pair and is re-emitted with the same energy but a change in direction giving rise to coherent scattering. X-ray diffraction results from interference effects between coherently scattered photons. Weakly bound electrons within the sample can also recoil and absorb some of the energy of the incident x-ray photons resulting in a shift to longer wavelengths producing incoherent or Compton scattering.

3. Crystalline X-Ray Diffraction and Synchrotron Experiments

In crystalline samples that display long range three dimensional periodicity the atoms are considered to define planes that partially reflect or transmit x-rays and thus act as atomic scale diffraction gratings for the x-ray beam. This results in the well known Bragg equation that relates the spacing between adjacent lattice planes (d) to the incident x-ray wavelength (λ) and the diffraction angle (θ):

$$n\lambda = 2d\sin\theta \tag{1}$$

Experiments conducted using monochromatic incident radiation are termed "angle dispersive" x-ray diffraction (ADXRD). These experiments are conventionally carried out using laboratory x-ray sources (e.g., Cu, Mo K_α) that provide specific x-ray wavelengths determined by the target. In the case of synchrotron radiation, a continuous range of x-ray wavelengths emanates from the source provided by a bending magnet or a "wiggler" array of magnets arranged in a N–S pattern along the direction of travel of the electron (or positron) beam contained within the ring. The result is a "white" beam that contains a very high intensity spectrum of x-ray wavelengths. If such a polychromatic incident source beam is used the intensity maxima in the scattered radiation spectrum are determined at fixed θ angle as a function of the energy. This constitutes an energy dispersive x-ray diffraction (EDXRD) experiment. The relation used to analyse EDXRD data is obtained by combining Eq (1) with Planck's law ($E = hc/\lambda$):

$$d = \frac{hc}{2E\sin\theta} \tag{2}$$

Planck's constant $h = 6.626 \times 10^{-34}$ Js, the speed of light $c = 2.998 \times 10^8$ ms^{-1} and θ is an angle fixed between the incident and sampled beam by a collimator placed before the detector. EDXRD was used in a pioneering study of a-SiO_2 at high pressure (*Meade et al.*, 1992). High pressure DAC experiments are now typically carried out using ADXRD at synchrotron sources (Figure 1).

The undeflected x-ray beam passing through the sample has very high intensity and would oversaturate the detector and so it is blocked by a cylindrical stop placed in the beam path: that corresponds to the dark (unexposed) spot in the centre of the image (bottom right). The spots and concentric rings from lattice reflections of polycrystalline samples are integrated and plotted as a function of 2θ or d spacing using a data analysis programme such as Fit2D. Only a few broad rings are observed in the diffraction patterns of amorphous solids and liquids (Figure 1). Background contributions must be systematically eliminated or carefully measured and

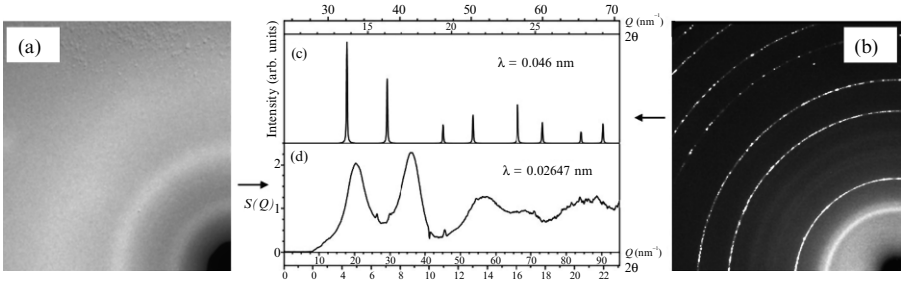

Figure 1. Monochromatic ADXRD images of amorphous (a) and polycrystalline Si (b) obtained using an image plate or CCD detector. Only the top left quadrants are shown. The a-Si pattern shows only a few diffuse rings. The data are integrated using Fit2D to plot intensity *vs* 2θ or *Q*. (c) is the integrated pattern from (b) after DAC background subtraction; (d) is *S*(*Q*) obtained from (a) following data processing described in the text.

subtracted in order to analyse the weak amorphous diffraction pattern. The x-ray scattering from amorphous materials is usually expressed as the reciprocal space correlation function *S(Q)* containing oscillations caused by interference effects between atom pairs with separations within a given range. A "first diffraction peak" (FDP) is also observed at low *Q* for amorphous materials correlated with nanoscale density fluctuations (*Elliot*, 1990; *Price et al.*, 1989) (Figure 2). *Q* is related to the x-ray wavelength and the scattering angle θ by:

$$Q = \frac{4\pi \sin\theta}{\lambda} \tag{3}$$

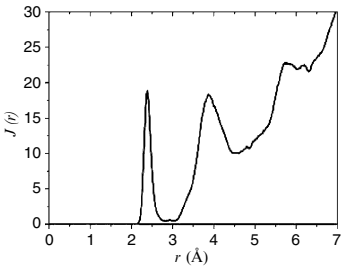

Figure 2. Radial distribution function *J(r)* for a-Si at ambient pressure.

4. Data Analysis and Theoretical Background

S(*Q*) is transformed into real space coordinates to yield a radial distribution function *J*(*r*) that expresses the number of atoms occurring at distances between *r* and *r* + *dr* from an arbitrary origin (*Fischer et al.*, 2006; *Zernicke and Prins*, 1927):

$$J(r) = 4\pi r^2 \rho(r) \tag{4}$$

$\rho(r)$ is defined to equal *0* below the minimal interatomic separation and is equivalent to the bulk density ρ_o at large *r*. Between these limits $\rho(r)$ exhibits oscillations due to short- and medium-range ordering within the amorphous material (Figure 2). The spherically averaged coherent scattering from an assembly of atoms is given by the Debye formula (*Debye,* 1915):

$$I^{coh}(Q) = \sum_1^N \sum_1^N f_n(Q) f_m(Q) \frac{\sin(Qr_{nm})}{Qr_{nm}} \tag{5}$$

where *f* is the atomic scattering factor and r_{nm} the distance between atoms *m* and *n*. For a monatomic system this reduces to:

$$I^{coh}(Q) = Nf^2(Q) + 2f^2(Q) \sum \sum_{n \neq m} \frac{\sin(Qr_{nm})}{Qr_{nm}} \tag{6}$$

Taking $4\pi r^2 \rho(r) dr$ as the average atoms in an interval *dr* from an arbitrary origin, and $\rho(r)$ the atomic density at distance *r*, the number of pairs of length *r* is $(N/2)\ 4\pi r^2 \rho(r) dr$ and the double sum is replaced by an integral:

$$I^{coh}(Q) = Nf^2(Q) + Nf^2(Q) \int_V 4\pi r^2 \rho(r) \frac{\sin(Qr_{nm})}{Qr_{nm}} dr \tag{7}$$

The integration is performed over the x-ray illuminated sample volume *V*. Introducing the average atomic density ρ_o:

$$I^{coh} = Nf^2 \left[1 + \int_V 4\pi r^2 [\rho(r) - \rho_o] \frac{\sin Qr_{nm}}{Qr_{nm}} dr + \rho_o \int_V 4\pi r^2 \frac{\sin Qr_{nm}}{Qr_{nm}} dr \right] \tag{8}$$

The last term involves small angle scattering that is usually obscured by the undeflected beam. The interference function, $S(Q)$, is given by:

$$S(Q) = \frac{I^{coh}(Q)}{Nf^2} = 1 + \int_0^\infty 4\pi r^2 [\rho(r) - \rho_o] \frac{\sin(Qr_{nm})}{Qr_{nm}} dr \tag{9}$$

This expression is Fourier transformed to find:

$$F(r) = 4\pi r[\rho(r) - \rho_o] = \frac{2}{\pi} \int_0^{Q_{\max}} Q[S(Q) - 1] \sin(Qr) dQ \tag{10}$$

where $F(r)$ is a real space distribution function. The corresponding pair distribution function $g(r)$ is given by:

$$g(r) = 1 + \frac{F(r)}{4\pi r \rho_o} \tag{11}$$

with $J(r) = 4\pi r^2 g(r)\rho_o$. (12)

5. Diamond Cell Experiments

In most DAC experiments the incident and scattered x-rays pass through the diamond windows and the maximum Q range is set by the incident x-ray wavelength and by the accessible angle for the scattered beam (Figure 3).

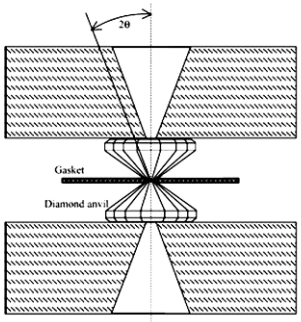

Figure 3. In the axial "through diamond" geometry generally used for synchrotron x-ray diffraction studies the accessible Q range is determined by the incident beam energy or wavelength and the opening angle (2θ) for the scattered x-ray beam from the sample (*Shen et al.*, 2007).

A large background signal can arise in all high-pressure scattering experiments as the x-ray beam passes through cell windows or assemblies containing the sample and these must be eliminated or carefully measured and subtracted before analysis of the amorphous diffraction data. In large press experiments this can be reduced using EDXRD with careful spatial collimation of the incident and scattered radiation (*Crichton et al.*, 2001) or by employing a Soller slit assembly (*Mezouar et al.*, 2002; *Yaoita et al.*, 2007). In ADXRD DAC experiments the background is measured independently and subtracted from the observed scattering (*Eggert et al.*, 2002). The experimentally observed scattering (I^{exp}) contains sample and background contributions:

$$I^{\exp}(Q) = T(Q)I^{samp}(Q) + sI^{bkgd}(Q) \tag{13}$$

The sample scattering (I^{samp}) passes through the down-stream diamond anvil and backing plate (Figure 3) hence is modified by a DAC transmission factor, $T(Q)$. This can be calculated from the cell geometry and the absorption coefficients of the diamond and backing plate materials at the operating wavelength. The background scattering (I^{bkgd}) contains Bragg peaks and Compton scattering from the diamond anvils. These background contributions are usually evaluated by recording an "empty" cell pattern by placing the cell including the gasket but without the sample back into the beam in exactly the same way as during the experiment and recording a background in the same conditions. It is often found that the scale factor s in Eq (13) must be adjusted due to variations in the incident beam intensity during the course of the experiment. Once the scattering from the sample is known it is expressed as a sum of coherent, Compton (incoherent) and multiple scattering contributions. Normalisation must be performed to report the intensity in electronic units required for Fourier transform of the interference function:

$$NI^{samp}(Q) = I^{coh}(Q) + I^{incoh}(Q) + I^{multiple}(Q) \tag{14}$$

The Krogh-Moe–Norman factor N is calculated as (*Krogh-Moe*, 1956; *Norman*, 1957):

$$N = \frac{-2\pi^2 n_0 Z^2 + \int_0^{Q_{\max}} ([f^2(Q) + I^{incoh}(Q)]Q^2)dQ}{\int_0^{Q_{\max}} [I^{samp}(Q)]Q^2 dQ} \tag{15}$$

Here n_0 is the average number density, Z the atomic number and f (Q) the atomic form factor. $Q^{\max}$ is the maximum extent for the integrations. The Compton contribution (I^{incoh}) is obtained theoretically (*Hadju*, 1972). Multiple scattering contributions are usually neglected in x-ray scattering experiments. The resulting interference function is:

$$S(Q) = \frac{1}{f^2(Q)}\left[NI^{samp}(Q) - I^{incoh}(Q)\right] \tag{16}$$

This is then Fourier transformed to give the real space distribution function $F(r)$. Errors arise from uncertainties in the normalisation procedure due to uncertainties in determining ρ_o at high pressure and the limited Q range of the integrals in the expression for N. Also atomic scattering factors are not known precisely over the whole Q range. Truncation errors due to the finite Q range involved in the Fourier transform of $S(Q)$ introduce unexpected oscillations in $F(r)$ (*Kaplow et al.*, 1965). An iterative method

for estimating $S(Q)$ and $F(r)$ within the experimental constraints of high pressure experiments in the DAC was developed by *Eggert et al.* (2002) based on pioneering work by *Kaplow et al.* (1965) and was used by *Shen et al.* (2004). In their work, *Eggert et al.* (2002) showed a method for extracting ρ_o and the background scale factor s from experimental x-ray scattering data that leads to the possibility of measuring densities of amorphous materials in the DAC at high pressure.

6. Polyamorphism in Amorphous Silicon

We now illustrate the application of amorphous synchrotron x-ray diffraction in the DAC at high pressure to study polyamorphism in a-Si. The field of polyamorphism in solid amorphous materials is related to the occurrence of density-driven liquid–liquid phase transitions thought to be present in a wide variety of substances (*Ponyatovsky and Barkalov*, 1992; *Angell*, 1995; *Brazhkin et al.*, 1997; *McMillan*, 2004; *Poole et al.*, 1997). The field began with observations of the high- and low-density (HDA, LDA) polyamorphic transformations of amorphous solid H_2O and both x-ray and neutron scattering have been carried out at high pressure to determine the structures of the two forms (*Loerting and Giovambattista*, 2006; *Angell*, 2004; *Bowron et al.*, 2006; *Mishima et al.*, 1985, 1998; *Nelmes et al.*, 2006). The polyamorphism is likely associated with an underlying density-driven liquid–liquid or liquid–fluid phase transition as observed for supercooled Y_2O_3–Al_2O_3 (*Aasland and McMillan*, 1994; *Wilding and McMillan*, 2001; *Wilding et al.*, 2002, 2006) and phosphorus at high pressure and temperature (*Katayama et al*., 2000, 2004; *Monaco et al*., 2003). We used synchrotron x-ray diffraction in the DAC to study the structural changes occurring in a-Si during the polyamorphic transition between its amorphous semiconductor (LDA) form to a new metallic polyamorph (HDA) as a function of pressure (*Imai et al.,* 1996; *Daisenberger et al.*, 2007; *Deb et al.*, 2001; *McMillan et al.*, 2007; *Ponyatovsky and Barkalov*, 1992).

We first determined the LDA-HDA transition in a-Si using Raman scattering combined with electrical conductivity studies, and later by ADXRD experiments at ESRF combined with MD simulations (*Daisenberger et al.*, 2007; *McMillan et al.*, 2007). The simulations permitted us to interpret the amorphous $S(Q)$ data and provided a link between the density-driven polyamorphism in the solid amorphous material and the liquid–liquid transition predicted to occur in the supercooled liquid state (*McMillan et al.*, 2007; *Ponyatovsky and Barkalov*, 1992; *Angell et al.*, 1996). For the amorphous diffraction study we did not use a pressure transmitting medium because its scattering would have had to be determined independently and

subtracted. We also did not add a pressure calibrant such as ruby to the run to avoid having additional strong crystalline reflections present along with the amorphous pattern. Instead, we carried out prior laboratory calibration of the He membrane pressure required to reach particular pressures in the DAC (*Daisenberger et al.*, 2007).

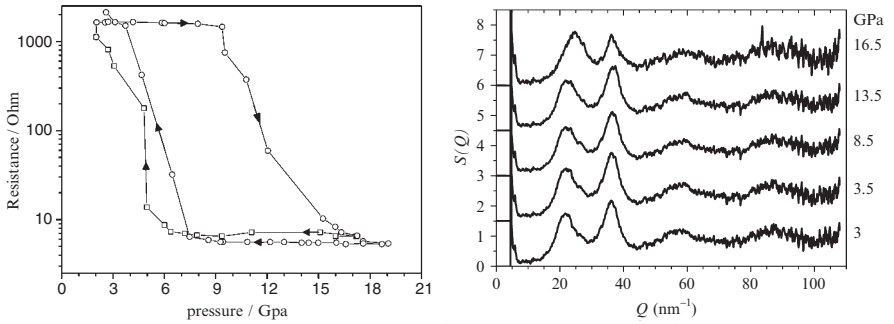

Figure 4. Left: Electrical resistance measurements carried out during the polyamorphic LDA-HDA transition in a-Si in the DAC as a function of pressure during compression and decompression cycles. *Right*: *S(Q)* data measured at ESRF ID15 during compression of a-Si showing the shift in position and change in relative intensity of the FDP and SDP signals during the polyamorphic transition (*Daisenberger et al.,* 2007; *McMillan et al.,* 2007).

At low pressure $S(Q)$ exhibits two main features: a first diffraction peak (FDP) at 2.18 $Å^{-1}$, and a second (SDP) at 3.63 $Å^{-1}$ (Figure 4). As P is increased the FDP moves to 2.23 $Å^{-1}$ then shifts abruptly to larger Q (2.48 $Å^{-1}$) and becomes more intense than the SDP (*Daisenberger et al.*, 2007). During microfocusing experiments carried out later at ID27, partly crystalline regions could be avoided (*McMillan et al.*, 2007). Fourier transformation of the low pressure *S(Q)* reveals *g(r)* features at 2.36 and 3.83 Å due to Si–Si distances within linked $SiSi_4$ tetrahedra. At high P, the FDP shifts to longer values and the SDP to ~3.40 Å consistent with higher coordinated species within the HDA polyamorph.

7. Amyloid Fibrils at High Pressure

Amyloid fibrils are fibrous structures that originate from the self-assembly of polypeptides. Their formation is linked to diseases associated with protein misfolding including Alzheimer's, Parkinson's and variant CJD (*Chiti and Dobson*, 2006; *Dobson*, 2003). In recent years, it has been suggested that such protein and peptide fibrils might provide novel nanoscaffolding materials due to their remarkable mechanical properties. Recent analyses

indicated that insulin and other fibrils possess high strength and stiffness parameters comparable to steel and silk. In our work we used synchrotron x-ray diffraction in a DAC to study the high-pressure stability and compressibility of mature amyloid fibrils of insulin and the transthyretin 105–115 (TTR) peptide that are useful model systems to study fibrillar structures and their formation.

The fibril structure is thought to consist of a cross-β arrangement in which the strands run perpendicular to the fibre and the β-sheets parallel to this axis, forming a protofilament. Several protofilaments are then wound together to form a fibril 60–70 Å across. Although the structure is highly organised it is not crystalline and x-ray diffraction patterns show only a few broad reflections (Figure 5). Most studies have been carried out for mature fibrils that have been dried and aligned on a stretch frame. Two main features observed in fibre diffraction studies are a "meridional" reflection at 4.7 Å that corresponds to the strand–strand distance along the fibre and a broad “axial” reflection at 10.8 Å that indicates the spacing between β-sheets normal to the fibre axis. Because of the alignment procedure the rings observed in the monochromatic diffraction pattern are not complete. In our case we studied unaligned fibrils and full Laue rings were observed (Figure 5).

Fibrils prepared from insulin and the TTR105-115 peptide were loaded into a DAC using H_2O or silicone oil and ADXRD data were collected at the ESRF Swiss–Norwegian beamline. Observation of both axial and meridional reflections permitted calculation of the molar volume that we analysed to obtain compressibility values for the fibrils. Important differences observed between experiments carried out in H_2O and silicone oil revealed interesting features of the structure and its interaction with aqueous versus non-aqueous environments.

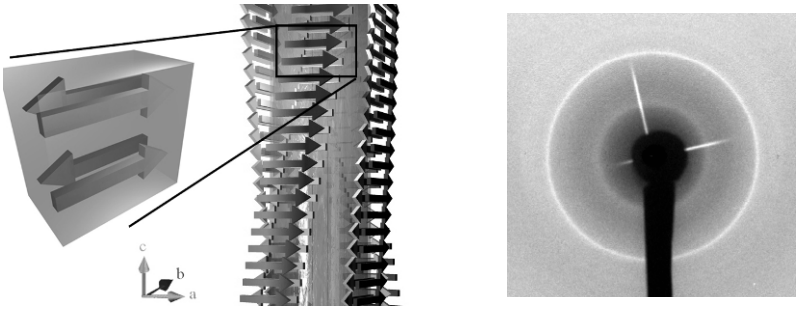

Figure 5. Structural model for amyloid protein fibrils showing the cross-β sheet assembly. *Right*: monochromatic diffraction pattern obtained in the DAC for amyloid fibrils at high pressure.

ACKNOWLEDGEMENTS

PFM acknowledges support from EPSRC SRF EP/D07357X and Portfolio EP/D504782 (joint with C.R.A. Catlow and P. Barnes). FM is a postdoctoral research fellow of the Research Foundation Flanders (FWO-Vlaanderen). DD is now supported by the Institute of Shock Physics. The work presented here is based on the Ph.D. theses of DD and RQC (*Daisenberger*, 2009; *Quesada Cabrera*, 2009). We thank V. Dmitriev (SNBL) and M. Mezouar ID27 at ESRF (Grenoble) for assistance with experiments.

References

Aasland S., P. F. McMillan, *Nature,* 369, 633 (1994).
Angell C. A., *Science,* 267, 1924 (1995).
Angell C. A., *Ann Rev Phys Chem,* 55, 559 (2004).
Angell C. A., S. Borick, M. Grabow, *J Non-Cryst Solids,* 205–207, 463 (1996).
Baldwin A. J., R. Bader, J. Christodoulou, C. E. MacPhee, C. M. Dobson, P. D. Barker, *J Am Chem Soc,* 128, 2162 (2006).
Bowron D. T., J. L. Finney, A. Hallbrucker, I. Kohl, T. Loerting, E. Mayer, A. K. Soper, *J Chem Phys,* 125, 194502 (2006).
Brazhkin V. V., S. V. Popova, R. N. Voloshin, *High Press Res,* 15, 267 (1997).
Chiti F., C. M. Dobson, *Ann Rev Biochem,* 75, 333 (2006).
Crichton W. A., M. Mezouar, T. Grande, S. Stolen, A. Grzechnik, *Nature,* 414, 622 (2001).
Daisenberger D., *Transformations Among Metastable Amorphous and Crystalline Forms of Silicon* (Ph.D. thesis, University College London, 2009).
Daisenberger D., P. F. McMillan, M. Wilson, D. Machon, R. Quesada-Cabrera, M. C. Wilding, *Phys Rev B,* 75, 224118 (2007).
Deb S. K., M. C. Wilding, M. Somyazulu, P. F. McMillan, *Nature,* 414, 528 (2001).
Debye P., *Ann Phys,* 46, 809 (1915).
Dewaele A., M. Mezouar, N. Guignot, P. Loubeyre, *Phys Rev B,* 76, 144106 (2007).
Dirix C., F. Meersman, C. E. MacPhee, C. M. Dobson, K. Heremans, *J Mol Biol,* 347, 903 (2005).
Dobson C. M., *Nature,* 426, 2003).
Duffy T. S., *Rep. Progr. Phys.,* 68, 1811 (2005).
Eggert J. H., G. Weck, P. Loubeyre, M. Mezouar, *Phys Rev B,* 65, 174105 (2002).
Elliot S. R., *Physics of Amorphous Materials* (Longman, London, 1990).

MICROPOROUS MATERIALS AT HIGH-PRESSURE: ARE THEY REALLY SOFT?

G. DIEGO GATTA*
Dipartimento di Scienze della Terra, Università degli Studi di Milano, Via Botticelli 23, I-20113 Milano, Italy

Abstract This is a review of the elastic behaviour and pressure-induced structural deformation mechanisms of zeolites, based on previously reported data. The relationship between microporosity and compressibility, the relationship between framework topology and principal *P*-induced structural deformation mechanisms, the *P*-induced over-hydration processes and the effect of the channel contents (*i.e.* nature of the cations and ionic valence, ionic radii, coordination number) on the elastic behaviour of this class of materials are discussed.

Keywords: Microporous materials, open-framework silicates, zeolites, high-pressure, elastic behavior, compressibility, phase-transitions, *P*-induced over-hydration

1. Introduction

Microporous materials form a class of compounds characterised by open framework structures, whose pores, in the form of channels or cages, have "free diameters" (*Baerlocher et al*., 2001) shorter than 20 Å. Materials with pores larger than 20 Å are commonly defined as "mesoporous materials". Zeolites, for example, are microporous framework materials. In nature, zeolites are found in several geological environments. Their crystal structure consists of a framework made by linked SiO_4–AlO_4–PO_4–tetrahedra. The tetrahedron is defined as the "primary building unit" of a zeolitic framework. Zeolite frameworks can also be viewed as an assemblage of polytetrahedral units. These units are usually defined as "secondary building units", which contain up to 16 tetrahedra. The number of the SBU's, which have been

*E-mail: diego.gatta@unimi.it

E. Boldyreva and P. Dera (eds.), *High-Pressure Crystallography: From Fundamental Phenomena to Technological Applications*, DOI 10.1007/978-90-481-9258-8_39,

observed up to the present time, is 20. A unit-cell always contains an integral number of SBU's.

Each zeolitic framework type contains open cavities, in which the channel content ("extra-framework content") lies. The presence of cavities is responsible for the low framework density (FD) of zeolites, which is defined as the number of tetrahedrally coordinated atoms (T-atoms) per 1,000 Å^3. For this class of materials, FD is lower than 20 T/1,000 Å^3. In natural zeolites, the channel content is usually represented by H_2O molecules and monovalent or bivalent cations, which are commonly exchangeable. In hydrated zeolites, dehydration occurs at temperatures lower than 400°C and is usually reversible (*Armbruster and Gunter,* 2000; *Coombs et al*., 1997; *Gottardi and Galli,* 1985). The general formula for common Si/Al-zeolites is:

$$A^{+}_{x} B^{2+}_{y} [Al_{(x+2y)} Si_{n-(x+2y)} O_{2n}] \cdot mH_2O \quad \text{(usually with } m < n\text{)}.$$

Zeolites with B-, Be-, Ga- and Ge-tetrahedral cations have been successfully synthesised. The cation-exchange capacity, the ionic conductivity, the reversible thermal transformations, the catalytic properties and some newly discovered photoluminescent features have made zeolites, and other microporous and mesoporous materials, an object of attention for their advanced technological applications. On this basis, the behaviour at high/low-temperature conditions of this class of open-framework materials has been investigated extensively. A few experiments have been devoted to the high-pressure (*HP*) behaviour and *HP*-induced structure evolution of zeolites or zeolite-like materials. Experiments on zeolites under pressure have been performed by in-situ X-ray/neutron powder and single-crystal diffraction or vibrational spectroscopies (IR/Raman) with diamond anvil cells or the large Paris–Edinburgh press (*Gatta*, 2008, and references therein). A limited number of experiments have also been devoted to the effect of pressure on the ionic conductivity of zeolites and to the *HP*-induced amorphization processes (*Gillet et al*., 1996; *Greaves et al.*, 2003; *Goryainov*, 2005; *Gulìn-Gonzàles and Suffritti*, 2004; *Huang and Havenga*, 2001; *Rutter et al*., 2000, 2001; *Secco and Huang*, 1999). Integrated theoretical and experimental approach have been also used to describe the *P*-induced structural evolution of some zeolites (*Ballone et al.*, 2002; *Betti et al.*, 2007; *Ferro et al.*, 2002; *Fois et al.*, 2005, 2008; *Gatta and Wells*, 2004, 2006; *Gatta et al*., 2009; *Sartbaeva et al*., 2008).

Some recent experiments have shown that the high-pressure behavior of microporous (and mesoporous) materials may be strongly influenced by the nature of the *P*-transmitting media used for the experiments: *i.e.* "penetrating"

or "non-penetrating" *P*-media (*Lee et al.*, 2002a, b, 2004a, b; *Likhacheva et al.*, 2007a, b; *Ori et al.*, 2008; *Seryotkin et al.*, 2005). Penetrating media represent a class of fluids that can penetrate into the zeolitic micropores at *HP*, implying a strong influence on the elastic behavior and on the *HP*-induced structural evolution of the open-framework materials. Water, for example, is able to penetrate micropores. Water-bearing *HP*-media (*e.g.* as the mix ethanol:methanol:water = 16:3:1) or elemental gaseous media (*e.g.* helium, nitrogen, neon, argon, xenon) are potentially penetrating media. Complex and larger molecules than water (methanol, ethanol, isopropanol, glycerol, silicon–oils, perfluorether, fluorinert FC-75), or solid media at room conditions (*e.g.* NaCl, KCl), are nominally non-penetrating media. According to *Gatta* (2008), the *HP*-induced penetrability is controlled by several variables: (1) the "free diameters" (*Baerlocher et al.*, 2001) of the framework channels; (2) the nature of the channel content, and (3) the $P(H_2O)$, due to the amount of water contained in the *P*-media. The *P*-induced penetration processes opened a new scenario in the use of microporous materials: the sorption selectivity, governed by the channels/cages configurations, makes these materials excellent "nano-reactors", since space confinement could also lead to the formation of (low-dimensionality) supramolecular systems (*Fois et al.*, 1999).

The aim of this work is a review of the *HP*-behaviour of natural and synthetic zeolites in order to analyse: (1) their elastic behaviour, (2) the relationship between microporosity and compressibility (and in particular the relationship between shape and orientation of the cavities and elastic anisotropy), (3) the relationship between framework topology and principal *P*-induced structural deformation mechanisms, (4) the *P*-induced over-hydration processes and (5) the effect of the channels content (*i.e.* nature of the cations and ionic valence, ionic radii, coordination number) on the elastic behaviour of this class of materials, on the basis on published data.

2. Compressional Behavior and Stability Field of Zeolites

For a comparative elastic analysis of zeolites investigated at high-pressure, the (volume) compressibilities have been here recalculated using the Birch–Murnaghan Equation-of-State (BM-EoS, *Birch*, 1947; *Angel*, 2000), because in previous studies the elastic parameters have been calculated simply by linear regression of *P–V* data, or by using different isothermal EoS adopting different weighting schemes for the EoS-fit (using weighted or un-weighted data by the uncertainties in *P* and *V*). The BM-EoS is based upon the assumption that the high-pressure strain energy in a solid can be expressed as a Taylor series in the Eulerian finite strain,

$$f_E = [(V_0/V)^{2/3} - 1]/2 \quad (1)$$

(V_0 and V represent the cell volume, or molar volume, under room and *HP* conditions respectively). Expansion in the Eulerian strain polynomial truncated to the fourth-order (in energy) has the following form:

$$P = 3K_0 f_E (1+2f_E)^{5/2} \{1 + 1.5(K' - 4) f_E + 1.5[K_0K'' + (K' - 4)\cdot (K' - 3) + 35/9] f_E^2\}, \quad (2)$$

where K_0 represents the bulk modulus [$K_0 = -V_0(\partial P/\partial V)_{P=0} = 1/\beta_0$, where β_0 is the volume compressibility coefficient], $K' = (\partial K_0/\partial P)$ and $K'' = (\partial^2 K_0/\partial P^2)$. According to *Gatta* (2008), for low-P values and/or for $V_0/V <$ 10%, a truncated second-order BM-EoS can be adequately used for fitting the experimental data. In this case, the refinable parameters are only V_0 and K_0 (*i.e.* K' is fixed to 4).

TABLE 1. Elastic parameters of zeolites

	Framework type	FD (T/1000Å^3)	K_0 (GPa)	K'	$K_0(a) : K_0(b) : K_0(c)$	*Note*	*Ref.*
Natrolite	NAT	17.8	43(2)	4.0	1.10 : 1 : 3.73	*P*>~1 GPa [*Fdd*2]	*Gatta* (2005)
Scolecite	NAT	17.8	54.6(6)	4.0	1.43 : 1 : 1.04	[*Cc*]	*Gatta* (2005)
Thomsonite	THO	17.7	49(1)	4.0	1 : 1.08 : 2.60	[*Pncn*]	*Gatta* (2005)
Edingtonite	EDI	16.6	59.3(4)	4.0	1 : 1 : 1.71	[$P\bar{4}2_1m$]	*Gatta* (2005)
			59.3(2)	4.0	1 : 1.00 : 1.43	[$P\,2_12_12$]	
Analcime	ANA	18.5	56(3)	4.0	1 : 1 : 1	*P*<1.0(8) GPa [$Ia\bar{3}d$]	*Gatta et al.* (2006)
			19(2)	6.8(7)	2.64 : 1.82 : 1	*P*>1.0(8) GPa [$P\bar{1}$]	
Leucite	ANA	18.5	41.9(6)	4.0	1 : 1 : 2.26	*P*<2.5(3) GPa [$I4_1$/a]	*Gatta et al.* (2008)
			33.2(5)	4.0	1.03 : 1 : 1.02	*P*>2.5(3) GPa [$P\bar{1}$]	
Pollucite	ANA	18.5	41(2)	4.0	1 : 1 : 1	*P*<0.7(1) GPa [$Ia\bar{3}d$]	*Gatta et al.* (2009)
			25.1(9)	6.5(4)	1.10 : 1 : 1.09	*P*>0.7(1) GPa [$P\bar{1}$]	
Wairakite	ANA	18.5	39(3)	4.0	1.38 : 2.69 : 1	*P*<2.8(4) GPa [*I*2/*a*]	*Ori et al.* (2008)
			24(3)	4.0	2.92 : 6.11 : 1	*P*>2.8(4) GPa [$P\bar{1}$]	
Laumontite	LAU	17.8	59(1)	4.0		*P*>~0.2 GPa [*C*2/*m*]	*Lee et al.* (2004b)
Yugawaralite	YUG	18.3	34(1)	4.0		*P*<~4 GPa [*Pc*]	*Arletti et al.* (2003)
Phillipsite	PHI	15.8	67(2)	4.0	1.41 : 1 : 2.26	[$P2_1$/m]	*Gatta and Lee* (2007)
Gismondine	GIS	15.3	63.8(2)	4.0		*P*<~7.4 GPa [$P2_1/c$]	*Ori et al.* (2008)
Sodalite	SOD	17.2	51(1)	4.0		[$P\bar{4}3n$]	*Hazen and Sharp* (1988)
Zeolite-A	LTA	12.9	22.1(3)	4.0		[$Fm\bar{3}c$]	*Arletti, et al.* (2003)
			19.6(6)	5.1(3)			
Levyne	LEV	15.2	56(4)	4.0	-	*P*<~1GPa [$R\bar{3}c$]	*Gatta et al.* (2005)
			48(1)	4.0	1 : 1 : 1.42	*P*>~1 GPa [$R\bar{3}c$]	
Zeolite-Y	FAU	12.7	38(2)	4.0		*P*<~2.4 GPa [$Fd\bar{3}m$]	*Colligan et al.* (2004)
Cd-RHO	RHO	14.1	40(7)	4.0		*P*>~1 GPa	*Lee et al.* (2001)
Mordenite	MOR	17.2	41(2)	4.0	2.41 : 1 : 1.31	[$Im\bar{3}m$]	*Gatta and Lee (*2006)
Bikitaite	BIK	20.2	44.2(4)	4.0	4.81 : 1.44 : 1	[*P*1]	*Comodi et al.* (2003)
			45(1)	4.0			*Ferro et al.* (2002)
Heulandite	HEU	17.1	27.5(2)	4.0	1 : 1.65 : 1.98	[*C*2/*m*]	*Comodi et al.* (2001)
Cancrinite $Na_6Cs_2Ga_6Ge_6O_{24}\cdot Ge(OH)_6$	CAN	16.6	36(2)	9(1)	1.29 : 1.29 : 1	[$P6_3mc$]	*Gatta and Lee* (2008)

Note: FD values are based on the idealised DLS frameworks according to *Baerlocher et al.* (2001). Zeolite-Y data are based on the experiment with silicon-oil as *P*-fluid. For *HP*-experiments performed on both single-crystal and powder (*i.e.* scolecite, bikitaite, heulandite), only the more accurate single-crystal data were used for the EoS-fit. For natrolite and laumontite only the EoS of the over-hydrated *HP*-phase was calculated. *P*-induced over-hydration effect was observed in natrolite (*Lee et al.*, 2002a, 2002b, 2004a), thomsonite (*Likhacheva et al.,* 2007a), scolecite (*Likhacheva et al*., 2007b), gismondine (*Betti et al*., 2007; *Ori et al.* 2008), laumontite (*Lee et al.*, 2004b), Zeolite-A (*Hazen and Finger*, 1984), -Y (*Colligan et al.*, 2004).

The "axial bulk moduli" were calculated with "linearized" BM-EoS (*Angel*, 2000), simply by substituting the cube of the individual lattice parameter (a^3, b^3, c^3) for the volume. The (isothermal) elastic anisotropy can be then described as: $K_0(a) : K_0(b) : K_0(c)$.

The elastic parameters (in terms of bulk modulus and its *P*-derivatives) and the elastic anisotropy of zeolites, based on the data previously published, were then calculated with the EOS-FIT5.2 program (*Angel*, 2001), using the weighted data by uncertainties in *P* and *V,* and are reported in Table 1.

Some zeolites undergo *P*-induced phase transitions. The transition pressures for several zeolites are reported in Table 1 along with the elastic parameters of the low-*P* and high-*P* polymorphs.

When nominally penetrating *P*-media are used, in particular H_2O-bearing mix, some zeolites show *P*-induced phase-transition due to an over-hydration effect, which implies a change of the chemistry of the system. Table 1 includes zeolites which show *P*-induced over-hydration effect.

3. *P*-Induced Structural Evolution

A comparison of the structural refinements of zeolites at different pressures, allows us to highlight the main *P*-induced deformation mechanisms in this class of materials.

Several studies (*Comodi et al.*, 2002; *Gatta et al.*, 2003, 2004a, b) showed that pressure increase does not produce any relevant effect on the "primary building units" (*i.e.* the tetrahedra) in microporous frameworks, as intra-tetrahedral bond distances (*i.e.* T–O) and angles (*i.e.* O–T–O) are only slightly modified in response to the applied pressure. These experimental findings are valid at least for $P < 5$ GPa. The main deformation mechanisms, therefore, act on inter-tetrahedral connections, as showed by T–O–T angle variations. In addition, in open frameworks structures with SBUs characterized by three-dimensional closed form, the SBUs themselves can behave as "rigid units" (with respect to unit-cell compressibility) in response to applied pressure and, therefore, the main deformation mechanisms are represented by co-operative rotation of the SBU. Two excellent examples in this respect are given by the heulandite ($[(Na,K)Ca_4(Al_9Si_{27}O_{72})\cdot 24H_2O$, HEU framework type, *Armbruster and Gunter*, 2001; *Baerlocher et al.,* 2001; *Comodi et al*., 2001) and by the "fibrous zeolites" group (*Gatta*, 2005, and references therein).

In heulandite, *Comodi et al.* (2001) showed that the main deformation is represented by a shortening of the 4–4 = 1 ($T_{10}O_{20}$) SBU zig-zag chain along [102], with a significant decrease of the inter-SMUs T5–T5–T5 angle (*i.e.* 162.4(1)° at 0.0001 GPa and 156.2(3)° at 3.40 GPa) (Figure 1). The SBU bulk modulus is 63(8) GPa, significantly higher than the unit-cell

value [K_0 = 27.5(2) GPa, Table 1] and than the estimated bulk moduli of the three systems of channels {*i.e.* [001]-channels: 19(2) and 10(2) GPa; [100]-channel: 18(1) GPa}. The kinking of the SBUs in the heulandite framework leads to a compression of the channels with a significant increase of the ellipticity (Figure 1).

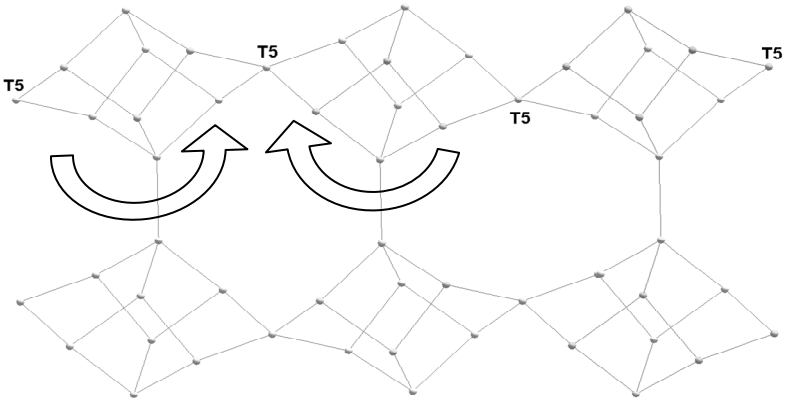

Figure 1. Skeletal representation of the heulandite-type framework (made by 4─4 = 1 SBU) and main deformation mechanism at high-pressure. The T5─T5─T5 angle decreases from 162.4(1)° at 0.0001 GPa to 156.2(3)° at 3.40 GPa.

"Fibrous zeolite" (FZ) structures are built on the 4 = 1 (T_5O_{10}) SBUs, which form chains with tetragonal topological symmetry (Figure 2). Three different cross-linking combinations of the chains lead to three different topologies of the fibrous zeolite frameworks: EDI (edingtonite-like), NAT (natrolite-like) and THO (thomsonite-like). All the fibrous zeolites show 8-membered ring channels running along the [001] and 8-membered ring channels running along the [110] in EDI, [110] in NAT and [010] in THO. The nature of the channel content and Si/Al-ordering make the crystal chemistry of this zeolite group more complex (*Gatta* 2005, Table 1). *Gatta* (2005) showed that in all the fibrous zeolites the same *P*-induced main deformation mechanism is represented by the cooperative rotation of the SBU around the chain-axis (Figure 2). This mechanism leads to the compression of the 8-membered ring channels along [001] with a significant increase of the ellipticity in response to the applied pressure (Figure 2). In addition, such a compression mechanism is independent of the nature of channel content, of the SBU-chains cross-linking geometry (*i.e.* it occurs in EDI, NAT and THO framework type) and of the Si/Al-distribution. A change of the unit-cell compressibility among the FZ was observed in response to the

extra-framework content, and the elastic anisotropy appears to be influenced by the tetragonal topological symmetry of the framework (Table 1).

In other zeolitic frameworks in which the SBU are not represented by "3D closed forms" (*e.g.* 4, 5-1, 6, 6-2, 8 SBU), it is not possible to identify a "rigid unit". However, the main deformation mechanisms are represented by inter-tetrahedral tilting which lead to a compression of the pores increasing their ellipticity.

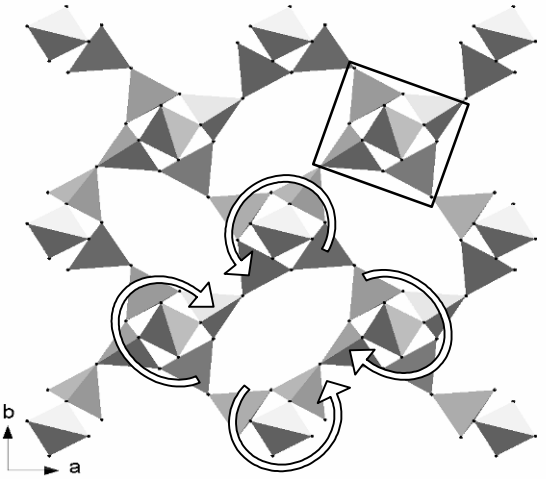

Figure 2. Polyhedral representation of the EDI framework type viewed down [001]. The 4 = 1 SBU is inscribed in the square. The *P*-induced anti-rotation mechanism of the SBUs is shown.

4. Concluding Remarks

4.1. COMPARATIVE ELASTIC ANALYSIS

The comparative elastic analysis of zeolites here performed, on the basis of recalculated elastic parameters, allows us to make two main considerations:

1. The range of compressibility among this class of microporous silicates is large [*i.e.* K_0 ranging between 20 and 65 GPa, Table 1]. These experimental findings show that microporosity does not necessarily imply high compressibility. Several zeolites reported in Table 1 are, unexpectedly, less compressible than many rock-forming silicates, such as α-quartz (*Angel et al*. 1997), Na-feldspars (*Benusa et al.*, 2005), Na-scapolites (*Comodi et al.*, 1990), and some tri-octahedral and di-octahedral micas (*Zanazzi and Pavese*, 2002, and references therein). Open-framework structures are intuitively expected to be highly compressible, because the tetrahedral tilting can lead to a channel compression accommodating the effects of pressure. However, the interaction

between the tetrahedral framework and the channel content (molecules + cations) may hinder the compression of the channels. This would explain why some zeolites are less compressible then other denser silicates. On the whole, the answer to the question "Does porous mean soft?" is "No".

2. Any attempt to find a credible relationship between microporosity and compressibility has been, to date, unsuccessful. For example, the compressibility of zeolites is not directly controlled by the microporosity described in terms of "framework density" (*Baerlocher et al.*, 2001). In fact, the bulk moduli of some isotypic fibrous zeolites (*e.g.* natrolite and scolecite) are different even though their FD is similar (Table 1). Or, more significantly, zeolites with completely different structure topology show drastically different bulk moduli despite their similar FD, as observed for scolecite and heulandite (Table 1).

4.2. FLEXIBILITY OF OPEN-FRAMEWORK STRUCTURES

Analysis of the *P*-induced structural evolution in zeolites allows us to make some general considerations:

1. The flexibility observed in open-framework structures is governed by a few specific deformation modes, based on tetrahedral tilting of stiff tetrahedra around oxygens that behave as hinges. In some open-framework structures is possible to identify secondary "rigid units" represented by a small number of tetrahedra in 3D closed form. However, such units are not completely rigid and contribute to the unit-cell compressibility.

2. When a non-penetrating *P*-medium is used, *P*-induced tetrahedral tilting usually leads to a continuous rearrangement of the framework without any phase-transition, but may induce "displacive" phase-transitions, as observed for the zeolites with ANA framework type (Table 1).

3. The *P*-induced main deformation mechanisms are governed by the tetrahedral framework (and its topological configuration) and are independent of the Si/Al-distribution and of the channels content. The extra-framework content controls, however, the compressibility of the channels/cages, implying a different unit-cell compressibility in isotypic structures (e.g. fibrous zeolites).

4. Usually, the open framework structures accommodate the effect of pressure with an increase in the ellipticity of the channel systems, while maintaining the original elliptical configuration (i.e. without any "inversion" in ellipticity).

References

Angel, R.J., 2000, Equation of state, in: *High-Temperature and High-Pressure Crystal Chemistry* (Eds R.M. Hazen, R.T. Downs), Reviews in Mineralogy and Geochemistry, Mineralogical Society of America and Geochemical Society (Washington, DC), **41**: 35–59.

Angel, R.J., 2001, EOS-FIT V6.0. Computer program. Crystallography Laboratory, Dept. Geological Sciences, Virginia Tech, Blacksburg, VA.

Angel, R.J., Allan, D.R., Miletich, R., and Finger, L.W., 1997, The use of quartz as an internal pressure standard in high-pressure crystallography. *J. Appl. Cryst.* **30**:461–466.

Armbruster, T., and Gunter, M.E., 2001, Crystal structures of natural zeolites, in: *Natural Zeolites: Occurrence, Properties, Application* (Eds D.L. Bish, D.W. Ming), Reviews in Mineralogy and Geochemistry, Mineralogical Society of America and Geochemical Society (Washington, DC), **45**:1–57.

Arletti, R., Ferro, O., Quartieri, S., Sani, A., Tabacchi, G., and Vezzalini, G., 2003, Structural deformation mechanisms of zeolites under pressure. *Am. Mineral.* **88**:1416-1422.

Baerlocher, Ch., Meier, W.M., and Olson, D.H., 2001, *Atlas of zeolite framework types*, 5th edn, Elsevier, Amsterdam.

Ballone, P., Quartieri, S., Sani, A., and Vezzalini, G., 2002, High-pressure deformation mechanism in scolecite: A combined computational-experimental study. *Am. Mineral.* **87**:1194–1206.

Benusa, M.T., Angel, R.J., and Ross, N.L., 2005, Compression of Albite, $NaAlSi_3O_8$. *Am. Mineral.* **90**:1115–1120.

Betti, C., Fois, E., Mazzucato, E., Medici, C., Quartieri, S., Tabacchi, G., Vezzalini, G., and Dmitriev, V., 2007, Gismondine under H*P*: deformation mechanism and re-organization of the extra-framework species. *Microp. Mesop. Mater.* **103**:190–209.

Birch, F., 1947, Finite elastic strain of cubic crystal. *Phys. Rev.* **71**:809–824.

Colligan, M., Forster, P.M., Cheetham, A.K., Lee, Y., Vogt, T., and Hriljac, J.A., 2004, Synchrotron X-ray powder diffraction and computational investigation of purely siliceous zeolite Y under pressure. *J. Am. Chem. Soc.* **126**:12015–12022.

Comodi, P., Mellini, M., and Zanazzi, P.F., 1990, Scapolites: Variation of structure with pressure and possible role in the storage of fluids. *Eur. J. Mineral.* **2**:195–202.

Comodi, P., Gatta, G.D., and Zanazzi, P.F., 2001, High-pressure structural behavior of heulandite. *Eur. J. Mineral.* **13**:497–505.

Comodi, P., Gatta, G.D., and Zanazzi, P.F., 2002, High-pressure behaviour of scolecite. *Eur. J. Mineral.* **14:**567–574.

Comodi, P., Gatta, G.D., and Zanazzi, P.F., 2003, Effects of pressure on the structure of bikitaite. *Eur. J. Mineral.* **15**:247–225.

Coombs, D.S., Alberti, A., Armbruster, T., Artioli, G., Colella, C., Galli, E., Grice, J.D., Liebau, F., Mandarino, J.A., Minato, H., Nickel, E.H., Passaglia, E., Peacor, D.R., Quartieri, S., Rinaldi, R., Ross, M., Sheppard, R.A., Tillmanns, E., and Vezzalini, G., 1997, Recommended nomenclature for zeolite minerals: report of the Subcommittee on Zeolites of International Mineralogical Association, Commission on new minerals and minerals names. *Can. Mineral.* **35**:1571–1606.

Ferro, O., Quartieri, S., Vezzalini, G., Fois, E., Gamba, A., and Tabacchi, G., 2002, High-pressure behaviour of bikitaite: An integrated theoretical and experimental approach. *Am. Mineral.* **87:**1415–1425.

Fois, E., Tabacchi, G., Quartieri, S., and Vezzalini, G., 1999, Dipolar host/guest interactions and geometrical confinement at the basis of the stability of one-dimensional ice in zeolite bikitaite. *J. Chem. Phys.* **111**:355–359.

Fois, E., Gamba, A., Tabacchi, G., Arletti, R., Quartieri, S., and Vezzalini, G., 2005, The "template" effect of the extra-framework content on zeolite compression: The case of yugawaralite. *Am. Mineral.* **90**:28–35.

Fois, E., Gamba, A., Medici, C., Tabacchi, G., Quartieri, S., Mazzucato, E., Arletti, R., Vezzalini, G., and Dmitriev, V., 2008, High pressure deformation mechanism of Li-ABW: synchrotron XRPD study and ab initio molecular dynamics simulations. *Microp. Mesop. Mater.* **115**:267–280.

Gatta, G.D., 2005, A comparative study of fibrous zeolites under pressure. *Eur. J. Mineral.* **17**:411–422.

Gatta, G.D., 2008, Does porous mean soft? On the elastic behaviour and structural evolution of zeolites under pressure. *Z. Kristallogr.* **223**:160–170.

Gatta, G.D., and Lee, Y., 2006, On the elastic behaviour of zeolite mordenite: A synchrotron powder diffraction study. *Phys. Chem. Miner*. **32**:726–732.

Gatta, G.D., and Lee, Y., 2007, Anisotropic elastic behaviour and structural evolution of zeolite phillipsite at high pressure: A synchrotron powder diffraction study. *Microp. Mesop. Mater.* **105**:239–250.

Gatta, G.D., and Lee, Y., 2008, Pressure-induced structural evolution and elastic behaviour of $Na_6Cs_2Ga_6Ge_6O_{24} \cdot Ge(OH)_6$ variant of cancrinite: A synchrotron powder diffraction study. *Microp. Mesop. Mater.* **116**(1–3):51–58.

Gatta, G.D., and Wells, S.A., 2004, Rigid unit modes at high pressure: An explorative study of a fibrous zeolite-like framework with EDI topology. *Phys. Chem. Miner.* **31**:465–474.

Gatta, G.D., and Wells, S.A., 2006, Structural evolution of zeolite levyne under hydrostatic and non-hydrostatic pressure: geometric modelling . *Phys. Chem. Miner.* **33**:243–255.

Gatta, G.D., Comodi, P., and Zanazzi, P.F., 2003, New insights on high-pressure behaviour of microporous materials from X-ray single-crystal data. *Microp. Mesop. Mater.* **61**:105–115.

Gatta, G.D., Boffa Ballaran, T., Comodi, P., and Zanazzi, P.F., 2004a, Isothermal equation of state and compressional behaviour of tetragonal edingtonite. *Am. Mineral.* **89**:633–639.

Gatta, G.D., Boffa Ballaran, T., Comodi, P., and Zanazzi, P.F., 2004b, Comparative compressibility and equation of state of orthorhombic and tetragonal edingtonite. *Phys. Chem. Miner.* **31**:288–298.

Gatta, G.D., Comodi, P., Zanazzi, P.F., and Boffa Ballaran, T., 2005, Anomalous elastic behavior and high-pressure structural evolution of zeolite levyne. *Am. Mineral.* **90**:645–652.

Gatta, G.D., Nestola, F., and Boffa Ballaran, T., 2006, Elastic behavior, phase transition and pressure induced structural evolution of analcime. *Am Mineral.* **91**:568–578.

Gatta, G.D., Rotiroti, N., Boffa Ballaran, T., and Pavese A., 2008, Leucite at high-pressure: Elastic behaviour, phase stability and petrological implications. *Am. Mineral.* **93**:1588–1596.

Gatta, G.D., Rotiroti, N., Boffa Ballaran, T., Sanchez-Valle, C., and Pavese A., 2009, Elastic behavior and phase-stability of pollucite, a potential host for nuclear waste. *Am. Mineral.* **94**(8–9):1137–1143.

Gillet, P., Malézieux, J.M., and Itié, J.P., 1996, Phase changes and amorphization of zeolites at high pressure: The case of scolecite and mesolite. *Am. Mineral*. **81**:651–657.

Goryainov, S.V., 2005, Pressure-induced amorphization of $Na_2Al_2Si_3O_{10} \cdot 2H_2O$ and $KAlSi_2O_6$ zeolites. *Physica Status Solidi* **202:**R25–R27.

Gottardi, G., and Galli, E., 1985, *Natural Zeolites*, Springer-Verlag, Berlin.

Greaves, G.N., Meneau, F., Sapelkin, A., Colyer, L.M., Gwynn, I.A., Wade, S., and Sankar, G., 2003, The rheology of collapsing zeolites amorphized by temperature and pressure**.** *Nature Mat.* **2**(9):622–629.

Gulín-González, J., and Suffritti, G.B., 2004, Amorphization of calcined LTA zeolites at high pressure: a computational study. *Microp. Mesop. Mater*. **69**:127–134.

Hazen, R.M., and Finger, L.W., 1984, Compressibility of zeolite 4A is dependent on the molecular size of the hydrostatic pressure medium. *J. Appl. Phys.* **56**:1838–1840.

Hazen, R.M., and Sharp, Z.D., 1988, Compressibility of sodalite and scapolite. *Am. Mineral.* **73**:1120–1122.

Huang, Y., and Havenga, E.A., 2001, Why do zeolites with LTA structure undergo reversible amorphization under pressure? *Chem. Phys. Lett.* **345**:65–71.

Lee, Y., Hriljac, J.A., Vogt, T., Parise, J.B., Edmondson, M., Anderson, P., Corbin, D., and Nagai, T., 2001, Phase transition of zeolite Rho at high-pressure. *J. Am. Chem. Soc.* **123:**8418–8419.

Lee, Y., Vogt, T., Hriljac, J.A., Parise, J.B., and Artioli, G., 2002a, Pressure-induced volume expansion of zeolites in the natrolite family. *J. Am. Chem. Soc.* **124**:5466–5475.

Lee, Y., Vogt, T., Hriljac, J.A., Parise, J.B., Hanson, J.C., and Kimk, S.J., 2002b, Non-framework cation migration and irreversible pressure-induced hydration in a zeolite. *Nature* **420**:485–489.

Lee, Y., Martin, D., Hriljac, J.A., and Vogt, T., 2004a, Formation and manipulation of confined water wires. *Nanoletters* **4**:619–621.

Lee, Y., Hriljac, J.A., and Vogt, T., 2004b, Pressure-induced migration of zeolitic water in laumontite. *Phys. Chem. Miner.* **31**:421–428.

Likhacheva, A.Yu., Seryotkin, Yu.V., Manakov, A.Yu., Goryainov, S.V., Ancharov, A.I., and Sheromov, M.A., 2007a, Pressure-induced over-hydration of thomsonite: a synchrotron powder diffraction study. *Am. Mineral.* **92**:1610–1615.

Likhacheva, A.Yu., Seryotkin, Yu.V., Manakov, A.Yu., Goryainov, S.V., Ancharov, A.I., and Sheromov, M.A., 2007b, Pressure-induced over-hydration in scolecite: A synchrotron powder diffraction study. Z. Kristallogr. Supplements (EPDIC 2006) **S26**:405–410.

Ori, S., Quartieri, S., Vezzalini, G., and Dmitriev, V., 2008, Pressure-induced over-hydration and water ordering in gismondine: A synchrotron powder diffraction study. *Am. Mineral.* **93**:1393–1403.

Rutter, M.D., Secco, R.A., and Huang, Y., 2000, Ionic conduction in hydrated zeolite Li-, Na- and K-A at high pressures. *Chem. Phys. Lett.* **331:**189–195.

Sartbaeva, A., Gatta, G.D., and Wells, S.A., 2008, Flexibility window controls pressure-induced phase transition in analcime. *Europhysics Letters* **83**:26002 (5pp).

Secco, R.A., and Huang, Y., 1999, Pressure-induced disorder in hydrated Na-A zeolite. *J. Phys. Chem. Solids* **60**:999–1002.

Seryotkin, Y.V., Bakakin, V.V., Fursenko, B.A., Belitsky, I.A., Joswig, W., and Radaelli, P.G., 2005, Structural evolution of natrolite during over-hydration: a high-pressure neutron diffraction study. *Eur. J. Mineral.* **17**:305–313.

Zanazzi, P.F., and Pavese, A., 2002, Behavior of micas at high pressure and high temperature, in: *Micas: Crystal Chemistry and Metamorphic Petrology* (Eds A. Mottana, F.P. Sassi, J.B. Thompson, Jr., S. Guggenheim), Review in Mineralogy and Geochemistry, Mineralogical Society of America and Geochemical Society (Washington, DC), **45**:99–116.

HYDROGEN BONDING IN MINERALS AT HIGH PRESSURES

BJORN WINKLER*
Kristallographie, Institute of Geowissenschaften, Goethe Universitaet, Altenhoeferallee 1, D-60438 Frankfurt am Main, Germany

Abstract Pressure-induced changes in hydrogen bonds in minerals are relevant for an understanding of a variety of processes. They can be studied by diffraction and spectroscopy and density functional theory calculations. Here, the current state-of-the-art of experimental and modeling approaches is discussed.

Keywords: Hydrogen bond, minerals, spectroscopy, density functional theory

1. Hydrogen Bonding

Hydrogen bonds influence structure–property relations in a very large variety of compounds. The present contribution is limited to those hydrogen bonds in minerals, where both the donor and the acceptor atoms oxygen atoms. Then, the hydrogen bond system can be written as *R*-O–H¨O-*R*', where R and R' represent parts of the structure, O–H represents a predominantly covalent bond between the donor atom and the hydrogen atom with a typical distance of *d*(OH) ~1 Å, and *d*(H¨O) represents the hydrogen bond between the hydrogen and the acceptor atom, with a typical distance of *d*(H¨O) ~ 1.5–1.72 Å.

The concept of hydrogen bonding was introduced first to describe the interaction between water molecules in 1920. Since then numerous studies have been devoted to elucidate structure–property relations of hydrogen bonds. A comprehensive classic introduction is the book by *Pimentel and McClellan* (1959). Correlations between structural features and spectroscopic observations have been extensively discussed by *Novak* (1974). A similar discussion, focusing on minerals, has been presented by *Libowitzky* (1999).

* E-mail: b.winkler@kristall.uni-frankfurt.de

E. Boldyreva and P. Dera (eds.), *High-Pressure Crystallography: From Fundamental Phenomena to Technological Applications*, DOI 10.1007/978-90-481-9258-8_40,

General aspects of infrared spectroscopic studies of minerals have been reviewed by *Farmer* (1974) and *Rossman* (1988). The special case of minerals where the hydrogen bond occurs between a water molecule and the structure has been summarized by *Winkler* (1996). A recent book edited by *Keppler and Smyth* (2006) contains a wealth of information on 'water' in anhydrous minerals.

As the hydrogen bond is important, numerous experimental techniques are employed to study the detailed atomic arrangement and the dynamics of -O–H¨O- groups. In the following, a brief overview of the advantages and short-comings of different diffraction and spectroscopic approaches with respect to high pressure investigations will be given.

2. Diffraction Studies of Hydrogen Bonds at High Pressure

The determination of the atomic positions by diffraction methods offers unique insights which cannot be obtained from spectroscopic studies. However, the hydrogen atom has only one electron and hence contributes only a small amount to the structure factor in x-ray diffraction studies. For neutron diffraction, the very large incoherent scattering cross section of the hydrogen atoms is problematic in powder diffraction studies, but unproblematic for single crystal studies.

2.1. SINGLE CRYSTAL STUDIES

2.1.1. *Single Crystal X-Ray Diffraction Studies*

The determination of the atomic coordinates of hydrogen atoms at ambient pressure in inorganic or 'small molecule' compounds is comparatively straightforward by laboratory x-ray diffraction experiments if a single crystal of sufficient quality is available. Diamond anvil cells, however, allow only a restricted access to reciprocal space, and hence the achievable resolution is limited.

Most high pressure x-ray single crystal diffraction studies up to now used alcohol or silicon oil as pressure transmitting media, which effectively limits these studies to a maximum pressure of ~10 GPa (*Angel et al*., 2007). At higher pressures the deviatoric stress exerted by the pressure medium leads to a deterioration of the quality of the crystal. The use of noble gases as pressure media allows experiments at much higher pressures. For example, reflections of diaspore were not significantly broadened even at 50 GPa when helium was used as a pressure medium *(Friedrich et al.*, 2007).

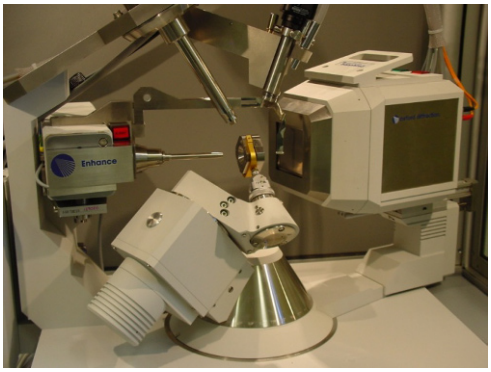

Figure 1. Diamond anvil cell mounted on a laboratory κ-diffractometer.

Nevertheless, the atomic coordinates of hydrogen atoms have not been determined in high pressure single crystal diffraction studies up to now (e.g. zoisite: *Comodi and Zanazzi*, 1997; chondrodite: *Friedrich et al*., 2002; bikitaite: *Comodi et al.*, 2003; diaspore: *Friedrich et al*., 2007; gypsum: *Comodi et al*., 2008). It is, however, possible to locate the acceptor and the donor oxygen. In conjunction with additional spectroscopic data, this has been used to infer hydrogen positions, but this approach will be critically discussed below.

2.1.2. *Single Crystal Neutron Diffraction Studies*

The use of 'panoramic' diamond or moissanite anvil cells with large anvils for single crystal neutron Laue diffraction experiments is potentially very promising. A successful feasibility study on natrolite in a moissanite anvil cell at ambient pressure at VIVALDI@ILL gave satisfactory structural parameters (*McIntyre et al*., 2005), but no high pressure studies on hydrous mineral have been published yet. The main advantages of this approach are that natural (i.e. protonated) samples can be employed and that measurements are comparatively fast. The main problem seems to be the indexing of the reflections.

2.2. POWDER DIFFRACTION STUDIES

The determination of atomic coordinate of hydrogen atoms in chemically and structurally complex minerals by high pressure x-ray powder diffraction studies seems to be currently out of reach. Neutron powder diffraction using deuterated samples is a potentially attractive alternative. Powder neutron diffraction at high pressures is generally performed on high flux, medium resolution diffractometers, such as PEARL@ISIS. Neutron powder diffraction

in high pressure cells such as the Paris–Edinburg cell or the TAP cell is limited to about ~15 GPa. The use of deuterated samples is required in order to minimize incoherent scattering. Then, deuterium positions in structurally not too complex compounds such as brucite (*Parise et al*., 1994), clinochlore (*Welch and Marshall,* 2001), chondrodite (*Friedrich et al*., 2002), or katoite (*Lager et al*., 2005) can be obtained.

3. Spectroscopic Studies of Hydrogen Bonds at High Pressure

3.1. RAMAN AND INFRARED SPECTROSCOPIC STUDIES

The dynamics of hydrogen bonds in crystals, melts, and glasses are routinely characterized using infrared or, to a lesser extent, Raman spectroscopy. Weak hydrogen bonds typically have O–H-stretching frequencies of ν(OH) ~ 3,600 cm^{-1} (450 meV, 108 THz), intermediate hydrogen bonds have ν(OH) ~ 2,800–3,100 cm^{-1}, and strong hydrogen bonds have ν(OH) < 2,700 cm^{-1}.

Infrared and Raman spectroscopic studies of pressure induced changes of hydrogen bonds in minerals are now well established. Diamond anvil cell experiments allow to obtain IR and Raman spectra in transmission or back scattering, and as the opening angle of the DAC is not a limiting factor, experiments at megabar pressures are feasible. One of the first studies aimed to determine the pressure-induced changes of the OH stretching vibration in a silicate was a single crystal study of orthozoisite (*Winkler et al*., 1989) (Figure 2).

The observed linear pressure induced red-shift of the OH-stretching vibration is shown in Figure 2. A red-shift (i.e. a shift to lower energies) is the expected behavior, since the hydrogen bond is shortened on compression, leading to a lengthening and weakening of the covalent O–H bond, with a concomitant decrease of ν(OH). Numerous studies have quantified similar pressure-induced red-shifts in other minerals. For brucite, $Mg(OH)_2$, the pressure-induced red-shift of the OH-stretching vibration is −0.6 cm^{-1}/GPa (*Kruger et al*., 1989), while isostructural portlandite, $Ca(OH)_2$, shows a shift of −2.1 to −3.5 cm^{-1}/GPa (*Kruger et al*., 1989; *Shinoda et al*., 2000). There are, however, also examples where the OH stretching frequency is either unaffected by increasing pressure or shifts to higher energies with increasing pressure. In katoite, ν(OH) remains constant at about 3,660 cm^{-1} up to pressures of approximately 5 GPa. In nominally anhydrous coesite, SiO_2, hydrogen can be incorporated through the hydrogarnet substitution and pressure-induced blue shifts of ~7 cm^{-1}/GPa have been observed (*Koch-Müller et al*., 2003). In chloritoids, the two symmetrically distinct hydrogen bonds behave very differently, as the high energy one displays a pressure-induced blue shift of ~5 cm^{-1}/GPa, while the second O–H stretch, corres-

ponding to a hydrogen bond of intermediate strength (ν $(OH)_{chloro}$ ~ 2,990 cm^{-1}), shifts to lower energies by −11 cm^{-1}/GPa (*Koch-Müller et al*., 2002). Nearly all hydrogen stretching frequencies in serpentine minerals shift to higher wave numbers (by about 1–10 cm^{-1}/GPa) (*Auzende et al*., 2004). In topaz, the pressure-induced shift is 0.6(3) cm^{-1}/GPa to higher energies (*Bradbury and Williams,* 2003).

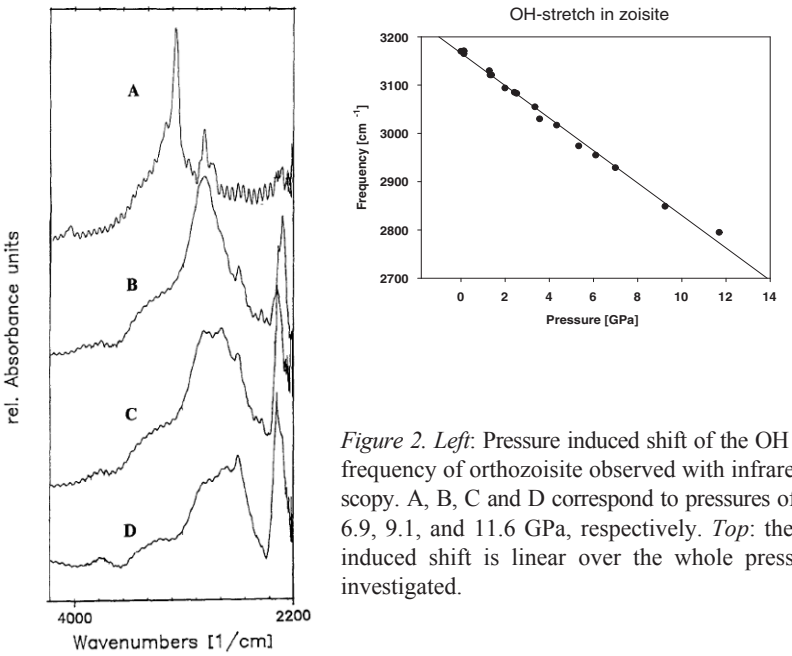

Figure 2. Left: Pressure induced shift of the OH stretching frequency of orthozoisite observed with infrared spectroscopy. A, B, C and D correspond to pressures of 0.1 MPa, 6.9, 9.1, and 11.6 GPa, respectively. *Top*: the pressure-induced shift is linear over the whole pressure range investigated.

3.2. OTHER SPECTROSCOPIC STUDIES

The dynamics of hydrogen bonds can be investigated with a variety of other spectroscopic techniques (see e.g. *Winkler,* 1996). However, most of these cannot easily be used in high pressure studies. For example, quasi-elastic and inelastic neutron scattering is an established method to study hydrogen dynamics. Both approaches exploit the unusually large incoherent scattering cross section of the hydrogen atom, which facilitates the observation of its dynamics. Instruments like TOSCA@RAL can, in principle, be used for high pressure experiments, but this has not been demonstrated yet.

High pressure coherent inelastic neutron scattering has been used to study lattice dynamics of hydrogen bonded systems such as ice (*Strässle et al*., 2004). However, the use of large volume cells limits the pressure to a few GPa, samples have to be deuterated and only the dispersion of low frequency phonons can be observed.

Recently, it was shown that inelastic x-ray spectroscopy, IXS, provides a unique opportunity to study both high and low frequency vibrations and can be used to determine the dispersion relation of the OH-stretching vibration (*Winkler et al*., 2008). However, currently counting times for the high frequency vibrations are already rather large at ambient pressure for samples of an optimal thickness (several hundred micrometer), and hence the requirement of much thinner samples for DAC experiments currently precludes the application of this technique to high pressure experiments. With more intense sources, however, this restriction will be lifted.

4. Atomistic Modeling Studies of Hydrogen Bonds at High Pressure

Currently, the most reliable atomistic modeling approach to study hydrogen bonding in crystals at high pressure are density functional theory, DFT, based calculations. DFT calculations are predictive, and can be used to locate hydrogen atoms (*Milman and Winkler,* 2001). Furthermore, DFT calculations allow one to compute phonon dispersion curves, either through density functional perturbation theory or through a finite displacement algorithm (*Baroni et al*., 2001, *Refson et al*., 2006). Modern approaches allow one to compute frequencies and intensities of Raman and IR-spectra. The role of anharmonicity has extensively been discussed recently (*Balan et al*., 2007) and a theoretical evaluation of IR absorption coefficients in minerals has been presented by *Balan et al.* (2008).

5. Example I: Zoisite

Zoisite, $Ca_2Al_2(Al_{1-p}Fe_p)(SiO_4)(Si_2O_7)O(OH)$ is the orthorhombic iron-poor end-member of the epidote group. The influence of pressure on the OH valence vibration in zoisite has been studied up to 11.6 GPa by infrared spectroscopy (*Winkler et al*., 1989). As has been mentioned above (Figure 2) ν(OH) shifts linearly to lower wave numbers by −33.9 cm^{-1}/GPa. In a similar study of the structurally related clinozoisite, (*Bradbury and Williams,* 2003) the pressure induced shift was found to be −5.1(9) cm^{-1}/GPa only. A comparison with pressure-induced shifts in other minerals (see above) suggests that the findings for orthozoisite are unusual. Extensive DFT calculations with different basis sets and different approaches to obtain the phonon frequencies confirmed that orthozoisite has an unusually large pressure-dependence of the stretching frequency (*Winkler et al*., 2008). This is due to the nearly linear hydrogen bond in orthozoisite, which, on compression, leads to an increase of *d*(OH) by about 2.5% at 10 GPa, which is significantly

larger than in clinozoisite, where the hydrogen bond is slightly kinked and consequently *d*(OH) increases only by 0.5% on pressure increase to 10 GPa.

6. Example II: Diaspore

Diaspore, α-AlOOH, (Figure 3) is a chemically and structurally simple model system with a hydrogen bond of intermediate strength. Its compression has been studied by singly crystal x-ray diffraction up to 50 GPa (*Friedrich et al*., 2007). This study confirmed the predicted compression behavior (*Winkler et al*., 2001). There are no high pressure experimental IR spectra available, but the reliability of the model with respect to an accurate description of the lattice dynamics, including the OH stretching vibration, has been confirmed by inelastic x-ray spectroscopy (*Winkler et al*., 2008).

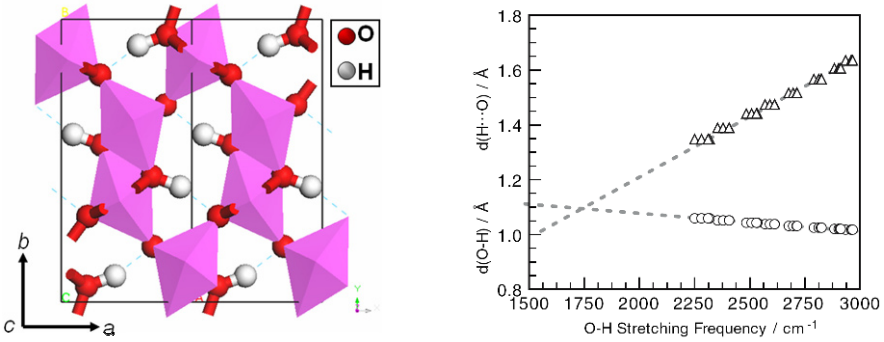

Figure 3. Left: The structure of diaspore, α-AlOOH. *Right*: DFT calculations predict pressure-induced structural changes which cause shifts in the OH-stretching frequencies. The maximum pressure in the calculation was 50 GPa.

Correlations between structural parameters and stretching frequencies have extensively been discussed in the past (e.g. *Novak*, 1974; *Libowitzky,* 1999). Figure 3 shows the dependence of the OH stretching frequency on the distance between the acceptor and donator atoms in diaspore. When this behavior is superimposed on the correlation between structural parameters and stretching frequencies derived at ambient pressure (Figure 4), it is obvious, that the pressure-induced changes differ significantly from what would have been expected from the correlation derived at ambient pressure. This has been also observed for other compounds (e.g. zoisite: *Winkler et al*., 2008). Hence, correlation functions between structural parameters and stretching frequencies obtained at ambient pressure cannot be used for the derivation of hydrogen positions in high pressure experiments.

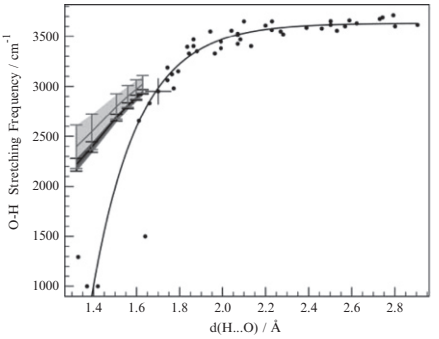

Figure 4. The points show the correlation between d(H···O) and ν(OH) at ambient pressure (after *Libowitzky,* 1999). Points with error bars are from high pressure DFT calculations for diaspore.

References

Angel, R.J., Bujak, M., Zhao, J., Gatta, G.D., and Jacobsen, S.D., (2007), *Journal of Applied Crystallograph*y, 40, 26–32.

Auzende, A., Daniel, I., Reynard, B., Lemaire, C., and Guyot, F., (2004), *Physics and Chemistry of Minerals*, 31, 269–277.

Balan, E., Refson, K., Blanchard, M., Delattre, S., Lazzeri, M., Ingrin, J., Mauri, F., Wright, K., and Winkler, B., (2008), *American Mineralogist*, 93, 950–953.

Balan, E., Lazzeri, M., Delattre, S., Meheut, M., Refson, K., Winkler, B., (2007) *Physics and Chemistry of Minerals*, 34, 621–625.

Baroni, S., de Gironcoli, S., Dal Corso, A., and Giannozzi, P., (2001), *Reviews of Modern Physic*s, 73, 515–562.

Bradbury, S.E., and Williams, Q., (2003), *American Mineralogist*, 88, 1460–1470.

Clark, S.J., Segall, M.D., Pickard, C.J., Hasnip, P.J., Probert, M.J., Refson, K., and Payne, M.C., (2005), *Zeitschrift für Kristallographie*, 220, 567–570.

Comodi, P., Gatta, G.D., and Zanazzi, P.F., (2003), *European Journal of Mineralogy*, 15, 247–255.

Comodi, P., Nazzareni, S., Zanazzi, P.F., and Speziale, S., (2008), *American Mineralogist,* 1530–1579.

Comodi, P., and Zanazzi, P.F., (1997), *American Mineralogist*, 82, 61–68.

Farmer, V.C. (ed) (1974) The infrared spectra of minerals. Mineralogical Society, London.

Friedrich, A., Lager, G.A., Ulmer, P., Kunz, M., and Marshall, W.G., (2002), *American Mineralogist,* 87, 931–939.

Friedrich, A., Haussühl, E., Boehler, R., Morgenroth, W., Juarez-Arellano, E.A., and Winkler. B., (2007), *American Mineralogist,* 92, 1640–1644.

Keppler, H., and Smyth, J.R., (eds) (2006) Water in nominally anhydrous minerals. Reviews in mineralogy and geochemistry, vol. 62. Mineralogical Society of America, Washington, DC.

Koch-Müller, M. Hofmeister, A.M., Fei, Y., and Liu, Z., (2002), *American Mineralogist,* 87,609–622.

Koch-Müller, M., Dera, P., Fei, Y., Reno, B., Sobolev, N., Hauri, E., and Wysoczanski, R., (2003), *American Mineralogist,* 88, 1436–1445.

Kruger, M.B., Williams, Q., and Jeanloz, R., (1989), *Journal of Chemical Physics,* 91, 5910–5915.

Lager, G.A, Marshall, W.G., Liu, X., and Downs, R.T., (2005), *American Mineralogist,* 90, 639–644.

Libowitzky, E., (1999), *Monatshefte für Chemie,* 130, 1047–1059.

McIntyre, G.J., Mélési, L., Guthrie, M., Tulk, C.A., Xu, J., and Parise, J.B., (2005), *Journal of Physics. Condensed Matter,* 17, S3017–S3024.

Milman, V., and Winkler, B., (2001), *Zeitschrift für Kristallographie,* 216,99–104.

Novak, A., (1974), Hydrogen bonding in solids correlation of spectroscopic and crystallographic data, Book series: Structure and bonding, Vol. 18, Springer Verlag, Berlin, pp 177─216.

Parise, J.B., Leinenweber, K., Weidner, D.J., Tan, K., and Von Dreek, R.B., (1994), *American Mineralogist,* 79, 193–196.

Pimentel, G.C., and McClellan, A.L., (1959), The hydrogen bond. W.H. Freeman. San Francisco, CA, 475 pp.

Refson, K., Tulip, P.R., and Clark, S.J., (2006), *Physical Review,* B 73, 155114.

Rossman, G.R., (1988) In: C HF (ed) Spectroscopic methods in mineralogy and geology. Reviews in mineralogy, vol 18. Mineralogical Society of America, Washington, DC, pp 193–206.

Shinoda, K., Nagai, and T., Aikawa, N., (2000), *Journal of Mineralogical and Petrological Sciences,* 95:65–70.

Strässle, T., Saitta, A.M., Klotz, S., and Braden, M., (2004), *Physical Review Letters,* 93, 225901.

Welch, M.D., and Marshall, W.G., (2001), *American Mineralogist,* 86, 1380–1386.

Winkler, B., (1996), *Physics and Chemistry of Minerals,* 23, 310–318.

Winkler, B., Gale, J.D., Refson, K., Wilson, D.J., and Milman, V., (2008), *Physics and Chemistry of Minerals,* 35, 25–35.

Winkler, B., Hytha, M., Pickard, C., Milman, V., and Warren, M., (2001), *European Journal of Mineralogy,* 13, 343–349.

Winkler, B., Langer, K, and Johannsen, P.G., (1989), *Physics and Chemistry of Minerals,* 16, 668–671.

NANOMATERIALS AT HIGH PRESSURE: SPECTROSCOPY AND DIFFRACTION TECHNIQUES

G.R. HEARNE*
School of Physics and DST-NRF Centre of Excellence in Strong Materials, University of the Witwatersrand, Private Bag 3, Wits 2050, Johannesburg, South Africa

Abstract Experiments have shown that the pressure response of a nanophase material is often quite different from that of the bulk analog. Transitions to high-pressure structural phases, mechanical–elastic properties and pressure-induced grain-size dependent amorphization are unlike those occurring in the bulk macrocrystalline analog. Attempts are made to rationalize why this should be the case from thermodynamic considerations. All of this will mainly be exemplified by the case of nano-TiO_2 on which there has been a surge of studies in recent years.

Keywords: Gibbs free energy, surface energy, nucleation and growth, critical diameter, pressure response, size-dependent amorphization, anatase

1. Introduction

Ultrafine nanometer grained materials have exhibited chemical, physical and mechanical properties significantly different (and often considerably improved) relative to those of their coarser-grained counterparts. In this work we consider the structural integrity of ultra-fine grained materials (e.g., down to grain sizes of several nanometers) under extreme pressure conditions in comparison to the pressure response of the macrocrystalline (bulk) analog.

Nanoanatase TiO_2 is used as the prime example, although cases of other materials will be cited. It may be noted that at grain size dimensions of

*Address: G.R. Hearne, Department of Physics, University of Johannesburg, P.O. Box 524, Auckland Park, 2006. E-mail: grhearne@uj.ac.za

E. Boldyreva and P. Dera (eds.), *High-Pressure Crystallography: From Fundamental Phenomena to Technological Applications*, DOI 10.1007/978-90-481-9258-8_41,

several nanometer (containing only several thousand atoms) *as many as ~25 % of the atoms are exposed at the surface of the particle-grain*. We anticipate, and will show, that the large surface-to-volume ratio in the nanomaterial impacts on the P–T response of these nanostructured entities (e.g., affects structural phase stability and mechanical–elastic properties).

2. Some Useful Thermodynamic Considerations

A (reconstructive) phase transition to a new structural phase occurs when the Gibbs free energy can be lowered. At a (pressure-induced) structural phase transition, the new (high-pressure, HP) phase nucleates within the matrix of the preceding (low pressure, LP) phase, see Figure 1. These spontaneously created particles are stable and grow if the initial diameter is greater than a critical value $d > d^*$, else it constitutes a cluster or embryo and collapses. This critical diameter exists because of the competition of two factors in the nucleation process. These are the energy reduction per unit volume (which drives the structural transition) $\Delta G_V = P \times \Delta V/V$ resulting from the volume change ΔV at the structural transition at pressure P, and the energy cost of order $\gamma \times d^2$ to form new interfaces (surfaces) with surface stress value γ (which is like surface tension) (*Cahn*, 1980).

Evaluating the critical size for the case of homogeneous nucleation of spherical particles of radius $r\ (= d/2)$, arises out of consideration of the Gibbs free energy change at the structural transition:

$$\Delta G = G_{HP} - G_{LP} = -\frac{4}{3}\pi r^3 \Delta G_V + 4\pi r^2 \gamma + \frac{4}{3}\pi r^3 \Delta G_S . \qquad (1)$$

The first two terms are from the competing effects of *volume-change energy decrease* and the *surface-interfacial energy cost (increase)* mentioned above. ΔG_S is the misfit strain energy (cost) per unit volume from the mismatch of the transformed volume in the host matrix.

Upon the emergence of a new phase at a structural phase transition, e.g., nucleation of spherical nuclei , the minimum or critical diameter d^* for self-sustaining growth of the nucleus and the nucleation energy barrier ΔG^* (which determines the nucleation rate) in the case of such homogeneous nucleation is given by (*Porter and Easterling*, 1992):

$$d^* = \frac{4\gamma}{\Delta G_V - \Delta G_S} \qquad (2)$$

and

$$\Delta G^* = \frac{16\pi\gamma^3}{3(\Delta G_V - \Delta G_S)^2}. \quad (3)$$

Both equations are dependent on the interfacial energy γ that exists between interfaces of the new phase and the host matrix. ΔG_V is the *magnitude* of the free energy reduction per unit volume due to the increase in density at the structural transition. Equations (2) and (3) above are derived from minimizing the total free-energy change, $d(\Delta G)/dr = 0$, in Eq (1). There are similar expressions for the case of heterogeneous nucleation, e.g., at grain boundaries and defects etc, and where there is a deviation in shape from spherical nucleation (*Porter and Easterling*, 1992).

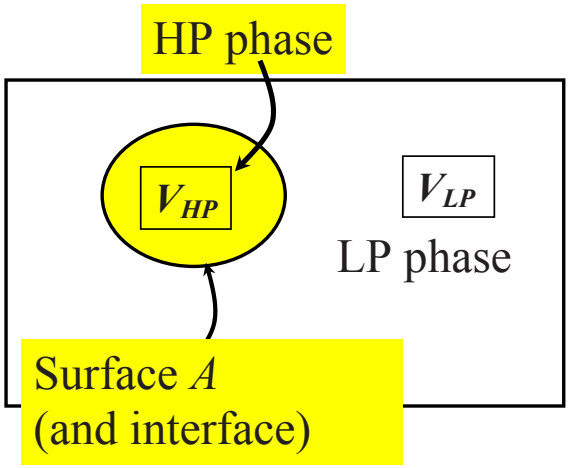

Figure 1. A schematic representation of the nucleation of the HP structural phase (having unit cell volume V_{HP}) within the LP phase matrix (having unit cell volume V_{LP}).

Perhaps it is now more apparent that, if we are dealing with nano-phase materials with grain sizes $d \sim d^*$ near to the "critical size", this is likely to have implications for structural transitions that would normally occur in (bulk) macrocrystalline analogs where $d >> d^*$. These considerations now find expression in a case study of pressurized nano-anatase TiO_2 presented in this manuscript.

3. Experimental Probes

Three primary techniques are used because of their convenient application as a probe of samples pressurized in the cavity of the diamond-anvil cell (DAC). These are listed below and have been used to investigate various nano-anatase samples pressurized in the DAC at room-temperature.

Synchrotron X-ray diffraction has the attributes of high photon flux (brilliance) and the possibility of focusing to small spot sizes (on the order of a few microns), compared with laboratory based instruments. But it is the tunability to short wavelengths that is most important. This ensures that sufficient Bragg reflections may be obtained from the limited exit-cone aperture typical of most DACs, to permit a reliable quantitative analysis from the diffraction pattern.

Raman inelastic light scattering by long wavelength optical phonons is a convenient and sensitive probe widely used to characterize local structural changes and monitor structural transitions in compounds.

X-ray absorption spectroscopy (XAS), through the analysis of the fine structure in the extended regime (EXAFS) of an X-ray absorption edge and of the pre-edge features (XANES), permits quite a detailed description of the local structure around a given atom, in this case the titanium, to be obtained.

Either Fluorinert FC70/FC77 (1:1) (for XRD and Raman measurements), or silicon oil (for XAS) have been used as the pressure-transmitting medium. Pressure determination was made by way of the ruby R1-luminescence line shift. This specific choice is for ease of loading and also to ensure that there is no interfering or background signals derived from the pressure-transmitting medium.

Details of the experimental conditions for each technique may be found in *Hearne et al.* (2004), *Pischedda et al.* (2006); *Flank et al.*, (2008).

4. Results: Exemplary Case of Nano-TiO_2

4.1. MACROCRYSTALLINE PRESSURE RESPONSE

Three different structural phases of TiO_2 exist in nature, namely anatase, rutile, and brookite. Other structures like the orthorhombic α-PbO_2 type phase and the monoclinic baddeleyite phase may be stabilized only under high pressure from a starting material of either anatase or rutile. At room temperature a single crystal of anatase undergoes the following sequence of structural transitions under high pressure (*Arlt et al.*, 2000): anatase ($I4_1/amd$)$\rightarrow^{\sim 5GPa}$ α-PbO_2-type phase ($Pbcn$) $\rightarrow^{\sim 15GPa}$ baddeleyite ($P2_1/c$). The orthorhombic α-PbO_2-type phase is retained upon decompression to ambient conditions. Ti has regular octahedral coordination by oxygen atoms in the tetragonal anatase, a distorted octahedral coordination in the orthorhombic α-PbO_2 type phase, and a sevenfold oxygen coordination in the monoclinic baddeleyite phase.

4.2. NANO-ANATASE 12 NANOMETER GRAIN SIZE – PRESSURE RESPONSE COMPARISON WITH MACROCRYSTALLINE ANATASE

The pressure evolution of the Raman spectra of nano-anatase is shown in Figures 2a and b, whereas Raman spectra at selected pressures of a bulk commercial sample are shown in Figure 2c. Under ambient conditions the most prominent Raman bands in nano-anatase are at 146.4 cm^{-1} (E_g), 396.9 cm^{-1} (B_{1g}), 518.1 cm^{-1} (A_{1g}/B_{1g} unresolved doublet) and 641.3 cm^{-1} (E_g); the band assignment is indicated in brackets (*Ohsaka et al.*, 1978). The pressure evolution of the Raman spectra of bulk anatase exhibits similar behavior to that reported in previous high pressure studies (*Lagarec and Desgreniers*, 1995). As the pressure increases to ~5.6 GPa, several weak peaks appear, characteristic of the α-PbO_2-type phase. As pressure increases further, the intensities of these new peaks increase and they are clearly discerned at pressures of ~7.5 GPa and beyond, see Figure 2c. Beyond this pressure radically new Raman bands become apparent in the range 225–280 cm^{-1} in addition to a prominent band at ~500 cm^{-1}; these are supposed to be characteristic of the high-pressure baddeleyite phase.

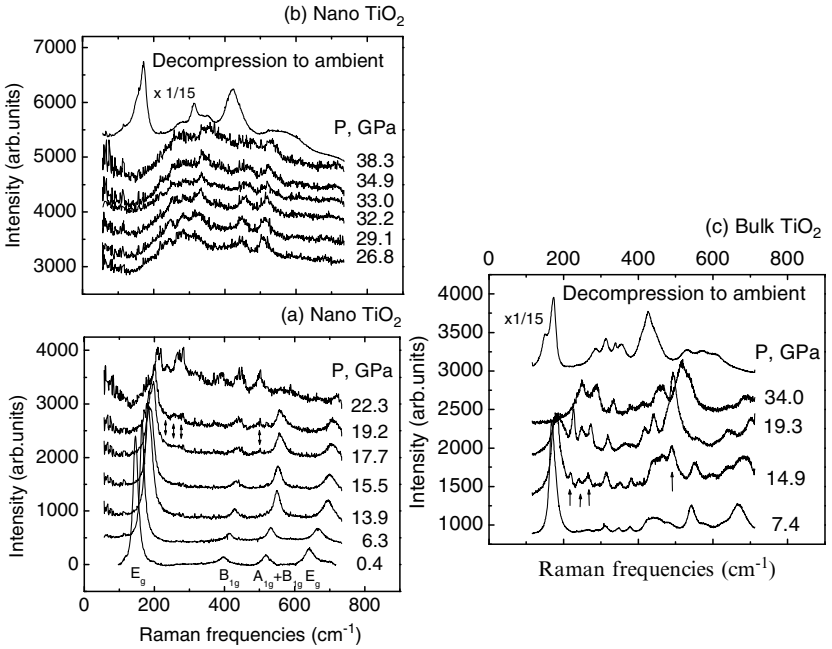

Figure 2. Raman spectra under high pressure of nanostructured anatase (a), (b); Panel (c) is for bulk anatase. The arrows in panels (a) and (c) are to delineate new modes specific to the high-pressure baddeleyite phase.

The pressure evolution of the Raman spectra of the nano-anatase compound is quite different. No new peaks appear in the spectra up to ~16 GPa which are all similar to the one at ambient pressure. Figure 2a shows that *the anatase phase in the nanostructured compound is stable to well beyond the first structural transition pressure found in bulk anatase*, i.e., ~5 GPa. When the pressure is increased to 17.7 GPa, see Figure 2a, a number of new bands of low intensity are discerned at ~235 cm^{-1}, ~250 cm^{-1}, ~275 cm^{-1} and ~500 cm^{-1}, which appear to be specific to the high-pressure baddeleyite phase (*Lagarec and Desgreniers,* 1995) and which persist to the maximum applied pressure of ~38 GPa. The nanophase sample transforms directly from the anatase to baddeleyite structure at 17.7 GPa without passage via the α-PbO_2-type intermediate (as in the macrocrystalline sample). However, when the nanophase sample is decompressed from the maximum pressure, the high-pressure baddeleyite phase is quenched to the α-PbO_2-type phase, similar to the behavior of the bulk compound, (see Figure 2b and c).

4.3. ULTRAFINE NANO-ANATASE , 6 NANOMETER GRAIN SIZE

Figure 3 displays all angle dispersive X-ray diffraction spectra taken at pressure for a ultrafine nano-TiO_2 sample having an average grain size of ~6 nm. The nano-anatase phase remains stable up to 18 GPa. *Note, that this is quite unlike the case of the bulk analog, which undergoes two different structural transitions up to this pressure.* Beyond 18 GPa evidence of structural disorder begins to set in as suggested by excessive peak-broadening and a diffuse halo emerging. The latter, manifested as an increase in background

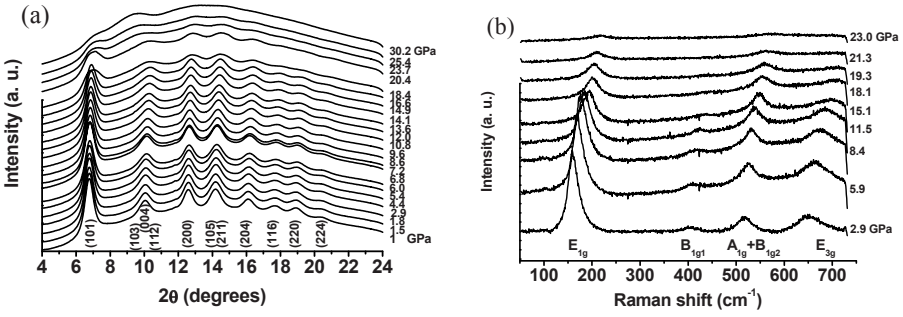

Figure 3. (a) High pressure powder x-ray diffraction spectra of ultrafine nano-anatase (d ~ 6 nm) up to 30 GPa at room temperature. (b) Raman spectra at room temperature of ultrafine nano-anatase up to high pressures of 23 GPa.

intensity (see Figure 3a), is supposed to signal the onset of disorder on a large length scale comparable to grain-size dimensions. The degree of disorder increases progressively at pressures beyond 18 GPa. At $P \sim 30$ GPa most of the diffraction lines disappear and a hump supposed to be characteristic of the highly disordered phase appears between 8° and 12° of 2θ. The material can be considered progressively more disordered and eventually near-amorphous at pressures beyond ~21 GPa, as corroborated by the Raman spectroscopy data shown in Figure 3b. The highly disordered or amorphous phase is quenchable after release of pressure.

5. Discussion

To estimate d^* from Eq (2) for the structural transition to the α-PbO_2-type intermediate, use the accepted value for the surface stress value i.e., $\gamma \approx 1.5$ Nm^{-1} (*Zhang and Banfield*, 1998). The reduction in free energy per unit volume due to density increase $\Delta G_V = P(\Delta V/V)$ is estimated by assuming the structural transition would occur at P~5 GPa and that the relative change in the unit-cell volume $\Delta V/V$ of ~10%, similar to bulk values (*Arlt et al.*, 2000). The estimated critical diameter is then d^*~15 nm, for the case where the misfit strain energy contribution has been neglected in Eq (2); if included then the critical diameter may be slightly larger.

Therefore the α-PbO_2-type intermediate will only nucleate and grow as a stable particle if it has a diameter $d > 15$ nm, else it constitutes a cluster or embryo and collapses. Since in one case the nano-phase anatase particles have average dimensions of $d \sim 12$ nm, they are therefore smaller than d^* and may be considered to be embryonic. It costs too much free energy of order $\gamma \times d^2$ in this case of a nano-particle of anatase of diameter $d < d^*$, compared to the energy reduction $P \times \Delta V$, to transform to a new structural phase with α-PbO_2 surfaces of dimension d^2.

From Eq (2) we again estimate the critical diameter for nucleation and growth of the baddeleyite phase at ~15 GPa using the relative volume reduction $\Delta V/V \sim 15\%$ at the anatase → baddeleyite transition, typical of what has been measured in a bulk single-crystal (*Arlt et al.*, 2000). Similar to arguments above a value for this critical diameter d^* ~4 nm is obtained if $\gamma \sim 1.5$ Nm^{-1} is used. The critical diameter d^* is appreciably smaller than the dimensions of a 12 nm anatase nano-particle. So nucleation and growth of the new baddeleyite phase out of the original (~12 nm) anatase nano-particle is plausible, consistent with the experimental observations.

What of the ultrafine 6 nm anatase which is seen to remain stable to high pressure without transforming to a new high pressure crystalline form (see Figure 3) As rationalized above for $d \approx d^*$: it would cost too much

surface energy $\sim \gamma \times d^2$ at high pressure to nucleate nano-domains $d \leq 6$ nm of the new high-pressure baddeleyite phase. So, ultrafine nano-anatase grains remain stable to much higher pressure, until there is sufficient energy reduction from volume collapse into a disordered (amorphous) network. The pressure dependence of the melting temperature T_M *in the nanophase material* may be an alternative explanation; where T_M has decreased to intersect the room-temperature isotherm (*Deb et al.*, 2001).

The relative change of the monotonically decreasing unit-cell volume versus pressure for the 6 nm nano-anatase is used in the range 6–18 GPa to obtain a bulk modulus ("stiffness") of B = 237 GPa, from an equation-of-state fit to the *P–V* data, see refs (*Pischedda et al.*, 2006; *Swamy et al.*, 2003). This is an enhanced bulk modulus at room-temperature incomparison with the macrocrystalline counterpart for which the bulk modulus is 180 GPa (*Arlt et al.*, 2000). *The nanophase material is appreciably less deformable (compressible), than the macrocrystalline analog.*

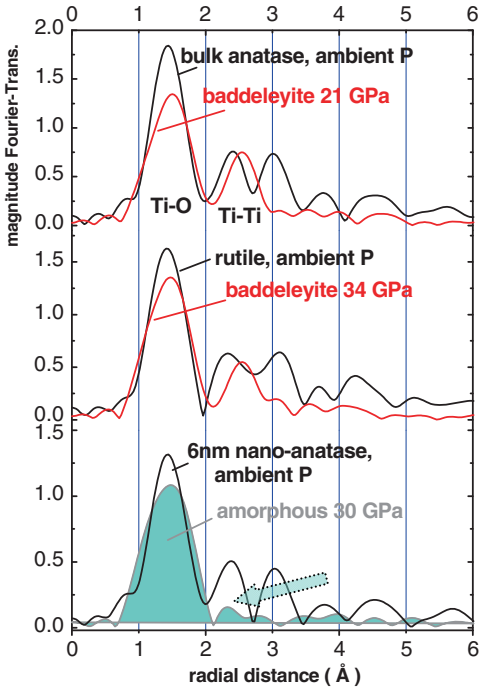

Figure 4. Pseudo radial distribution functions indicative of the Ti atomic local environment, obtained from the Fourier Transform of the Ti *K*-edge EXAFS oscillations of TiO_2. This shows Ti–O nearest-neighbor and Ti–Ti next-nearest neighbor features for different structural phases. Bottom panel shows the result for the high-density amorphous phase (shaded) of the 6 nm sample, where there are no structural signatures of significance (arrow) beyond radial distances of 2 Å.

To what extent (i.e., on what length scale) is this sample disordered at high densification (P > 20 GPa)? By means of the technique of X-ray absorption spectroscopy (XAS), very sensitive to the kind of local order around one given atom, namely the titanium, there is evidence that nano-anatase of an average grain size ~6 nm exhibits a pressure driven disorder on a scale of ~2 Å. This is shown in the Ti *K*-edge analyses of Figure 4, where second nearest neighbor (Ti–Ti) peaks in the pseudo radial distribution function are not discerned. This is supposed to be indicative of a purely amorphous network, *i.e.* with a disorder beyond the first nearest neighbor shell. This amorphization onset in the 15–20 GPa range is evident in either the EXAFS or through the behavior of the titanium pre-edge peaks (*Flank et al.*, 2008).

6. Final Comments

The "nano specific" features of, and grain-size effects on, the pressure response (ultra-stability, enhanced stiffness, high density amorphization) are not unique to the TiO_2 system. Other examples include both nano-structured silicon (*Tolbert et al.*, 1996; *Deb et al.*, 2001) and iron-oxide (*Jiang et al.*, 1998), to name but a selected few examples. These findings may eventually have important applications in nano-materials science and technology, e.g., for the development of new ultra-stable and ultra-strong variants of the bulk analogs.

ACKNOWLEDGEMENTS

Much of the research presented here has been funded from NRF and CoE sources (SA). It is also a pleasure to acknowledge the inputs from post-doctoral associates and international collaborators in France (Synchrotron-SOLEIL, IMPMC-Paris).

References

Arlt, T., Bermejo, M., Blanco, M.A., Gerward, L., Jiang, J.Z., Olsen, J.S., and Recio, J.M., 2000, High-pressure polymorphs of anatase TiO_2, *Phys. Rev. B* **61**: 14414–14419.

Cahn, J.W., 1980, Surface stress and the chemical equilibrium of small crystals – I. The case of the isotropic surface, *Acta Metall.* **28**: 1333–1338.

Deb, S.K., Wilding, M., Somayazulu, M., and McMillan, P.F., 2001, Pressure-induced amorphization and an amorphous-amorphous transition in densified porous silicon, *Nature* **414**: 528–530.

Flank, A.-M., Lagarde, P., Itie, J.-P., Polian, A., and Hearne, G.R., 2008, Pressure-induced amorphization and a possible polyamorphism transition in nanosized TiO_2. An X-ray absorption spectroscopy study, *Phys. Rev. B* **77**: 224112.

Hearne, G.R., Zhao, J., Dawe, A.M., Pischedda, V., Maaza, M., Nieuwoudt, M.K., Kibasomba, P., Nemraoui, O., and Comins J.D., 2004, Effect of grain size on the structural transitions in anatase TiO_2: A Raman spectroscopy study at high pressure, *Phys. Rev. B* **70**: 134102.

Jiang, J.Z., Olsen, J.S., Gerward, L., and Morup, 1998, Enhanced bulk modulus and transition pressure in γ-Fe_2O_3 nanocrystals, *Europhys. Lett.* **44**: 620–626.

Lagarec, K., and Desgreniers, S., 1995, Raman study of single crystal anatase TiO_2 up to 70 GPa, *Solid State Comm.* **94**(7): 519–524.

Ohsaka, T., Izumi, F., and Fujiki, Y., 1978, Raman spectrum of anatase, TiO_2, *J. Raman Spectrosc.* **7**: 321–324.

Pischedda, V., Hearne, G.R., Dawe, A.M., and Lowther, J.E., 2006, Ultra-stability and enhanced stiffness of ~6 nm TiO_2 nano-anatase and eventual pressure-induced disorder on the nanometer scale, *Phys. Rev. Lett.* **96**: 035509.

Porter, D.A., and Easterling, K.E., 1992, *Phase Transformations in Metals and Alloys*, 2nd. ed., Chapman & Hall, London, pp. 265–267.

Swamy, V., Dubrovinsky, L.S., Dubrovinskaia, N.A., Simionovici, A.S., Drakopoulos, M., Dimitriev, V., and Weber, H.-P., 2003, Compression behavior of nanocrystalline anatase TiO_2, *Solid State Commun.* **125** (2): 111–115.

Tolbert, S.H., Herhold, A.B., Brus, Louis E., and Alivisatos, A.P., 1996, Pressure-induced structural transformations in Si nanocrystals: surface and shape effects, *Phys. Rev. Lett*. **76**: 4384–4387.

Zhang, H., and Banfield, J.F., 1998, Thermodynamic analysis of phase stability of nano-crystalline titania, *J. Mater. Chem.* **8**: 2073–2076.

ANALYSIS OF THE TOTAL SCATTERING USING THE QUANTITATIVE HIGH PRESSURE PAIR DISTRIBUTION FUNCTION: PRACTICAL CONSIDERATIONS

J.B. PARISE[1,2*], L. EHM[1,3], F.M. MICHEL[4]
[1]*Mineral Physics Institute,* [2]*Department of Geosciences, Department of Chemistry, Stony Brook University, Stony Brook NY 11794-2100, USA,* [3]*Brookhaven National Laboratory, Upton NY 11973, USA,* [4]*Stanford Synchrotron Radiation Laboratory, Stanford, CA, USA*

Abstract Technical developments in high energy (E > 60 keV) total x-ray scattering at synchrotron storage rings allow collection of quantitative data from samples in high pressure devices. The infrastructure now in place facilitates advances in our understanding of how disorder, composition, P and T interact to stabilize and to properties of disordered crystalline, nano-crystalline, glassy and liquid materials at high PT. Key developments include over sampling using area detectors, focusing of beams with E > 80 keV and modifications to diamond anvil cells that in combination mitigate problems that limit the resolution and precision with which disordered materials can be studied.

Keywords: PDF, high-energy x-ray scattering, synchrotron

1. Introduction

Crystallographers determine the atomic-level structure of materials. Regardless of the state of the sample – crystalline, nano-crystalline, liquid, glassy – the basic theory of elastic scattering required to determine the atomic arrangement in materials is the same (*Warren*, 1969; *Cowley*, 1975). The compromises that accompany collection and interpretation of data when the sample is contained in a high-pressure vessel will be different from

* E-mail: jparise@notes.cc.sunysb.edu

E. Boldyreva and P. Dera (eds.), *High-Pressure Crystallography: From Fundamental Phenomena to Technological Applications*, DOI 10.1007/978-90-481-9258-8_42,

those required when the sample to collected at ambient conditions. The basic theory is the same however: diffraction or elastic scattering arises from the interference of radiation scattered from atoms, arranged periodically or not, and the x-ray and neutron interference patterns contain amplitude information but not phase.

Techniques developed to precisely determine crystal structure using single crystal and powder Bragg scattering data are well established and applicable straightforwardly to data collected at high pressures (HP). For disordered materials the inherently lower signal-to-background discrimination of the powder diffraction experiment is compound by the need to measure diffuse scattering that may be several orders of magnitude weaker than Bragg scattering. Maximizing the elastic component to the scattering from samples held in pressure cells is especially challenging, and minimize parasitic and Compton scattering from cells is therefore a priority.

2. Technical Developments

Recent technical developments now allow us to study a variety of important disordered materials *in situ,* over a wide range of conditions, with unprecedented precision (*Ehm et al.*, 2009). These technical developments include protocols for the collection of reliable data from diamond anvil cells (*Parise et al.*, 2005a*; Martin et al.*, 2005) and large volume devices (*Chapman et al.*, 2007); determining the present limits on model discrimination for nanomaterials at both ambient (*Michel et al.*, 2007, 2008) and high P (*Ehm et al.*, 2009, 2007), the combined use of ultrasonic and scattering techniques at HP to unambiguously reveal transitions in amorphous materials (*Antao et al.*, 2008) and integrating the use of theory to complement data taken from HP devices (*Yang et al.*, 2008, 2009).

2.1. HIGH ENERGY X-RAY SCATTERING

Investigations of glasses, nano-crystalline materials, and other poorly crystalline materials (*Tulk et al.*, 2002; *Guthrie et al.*, 2004; *Mei et al.*, 2006, 2007) benefit from scattering of high energy x-rays chiefly because of the increased penetrating power at high energies. The increased coverage of Q-space ($Q = 4\pi\sin\theta/\lambda$) in a single exposure using shorter wavelength radiation is also compatibility with modern area detectors (*Chupas et al.*, 2007). Focused x-rays with $E > 60$ keV ($\lambda < 0.2$ Å) allow high brightness experiments in diamond anvil cells while measurement of total elastic scattering to $Q > 25 Å^{-1}$ minimizes Fourier ripple and provide a remarkable

opportunity for quantitative high-pressure pair distribution function (QHP-PDF; *Parise et al.*, 2004) analysis.

2.2. THE PAIR DISTRIBUTION FUNCTION TECHNIQUE

Obtaining reliable data requires minimizing parasitic scattering. We have made a start on this problem in a series of recent experiments using high brightness high-energy x-ray scattering we (*Parise et al.*, 2005a; *Martin et al.*, 2005; *Mei et al.*, 2006) and several other groups (*Sheng et al.*, 2007; *Sen et al.*, 2006) are obtaining exciting results (see Part II). In the examples below, we review some of our recent work in high-pressure devices aimed at collecting data suitable for the study of the total scattering at high pressure.

The PDF, G(r), gives the probability of finding an atom at a given distance r from another atom and can be considered as a bond length distribution (*Egami et al.*, 2003):

$$G(r) = 4\pi r[\rho(r) - \rho_0] = \frac{2}{\pi}\int_0^\infty Q[S(Q) - 1]\sin(Qr)dQ \quad (1)$$

where $\rho(r)$ is the microscopic pair density, ρ_0 is the average number density, and Q is the magnitude of the scattering vector ($Q = (4\pi\sin\theta)/\lambda$). Experimentally it is not possible to measure data up to infinite Q, and the cutoff at finite values of Q_{max} decreases the real space resolution of the PDF. This causes some aberrations in the form of "termination ripples" which propagate through $G(r)$ as high frequency noise. For both x-ray and neutron scattering experiments, high energies are required in order to access high values of Q_{max} to obtain the most accurate Fourier transform of the reduced structure function $F(Q)$.

The PDF is obtained from the powder diffraction (x-ray or neutron) via a Fourier transform of the normalized total scattering intensity, S*(Q)*:

$$S(Q) = 1 + [I^{coh}(Q) - \sum c_i |f_i(Q)|^2] / \left|\sum c_i f_i(Q)\right|^2 \quad (2)$$

where $I^{coh}(Q)$ is the coherent scattering intensity per atom, c_i is the atomic concentration and f_i is the x-ray scattering factor for species i.

Conventional high real-space resolution measurements typically make use of energy resolving point detectors, such as high-purity germanium, that are scanned over wide angular ranges. These measurements are very slow and generally are unsuitable for studies in the diamond anvil cell where sample volumes are typically less than 10^{-2} mm^3. For large volume devices such as the Paris–Edinburgh cell the use of a point counter with tight collimation provides excellent signal-to-noise discrimination, at the expense of 8-h data collection times. Recent advances in measurement strategies for

quantitative PDF analysis reduced data collection times by several orders of magnitude over the conventional scanning approach based on point by point detection (*Martin et al.*, 2005; *Chupas et al.*, 2003), by combining high energy x-rays (>60 keV) with imaging plate (IP) or amorphous Si (a-Si) area detectors to measure the scattered intensity to moderately high values of momentum transfer ($Q_{max} < 30$ Å^{-1}). In combination with modified high pressure cell designs (*Martin et al.*, 2005; *Chupas et al.*, 2003), imaging plate and amorphous silicon detectors (*Chupas et al.*, 2003, 2007), provide moderate resolution PDF data in tens of minutes for large volume devices and hours for the DAC, rather than hours or not at all. This combination of focusing, detectors and HP cells enables previously impractical parametric and in-situ studies of complex functional materials. Consequently, such studies based on this approach have become more routine/widespread and this approach has rapidly become the method of choice for HP PDF measurements for a growing number of users at synchrotron facilities.

2.3. QUANTITATIVE TOTAL SCATTERING STUDIES AT HIGH P

Trial measurements (Figures 1 and 2) demonstrated scattering to 20 Å^{-1} is sufficient for high quality PDFs of crystalline gold reference in a standard diamond anvil cell (*Martin et al.*, 2005) with un-perforated diamonds (Figure 3). Diffraction patterns were collected using a MAR345 imaging plate detector. Data treatment included subtraction of background, determined from exposures at ambient-P without the sample in position, and exclusion of single-crystal diamond spots (Figure 1), followed by integration with Fit2D (*Hammersley et al.*, 1996). To avoid saturation of the detector on any single exposure, and to obtain optimal counting statistics, data were obtained by averaging many short exposures. Typically, data were collected for ten 5-s exposures, which were averaged to attain optimum counting statistics. Integrated data was processed to PDFs using the program PDFgetX2 (*Qiu et al.*, 2004), where standard corrections as well as those unique to the image plate geometry were applied (*Chupas et al.*, 2003). Full profile fitting of the PDF was performed using program PDFFIT (*Proffen and Billinge*, 1999).

The DAC is versatile, portable and easily interfaced to LT and resistive heating apparatus. For selected problems, large samples in the gas cell or Paris–Edinburgh cell will be required. The use of area detectors usually precludes the use of diffracted beam collimation. This is not so problematic for diamond cell studies where contributions by Bragg scattering from single crystal diamond anvils can be excluded ex post facto using software such as Fit2D (*Hammersley et al.*, 1996); the loss of information on the area detector is not so severe since integration around the Debye rings provides

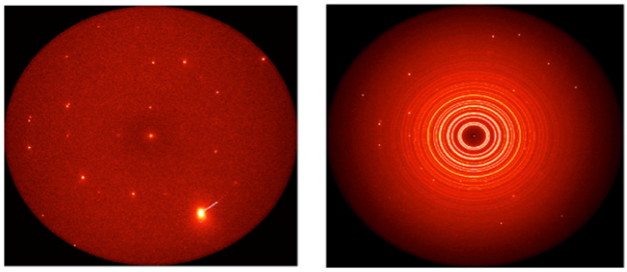

Figure 1. Typical two-dimensional sample exposure illustrating the single crystal diamond spots alongside sample powder diffraction. These spots, including the surrounding diffuse scatter, must be carefully masked prior to data integration. To avoid saturation of the detector and obtain optimal counting statistics, the bright spots from the diamond anvils demonstrate the need to average many short exposures. The intensity of parasitic DAC Compton scatter is best observed when comparing the central beamstop shadow with adjacent background intensity. The diamond anvil Compton scatter and sample diffuse scatter cannot be distinguished by eye.

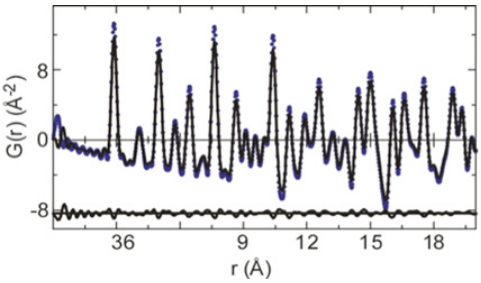

Figure 2. A plot comparing the PDF of gold taken from a 1 mm capillary (solid black) versus that taken in the DAC at 1 bar (dash blue). The difference plot below (solid black) shows no asymmetry about PDF Au–Au correlations suggesting the DAC background correction is valid.

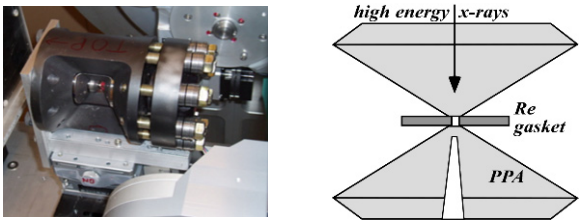

Figure 3. (Left) moissonite (SiC) anvil cell of the type being developed by the Carnegie Institution for SNAP at the SNS and capable of pressure >35 GPa and large volume. (Right) schematic drawing of a DAC with a single perforated anvils. PPA: Partial Perforated Anvil made of 0.25-carat diamond with a conical hole. Most scattering of high-energy x-rays by the upstream diamond is masked by an extended heavy metal gasket (rhenium in this case). Provided the transmitted beam is aligned to the perforation, contributions from the downstream diamond are minimized.

sufficient statistics. Some difficulty arises in the case of large volume high pressure devices (LVHPD) were components in the beam tend to give rise to parasitic scattering around the whole Debye ring (*Chen et al.*, 1998, 2000). When measurement of the diffuse elastic contribution to the pattern is important, as they are for total scattering, subtraction techniques may eliminate the diffuse scattering component. For this reason, use of a radial collimator (*Mezouar et al.*, 2002; *Crichton et al.*, 2003; *Parise et al.*, 2005b) along with a large sample size in a LVHPD is advantageous for quantitative studies of glassy and cryptocrystalline materials.

2.4. QUANTITATIVE HIGH PRESSURE PAIR DISTRIBUTION FUNCTION (QHP-PDF) ANALYSIS: CURRENT PRACTICE

Comparison of parameters derived from both the Rietveld technique (*Toby*, 2001; *Larson and Von Dreele*, 2000) and PDF refinement were consistent and demonstrated the corrections used for background and Compton scattering were valid (Figures 1 and 2, *Martin et al.*, 2005). Several potential pitfalls are avoided by looking at heavy scatterers such as gold including the dominance of sample scattering compared to the coherent scattering contributions from the methanol:ethanol (4:1) pressure-transmitting medium at 80 keV. The correlations from the alcohol pressure medium must exist however and will become more obvious when light elements are used. This will require some combination of samples being loaded in He, elimination of the pressure medium, perhaps along with heating of the sample to eliminate deviatoric stress, and the collection and proper normalization of blanks for subtraction of the pressure-medium contribution.

The protocol described above works well for heavy scatterers, and for lighter scatterers it is essential to properly correct for background to remove long-wavelength errors in $S(Q)$, which will Fourier transform into physically meaningless peaks in the low-r(Å) region of the PDF. Tests of the validity of background correction included comparison of PDFs from gold in a capillary versus gold in the DAC at ambient-P; we found the difference in PDF between the capillary and DAC is minimal (Figure 2).

The significant contribution to the background from diamond will need to be addressed (*Martin et al.*, 2005) for studies of glasses, melts and light elements, since in these cases Compton scattering can overwhelm the signal of interest. One solution is to increase signal-to-noise discrimination by removing some of the diamond from the beam path using perforated diamond anvils with the geometry shown in Figure 3 or by using two in-line perforated diamonds. In the case shown in Figure 3, a conical hole of about 0.5 mm maximum and 80 μm minimum diameter is perforated into the downstream diamond to within 200 μm of a 350 μm-culet for example.

Compton scattering is significantly reduced (Figure 4). It is important in this case to focus the incident beam rather than to use beam slits to define the beam size. This maximizes the x-ray flux on the sample. Beamline optics at beamline 1-ID at the APS are well matched to the studies of nanocrystalline and glassy materials at high PT. Focused (20 μm spot size) x-rays with energies in the 80–120 keV range provide data to $Q > 20$ Å^{-1} with standard imaging plate geometries, while minimizing background from the DAC (Figure 4). Most Compton scattering arises from the downstream diamond and only this diamond needs to be perforated; the upstream scattering is easily masked by use of a high Z gasket materials such as Re or W.

The high-energy x-rays at beamline 1-ID are delivered by a bent double-Laue monochromator followed by vertically focusing refractive lenses. The liquid nitrogen cooled monochromator (*Shastri et al.*, 2002) consists of two bent Si(111) Laue crystals arranged to sequential Rowland conditions and provides high flux in a beam of preserved source brilliance (divergence and size). The focusing refractive lenses, placed immediately after the monochromator, are of either the cylindrical aluminum or saw-tooth silicon (*Shastri*, 2004) types, giving line-foci of 16–80 μm in vertical size at the end-station, with flux density gains in the range 6–20.

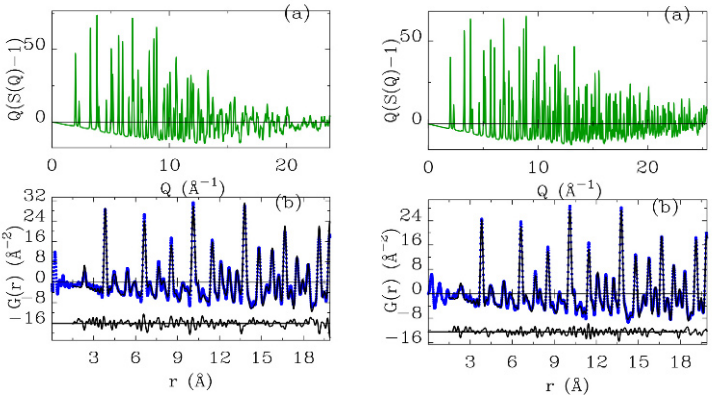

Figure 4. Diagrams showing (a) Q[$S(Q)$-1] and (b) $G(r)$ for nano-CeO_2 in (*left*) a diamond anvil cell fitted with un-perforated diamonds and (*right*) fitted with perforated diamonds (Figure 3). The decrease in contributions to the overall scattering from diamonds in the perforated cell leads to much better signal to noise discrimination at high Q, an important factor in deriving better resolved real space correlation functions containing fewer "ripples" due to Fourier termination errors. The experimentally determined $G(r)$ in each case is shown as a dotted line and the model derived values are shown as a continuous line. The difference curve (black line) is plotted below and on the same scale as the experimental and model-derived curves.

The combination of focusing, perforated diamonds and area detectors have allowed QHP-PDF studies of nano-crystalline and glassy materials composed of first row transition and main group elements. Studies of low Z elements are tractable. Some recent results are discussed in the next chapter.

ACKNOWLEDGEMENT

This work is supported by the National Science Foundation (DMR-0800415).

References

Antao, S.M., C.J. Benmore, E. Bychkov, and J.B. Parise (2008) Network rigidity in $GeSe_2$ glass at high pressure. Physical Review Letters, 100: 115501.

Chapman, K.W., P.J. Chupas, C.A. Kurtz, D.R. Locke, J.B. Parise, and J.A. Hriljac (2007) Hydrostatic low-range pressure applications of the Paris-Edinburgh cell utilizing polymer gaskets for diffuse X-ray scattering measurements. Journal of Applied Crystallography, 40: 196–198.

Chen, J., D.J. Weidner, M.T. Vaughan, R. Li, J.B. Parise, C. Koleda, and K.J. Baldwin (1998) Time resolved diffraction measurements with an imaging plate at high pressure and temperature. Reviews in High Pressure Science and Technology, 7: 272–274.

Chen, J., D.J. Weidner, M.T. Vaughan, J.B. Parise, J. Zhang, and Y. Xu (2000) A Combined CCD/IP Detection System for Monchromatic XRD Studies at High Pressure and Temperature, in Science and Technology of High Pressure, M.H. Manghnani, W.J. Nellis, and M.F. Nicol, Editors. Universities Press Ltd.: Hyderabad, India, pp. 1035–1038.

Chupas, P.J., X.Y. Qiu, J.C. Hanson, P.L. Lee, C.P. Grey, and S.J.L. Billinge (2003) Rapid-acquisition pair distribution function (RA-PDF) analysis. Journal of Applied Crystallography, 36: 1342–1347.

Chupas, P.J., K.W. Chapman, and P.L. Lee (2007) Applications of an amorphous silicon-based area detector for high-resolution, high-sensitivity and fast time-resolved pair distribution function measurements. Journal of Applied Crystallography, 40: 463–470.

Crichton, W.A., M. Mezouar, G. Monaco, and S. Falconi (2003) Phosphorus: New in situ powder data from large-volume apparatus. Powder Diffraction, 18: 155–158.

Cowley, J.M. (1975) Diffraction Physics. Amsterdam: North-Holland.

Egami, T. and S.J.L. Billinge (2003) Underneath the Bragg Peaks: Structural Analysis of Complex Materials. Pergamon Materials Series, R.W.Cahn, Editor. Kidlington: Elsevier. Vol. 7, 316 pp.

Ehm, L., S.M. Antao, J. Chen, D.R. Locke, M.F. Michel, C.D. Martin, T. Yu, J.B. Parise, P.J. Chupas, P.L. Lee, S.D. Shastri, and Q. Guo (2007) Studies of local and intermediate range structure in crystalline and amorphous materials at high pressure using high-energy X-rays. Powder Diffraction, 22: 108–112.

Ehm, L., F.M. Michel, S.M. Antao, C.D. Martin, P.L. Lee, S.D. Shastri, P.J. Chupas, and J.B. Parise (2009) Structural changes in nanocrystalline mackinawite (FeS) at high pressure. Journal of Applied Crystallography, 42: 15–21.

Guthrie, M., C.A. Tulk, C.J. Benmore, J. Xu, J.L. Yarger, D.D. Klug, J.S. Tse, H.K. Mao, and R.J. Hemley (2004) Formation and structure of a dense octahedral glass. Physical Review Letters, 93: 115502.

Hammersley, A.P., S.O. Svensson, M. Hanfland, A.N. Fitch, and D. Hausermann (1996) Two-dimensional detector software: from real detector to idealised image or two-theta scan. High Pressure Research, 14: 235–248.

Larson, A.C. and R.B. Von Dreele (Editors) (2000) GSAS Manual, in Secondary GSAS Manual, Secondary. Los Alamos, NM: Los Alamos National Laboratory.

Martin, C.D., S.M. Antao, P.J. Chupas, P.L. Lee, S.D. Shastri, and J.B. Parise (2005) Quantitative high-pressure pair distribution function analysis of nanocrystalline gold. Applied Physics Letters, 86: 061910-1.

Mei, Q., C.J. Benmore, R.T. Hart, E. Bychkov, P.S. Salmon, C.D. Martin, F.M. Michel, S.M. Antao, P.J. Chupas, P.L. Lee, S.D. Shastri, J.B. Parise, K. Leinenweber, S. Amin, and J.L. Yarger (2006) Topological changes in glassy $GeSe_2$ at pressures up to 9.3 GPa determined by high-energy x-ray, and neutron diffraction measurements. Physical Review B, 74: 014203-01.

Mei, Q., C.J. Benmore, and J.K.R. Weber (2007) Structure of liquid SiO_2: A measurement by high-energy x-ray diffraction. Physical Review Letters, 98: 057802.

Mezouar, M., P. Faure, W. Crichton, N. Rambert, B. Sitaud, S. Bauchau, and G. Blattmann (2002) Multichannel collimator for structural investigation of liquids and amorphous materials at high pressures and temperatures. Review of Scientific Instruments, 73: 3570–3574.

Michel, F.M., L. Ehm, G. Liu, W.Q. Han, S.M. Antao, P.J. Chupas, P.L. Lee, K. Knorr, H. Eulert, J. Kim, C.P. Grey, A.J. Celestian, J. Gillow, M.A.A. Schoonen, D.R. Strongin, and J.B. Parise (2007a) Similarities in 2-and 6-line ferrihydrite based on pair distribution function analysis of X-ray total scattering. Chemistry of Materials, 19: 1489–1496.

Michel, F.M., L. Ehm, S.M. Antao, P. Lee, P.J. Chupas, G. Liu, D.R. Strongin, M.A.A. Schoonen, B.L. Phillips, and J.B. Parise (2007b) The structure of ferrihydrite, a nanocrystalline material. Science, 316: 1726–1729.

Michel, F.M., S. Debnath, D.R. Strongin, L. Ehm, P. Lee, P.J. Chupas, C. Tarabrella, M.A.A. Schoonen, and J.B. Parise (2008) Ferrihydrite, the iron core in native horse-spleen ferritin. Science (submitted).

Parise, J.B., S.M. Antao, F.M. Michel, C.D. Martin, P.J. Chupas, S.D. Shastri, and P.L. Lee (2005a) Quantitative high-pressure pair distribution function analysis. Journal of Synchrotron Radiation, 12: 554–559.

Parise, J.B., S.M. Antao, C.D. Martin, and W. Crichton (2005b) Diffraction studies of order-disorder at high pressures and temperatures. Powder Diffraction, 20: 80–86.

Proffen, T. and S.J.L. Billinge (1999) PDFFIT, a program for full profile structural refinement of the atomic pair distribution function. Journal of Applied Crystallography, 32: 572–575.

Qiu, X., J.W. Thompson, and S.J.L. Billinge (2004) PDFgetX2: a GUI-driven program to obtain the pair distribution function from X-ray powder diffraction data. Journal of Applied Crystallography, 37: 678.

Shastri, S.D. (2004) Combining flat crystals, bent crystals and compound refractive lenses for high-energy X-ray optics. Journal of Synchrotron Radiation, 11: 150–156.

Shastri, S.D., K. Fezzaa, A. Mashayekhi, W.K. Lee, P.B. Fernandez, and P.L. Lee (2002) Cryogenically cooled bent double-Laue monochromator for high-energy undulator X-rays (50–200 keV). Journal of Synchrotron Radiation, 9: 317–322.

Sheng, H.W., H.Z. Liu, Y.Q. Cheng, J. Wen, P.L. Lee, W.K. Luo, S.D. Shastri, and E. Ma (2007) Polyamorphismin a metallic glass. Nature Materials, 6: 192–197.

Sen, S., S. Gaudio, B.G. Aitken, and C.E. Lesher (2006) Observation of a pressure-induced first-order polyamorphic transition in a chalcogenide glass at ambient temperature. Physical Review Letters, 97: 025504.

Toby, B.H. (2001) EXPGUI, a graphical user interface for GSAS. Journal of Applied Crystallography, 34: 210–213.

Tulk, C.A., C.J. Benmore, J. Urquidi, D.D. Klug, J. Neuefeind, B. Tomberli, and P.A. Egelstaff (2002) Structural studies of several distinct metastable forms of amorphous ice. Science, 297: 1320–1323.

Warren, B.E. (1969) X-ray Diffraction. Reading, MA: Addison–Wesley.

Yang, L., C.A. Tulk, D.D. Klug, L. Ehm, D. Martin, B.C. Chakoumakos, J.J. Molaison, and J.B. Parise. (2008 of Conference) A New Hexagonal Phase for Pressure-Quenched Xe Clathrate Hydrate. in American Crystallographic Association Book of Abstracts (http://neutrons.ornl.gov/conf/aca2008/abstracts.shtml). Oak Ridge Tennessee: ACA Volume: Pages.

Yang, L., C.A. Tulk, D.D. Klug, I.L. Moudrakovski, C.I. Ratcliffe, J.A. Ripmeester, B.C. Chakoumakos, L. Ehm, C.D. Martin, and J.B. Parise (2009) Synthesis and characterization of a new structure of gas hydrate. Proceedings of the National Academy of Sciences, 97: 13484–13487.

ANALYSIS OF THE TOTAL SCATTERING USING THE QUANTITATIVE HIGH PRESSURE PAIR DISTRIBUTION FUNCTION: CASE STUDIES

L. EHM[1,2*], F.M. MICHEL[3], J.B. PARISE[1,4]
[1]*Mineral Physics Institute, Stony Brook University, Stony Brook NY 11794-2100, USA,* [2]*Brookhaven National Laboratory, Upton NY 11973, USA,* [3]*Stanford Synchrotron Radiation Laboratory, Stanford CA, USA,* [4]*Department of Geosciences, and Department of Chemistry, Stony Brook University, Stony Brook NY 11794-2100, USA*

Abstract X-ray total scattering and pair distribution function analysis have been used to investigate the structural changes in nano-crystalline mackinawite (FeS), with three distinct particle sizes, at high pressure. Nano-crystalline mackinawite undergoes an irreversible first-order phase transition at about 3 GPa from tetragonal mackinawite to orthorhombic FeS-II. The transition mechanism and the grain size effect on the transition pressure and the compressibility have been determined.

Keywords: Iron sulfide, pair distribution function, phase transition

1. Introduction

The structural comparison between bulk and nano-crystalline materials is challenging, due to the difficulties in determining the atomic arrangements in nano-crystalline materials. The diffraction data of nano-materials are degraded due to broadening of the Bragg peaks and the build-up of diffuse scattering is significant, as particle sizes approach the coherence length of the radiation used to study these materials. Conventional structure determination and structure refinement techniques often fail on nano-crystalline materials, since the evaluation neglects the information in the diffuse scattering

* E-mail: lars.ehm@stonybrook.edu

E. Boldyreva and P. Dera (eds.), *High-Pressure Crystallography: From Fundamental Phenomena to Technological Applications*, DOI 10.1007/978-90-481-9258-8_43,

and only uses the Bragg contribution to the scattering signal. Additional difficulties during the structure determination of nano-crystalline compounds are introduced by capping agents widely used to stabilize nano-particles.

The combination of focusing, perforated diamonds and area detectors have allowed quantitative high pressure pair distribution function (QHP-PDF) studies of nano-crystalline and glassy materials composed of first row transition and second main group elements (*Ehm et al.*, 2009; *Martin et al.*, 2005; *Mei et al.*, 2006; *Parise et al.*, 2005, 2009). Recent results on the high-pressure behavior of capping agent free nano-crystalline FeS are discussed below.

2. Case Study Iron Sulfide FeS

Iron sulfides are of major importance in geological, environmental and planetary science (*Schippers and Jorgensen*, 2002; *Fei et al.*, 1995; *Wilkin et al.*, 1996). The phase relations in this system are complex and not fully resolved. At ambient conditions the composition FeS crystallizes in two modifications, the mackinawite (*Kouvo et al.*, 1963; *Lennie et al.*, 1995) and troilite (*Bertaut*, 1956) structures. The first step in the formation of iron sulfides under hydrothermal conditions is the nucleation of a reduced, short-range ordered iron monosulfide that is generally believed to be a precursor to crystalline mackinawite and pyrite (FeS_2) (*Benning et al.*, 2000; *Schoonen and Barnes*, 1991a, b). Recently, *Michel et al.* (2005) have used the x-ray total scattering technique to determine that this nano-crystalline compound is single phase and that its pair distribution function (PDF) can be modeled using the mackinawite structure. Nano-crystalline FeS can be reproducibly synthesized without stabilizing capping agents and the particle size of nano-crystalline mackinawite can be controlled by aging time and/or temperature (*Michel et al.* 2005). Therefore, the nano-crystalline form of mackinawite is an excellent material to explore its behavior at non-ambient conditions.

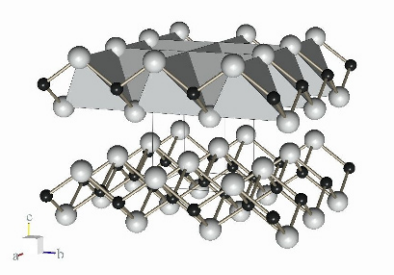

Figure 1. Crystal structure of mackinawite. The black spheres represent Fe^{2+} ions and the light gray spheres are S^{2-} ions. The coordination polyhedra of iron are plotted in gray.

Mackinawite (FeS) crystallizes in the space group *P*4/*nmm* with the lattice parameters a = 3.6735 (4) and c = 5.0328 (7) Å (*Lennie et al.*, 1995). Iron occupies the Wyckoff position 2*a* (0, 0, 0) and sulfur the position 2*b* (0, 1/2,1/4). The structure is composed of layers of edge-sharing FeS_4 tetrahedra stacked onto each other parallel to the *c* axis. The bonding in the layers is predominantly covalent, whereas the layers are connected by van der Waals forces (Figure 1). The FeS polymorph troilite has been extensively studied at high pressure (*King and Prewitt*, 1982), whereas the high-pressure behavior of mackinawite is unknown. The high-pressure behavior of nano-crystalline mackinwaite with three different particle sizes has been studied by x-ray total scattering and pair distribution function (PDF) analysis up to pressures of 9.2 GPa. The details of the high-pressure experiment have been exhaustively discussed elsewhere including in this volume (*Ehm et al.*, 2001; *Parise et al.*, 2009).

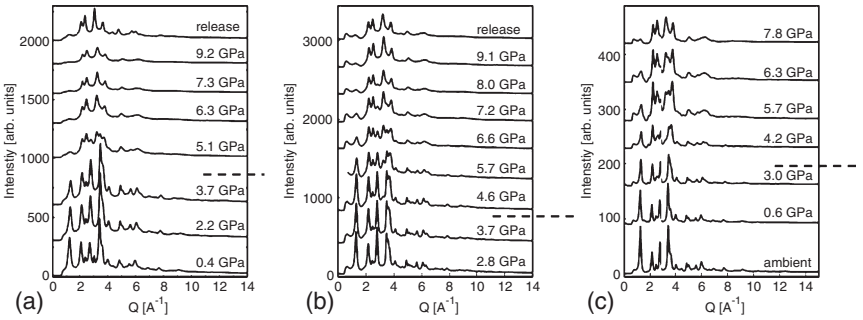

Figure 2. Pressure dependence of the diffraction patterns of nano-crystalline mackinawite with grain sizes of 6 nm (a), 7 nm (b) and 8 nm (c). The disappearance of the 001 reflection of mackinawite at Q of 1.2 $Å^{-1}$ is clearly visible above 3.7 GPa for the 6 and 7 nm samples, and 3.0 GPa for the 8 nm sample.

Figure 2 shows the evolution of the integrated diffraction patterns with pressure for three particle sizes. The disappearance of the 001 reflection of mackinawite at Q ~1.2 $Å^{-1}$ can be observed for all samples, indicating a pressure-induced phase transition. The transition pressure and the width of the two-phase region show particle size dependence. The onset of the phase transition is observed at 3.7 (2) GPa for the samples with particle sizes of 6 and 7 nm, whereas for the 8 nm sample the start of the phase transition is at 3.0 GPa. The diffraction patterns collected after pressure release show that the transition is irreversible. The pair distribution function of the low pressure phase can be fitted with the mackinawite structure model. Figure 3 shows the fit for the 6 nm sample at 0.4 (2) GPa.

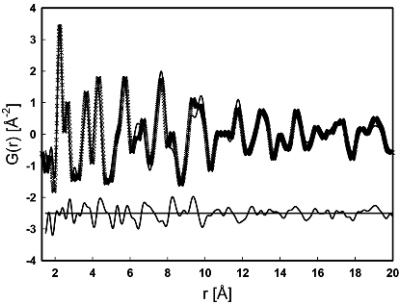

Figure 3. Observed (crosses) and calculated (solid line) PDF of mackinawite with a particle size of 6 nm at 0.4 (2) GPa. The difference curve between the measured and calculated PDF is plotted at the bottom of the figure.

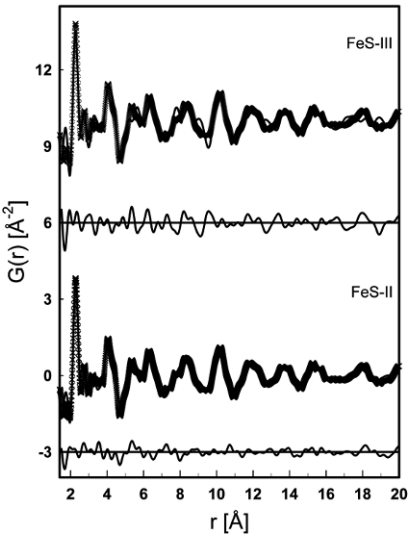

Figure 4. Observed (crosses) and calculated (solid line) PDF of FeS-II (*bottom*) and FeS-III (*top*) for the 7 nm sample at 9.1 (1) GPa. The associated difference curves between the measured and calculated PDFs are plotted beneath each fit.

The structure determination for the high-pressure phase of mackinawite from the total scattering data is not straightforward. Nanocrystalline materials show diffraction patterns with very few and overlapping Bragg peaks, and a pronounced diffuse component, making conventional crystallographic structure solution approaches inapplicable. However, initial structural model for the high-pressure phase can be developed on basis of the PDF. The first three maxima in the PDF at 2.277 (8), 2.75 (1) and 3.19 (1) Å have been assigned to specific atomic pairs on the basis of ionic radii and information

about high-pressure crystal chemistry (*Shannon*, 1976; *Hazen and Finger*, 1992). The maximum at 2.277 (8) Å represents a Fe–S distance with iron octahedrally coordinated by sulfur. Fe–Fe distances in face-sharing FeS_6 octahedra can be assigned to the maximum at 2.74 (1) Å. The third maximum at 3.19 (1) Å cannot be unambiguously associated with only one atomic pair. Most likely, two atomic pairs contribute to the maximum in the pair distribution function: S–S distances in a FeS_6 octahedron and Fe–Fe distances in edge-sharing FeS_6 octahedra. The distance and connectivity requirements derived from the PDF are met by three structures, troilite (*Bertaut*, 1956), its high-pressure polymorphs FeS-II (*King and Prewitt*, 1982) and FeS-III (*Nelmes et al.*, 1999). The troilite structure is only stable below 3.4 GPa (*King and Prewitt*, 1982) and can, therefore, be ruled out as a possible structure for the high-pressure phase of mackinawite. In order to determine the structure of the high-pressure phase of mackinawite, the FeS-II and FeS-III structural models were refined against the data sets collected at the highest pressure for the three different particle sizes.

The fits of the FeS-II and FeS-III structure models to the pair distribution function G(r) at 9.1 (1) GPa for the 7 nm sample are shown in Figure 4. The FeS-II structural model leads to a superior fit to the data with fewer refinable structural parameters than the FeS-III model. Although the fit to the FeS-II model is satisfactory, the close structural relationship between the type-II, type-III and troilite structures, which are distortions of the ideal NiAs ($B8_1$) structure, suggests caution in interpreting what is an ensemble of atoms with limited periodicity in terms of an exact structure model for a bulk periodic material. Within the limits of resolution of the data, we conclude that nanocrystalline mackinawite undergoes a pressure-induced phase transition to the FeS-II structure, or one very closely related to it, at about 3.0 GPa. Although the stability field for the bulk FeS-III structure is reached for all three samples, a second phase transition from the FeS-II structure to the FeS-III structure is not observed and this is not unexpected, since the phase transition pressures are usually significantly elevated in nanocrystalline materials, compared to the bulk material (*Variano et al.*, 1988).

FeS-II crystallizes in the space group *Pnma* with the lattice parameters a = 5.7449 (6), b = 3.3782 (4) and c = 5.8048 (6) Å (*King and Prewitt,* 1982; *Marshall et al.*, 2000). Iron and sulfur occupy the Wyckoff position 4*c* (x, 1/4, z), with x = 0.0117 (4) and z = 0.2038 (3) for iron, and x = 0.223 (1) and z = 0.576 (1) for sulfur. The MnP-type structure can be seen as an orthorhombically distorted variant of the NiAs structure type, with pronounced metal–atom zigzag chains. Iron is sixfold coordinated by sulfur, forming distorted octahedra. These octahedra are connected through edges and faces to each other.

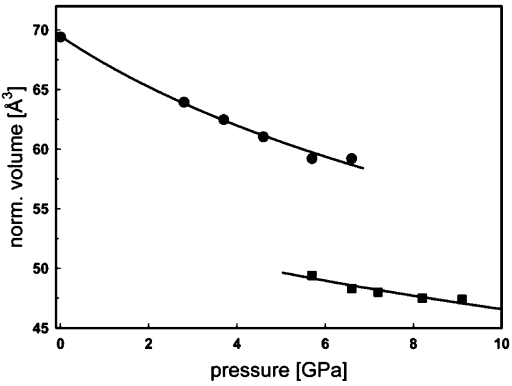

Figure 5. Evolution of the normalized (1 formula unit per unit cell) unit-cell volume for 7 nm mackinawite. The filled circles represent the low-pressure mackinawite structure, whereas the squares represent the high-pressure polymorph FeS-II. The lines result from fits of second-order Birch–Murnaghan equations-of-state to the low- and high-pressure phases of FeS.

The evolution of the normalized unit-cell volume is shown in Figure 5 for the sample with 7 nm particle size.

A volume discontinuity of 16.6 (4)% for the 6 nm sample, 16.8 (5)% for the 7 nm sample and 18.4 (5)% for the 8 nm sample is observed at the phase transition. The results of the fits of a second-order Birch–Murnaghan equation-of-state are given in Table 1. The bulk modulus for the mackinawite phase shows a small particle size dependency. The sample with the smallest grain size is the least compressible, whereas the 7 and 8 nm samples have the same bulk modulus. The bulk moduli determined for the FeS-II phase for the three nano-crystalline samples are significantly enhanced compared with the bulk modulus of bulk FeS-II (*King and Prewitt*, 1982; *Kusaba et al.*, 1997). The lattice compression of the mackinawite phase is highly anisotropic. The linear compressibilities parallel to the *c* axis are five to seven times larger than those along the *a* axis, with a small particle size dependence. The FeS-II structure shows almost no anisotropy in the lattice compression. The strong anisotropy of the linear compressibilities in the mackinawite phase can be understood by considering the different types of bonding in the structure. The lowest compressibility is found parallel to the *a* axis, where the structure consists of layers of ionic bonded FeS_4 tetrahedra, whereas the layers are connected by van der Waals forces along the *c*-axis direction. The compressibility parallel to the stacking direction **c** is five to seven times higher. This can be attributed to the ease with which the distance between the van der Waals bonded layers can be reduced compared with distorting the covalently bonded tetrahedra, which would require considerably more energy.

TABLE 1. Values of a second-order Birch–Murnaghan equation-of-state fit parameters.

	Mackinawite		FeS-II	
Particle size (nm)	V_0 (Å^3)	B_0 (GPa)	V_0 (Å^3)	B_0 (GPa)
6	69.9(2)	39(2)	104.7(1)	68(1)
7	69.5(6)	27(2)	108.0(2)	50(1)
8	70.0(3)	27(1)	106.9(4)	56(4)
Bulk[a]			112.8(3)	35(4)
Bulk[b]			107.5(6)	44(3)

[a] *King and Prewitt,* 1982

[b] *Kusaba et al.,* 1997

The phase transition from mackinawite to FeS-II observed at about 3 GPa is characterized by a change in the iron environment. The coordination of the Fe ions changes from a fourfold to a sixfold coordination. The two phases coexist over a wide pressure range, reflecting the first-order character of the transition. This is further supported by the observed discontinuities in the molar volume at the phase transition. The phase transition is irreversible and the high-pressure phase is metastably preserved at ambient conditions after pressure release. This behavior can be attributed to surface stabilization and grain size effects of the nanoparticles, since the pressure-induced phase transitions to FeS-II and FeS-III observed in bulk troilite are fully reversible. The phase transition is induced by the closure of the van der Waals gap in the mackinawite structure. The transition is reconstructive, since a change in the Fe coordination from four to six is observed and there exists no direct group/subgroup relationship between the space groups *P*4/*nmm* and *Pnma*.

3. Conclusions

Recent developments in focused high-energy beams, and modified diamond geometries, suggest that quantitative data suitable for PDF analysis and the derivation of refined structure models can be obtained from samples at high pressure, in the diamond anvil cell and other pressure vessels. It remains for the near future to rigorously test the suitability of the PDF technique for distinguishing between closely related models such as those, for example, related to the same aristotype. Several important classes of nano-materials fall into this category including those related to perovskite. It is clear at this early stage, however, that the total scattering experiments are suitable for a wide range of high-pressure studies in diamond anvil cells.

References

Benning, L.G., R.T. Wilkin, and H.L. Barnes, *Reaction pathways in the Fe-S system below 100°C.* Chemical Geology (2000), **167**(1–2): p. 25–51.

Bertaut, E.F., *Structure de FeS stoechiometrique.* Bulletin de la Societe francaise de Mineralogie et de Cristallographie (1956), **79**: p. 276–292.

Ehm, L., et al., *Structural changes in nanocrystalline mackinawite (FeS) at high pressure.* Journal of Applied Crystallography (2009), **42**: p. 15–21.

Fei, Y.W., et al., *Structure and density of FeS at high-pressure and high-temperature and the internal structure of Mars.* Science (1995), **268**(5219): p. 1892–1894.

Hazen, R.M. and L. Finger, *Comparative crystal chemistry*. (1992), Chichester/New York, Brisbane/Toronto/Singapore: Wiley.

King, H.E. and C.T. Prewitt, *High-pressure and high-temperature polymorphism of iron sulfide (FeS).* Acta Crystallographica Section B-Structural Science (1982), **38**(July): p. 1877–1887.

Kouvo, O., J.V.P. Long, and Y. Vuorelainen, *A Tetragonal Iron Sulfide.* American Mineralogist (1963), **48**(5–6): p. 511–524.

Kusaba, K., et al., *Structure of FeS under high pressure.* Journal of Physics and Chemistry of Solids (1997), **58**(2): p. 241–246.

Lennie, A.R., et al., *Synthesis and Rietveld crystal structure refinement of mackinawite, tetragonal FeS.* Mineralogical Magazine (1995), **59**(397): p. 677–683.

Lennie, A.R., K.E.R. England, and D.J. Vaughan, *Transformation of synthetic mackinawite to hexagonal pyrrhotite – a kinetic-study.* American Mineralogist (1995), **80**(9–10): p. 960–967.

Marshall, W.G., et al., *High-pressure neutron-diffraction study of FeS.* Physical Review B (2000), **61**(17): p. 11201–11204.

Martin, C.D., et al., *Quantitative high-pressure pair distribution function analysis of nanocrystalline gold.* Applied Physics Letters (2005), **86**(6): p. 061910.

Mei, Q., et al., *Topological changes in glassy $GeSe_2$ at pressures up to 9.3 GPa determined by high-energy x-ray and neutron diffraction measurements.* Physical Review B, (2006). **74**(1): p. 014203.

Michel, F.M., et al., *Short- to medium-range atomic order and crystallite size of the initial FeS precipitate from pair distribution function analysis.* Chemistry of Materials (2005), **17**(25): p. 6246–6255.

Nelmes, R.J., et al., *Structure of the high-pressure phase III of iron sulfide.* Physical Review B (1999), **59**(14): p. 9048–9052.

Parise, J.B., et al., *Quantitative high-pressure pair distribution function analysis.* Journal of Synchrotron Radiation (2005), **12**: p. 554–559.

Parise, J.B., L. Ehm, and F.M. Michel, *Analysis of total scattering using the quantitative high pressure pair distribution function: Practical considerations, High-Pressure Crystallography From Fundamental Phenomena to Technological Applications,* E. Boldyreva and P. Dera (Eds), (2010), p. 513–522.

Schippers, A. and B.B. Jorgensen, *Biogeochemistry of pyrite and iron sulfide oxidation in marine sediments.* Geochimica et Cosmochimica Acta (2002), **66**(1): p. 85–92.

Schoonen, M.A.A. and H.L. Barnes, *Reactions forming pyrite and marcasite from solution 1. Nucleation of Fes_2 below 100°C.* Geochimica et Cosmochimica Acta, (1991a), **55**(6): p. 1495–1504.

Schoonen, M.A.A. and H.L. Barnes, *Reactions forming pyrite and marcasite from solution 2. Via FeS precursors below 100ºC.* Geochimica et Cosmochimica Acta (1991b), **55**(6): p. 1505–1514.

Shannon, R.D., *Revised effective ionic radii and systematic studies of interatomic distances in halides and chalcogenides.* Acta Cryst. A (1976), **32**: p. 751–767.

Variano, B.F., et al., *Investigation of finite size effects in a 1st order phase-transition – high-pressure Raman-study of CdS microcrystallites.* Journal of Chemical Physics (1988), **88**(4): p. 2848–2850.

Wilkin, R.T. and H.L. Barnes, *Pyrite formation by reactions of iron monosulfides with dissolved inorganic and organic sulfur species.* Geochimica et Cosmochimica Acta (1996), **60**(21): p. 4167–4179.

HIGH-PRESSURE STUDIES OF PHARMACEUTICALS AND BIOMIMETICS. FUNDAMENTALS AND APPLICATIONS. A GENERAL INTRODUCTION

ELENA BOLDYREVA*
REC-008 Novosibirsk State University, Institute of Solid State Chemistry and Mechanochemistry SB RAS, Novosibirsk, ul. Kutateladze, 18, 630128, Russia

Abstract This chapter aims to give a general introduction into a series of several lectures to follow, which are dedicated to the fundamental and applied aspects of high-pressure research of pharmaceuticals, biomimetics and biomolecules. This is a relatively recent field in high-pressure science, as compared with more traditional applications for physics, geosciences, materials sciences. However, its importance is rapidly growing.

Keywords: Pharmaceuticals, polymorphism, intermolecular interactions, molecular crystals, hydrogen bonds, biomimetics, phase transitions, mechanochemistry

1. High Pressure and Pharmaceuticals

1.1. HOW CAN HIGH PRESSURE RESEARCH HELP?

Pharmaceutical industry is an important field of applications of high-pressure research. Research and development of drugs is well-supported financially, since the pharmaceuticals have an enormous market, and are "life-important" in the direct sense of the word. As Sir Derrick Dunlop, the first Chairman of the Committee on safety of drugs, UK, has said: "Modern drugs are like nuclear energy: they can be enormously helpful and enormously harmful".

*E-mail: eboldyreva@ngs.ru, eboldyreva@yahoo.com

E. Boldyreva and P. Dera (eds.), *High-Pressure Crystallography: From Fundamental Phenomena to Technological Applications*, DOI 10.1007/978-90-481-9258-8_44,

The main problems in pharmaceutical industry are related to obtaining (1) an *Active Pharmaceutical Ingredient* (API) either by chemical synthesis, or by extraction from natural and renewable resources, and (2) a *drug formulation*. A drug formulation is not only an active substance (API) itself, but also other additives present in the system. The formulation can be prepared as a solution, a spray, a liniment, or a tablet. If the formulation contains solid particles, what is most often the case, then the particle size and shape, the crystal structure, the presence of defects are important. Without changing the chemical composition of an API, just by modifying its solid form, one can influence on the properties relevant either for medical applications (solubility and dissolution kinetics, targeted delivery, bioavailability, pharmacokinetics), or for processing and storage (hygroscopicity, shelf-life, tabletting and filtering properties). Even if the forms do not differ much in their bioavailability and are produced with approximately equal efforts and costs, development an alternative form may be beneficial because the new forms are patentable, and production of a new form is not prevented by an already existing patent.

Mechanochemistry is being actively applied for synthesis and extraction of APIs, as well as for preparing new forms of APIs and new, modified drug formulations. Quite often, a new form is obtained not on purpose, but forms un-desirably and non-controlled during pharmaceutical processing involving mechanical treatment (grinding, tabletting), or on subsequent storage after these stages of the pharmaceutical processing.

Mechanical treatment can be carried out manually (grinding and co-grinding in a mortar), or in various special apparatures (mills, activators, extruders, etc.). Mechanical treatment using these devices (including a simple mortar!) is a very complex process, during which a sample is subject to locally increased temperature and pressure conditions, shear stresses, elastic and plastic deformation. Local melting (contact melting), sublimation, generation of fresh surfaces, are only some of the processes taking place at the moment of mechanical action. In most cases, the mechanical action is of pulse nature, not continuous, and therefore the relaxation process occurring in the time intervals between the pulses are important, and kinetic factors play a major role.

In contrast to this, hydrostatic loading of a sample is relatively (relatively!) easier to study and to interpret: the conditions are well-defined and controlled, the sample can be studied *in situ* by various experimental techniques, action on the sample is continuous. There are several possible ways, in which the studies of pharmaceuticals under hydrostatic pressure conditions can

develop. On one side, high pressure can be used on purpose, to obtain new polymorphs and new solvates of API either by direct crystallization from solution, or through solid-state polymorphic transformations. If quenchable, the new forms can be used for seeding, to produce larger amounts of the new forms metastable at ambient conditions. High-pressure experiments can be also helpful for improving the models, e.g. – the atom-atom potentials, used by various programs, "polymorph predictors", which are widely used in drug research and development for the theoretical search of new possible forms. On the other side, high-pressure experiments can assist in controlling the undesirable polymorphic transformations occurring during the pharmaceutical processing. Comparing the behavior of an API on tabletting and under hydrostatic pressure, one can understand better, if the phase transition on tabletting is induced by local pressure increase, or if it is due to local heating or shear stresses, so that the undesirable transformation can be prevented.

1.2. AN EXAMPLE – POLYMORPHISM OF PARACETAMOL

Although many papers on the polymorphic transformations in drugs on grinding or on tabletting have been published, and this phenomenon is being studied for almost a century, the first study of the effect of hydrostatic pressure on a drug substance, paracetamol (CH_3–NH–(C=O)–C_6H_5–OH), was carried out in the late 1990s only. We have carried out an x-ray single-crystal and powder diffraction study of the monoclinic and the orthorhombic polymorphs completed by IR-spectroscopy.

The results obtained in this early study are quite instructive for other systems as well. First, a pronounced difference in the behavior of single crystals and powders has been observed. No polymorphic transitions could be observed when a single crystal of the monoclinic polymorph in pentane-isopentane as pressure-transmitting medium was compressed up to 5 GPa, even if the crystal was kept under pressure for a year. Reversible anisotropic structural distortion was accompanied by continuous flattening of the molecules and shortening of the intermolecular NH…O and OH…O hydrogen bonds (see chapter by Boldyreva). At the same time, when a polycrystalline (powder) sample was compressed, an irreversible partial transformation of the monoclinic form into the orthorhombic polymorph was observed at pressure below 2 GPa. The transformation could be observed not on direct compression, but on decompressing the sample down from a higher pressure. After the pressure was increased again in the second cycle, the concentration

of the orthorhombic polymorph increased, but the transformation was never complete. Interestingly enough, the effect of grinding in the mortar was opposite to that of the hydrostatic compression: the orthorhombic polymorph transformed into the monoclinic one.

All these phenomena can be interpreted consistently, if one assumes, that the orthorhombic polymorph is the thermodynamically stable form at high pressure, but the transformation is kinetically hindered. In fact, a transformation of one polymorph into another would require a large structural rearrangement of hydrogen-bonded molecular chains, giving different two-dimensional layers and three-dimensional networks – inversion of every second chain. The orthorhombic polymorph is metastable at ambient conditions, but unless solvent inclusions are present in the sample, the form can be not only preserved at ambient conditions for an indefinitely long time, but also heated up to melting, without any polymorphic transformation. The transformation is limited by the nucleation of the new phase and is facilitated by shear stresses. Several years later, Fabbiani and Pulham, who are both lecturing at this School, have succeeded in obtaining the orthorhombic polymorph of paracetamol by crystallization from ethanol solutions at about 1.1 GPa. A few years later the Ceolin group in collaboration with Pulham has proved that the orthorhombic polymorph is the thermodynamically stable form at high pressures by calorimetry measurements.

1.3. THE ROLE OF THE LIQUID PHASE – DIFFERENT ASPECTS

Experiments with high-pressure crystallization of paracetamol from different solvents have eventually resulted in developing a general strategy of generating new polymorphs and solvates of molecular solids, in general, and of APIs, in particular. If several polymorphs are known at ambient conditions, the denser one might be the thermodynamically stable form at high pressure, and thus can be crystallized easily and reproduceably at high pressures, even if it is elusive, “disappearing” at ambient conditions. Varying the solvents, serving simultaneously as pressure-transmitting liquids, and varying the details of the compression–decompression procedure, one can obtain different polymorphs and solvates, many of which are quenchable and can be recovered after decompression. More on this approach and recent achievements see in the chapter by Fabbiani.

These experiments are valuable in themselves, but they also attract attention to one more important aspect of the high-pressure polymorphism of drugs, namely to the role of liquids in the transformation. No hydrostatic conditions can be achieved, if no liquid is present, and the choice of a liquid

determines the limits of the hydrostatic conditions. At the same time, a liquid is not necessarily completely inert with respect to the solid sample under pressure. It can be involved into the high-pressure transformation to a larger, or to a smaller extent, mediating the solid-state transformations, assisting in recrystallization, or also via the interaction with the surface and the extended defects. The first systematic experiments have already shown, that for the same solid sample a polymorphic transformation may occur in one liquid, and are not observed in another. This result is of a special importance for the pharmaceutical applications. Quite often, polymorphic transformations on tabletting could be observed for slurries, not for dry samples, and in other cases, the presence of the traces of solvent in a powder has simply not been controlled. A very hot topic today is mechanochemical synthesis by grinding. In many cases, a small amount of solvent ("solvent-drop grinding") is required, to make the reaction possible. The role of this liquid is being discussed actively, and one of the possible mechanisms can be related to solvent-assisted high-pressure polymorphism.

1.4. TAKE-HOME MESSAGE

High-pressure research is finding ever more applications in drug development.

It is always good for the manufacturer to keep high-pressure polymorphism under control – either to produce new forms, or to avoid the occurrence of undesired forms on processing.

Model pressure experiments help to understand the complicated processes during treatment of drugs and drug formulations.

High-pressure experiments help to distinguish the role of pressure from those of heating (melting, sublimation), or shear stresses in the "dry chemical reactions", in the mechanical modification and mechanochemical synthesis of drugs and drug formulations.

2. High Pressure and Biomimetics

2.1. PRESSURE AND BIOLOGICAL SYSTEMS

Another rapidly developing field of high-pressure research is related to biological applications. Conformational transitions in biological molecules are necessary for their normal functioning; at the same time, wrong conformations (mis-folding) may account for the disfunction of the biomolecules, and result in fatal deseases, such as bovine spongiform encephalopathy (BSE, also known as "mad cow disease") in cattle and Creutzfeldt–Jakob

disease (CJD) in humans, fatal familial insomnia, Parkinson's and Alzheimer's diseases. Conformational changes in viruses occur, when the virus aims to penetrate a cell. Therefore, theoretical and experimental studies of conformational transitions in biomolecules are of primary importance.

High pressure is a tool that makes it possible to access high-energy conformational states, which play the primary role for the functioning of biomolecules *in vivo*. On the other hand, high pressure can result in the conformational transitions, even in the denaturation, which account for the inactivation of pathogens (viruses and bacteria) in medicine and in food industry. High pressure research helps to understand the adapting mechanisms of piezophiles to their extreme living conditions. Recent experimental achievements make it possible to study the biological molecules at high pressures *in situ* by spectroscopic techniques, calorimetry, or high-resolution x-ray diffraction. Chapters by Winter and Fourme cover various fundamental and applied aspects of these topics.

2.2. CRYSTALS OF AMINO ACIDS AS MODELS OF BIOLOGICAL SYSTEMS

In addition to the direct studies of biomolecules at high pressures, one can study the crystals of small organic molecules, which mimic some structural or dynamic features of the biomolecules. Crystals of amino acids have been considered as such model systems (biomimetics) since the early work by Bernal and Pauling. In their structures the molecules of amino acids are present as zwitter-ions linked with each other in the head-to-tail chains via bifurcated NH…O hydrogen bonds. These chains are very robust and are preserved even during phase transitions. They can be considered as models of the peptide chains, although they do not contain any peptide bonds. The head-to-tail chains are further linked via hydrogen bonds into two-dimensional layers, helices, double-sheets, three-dimensional frameworks, nanoporous structures, mimicking fragments of the secondary structure of proteins. At the early stage of structural analysis, the main attention was paid to the static aspects of crystal structures, whereas now the study of the dynamics becomes ever more important. The properties of individual intramolecular bonds, of the intermolecular hydrogen bonds, the dynamics of certain molecular fragments and the molecules as a whole are now the main focus of the studies. More details on amino acids under pressure see in chapter by Freire.

2.3. PROPERTIES OF THE INDIVIDUAL BONDS

A recent trend in the biophysical research is probing the properties of individual bonds in biomolecules using atomic force microscopy (AFM). This technique *stretches* the bonds and makes it possible to estimate their force constants from the experiment. The experiments under hydrostatic pressure conditions are complementary to those with AFM, since they allow one to probe individual bonds on *compression*. The state of art of the research in this field is covered in chapters by Winter and Fourme.

2.4. DYNAMICS OF BIOPOLYMERS AND PHASE TRANSITIONS IN CRYSTALS

The pioneering research on the dynamics of amino acids in the crystalline state has been carried out using Raman spectroscopy, and Freire will cover this topic in his lecture. X-ray diffraction brings a new dimension into the studies, providing direct data on the structural rearrangements during the phase transitions, which have much in common with the conformational changes in biological systems. As examples, one can refer to pressure-induced phase transitions in the polymorphs of glycine, L- serine and L-serine hydrate, β-alanine, L- and DL-cysteine. The stability of the polymorphs of glycine with respect to pressure-induced phase transitions depends on the starting form, what indicates at the kinetic rather than thermodynamic control of the process (Figure 1). In the course of the irreversible γ- to δ- transformation the triple helices unravel giving sheets, and a similar process is observed in fibrous peptides, like collagen, and is related to aging and growth. A series of phase transitions in the crystals of L-serine is of another type: the single crystal is preserved, the interface propagates jump-wise throughout the crystal after a waiting time. As pressure increases, the head-to-tail chains are first compressed continuously, as springs, till a certain limit (Figure 2), and then, at the transition point, they expand jump-wise due to the rotation of the $–CH_2OH$ side chains and a change in the intermolecular hydrogen-bonding network (Figure 3). This process can be related to the functioning of the serine-serine zippers in the membrane proteins. In general, the crystals of amino acids make a link between the materials, deformation and destruction of which must be described in terms of plastic and elastic deformation involving dislocations and cracks, and the biopolymers, mechanical properties of which are determined basically by the dynamics of hydrogen-bonded molecular fragments.

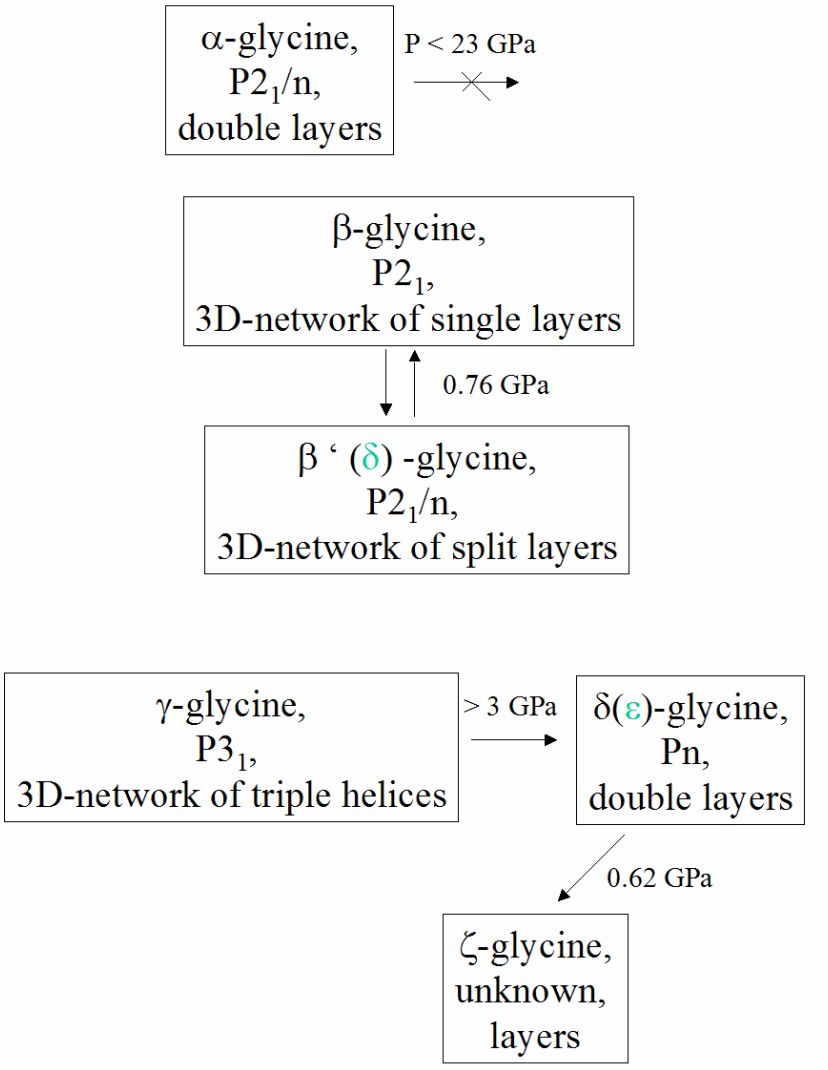

Figure 1. A schematic presentation of the pressure-induced phase transitions between the polymorphs of glycine (From *Boldyreva*, 2008).

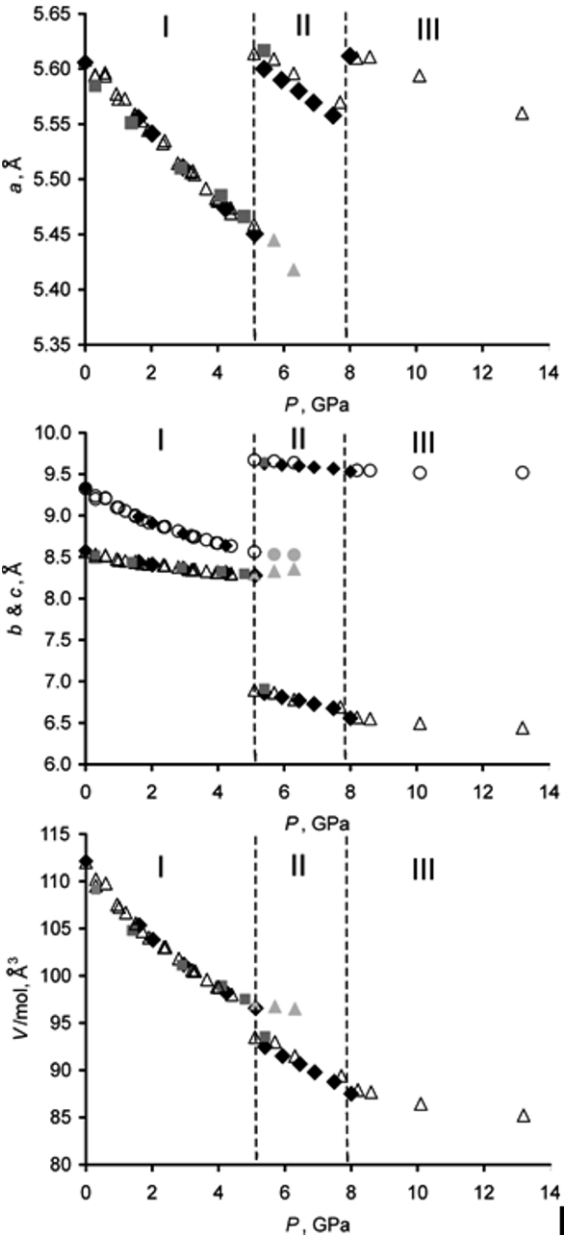

Figure 2. Changes in the cell parameters and volume accompanying pressure-induced phase transitions in L-serine. The NH…O bonded head-to-tail chains of zwitter-ions along axis ***a*** act as "springs" (From *Boldyreva et al.*, 2006).

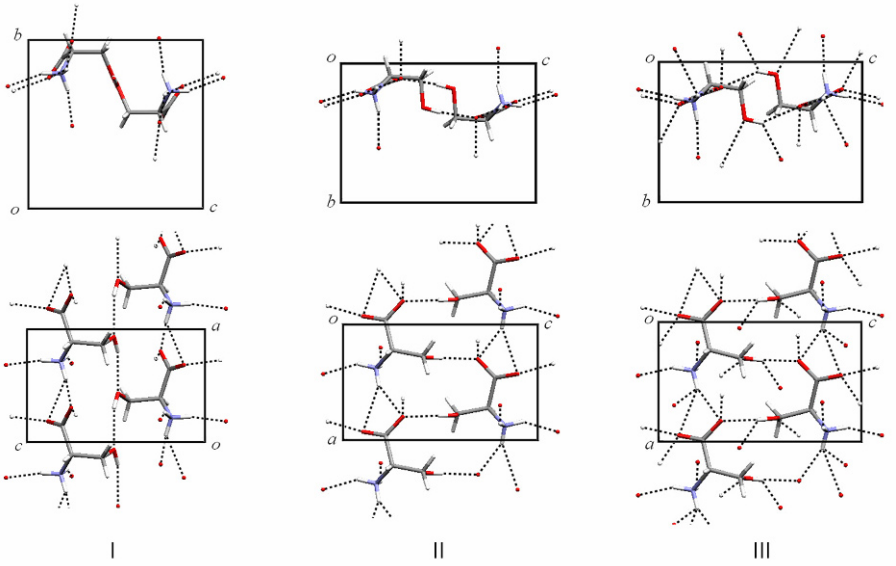

Figure 3. The rotation of the $-CH_2OH$ side chains and a change in the intermolecular hydrogen-bonding network (dotted lines) accompanying the pressure-induced transitions from the ambient-pressure (I) to the two high-pressure (II, III) polymorphs of L-serine; the process is similar to the functioning of "serine-serine zippers" (From *Boldyreva et al.*, 2006).

Further Reading

This field has been reviewed recently in several papers, in which the references to the original publications can be easily found. More references see in the lectures of other lecturers, mentioned above.

References

Boldyreva, E.V., 2004, High pressure and supramolecular systems, *Russian Chem. Bulletin*, **53**(7): 1315–1324.

Boldyreva, E.V., 2007, High-pressure studies of crystalline amino acids and simple peptides. In: *Proceed. IV-th Intern. Confer. High Press. Biosci. Biotech.*, Presented by J-STAGE, Tsukuba, Japan, September, 25th–26th 2006, Eds. F. Abe, A. Suzuki, Japan Science and Technology Agency: Saitama, Japan, **1**(1): 28–46.

Boldyreva, E.V., 2007, Crystalline amino acids – a link between chemistry, materials science and biology, In: *Models, Mysteries, and Magic of Molecules*, Eds. J.C.A. Boeyens, J.F. Ogilvie, Springer Verlag, 169–194.

Boldyreva, E.V., 2007, High-pressure polymorphs of molecular solids: when are they formed, and when are they not? Some examples of the role of kinetic control, *Cryst. Growth Des*, **7**(9): 1662–1668.

Boldyreva, E.V., 2008, High-pressure diffraction studies of molecular organic solids. A personal view, *Acta Crystallogr. A*., **64**(1): 218–231.

Boldyreva, E.V., 2009, Combined X-ray diffraction and Raman spectroscopy studies of phase transitions in crystalline amino acids at low temperatures and high pressures. Selected examples, *Phase Transitions*, **82**(4): 303–321.

Boldyreva, E.V., Drebushchak, T.N., Shakhtshneider, T.P., Sowa, H., Ahsbahs, H., Goryainov, S.V., Ivashevskaya, S.N, Kolesnik, E.N., Drebushchak, V.A., Burgina, E.B., 2004, Variable-temperature and variable-pressure studies of small-molecule organic crystals, *Arkivoc*, **XII**: 128–155.

Boldyreva, E.V., Sowa, H., Ahsbahs, H., Goryainov, S.V., Chernyshev, V.V., Dmitriev, V.P., Seryotkin, Yu.V., Kolesnik, E.N., Shakhtshneider, T.P., Ivashevskaya, S.N., and Drebushchak, T.N., 2008, Pressure-induced phase transitions in organic molecular crystals: a combination of x-ray single-crystal and powder diffraction, Raman and IR-spectroscopy, *J. Phys. Conf. Ser.*, **121**: 022023.

Fabbiani, F.P.A., Pulham, C.R., 2006, High-pressure studies of pharmaceutical compounds and energetic materials, *Chem. Soc. Rev*., **35**(10): 932–942.

Fabbiani, F.P.A., Allan, D.R., David, W.I.F., Moggach, S.A., Parsons, S., Pulham, C.R., 2004, High-pressure recrystallisation – A route to new polymorphs and solvates, *Cryst. Eng. Comm.*, **6**: 504–511.

Fabbiani, F.P.A., Allan, D.R., Marshall, W.G., Parsons, S., Pulham, C.R., Smith, R.I., 2005, High-pressure recrystallisation – A route to new polymorphs and solvates of acetamide and parabanic acid, *J. Cryst. Growth*, **275**(1–2): 185–192.

Wood, P.A., McKinnon, J.J., Parsons, S., Pidcock, E., Spackman, M.A., 2008, Analysis of the compression of molecular crystal structures using Hirshfeld surfaces, *CrystEngComm*, **10**(4): 368–376.

Moggach, S.A., Parsons, S., Wood, P.A., 2008, High-pressure polymorphism in amino acids, *Cryst. Rev*., **14**(2): 143–184.

Oswald, I.D.H., Chataigner, I., Elphick, S., Fabbiani, F.P.A., Lennie, A.R., Maddaluno, J., Marshall, W.G., Prior, T.J., Pulham, C.R., Smith, R.I., 2009*,* Putting pressure on elusive polymorphs and solvates, *CrystEngComm*, **11**(2): 359–366.

NEW FRONTIERS IN PHYSICAL FORM DISCOVERY: HIGH-PRESSURE RECRYSTALLIZATION OF PHARMACEUTICALS AND OTHER MOLECULAR COMPOUNDS

FRANCESCA P. A. FABBIANI*
GZG, Abteilung Kristallographie, Georg-August Universität Göttingen, Goldschmidtstr. 1, 37077, Göttingen, Germany

Abstract What is the underlying motivation for physical form discovery in the pharmaceutical industry? Can high-pressure techniques help with this task? After a brief introduction on high-pressure methodologies for the study of molecular compounds, the technique of high-pressure recrystallization from solution is described in some detail.

Keywords: Physical form discovery, pharmaceuticals, DAC, crystallization

1. Introduction

1.1. PHYSICAL FORM DISCOVERY

The term "physical form" describes a particular ensemble of molecules (or atoms) in the solid state. The term is widely used in the pharmaceutical industry (*Gardner et al*., 2004), where the molecule under consideration is typically pharmaceutically active and is also known as an active pharmaceutical ingredient (API). Two main types of physical forms can be distinguished, namely amorphous and crystalline. Crystalline forms can be further divided into one-component phases, also known as polymorphs (different crystal structures of the API) (*Bernstein*, 2002), and multi-component phases [salt (*Stahl and Wermuth*, 2002; solvate, hydrate (*Khankari and Grant*, 1995) and co-crystal forms (*Almarsson and Zaworotko*, 2004; *Stahly*, 2007) of the API], where the covalent bonding of the API is kept intact and for which polymorphism can also be observed.

* E-mail: ffabbia@gwdg.de

E. Boldyreva and P. Dera (eds.), *High-Pressure Crystallography: From Fundamental Phenomena to Technological Applications*, DOI 10.1007/978-90-481-9258-8_45,

The efficacy of a drug is largely determined by its structure in solution since this is where the drug-receptor interactions take place. So where does the interest in the solid state stem from? Different physical forms have different physicochemical properties, such as density, hardness, tablettability, refractive index, melting point, enthalpy of fusion, vapor pressure, solubility, dissolution rate and color (*Grant*, 1999). These properties play a major role in devising a controlled formulation, stable storage and safe mode of administration of drugs. For instance, the anti-inflammatory drug dexamethasone is administered as water-insoluble dexamethasone in tablet formulation but as highly water-soluble dexamethasone sodium phosphate for oral solution and injection (extract from the British National Formulary, http://www.bnf.org).

New forms can be observed at different stages of a drug life: various pharmaceutical processes can lead to phase changes, which can alter the bioavailability of the drug and its performance (*Brittain and Fiese*, 1999), as well as lead to substantial revenue loss for the pharmaceutical company. Hence, the control of a physical from and understanding of its physical properties are very important if problems with stability, manufacturing, regulatory bodies (*Byrn et al*., 1995) and patent protection are to be avoided (*Hilfiker*, 2006). Surprise is an unwanted element in an industrial environment. The often quoted example of the HIV protease inhibitor Ritonavir illustrates this effectively: after a new, more stable and less soluble polymorph appeared almost 2 years after FDA approval, the existing product, which contained a metastable form of the API, had to be withdrawn from the market until a new formulation was devised (*Bernstein*, 2002).

1.2. SCREENING FOR PHYSICAL FORMS

Physical from discovery can be a serendipitous process (*Bernstein*, 2002), but can also be part of a systematic and rational search. The industrial approach to this involves solution crystallization processes in which parameters such as solvent, temperature and concentration are varied in a rapid and systematic manner, through robotic high-throughput screening technologies that can use volumes as little as 50 μl (*Gardner et al*., 2004). For basic research programs that are typically based in academia, automated platforms represent more an exception rather than the norm. These platforms tend to be less geared towards high throughput and more towards better control over crystallization parameters, and use significantly larger volumes (3–8 ml) (*Florence et al*., 2006). As pointed out by G.P. Stahly (2007): “It is a mistake...to believe that any high-throughput system can

increase the merit of a screen simply by its use...thousands of experiments are not needed to find polymorphs...Some sample generation techniques are less amenable to automation than others, and these should not be eliminated from screening...". Hence, isolated physical forms should also be screened by variation of temperature, relative humidity, vapor, slurry conversion and solvent-assisted grinding. Important techniques that are used to study and characterize physical forms include IR, Raman and solid-state NMR spectroscopy, differential scanning calorimetry (DSC), thermal gravimetric analysis (TGA), thermal microscopy, powder and single-crystal x-ray diffraction (*Hilfiker*, 2006).

In the pharmaceutical industry, the phyisicochemical properties of physical forms are investigated to facilitate the selection of the best form for drug product. Even if certain forms may not be of immediate interest from a selection point of view, a comprehensive screening offers maximum patent protection and enables rapid solution of problems which may be encountered in later stages of a drug life. However, in practice, budgetary and time constraints may limit the extent of screening. In general, "no amount of screening can guarantee that all polymorphs of a given substance have been found" (*Stahly*, 2007). Developments in the use of computational methods to predict crystal structures of polymorphs, and more recently of co-crystals and salts (see *e.g. Day et al*., 2009; *Price*, 2009), indicate that *in silico* polymorph screening does in some cases offer the ability to say when an experimental screening is complete, although there remain substantial challenges before these techniques can be widely and routinely applied.

In the pharmaceutical industry, pressure is not used as a screening parameter: virtually all crystallization studies are performed under ambient-pressure conditions. The only exceptions are a few processes that use supercritical fluids as solvents, but the pressures rarely exceed 0.01 GPa (*Tozuka et al*., 2003). Of more long-standing interest is the effect of mechanical action on solid drugs (*Boldyrev*, 2004 and refs. therein): manufacturing processes like milling and tabletting can cause localized increases in pressure and shear stress that can induce phase transitions (*Boldyreva*, 2003; *Fabbiani and Pulham*, 2006, and refs. therein). The first high-pressure compression experiments on pharmaceuticals date back to (*Bridgman*, 1931). More recent studies include the solvate-mediated transition and compression studies on indomethacin (*Okumura et al.*, 2006), fenacetine (*Shakhtshneider et al*., 1998, 1999), paracetamol (*Boldyreva et al*., 2000, 2002; *Shakhtshneider et al*., 1998, 1999) and chlorpropamide A (*Boldyreva et al*., 2006). In the following pages we will indeed see that pressure is a powerful tool for accessing new physical forms.

2. Contributions of High-Pressure Methods to Physical Form Discovery

2.1. HIGH-PRESSURE RESEARCH

Within the Physics and Geosciences communities, pressure is a well-known thermodynamic variable for inducing phase transitions in a wide range of materials (*e.g.* metals, alloys, minerals and ices) (*Hazen and Downs*, 2000; *Katrusiak and McMillan*, 2004; *Tonkov and Ponyatovsky*, 2005). In comparison, the use of pressure as a variable for studying the chemistry of the organic solid-state has only begun relatively recently. In contrast to experiments that for example aim at synthesizing novel super hard materials (*McMillan*, 2003) or at reproducing the extreme conditions found in planets' interiors, where pressures reach several hundreds of gigapascal and temperatures several thousand kelvin, experiments for studying soft matter can be performed at ambient temperature and comparably low high pressures, with rich polymorphism observed *well below* 10 GPa.

The response of a system to an applied pressure can be understood by invoking Le Châtelier's principle: pressure causes the equilibrium to shift in favor of the state that occupies the smallest volume. Note that pressure–volume work has the dimensions of energy: for instance, the free-energy change for compression in the multimegabar range can be in excess of 100 kJ mol^{-1} (*Hemley*, 2000), whereas for a protein unfolding at around 500 MPa, the total energy input in the system is only of the order of 15 kJ mol^{-1} (*Meersman et al*., 2006).

The difference in pressure regimes used for inducing structural changes in different materials can be rationalized in terms of a hierarchy of the binding forces that hold together molecules and atoms in a crystal. In general, the first structural response to an applied pressure is the shortening of the weaker and more compressible *intermolecular* interactions (H-bonding, van der Waals, C–H…π, *etc.*), accompanied by reduction of structural voids and changes in the molecular conformation, if the molecule has some conformational flexibility. This leads to the formation of more densely packed materials through direct compression of the same one phase and phase transitions to give new polymorphs. At higher pressures, *intramolecular* bonds are destabilized, *i.e.* the chemical bonding between atoms is affected, *e.g.* benzene becomes polymeric at 24–30 GPa (*Pruzan et al*., 1990).

2.2. HIGH-PRESSURE TECHNIQUES FOR PHYISCAL FORM DISCOVERY OF MOLECULAR COMPOUNDS

The experiments illustrated in this section are more conveniently and frequently carried out using the Diamond-Anvil Cell (DAC) for pressure generation (see *Katrusiak*, 2008 for a recent review on the DAC), followed by *in situ* diffraction and spectroscopy for material characterization. Other equipment is also available for pressure generation (*Hazen and Downs*, 2000; *Katrusiak and McMillan*, 2004). Depending on the physical nature of the molecular compound, three main methods are available for loading a DAC.

Samples that are in the liquid state are crystallized *in situ* by the application of pressure. This induces the formation of polycrystalline material, which is subsequently heated to grow a single crystal. Pressure-induced freezing of a pure liquid (*Bridgman*, 1931; *Fourme*, 1968) and more recently of a mixture of liquids (*Olejniczak et al*., 2009a; *Podsiadlo and Katrusiak*, 2008), is a very powerful method for accessing new polymorphs (*Dziubek and Katrusiak*, 2008; *Gajda et al*., 2006; *Hemley and Dera*, 2000; *Lozano-Casal et al.*, 2005; *McGregor et al*., 2006; *Olejniczak et al*., 2009b). However, it is less applicable to compounds such as API's that have melting points significantly higher than ambient temperature. The problem is made more difficult by the substantial increase in melting point induced in most substances by the application of pressure. Generally decomposition or some chemical reaction takes place before the compound melts.

Samples that have a melting point higher than 323 K are studied by direct compression, either as a single crystal or as a powder (*Boldyreva*, 2004, 2008; *Katrusiak*, 1991; *Wood et al*., 2008; *Moggach et al*., 2009 and refs. therein). Of particular notice is the large number of studies on amino acids (*Boldyreva*, 2007a, b, c, 2008, 2009; *Moggach et al*., 2008, and refs. therein). Direct compression can be effective for inducing phase transitions in some materials, in particular if the molecule under investigation has some degree of conformational flexibility. However, there is often a substantial kinetic barrier to be overcome before the molecules can rearrange, even though pressure may thermodynamically favor the transition. This was for example observed for the analgesic drug paracetamol: *Boldyreva et al*. (2002) demonstrated that the application of pressures in excess of 4 GPa to powder samples of form I resulted in the conversion into form II, but for kinetic reasons the conversion was incomplete, poorly reproducible, and no conversion was observed in a single crystal.

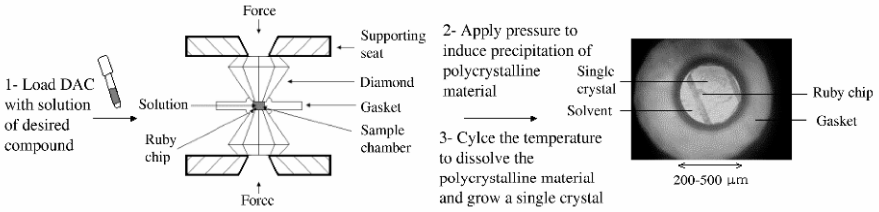

Figure 1. Schematic experimental procedure for *in situ* high-pressure crystallization.

Samples that have a melting point higher than 323 K can also be studied by *in situ* high-pressure recrystallization *from solution* (Figure 1).

The main advantages of this technique for physical form discovery are: (a) modest pressures, typically 0.1–2.0 GPa, are needed to induce precipitation of novel forms: for instance, paracetamol form II can be reproducibly crystallized at 0.5 GPa from aqueous solutions and recovered in bulk quantities (*Oswald et al*., 2009); (b) modest temperatures, typically <<373 K, are required for dissolving the precipitated material and growing single crystals; (c) different solvent and solute systems can be studied, thereby providing opportunities for preparing new multi-component crystals.

3. High-Pressure Crystallization: Some Experimental Aspects and Examples

By looking beyond ambient pressure crystallization conditions, the number of observed physical forms of molecular compounds, including those relevant to the pharmaceutical industry, is significantly increased. High-pressure crystallization has been used for preparing new polymorphs [phenanthre (*Fabbiani et al*., 2004), pyrene (*Fabbiani et al*., 2006), acetamide (*Fabbiani et al*., 2005a), leucine (*Yamashita et al*., 2007), piracetam (*Fabbiani et al*., 2005b, 2007)], new hydrates and solvates [parabanic acid (*Fabbiani et al*., 2005a), piracetam (*Fabbiani et al*., 2007), paracetamol (*Fabbiani et al*., 2003, 2004)], new salts (ciprofloxacin (*Fabbiani et al*., 2009), new co-crystals [paracetamol (*Oswald and Pulham*, 2007)] as well as for reproducibly crystallizing forms that are metastable at ambient pressure (paracetamol, maleic acid, malonamide (*Oswald et al*., 2009). The following are some useful guidelines for the preparation of a high-pressure crystallization experiment.

The solubility of the solute decreases with increasing pressure. This is a crucial requirement for performing the experiment and, from a thermodynamic point of view, usually implies that the volume change for dissolution

is positive. The effect of pressure on the solubility of organic compounds is to date a virtually unexplored area of research. In absence of experimental data, this problem is solved by trial and error, *i.e.* by doing the experiment. Examples reported in the literature where solubility increases with increasing pressure include those of C_{60} (*Sawamura and Fujita*, 2007), tetragonal lysozyme (*Kadri et al*., 2005; *Suzuki et al*., 2002), and subtilisin (*Suzuki et al*., 2002).

The solvent has a reasonably high freezing pressure. This creates a wide window for crystallization of the solute. That said, a novel physical form may also nucleate as a result of freezing of the solvent. For instance, the crystallization of high-pressure ice-VI has been ascribed as a possible factor for the nucleation of piracetam dehydrate (*Fabbiani et al*., 2007) and paracetamol monohydrate (*Oswald et al*., 2009).

The solute has a relatively high solubility in the chosen solvent. Ideally, solutions of concentration greater than *ca*. 0.4 M should be prepared. Usually, the higher the concentration, (a) the lower the crystallization pressure; (b) the more material precipitates, thereby facilitating its characterization by diffraction methods; (c) the higher the chances of recovering high-pressure phases at ambient-pressure conditions. It is always advisable to study the crystallization of solutions where the nature of the solvent, concentration and crystallization pressure are varied. Figures 2 and 3 illustrate that high-pressure crystallization from solution, in combination with ambient pressure screening, is a very powerful tool for accessing new forms of the nootropic drug piracetam and the antibiotic ciprofloxacin.

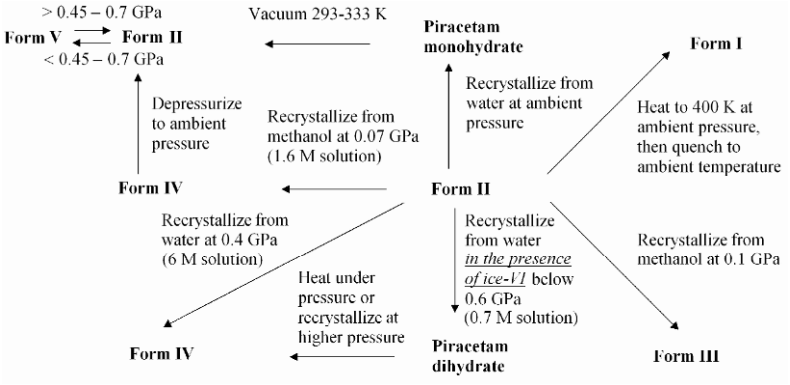

Figure 2. Phase transformation and crystallization diagram for piracetam (*Fabbiani et al*., 2007).

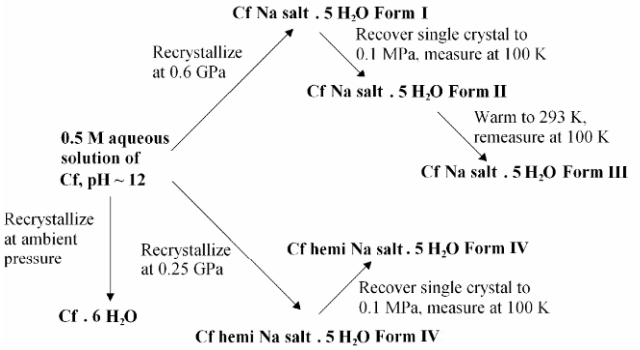

Figure 3. Phase transformation and crystallization diagram for ciprofloxacin (Cf) (*Fabbiani et al.*, 2009).

The volume of the sample chamber is maximized. This can be achieved by drilling a hole of large diameter through the gasket material and by minimizing the gasket pre-indentation, provided modest pressures are applied and diamonds with large culets are available. Typical DAC volumes are in the 0.005–0.025 mm^3 (1 mm^3 = 1 μl) range, making high-pressure crystallization ideally suited for experiments where only a small amount of material is available: a few crystallites can in fact be directly loaded in a DAC and dissolved *in situ*, though this way an estimate of concentration can be very troublesome.

4. Future Challenges

Experimental evidence shows that high-pressure crystallization from solution can provide access to zones of thermodynamic stability that are either inaccessible or metastable under ambient conditions, thereby expanding the search space in a crystallization search for novel physical forms. What does the future hold for the technique?

Larger molecules. Apart from a few exceptions (*Girard et al*., 2007 and refs. therein, *Katrusiak and Dauter*, 1996, *Prescimone et al*., 2008) the vast majority of compounds that have been studied by high-pressure crystallographic methods are small molecules, with crystals comprising < 20 non H-atoms in the asymmetric unit. In between the small molecules and macromolecules classes, a vast number of "large small molecules" up to 100 non-H atoms, remain unexplored to date. Recent examples of high-pressure salts (*Fabbiani et al*., 2009) and co-crystals (*Oswald and Pulham*, 2008) formation indicate that low solubility and molecular complexity can be increased so that many larger molecules, including API's, are now

amenable to high-pressure crystallization studies. This only adds to the motivation to further develop *in situ* high-pressure diffraction, at both synchrotron and laboratory level. High-pressure has been shown to be a potential tool for the preparation of high quality protein crystals, and x-ray diffraction studies were carried out on depressurized protein crystals that were crystallized in high-pressure vessels (*Kadri et al*., 2005). In the future, it may be possible to improve crystal quality *and* monitor the changes in protein conformation by performing both crystallization and diffraction *in situ* at high pressure.

Structure solution. The environment within a high-pressure cell is small, confined and sealed and apart from not having control of the nucleation sites inside the DAC (*e.g.* gasket edge or ruby chip), these restrictions can be used as an advantage when it comes to crystal growing. Perhaps the most frustrating lack of control is that to date, the *in situ* grown crystal cannot be oriented for optimal collection of x-ray diffraction data. Structure solution (and refinement) of novel high-pressure forms of larger molecules are foreseen to be heavily dependent on methods "borrowed" from protein crystallography and from powder diffraction that use incomplete and low-resolution data (*Favre-Nicolin and Černý*, 2002, *Markvardsen et al*., 2002, *Palatinus et al*., 2007, *Rossmann*, 2001). Technical advances in high-pressure powder diffraction (neutron and x-ray) will also play an important role for the characterization of high-pressure phases for which single crystals cannot be obtained.

Understanding the effects of pressure on a structural level. An important general aspect of physical form discovery is the systematic investigation of structural relationships that can, for example, underpin solid-state transformations. A variety of recent approaches have been shown to provide qualitative and quantitative insight in crystal structure analysis (*Gavezzotti*, 2007, *Gelbrich and Hursthouse*, 2005, *Spackman and Jayatilaka*, 2009).

Routine, reproducible and recoverable. These are important qualifiers that would make the technique of high-pressure crystallization a viable and attractive additional screening tool in the pharmaceutical industry. The instances of recovery of high-pressure phases of organic compounds reported in the literature are not numerous (*Fabbiani et al*., 2009, *Goryainov et al*., *2006*, *Olejniczak and Katrusiak*, 2008, *Oswald et al*., 2009, *Yamashita et al*., 2007). It is often observed that on decompression the crystal either transforms to a more stable phase, or, as is often encountered with crystals grown *in situ* from solution, it dissolves completely. Increased solubility is not an unexpected outcome for a metastable phase. The problem of solubility is exacerbated when using a DAC, which does not allow a very controlled and rapid way of decreasing the pressure or removing the solvent of crystallization. Performing decompression experiments at low temperatures

may delay the onset and rate of dissolution, though temperatures at which the solvent crystallizes should be avoided, *e.g.* if water is used as crystallization solvent, low temperatures can lead to icing and subsequent crystal damage and/or phase transition. These considerations clearly highlight a need for: (a) investigating the reproducibility of high-pressure crystallizations and (b) explore optimal strategies for recovery of high-pressure phases through (c) the development of alternative easy-to-use high-pressure apparatus tailored for bulk crystallization and subsequent recovery, as testified by the research efforts of some groups (*Oswald et al*., 2009).

ACKNOWLEDGEMENTS

My own work on high-pressure crystallization would not have been possible without the support and enthusiasm of numerous collaborators. I am particularly indebted to Colin Pulham (University of Edinburgh) for inspiring and supervising much of my early work. Simon Parsons (University of Edinburgh) and Dave Allan (Diamond) are also gratefully acknowledged. I would also like to thank Stephen Moggach, Iain Oswald, Patricia Lozano-Casal (University of Edinburgh), Peter Wood (CCDC), Alice Dawson (University of Dundee), Werner Kuhs, Heidrun Sowa and Birger Dittrich (University of Göttingen), Norman Shankland, Alastair Florence (University of Strathclyde), Kenneth Shankland (University of Reading), Mark Spackman, Joshua McKinnon (University of Western Australia), Mike Hursthouse (University of Southampton), Thomas Gelbrich (University of Innsbruck), Demi Levendis (University of the Witwatersrand), Bill Marshall, Bill David, Kevin Knight, Ronald Smith (ISIS), John Warren, Alistair Lennie (SRS Daresbury), Gernot Buth (Anka) and Jürgen Graf (Incoatec). This work has been financially supported by the Leverhulme Trust and the Alexander von Humboldt Foundation.

References

Almarsson, Ö., and Zaworotko, M.J., 2004, Crystal engineering of the composition of pharmaceutical phases. Do pharmaceutical co-crystals represent a new path to improved medicines? *Chem. Commun.*: 1889–1896.

Bernstein, J. 2002, *Polymorphism in Molecular Crystals*, Clarendon Press, Oxford.

Boldyrev, V.V., 2004, Mechanochemical modification and synthesis of drugs, *J. Mater. Sci.* **39**: 5117–5120, and references therein.

Boldyreva, E.V., 2003 High-pressure studies of the anisotropy of structural distortion of molecular crystals, *J. Mol. Struct.* **647**: 159–179, and references therein.

Boldyreva, E.V., 2004, Molecules in strained environment, in: *High-Pressure Crystallography*, edited by A. Katrusiak and P.F. McMillan, Kluwer, Dordrecht, pp. 495–512.

Boldyreva, E.V., 2007a, Crystalline amino acids – a link between chemistry, materials science and biology, In: *Models, Mysteries, and Magic of Molecules*, edited by J.C.A. Boeyens, J.F. Ogilvie, Springer Verlag, New York, pp. 169–194.

Boldyreva, E.V., 2007b, High-pressure polymorphs of molecular solids: when are they formed, and when are they not? Some examples of the role of kinetic control, *Cryst. Growth Des.* **7**(9): 1662–1668, and reference therein.

Boldyreva, E.V., 2007c, High-pressure studies of crystalline amino acids and simple peptides/ *Proceedings of the IV-th International Conference on High Pressures in Biosciences and Biotechnology*, Presented by J-STAGE, Tsukuba, Japan, September, 25th–26th 2006, edited by F. Abe, A. Suzuki, Japan Science and Technology Agency: Saitama, Japan, **1**(1): 28–46.

Boldyreva, E.V., 2008, High-pressure diffraction studies of molecular organic solids. A personal view, *Acta Cryst. A* **64**: 218–231, and reference therein.

Boldyreva, E.V., 2009, Combined X-ray diffraction and Raman spectroscopy studies of phase transitions in crystalline amino acids at low temperatures and high pressures. Selected examples / *Phase Transitions*, **82**(4): 303–321.

Boldyreva, E.V., Shakhtshneider, T.P., Vasilchenko, M.A., Ahsbahs, H., and Uchtmann H., 2000, Anisotropic crystal structure distortion of the monoclinic polymorph of acetaminophen at high hydrostatic pressure, *Acta Cryst. B.* **56**: 299–309.

Boldyreva, E.V., Shakhtshneider, T.P., Ahsbahs, H., Sowa, H., and Uchtmann, H., 2002, Effect of high pressure on the polymorphs of paracetamol, *J. Therm Anal. Calorim.* **66**: 437–452.

Boldyreva, E.V., Dmitriev, V.P., and Hancock, B.C., 2006, Effect of pressure up to 5.5 GPa on dry powder samples of chlorpropamide form-A, *Int. J. Pharm.* **327**: 51–57.

Bridgman, P.W., 1931, *The Physics of High Pressure*, G. Bell & Sons, London.

Brittain, H.G., and Fiese, E.F., 1999, Effects of pharmaceutical processing on drug polymorphs and solvates, in: *Polymorphism in Pharmaceutical Solids*, edited by H.G. Brittain, Marcel Dekker, New York, pp. 331–361.

Byrn, S., Pfeiffer, R., Ganey, M., Hoiberg, C., Poochikian, G., 1995, Pharmaceutical solids: a strategic approach to regulatory considerations, *Pharm. Res.* **12**: 945–954.

Day, G.M., Cooper, T.G., Cruz-Cabeza, A.J., Hejczyk, K.E., Ammon, H.L., Boerrigter, S.X.M., Tan, J.S., Della Valle, R.G., Venuti, E., Jose, J., Gadre, S.R., Desiraju, G.R., Thakur, T.S., van Eijck, B.P., Facelli, J.C., Bazterra, V.E., Ferraro, M.B., Hofmann, D.W.M., Neumann, M.A., Leusen, F.J.J., Kendrick, J., Price, S.L., Misquitta, A.J., Karamertzanis, P.G., Welch, G.W.A., Scheraga, H.A., Arnautova, Y.A., Schmidt, M.U., van de Streek, J., Wolf, A.K., and Schweizer, B., 2009, Significant progress in predicting the crystal structures of small organic molecules – a report on the fourth blind test, *Acta Cryst. B* **65**: 107–125.

Dziubek, K.F., and Katrusiak, A., 2008, Polar symmetry in new high-pressure phases of chloroform and bromoform, *J. Phys. Chem. B* **112**: 12001–12009.

Fabbiani, F.P.A., and Pulham, C.R., 2006, High-pressure studies of pharmaceutical compounds and energetic materials, *Chem. Soc Rev.* **35**: 932–942.

Fabbiani, F.P.A., Allan, D.R., Dawson, A.D., David, W.I.F., McGregor, P.A., Oswald, I.D.H., Parsons, S., and Pulham, C.R., 2003, Pressure-induced formation of a solvate of paracetamol, *Chem. Commun.*: 3004–3005.

Fabbiani, F.P.A., Allan, D.R., David, W.I.F., Moggach, S.A., Parsons, S., and Pulham, C.R., 2004, High-pressure recrystallisation – a route to new polymorphs and solvates, *CrystEngComm.* **6**: 504–511.

Fabbiani, F.P.A., Allan, D.R., Marshall, W.G., Parsons, S., Pulham, C.R., and Smith, R.I., 2005a, High-pressure recrystallisation – a route to new polymorphs and solvates of acetamide and parabanic acid, *J. Cryst. Growth* **275**: 185–192.

Fabbiani, F.P.A., Allan, D.R., Parsons, S., and C.R. Pulham, 2005b, An exploration of the polymorphism of piracetam using high pressure, *Cryst. Eng. Comm.* **7**(29): 179–186.

Fabbiani, F.P.A., Allan, D.R., Parsons, S., and Pulham, C.R., 2006, Exploration of the high-pressure behaviour of polycyclic aromatic hydrocarbons: naphthalene, phenanthrene and pyrene, *Acta Cryst.* B **62**: 826–842.

Fabbiani, F.P.A., Allan, D.R., David, W.I.F., Davidson, A.J., Lennie, A.R., Parsons, S., Pulham, C.R., and Warren, J.E., 2007, High-pressure studies of pharmaceuticals: an exploration of the behavior of piracetam. *Cryst. Growth Des.* **7**(4): 1115–1124.

Fabbiani, F.P.A., Dittrich, B., Florence, A.J., Gelbrich, T., Hursthouse, M.B., Kuhs, W.F., Shankland, N., and Sowa, H., 2009, Crystal structures with a challenge: high-pressure crystallisation of ciprofloxacin sodium salts and their recovery to ambient pressure, *Cryst. Eng. Comm.* **11**(7): 1396–1406.

Favre-Nicolin, V., and Černý, R., 2002, FOX, free objects for crystallography: a modular approach to ab initio structure determination from powder diffraction *J. Appl. Cryst.* **35**: 734–743.

Florence, A.J., Johnston, A., Price, S.L., Nowell, H., Kennedy, A.R., and Shankland, N., 2006, An automated parallel crystallisation search for predicted crystal structures and packing motifs of carbamazepine, *J. Pharm. Sci.* **95**: 1918.

Fourme, R., 1968, Appareillage pour études radiocristallographiques sous pression et à température variable, *J. Appl. Cryst.* **1**: 23–30.

Gajda, R., Dziubek, K. F., and Katrusiak, A., 2006, Absence of halogen . . . halogen interactions in chlorotrimethylsilane polymorphs, *Acta Cryst. B* **62**: 86–93.

Gardner, C.R., Walsh, C.T., and Almarsson, Ö., 2004, Drugs as materials: valuing physical form in drug discovery, *Nat. Rev. Drug Discov.* **3**(11): 926–934.

Gavezzotti, A., 2007, *Molecular Aggregation: Structure Analysis and Molecular Simulation of Crystals and Liquids*, Oxford University Press, Oxford.

Gelbrich, T., and Hursthouse, M.B., 2005, A versatile procedure for the identification, description and quantification of structural similarity in molecular crystals, *Cryst. Eng. Comm.* **7**: 324–336.

Girard, E., Dhaussy, A.-C., Couzinet, B., Chervin, J.-C., Mezouar, M., Kahn, R., Ascone, I., and Fourme, R., 2007, Toward fully fledged high-pressure macromolecular crystallography, *J. Appl. Cryst.* **40**: 912–918, and references therein.

Goryainov, S.V., Boldyreva, E.V., and Kolesnik, E.N., 2006, Raman observation of a new (ζ) polymorph of glycine? *Chem. Phys. Lett.* **419**: 496–500.

Grant, D.J.W., 1999, Theory and origin of polymorphism, in: *Polymorphism in Pharmaceutical Solids*, edited by H. G. Brittain, Marcel Dekker, New York, pp. 1–33.

Hazen, R.M., and Downs, R.T., (Eds.), 2000, *High-Temperature and High-Pressure Crystal Chemistry*, The Mineralogical Society of America, Washington, D.C., **41**.

Hemley, R.J., 2000, Effects of high pressure on molecules, *Annu. Rev. Phys. Chem.* **51**:763–800.

Hemley, R.J., and Dera, P., 2000, Molecular crystals, in: *High-Temperature and High-Pressure Crystal Chemistry*, edited by R.M. Hazen and R.T. Downs, The Mineralogical Society of America, Washington, D.C., **41**, pp. 355–420.

Hilfiker, R., (Ed.), 2006, *Polymorphism in the Pharmaceutical Industry*, Wiley-VCH: Weinheim.

Kadri, A., Lorber, B., Charron, C., Robert, M.-C., Capelle, B., Damak, M., Jenner, G., and Giegé, R., 2005, Crystal quality and differential crystal-growth behaviour of three proteins crystallized in gel at high hydrostatic pressure, *Acta Cryst. D* **61**: 784–788.

Katrusiak, A., 1991, High-pressure X-ray diffraction studies on organic crystals, *Cryst. Res. Technol.* **26**: 523–531, and references therein.

Katrusiak, A., 2008, High-pressure crystallography, *Acta Cryst. A* **64**: 135–148.

Katrusiak, A., and Dauter, Z., 1996, Compressibility of lysozyme protein crystals by X-ray diffraction, *Acta Cryst. D* **52**: 607–608.

Katrusiak, A., and McMillan, P., 2004, (Eds.) *High-Pressure Crystallography*, Kluwer, Dordrecht.

Khankari, R.K., and Grant, D.J.W., 1995 Pharmaceutical hydrates, *Thermochim. Acta* **248**:61–79.

Lozano-Casal, P., Allan, D.R., and Parsons, S., 2005, Pressure-induced polymorphism in cyclopropyl-amine, *Acta Cryst. B* **61**: 717–723.

Markvardsen, A.J., David, W.I.F., and Shankland, K., 2002, A maximum likelihood method for global optimization based structure solution from powder diffraction data, *Acta Cryst. A* **58**: 316–326.

McGregor, P.A., Clark, S.J., Allan, D.R., and Parsons, S., 2006, Hexamer formation in tertiary butyl alcohol (2-methyl-2-propanol, $C_4H_{10}O$), *Acta Cryst. B* **62**: 599–605.

McMillan, P.F., 2003, Chemistry of materials under extreme high-pressure-high-temperature conditions, *Chem. Commun.* **8**: 919–923.

Meersman, F., Dobson, C.M., and Heremans, K., 2006, Protein unfolding, amyloid fibril formation and configurational energy landscapes under high pressure conditions, *Chem. Soc. Rev.* **35**: 908–917.

Moggach, S.A., Parsons, S., and Wood, P.A., 2008, High pressure polymorphism in amino acids, *Crystallogr. Rev.* **14**: 143–184, and references therein.

Moggach, S.A., Bennett, T.D. and Cheetham, A.K., 2009, The Effect of Pressure on ZIF-8: increasing pore size with pressure and the formation of a high-pressure phase at 1.47 GPa, *Angew. Chem. Int. Ed.* **48**(38): 7087–7089.

Okumura, T., Ishida, M., Takayama, K., and Otsuka, M., 2006, Polymorphic transformation of indomethacin under high pressures, *J. Pharm. Sci.* **95**: 689–700.

Olejniczak, A., and Katrusiak, A., 2008, Supramolecular reaction between pressure-frozen acetonitrile phases α and β, *J. Phys. Chem. B* **112**: 7183–7190.

Olejniczak, A., Katrusiak, A., and Vij, A., 2009a, Halogenoxygen aggregation and disorder modes in pressure frozen XCF_2CF_2X:1,4-dioxane (X = Br, I) complexes, *Cryst. Eng. Comm*. **11**(7): 1240–1244.

Olejniczak, A., Katrusiak, A., Metrangolo, P., and Resnati, G., 2009b, Molecular association in 2-bromo-2-chloro-1,1,1-trifluoroethane (Halothane), *J. Fluor. Chem.* **130**: 248–253.

Oswald, I.D.H., and Pulham, C.R., 2008, Co-crystallisation at high pressure – an additional tool for the preparation and study of co-crystals, *Cryst. Eng. Comm.* **10**: 1114–1116.

Oswald, I.D.H., Chataigner, I., Elphick, S., Fabbiani, F.P.A., Lennie, A.R., Maddaluno, J., Marshall, W. G., Pulham, C.R., Prior, T.J., and Smith, R.I., 2009, Putting pressure on elusive polymorphs and solvates, *Cryst. Eng. Comm.* **11**: 359–366.

Palatinus, L., Steurer, W., and Chapuis, G., 2007, Extending the charge-flipping method towards structure solution from incomplete data sets, *J. Appl. Cryst.* 40: 456–462.

Podsiadło, M., and Katrusiak, A., 2008, Competing patterns of weak directional forces in pressure-frozen CH_2ClI and CH_2I_2, *J. Phys. Chem. B* **112**: 5355–5362.

Prescimone, A., Milios, C. J., Moggach, S. A., Warren, J. E., Lennie, A. R., Sanchez-Benitez, J., Kamenev, K., Bircher, R., Murrie, M., Parsons, S., and Brechin, E. K., 2008, [Mn_6] under pressure: a combined crystallographic and magnetic study, *Angew. Chem., Int. Ed.* **47**(15): 2828–2831.

Price, S.L., 2009, Computed crystal energy landscapes for understanding and predicting organic crystal structures and polymorphism, *Acc. Chem. Res.* **42**(1): 117–126.

Pruzan, P., Chervin, J.C., Thiery, M.M., Itie, J.P., Besson, J.M., Forgerit, J.P., and Revault, M.J., 1990, Transformation of benzene to a polymer after static perssurization to 30 GPa, *Chem. Phys.* **92**: 6910–6915.

Rossmann, M.G., 2001, Molecular replacement - historical background, *Acta Cryst. D* **57**: 1360–1366.

Sawamura, S., Fujita, N., 2007, High-pressure solubility of fullerene C_{60} in toluene. *Carbon* **45**(5): 965–970.

Shakhtshneider T.P., Boldyreva E.V., Vasilchenko M.A., Ahsbahs, H., Uchtmann, H., 1999, Anisotropy of structural strain in molecular organic crystals on hydrostatic compression, *J. Struct. Chem*. **40**(6): 1140–1148.

Shakhtshneider T.P., Boldyreva E.V., Vasilchenko M.A., Ahsbhas, H., Uchtmann, H., 1998, A comparison of the anisotropy of hydrostatic compression of the crystalline structures of paracetamol and phenacetine, *Doklady Phys. Chem.* **363**(6): 783–786.

Spackman, M.A., and Jayatilaka, D., 2009, Hirshfeld surface analysis, *Cryst. Eng. Comm* **11**: 19–32.

Stahl, P.H., and Wermuth, C.G., (Eds.) 2002, *Handbook of Pharmaceutical Salts: Properties, Selection and Use*, Wiley-VCH, Chichester.

Stahly, G.P., 2007, Diversity in single- and multiple-component crystals. The search for and prevalence of polymorphs and cocrystals, *Cryst. Growth Des.* **7**(6): 1007–1026.

Suzuki, Y., Sazaki, G., Miyashita, S., Sawada, T., Tamura, K., Komatsu, H., 2002, Protein crystallization under high pressure, *Biochim. Biophys. Acta* **1595**: 345–356.

Tonkov, E.Yu., and Ponyatovsky, E.G., 2005, *Phase Transformations of Elements under Pressure*, CRC Press, Boca Raton, FL.

Tozuka, Y., Kawada, D., Oguchi, T., Yamamoto, K., 2003, Supercritical carbon dioxide treatment as a method for polymorph preparation of deoxycholic acid, *Int. J. Pharm.* **263**: 45–50.

Wood, P.A., Forgan, R.S., Lennie, A.R., Parsons, S., Pidcock, E., Tasker, P.A., and Warren, J. E., 2008, The effect of pressure and substituents on the size of pseudo-macrocyclic cavities in salicylaldoxime ligands, *Cryst. Eng. Comm.* **10**: 239–251.

Yamashita, M., Inomata, S., Ishikawa, K., Kashiwagi, T., Matsuo, H., Sawamura, S., and Kato, M., 2007, A high-pressure polymorph of L-α-leucine, *Acta Cryst. E* **63**: o2762–o2764.

PRESSURE-INDUCED PHASE TRANSITIONS IN CRYSTALLINE AMINO ACIDS. RAMAN SPECTROSCOPY AND X-RAY DIFFRACTION

PAULO T. C. FREIRE*
Departamento de Física – Universidade Federal do Ceará
C.P. 6030 Fortaleza – CE, 60455-760 Brazil

Abstract In this lecture I give a general overview of the behavior of amino acid crystals under high pressure conditions. This chapter presents a summary of the main results published in the literature obtained using Raman spectroscopy and x-ray diffraction.

Keywords: Amino acid, high pressure, Raman spectroscopy, phase transition

1. Introduction

Amino acids are the small molecules that constitute the "building block" of all proteins of living beings. They have both carboxylic and amino groups and have a general formula NH_2–CH(R)–COOH, where R is a side chain that characterizes the different molecules (for example, glycine, R: H; alanine, R: CH_3; valine: $(CH_3)_2CH$, etc). Amino acids can be classified as essential or non-essential, according to their importance for the humans. The essential amino acids, which are produced by plants and bio-organisms, must be present in the human food, while the non-essential amino acids are synthesized in our organisms. From a chemical point of view the 20 amino acids can be classified, for example, according to their side chain polarity: (i) non-polar: glycine, alanine, valine, leucine, isoleucine, phenylalanine, cysteine, methionine, tryptofan and proline; (ii) polar: serine, threonine, asparagine, glutamine, aspartic acid, glutamic acid, tyrosine, lysine, arginine and histidine.

*E-mail: tarso@fisica.ufc.br

E. Boldyreva and P. Dera (eds.), *High-Pressure Crystallography: From Fundamental Phenomena to Technological Applications*, DOI 10.1007/978-90-481-9258-8_46,

In the last years an increasing interest in vibrational and structural properties of amino acid crystals has been observed (*Boldyreva*, 2007a, b; *Jenkins et al.*, 2005; *Moggach et al.*, 2008). One of the reasons is because amino acids constitute molecular systems, where van der Waals interactions and hydrogen bonds play important roles in the stability of the crystalline structure; in this case amino acid assumes a zwitterions conformation, NH_3^+–CH(R)–COO^-. Another important point is the possibility of producing polymorphs under different external conditions, which is a subject of crucial importance within the pharmaceutical industry because different polymorphs of the same drug compound may have very distinct physical and chemical properties affecting bioavailability, processing, dissolution rate and stability, among others. As a third point, amino acids can be used as models to examine the intermolecular bonding in life processes and finally, just to cite a few points, the vibrational spectra of these molecules serve to obtain information regarding molecular conformation, confirming *ab initio* calculations and giving insights into the topology of more complex molecules.

Although a universe of aspects can be discussed related to this fascinating subject (isomerism and the origin of chirality, catalysis, biochemical reactions, chemical synthesis, peptide bond formation, among others) we will be restricted to the vibrational aspects of solid amino acids, in particular, the influence of high pressure on some physical properties of the amino acid crystals. Among the systems we will consider, are glycine, alanine, valine, methionine and asparagine.

2. Polymorphism and Glycine

Polymorphism is a pivotal point of solid-state physics and pharmaceutical science. The problem can be discussed in several aspects (*Boldyreva et al.*, 2003a): (i) given a certain compound, to find experimentally or to predict all the possible polymorphs; (ii) to find experimentally or to predict, which of the polymorphs will be formed under special experimental conditions. The theoretical prediction, in fact, is a very complex task. As pointed out by recent works, some success has been obtained for small molecules but, up to now, in general terms, the structural prediction is not a routine work (*Datta and Grant*, 2004).

We expect that some new polymorphs of amino acids can be obtained under extreme conditions, in particular, under high-pressure conditions. But before we can understand such modifications induced by pressure application, attention must be paid to another aspect. This aspect is related to the original phase composition in the sample we investigate.

For example, let us consider the simplest amino acid, glycine, the only non-chiral one. It shows an interesting and complex polymorphism at ambient pressure and room temperature. The α-form crystallizes in a monoclinic $P2_1/n$ structure, has hydrogen bonds in double antiparallel layers. The β-form crystallizing also in a monoclinic structure ($P2_1$) with individual parallel polar layers linked by hydrogen bonds in a three-dimensional network. The γ-form has a trigonal ($P3_1$ space group) structure with zwitterions forming polar helixes linked in a three dimensional network (*Iitaka*, 1958, 1959, 1960, 1961; *Marsh*, 1958). So, the way, how the zwitterions are linked in the solid structure through the hydrogen bond network, makes the various polymorphs different.

The problem is to obtain a pure polymorph via crystallization. In fact, the work of (*Boldyreva et al.*, 2003a) has shown that α-, β- and γ-polymorphs generally crystallize simultaneously from the same solution. As a consequence, the first step in order to perform high pressure studies on glycine is to obtain a pure polymorph. A detailed and careful indication how to obtain pure polymorphs of glycine is given in (*Boldyreva et al.*, 2003a).

Let us suppose we know the original phase of the glycine crystal. The question now is: what will occur when we subject such a material to high pressure conditions? The answer to this question was given in a series of papers (*Boldyreva*, 2004; *Boldyreva et al.*, 2003b, 2004a, b, 2005a; *Bordallo et al.*, 2008; *Dawson et al.*, 2005; *Goryainov et al.*, 2005, 2006; *Murli et al.*, 2003), and a résumé is given below.

Among the techniques that can be used to answer this question two were more frequently used: Raman spectroscopy and x-ray diffraction. First of all, let us understand what is expected when we record a Raman spectrum. The peaks appearing in the spectrum correspond to vibrational transitions as a consequence of the scattering of light from the material. In this way light scattered from a crystal has precious coded information about the vibrational properties of the material. For amino acid crystals, in a general way, we can separate the spectrum in two different regions: (i) high-wavenumber region, $\omega > 200$ cm^{-1}, where we can observe the so called "internal modes", corresponding to vibrations associated to a part of the molecule; (ii) low-wavenumber region, $\omega < 200$ cm^{-1}, where the "external modes" are observed. The number 200 cm^{-1} at the separation is not a fixed point. In fact, in some situations internal modes are observed for $\omega < 200$ cm^{-1}, as the torsional vibration of CO_2 unit, which is observed at about 170 cm^{-1} for most amino acid crystals.

Because in the external mode region we can observe the lattice modes of the crystal, it constitutes a very interesting place to observe changes on the unit cell: change of symmetry will be understood as change on the behavior of lattice modes. (Some attention must be paid related to the change in the

external mode region. There are materials, in which the changes of low wavenumber modes are associated not to phase transitions, but to the movement of domain walls).

Murli et al. (2003) have observed that the external modes in α-glycine shift to higher frequencies with increasing pressure and there are no unambiguous discontinuities up to 23 GPa. Although some slope changes related to internal modes are observed at ~ 3 GPa and above 13 GPa, many of the observed bands show broadening, all features pointing to a stability of the ambient pressure of the α-glycine structure. The changes at ~ 3 GPa can be explained by structural rearrangement involving intra-layer N–H…O hydrogen bond (*Murli et al.*, 2003).

For β-glycine, great changes were observed in the Raman spectra at ~ 0.76 GPa (*Goryainov et al.*, 2005). Jumps and kinks at the curve of the wavenumber as a function of pressure were interpreted as an evidence of the phase transition undergone by the crystal. The phase transition was reversible, but after several cycles the single crystal cracked. The phase transition involves some rearrangement in the hydrogen bond network and rotations of the zwitterions. Another important observation is that C–H and N–H stretching vibrations exhibit significant positive shifts at transition indicating that the structure gets denser at high pressure (*Goryainov et al.*, 2005). These conclusions from the Raman spectroscopy have been confirmed later by x-ray diffraction (*Dawson et al.*, 2005, *Tumanov et al.*, 2008).

The high pressure phase formed from γ-glycine (called δ-phase) was originally described in (*Boldyreva et al.*, 2003b, *Boldyreva*, 2004, *Boldyreva et al.*, 2004a, b, 2005a), and these observations were later confirmed (*Bordallo et al.*, 2008; *Dawson et al.*, 2005; *Goryainov et al.*, 2006; *Mishra et al.*, 2008). The new phase begins to appear at ~2.74 GPa, but the initial γ-form and the new δ-form coexist in a wide range of pressures. However, the new phase is the main component in the pressure range 4.17–7.85 GPa. If the γ-polymorph is kept for a long time in the slow-neutrons beam, the transformation into the δ-polymorph is observed at much lower pressures, about 0.8 GPa (*Bordallo et al.*, 2008). The packing of glycine zwitterions in the high-pressure δ-phase appears to be in many respects similar to the arrangement of the zwitterions in the α- and β-polymorphs, different from that in the initial γ-form (*Boldyreva et al.*, 2004a, b, 2005a; *Dawson et al.*, 2005).

However, the process is even more complex than that. On decompression from 7.85 GPa, the δ-form exists down to the 0.95–0.2 GPa, when new peaks in the x-ray diffraction pattern appear, which could not be indexed assuming the presence of the δ-form only. In a beautiful work, *Goryainov et al.* (2006) have shown, that the new peaks could be assigned to an additional phase; this is in fact an example of a problem, where Raman scattering could be fundamental to solve an open problem related to

understanding a new phase. Combining optical microscopy observations with Raman spectroscopy, it was possible to find, that the samples formed on decompression of δ-phase down to 0.62 GPa consist of two different regions – a light one, which was the original δ-phase, and a dark one – a new ζ-phase. The 0.62 GPa is special in the sense that if one stops changing pressure at this value the dark region increases up to a maximum. However, further decreasing of pressure down to ambient does not destroy the remaining light region. In other words, the δ- and ζ-phases are both present at 0 GPa after decreasing pressure for some time, after what they convert into the α-form. Similar observations have been reported later for the transitions on compression-decompression in the completely deuterated γ-glycine (*Mishra et al.*, 2008).

3. Aliphatic Amino Acids

Alanine is the simplest chiral amino acid. Over the years it has been observed that alanine is a very complex system. For example, a localization of energy in low-frequency bands was observed (*Migliori et al.*, 1988), as well as a negative thermal expansion along a certain axis (*Lehmann et al.*, 1972), and some others unusual effects (*de Souza et al.*, 2007). Under temperature variations, L-alanine seems to be stable (in the sense that the room temperature orthorhombic structure does not change in the 20–400 K interval), although particular changes have been observed at low temperatures (*Barthes et al.*, 2004).

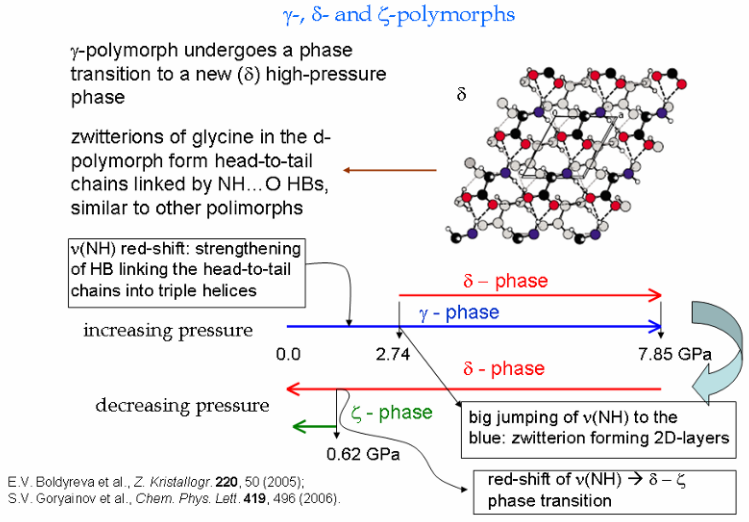

Figure 1. Representation of the transitions between the δ –, γ- and ζ-phases of glycine.

The question here is to understand vibrational and structural properties of L-alanine under high pressure conditions. Again, Raman spectroscopy and x-ray diffraction experiments can provide an almost complete answer to the problem.

Figure 2 gives the evolution of the Raman spectra of L-alanine under pressure variation in the low wavenumber region. As we commented, this region spans the lattice mode vibrations. Modifications of the Raman spectra, as a consequence, can be associated to changes of the symmetry of the unit cell. Figure 2 shows that above ~2.2 GPa a new peak appears in the Raman spectrum suggesting that L-alanine undergoes a phase transition (*Teixeira et al.*, 2000). In order to understand this phenomenon better, an x-ray diffraction study under high pressure was performed at Hasylab-Desy in Hamburg, Germany (Figure 3). The results showed that at high pressure two doublets, 110/001 and 120/021, of the orthorhombic structure merge into single peaks. This was interpreted as the sample undergoing a structural phase transition from the orthorhombic to the tetragonal symmetry (*Olsen et al.*, 2008).

The experiment done with x-ray diffraction was able to reach a pressure of 12 GPa, well beyond the maximum pressure obtained from the Raman experiment, 4.2 GPa. As a consequence, it was possible to observe that at still higher pressures, new lines appeared at the diffraction pattern, indicating a further structural change. This new structure has a lower symmetry and through the use of a particular code a new phase was indexed supposing the existence of a monoclinic unit cell above 9 GPa. So, using Raman scattering and x-ray diffraction experiments it was possible to establish the following

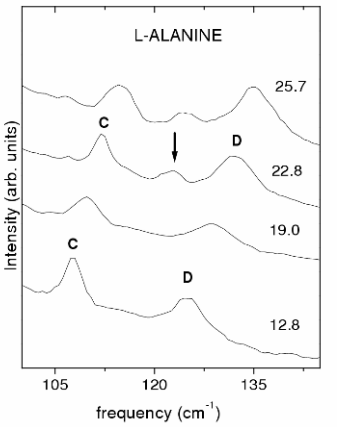

Figure 2. Raman spectra of L-alanine in the low-wavenumber region for different pressures (in kbar) (*Teixeira et al.*, 2000).

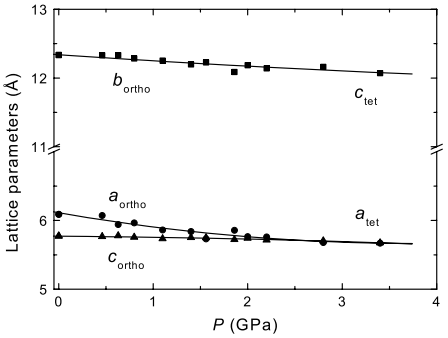

Figure 3. The unit-cell parameters of L-alanine as a function of pressure (*Olsen et al.*, *2008*).

sequence of phase transitions undergone by L-alanine crystal: orthorhombic → (2.3 GPa) tetragonal → (9 GPa) monoclinic. The original structure was observed on decompression, indicating that the phase transitions are reversible.

Now let us discuss the results related to another aliphatic amino acid submitted to high pressure conditions: L-leucine. These molecules crystallize in a monoclinic structure (*Harding and Howieson*, *1976*). Three different polymorphs are known at ambient pressure: (i) phase I, corresponding to the room temperature structure; (ii) phase II, corresponding to the structure for T >353 K (*Façanha Filho et al.*, 2008) and (iii) phase III, precipitating from a solution at 200 Ma (*Yamashita et al.*, 2007). Submitting L-leucine crystal to high pressure conditions we obtain interesting results; Figures 4 and 5 will help us to understand the phenomena.

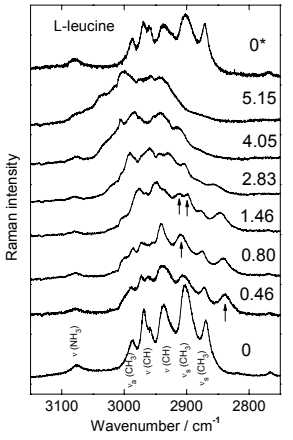

Figure 4. Raman spectra of L-leucine crystal at different pressures (GPa) (*Façanha Filho et al.*, 2009).

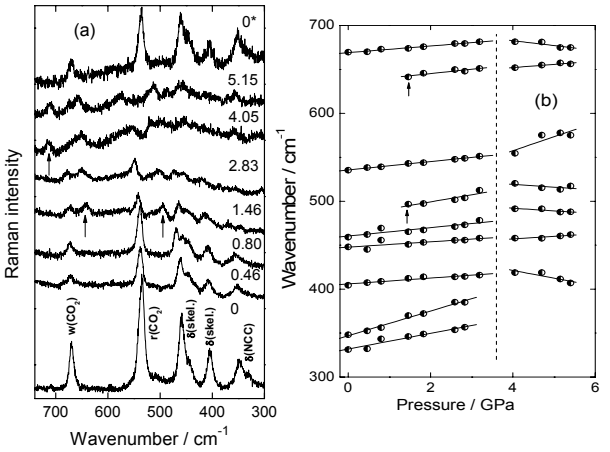

Figure 5. Evolution of Raman spectra of L-leucine crystal in the spectral range 300–740 cm^{-1} at different pressures (GPa) (*Façanha Filho et al.*, 2009).

Raman spectra of L-leucine crystal in the high wavenumber region for selected pressures (in GPa) are shown in Figure 4. Compressing sample we observe that the intensity of all bands decreases and a new band (marked by an arrow) appears at ~ 0.46 GPa. Another change is observed between 0.80 and 1.46 GPa, i.e., a band splits (marked by arrows in Figure 4). With pressure increases above 1.46 GPa, the intensity of peaks continues to decrease, but the spectrum seems to maintain the same profile (*Façanha Filho et al.*, 2009).

Figure 5 shows the Raman spectrum of L-leucine crystal for several pressures in the 300–740 cm^{-1} range. The changes between 0 and 0.46 GPa are not so evident as in the previous Figure. However, the changes between 0.80 and 1.46 GPa are more pronounced and include the change of relative intensities and the appearance of two new peaks in the spectrum at 1.46 GPa. Additionally, the spectra measured at 2.83 and 4.05 GPa differ. This region also shows strong discontinuities in the dω/dP curve as shown in Figure 5b. It is interesting to note the splitting of a band associated to deformation of CO_2^- unit. It may be understood as a consequence of changes in the intermolecular coupling. Since such an intermolecular coupling originates from the hydrogen bonds between CO_2^- and NH_3^+ units of the adjacent molecules, one can suppose that the phase transition involves a large variation of one or more of the hydrogen bonds among leucine molecules. The Raman spectra of the low-wavenumber region (not shown in this text) confirms anomalies in the regions 0–0.46 GPa and 0.80–1.46 GPa, as well as above 3.6 GPa. Together with the behavior of internal

modes we can interpret all the results as a change in the conformation of molecules of L-leucine, possibly including modification of symmetry of the unit cell. Further works involving x-ray diffraction will help us to understand these transformations better.

4. Sulfur-Containing Amino Acids

There are two sulfur-containing amino acids. One of them is L-cysteine, a sulfur-containing amino acid with the thiol side-chain, which is involved in metal-binding in proteins. At atmospheric pressure L-cysteine crystallizes in an orthorhombic (*Kerr and Ashmore*, *1973*) and a monoclinic structure (*Harding and Long*, *1968*), similarly to L-isoleucine crystal that presents both orthorhombic and monoclinic stable structures at 1 atm (*Almeida et al.*, 2006). In the orthorhombic L-cysteine the hydrogen of thiol group is disordered, forming either SH…S or SH…O bonds. As has been observed also for other amino acids, the unit cell parameters change anisotropically with increasing pressure: while *b*-axis shortens only by 1.3% between 0 and 1.8 GPa, the *a*-axis decreases by 8.6%. The changes in the cell parameters are accompanied by the changes in the values of the NCCS and NCCO torsional angles and the compression of hydrogen bonds, which is different for different bonds (*Moggach et al.*, 2006a). The behavior of cysteine at high pressure is representative for other amino acids.

At 1.8 GPa L-cysteine undergoes a phase transition. At this pressure value the N…O distance has a normal dimension, common to other amino acids. However, the S…S distances are quite short, and in order to accomplish such an approximation between sulfur atoms, the NCCS torsion angle changes, explaining the occurrence of the phase transition. In other words, the structural change lets the tension produced by the proximity of S…S bond relax, and the new conformation remains stable up to 4.2 GPa. On releasing pressure down to 1.7 GPa, L-cysteine undergoes a new phase transition, forming a phase, where two alternated zones are present. One of the zones has a structure similar to the ambient-pressure phase and the other zone has a structure like the high-pressure phase. For this reason, it is believed that at this pressure, L-cysteine is in an “intermediate” phase (*Moggach et al*., 2006a), or a mixture of phases. A similar effect has been observed for L-methionine (*Lima et al.*, 2008). Finally, after releasing pressure down to 1 atm the original, the orthorhombic phase is recovered. Further insights could be achieved by Raman spectroscopy and a comparison of the behavior of L- and DL-cysteine under pressure was given by *Minkov et al.* (2008).

L-methionine is another proteic amino acid that possesses sulfur in its molecule. It crystallizes in a monoclinic structure with four molecules per unit cell. Differently from L-cysteine, where S belongs to a side chain and forms a hydrogen bond through the sulfhydryl group, in L-methionine, sulfur atom belongs to the skeletal structure of the amino acid. As in all the other amino acids, the hydrogen bonds are formed between NH_3^+ and CO_2^- groups of the different molecules.

The Raman spectra of a L-methionine crystal at pressures from 0.1 to 4.7 GPa in the 500–700 cm^{-1} region are shown in Figure 6a. One can assign the bands as the rocking of CO_2^-, $\rho(CO_2^-)$, at 543 cm^{-1}; the stretching vibration of SC, at 659 cm^{-1}, the wagging of CO_2^-, at 683 cm^{-1} With increasing pressure, very interesting changes in the Raman spectra are observed. Firstly, the linewidth of the band $r(CO_2^-)$ increases above 1.1 GPa, and at 2.7 GPa this bands split completely. Secondly, the other two bands are shifted to higher frequencies; in the spectrum at 2.1 GPa one can notice not only these two weak bands. Possibly, at this pressure value the original crystal transforms into a mixture of phases. With further increase of pressure, the two original bands vanish and the intensity of the new band increases. This new band is observed up to 4.7 GPa. By releasing the pressure, the characteristic monoclinic-phase Raman spectrum features are recovered, although at a lower value, i.e., below 1.3 GPa, so that a hysteresis is ~ 0.8 GPa. The spectra at 1.8 GPa (Figure 6a) and at 0.7 GPa (Figure 6b) are qualitatively the same (*Lima et al.*, 2008).

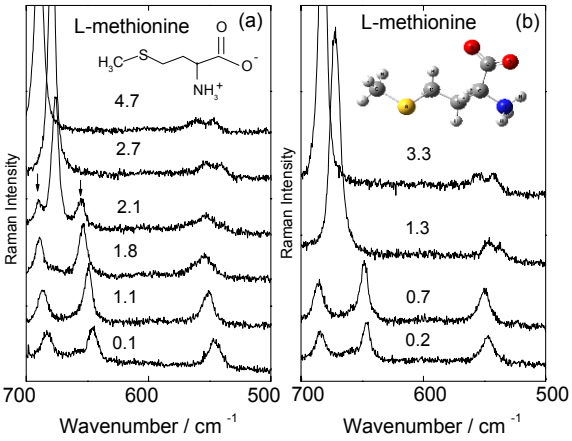

Figure 6. Raman spectra of L-methionine crystal in the spectral range 500–700 cm^{-1} at different pressures (GPa) (*Lima et al.*, 2008).

5. Other Amino Acids

Beyond these, other amino acid crystals have been investigated by Raman spectroscopy and/or by x-ray diffraction under high pressure conditions. Very interesting results have been obtained for monohydrated L-asparagine (*Moreno et al.*, 1997), L-threonine (*Silva et al.*, 2000), L-serine (*Boldyreva et al.*, 2005b, 2006a, b; *Drebushchak et al.*, 2006; *Kolesnik et al.*, 2005; *Moggach et al.*, 2005, 2006), DL-serine (*Boldyreva et al.*, 2006a; *Murli et al.*, 2006), deuterated L-alanine (*Goncalves et al.*, 2009), and L-isoleucine (*Sabino et al.*, 2009).

For example, three different phase transitions for pressures lower than 1.3 GPa have been observed in the crystal of the monohydrated L-asparagine (*Moreno et al.*, 1997). The first phase transition apparently occurs at pressures of ~0.2 GPa, a very low value when compared with all other amino acid crystals investigated up to now. In fact, only L-cysteine, which undergoes a phase transition at ~0.1 GPa (*Minkov et al.*, 2008), also has a phase transition at such a very low pressure value.

Many have to be studied yet!

References

Almeida, F.M., Freire, P.T.C., Lima, R.J.C., Remédios, C.M.R., Mendes Filho, J., Melo, F.E.A., 2006, Raman spectra of L-isoleucine crystals. *J. Raman Spectrosc*. **37**: 1296.

Barthes, M., Bordallo, H.N., Dénoyer, F., Lorenzo, J.-E., Zaccaro, J., Robert, A., Zontone, F., 2004, Micro-transitions or breathers in L-alanine? *Eur. Phys. J. B* **37**: 375.

Boldyreva, E.V., 2004, High-pressure-induced structural changes in molecular crystals preserving the space group symmetry: anisotropic distortion/isosymmetric polymorphism. *Cryst. Eng.* **6**: 235.

Boldyreva, E.V., 2007a, Crystalline amino acids – a link between chemistry, materials sciences and biology. In *Models, Mysteries, and Magic of Molecules*; Boeyens JCA, Ogilvie JF, Eds. Springer-Verlag: New York, pp. 169–194.

Boldyreva, E.V., 2007b, High-pressure polymorphs of molecular solids: When are they formed, and when are they not? Some examples of the role of kinetic control. *Cryst. Growth Des.* **7**, 1662.

Boldyreva, E.V., Drebushchak, V.A., Drebushchak, T.N., Paukov, I.E., Kovalevskaya, T.A., Shutova, E.S., 2003a, Polymorphism of glycine: Thermodynamic aspects. Part I – Relative stability of the polymorphs. *J. Therm. Anal. Cal*. **73**: 409.

Boldyreva, E. V., Ahsbahs, H., Weber, H.-P., 2003b, A comparative study of pressure-induced lattice strain of α- and γ-polymorphs of glycine, *Z. Krist.* **218**: 231–236.

Boldyreva, E.V., Ivashevskaya S.N., Sowa H., Ahsbahs H., Weber H.-P., 2004a, Effect of hydrostatic pressure on the γ-polymorph of glycine: a phase transition, *Mater. Struct.,* **11**(1a): 37–39.

Boldyreva, E.V., Ivashevskaya SN, Sowa H, Ahsbhs H, Weber H.-P., 2004b, Effect of high pressure on crystalline glycine: A new high-pressure polymorph. *Dok. Phys. Chem*. **396**: 111.

Boldyreva, E.V., Ivashevskaya, S.N., Sowa, H., Ahsbahs, H., Weber, H-P., 2005a, Effect of hydrostatic pressure on the γ-polymorph of glycine 1. A polymorphic transition into a new δ-form. *Z. Kristallogr*., **220**: 50.

Boldyreva, E.V., Kolesnik, E.N., Drebushchak, T.N., Ahsbahs, H., Beukes, J.A., Weber, H.-P., 2005b, A comparative study of the anisotropy of lattice strain induced in the crystals of L-serine by cooling down to 100 K or by increasing pressure up to 4.4 GPa, *Z. Kristallogr.* **220** (1): 58–65.

Boldyreva, E.V., Kolesnik, E.N., Drebushchak, T.N., Sowa, H., Ahsbahs, H., Seryotkin, Y.V., 2006a, A comparative study of the anisotropy of lattice strain induced in the crystals of DL-serine by cooling down to 100 K, or by increasing pressure up to 8.6 GPa. A comparison with L-serine. *Z. Kristallogr*. **221**: 150.

Boldyreva, E.V., Sowa, H., Seryotkin, Yu.V., Drebushchak, T.N., Ahsbahs, H. Chernyshev, V., Dmitriev, V., 2006b, Pressure-induced phase transitions in crystalline L-serine studied by single-crystal and high-resolution powder X-ray diffraction. *Chem. Phys. Lett*. **429**: 474–478.

Bordallo, H.N., Boldyreva, E.V., Buchsteiner, A., Koza, M.M., Landsgesell, S., 2008, Structure-property relationships in the crystals of the smallest amino acid: An incoherent inelastic neutron scattering study of the glycine polymorphs, *J. Phys. Chem. B.* **112**: 8748.

Datta, S., Grant, D.J.W., 2004, Crystal structures of drugs: Advances in determination, prediction and engineering, *Nat. Drug Discov*. **3**: 42.

Dawson, A., Allan, D.R., Belmonte, S.A., Clark SJ, David WIF, McGregor PA, Parsons S, Pulham CR, Sawyer L., 2005, Effect of high pressure on the crystal structures of polymorphs of glycine. *Cryst. Growth Des*. **5**: 1415.

Drebushchak, T.N., Sowa, H., Seryotkin, Yu.V., Boldyreva, E.V., Ahsbahs, H., 2006, L-Serine III at 8.0 GPa, *Acta Cryst. E.* **62**: 4052–4054.

Façanha Filho, P.F., Freire, P.T.C., Lima, K.C.V., Filho, J.M., Melo, F.E.A., Pizani, P.S., 2008, High-temperature Raman spectra of L-leucine crystals. *Braz. J. Phys.* **38:** 131.

Façanha Filho, P.F., Freire, P.T.C., Melo, F.E.A., Lemos, V., Filho, J.M., Pizani, P.S., Rossatto, D.Z., 2009, Pressure-induced phase transitions in L-leucine crystal. *J. Raman Spectr.* **40:** 46.

Gonçalves, R.O., Freire, P.T.C., Bordallo, H.N., Lima Jr. J.A., Melo, F.E.A., Filho, J.M., Argyriou, D.N., Lima, R.J.C., 2009, High-pressure Raman spectra of deuterated L-alanine crystal. *J. Raman Spectr.* **40:** 958.

Goryainov, S.V., Kolesnik, E.N., Boldyreva, E.V., 2005, A reversible pressure-induced phase transition in β-glycine at 0.76 GPa. *Physica B.* **357:** 340.

Goryainov, S.V., Boldyreva, E.V., Kolesnik, E.N., 2006, Raman observation of a new (ζ) polymorph of glycine? *Chem. Phys. Lett.* **429:** 496.

Harding, M.M., Howieson, R.M., 1976, L-Leucine. *Acta Cryst. B.* **32:** 633.

Harding, M.M., Long, H.A., 1968, The crystal and molecular structure of L-cysteine. *Acta Cryst. B.* **24:** 1096.

Iitaka, Y., 1958, The crystal structure of γ-glycine, *Acta Cryst.* **11:** 225–226.

Iitaka, Y., 1959, The crystal structure of β-glycine, *Nature* **183**(4658): 390–391.

Iitaka, Y., 1960, The crystal structure of β-glycine, *Acta Crys*t. **13:** 35–45.

Iitaka, Y., 1961, The crystal structure of γ-glycine, *Acta Cryst*. **14:** 1–10.

Jenkins, A.L., Larsen, R.A., Williams, T.B., 2005, Characterization of amino acids using Raman spectroscopy. *Spectr. Acta A.* **61:** 1585.

Kerr, K.A., Ashmore, J.P., 1973, Structure and conformation of orthorhombic L-cysteine. *Acta Cryst. B.* **29:** 2124.

Kolesnik, E.N., Goryainov, S.V., Boldyreva, E.V., 2005, Different behavior of L- and DL-serine crystals at high pressures: phase transitions in L-serine and stability of the DL-serine structure. *Dokl. Phys. Chem*. **404**, Part 1: 169.

Lehmann, M.S., Koetzle, T.F., Hamilton, W.C., 1972, Precision neutron diffraction structure determination of protein and nucleic acid components. I. The crystal and molecular structure of the amino acid L-alanine. *J. Am. Chem. Soc.* **94:** 2657.

Lima Jr., J.A., Freire, P.T.C., Melo, F.E.A., Lemos, V., Mendes Filho, J., Pizani, P.S., 2008, High-pressure Raman spectra of L-methionine crystal. *J. Raman Spectr*. **39:** 1356.

Marsh, R.E. A refinement of the crystal structure of glycine. *Acta Cryst*. 1958, 11, 654–663.

Migliori, A., Maxton, P.M., Clogston, A.M., Zrngiebl, E., Lowe, M., 1988, Anomalous temperature dependence in the Raman spectra of l-alanine: evidence for dynamic localization. *Phys. Rev. B.* **38**: 13464.

Minkov, V.S., Krylov, A.S., Boldyreva, E.V., Goryainov, S.V., Bizyaev, S.N., Vtyurin, A.N., 2008, Pressure-induced phase transitions in crystalline L- and DL-cysteine. *J. Phys. Chem. B.* **112:** 8851.

Mishra, A.K., Murli, C., Sharma, S.M., 2008, High pressure Raman spectroscopic study of deuterated γ-glycine, *J. Phys. Chem. B*. **112** (49)**:** 15867–15874.

Moggach, S.A., Allan, D.R., Morrison, C.A., Parsons, S., Sawyer, L., 2005, Effect of pressure on the crystal structure of L-serine-I and the crystal structure of L-serine-II at 5.4 GPa, *Acta Cryst. B*. **61:** 58–68.

Moggash, S.A., Allan, D.R., Clark, S.J., Gutmann, M.J., Parsons, S., Pulham, C.R., Sawyer, L., 2006a, High-pressure polymorphism in L-cysteine: the crystal structures of L-cysteine-III and L-cysteine-I.V *Acta Cryst. B.* **62:** 296.

Moggach, S.A., Marshall, W.G., Parsons, S., 2006b, High-pressure neutron diffraction study of L-serine-I and L-serine-II, and the structure of L-serine-III at 8.1 GPa. *Acta Cryst. B.* **62:** 815.

Moggach, S.A., Parsons, S., Wood P.A., 2008, High pressure polymorphism in amino acids, Crystallogr. Rev. **14:** 143–184.

Moreno, A.J.D., Freire, P.T.C., Melo, F.E.A., Silva, M.A.A., Guedes, I., Mendes Filho, J., 1997, Pressure-induced phase transitions in monohydrated l-asparagine aminoacid crystals. *Solid State Commun*. **103:** 655.

Murli, C., Sharma, S.K., Karmakar, S., Sikka, S.K., 2003, α-Glycine under high pressures: A Raman scattering study. *Physica B.* **339:** 23.

Murli, C., Vasanthi, R., Sharma, S.M., 2006, Raman spectroscopic investigations of dl-serine and dl-valine under pressure. *Chem. Phys*. **331:** 77.

Olsen, J.S., Gerward, L., Freire, P.T.C., Filho, J.M., Melo, F.E.A., Souza Filho, A.G., 2008, Pressure-induced phase transformations in l-alanine crystals. *J. Phys. Chem. Solids* **69:** 1641.

Sabino, A.S., De Sousa, G.P., Luz-Lima, C., Freire, P.T.C., Melo, F.E.A., Mendes Filho, J., 2009, High-pressure Raman spectra of L-isoleucine crystals. *Solid State Commun.* **149:** 1553.

Silva, B.L., Freire, P.T.C., Melo, F.E.A., Mendes Filho, J., Pimenta, M.A., Dantas, M.S.S., 2000, High-pressure Raman spectra of L-threonine crystal. *J. Raman Spectr.* **31:** 519.

de Souza, J.M., Freire, P.T.C., Bordallo, H.N., Argyriou, D.N., 2007, Structural isotopic effects in the smallest chiral amino acid: observation of a structural phase transition in fully deuterated alanine. *J. Phys. Chem. B.* **111:** 5034.

Teixeira, A.M.R., Freire, P.T.C., Moreno, A.J.D., Sasaki, J.M., Ayala, A.P., Mendes Filho, J., Melo, F.E.A., 2000, High-pressure Raman study of L-alanine crystal. *Solid State Commun.* **116:** 405.

Tumanov, N.A., Boldyreva, E.V., Ahsbahs, H., 2008, Structure solution and refinement from powder or from single-crystal diffraction data? Pro and contras: an example of the high-pressure beta´-polymorph of glycine: *Powder Diffract.* **23:** 307–316.

Yamashita, M., Inomata, S., Ishikawa, K., Kashiwagi, T., Matsuo, H., Sawamura, S., Kato, M., 2007, A high-pressure polymorph of L-leucine. *Acta Cryst. E.* **63:** o2762.

EXPLORING THE ENERGY AND CONFORMATIONAL LANDSCAPE OF BIOMOLECULES UNDER EXTREME CONDITIONS

ROLAND WINTER*
TU Dortmund University, Physical Chemistry - Biophysical Chemistry, Otto-Hahn Straße 6, D-44227 Dortmund, Germany

Abstract High hydrostatic pressure has been used as a physical parameter for studying the stability of biomolecular systems, such as lipid bilayers, DNA and proteins, but also because high pressure is an important feature of certain natural environments. By using a variety of spectroscopic, calorimetric and scattering techniques, the temperature and pressure dependent structure and phase behavior of these systems has been studied and will be discussed. We also introduce pressure as a kinetic variable. Applying the pressure-jump relaxation technique in combination with time-resolved synchrotron X-ray diffraction and spectroscopic techniques, the kinetics of lipid phase transitions and folding reactions of proteins has been studied. Finally, recent advances in using pressure for studying misfolding and aggregation of proteins will be elucidated.

Keywords: High pressure, phase diagrams, model biomembranes, protein stability, protein folding, protein aggregation

1. Introduction

Remarkably, the greatest portion of our biosphere is in the realm of environmental extremes, and for several decades now, the limits of the existence of life have been pushed to unexpected extremes of pressure, temperature, pH and salinity (*Daniel et al.*, 2006). Although hydrostatic pressure significantly influences the structural properties and thus functional characteristics of cells,

* E-mail: roland.winter@tu-dortmund.de

E. Boldyreva and P. Dera (eds.), *High-Pressure Crystallography: From Fundamental Phenomena to Technological Applications*, DOI 10.1007/978-90-481-9258-8_47,

this has not prevented life from invading the cold and high pressure habitats of marine depths (70% of the surface of the earth is covered by oceans, and the average pressure on the ocean floor is about 380 bar (0.1 MPa = 1 bar, 1 GPa = 10 kbar)). For example, deep-sea sediments and hydrothermal vents are densely crowded with barophilic-thermophilic (i.e., pressure- and heat-adapted species). Psychrophilic-barophilic (cold- and pressure-adapted) species, which live at ~2°C, are found on the deepest ocean floor (~11,000 m) in the Mariana Trench and in deep-sea sediments. Close to hydrothermal vents, generally several thousand meter under the sea surface, even organisms far more complex than bacteria can be found at conditions of high hydrostatic pressure (HHP) (~300 bar) and high temperature (up to ~120°C) (*Bartlett*, 2002; *Yayanos*, 1986). Interest in pressure as a thermodynamic and kinetic variable has been growing also in physico-chemical studies of biological materials in recent years (*Daniel et al.*, 2006; *Heremans and Smeller*, 1998; *Silva et al.*, 2001; *Winter*, 2002; *Winter et al.*, 2007), for the following reasons: (i) Changing temperature of a biochemical system at atmospheric pressure produces a simultaneous change in thermal energy and volume; therefore, to separate thermal and volume effects, one must carry out also pressure dependent experiments. (ii) Because noncovalent interactions play a primary role in the stabilization of biochemical systems, the use of pressure allows one to change, in a controlled way, the intermolecular interactions without the major perturbations often produced by changes in temperature or cosolvent concentration. (iii) Pressure affects chemical equilibria and reaction rates. Le Châtelier's principle predicts that the application of pressure shifts an equilibrium towards the state that occupies a smaller volume, and accelerates processes for which the transition state has a smaller volume than the ground state. With the knowledge of ΔV^{o} and $\Delta V^{\#}$ values, one can then draw valuable conclusions about the nature of the reaction and its mechanism. (iv) The viscosity of the solvent can be changed continuously by pressure. (v) One can extend the range of conditions and carry out experiments at subzero temperatures still within the liquid state. For example, protein solutions can be studied at subzero temperatures to investigate their cold-denaturation behavior.

Pressures used to investigate biochemical systems generally range from 1 bar to 10 kbar. Such pressures only change intermolecular distances and affect conformations, but do not change covalent bond distances or bond angles. The covalent structure of low molecular mass biomolecules (peptides, lipids, saccharides), as well as the primary structure of macromolecules (proteins, nucleic acids and polysaccharides), is generally not perturbed by pressures up to ~20 kbar. Pressure acts predominantly on the conformation, supramolecular structure and topology of biomolecular systems.

In this short review, we will discuss selected results of studies on the high pressure structure and phase behavior of simple biomolecular systems, such as model biomembrane systems and proteins. High pressure biophysical studies generally call for unique experimental methods, which have been developed in recent years as well. The principles and applications can be found elsewhere (*Akasaka*, 2006; *Arnold et al.*, 2003; *Jonas*, 1991; *Winter*, 2001, 2002; *Winter and Czeslik*, 2000, and refs. therein).

2. Pressure Effects on Biomolecular Systems Introduction

2.1. LIPID BILAYERS AND MODEL BIOMEMBRANE SYSTEMS UPON PRESSURIZATION

The basic structural element of biological membranes consists of a lamellar phospholipid bilayer matrix. Even though most lipids possess two acyl-chains and one hyphrophilic headgroup, the composition of the chains and the headgroup can vary significantly in cellular membranes. Also, the lipid composition is very different in different cell types of the same organism, or even in different organelles of the same cell. Lipid bilayers display various phase transitions including a chain melting transition. In excess water, saturated phospholipids often exhibit two thermotropic lamellar phase transitions, a gel-to-gel ($L_{\beta'}$-$P_{\beta'}$) pretransition and a gel-to-liquid-crystalline ($P_{\beta'}$-L_{α}) main (chain melting) transition at a higher temperature, T_m (Figure 1).

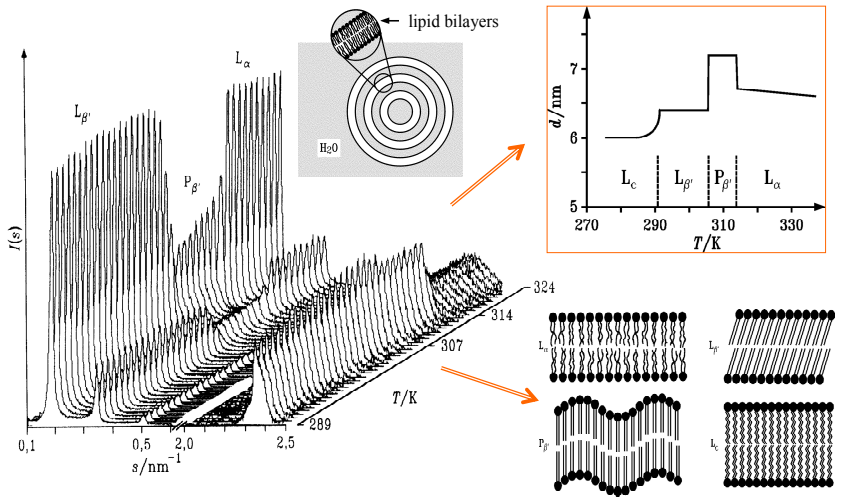

Figure 1. Temperature dependent synchrotron X-ray diffration data of DPPC in exess water, the lamellar *d*-spacings, and a schematic drawing of various lipid bilayer phases (L_c, lamellar crystalline; $L_{\beta'}$, $P_{\beta'}$, lamellar gel; L_{α}, lamellar liquid-crystalline).

In the physiologically more relevant fluid-like L_α phase, the acyl-chains of the lipid bilayers are conformationally disordered ("melted"), whereas in the gel (solid-ordered) phases, the chains are more extended and ordered. Biological membranes can also melt. Typically, such melting transitions are found about 10°C below body or growth temperatures. It seems that biological membranes adapt their lipid compositions such that the temperature distance to the melting transition is maintained. The same may hold true for adaptation to high pressure conditions. In fact, in addition to thermotropic lipid phase transitions, a variety of pressure-induced phase transformations have been observed (*Winter*, 2002; *Winter and Czeslik*, 2000; *Winter et al.*, 2007).

A common slope of ~22°C/kbar has been observed for the gel–fluid phase boundary of saturated phosphatidylcholines as shown in Figure 2. Assuming the validity of the Clapeyron relation describing first-order phase transitions for this quasi-one-component lipid system, $dT_m/dp = T_m\Delta V_m(T_m, p)/\Delta H_m(T_m, p)$, the positive slope can be explained by an endothermic enthalpy change, ΔH_m, and a partial molar volume increase, ΔV_m, for the gel-to-fluid transition. The transition enthalpy at atmospheric pressure is about 36 kJ/mol for DPPC at ambient pressure and decreases slightly with pressure. Similarly, ΔV_m decreases essentially linearly with increasing pressure ($d\Delta V_m/dp$)= -4.93 $cm^3 \cdot mol^{-1}$ $kbar^{-1}$).

Similar transition slopes have been determined for the mono-*cis*-unsaturated lipid POPC, the phosphatidylserine DMPS, and the phosphatidylethanolamine DPPE. Only the slopes of the di-*cis*-unsaturated lipids DOPC and DOPE have been found to be markedly smaller. The two *cis*-double bonds of DOPC and DOPE lead to very low transition temperatures and slopes, as they impose kinks in the linear conformations of the lipid acyl-chains, thus creating significant free volume fluctuations in the bilayer so that the ordering effect of high pressure is reduced. Hence, in order to remain in a physiological relevant, fluid-like state at high pressures, more of such *cis*-unsaturated lipids are incorporated into cellular membranes of deep sea organisms, one example of homeoviscous adaption (*Cossins and Macdonald*, 1986; *Yayanos*, 1986). While increasing pressure is accompanied by an increase of the concentration of unsaturated chains, the abundance of saturated chains is lowered.

Pressure generally increases the order of membranes, thus mimicking the effect of cooling. However, applying high pressure can lead to the formation of additional ordered phases, which are not observed under ambient pressure conditions, such as a partially interdigitated high pressure gel phase, $L_{\beta i}$, found for phospholipid bilayers with acyl-chain lengths ≥ C_{16}. To illustrate this phase variety, the results of a detailed SAXS/SANS and FT-IR spectroscopy study of the *p*,*T*-phase diagram of DPPC in excess water are shown in Figure 3a. At much higher pressures as shown here,

even further ordered gel phases appear, differing in the tilt angle of the acyl-chains and the level of hydration in the headgroup area (*Winter and Czeslik*, 2000). Even at pressures where the bulk water freezes, the lamellar structure of the membrane is preserved.

Cholesterol effect. Cholesterol constitutes up to ~50% of the lipid content of animal cell membranes. Due to both its amphiphilic character and size, it is inserted into phospholipid membranes. Cholesterol thickens liquid-crystalline bilayers and increases the packing density of the lipid acyl-chains in a way that has been referred to as "condensing effect". Measurements of the acyl-chain orientational order of the lipid bilayer system by measuring the ^{2}H-NMR spectra or the steady-state fluorescence anisotropy of the embedded fluorophore TMA-DPH (*Eisenblätter and Winter*, 2006; *Zein and Winter*, 2000), clearly demonstrate the ability of cholesterol and other plant or bacterial sterols to efficiently regulate the structure, motional freedom and hydrophobicity of biomembranes (Figure 4).

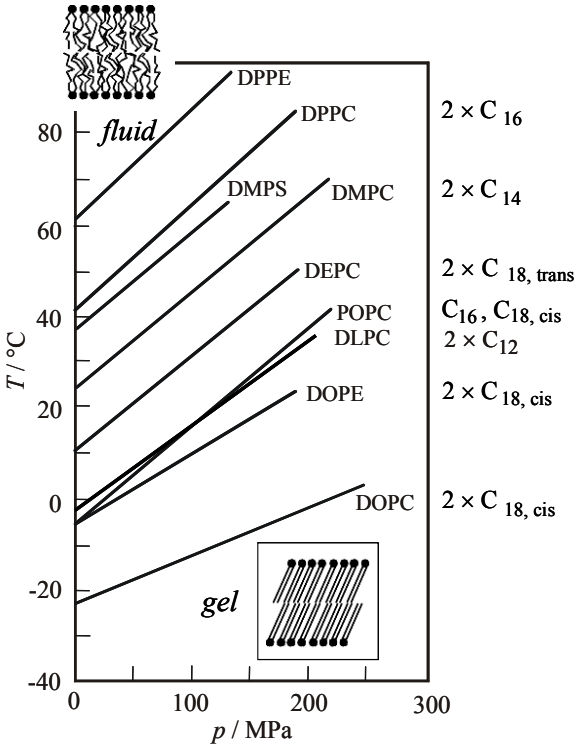

Figure 2. T, *p*-phase diagram for the main (chain-melting) transition of different phospholipid bilayer systems. The fluid-like L_α-phase is observed in the low-pressure, high-temperature region of the phase diagram; the ordered gel phase regions appear at low temperatures and high pressures, respectively. The lengths and degree of unsaturation of the acyl-chains of the various phospholipids are denoted on the right-hand side of the figure.

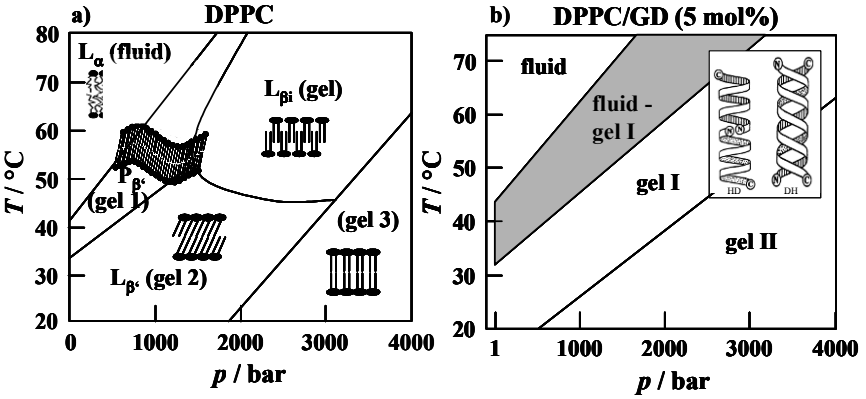

Figure 3. (a) *T*, *p*-phase diagram of DPPC bilayers in excess water. Besides the Gel 1 ($P_{\beta'}$), Gel 2 ($L_{\beta'}$) and Gel 3 phase, an additional crystalline gel phase (L_c) can be induced in the low-temperature regime after prolonged cooling which is not shown here). (b) Phase diagram of DPPC-gramicidin D (GD) (5 mol%) in excess water as obtained from diffraction and spectroscopic data. The inset shows a schematic view of the helical dimer (HD) and double helix (DH) conformation of GD.

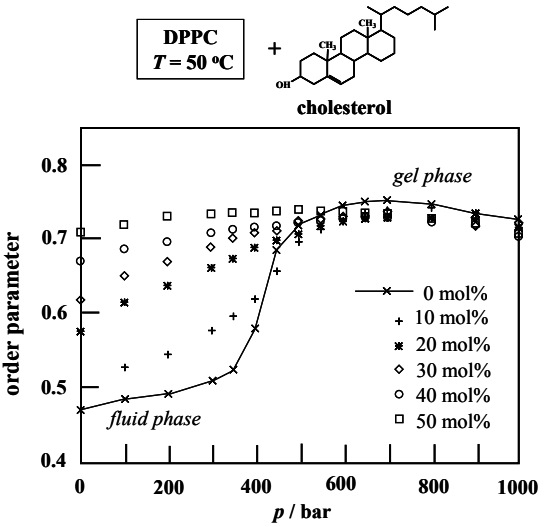

Figure 4. Pressure dependence of the mean chain order parameter as determined from steady-state fluorescence anisotropy measurements of TMA-DPH in DPPC unilamellar vesicles at different cholesterol concentrations (at $T = 50°C$).

The mean chain order parameter *S* of pure DPPC at $T = 50°C$ increases slightly up to about 400 bar, where the pressure-induced liquid-crystalline to gel phase transition takes place. Since *S* essentially reflects the mean

order parameter of the lipid acyl-chains, these results indicate that increased pressures cause the chain region to be ordered in a manner similar to that which occurs upon decreasing the temperature. Addition of increasing amounts of cholesterol leads to a drastic increase of *S*-values in the lower pressure region, whereas the corresponding data at higher pressures in the gel-like state of DPPC are slightly reduced. For concentrations above ~30 mol% cholesterol, the main phase transition can hardly be detected any more. At a concentration of ~40–50 mol% cholesterol, the order parameter values are found to be almost independent of pressure. These data and further FT-IR spectroscopic pressure studies clearly demonstrate the ability of sterols to efficiently regulate the structure, motional freedom and hydrophobicity of lipid membranes, so that they can withstand even drastic changes in environmental conditions, such as in external pressure and temperature.

Lipid mixtures and model raft membranes. To increase the level of complexity, *T*, *p*-phase diagrams of binary mixtures of saturated phospholipids have been determined as well (*Winter and Czeslik*, 2000; *Winter et al.*, 1999). Studies were also carried out on the phase behavior of cholesterol-containing ternary lipid mixtures, containing an unsaturated lipid like a phosphatidylcholine and a saturated lipid like sphingomyelin (SM) or DPPC next to cholesterol. Such lipid systems are supposed to mimic distinct liquid-ordered lipid regions, called "rafts", which seem to be also present in cell membranes and are thought to be important for cellular functions such as signal transduction and the sorting and transport of lipids and proteins (*Eisenblätter and Winter*, 2006). Lipid domain formation can be influenced by temperature, pH, calcium ions, protein adsorption, and may be expected to change upon pressurization as well. We determined the liquid-disordered/liquid-ordered (l_d / l_o) phase coexistence region of canonical model raft mixtures such as DOPC/DPPC/cholesterol (1:2:1), which extends over a rather wide temperature range. An overall fluid phase without domains is reached at rather high temperatures (above ~45°C), only (*Jeworrek et al.*, 2008). Upon pressurization at ambient temperatures, an overall (liquid- and solid-) ordered state is reached at pressures of about 1 kbar (Figure 5). Interestingly, in this pressure range of ~1–2 kbar, ceasing of membrane protein function in natural membrane environments has been observed for a variety of systems (*Chong et al.*, 1985; *Kato et al.*, 2002; *Linke et al.*, 2008; *Powalska et al.*, 2007; *Ulmer et al.*, 2002), which might be related with the membrane matrix reaching a physiologically unacceptable overall ordered state at these pressures. In addition, morphological transitions of lipid vesicles may occur in this pressure range (*Nicolini et al.*, 2006).

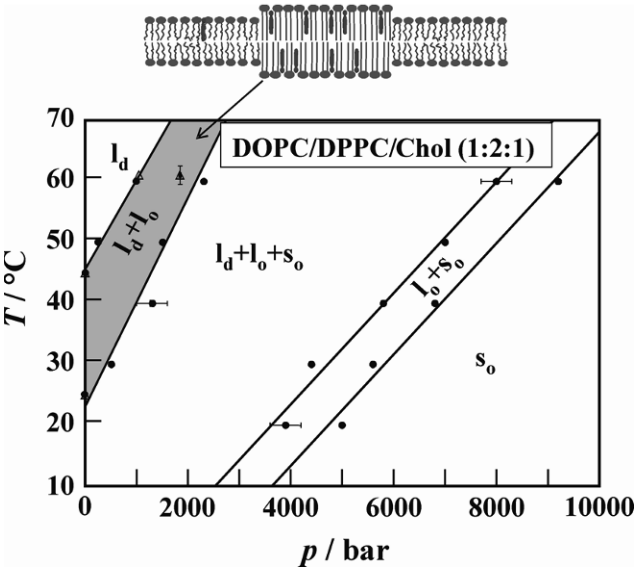

Figure 5. *p*,*T*-phase diagram of the ternary lipid mixture DOPC/DPPC/Chol (1:2:1) in excess water as obtained from FT-IR spectroscopy (•) and SAXS (Δ) data. The raft-like l_d+l_o two-phase coexistence region is marked in grey and depicted schematically in the drawing at the top.

Effects of peptide incorporation and biological membranes. Membrane proteins can constitute about 30% of the entire protein content of a cell and so, rest to a varying extent in the lipid environment where they act as anchors, enzymes or transporters. Membrane lipids and proteins influence each other directly as a result of their biochemical nature and in reaction to environmental changes. Pressure studies are still very scarce. Figure 3b shows the effect of the incorporation of the model channel peptide gramicidin D (GD) on the structure and phase behavior of phospholipid bilayers. Gramicidin is polymorphic, being able to adopt a range of structures with different topologies. Common forms are the dimeric single-stranded right-handed $\beta^{6.3}$-helix with a length of 24 Å (which is generally observed in the fluid phase), and the antiparallel double-stranded $\beta^{5.6}$-helix, being approximately 32 Å long (which often prevails in the gel phase). For comparison, the hydrophobic fluid bilayer thickness is about 30 Å for DPPC bilayers, and the hydrophobic thickness of the gel phases is larger by 4–5 Å. Depending on the gramicidin concentration, significant changes of the lipid bilayer structure and phase behavior were observed. These include disappearance of certain gel phases formed by the pure DPPC system, and the formation of broad two-phase coexistence regions at higher gramicidin concentrations (Figure 3b). Hence, not only the lipid bilayer structure and *T*,

p-dependent phase behavior drastically depends on the polypeptide concentration, but also the peptide conformation (and hence function) can be significantly influenced by the lipid environment. No pressure-induced unfolding of the polypeptide is observed up to 10 kbar. For large integral and peripheral proteins, however, pressure-induced changes in the physical state of the membrane may lead to a weakening of protein–lipid interactions as well as to protein dissociation. For example, the influence of hydrostatic pressure on the activity of Na^+, K^+-ATPase was studied using a kinetic assay. The data show that the activity, *k*, of Na^+, K^+-ATPase is inhibited reversibly by pressures below 2 kbar. The plot of ln*k versus p* reveals an apparent activation volume of the pressure-induced inhibition reaction which amounts to $\Delta V^{\neq} = 47$ mL mol^{-1}. At higher pressures, exceeding 2 kbar, the enzyme is inactivated irreversibly due to protein unfolding and interface separation (*Chong et al.*, 1985; *Kato et al.*, 2002; *Powalska et al.*, 2007).

2.2. PRESSURE EFFECTS ON PROTEIN STRUCTURE AND STABILITY

Since the discovery of HHP-induced protein unfolding and denaturation by Nobel laureate P.W. Bridgman in 1914, it has been shown in many studies now that hydrostatic pressure may lead to disruption of the intermolecular interactions maintaining the native protein structure, which is accompanied by a decrease of the volume of the protein–water system, and simultaneous unfolding (*Heremans and Smeller*, 1998; *Mishra and Winter*, 2008; *Silva et al.*, 2001; *Winter*, 2002; *Winter et al.*, 2007). The appropriate way of expressing the thermodynamic stability of a protein appears to be a multi-dimensional function of temperature, pressure and solution conditions, yielding an energy landscape as a multi-dimensional surface. When the solution conditions (pH, ionic strength, salt and cosolvent concentration) are kept constant, the stability of the protein is a simultaneous function of temperature and pressure, only. The Gibbs free energy difference between the denatured (unfolded) and native state, relative to some reference point T_0, p_0 (e.g., the unfolding temperature at 25°C and ambient pressure), can be approximated – assuming a second-order Taylor series of $\Delta_u G(T, p)$ expanded with respect to T and p around T_0, p_0 – as:

$$\Delta_u G = \Delta_u G_0 + \frac{\Delta_u \kappa}{2}(p - p_0)^2 + \Delta_u \alpha (p - p_0)(T - T_0) - \Delta_u C_p \left[T\left(\ln \frac{T}{T_0} - 1 \right) + T_0 \right] + \Delta_u V_0 (p - p_0) - \Delta_u S_0 (T - T_0) \quad (1)$$

where $\Delta_u\kappa$, $\Delta_u\alpha$, and Δ_uC_p refer to the changes in compressibility, expansibility and heat capacity upon unfolding (u). The transition line, where the protein unfolds upon a temperature of pressure change, is given by $\Delta_uG = 0$. The physically relevant solution of the curve in the p,T-plane has an elliptic-like shape (Figure 6a). As also indicated in Figure 6, the slope of the p,T-phase boundary between liquid water and ice I is negative. Hence, an increase in pressure extends the stability range of the liquid water phase to subzero °C temperatures (e.g., −18°C at ~2 kbar). The possibility to explore the subzero °C temperature region at slightly elevated pressures can therefore be used to study the cold denaturation process of proteins. At low temperatures, a marked decrease of the hydration enthalpy term (increase of favourable, low energy interactions between water and the protein interface) leads to the destabilisation of the native structure. Thus, with the enthalpy change of unfolding being a function of temperature, at a temperature low enough, the Gibbs free energy of unfolding Δ_uG becomes negative and the protein will unfold under the release of heat. While the heat-induced denaturation, which is mainly driven by a large positive configurational entropy change, is mostly a highly cooperative process leading to a largely unfolded conformation, cold denaturation, which is fostered by the number and strength of interfacial H-bonds at low temperatures, is known to be a milder form of unfolding, leading to a partial unfolding of the protein, only.

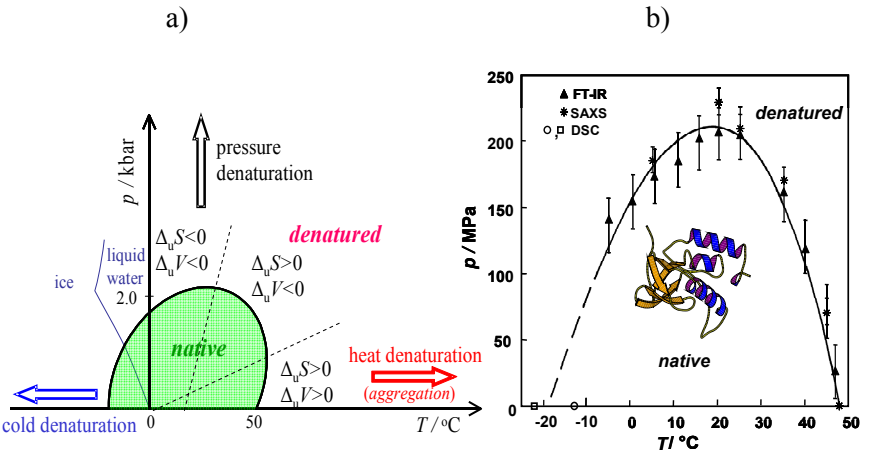

Figure 6. (a) Schematic pressure, temperature stability diagram of a typical monomeric protein. The different routs of unfolding of the native protein (green area), as well as the corresponding thermodynamic properties are depicted. Heat denaturation is often accompanied by irreversible aggregation. The water/ice I phase transition line is given as well. (b) As an example, the p,T-stability diagram of SNase at pH 5.5 as obtained by SAXS, FT-IR and DSC measurements is shown (*Panick et al.*, 1998).

According to the stability diagram shown in Figure 6a, pressure can be used to destabilize proteins at ambient temperatures, which is facilitated by a combination of factors: HHP leads to a weakening of hydrophobic interactions in general. Moreover, the presence of cavities within the folded proteins or in the interface of oligomers can favor the unfolding or dissociation of these structures. If the water molecules fill the cavities when they become accessible upon unfolding or dissociation of the proteins, this leads to a volume decrease and the event is hence favored under high pressure. Also the dissociation of electrostatic interactions leads to a marked reduction in the volume caused by electrostrictive effects of water molecules around the unpaired charged residues exposing charged groups. In a similar way, solvation of polar groups results in a decrease in volume of the water molecules.

The stability diagrams and the folding reactions of oligomers and protein complexes are more complex. At pressures of 4–8 kbar, most small monomeric proteins unfold reversibly. Oligomeric proteins and multiprotein assemblies often dissociate into individual subunits already at pressures of 1–2 kbar (Figure 7).

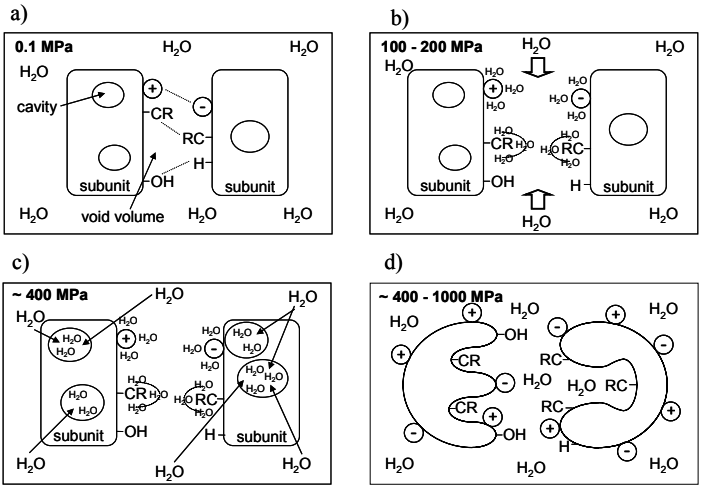

Figure 7. Schematic representation of the effects of pressure on oligomeric proteins: (a) native dimeric protein with cavities/voids; (b) dissociation of the oligomer, hydration with electrostriction of polar/ionic groups, hydrophobic hydration of unpolar groups (–CR), release of void volume; (c) weakening of hydrophobic interactions provides pathways for water to penetrate into the interior of the protein, swelling of the core - molten-globule like state; (d) unfolding of subunits, disruption of the secondary/tertiary structure (hydration of residues not plotted here), loss of cavity volume within protein (Adapted from *Boonyaratanakornkit et al.*, 2002).

Also with respect to the kinetics of the folding reaction, pressure studies are of particular use, as they allow to evaluate the volume profile during the folding process (or other biomolecular reactions (*Conn et al.*, 2006, 2008; *Winter et al.*, 2007; *Woenckhaus et al.*, 2000) and to characterize the nature of the barrier to folding or unfolding and the corresponding transition state. Moreover, pressure studies present an important advantage due to the generally observed positive activation volume for folding, the result of which is to slow down the folding reaction substantially, in turn allowing for relatively straightforward measurements of structural order parameters characteristic for folding intermediate states, that are difficult or even impossible to quantify on much faster timescales corresponding to ambient pressure conditions (*Panick et al.*, 1998; *Winter et al.*, 2007).

As an example, we discuss the pressure-induced unfolding and refolding of staphylococcal nuclease (SNase), a small protein of about 17.5 kDa containing 149 amino acids (*Panick et al.*, 1998). Analysis of the high pressure SAXS data at 25°C revealed that over a pressure range from atmospheric to ~3 kbar, the radius of gyration R_g of the protein doubles from roughly 17 Å for native SNase twofold to nearly 35 Å. Deconvolution of the FT-IR amide I' absorption band reveals a pressure-induced denaturation process that is evidenced by an increase in disordered and turn structures and a drastic decrease in the content of β-sheets and α-helices. Contrary to the temperature-induced unfolded state, the pressure-induced denatured state retains some degree of secondary structure and the protein molecules cannot be described as a fully extended random polypeptide coil. Assuming the pressure-induced unfolding transition of SNase to occur essentially as a two-state process, analysis of the FT-IR pressure profiles yields a standard Gibbs free energy change for unfolding of $\Delta G^o = 17$ kJ·mol^{-1} and a volume change for unfolding of $\Delta V^o = -80$ mL·mol^{-1}. The pressure midpoints at several temperatures obtained from the FT-IR and SAXS profiles are plotted as a *p*,*T*-phase diagram in Figure 6b. It exhibits the elliptic-like curvature which is typical of monomeric proteins.

2.3. USING PRESSURE FOR STUDYING PROTEIN AGGREGATION AND AMYLOIDOGENESIS

Protein folding is one of the most crucial steps during the life of a protein. If some failure occurs in achieving the native conformation, this will render the polypeptide inactive, or even worse, it can produce a misfolded molecule that can interfere or block components of the cellular machinery to the point of causing cell malfunction or even death. In recent years, it has become evident that a wide range of human diseases are associated with aberrations in the folding process. These diseases, which are also coined

"protein conformational diseases", include Alzheimer's disease (Aβ-peptide), Parkinsons's disease (α-synuclein), prion protein related encephalopathies, and type II diabetes mellitus (islet amyloid peptide, IAPP). In an attempt to probe the stability and energetics of amyloid fibrils, besides temperature, pH and cosolvent dependent studies, also pressure perturbation has been in the focus, recently (*Cordeiro et al.*, 2004; *Foguel et al.*, 2003; *Grudzielanek et al.*, 2006; *Marchal et al.*, 2003; *Meersman et al.*, 2006; *Mishra and Winter*, 2008).

The susceptibility of protein aggregates to pressure largely depends on the degree of the structural order of the aggregate: fresh, amorphous aggregates are more sensitive to pressure and prone to refolding to the native state than mature amyloid fibrils. In the latter case, the effectiveness of pressure-induced dissociation depends on the particular mode of polypeptide backbone and side chain packing that allows reducing remaining void volumes. The pressure-sensitivity of fresh aggregates and the insensitivity of most mature fibrils to HHP allow not only to differentiate between various stages of the amyloid-formation, but also to obtain reliable thermodynamic data on the transformation process.

As an example, we show pressure effects on insulin at various stages of the aggregation process (Figure 8). The capacity to bind the fluorophor thioflavine T (ThT) is used as a measure of fibril formation, which is indicated by an increase of fluorescence intensity upon binding to fibrillar species. Clearly, at the early stages of insulin aggregation, where oligomeric species are formed in the nucleation and growth process, only, pressure leads to dissociation. These oligomers are stabilized mainly by electrostatic and hydrophobic interactions, yet they lack the precise packing of mature insulin fibrils. This renders them susceptible to pressure-induced dissociation. Uncommon to their precursors, the pressure-insensitivity of mature insulin fibrils demonstrates that extensive hydrogen bonding and optimised side chain packing are crucial for their stability.

Some amyloid fibrils (in particular protofibrils) might exhibit a larger partial specific volume than that of the composing proteins, because the assembly process, which involves various conformational transitions of native structures to non-native β-sheets, could create new water-excluded cavities and induce hydrophobic pockets. In these cases, HHP has a potential to dissociate also amyloid fibrils. For example, it has been shown that moderate pressures (1–3 kbar) can dissociate amyloid fibrils of transthyretin, β_2-microglobulin and α-synuclein. One of the most thrilling prospects for application of high pressure in protein aggregation research is the idea of destroying prion infectivity through pressure treatment.

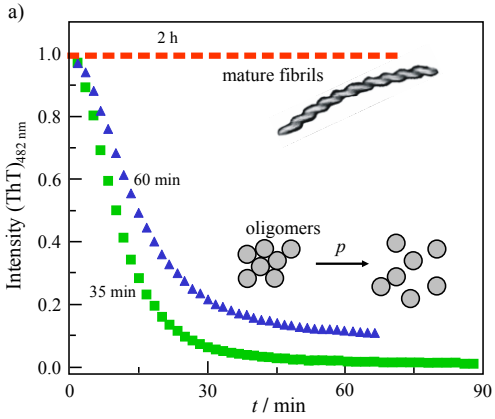

Figure 8. Characteristic features of the high-pressure treatment of 0.5 wt.% insulin in water (0.1 M NaCl, T = 60°C) at different stages of the aggregation process. The decay of the normalized ThT intensity upon a pressure increase to 1 kbar after progressively longer incubation times is shown. At 35 and 60 min, the oligomeric states prevail, whereas at 2 h, the mature fibrillar state of insulin is reached, which exhibits pressure resistance (*Mishra and Winter*, 2008).

Figure 9 shows a schematic energy landscape for protein folding and aggregation phenomena. At the high energy, high entropy surface, a multitude of unfolded conformations are present. "Funneling" on a rugged energy surface or "landscape" occurs towards the natively folded state via rapid intramolecular contact formation. By a – generally slow – nucleation process and subsequent autocatalytic aggregation reaction of particularly partially unfolded structures (induced by mutations, particular cosolvents, pH, etc.), formation of aggregates and amyloid fibrils via intermolecular contacts may occur, and the system enters the aggregation funnel. Within the aggregation funnel, loosely packed oligomeric or amorphous aggregates as well as – generally several – amyloid fibrillar states (strains) with different packing properties and with deep energy minima may form, hence exhibiting conformational polymorphism. Dissociation of protein aggregates and, under favourable conditions, also amyloid fibrils is possible upon application of HHP. We may assume that an amyloid structure without optimal packing will enable formation of various isoforms, suggesting the structural basis of multiple forms of amyloid fibrils in contrast to the unique native fold of functioning proteins.

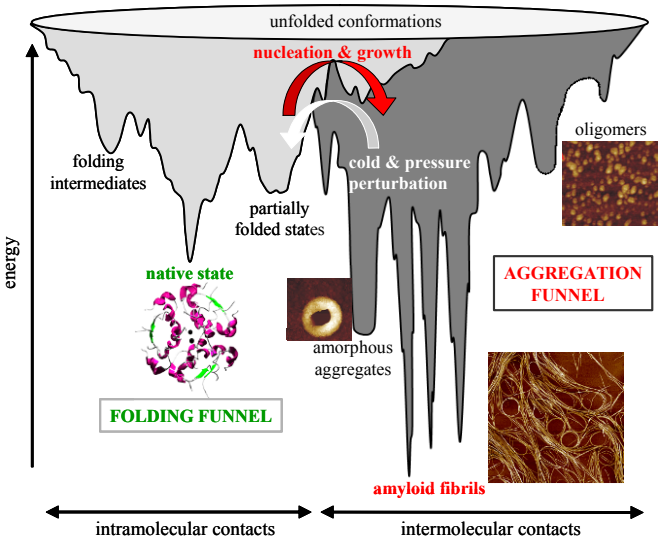

Figure 9. Schematic energy landscape for protein folding and aggregation/amyloid formation. While the protein attains the native conformation at its global energy minimum under normal physiological conditions, the amyloidogenic stacking of many protein molecules may lead to lower energies beyond this level in the aggregation funnel. At low temperature and high pressure, dissociation of less densely packed protein aggregate and fibrils is possible (*Mishra and Winter*, 2008).

3. Concluding Remarks

We conclude that pressure work on biomolecular systems can yield a wealth of enlightening new information on their structure, energetics and phase behavior and on the transition kinetics between various states, and might promise fulfilment of the challenge set forth by W. Kauzmann: “Until more searching is done in the darkness of high-pressure studies, our understanding of the hydrophobic effect must be considered incomplete”. It is clear that the application of the pressure variable in this research area has only just started and many interesting results are expected in the near future. These pressure studies are also important for the development of new technological and pharmaceutical applications, such as high pressure food processing, inactivation of food allergens, separation of protein complexes (inclusion bodies), supercritical biocatalysis, and micellar baroenzymology.

Abbreviations. GD gramicidin D, DLPC 1,2-dilauroyl-*sn*-glycero-3-phosphatidylcholine (di-$C_{12:0}$), DMPC 1,2-dimyristoyl-*sn*-glycero-3-phosphatidylcholine (di-$C_{14:0}$), DMPS 1,2-dimyristoyl-*sn*-glycero-3-phosphatidylserin (di-$C_{14:0}$), DPPC 1,2-dipalmitoyl-*sn*-glycero-3-phosphatidylcholine (di-$C_{16:0}$), DPPE 1,2-dipalmitoyl-*sn*-glycero-3-phosphatidylethanolamine (di-$C_{16:0}$); DSPC 1,2-distearoyl-*sn*-glycero-3-phosphatidylcholine (di-$C_{18:0}$), DOPC 1,2-dioleoyl-*sn*-glycero-3-phosphatidylcholine (di-$C_{18:1,cis}$), DOPE 1,2-dioleoyl-*sn*-glycero-3-phosphatidylethanolamine (di-$C_{18:1,cis}$), DEPC 1,2-dielaidoyl-*sn*-glycero-3-phosphatidylcholine (di-$C_{18:1,trans}$), POPC 1-palmitoyl-2-oleoyl-*sn*-glycero-3-phosphatidylcholine ($C_{16:0}$,$C_{18:1,cis}$), SAXS (WAXS) small(wide)-angle X-ray scattering, CD circular dichroism, FT-IR Fourier-transform infrared, NMR nuclear magnetic resonance, SNase staphylococcal nuclease, TMA-DPH 1-(4-trimethylammonium-phenyl)-6-phenyl-1,3,5-hexatriene, ΔV^0 volume change of reaction, $\Delta V^{\#}$ activation volume of reaction.

References

Akasaka, K., 2006, Probing conformational fluctuation of proteins by pressure perturbation, *Chem. Rev.* **106**: 1814–1835.

Arnold, M.R., Kalbitzer, R.H., and Kremer, W., 2003, High-sensitivity sapphire cells for high pressure NMR spectroscopy on proteins, *J. Magn. Reson.* **161**: 127–131.

Bartlett, D.H., 2002, Pressure effects on in vivo microbial processes, *Biochim. Biophys. Acta*. **1595**: 367–381.

Boonyaratanakornkit, B.B., Park, C. B., and Clark, D. S., 2002, Pressure effects on intra- and intermolecular interactions within proteins, *Biochim. Biophys. Acta.* **1595**: 235–249.

Chong, P.L.-G., Fortes, P.A.G., and Jameson, D.A., 1985, Mechanisms of inhibition of (Na,K)-ATPase by hydrostatic pressure studied with fluorescent probes, *J. Biol. Chem.*, **260**: 14484–14490.

Conn, C.E., Ces, O., Mulet, X., Finet, S., Winter, R., Seddon, J.M., and Templer, R.H., 2006, Dynamics of structural transformations between lamellar and inverse bicontinuous cubic lyotropic phases, *Phys. Rev. Lett.* **96**: 108102.

Conn, C.E., Ces, O., Squires, A.M., Mulet, X., Winter, R., Finet, S., Templer, R.H., and Seddon, J.M., 2008, A pressure-jump time-resolved X-ray diffraction study of cubic - Cubic transition kinetics in monoolein, *Langmuir* **24**: 2331–2340.

Cordeiro, Y., Kraineva, J., Ravindra, R., Lima, L.M.T.R., Gomes, M.P.B., Foguel, D., Winter, R., and Silva, J.L., 2004**,** Hydration and packing effects on prion folding and β-sheet conversion: High pressure spectroscopy and pressure perturbation calorimetry studies, *J. Biol. Chem.* **279**: 32354–32359.

Cossins, A.R., and Macdonald, A.G., 1986, Homeoviscous adaptation under pressure. III. The fatty acid composition of liver mitochondrial phospholipids of deep-sea fish, *Biochim. Biophys. Acta – Biomembranes*. **860**: 325–335.

Daniel, I., Oger, P., and Winter, R., 2006, Origins of life and biochemistry under high-pressure conditions, *Chem. Soc. Rev.* **35**: 858–875.

Eisenblätter, J., and Winter, R., 2006, Pressure effects on the structure and phase behavior of DMPC-gramicidin lipid bilayers: A synchrotron SAXS and 2H-NMR spectroscopy study, *Biophys. J.* **90**: 956–966.

Foguel, D., Suarez, M.C., Ferrao-Gonzales, A.D., Porto, T.C.R., Palmieri, L., Einsiedler, C.M., Andrade, L.R., Lashuel, H.A., Lansbury, P.T., Kelly, J.W., and Silva, J.L., 2003, Dissociation of amyloid fibrils of α-synuclein and transthyretin by pressure reveals their reversible nature and the formation of water-excluded cavities, *Proc. Natl. Acad. Sci. USA*. **100**: 9831–9836.

Grudzielanek, S., Smirnovas, V., and Winter, R., 2006, Solvation-assisted pressure tuning of insulin fibrillation: From novel aggregation pathways to biotechnological applications, *J. Mol. Biol.* **356**: 497–509.

Heremans, K., and Smeller, L., 1998, Protein structure and dynamics at high pressure, *Biochim. Biophys. Acta*. **1386**: 353–370.

Jeworrek, C., Pühse, M., and Winter, R., 2008, X-ray cinematography of phase transformations of three-component lipid mixtures: A time-resolved synchrotron X-ray scattering study using the pressure-jump relaxation technique, *Langmuir*. **24**: 11851–11859.

Jonas, J., ed., 1991, *High Pressure NMR*, Springer-Verlag, Berlin.

Kato, M., Hayashi, R., Tsuda, T., and Taniguchi, K., 2002, High pressure-induced changes of biological membrane: Study on the membrane-bound Na^+/K^+-ATPase as a model system, *Eur. J. Biochem.* **269**: 110–118.

Linke, K., Periasamy, N., Ehrmann, M., Winter, R., and Vogel, R.F., 2008, Influence of high pressure on the dimerization of ToxR, a protein involved in bacterial signal transduction, *Appl. Environ. Microbiol.* **74**: 7821–7823.

Marchal, S., Shehi, E., Harricane, M.C., Fusi, P., Heitz, F., Tortora, P., and Lange, R., 2003, Structural instability and fibrillar aggregation of non-expanded human ataxin-3 revealed under high pressure and temperature, *J. Biol. Chem.* **278**: 31554–31563.

Meersman, F., Dobson, C.M., and Heremans, K., 2006, Protein unfolding, amyloid fibril formation and configurational energy landscapes under high pressure conditions, *Chem. Soc. Rev.* **35**: 908–917.

Mishra, R., and Winter, R., 2008, Cold- and pressure-induced dissociation of protein aggregates and amyloid fibrils, *Angew. Chem. Int. Ed.*, **47**: 6518–6521.

Nicolini, C., Celli, A. Gratton, E., and Winter, R., 2006, Pressure tuning of the morphology of heterogeneous lipid vesicles: A two-photon-excitation fluorescence microscopy study, *Biophys. J.* **91**: 2936–2942.

Panick, G., Malessa, R., Winter, R., Rapp, G., Frye, K. J., and Royer, C. A., 1998, Structural characterization of the pressure-denatured state and unfolding/refolding kinetics of staphylococcal nuclease by synchrotron small-angle X-ray scattering and Fourier-transform infrared spectroscopy, *J. Mol. Biol.* **275**: 389–402.

Powalska, E., Janosch, S., Kinne-Saffran, E., Kinne, R.K.H., Fontes, C.F.L., Mignaco, J.A., and Winter, R., 2007, Fluorescence spectroscopic studies of pressure effects on Na^+, K^+-ATPase reconstituted into phospholipid bilayers and model raft mixtures, *Biochemistry*. **46**: 1672–1683.

Silva, J.L., Foguel, D., and Royer, C.A., 2001, Pressure provides new insights into protein folding, dynamics and structure, *Trends Biochem. Sci.* **26**: 612–618.

Ulmer, H.M., Herberhold, H., Fahsel, S., Gänzle, M.G., Winter, R., and Vogel, R.F., 2002, Effects of pressure-induced membrane phase transitions on inactivation of HorA, an ATP-dependent multidrug resistance transporter, in Lactobacillus plantarum, *Appl. Environ. Microbiol.* **68**: 1088–1095.

Winter, R., 2001, Effects of hydrostatic pressure on lipid and surfactant phases, *Curr. Opin. Colloid Interface Sci.* **6**: 303–312.

Winter, R., 2002, Synchrotron X-ray and neutron small-angle scattering of lyotropic lipid mesophases, model biomembranes and proteins in solution at high pressure, *Biochim. Biophys. Acta*. **1595**: 160–184.

Winter, R., and Czeslik, C., 2000, Pressure effects on the structure of lyotropic lipid mesophases and model biomembrane systems, *Z. Kristallogr.* **215**: 454–474.

Winter, R., Gabke, A., Czeslik, C., and Pfeifer, P., 1999, Power-law fluctuations in phase-separated lipid membranes, *Phys. Rev. E*. **60**: 7354–7359.

Winter, R., Lopes, D., Grudzielanek, S., and Vogtt, K., 2007, Towards an understanding of the temperature / pressure configurational and free-energy landscape of biomolecules, *J. Non-Equilib. Thermodyn.* **32**: 41–97.

Woenckhaus, J., Köhling, R., Winter, R., Thiyagarajan, P., and Finet, S., 2000, High pressure-jump apparatus for kinetic studies of protein folding reactions using the small-angle synchrotron x-ray scattering technique, *Rev. Sci. Instrum.* **71**: 3895–3899.

Yayanos, A.A., 1986, Obligately barophilic bacterium from the Mariana Trench, *Proc. Natl. Acad. Sci. USA*. **83**: 9542–9546.

Zein, M., and Winter, R., 2000, Effect of temperature, pressure and lipid acyl chain length on the structure and phase behaviour of phospholipid-gramicidin bilayers, *Phys. Chem. Chem. Phys.* **2**: 4545–4551.

HIGH-PRESSURE CRYSTALLOGRAPHY OF BIOMOLECULES: RECENT ACHIEVEMENTS. I – INTRODUCTION, MATERIALS AND METHODS

ROGER FOURME[1*], ISABELLA ASCONE[1†], MOHAMED MEZOUAR[2], ANNE-CLAIRE DHAUSSY[3], RICHARD KAHN[4], ERIC GIRARD[4]
[1]*Synchrotron SOLEIL, 91192 Gif sur Yvette, France,* [2]*ESRF, 38027 Grenoble, France,* [3]*CRISMAT, Ensicaen, 14000 Caen, France,* [4]*Institut de Biologie Structurale, 38027 Grenoble, France*

Abstract High-pressure molecular biophysics is a developing field for three main reasons. Pressure has a unique potential, in particular for the exploration of the energy landscape of biomolecules. Progress in instrumentation has extended the range of biophysical techniques under pressure and often relaxed technical constraints on sample confinement. Two high-resolution structural methods are now available at high pressure, NMR and macromolecular crystallography (HPMX). We describe materials and methods of HPMX, now a full-fledged technique taking advantage of purposely-built diamond-anvil cell, ultra-short wavelength synchrotron radiation and improved crystal-loading procedures.

Keywords: High pressure, crystallography, diamond anvil cell, macromolecules

1. High-Pressure Molecular Biophysics: An Introduction

The interest of pressure in biosciences was confined for a long time on marine biology and deep-sea diving. New aspects of deep-sea biology were added with the discovery of organisms that not only survive but thrive under extreme conditions, then of obligate barophile organisms (i.e. not able

[*]E-mail: roger.fourme@synchrotron-soleil.fr
[†] Present address: ENSCP, 75231 Paris, France

E. Boldyreva and P. Dera (eds.), *High-Pressure Crystallography: From Fundamental Phenomena to Technological Applications*, DOI 10.1007/978-90-481-9258-8_48,

to grow at ambient pressure) (*Horikoshi and Grant*, 1998; *Yayanos and Delong*, 1987). The range of pressure and extent of biosphere are further increased when including Earth crust and bacterial organisms within. The theme of life adaptation under extreme conditions encompasses basic questions such as the onset of life on Earth and its possible occurrence on other stellar objects. Another feature of high-pressure bioscience is the importance of applied research and industrial applications. Hydrostatic pressure is broadly used by industry and biotechnology, for instance for food extraction and/or preservation since the late 1980s (*Balny et al.*, 1992; *Mozhaev et al.*, 1994). Medical and pharmaceutical applications of high pressure directed at viruses, bacteria and prions are expanding. Fundamental research was pioneered by *P.W. Bridgman* (1914), then continued during several decades with scarce publications of a small community and emerged really since the 1960s and 1970s (*Gross and Jaenicke*, 1994). The interest for high-pressure biophysics has increased since a few years, for several basic reasons: (i) Pressure has a unique potential for the exploration of the so-called energy landscape of a biomolecule. This important aspect is developed below. (ii) Progress in instrumentation have extended the range of biophysical techniques under pressure and often relaxed technical constraints on sample confinement. (iii) High-resolution structural methods, namely nuclear magnetic resonance and macromolecular crystallography, have been adapted to high pressure (HPNMR and HPMX). These powerful newcomers complete low-resolution methods, small-angle neutron (SANS) and x-ray scattering (SAXS), and long-established spectroscopic techniques (V/UV, Raman, IR). Accordingly, there is now a toolbox for integrated structural biology under high pressure, including structural and dynamical aspects. For several techniques, in particular MX, SAXS and IR spectro-microscopy, synchrotron radiation is a crucial tool.

2. Pressure as a Tool to Explore the Energy Landscape

Proteins, as well as other biological macromolecules, have been designed by natural selection not just for the ground or “native” state but also for higher-energy, “non-native”, states that are involved in function, folding and unfolding (*Anfinsen*, 1973). These conformers are distributed in a wide conformational space, from the folded state to the totally unfolded state(s). Their free energies are different, but differences are small, at most a few kcal mol^{-1}. They have also different partial molar volumes (i.e. the effective volumes of conformers in an aqueous environment including the contribution from hydration) and as a general empirical rule, the partial molar volume of a protein decreases in parallel with the decrease of its conformational order.

The partial volume difference ΔV between the unfolded and folded states is negative in the vast majority of cases and is in the range 20–100 ml mol^{-1}. Pressure displaces equilibrium toward more compact phases (an application of Le Chatelier's principle), and accordingly displaces equilibria toward conformers of lower partial-volume. How this displacement proceeds can be understood on the following example (*Akasaka*, 2006), a hypothetical protein solution with two sub-ensembles of conformers: the native sub-ensemble (N), and another sub-ensemble (I) attached to a partially unfolded conformer. N and I conformers differ in topology, in free energy ($\Delta G = G_I - G_N$) and in partial molar volume ($\Delta V = V_I - V_N$). Under an isothermal compression at p:

$$\Delta G = G_I - G_N = \Delta G(p_0) + \Delta V_0(p-p_0) - \tfrac{1}{2}(\Delta\beta)V_0(p-p_0)^2 \qquad (1)$$

where the subscript zero is related to values at ambient pressure and temperature, β is the isothermal compressibility ($\beta = -V^{-1}(\partial V/\partial P)_T$), $\Delta\beta$ is the variation of β between p and p_0. As the term proportional to $\Delta\beta$ can often be neglected in a relatively narrow pressure range, then:

$$\Delta G \approx \Delta G(p_0) + \Delta V_0(p-p_0) \qquad (2)$$

The equilibrium constant K between the two conformers is related to the free-energy difference by the relation:

$$K = [I]/[N] = \exp(-\Delta G/RT). \qquad (3)$$

In Eq (2), $\Delta G(p_0)$ is >0 (as conformer N is more stable than conformer I at ambient pressure). As p increases, the second term, which is <0 ($\Delta V_0 < 0$), is going to counterbalance $\Delta G(p_0)$, so that K increases. Let us take a representative example at T = 293 K (RT = 0.582 kcal mol^{-1}) with $\Delta G(p_0)$ = 2 kcal mol^{-1}, $\Delta V_0 = -50$ ml mol^{-1} (-5.10^{-5} m^3 $mole^{-1}$) and p = 4 kbar (4.10^8 Pa). With these values, the fraction of (N) state is 97% at ambient pressure, whereas the fraction of the more compact (I) state is 94% at 4 kbar. Such selective population enhancement was demonstrated first by NMR (review in *Akasaka*, 2006). In an isothermal variable-pressure experiment, the protein gains only a few kcal mol^{-1} through the mechanical energy supplied by pressure. Application of pressure affects internal interactions exclusively by changes in the distances (volumes) of the components, whereas the total energy of the system remains almost constant. In an isobaric variable-temperature experiment, the situation is very different. Free-energy difference ΔG between the two conformers results from the balance of the enthalpic and entropic terms, ΔH and $-T\Delta S$, which differ only in second (or higher)-order term. In a thermal transition, each term increases substantially with temperature (ΔH > 100 kcal mol^{-1}), so that the system gains a substantial amount of internal energy and entropy. Accordingly, pressure perturbation

is uniquely suited to explore the conformational space of proteins and other biomolecules. This exploration is selective because, in principle, low-lying substates can be promoted and investigated in a well-defined thermodynamic state. Increasing pressure will ultimately lead to destruction of the tertiary structure by denaturation, preceded in the case of oligomeric proteins by dissociation of the quaternary structure in smaller units (*Weber*, 1992a, b).

3. The Importance of High-Resolution Structural Information

Pressure modifies volume, i.e. distances between components, so that an accurate description of these changes is crucial to understand these mechanisms. Most results on the effect of pressure on biomolecules have been obtained with spectroscopic methods (in particular fluorescence and infrared spectroscopy) and, less commonly, with low spatial-resolution structural techniques. The adaptation of higher-resolution structural biology methods was a major step forward. HPNMR is presently limited in pressure range (≈300 MPa) and in molecular weight of macromolecules. Those limits do not apply to HPMX. After the pioneering work in 1987 on tetragonal crystals of a small protein, hen egg-white lysozyme (HEWL) compressed at 100 MPa (*Kundrot and Richards*, 1987), few new HPMX studies were published during more than a decade. A diamond-anvil cell was used for compressibility measurements on HEWL crystals (*Katrusiak and Dauter*, 1996). Since 2001, there is a renewal of HPMX (*Fourme et al.*, 2001), which is now a full-fledged technique (*Fourme et al.*, 2009; *Girard et al.*, 2007).

4. Conventional Macromolecular Crystallography: A Reminder

X-ray crystallography is by far the most important method of structural biology as it can provide a detailed picture at atomic or near-atomic resolution of the global structure of biological macromolecules such as proteins, nucleic acids and macromolecular assemblies of nearly arbitrary size and complexity. Files of new structures are archived in the Protein Data Bank (PDB). An increasing number of new or potential drugs are based on the knowledge of the 3D structure of a particular target and systematic studies of target-inhibitor complexes. Systematic investigations of the 3D structures of proteins encoded by specific genomes are performed in national or worldwide structural genomics initiatives.

The crystal is mounted on a single or multi-axis goniometer and rotates (or oscillates) about a single axis. This rotation is not continuous, but is divided into contiguous angular intervals which are small (typically 0.3–1°)

in order to avoid background accumulation (with recent pixel detectors, the dream of a continuous rotation becomes possible). Using x-rays with a wavelength of typically 1 Å, data are collected on a series of frames produced by the detector. Each frame is the digitized record of diffraction by the crystal and parasitic scattering coming from various sources (diffuse elastic scattering and Compton scattering from the sample and mother liquor surrounding the crystal, scattering by air, fluorescence from the sample…). Frames are processed in parallel to data acquisition. Usually, the number of Bragg spots in each frame is so large that one or two frames are sufficient to get a list of possible unit cells and lattice types, an advantage of complexity. Bragg spots can then be indexed. After successful indexation, various parameters are refined in order to improve the agreement between predicted and observed spot locations. A box centred on each reflection can then be predicted and background-subtracted integrated intensities are determined. Measurements from various frames and (possibly) from different crystals are subjected to sophisticated rescaling procedures, which also partially correct for the effects of degradation and absorption. The final merged data set is used for the subsequent crystal structure analysis. Merged data are divided in resolution shells and various indicators help to define the quality of the set. The resolution of the data set is given by the minimum 'useful' d value (in Bragg's equation) of the data set, where 'useful' is defined on the basis of a cutoff for the ratio I/σ (for instance $I/\sigma = 2$). R_{merge} gives the average deviation of measurements of intensities of equivalent reflections (i.e. which should have ideally the same integrated intensity). Completeness is the ratio of the number of measured reflections to the theoretical number of reflections at a given resolution. Redundancy is the average number of measurements of the same reflection or its equivalent reflections. Mosaicity results from the convolution of the intrinsic angular width of reflections by an instrumental function which depends mainly on relative x-ray bandwidth and beam divergence.

5. Materials and Methods of HPMX

5.1. DIAMOND-ANVIL CELL

High pressure brings additional constraints to standard MX data collection. (1) The compressed crystal must remain visible. (2) Its actual pressure must be known and kept constant during data collection. (3) The sample must be compressed in a liquid phase, in order to preserve hydrostatic compression, accordingly cryocooling (a standard procedure in conventional MX) is excluded. The temperature range compatible with HPMX is from −5°C to moderately high temperature (60–120°C, depending on the stability domain).

(4) The useful apertures of the pressure cell for x-rays must be sufficient for angle-dispersive data collection. (5) Absorption of x-rays by cell walls must be either very small or accurately corrected for each Bragg reflection.

These various requirements can be met with diamond-anvil cells (DAC). The principle of DAC (*Weir et al.*, 1959) and various implementations are given in other presentations in this school. Two co-axial diamond anvils are mounted on metal supports, one which is part of the cell body and the second which is attached to a piston on which thrust can be applied. The sample is compressed in a cavity drilled in a metallic gasket squeezed between the two diamonds (*Van Valkenburg*, 1962). The thrust applied to diamonds is generated by screws (*Merrill and Bassett*, 1974) or by applying a variable pressure from an external gas source to either an annular piston (*Fourme*, 1968) or a toroidal membrane (*Le Toullec et al.*, 1988) incorporated in the cell. For our experiments, we use cylindrically-symmetric DAC of the cylinder-piston type. Each DAC with the associated pneumatic system is an autonomous unit which can be transported at will from the high pressure laboratory (where the gaskets are prepared and the cell loaded) to the ID27 beamine at ESRF (*Mezouar et al.*, 2005). The installation of DAC on the goniometer is fast and reproducible. It is convenient to use a pair of DAC, one being loaded while the other is used for data collection. We have successfully used membrane cells (*Le Toullec*, 1988) (Figure 1A). Our latest DAC is provided with a piston system (Figures 1B and 1C) and its main characteristics are the following. Diamonds are inserted in a conical seat, providing both a good mechanical strength and broad aperture (*Boehler and de Hantsetters*, 2004). The diamond culet is a 16-sided polygon in a circle of diameter 800 μm, so that the ratio between piston and culet areas is ≈1,400. The cavity in the Inconel or copper gasket is machined either by drilling or by electro-erosion. Typical diameter and thickness of the cavity ready for operation are respectively 350–400 and 150–200 μm. The useful aperture for x-rays is ~85°. The cell is equipped with a removable heating device with two sensors in contact with the gasket. The temperature of the gasket can be adjusted and regulated from ambient temperature to 120°C. The piston system ensures thrust reversibility. This cell has been designed for pressure cycling and coupled P–T annealing (*Girard et al.*, 2010).

The relation between the pressure in the pneumatic circuit and the actual pressure in the sample cavity depends on the characteristics and history of each gasket and each particular loading. The determination of the actual pressure is based as usual (*Forman et al.*, 1972) on the wavelength shift of the fluorescence emission from a ruby microsphere inserted in the compression chamber. Emission wavelengths at 1 bar may slightly differ from one ruby chip to another (depending on size, preparation, annealing etc.). Accordingly, calibration at 1 bar is performed with emission lines of neon

emitted by a small lamp and pressure-induced wavelength shifts are determined by differential measurements. Finally, the sensitivity and the precision of the pressure determination are about 20 and 100 bar respectively. The same optical system (PRL from Betsa, France) is also used to image the sample.

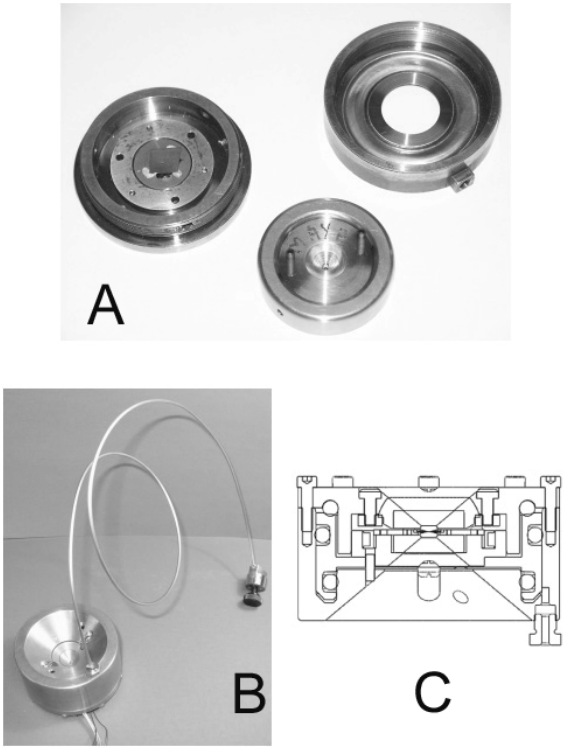

Figure 1. Diamond-anvil cells for HPMX. A: Main components of the membrane cell. B: View of the piston cell. C: Schematic section through the piston cell.

5.2. INSTRUMENTATION ON ID27

The beamline (*Mezouar et al.*, 2005) incorporates a two-circle goniometer (rotations are about a vertical ω-axis and a χ-axis in the horizontal plane) installed on a stacking of three orthogonal translation tables. All experiments are performed with the detector normal to the x-ray beam. A photodiode, located between the DAC and the detector, is used for sample centring (as described later) as well as for rapid check of alignment after each compression. This diode is mounted on a pneumatic actuator that sets it on or off the x-ray beam.

The optimal x-ray beam for HPMX is a quasi-plane (i.e. very low divergence, narrow $\delta\lambda/\lambda$) wave of ultra-short wavelength and very high intensity (*Fourme et al.*, 2001, 2003). For a given detector, the wavelength can be adjusted in order to both maximize the detection efficiency for elastic scattering and reduce the detection efficiency for Compton scattering, thereby increasing the signal to noise ratio. Interestingly, this effect is more effective at large Bragg angles, i.e. for the higher resolution data. For instance, in the case of an imaging plate detector with a sensitive layer containing BaFBr:Eu^{2+}, the optimal wavelength is 0.3305 Å.

A very good detector should combine a "reasonable" detective quantum efficiency (DQE) at ultra-short wavelength, a large surface, a small point spread function (PSF), a very low intrinsic noise and a fast readout (*Fourme et al.*, 2001). Current MX detectors have a poor DQE at short wavelengths. As many photons are not detected, the crystal must be overexposed at the expense of its lifetime. Better detectors are urgently needed for the development of ultrashort-wavelength data collection. In the case of CCD detectors, a thicker phosphor may be deposited, at the expense of some degradation of the PSF. High-Z elements can also be considered (e.g. CdTe pixel detectors).

5.3. LOADING A CRYSTAL IN THE DAC

With the piston DAC (Figures 1B and C) open, a square piece of metal sheet is inserted between the two diamond culets, with its corners placed in the two orthogonal grooves at the surface of the lower diamond support, which ensures a reproducible position. Then the cell is closed, i.e. the cap bearing the upper diamond is put in place. An appropriate thrust on the piston produces an indentation in the sheet. After dismounting the cap, the sheet is removed and a hole is machined by spark-erosion or by drilling at the center of the indentation. After ultrasonic cleaning, the piece of metal is replaced on top of the lower diamond, exactly as it was during indentation. A crystal is fished in the crystallization drop using a nylon loop (from Hampton), then quickly transferred to a small drop (3–4 μl) of mother liquor covering the indentation. The drop must be deposited just before the deposition of the crystal, in order to reduce evaporation of its most volatile components. Then the crystal is gently pushed into the cavity. A tiny spherical ruby chip is deposited at the center of the piston anvil. Finally, the cell is closed. A moderate pressure on the piston seals the cavity, the metal sheet acting as a gasket. By increasing the thrust, the volume of the cavity, which is filled with an invariant quantity of matter, decreases gradually with a concomitant increase of pressure. Bubbles in the cavity after sealing (except if very small) are to be avoided as their removal will require an additional contraction of the cavity, hence the application of an abnormally

high thrust. The mother liquor used for crystallization is generally used also to compress the crystal, after increasing the fraction of precipitant. Pure water becomes solid at about 1 GPa at room temperature. Mother liquors, which are complex mixtures, can generally remain liquid at higher pressures than water. For instance, addition of MPD allowed us to keep a liquid phase up to at least 2 GPa (*Girard et al.*, 2007). When crystals adopt a limited number of orientations with respect to culets, depending on their habit, different orientations can be obtained thanks to a splinter of diamond (from a broken anvil) deposited in the cavity. When crystals are much smaller than the cavity, several crystals are loaded together. These tricks are very efficient for the collection of high completeness data.

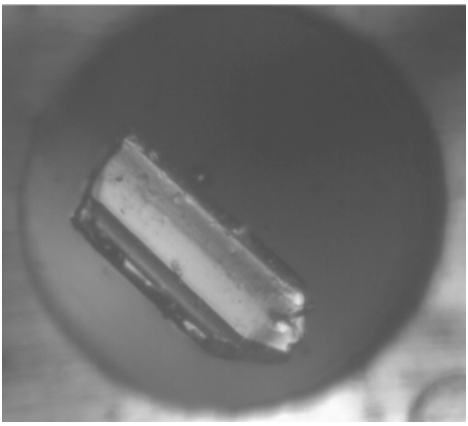

Figure 2. Crystal of a biomolecule (an octanucleotide) loaded in the diamond anvil cell. The diameter of the cavity drilled in the gasket is 400 μm.

5.4. CENTERING THE SAMPLE ON THE GONIOMETER AND DATA COLLECTION

After sample loading, the DAC is attached on the χ-cradle of the goniometer set at $\omega = 0$. The centre of the compression cavity must be accurately located on both the goniometer rotation axis and the undulator beam pathway. This is achieved by measuring the transmission of x-rays through the DAC while translating and rotating the cell, a standard procedure on ID27.

Data collection is performed by the rotation method. The beam is collimated by slits to typically 40–60 μm in both directions, which defines the irradiated zone on the sample. Successive frames are observed on the computer monitor and, in most cases, data integration proceeds on-line using XDS (*Kabsch*, 1993). Irradiating successively different regions of the sample during data collection is an efficient way to alleviate the relatively fast degradation of crystals exposed to x-rays at room temperature.

References

Akasaka, K., 2006, Probing conformational fluctuations of proteins by pressure perturbation, *Chem. Rev.* **106**:1814–1835.

Anfinsen, C.B., 1973, Principles that govern the folding of protein chains, *Science* **181**:223–230.

Balny, C., Hayashi, R., Heremans, K., and Masson, P. (ed.), 1992, *High pressure and biotechnology*, Colloque INSERM **224**, John Libbey, London.

Boehler, R., and de Hantsetters, K., 2004, New anvil designs in diamond-cells, *High Press. Res.* **24**:1–6.

Bridgman, P.W., 1914, The coagulation of albumin by pressure, *J. Biol. Chem.* **19**:511–512.

Forman, R.A., Piermarini, G.J., Barnett, J.D., and Block, S., 1972, Pressure measurement made by the utilization of ruby sharp-line luminescence, *Science* **176**: 284–285.

Fourme R., 1968, Appareillage pour études radiocristallographiques sous pression et à température variable, *J. Appl. Cryst*. **1**:23–29.

Fourme, R., Girard, E., Kahn, R., Ascone, I., Mezouar, M., Dhaussy A.C., Lin, T.W., and Johnson, J.E., 2003, Using a quasi-parallel X-ray beam of ultra-short wavelength for high-pressure virus crystallography: implications for standard macromolecular crystallography, *Acta Cryst. D* **59**:1767–1772.

Fourme, R., Girard, E., Kahn, R., Dhaussy, A.-C., and Ascone, I., 2009, Advances in high-pressure biophysics: status and prospects of macromolecular crystallography, *Ann. Rev. Biophys.* **38**:153–171.

Fourme, R., Kahn, R., Mezouar, M., Girard, E., Hoerentrup, C., Prange, C., Ascone, I., 2001, High pressure protein crystallography (HPPX): instrumentation, methodology and results of data collection on lysozyme crystals, *J. Synchrotron Rad.* **8**:1149–1156.

Girard, E., Dhaussy, A.-C., Couzinet, B., Chervin, J. C., Mezouar, M., Kahn, R., Ascone, I., and Fourme, R., 2007, Toward full-fledged high-pressure macromolecular crystallography (HPMX), *J. Appl. Cryst.* **40**:912–918.

Girard, E., Fourme, R., Ciurko, R., Joly, J., Bouis, F., Legrand, P., Jacobs, J., Dhaussy, A.-C., Ferrer, J.-L., Mezouar, M. and Kahn, R., 2010, Macromolecular crystallography at high pressure with pneumatic diamond-anvil cells handled by a six-axis robotic arm, *J. Appl. Cryst.* **43**: xxx–xxx.

Girard, E., Prangé, T., Dhaussy, A.-C., Migianu, E., Lecouvey, M., Chervin, J.-C., Mezouar, M., Kahn, R., Fourme, R., 2007, Adaptation of base-paired double-helix to extreme hydrostatic pressure, *Nucl. Acids Res*. **35**(14):4800–4808.

Gross, M., and Jaenicke, R., 1994, The influence of high hydrostatic pressure on structure, function and assembly of proteins and protein complexes, *Eur. J. Biochem*. **221**:617–630.

Horikoshi, K., and Grant, W.D., 1998, *Extremophiles. Microbial life in extreme environments,* Wiley-Liss, New York.

Kabsch, W., 1993, Automatic processing of rotation diffraction data from crystals of initially unknown symmetry and cell constants, *J. Appl. Cryst.* **26**:795–800.

Katrusiak, A., and Dauter, Z., 1996, Compressibility of lysozyme crystals by X-ray diffraction, *Acta Cryst. D* **52**:607–608.

Kundrot, C.E., and Richards, F.M., 1987, Crystal structure of hen egg-white lysozyme at a hydrostatic pressure of 1000 atmospheres, *J. Mol. Biol*. **193**:157–170.

Le Toullec, R., Pinceaux, J.-P., and Loubeyre, P., 1988, The membrane diamond anvil cell: a new device for generating continuous pressure and temperature variations, *High Press. Res.* **1**:77–90.

Merrill, L.L., and Bassett, W.A., 1974, Miniature diamond anvil pressure cell for single crystal X-ray diffraction studies, *Rev. Sci. Instrum*. 45:290–294.

Mezouar, M., Crichton, W.A., Bauchau, S., Thurel, F., Witsch, H., Torrecillas, F, Blattmann, G., Marion, P., Dabin, Y., Chavanne, J., Hignette, O., Morawe, C., and Borel, C., 2005, Development of a new state-of-the-art beamline optimized for monochromatic single-crystal and powder X-ray diffraction under extreme conditions at the ESRF, *J. Synchrotron. Rad.* **12**:659–664.

Mozhaev, V.V., Heremans, K., Franks, J., Masson, P., and Balny, C., 1994, Exploiting the effect of high hydrostatic pressure in biotechnological applications, *Trends Biotechnol.* **12**:493–501.

Van Valkenburg A., 1962, Visual observations of high pressure transitions, *Rev. Sci. Instrum.* **33**:1462.

Weber, G., 1992, *Protein interactions*, Chapman & Hall, New York, pp. 211–214.

Weber, G., 1992, Thermodynamics of the association and the pressure dissociation of oligomeric proteins, *J. Phys. Chem.* **97:**7108–7115.

Weir, C.E., Lippincott, E.R., Van Valkenburg, A., Bunting, E.N., 1959, Infrared studies in the 1-micron to 15-micron region to 30,000 atmospheres, *J. Res. Natl. Bur. Stand. - Phys. Chem.* **63A**:55–62.

Yayanos, A.A., and Delong, E.F., 1987, Deep-sea bacterial fitness to environmental temperatures and pressures. In: *Current perspectives in high pressure biology*, edited by H.W. Jannasch et al., Academic Press, London, pp. 17–32.

HIGH-PRESSURE CRYSTALLOGRAPHY OF BIOMOLECULES: RECENT ACHIEVEMENTS. II – APPLICATIONS

ROGER FOURME[1*], ISABELLA ASCONE[1†],
RICHARD KAHN[2], ERIC GIRARD[2]
[1]*Synchrotron SOLEIL, 91192 Gif sur Yvette, France,*
[2]*Institut de Biologie Structurale, 38027 Grenoble, France*

Abstract This chapter gives various applications around the general theme of macromolecular crystallography (MX) and high pressure (HP). We first describe high-pressure cooling where crystallographic data collection is performed at ambient pressure. Then we give selected examples with data collection at high pressure (HPMX); they include compressibility measurements and structural studies on polynucleotides, an oligomeric protein and a virus capsid. Finally, we show that high pressure and methods developed for HPMX have impacts on conventional MX.

Keywords: High pressure, crystallography, nucleic acid, protein, virus, compressibility, xenon

1. High-Pressure Cooling

The method consists in cryocooling a protein crystal while it is compressed in helium gas up to about 500 MPa, then releasing pressure. Subsequent data collection is performed on the cooled sample at atmospheric pressure. The goal is to quench pressure-induced collective movements of the polypeptide chain. Responses of sperm whale myoglobin crystals to active compression in a beryllium cell and after high-pressure cooling were accurately compared (*Urayama et al.*, 2002). Similar responses were found for several major collective displacements, but not for others. Presumably, modifications due to high pressure were only partially preserved by high-pressure cooling

* E-mail: roger.fourme@synchrotron-soleil.fr
† Present address: ENSCP, 75231 Paris, France

E. Boldyreva and P. Dera (eds.), *High-Pressure Crystallography: From Fundamental Phenomena to Technological Applications*, DOI 10.1007/978-90-481-9258-8_49,

and superimpose with those induced by cooling. Indeed, in this method, the thermodynamic state of the sample is not well defined. An interesting application of this method is to trap small modifications induced by pressure in a protein. The effect of these modifications is monitored in parallel by another method, e.g. spectroscopy, and correlated with function. This principle was applied to correlate alterations of the structure of a fluorescent protein, citrine, with the accompanying spectral shift (*Barstow et al.*, 2008).

High pressure cooling is also used in conventional MX to improve crystal diffraction with respect to standard cryocooling, without recourse to cryoprotectants (*Kim et al.*, 2005). The formation of high-density amorphous ice is responsible for this improvement (*Kim et al.*, 2008).

2. Impact of High Pressure and HPMX Procedures on Conventional MX

2.1. APPLICATIONS OF LOW-PRESSURE GAS BINDING TO PROTEINS

Gas ligands such as oxygen, carbon monoxide, nitric oxide, xenon and krypton interact very weakly with the host protein due to their small sizes and hydrophobicity. Pressurizing native crystals with gas at low pressure (<10 MPa) may increase binding and reveal binding sites. Xenon or krypton reversibly bound in hydrophobic cavities of pressurized proteins (Figure 1) can be used to solve the crystallographic "phase problem". On the one hand, these heavy atom derivatives are generally highly isomorphous, because

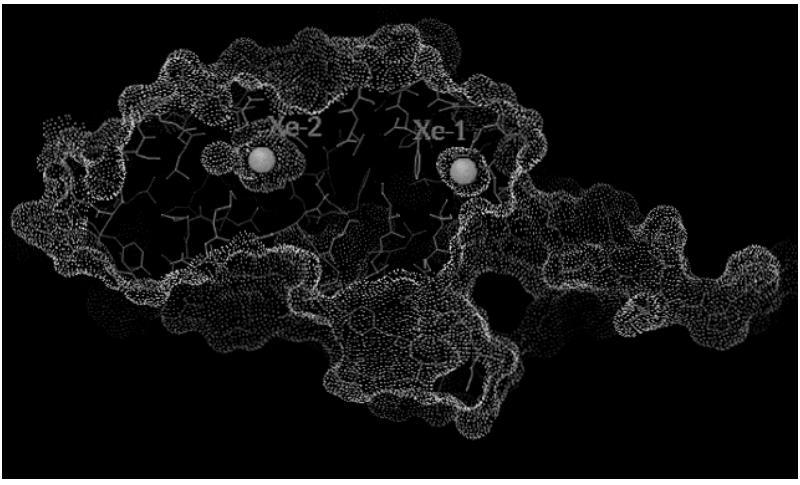

Figure 1. Xenon binding sites in the ligand-binding domain of the human nuclear receptor RXR (*Bourguet et al.*, 1995).

the perturbation to the native structure is very small. On the other hand, anomalous scattering of xenon and krypton can be used for SAD and MAD phasing. The use of Xe was introduced in 1965 (*Schoenborn et al.*, 1965). A simple technique was later described to make such derivatives (*Schiltz et al.*, 1994) and the method is now commonly used (*Schiltz et al.*, 2003). Xe is also used to reveal the pathway of gases (*Montet et al.*, 1997).

2.2. PRESSURE AS A TOOL FOR IMPROVING ORDER IN MACROMOLECULES AND CRYSTALS

Isothermal compression leads to the ordering of molecules or a decrease in the entropy of system. The resolution that can be obtained in a crystallographic experiment depends on the quality of crystal order. The quality of pre-existing crystals may be improved by compression in the DAC, with subsequent data collection at high pressure. A spectacular effect was observed for Cowpea Mosaic Virus (CpMV) crystals (*Girard et al.*, 2005), but this is a particular case where pressure improves the packing of nearly spherical particles featuring some orientational disorder at atmospheric pressure (*Lin et al.*, 2005). Application of pressure and pressure/temperature annealing might become a standard way of improving the long-range order of crystals. There are also protein structures where a portion of electron density is not visible due to disorder: pressure might be useful in such cases by increasing steric constraints.

2.3. TRANSFER OF HPMX PROCEDURES TO CONVENTIONAL MX

The constraints of HPMX, including data collection at room temperature, led us to careful examination of how to improve the signal-to-noise ratio in data collection and more generally how to increase the data collection efficiency (defined as the information content collected per unit volume of crystal). Our results suggest that some experimental conditions used during HPMX data collection (in particular: use of a quasi-parallel beam of ultra-short wavelength with very narrow collimation, irradiation of successive crystal zones, large detector placed at a long crystal-to-detector distance) should also be considered for standard data collection (*Fourme et al.*, 2003). A problem must be solved in order to fully exploit potential advantages of ultra-short wavelengths: the low detective quantum efficiency of current MX detectors for high-energy photons. As only a small fraction of diffracted photons is detected, crystals are over-irradiated. The situation might be improved, e.g. by using either CCD detectors with a thicker phosphor or heavy elements pixel detectors.

3. Compressibility of Crystals and Macromolecules

A number of experimental works and computer simulations have appeared on isothermal compressibility and its pressure dependence (review in *Kharakoz*, 2000). Most determinations of protein compressibility are performed by ultrasonic measurements in aqueous solutions at frequencies of the order of 10 MHz. The adiabatic compressibility, which is close to isothermal compressibility for aqueous solutions at room temperature, is measured as $1/(\rho u^2)$ (Laplace relation), where ρ is the solution density and u the sound velocity in the medium. This method allows accurate measurements of the apparent compressibility of the protein (i.e. including contributions from protein and from hydration). In contrast, the intrinsic compressibility of the protein is not accurately determined as it depends on the approach used to evaluate the hydration contribution. Like ultrasonic measurements, other approaches including measurements of the dynamic Young's modulus, NMR spectra and molecular dynamics simulation have provided values in the range 0.1–0.2 GPa^{-1} when extrapolated at atmospheric pressure (*Kharakoz*, 2000). Accordingly, intrinsic compressibilities were not accurately determined, and even less the variation of compressibility with pressure. HPMX is a method, by which the isothermal compressibility of crystals $\chi = -V^{-1}(\partial V/\partial P)_T$ can be determined from measurements of unit-cell parameters. Such measurements were first reported in a pioneering HPMX study of tetragonal hen egg-white lysozyme crystals (tHEWL) at a single pressure (*Kundrot and Richards*, 1987), then of orthorhombic hen egg-white lysozyme crystals (oHEWL) at three different pressures (*Katrusiak and Dauter*, 1996). Besides this basic information, a single accurate crystal structure allows to determine the molecular volume from atomic coordinates and several structures determined at different pressures give access to molecular compressibility and its pressure-dependence. Such determinations were performed for the octanucleotide d(GGTATACC) (*Girard et al.*, 2007) and for HEWL on the basis, in each case, of four crystal structures. For another globular protein, bovine erythrocyte Cu,Zn superoxide dismutase, the unit-cell compressibility and information on the molecular compressibility were derived from crystal structures at atmospheric pressure and at 0.57 GPa. Data available on the unit-cell compression of orthorhombic lysozyme were re-analyzed in the light of results from the tetragonal crystal. Finally, once the unit-cell volumes and the volumes of the molecular fraction in the cell were determined, the solvent behaviour was simulated. The apparent solvent compressibility in the crystalline state was determined from the solvent-excluded volume per unit-cell, calculated from both molecular and unit-cell volumes and taking into account effects of crystal packing. For several of the five crystalline

systems under study, there was evidence of abnormal apparent solvent compressibility, and this result was critically discussed (*Ascone et al.*, 2010).

4. New Properties of the Double-Helix Base-Paired Architecture

Until recently, the behaviour of nucleic acids under high pressure had been investigated by spectroscopic techniques in solution only. The first HPMX study of a nucleic acid was performed on the octanucleotide d(GGTATACC) (*Girard et al.*, 2007). This relatively small biomolecule (322 non-hydrogen atoms) is a model of the A-form of DNA. At atmospheric pressure, the structure features super-helices of duplexes down the unique axis of the hexagonal $P6_1$ space group. The central channel of the super-helix has just the appropriate diameter to host oriented molecules of another form of DNA, the B form, which are reminiscent of the A-B equilibrium in solution. These molecules are disordered around the channel axis; accordingly they produce a fibre diffraction pattern of B-DNA (*Doucet et al.*, 1989). In this system, both A- and B-forms of DNA can be simultaneously monitored against external hydrostatic pressure using Bragg reflections of the crystallized A-DNA and the fibre pattern of B-DNA.

Single crystals of the octanucleotide were gradually compressed from ambient pressure to 2 GPa in a solution containing 35% of MPD. The compressibility curve up to 1.9 GPa was derived from measurements of unit-cell parameters. Four complete diffraction data sets at high resolution (1.60–1.65 Å) were recorded at ambient pressure, 0.55, 1.04 and 1.39 GPa, and the structures were fully refined. The double-helix features a large axial compressibility of the molecule. The base-stacking shrinkage is 2.6 Å for the full octamer length (a relative contraction of 11%). The average base-pair step varies from 2.92 to 2.73 Å. The transversal compressibility is negligible. The molecule reacts under high pressure as a molecular spring and, during compression, the geometry of Watson–Crick base-pairings (which carry genetic information) is preserved. A wedge effect due to packing is probably at the origin of crystal degradation beyond 1.6 GPa. The strong meridional reflections of the fibrous B-DNA are visible up to at least 2 GPa, which shows that the double-helix is preserved. They monitor the shortening of the average base-pair step, with a decrease from 3.34 Å at ambient pressure to 3.07 Å at 2 GPa. Accordingly, the double-helix topology is remarkably adapted to high pressure and the adaptation of such architectures to harsh conditions may have played an important role at the prebiotic stage and in the first steps of the emergence of life.

Crystals of the dodecamer $d(CGCGTTAACGCG)_2$ were selected to study the behavior of B-DNA in the crystalline state. Diffraction is lost at

700–800 MPa. This loss is clearly not due to denaturation of the double-helix, which was found stable up to at least 2 GPa in the previous study. In the orthorhombic $P2_12_12_1$ space-group, molecules are arranged in parallel files, a packing which is easily perturbed by pressure (*T. Prangé et al.*, unpublished results).

5. The Pressure-Induced Structure–Function Modifications and Dissociation of an Oligomeric Enzyme

Another important effect of pressure is the destabilization of the quaternary structure of oligomeric proteins. A simple explanation of the mechanism by which pressure leads to dissociation of such systems has been proposed: compression of the weaker protein–protein interactions results in preferential destabilization of the subunit interactions and shifts the equilibrium toward the formation of the shorter and stronger subunit-water bonds. It is also possible to invoke the formal Le Chatelier–Braun's principle. There is a net volume decrease at dissociation which stems primarily from the filling with solvent of structural voids that exist in the oligomer and from the electrostriction of solvent when charged groups at the monomer surface are exposed after dissociation. This destabilization occurs in most cases at fairly low pressure (100–300 MPa), before denaturation of the tertiary structure of subunits.

A multi-faceted study of the effect of pressure on an oligomeric protein, urate oxidase (UOx) from *Aspergillus flavus* was performed (*Girard et al.*, 2010). UOx belongs to the purine degradation pathway. It catalyzes the oxidation of uric acid to a primary reaction intermediate, 5-hydroxyisourate, with release of hydrogen peroxide at physiological or basic pH. It is functionally active as a homo-tetramer. This enzyme, which is not produced in humans, is used to resolve hyperuricemic disorders that can occur in chemotherapy treatment where DNA is massively degraded. The structure of the 135 kDa UOx tetramer complexed with the competitive inhibitor 8-azaxanthin was first determined at atmospheric pressure, using orthorhombic crystals (space group I222) diffracting at high resolution. The asymmetric unit contains one monomer, and subunits (A, B, C, D) are related by the crystallographic twofold axis. The A-B (or C-D) dimer consists of a 16-stranded beta-barrel structure with eight alpha-helices outside the barrel. The association of two such dimers forms the active homo-tetramer crossed by a 50 Å long and 12 Å in diameter tunnel along the twofold axis. The four active sites in each tetramer are located at the interfaces of A–B and C–D dimers, which have by far the largest contact zones (Figure 2). These crystals were selected for HPMX study.

Figure 2. Structure at 140 MPa of the urate oxidase homotetramer complexed with the competitive inhibitor 8-azaxanthin (*Colloc'h et al.*, 2006).

Although this enzyme is very stable at ambient conditions, it is quite sensitive to high pressure. Diffraction is lost at about 200 MPa. The crystal structure was first solved at 140 MPa and 2.3 Å resolution (*Colloc'h et al.*, 2006). After these first results, a new crystallographic study was performed at a somewhat higher pressure (150 MPa) and improved resolution (2 Å). The HP crystal structure has revealed complex modifications. On the one hand, there are discrete signs of the onset of tetramer dissociation, such as an increase of the average B-factor instead of a decrease as generally observed, and a slight elongation of H-bonds at the main interfaces (A–C and A–B). The expected variation would be a contraction by ~0.015 Å since the value found in proteins for elastic compression is ~0.1 Å.GPa^{-1}. On the other hand, under pressure, the hydrophobic cavity contracts and the active site swells, through increased bond-length distances between atoms belonging to different subunits and decreased bond-length distances between atoms belonging to the same subunit. This conformation probably corresponds to an enzymatic substate where the active site can accommodate a larger ligand. During the reaction, swelling is necessary to accommodate the incoming protonated substrate and the large non-planar product 5-HIU. Accordingly, this work confirms that high-pressure perturbation allows promoting and trapping protein conformation states of biological significance.

Increasing pressure beyond ~175 MPa leads to the irreversible dissociation of the tetramer, followed by aggregation. Small angle X-ray scattering (SAXS) experiments have shown that the pressure-induced tetramer dissociation produces monomeric intermediates, which are sufficiently stable

for being observed in the course of a SAXS experiment. The substrate-like inhibitor disfavours the dissociation of the tetramer. Finally, from HPMX, SAXS, fluorescence spectroscopy experiments and enzymatic activity measurements, a coherent model of the pressure-induced destabilization of the functional UOX tetramer was proposed both in the apo and in the inhibitor-bound forms.

6. Elastic Compression of the Capsid of Cowpea Mosaic Virus

CpMV is a plant virus. The 3D-structure of the capsid had been determined at ambient pressure in the cubic body-centred space group I23 (a = 317 Å) and refined at 2.8 Å resolution by *Lin et al.* (1999). In crystallization drops, only a small fraction of crystals conforms to characteristics of the I23 space group, in which Bragg reflections with h + k + l odd are strictly forbidden. These crystals have a low mosaicity and diffract at 2.6–2.8 Å resolution, which reveals a good long-range order. For most crystals in the drops, diffraction patterns show weak reflections with h + k + l odd, the mosaicity is large and the resolution is modest (4–5 Å). These features have been interpreted by small random rotations of quasi-spherical capsids about their centre of gravity (*Lin et al.*, 2005), that perturb the periodicity of the I23 structure. This disorder has plagued previous structural studies at ambient pressure.

We found that compressing disordered crystals beyond about 240 MPa systematically removed "odd" reflections, reduced mosaicity and improved resolution. In this way, I23 crystals are systematically obtained, which diffract up to about 400 MPa. We collected a highly-complete data set at 330 MPa. The structure was fully refined at 2.8 Å resolution (HP structure). Using original diffraction data from *Lin et al.* (2005), the I23 structure at ambient pressure was also refined using the same programs and the same procedure, and served as reference (AP structure). The two structures were compared. The most interesting effects of pressure on the capsid include the compression of the capsid, the large reduction of the cavity volumes, the increase of buried surfaces, and the shortening of H-bond lengths by about 0.1 Å. GPa^{-1} on average (this value is highly significant as it is based on a histogram of H-bond lengths variations between AP and HP incorporating about 600 values). All these features are characteristic of elastic compression within the same conformation subset. Further, the origin of disorder was confirmed and described in terms of inter-capsid interactions: high pressure produces shorter interactions and new connections mediated by water molecules, thus restoring the body-centered lattice, the long-range order in the crystal and high-quality diffraction. This work was the first

HPMX study of a virus and showed that high-quality HP data can be collected on a large assembly (*Girard et al.*, 2005).

7. Conclusion

HPMX is now a full fledged technique that is widely applicable (*Fourme et al.*, 2009). The methods of HPMX may be also an inspiration for conventional MX. Although HPMX can be performed using conventional X-ray equipment in laboratories, exploiting the full potential of HPMX requires synchrotron radiation. The access to existing high-pressure beamlines is limited due to overbooking. So that systematic investigations which would be required to, e.g. probe the ordering effects of high pressure on crystals, are in practice very difficult.

References

Barstow, B., Ando, N., Kim, C.U., Gruner, S.M., 2008, Alteration of citrine structure by hydrostatic pressure explains the accompanying spectral shift, *Proc. Natl. Acad. Sci. USA* **105**:13362–13366.

Bourguet, W., Ruff, M., Chambon, P., Gronemeyer, H., Moras, D., 1995, Crystal structure of the ligand-binding domain of the human nuclear receptor RXR-α, *Nature* **375**: 377–382.

Colloc'h, N., Girard, E., Dhaussy, A.-C., Kahn, R., Ascone, I., Mezouar, M., Fourme, R., 2006, High-pressure macromolecular crystallography: The 140-MPa crystal structure at 2.3 Å resolution of urate oxidase, a 135-kDa tetrameric assembly, *Biochim. Biophys. Acta* **1764**:391–397.

Doucet, J., Benoit, J.-P., Cruse, W.B.T., Prangé, T., and Kennard, O., 1989, Coexistence of A- and B-form DNA in a single crystal lattice, *Nature* **337**:190–193.

Fourme, R., Girard, E., Kahn, R., Ascone, I., Mezouar, M., Dhaussy, A.-C., Lin, T., Johnson, J.E., 2003, Using a quasi-parallel X-ray beam of ultra-short wavelength for high-pressure virus crystallography: implications for standard macromolecular crystallography, *Acta Cryst. D* **59**:1767–1772.

Fourme, R., Girard, E., Kahn, R., Dhaussy, A.-C., Ascone, I., 2009, Advances in high-pressure biophysics: status and prospects of macromolecular crystallography, *Ann. Rev. Biophys.* **38**:153–171.

Girard, E., Kahn, R., Mezouar, M., Dhaussy, A.-C., Lin, T., Johnson, J.E., Fourme, R., 2005, The first crystal structure of a macromolecular assembly under high pressure: CpMV at 330 MPa, *Biophysical J.* **88**:3562–3571.

Girard, E., Marchal, S., Perez, J., Finet, S., Kahn, R., Fourme, R., Marassio, G., Dhaussy A.-C., Prangé, T., Giffard, M., Dulin, F., Bonneté, F., Lange, R., Abraini, J.H., Mezouar, M. and Colloc'h N., 2010, Structure –function perturbation and dissociation of tetrameric urate oxidase by high hydrostatic pressure, *Biophys. J.* **98**(10):2365–2373.

Girard, E., Prangé, T., Dhaussy, A.-C., Migianu, E., Lecouvey, M., Chervin, J.-C., Mezouar, M., Kahn, R., Fourme, R., 2007, Adaptation of base-paired double-helix to extreme hydrostatic pressure. *Nucl. Acids Res.* **35**(14):4800–4008.

Katrusiak, A., Dauter, Z., 1996, Compressibility of lysozyme crystals by X-ray diffraction. *Acta Cryst. D* **52**:607–608.

Kharakoz, D.P., 2000, Protein compressibility, dynamics, and pressure, *Biophys. J.* **79**:511–525.

Kim, C.U., Kapfer, R., Gruner, S.M., 2005, High pressure cooling of crystals without cryoprotectants, *Acta Cryst. D* **61**: 881–890.

Kim, C.U., Chen, Y.F., Tate, M.W., Gruner, S.M., 2008, Pressure-induced high-density ice in protein crystals, *J. Appl. Cryst.* **41**:1–7.

Kundrot, C.E., and Richards, F.M., 1987, Crystal structure of hen egg-white lysozyme at a hydrostatic pressure of 1000 atmospheres, *J. Mol. Biol.* **193**:157–170.

Lin, T., Chen, Z., Usha, R., Stauffacher, C.V., Dai, J.-B., Schmidt, T., Johnson, J.E., 1999, The refined crystal structure of cowpea mosaic virus at 2.8 A° resolution, *Virology* **265**:20–34.

Lin, T., Schildkamp, W., Bister, K., Doerschuk, P.C., Somayazulu, M., Mao, H., and Johnson, J.E., 2005, The mechanism of high-pressure-induced ordering in a macromolecular crystal, *Acta Cryst. D* **61**(6):737–743.

Montet, Y., Amara, P., Volbeda, A., Vernede, X., Hatchikian, E.C., 1997, Gas access to the active site of Ni-Fe hydrogenases probed by X-ray crystallography and molecular dynamics, *Nature Structural Biology* **4**:523–526.

Schiltz, M., Prangé, T., and Fourme, R., 1994, On the preparation and X-ray data collection of isomorphous xenon derivatives, *J. Appl. Cryst.* **27**: 950–960.

Schiltz, M., Fourme, R., and Prangé, T., 2003, The use of noble gases Xenon and Krypton as heavy atoms in protein structure determination for phasing, *Methods Enzymol.* **374**:83–119.

Schoenborn, B.P., Watson, H.C., and Kendrew, J.C., 1965, Binding of xenon to sperm whale myoglobin, *Nature* **207**:28–30.

Urayama, P., Phillips, G.N., and Gruner, S.M., 2002, Probing substates in sperm whale myoglobin using high-pressure crystallography, *Structure* **10**:51–60.